ONS

NBS SPECIAL PUBLICATION 414

U.S. DEPARTMENT OF COMMERCE / National Bureau of Standards

Laser Induced Damage In Optical Materials: 1974

NATIONAL BUREAU OF STANDARDS

The National Bureau of Standards [1] was established by an act of Congress March 3, 1901. The Bureau's overall goal is to strengthen and advance the Nation's science and technology and facilitate their effective application for public benefit. To this end, the Bureau conducts research and provides: (1) a basis for the Nation's physical measurement system, (2) scientific and technological services for industry and government, (3) a technical basis for equity in trade, and (4) technical services to promote public safety. The Bureau consists of the Institute for Basic Standards, the Institute for Materials Research, the Institute for Applied Technology, the Institute for Computer Sciences and Technology, and the Office for Information Programs.

THE INSTITUTE FOR BASIC STANDARDS provides the central basis within the United States of a complete and consistent system of physical measurement; coordinates that system with measurement systems of other nations; and furnishes essential services leading to accurate and uniform physical measurements throughout the Nation's scientific community, industry, and commerce. The Institute consists of a Center for Radiation Research, an Office of Measurement Services and the following divisions:

Applied Mathematics — Electricity — Mechanics — Heat — Optical Physics — Nuclear Sciences [2] — Applied Radiation [2] — Quantum Electronics [3] — Electromagnetics [3] — Time and Frequency [3] — Laboratory Astrophysics [3] — Cryogenics [3].

THE INSTITUTE FOR MATERIALS RESEARCH conducts materials research leading to improved methods of measurement, standards, and data on the properties of well-characterized materials needed by industry, commerce, educational institutions, and Government; provides advisory and research services to other Government agencies; and develops, produces, and distributes standard reference materials. The Institute consists of the Office of Standard Reference Materials and the following divisions:

Analytical Chemistry — Polymers — Metallurgy — Inorganic Materials — Reactor Radiation — Physical Chemistry.

THE INSTITUTE FOR APPLIED TECHNOLOGY provides technical services to promote the use of available technology and to facilitate technological innovation in industry and Government; cooperates with public and private organizations leading to the development of technological standards (including mandatory safety standards), codes and methods of test; and provides technical advice and services to Government agencies upon request. The Institute consists of a Center for Building Technology and the following divisions and offices:

Engineering and Product Standards — Weights and Measures — Invention and Innovation — Product Evaluation Technology — Electronic Technology — Technical Analysis — Measurement Engineering — Structures, Materials, and Life Safety [4] — Building Environment [4] — Technical Evaluation and Application [4] — Fire Technology.

THE INSTITUTE FOR COMPUTER SCIENCES AND TECHNOLOGY conducts research and provides technical services designed to aid Government agencies in improving cost effectiveness in the conduct of their programs through the selection, acquisition, and effective utilization of automatic data processing equipment; and serves as the principal focus within the executive branch for the development of Federal standards for automatic data processing equipment, techniques, and computer languages. The Institute consists of the following divisions:

Computer Services — Systems and Software — Computer Systems Engineering — Information Technology.

THE OFFICE FOR INFORMATION PROGRAMS promotes optimum dissemination and accessibility of scientific information generated within NBS and other agencies of the Federal Government; promotes the development of the National Standard Reference Data System and a system of information analysis centers dealing with the broader aspects of the National Measurement System; provides appropriate services to ensure that the NBS staff has optimum accessibility to the scientific information of the world. The Office consists of the following organizational units:

Office of Standard Reference Data — Office of Information Activities — Office of Technical Publications — Library — Office of International Relations.

---

[1] Headquarters and Laboratories at Gaithersburg, Maryland, unless otherwise noted; mailing address Washington, D.C. 20234.
[2] Part of the Center for Radiation Research.
[3] Located at Boulder, Colorado 80302.
[4] Part of the Center for Building Technology.

Laser Induced Damage In Optical Materials: 1974

Proceedings of a Symposium Sponsored by
Office of Naval Research
The American Society for Testing and Materials
And by the National Bureau of Standards

May 22-23, 1974
NBS Boulder, Colorado 80302

Edited by

Alexander J. Glass
Lawrence Livermore Laboratory
Livermore, California 94550

and

Arthur H. Guenther
Air Force Weapons Laboratory
Kirkland AFB, New Mexico 87117

U.S. DEPARTMENT OF COMMERCE, Frederick B. Dent, *Secretary*
NATIONAL BUREAU OF STANDARDS, Richard W. Roberts, *Director*

Issued December 1974

Library of Congress Cataloging in Publication Data

Symposium on Laser Damage in Optical Materials. 6th. Boulder, Colo., 1974.
Laser induced damage in optical materials, 1974.

(NBS Special Publication; 414)
Supt. of Docs. No.: C 13.10:414
1. Optical materials—Defects—Congresses. 2. Laser radiation—Congresses. 3. Laser materials—Defects—Congresses. I. Glass, Alexander J., 1933- ed. II. Guenther, Arthur Henry, 1931- ed. III. United States. Office of Naval Research. IV. American Society for Testing and Materials. V. United States. National Bureau of Standards. VI. Title. VII. Series: United States. National Bureau of Standards. Special Publication; 414.
QC100.U57 No. 414 [QC374] 389'.08s [621.36] 74-26935

National Bureau of Standards Special Publication 414

Nat. Bur. Stand. (U.S.), Spec. Publ. 414, 256 pages (Dec. 1974)

CODEN: XNBSAV

U.S. GOVERNMENT PRINTING OFFICE
WASHINGTON: 1974

For sale by the Superintendent of Documents, U.S. Government Printing Office, Washington, D.C. 20402
(Order by SD Catalog No. C13.10:414). Price $3.15
Stock Number 0303-01355

Foreword

These proceedings report in detail the formal papers presented at the 6th Annual Symposium on Laser Damage in Optical Materials held at the National Bureau of Standards, Boulder, Colorado on May 22 and 23, 1974. This meeting was jointly sponsored by the Office of Naval Research, National Bureau of Standards, and the American Society of Testing and Materials. The major topics covered were damage at dielectric surfaces, damage due to self-focusing, damage to dielectric coatings, and damage to mirrors and windows in the infrared, as well as theoretical and laser system studies and the reporting of fundamental properties important in the damage process. Furthermore, several papers dealing with improved diagnostic techniques were heard.

Because of the growing importance and acceptance of machined components in high power laser systems, a workshop on the machining of optics was held, under the coordination of Captain T. T. Saito of the Air Force Weapons Laboratory. Nine papers on various facets of the topic were presented dealing with machining procedures, surface characterization of machined elements, coating of machined components and the polishing and damage resistance of polished, coated, and bare machined metal reflectors. Abstracts of these papers are included in the Symposium Proceedings proper.

The co-chairmen, Dr. Alexander J. Glass of Lawrence Livermore Laboratory, Livermore, California, and Dr. A. H. Guenther of the Air Force Weapons Laboratory, Kirtland AFB, New Mexico, take full responsibility for the summary, conclusions, and recommendations contained in this report, as well as the summaries of the discussions at the conclusion of each presentation. It is suggested that individuals interested in the subject of this meeting obtain copies of those publications referenced in the bibliography contained in the summary and conclusions.

It is our intention to convene another symposium next year in Boulder during May to update and document the state of the art of Laser Damage in Optical Materials at that time. This meeting will cover the subject historically presented at these symposia with additional emphasis on thin film damage, machined optics, the problem of the damage of materials and components at 10.6 μm, as well as address ourselves to the subject of optical system reliability as influenced by laser applications. Hopefully, reports relating to very short pulses, short wavelengths, and multipulse damage effects will be heard. We wish to encourage the reader to contact us on matters pertinent to the intent of these conferences.

A. H. Guenther

CONTENTS

MATERIAL CHARACTERIZATION AND INSTRUMENTATION

DAMAGE DIAGNOSTICS

THEORETICAL STUDIES

APPENDIX I

Laser Induced Damage in Optical Materials
6th ASTM Symposium
May 22-23, 1974

The Sixth ASTM-ONR-NBS Symposium on Laser Induced Damage in Optical Materials was held at the National Bureau of Standards in Boulder, Colorado on May 22-23, of this year. These Symposia are held as part of the activities in Subcommittee II on Lasers and Laser Materials, of the ASTM. Subcommittee II is charged with the responsibilities of formulating standards and test procedures for laser materials, components, and devices. The Chairman of Subcommittee II is Haynes Lee, of Owens-Illinois, Inc. Co-chairmen for the Damage Symposia are Dr. Arthur Guenther, Chief Scientist of the Air Force Weapons Laboratory, and Dr. Alexander J. Glass, Head, Theoretical Studies, Y Division, Lawrence Livermore Laboratory.

Over 150 attendees at the Symposium heard 31 papers on topics relating to laser induced damage in crystalline and non-linear optical materials, at dielectric surfaces, and in thin film coatings as well as discussions of damage problems in the infrared region due both to cw and pulsed irradiation. In addition, several reports on the theoretical analysis of laser-materials interaction relative to the damage process were given, along with tabulations of fundamental materials properties of importance in evaluation of optical material response to high power laser radiation. Attention was given to high power laser system design considerations which relate to improved system performance and reliability when various damage mechanisms are operable in such systems.

Because of the growing importance and acceptance of machined components in high power laser systems, a workshop on the machining of optics was held, under the coordination of Captain T. T. Saito of the Air Force Weapons Laboratory. Nine papers on various facets of the topic were presented dealing with machining procedures, surface characterization of machined elements, coating of machined components, and the polishing and damage resistance of polished, coated, and bare metal reflectors. Abstracts on these papers are included in the Symposium Proceedings proper.

The proceedings of these Symposia represent the major sources of information in the field of laser induced damage in optical materials. The Symposia themselves, along with the periodic meetings of Subcommittee II, provide a unique forum for the exchange of information regarding laser materials specifications among the manufacturers and users of laser devices, components, and systems. The Symposia also serve as a mechanism of information gathering to enable the Subcommittee to write informed and realistic specifications.

Key words: IR windows and mirrors; laser damage; laser materials; self-focusing; thin films.

1. Principal Conclusions

The sixth annual Symposium on Damage in Laser Materials, sponsored by the American Society of Testing and Materials (ASTM), in conjunction with the National Bureau of Standards (NBS), and the Office of Naval Research (ONR), was held at NBS in Boulder, Colorado on the 22nd and 23rd of May. Over 150 experts on laser materials, components and systems were in attendance. The participants were drawn from government, industrial, and university laboratories. The attendees included several foreign representatives from organizations such as the Laboratoire Nationale D'Essais, in Paris, France; Commissariat d'Energie Atomique, in Limeil, France; CRDV, in Quebec, Canada; and ITT Europe, in Harlow, England.

In conjunction with the ASTM Symposium, the National Bureau of Standards played host to three other meetings on related subjects, a review of ARPA programs on laser materials, a day-long workshop on Optical Surface and Coating Science, sponsored jointly by the ASTM and ARPA, and an evening workshop on Machining of Optics, organized by the Air Force Weapons Laboratory. New techniques of surface preparation, especially bowl feed polishing, ion polishing, and diamond turning, as well as methods for the quantitative characterization of super-smooth surfaces, were the principal topics of discussion at these ancillary meetings.

Of the thirty-one papers presented at the symposium, more than one-third gave experimental results on damage measurements. These included measurements of thresholds in bulk materials, at dielectric surfaces, at metal surfaces, in nonlinear optics crystals, and in multilayer dielectric films. These measurements, for the most part, were carried out with well-characterized lasers, on carefully prepared surfaces, and thus represent information of wide applicability.

The remaining papers dealt with improved methods of surface preparation, characterization of materials, instrumentation, damage diagnostic techniques, basic damage phenomena, and system design. The emphasis, throughout the symposium, was on the improvement of damage thresholds, particularly at surfaces and in thin films, due to improved techniques of preparation and fabrication.

In the design of large laser systems, such as those currently under construction, damage considerations impose severe limits on system design. The improved understanding of index nonlinearity in transparent dielectrics, its origin, magnitude, and consequences, all confirmed by agreement between experiment and theory, makes it possible to design large glass systems for optimal operation, avoiding beam degradation and damage due to self-focusing effects. Correspondingly, in CW systems, the understanding of thermally induced distortion, and availability of reliable material parameters, makes it possible to design such systems to operate safely within the limits imposed by thermal distortion. The optimal design is sensitive not only to the material parameters of the system, but to the control of the beam profile in space and time as well.

Current short pulse systems are limited by surface damage at coated elements to operating fluxes of a few J/cm^2. There still remains considerable room for improvement in thin film damage levels since the observed thresholds are far below intrinsic limits. This indicates that damage in coatings is still dominated by defects and impurities. The same coatings, obtained from different manufacturers, exhibit different damage thresholds, indicating a sensitivity of the surface condition to the fabrication process. Thin film coatings are very complicated structures, requiring full characterization in terms of materials, residual stress, adherence to the substrate, morphology (crystalline or amorphous), and, of course, purity and freedom from defects. Current indications are that sputtered films exhibit better damage resistance than vacuum-deposited films. The exact cause of this difference, and its susceptibility to improvement by refined techniques, is still uncertain.

As far as surface preparation is concerned, new etching techniques continue to be advanced. The surface properties of both infrared materials and glass can be improved by use of appropriate chemical etch, to obtain thresholds close to the intrinsic bulk level. Super-polishing and sputter-cleaning of surfaces also improve their damage properties, by removal of defects and polishing residue.

The new interest in metal mirrors arises in part from the use of diamond turning in surface preparation. This technique tends to leave a very clean surface, free of defects, debris, and contamination, which is resistant to both damage and deterioration.

In order to evaluate improved methods of surface preparation, better surface diagnostics have been developed. In particular, increasing use has been made of surface scattering measurements, to obtain measures of rms surface roughness down to ten Angstrons. Additionally, selective surface probes, such as Auger spectroscopy, low energy electron diffraction, and scanning electron microscopy give reliable information on surface composition, contamination, and structure. A strong correlation between surface scattering and damage threshold has been established, as has the appearance of increased scattering after damage.

It is becoming possible to design materials for high damage resistance. The index nonlinearity has been related to the refractive index value and dispersion, and to the Raman spectrum of the materials so that a capability exists to predict the value of n_2 from a knowledge of the index dispersion and Raman scattering. For a broad class of materials, an empirical relation exists correlating higher refractive index with lower surface damage threshold.

Compositional purity is also a factor in determining damage levels. In alkali halides, for example, extremely high damage levels have been obtained in materials grown by reactive atmospheric processing (RAP). These improved values indicate that earlier work on avalanche breakdown levels in alkali halides as a function of frequency may not have tested the intrinsic property of the materials, but may have been influenced by impurities. Specific remedies have evolved for certain materials. Thus, in $LiNbO_3$, oxygen enrichment of the surface leads to a higher damage threshold, since it reduces surface absorption. In general, purity of materials, care in preparation, and careful removal of chemical residues and defect structures are all essential to approach the intrinsic damage limit in any material.

Care must be exercised in extrapolating damage values from small area test results to large area applications. Optical damage always finds the weakest spot on the surface, so that the average properties of the sample may not accurately reflect the operational value of damage resistance.

In conclusion, there have been significant advances in both understanding of damage processes and in the measurement of relevant parameters in the past year. Intrinsic processes are very well understood. Extrinsic processes are hard to characterize, and the emphasis is now placed on the use of careful techniques for material preparation, to reduce the presence of extrinsic influences on material damage.

2. Summary of Papers

The papers presented at the 1974 Symposium have been grouped under six headings: Damage Factors in System Design; Experimental Damage Results; Surface Preparation and Improvement; Material Characterization and Instrumentation; Damage Diagnostics, and Theoretical Studies. One-third of the papers presented fall under the heading of Experimental Damage Results. This group includes information on new materials and on composite elements, over a range of conditions from picosecond pulses to CW. As in previous years, the purpose of these summaries is to provide the reader with a concise overview of the conference papers, and to direct his attention to those papers of greatest interest to him.

2.1 Damage Factors in System Design

The degradation of system performance, and the limitations imposed by damage phenomena are overriding considerations in the design of large laser systems. It is now well established that the two phenomena which limit the design of large glass systems for laser fusion are small-scale self-focusing, and parasitic oscillation. Techniques which have been developed to reduce the effect of both phenomena were described at the Symposium.

Kent Moncur of KMSF presented a paper in which he discussed the consequences of the index nonlinearity in glass lasers, and techniques whereby the beam profile in large glass systems can be controlled. He made particular reference to the KMS laser system, which operates at 5 to 10 GW/cm^2. He concluded that, at this power level, self-phase modulation was inconsequential, but that both large-scale beam distortion (nonlinear lensing) and small-scale self-focusing (beam break-up) posed serious design problems. To avoid the development of self-focusing, he advocated the use of apodizing techniques (soft aperatures), and described several apodizer designs for high power use. In particular, dielectric coated glass apodizers withstand power levels of $5J/cm^2$, but can only be fabricated with relatively small gradients in transmission. Other apodizer techniques were also discussed. Without the use of apodization, as much as 50% of the beam power can be scattered into a halo, which is of small angular divergence, but outside the desired beam angle. The development of small scale self-focusing can, of course, lead to physical damage in the glass itself.

Erlan Bliss, of Lawrence Livermore Laboratory, reported on studies of self-focusing effects in both rod and disk amplifiers. Like Moncur, he analyzed the problems of whole-beam lensing and small-scale, self-focusing separately. To observe lensing, he passed a high intensity beam through an umpumped glass rod, and passed a reference beam from the same source along a parallel path, photographing both beam profiles at a distance of several meters. The lensing effect was quite apparent. A more detailed observation of self-focusing was provided by use of a Mach-Zehnder interferometer, in which the intensity dependent refractive index change was observed directly, as a function of time. Analyses of these observations yielded values of n_2 for laser glass and YAG in good agreement with results obtained from ellipse rotation measurements.

By use of a shear plate interferometer, a phase and amplitude perturbation of known modulation depth and spatial frequency can be generated on an intense beam. The growth of this perturbation can then be observed, by passing the modulated beam through a nonlinear medium, in this case laser glass. By this technique, Bliss was able to test the predictions of both the linearized theory of small-scale self-focusing, and the full, nonlinear computation. Agreement was excellent between experimental results and the detailed numerical calculations, and it was found that the linearized theory, discussed by several speakers at this symposium in 1973, provided an accurate description of the modulation growth, even when significant deviation of the fringe shape from sinusoidal was seen.

In disk lasers, the presence of intermittent regions of linear material allows diffraction to reduce the growth of instabilities at high spatial frequencies. For the same power level, the small-scale self-focusing in a disk amplifier and rod amplifier were compared. As expected, the structure which developed in the disk system exhibited lower spatial frequencies than seen in the same length of glass in a rod system.

At the Naval Research Laboratory, John McMahon has been developing techniques for the suppression of parasitics in flash lamp pumped, Nd: glass, rod amplifiers. He identified four kinds of parasitics, as follows. A circumferential mode can build up due to reflection around the interface between the rod and the cooling water (Mode #1), or around the water jacket outside the rod, but with gain paths through the rod (Mode #2). Similarly, longitudinal modes can build up, due to reflections at the end of the rod, either due to internal reflection at the rod surface (Mode #3) or at the water jacket surface (Mode #4). Modes 2 and 4 can be suppressed by the introduction of samarium salts, which absorb at 1.06 μm, into the cooling water. Modes 1 and 3, which develop due to reflection at the rod-interface, are suppressed by index matching the cooling liquid to the rod. The index matched coolant must be chemically stable, even when exposed to flash lamp irradiation, and transparent to the pump radiation. A solution of Zinc Chloride (for index matching), Samarium Chloride (for 1.06 μm absorption) and HCI (for chemical stabilization) was found to be satisfactory for this purpose. The end-reflected mode could be further suppressed by anti-reflection coating the end of the rod, but this technique may not be directly applicable to long amplifier chains where feedback can occur from other sources.

Using parasitic suppression, it looks as if gain-diameter products of $\alpha D = 0.6$ are achievable. Without stabilization, a value of $\alpha D = 0.2$ is marginally unstable. Parasitic suppression allows the use of higher gains, and therefore reduces the length of glass in the system. Thus higher power densities can be propagated without small-scale self-focusing. McMahon proposed that stabilized rod amplifiers are more attractive than disk amplifiers up to 100 mm diameter apertures.

For CW or repetitively pulsed systems, thermal distortion and passive distortion must also be considered. In multi-element systems, the requirements on the surface figure and bulk homogeneity of each element must be developed in terms of the total system performance.

A most important paper by H. E. Bennett and P. C. Archibald of the Naval Weapons Center considered the requirements for high power laser mirrors and components, not from an individual component standpoint, but rather from consideration of total system performance and intended operational functions. These total system considerations place very severe requirements on individual components to avoid disastrous

cummulative effects and minimize the need for active wavefront correction elements. These severe requirements are a) maintenance of excellent figure under thermal load, b) high damage threshold and absence of damage initiating sites and finally c) low scatter. Maréchal's criterion related the cumulative phase distortion to the possible peak on-axis energy at the focal point. For a 10 component system at 3.8 μm, these conditions demand that each component have a figure of $\lambda/8$ in the visible, and thermal distortion < 1000 Å, with high and uniform reflectivity over the total aperature. The interaction of various factors contributing to system performance was evaluated so that various system design and tolerance specifications could be made, e.g., initial and thermally induced distortion. For the case presented above, the sources of wavefront distortion resulting from 1) non-uniformity in the active laser medium, 2) distortion from figure errors, 3) refractive index variations and 4) atmospheric non-uniformities were made. It was shown that in many cases there was a need for apodization or active wavefront correction to maintain a high on-axis intensity at the focus of the system. The general conclusion of this paper, based on achieving high on-axis intensity, quantifies the requirements for improved state-of-the-art polishing and figuring procedures, and reduction of thermally induced distortion particularly from coating absorption and microroughness. Additionally, the mirror elements should possess high catastrophic damage resistance with minimum backscatter. It was pointed out that investigation of short wavelength scattering is a powerful non-destructive tool in addressing many important properties which ultimately influence the total system performance.

In a weakly absorbing window material, especially at 10.6 μm, the effects of thermal lensing and birefringence will introduce depolarization and aberration into the transmitted beam. M. Flannery and J. Marburger, of the University of Southern California, have analyzed this problem with an aberration matrix formulation, and developed a convenient description of the ensuing beam distortion in terms of two characteristic parameters, which are tabulated for 16 common IR window materials.

The significance of these parameters is as follows. The authors consider a plane-polarized Gaussian equiphase beam on the window, with the electric field distribution given by $\underline{E} = \hat{x}\, E_{in} \exp(-r^2/w^2)$. The thermal lensing which such a beam introduces is characterized by a dimensionless time t, which is the ratio of the Gaussian diffraction length, $kw^2/4$, to the instantaneous effective focal length of the induced thermal lens at the center of the beam. Clearly, the ratio is proportional to the energy density deposited in the window material. The spherical aberration introduced in the beam is given simply by $2t/w^4$. Serious aberration is expected to occur when $t \sim \pi/4$, and at a value of $t \approx 3$, the on-axis intensity is reduced to one-half its unperturbed value. The authors tabulate the ratio $t/\ell \int_0^t I_o(t')dt'$, (where ℓ is the window thickness), which is a number characteristic of window materials. It ranges in value from -1.49 mm/Joule for KBr, to 1.95×10^5 mm/Joule for Irtran-6. Thus, one would expect the same thermal lensing effect to occur for Irtran-6 at 10^{-5} times the transmitted energy, in a beam of the same radius, as in KBr.

The effect of birefringence is characterized by a parameter σ, which is also characteristic for a given material. The effect of birefringence is to introduce oscillations in the intensity, in the aperture plane. In the focal plane, this gives rise to an increased beam divergence, and less on-axis intensity. Significant depolarization effects are seen for values of $\sigma \sim 2$. For all the tabulated materials, the authors find $\sigma << 1$, except for KCl, in which case $\sigma = -1.344$, and KBr, for which $\sigma = -0.598$. This paper reduces a difficult and complex problem to simple form, and provides a useful basis of comparison of window materials, both for the materials tabulated in the paper, and whatever new materials may be developed.

2.2 Experimental Damage Results

The main purpose of the ASTM Symposium is to generate understanding of damage phenomena in laser materials, and to translate this understanding into improved material and system performance. The measurement and tabulation of relevant material parameters, especially damage thresholds, is an integral part of this process. In one-third of the papers presented at this Symposium, damage measurement results were reported. In such measurements, the characterization of the laser output, in terms of wavelength, pulse duration, peak intensity, as well as careful characterization of the material tested, in terms of purity, homogeneity, defect and impurity levels, are essential. Damage investigators seek correlation between observed damage levels and materials properties; especially properties that can be characterized in passive, non-destructive measurements. The measured damage values must be interpreted as being valid only under the conditions of test, but provide a basis of comparison of materials, when comparative measurements are carried out on several materials by the same investigator.

The first paper, on damage resistance of dielectric coatings subjected to picosecond pulses, was presented by B. Newnam of the Los Alamos Scientific Laboratory. Employing a single 30 psec, 1.06 μm pulse from a TEM_{oo} YAG laser he exposed two types of reflective coatings from several experienced commercial manufacturers over a 0.74 mm radius spot size using a 2 m focal length lens. This state-of-the-art survey was accomplished by suppling seven coating companies with common, low-scatter superpolished BK-7 glass substrates fabricated by a separate optical finishing company. All films were e-beam deposited in a $G(HL)^9HL^2A$ $(H,L = \frac{\lambda}{4})$ configuration using TiO_2 and SiO_2 and, as additional optional coating materials, ZrO_2 and SiO_2. Single shot thresholds were determined both by spark threshold using a filtered photo-multiplier tube, and by changes in laser-induced scatter (LIS) observed both visually and photometrically. Measurements on samples from different manufacturers yielded a range in damage resistance of 1 to 4 J/cm^2 for the TiO_2/SiO_2 coatings and 0.5 to 2 J/cm^2 for the ZrO_2/SiO_2 coatings. From all manufacturers where both types of coatings were supplied, this reduced damage resistance for the ZrO_2/SiO_2 samples was indicated. It was concluded that the variance in results for a specific design

from each of several suppliers was related to the coating procedures and starting material purity employed. There was a general but not strong relation between initial scatter and damage resistance. Reflectors which exhibited a large amount of diffuse weak signal scatter generally exhibited lower thresholds. It is worth mentioning that based upon several intrinsic physical properties, the ZrO_2/SiO_2 films should have been more damage resistant that the observed result, in which they were only one-half as damage resistant as the TiO_2/SiO_2 coatings. Consideration of energy requirements for melting and calculated linear absorption coefficients suggest the order $ZrO_2 > TiO_2$ in damage threshold. One must therefore look for other possible processes such as multiphoton absorption (not very probable), or film defects. This latter cause is more likely the culprit as may be suggested from the observed inverse relation of scattering and damage resistance.

A closely related study by G. W. Leppelmeier and M. Finkelstein of the Lawrence Livermore Laboratory concerned the investigation of a variety of coated and uncoated elements from different manufacturers. The damage threshold of multi-layer dielectric films used as polarizing beamsplitters, mirrors and anti-reflection coating, deuterated KDP, several high-Verdet glasses and micro-machined silver was determined. The 1J, 125 ± 25 psec laser at 1.06 μm used in this study exhibited less than 4% spatial and temporal ripple. A main concern in this work was not only assessment of the damage sensitivity of the above-commercial components, but evaluation of the availability of large area, defect free elements which yielded high damage thresholds and did not exhibit low level non-linear beam distortion. Specific film designs were not dictated by the authors, but it was found that the high index layers generally contained Zr or Ti sometimes with K and Ce added. It was assumed that the lower index material was SiO_2. The multi-layer dielectric-coated BK-7 polarizers were normally constructed in 20 to 30 layers and tested at 56.5 ± 0.2°. Samples from seven manufacturers resisted damage from 1.8 to 5.8 J/cm^2 and damaged at levels from 1.5 to 6.7 J/cm^2. Seven companies also supplied their best anti-reflection coatings on LLL provided EY-1 substrates. Damage resistance was from 2 to 5.4 J/cm^2 and damage was produced from 2.8 to 6.2 J/cm^2. The damage hierarchy for these two types of coatings was not the same from different suppliers. In the tests on mirrors, micro-machined silver damaged at levels considerably lower than coated glass reflectors, by a factor ranging from 1.5 to 3X. Results were also reported on three Faraday rotator glasses Hoya FR-4, FRN-5 and Owens Illinois EY-1 and several potassium dihydrogen phosphates crystals with varying degrees of deuteration. All Faraday rotator glasses were quite tough, resisting damage from 4.0 to 7.2 J/cm^2. All KDP samples resisted damage from 2.5 to 30 J/cm^2. In conclusion, the goal of achieving reliable optical elements which do not damage at levels below 2.0 J/cm^2 for subnanosecond exposures was largely achieved. However, it was stressed that for nanosecond and sub-nanosecond work there is a necessity for beams which are very clean, spatially and temporally, in order to avoid self-focusing and prevent local maxima in energy density. It was quite clear here, as in Newnam's work, that damage sensitivity is process-dependent, and that processing techniques to fabricate large aperture elements free of defects, which will be uniform and damage-resistant, remain to be developed.

With their obvious interest in high power CO_2 systems for laser fusion applications, the Los Alamos Scientific Laboratory is pursuing damage assessments of numerous optical elements subjected to nanosecond duration pulses. At this meeting, E. Stark, Jr. and W. Reichelt reported recent results on ZnSe, AR-coated NaCl and micromachined mirrors subjected to these short duration exposures. For chemical vapor deposited (CVD) ZnSe with many voids and inclusions, damage to uncoated samples occurred in the bulk at about 1.5 J/cm^2. For AR-coated ZnSe, from two manufacturers, results indicated damage levels of 2.5 J/cm^2 for coatings with reduced defect concentration, while for other samples, containing more irregular and ragged defects, the damage level was approximately 1.7 J/cm^2. NaCl which was AR-coated with a $\lambda/4$ layer of NaF damaged at 2.0 J/cm^2, while the uncoated NaCl exhibited damage at levels of 3.0 to 4.5 J/cm^2 depending on the quality of surface finish. Finally, micro-machined OFHC copper mirror substrates electroplated with 0.013 cm of gold or copper were fabricated. These mirrors and coatings, after further micro-machining at the Y-12 facility at Oak Ridge, Tennessee yielded damage levels in excess of 4 J/cm^2. This was attributed to the removal of defects and polishing debris from the surface.

A comprehensive study of pulsed CO_2 laser damage in infrared windows, reflectors and coatings was reported by V. Wang, J. E. Rudisill, C. R. Giuliano, M. Braunstein, and A. Braunstein of the Hughes Research Laboratories. Their results were obtained using a 600 nsec, TEM_{00} 10.6 μm CO_2 laser, described at previous meetings of this symposium series. An interesting result was that while a reduction in void and inclusion density in ZnSe led to considerably less measurable scatter, there was only a relatively smaller increase in damage threshold under these pulsed exposures. Specifically, in the more imperfect ZnSe window substrates which exhibited an absorption coefficient of 0.0030 cm^{-1}, damage was obtained at 30 to 40 J/cm^2. For the substrates which showed a scattering level only one-tenth as great, and an absorption coefficient of 0.0021 cm^{-1}, damage was observed at 55 J/cm^2. However, in the former case, damage was always characterized by inclusion damage, while for the more damage resistant sample damage was either inclusion-initiated or localized surface breakdown. In tests of thin films deposited on either RAP grown KCl or ZnSe substrates, significant correlation between absorption and damage threshold was achieved. For example, $\lambda/4$ wave films of ThF_4, As_2S_3 and ZnSe on KCl of absorption of 10 cm^{-1}, $<|$cm^{-1} and < 0.6 cm^{-1} respectively, damaged at levels of 80 J/cm^2, 120 J/cm^2 and 140 J/cm^2. However, an anti-reflection coating of ZnSe/ThF_4 on KCl with reflectivity $< 0.2\%$ per surface damaged at a threshold of 60 J/cm^2. In tests of ThF_4/ZnS AR coatings on ZnSe, damage was limited by the substrate to 25 to 40 J/cm^2. Similar damage determinations on coated and bare metal reflectors were also obtained. $(ThF_4/ZnSe)^2$ on Mo, with an absorption coefficient of 0.22 cm^{-1}, damaged at 50 J/cm^2 while for $(ThF_4/ZnSe)^3$ on Mo, with an increased absorption coefficient of 0.32^{-1}, the damage threshold was reduced to 30 J/cm^2. By comparison, an Ag/$(ThF_4/ZnSe)^2$ coating on Al/E-Ni exhibited an absorption coefficient

of 0.2 cm^{-1} and a damage level of 270 J/cm^2. In the first two cases surface conditioning was evident. The last set of experiments concerned bare metal reflectors. For three samples of conventional polished Cu, Mo sputtered on Mo, and polished and etched OHFC Cu, damage was noticed at 90-150 J/cm^2, 4-8 J/cm^2 and 750 J/cm^2 respectively. Obviously in the case of the two Cu samples there was a considerably lower concentration of impurities or surface defects in the etched sample. Here again the results seem to point to inclusions of surface contaminants and surface defects as important factors limiting the damage resistance of this class of materials.

Laser induced damage studies of KCl, grown by reactive atmosphere processing (RAP), was reported by S. D. Allen, M. Braunstein, C. Guiliano, and V. Wang all of the Hughes Research Laboratories. The same high power pulsed CO_2 laser used in the previous paper was employed. This investigation centered on a comparison of the damage resistivity of variously processed bulk and surface components made of high grade KCl. Each sample was examined in great detail by Auger, LEED, and SEM techniques, in concert with evaluation of the absorption characteristics of the individual samples. Samples of both single crystal and press forged RAP grown KCl were compared with commercially available KCl after both conventional and chemical etch surface processing. For the press forged samples fabricated at 250°C at a rate of 0.05 inch per minute per inch of remaining length, the resultant grain size averaged 5 to 10 μm in diameter.

Extending the work of J. W. Davisson of the Naval Research Labs, a chemical treatment of immersion in concentrated HCl for one to two minutes was rapidly followed by an isopropyl alcohol rinse. Finally, the residual alcohol and acid were removed by the vapor from a freon TF degreaser. In all cases studied the absorption of the conventionally polished materials (initial values of 0.00045 to 0.002 cm^{-1}) was reduced considerably (to 0.00013 to 0.0014 cm^{-1}) depending on sample type, source, and fabrication process. Furthermore, the chemically etched samples were less subject to environmental factors which induce fogging. Similar improvements in Auger scans and LEED patterns were evident, indicating reduced contamination density and greater crystalline integrity. It was noted that further surface cleanliness could be achieved by Argon ion sputtering.

As was mentioned elsewhere in these proceedings, low surface scattering is an important property of optical elements in high power laser systems, and again the chemical etching process produced measurable reductions in scattering. Normalizing the scattering from mechanically polished single crystal KCl to 1.0, the chemically etched single crystal sample exhibited a scattering level of 0.45, while for press forged samples, scattering was reduced from 2.3 to 0.72 when the conventionally polished samples were further treated by an etch. However, the most important improvement was in surface damage threshold, where etched single crystal surfaces damaged at from 330 to 2700 J/cm^2 compared to values of 70 to 350 J/cm^2 for conventional polished RAP grown KCl. Etched, press-forged samples damaged at levels of 1500 to 1800 J/cm^2. For bulk damage in RAP grown samples of both single crystal and press forged fabrication, levels in excess of 4600 J/cm^2 was achieved. When these values are compared to other available data on the laser induced and DC breakdown strength of KCl and NaCl, it was concluded that the electron avalanche mechanism is primarily impurity mediated and furthermore that future improvements in optical strength can be made evident through improved process control and higher purity of starting materials.

Many proposals have been made to assess the desirability of one coating process versus another. In a study to answer this question for the specific case of germanium coated KCl elements subjected to 75 nanosecond pulsed CO_2 lasers, A. Golubovic, W. Ewing, J. Bruce, J. Comer, and D. Milam compared both sputtered and electron beam deposited coatings at the Air Force Cambridge Research Laboratory. This specific combination of coating material and substrate is important because KCl is hydroscopic, and thus subject to environmental degradation,as well as being easily marred. Germanium's high refractive index suggests it suitability as the first layer in a multi-layer AR-coating which can act as a protective covering as well. The substrates used were reactive atmosphere processed (RAP) and Czochralski grown KCl of [100] and [111] crystal orientation. All substrates were carefully polished, cleaned, chemically etched and finally sputter-etched with Ar. The sputtered films were deposited at a rate of 1 Å/sec at 20×10^{-3} Torr while the substrate was held at 75°C. The e-beam coating was deposited at 20 Å/sec with the initial pressure of 5×10^{-8} Torr increasing to 2×10^{-5} Torr during deposition of the 1 μm thick coating. Applying the "standard" scotch tape adhesive test both films exhibited weak adherence with the sputtered film slightly stronger. Auger analysis indicated that Ge $\leftrightarrows$ KCl diffusion was more complete on this sputtered sample. Damage tests indicated a range of thresholds of 0.96 to 1.18 J/cm^2 for the sputtered films, and 0.53 to 0.82 J/cm^2 for the e-beam coated samples. There was no correlation with crystal structure or growth procedures.

In an attempt to study the effects of intergranular boundaries devoid of defect material on the damage sensitivity of CVD grown ZnSe subjected to pulsed CO_2 laser irradiation, H. Posen, J. Bruce and D. Milam of the Air Force Cambridge Research Labs investigated the morphology and damage threshold of large grain and highly twinned samples. ZnSe was chosen because of its possible use as a high power window and coating material. This low bandgap material exhibits low absorption and high yield strength. All samples tested were sputter-cleaned to remove any carbon introduced in the growth technique. The polycrystalline ZnSe exhibited an absorption coefficient of $\beta = 0.0030 \pm 0.0004$ cm^{-1} while the highly twinned sample had a $\beta = 0.0070 \pm 0.002$ cm^{-1}. Twinning serves to strengthen material since it serves to form barriers to dislocation propagation. Generally ZnSe is available only as a polycrystalline aggregate, showing large grain misorientations with highly rectilinear intergranular bands (twins). In addition to classifying various crystal regions as to depth of twinning, refractive index variations and purity, they were unable to identify any major difference in damage threshold in this II-VI material correlated with boundary orientation of structure. There was some indication that the morphology of

damage was related to the orientation of the twin relative to the surface. Failure usually occured along the [110] cleavage plane. The damage sensitivity observations of this study should not be considered conclusive because of the difficulty of exposing only one type of crystal structure on the surface with a focal spot size which was large compared to the specific grain boundary locale.

In their continuing program on evaluation of new laser component materials, F. Varsanji and L. G. Deshazer of the University of Southern California reported their preliminary measurements on $LaCl_3$. This anisotropic crystalline substance has been proposed for use as a 10.6 μm window material, it being transparent from the visable to 25 μm. Their rather elaborate program of mechanical and optical property evaluation may be sufficiently complete for a more detailed presentation at a future date.

A paper dealing with CW 10.6 μm damage was given by J. S. Loomis and C. A. Huguley. The materials studied were coated and uncoated windows of KCl, NaCl and ZnSe. The main thrust of this study was to correlate temperature rise with intensity (to 70 kW/cm^2), focal spot size and irradiation time (1 to 30 sec) and to measure the distortion interferometrically on coated and uncoated elements. High strength materials, such as ZnSe and CdTe, had previously been observed to fail, by burning through under intense illumination, whereas, KCl and NaCl had been observed to fracture, or fail due to the melting of coatings. Fracture frequently occured after the high power laser was turned off abruptly.

Using a TEM_{oo} CO_2 laser of 500 watts output in a 4 mm beam, peak optical pathlength differences, in 632.8 nm fringes, of 3.3, 0.8, and 0.3 were recorded for samples of ZnSe, KCl and NcCl. Distortion was permanent only in one sample of KCl coated with As_2S_3. During this series of measurements temperature gradients stabilized within a few seconds after start of exposure. Thereafter, at each location, the temperature rise was linear. For samples of ZnSe and NaCl subjected to 70 kW/cm^2 loading, no stress pattern appreared.

At the Air Force Weapons Laboratory, T. T. Saito, C. B. Charlton and J. S. Loomis are continuing their comprehensive study of metal substrate mirrors for high power CW 10.6 μm applications. The main thrust of their effort is the damage assessment of mirrors prepared by conventional polishing and diamond machining with noble metal coatings, dielectric coatings and subsequently machined electroplated metal mirrors. After reporting in detail the output characteristic of their 1 kW cw TEM_{oo} CO_2 laser, focusing arrangement and intensity distribution (greater than 200 kW/cm^2) at the target surface, they reported extensive results on a wide variety of samples. In brief, they have found copper surfaces exhibit lower damage thresholds than molybdenum in contrast to pulsed findings. Silver and gold evaporated on metal substrates to yield reflectivities greater than 0.99 are found to withstand more than 200 kW/cm^2 irradiation over small areas. Diamond turned optics compete well with conventionally polished optics and, finally absorption is the major factor limiting the survivability of dielectric coatings. Some coatings, however, did survive test illuminations greater than 175 kW/cm^2. As in other reports of this meeting, precleaning or conditioning by irradiation at low levels resulted in greater ultimate damage resistance, probably by gentle removal of dust and other absorbing or scattering particles.

In an engineering study, W. S. Otaguro of McDonnell-Douglas investigated damage to infrared filters by inadvertant exposure to pulsed ruby laser radiation. Damage morphology, degradation of filter transmission and thresholds for damage from the highly absorbed ruby wavelength were measured. Filter samples were initially cooled to 10°K, for their intended use in infrared radiation sensor systems. The filters, of Ge/ZnS multilayer construction, transmitted from 8 to 14 μm. With damage defined at that level in which the passband transmission changed by 4%, Q-switched ruby TEM_{oo} laser pulses of 20 nsecs duration caused damage at $5MW/cm^2$. This observation was treated theoretically from a heat conduction approach based on intrinsic absorption of the multilayer materials. Results of experiment and theory were in general agreement.

2.3 Surface Preparation and Improvement

In actual systems, damage generally first occurs at optical surfaces. Surfaces are characterized by high concentrations of impurities, defects, and inhomogeneities. Thus, the resistance of an optical surface to damage can be greatly affected by the techniques of preparation used. Also, since surface damage is dominated by extrinsic factors, present values can be substantially improved.

It is generally agreed that by improved polishing techniques, smoother optical surfaces (lower rms roughness, and fewer cracks, scratches, and pits) can be obtained, and that smoother surfaces yield higher damage thresholds. M. Boling, J. A. Ringlien, and G. Dube, all of Owens-Illinois, challenged this concept in a paper reporting studies of surface damage at 1.06 μm in laser glass. They showed that, if greater smoothness is obtained by a polishing technique which leaves behind an absorbing residue, a reduced damage threshold will result.

Several other examples were presented which contradicted the hypothesis that smoother surfaces exhibit higher damage levels. Two quartz samples were polished by conventional methods. One was then subjected to an acid etch, which left pits of about 100 nm size on the surface. Both samples damaged at 300 to 350 J/cm^2. (This might be due to residual defects and impurities still present on the pitted surface, despite the etching process.)

Boling also showed results on two glass surfaces, one polished conventionally, with barnsite, and the other bowl-feed polished. The conventionally polished surface showed significant scratch and defect structure, while the bowl-feed polished surface was defect-free on a scale of 10 nm. Both surfaces damaged at about 150 J/cm^2, well below the intrinsic bulk level.

He then discussed the use of a boiling nitric acid etch, to raise the damage threshold of laser glass. Unlike the HF etch used earlier by Swain, nitric acid does not attack the silicate structure of the glass, so it does not alter the optical character of the surface. The etchant is heated to increase diffusion into the sample. For samples carefully polished with non-absorbing polishing compounds prior to etching, this technique yielded a threefold increase in surface damage threshold, from the 150 J/cm^2 quoted above to values close to 500 J/cm^2. This is very nearly the intrinsic limit of the medium.

Boling emphasized the point that surface smoothness alone does not guarantee a high damage threshold, and that chemical residues on or near the surface are of great importance in the damage process. The hot acid etch technique is promising as a method which will provide chemically clean surfaces, while not destroying the optical integrity of the surface.

It has been postulated that surface damage in $LiNbO_3$ arises due to a deficiency in oxygen at the surface, leading to a localized increase in the absorption at 1.06 μm. This hypothesis was tested by J. Potoskey and C. Giuliano, of the Hughes Research Laboratory, and C. Klein of the Hughes Aircraft Corporation. They tried two methods of adding oxygen to the $LiNbO_3$ surface, by bombarding the surface with oxygen in an argon-oxygen rf discharge, and by exposing the sample to oxygen gas at high pressure.

The treated surfaces were tested with a Nd:YAG laser pulse of 17.5 ns duration, focused onto a 64.5 μm spot. Damage threshold was determined by visual inspection. When the $LiNbO_3$ surface was bombarded with 300V oxygen ions in an rf discharge for 30 minutes, a 50% increase in the damage threshold was observed. The effect was persistent, and the sample retained its improved value up to several weeks after treatment. However, some regions of the crystal did not show improvement, an effect attributed to the presence of impurities or defects.

Under high pressure oxygen, the crystal showed similar improvement. Samples were exposed from a few minutes to 24 hours at pressures from 50 to 250 psig. No persistent effect was observed in this case, however. It appears as if surface damage in $LiNbO_3$ is partially attributable to oxygen deficiency, and partially due to defects and impurities. The former cause is amenable to treatment by oxygen enrichment.

J. Porteus, E. Teppo, and J. Dancy, of the Michelson Laboratory reported on studies of surface damage in $LiNbO_3$ and KCl, using both transmission electron microscopy, and Auger electron spectroscopy. Uncoated samples of $LiNbO_3$ polished with Al_2O_3, diamond dust, SiC/Glycerol, and "Syton" were examined, along with samples coated with a proprietary coating (probably $ThOF_2$ or ThF_4 overcoated with Al_2O_3) and $ThOF_2$. All samples were in the form usually used for Q-switches.

It has been hypothesized that surface acoustic waves play a role in surface damage in $LiNbO_3$. Experiments are now underway at the Michelson Laboratory to test this hypothesis in two ways. In one, surface waves will be generated with an interdigital transducer, to see if acoustic waves alone can generate surface pitting. In the other, a surface will be divided by saw cuts, and only one portion illuminated, to see if pits appear on the isolated regions. Only preliminary results have been obtained to date.

Auger spectra of damaged coated surfaces indicated the presence of trace impurities. On the proprietary coating, the Auger spectrometer indicated Nb, S, and Cl as being present. The presence of niobium was attributed to the disruption of the coating during the damage process and exposure of the underlying niobate. The origin of the other impurities was not determined. The other coating showed significant amounts of carbon, probably attributable to pump oil. The carbon was concentrated at the interface between the coating and the substrate. Only preliminary results were presented on KCl.

This paper represents the use of sophisticated surface diagnostics for studying damage phenomena. It is essential in systems as complicated as coated surfaces, that very specific diagnostics be available.

2.4 Material Characterization and Instrumentation

To develop a full understanding of the factors influencing damage processes requires detail characterization of the materials involved. Intrinsic, bulk physical properties of the materials are essential, and a measurement program has been established to provide these data. Of the extrinsic factors influencing damage, surface scattering is one of the most significant. Improved methods for measuring surface scattering have also been developed.

Partially under the auspices of the Advanced Research Projects Agency, A. Feldman, I. Malitson, D. Horowitz, R. M. Waxler and M. Dodge have established an infrared laser window material characterization program at the National Bureau of Standards. The main areas of precision measurement include refractive index, stress-optical constants (q_{ij}), the temperature dependence of refractive index, the thermal expansion coefficient and appropriate elastic compliances (S_{ij}). Details of their specific instruments design, performance and range of applicability were reported. The thrust of this intrinsic material characterization program is aimed at accurately predicting the distortion produced in infrared windows as a result of thermal loading. Currently under study are polycrystalline ZnSe, As_2S_3 glass, chalcogenide glass (Ge 33%, As 12%, Se 55%) and KCl. A few of the many important quantities already measured for KCl are the refractive index at 20°C of 1.6360 at 0.224 μm, 1.4374 at 14.3 μm and 1.4542 at 10.6 μm. The change of refractive index with temperature over the range of 20°C to 30°C is $-2.1 \times 10^{-5}/o_K$ @ 0.27 μm and $-2.5 \times 10^{-5}/o_K$ at 14.3 μm remaining fairly constant at ~ $-3 \times 10^{-5}/o_K$ between 3 μm and 6 μm. The fact that dn/dT is negative indicates that the variation of n with T is primarily due to a change in material density. At the spectral extremes where dn/dT is less negative, the temperature dependence

suggests a shift of U.V. and IR absorption edges to longer wavelengths. Results for stress optical constants q_{11}, q_{12}, $(q_{12} - q_{11})$, the elastic compliance S_{12} and refractive index, were given for As_2S_3, chalcogenide glass and polycrystalline ZnSe at 0.6328 μm, 1.15 μm and 10.6 μm.

M. J. Soileau and H. E. Bennett of the Naval Weapons Center, Michelson Laboratory, described a sensitive instrument for measuring bulk and surface scattering in optical components. The instrument, called the Optical Functional Tester (OFT), measures both reflecting and transmitting optics in the visible and infrared. Light from a He-Ne laser, operating at 0.633 μm, 1.15 μm, or 3.39 μm, illuminates the sample, and the scattered light from the desired sample volume is imaged on a pyroelectric detector by a Coblentz sphere, with a focal ratio of 0.5. Bulk and surface contributions to the scattering can be separately analyzed.

Samples of hot rolled KCl, hot forged KCl doped with divalent europium, "polytran" KCl, and CVD ZnSe have been tested. The europium-doped KCl and ZnSe samples showed more bulk scattering than the other samples tested. In both cases, the scattering decreased with increasing wavelength. At 1.15 μm, bulk scatter in Eu^{++}: KCl was about one-third that seen at 0.63 μm, while in ZnSe, the reduction was by about a factor of two.

The standard scratch and dig specifications, MIL-O-13830A, were compared to the OFT. Scratch and dig standard specimens were examined in the instrument. It was found that the standard specimens correlated poorly with actual scattering measurements. Thus, a #10 scratch yielded greater scattering than a #20 scratch, and the substrate on which the #10 scratch was scribed yielded higher scattering than the #20 scratch standard.

The OFT offers the advantage of automated, objective evaluation of optical components in terms of both bulk and surface scattering. Scratches and digs can be identified from a surface scan by the OFT. So-called scratch and dig standards are seen to be subjective at best, and can be misleading.

Another area of materials classification concerns the characterization of surfaces exposed to high intensity laser radiation. Jean Bennett of the Naval Weapons Center reported on several new instruments developed at the Michelson Laboratory specifically designed to perform these measurements accurately. The prime driving force for this work is to aid in the determination of surface structure and its relation to laser induced damage, and to calculate the magnitude and angular distribution of scattered light from surfaces prepared by various techniques. To accomplish this task effectively three main factors must be determined. These are a) the auto-covariance function, b) the rms roughness, and c) the height distribution function. These basic quantities along with the rms slope and slope distribution function should sufficiently characterize the geometrical character of normally encountered surfaces of interest. One should then be able to correlate scattered light with roughness, which can decrease intensity in the main beam, reduce spurious signals, and assess backscatter which may produce damage by feedback into the laser. Furthermore, mirror absorption can be increased by a factor of three in overly rough surfaces. In addition, geometrical roughness can lead to field enhancement and thus lower damage thresholds in short pulsed laser operations. To perform these assessments reliably and rapidly, an automated FECO (Fringes of Equal Chromatic Order) interferometer with a lateral resolution of ~ 2 μm and a depth resolution of a few Angstrons has been constructed. This instrument has already been employed to evaluate the surface character of several glasses, metals and crystals. These include Cervit, KCl, molybdenum, titanium and copper surfaces prepared by different techniques. On these samples there was a good correlation between rms roughness determined both by the TV FECO interferometer and those from visual observations of FECO fringes; however, these two methods did not agree absolutely, the visually determined values generally being larger than those determined by the automated system. The basis of this disagreement is under further study.

John C. Stover of Dow Chemical has attempted to assess the possible utility of other scattering concepts and geometries than those in normal use, such as total integrated scattering (TIS) etc., to evaluate surface character more easily, and arrive at a quantification of average surface parameters. He has attacked this problem from a theoretical standpoint with experimental verification of the scattering from sinusoidal reflection gratings produced by the interference of two coherent laser beams on photographic emulsions. He hopes to extend his analysis in this initial effort to obtain relations governing the light scattered from arbitrary surfaces (not necessarily Gaussion in roughness disturbation), resulting in an accurate spatial power spectral density function of these surfaces. Analyzing the previously described surface theoretically, where scalar theory should apply, he has achieved qualitative agreement with experiment. This work is now being expanded to arbitrary surfaces and correlated with standard surface characterization techniques in use at the Michelson Laboratory. Besides allowing the measurement of rms surface roughness, auto-covariance length, etc., the spatial power spectral density function should be useful at higher frequencies than presently employed techniques. The thrust of this research of course is to lead to correlation between geometrical surface character and damage threshold.

2.5 Damage Diagnostics

In any study of laser damage, it is essential to develop techniques to determine when and if damage has occurred, and, if it has, to identify the operative mechanism. Furthermore, there is a continuing search for precursors to damage which might provide a nondestructive test for damage studies. In the past, increased light scattering, and spark observation, combined with post-mortem observation, have been used to indicate when damage has occurred. A number of proposals have been put forward in past Damage Symposia for ways to identify which of several competing mechanisms is responsible for damage

under a given set of circumstances. This year, D. Milam, R. Broadury, R. Picard, all of the Air Force Cambridge Research Laboratory, and M. Bass of the University of Southern California, discussed the use of the statistics of sample survival time under continuous illumination as an indicator of the operative damage mechanism. For a given damage mechanism, the probability of damage per unit time at a given illumination level is assumed to be a known function, h(t). In an ensemble of N_o experiments, the number of sample sites surviving, without damage, to a time t is given by

$$\ln[N(t) / N_o] = {}_o\int^t h(t')\, dt'.$$

If the intensity level is constant, corresponding to an intensity I_0, then the log - survival function will be

$$\ln[N(t) / N_o] = {}_o\int^t h(I_o,t')\, dt'.$$

If more than one mechanism is operative the log-survival function will be a sum of similar integrals. For avalanche ionization, the function h(t) is constant (for constant illumination) and given by $A_o \exp(-k/E_0)$, where E_0 is the field amplitude. Thus, the log-survival curve is expected to be a straight line of constant negative slope, with the slope increasing in magnitude with increasing field. If both defect and intrinsic breakdown are occuring, a curve asymptotic to the two appropriate slopes will be observed.

For thermal absorption damage, the function h(t) is zero below a critical illumination level, and goes quickly to a large value as the critical deposited energy is reached. Thus, the log-survival curve approaches a step function in time, with the step being of shorter duration at higher power levels. More complicated curves arise if several types of absorbing inclusions are present. This hypothesis was tested using a single mode ruby laser which was shuttered with a fast Pockel's cell. The pulse had a rise time of 0.7 nanoseconds, and a power level of from 50 kW for 50 nanoseconds duration, to 200 kW in 20 nanoseconds. For transparent samples, the transmission of the pulse was monitored, and the decrease in transmission taken as indicative of damage. The beam was focused to a spot of from 3 to 100 μm in diameter.

For TiO_2-SiO_2 multilayer coatings, damage was seen to be due to absorption. The log-survival curve showed a sharp cutoff for fixed power, and the cutoff time was inversely proportional to the power. For ZrO_2, single-layer films deposited by e-gun evaporation, damage was seen to be due to absorbing inclusions. For Suprasil quartz, damage was attributed to defect-enhanced, avalanche ionization in the bulk material. The data presented showed reasonable agreement with the proposed theory, although in the case of Suprasil, there was considerable ambiguity in assigning the damage mechanism on the basis of the log-survival curves.

Concetto Giuliano of Hughes Research Laboratories, reported on the observation of transmitted, reflected and back-scattered light during the damage process, as a possible diagnostic test for damage detection. Samples were sapphire, illuminated with a 20 nanosecond, ruby laser pulse, focused to a 55 μm spot. Damage in this case is accompanied by a significant reduction in both transmitted and specularly reflected light, undoubtedly due to the formation of a strongly absorbing plasma in the damage region.

Time resolved measurements indicated that the reflection and transmission follow generally the same temporal behavior. The decrease in specular reflection is seen both for entrance and exit surface damage. Observations of the diffuse back scattering showed that, above the damage threshold, the back scattering spreads into a cone of angle 1.5 to 2.0 degrees. As the power is increased, back-scatter structure, in the form of spots and rings, appear. Temporal monitoring of the diffuse backscatter shows that it strongly increases at the time that the transmission cuts off, which is the time of first appearance of the damage plasma. Diffuse back scatter produces a sensitive observable for damage of this kind, since changes in backscatter are seen even when the absorption is weak. Guiliano was not able to observe a scattering increase reliably before damage was seen, so he could not establish a precursor test based on scattering.

A new diagnostic technique for detecting surface damage was proposed in a paper by R. Hart, G. Giuliano, and H. Dunlap of the Hughes Research Laboratory. They analyzed a sample of GaAs exposed to radiation at 0.69 μm from a ruby laser. The pulse duration was 20 ns, in a beam of 1.2 mm radius, and the observed damage levels were from 12 to 15 MW/cm^2.

The surface of the crystal was probed by observing the backscattering of 280 KeV alpha particles. By observing the scattering intensity as a function of energy loss, the scattering could be related to the depth of the scattering layer in the crystal. Backscattered particles were detected at an angle of 160° to the incident beam, with a cooled Si detector.

When the crystal was randomly oriented to the incident particle beam, the scattering was insensitive to the damage layer. However, when the beam was incident along the <100> crystal direction, ion channeling greatly reduced the backscatter signal. In this case, the signal increase due to surface damage was clearly discernible. The scattering layer due to damage extends only to about 17.5 nm. The transverse extent of the scattering layer correlates well with the laser profile.

It was remarkable that the scattering only extended to 17.5 nm, when the surface pits associated with the damage were from 2 to 4 μm in diameter. Beyond the surface layer, the channeling effect was relatively insensitive to the presence of damage.

TiO_2 and YVO_2 are birefringent materials of interest for use in laser applications. K. M. Leung and L. G. DeShazer of the University of Southern California, reported results on surface damage in uniaxial single crystals of each of these materials. Damage was induced by irradiation with a TEM_{oo} ruby laser. The damage mechanism was identified by recording the damage threshold as a function of irradiated spot size, for spot sizes from 52 μm to 215 μm. Damage was identified by the technique of laser-induced scattering. The mechanism of damage was confirmed by morphological investigation, using a scanning electron microscope.

Damage studies were carried out with the optic axis of the crystal both parallel to and perpendicular to the incident E-field. No difference was observed either in damage threshold, or in morphology. Damage was attributed to polishing inperfections in the case of TiO_2 and inclusions of YVO_4. Extrapolation of the observations to zero spot size yield intrinsic damage levels of 2.5 to 3 times the defect-dominated values.

2.6 Theoretical Studies

In recent years, there has been significant advance in the theoretical understanding of damage processes. Avalanche ionization, for example, has been exhaustively studied, as has self-focusing. Inclusion damage has been analyzed in several papers. Various theoretical models have been proposed to account for impurity absorption in otherwise transparent materials. As experimental data improves, and materials of greater purity become available, a corresponding increase in theoretical understanding can be achieved.

R. A. Shatas, J. D. Stettler, M. M. Narducci, S. S. Mitra and H. C. Meyer of the U. S. Army Missile Command, presented a theoretical discussion of alternatives to the avalanche breakdown process to explain the observed discrepancies in surface damage thresholds in semiconductors. After reviewing the phenomenological theory of avalanche breakdown, they discussed the conditions under which the Shockley theory can be extended from DC to optical frequencies. They show that as long as the optical frequency is less than the effective collision frequency, the avalanche theory can be expected to apply. Under this condition, there is a high probability of a "lucky" electron undergoing a momentum-reversing collision during the optical cycle, and thereby absorbing energy from the applied field. This condition is shown to occur in NcCl.

In semiconductors like GaAs however, the effective collision rate is too low for the avalanche theory to apply. The authors' propose that in these materials, collective excitations of the plasma may be responsible for the observed damage. They examine the threshold for both the two-stream instability and the parametric instability, and find that in GaAs, the predicted thresholds are in general agreement with experiment.

The threshold for both plasma instabilities is shown to increase linearly with the ratio of the laser frequency to the electron mobility. Observed thresholds in GaAs do not increase with increasing optical frequency, but decrease instead. This effect is attributed to the fact that the band gap in semiconductors is comparable to the frequency, so that at increased optical frequency, electrons can be excited into conduction states via lower order multiphoton processes.

Recently, there has been great interest in the determination of the third-order nonlinear susceptibility ($\chi^{(3)}$) of transparent dielectrics. R. Hellwarth, J. Cherlow, and T. T. Yang of the University of Southern California, discussed the determination of the so-called "nuclear" contribution to $\chi^{(3)}$ from analysis of the Raman scattering spectrum. This is the contribution to $\chi^{(3)}$ from heavy particle motion in the medium. By use of the Kramers-Krönig relation, both the scalar and tensor components of the nonlinear dielectric response function can be determined. These values lead directly to the non-electronic contribution to the nonlinear refractive index coefficient, n_2.

Samples tested included Homosil quartz, LSO and ED-4 laser glasses, and SF-7 and LaSF-7 optical glasses. In each case, the electronic nonlinearity was found to account for 70 to 85% of the reported nonlinear refractive index.

An intriguing relation between observed damage thresholds and material properties was put forward by J. Bettis and A. H. Guenther of the Air Force Weapons Laboratory, and A. J. Glass of the Lawrence Livermore Laboratory. They postulated that the electric field value at damage threshold in transparent dielectrics might correspond to some critical extension of the electron coordinate, corresponding to a critical distortion of the electron cloud in the polarizable molecule. Consideration of the local field correction then led to an empirical relation, that the threshold electric field value should vary as $N/(n^2-1)$, where N is the number density of molecules, and n the index of refraction of the material.

This hypothesis was compared with experimental results of several investigators. Thin film results of DeShazer showed generally good agreement. Data reported by Boling et al on surface damage in glasses showed a $1/(n^2-1)$ dependence, since the molecular densities were essentially the same for all materials tested. For vapor phase mixtures of thin film materials, reported by Austin, et al, a $1/(n^2-1)$ dependence was found, but the observed damage thresholds were found to be in poor agreement with $N/(n^2-1)$. No explicit explanation of this anomaly was offered.

The most elaborate comparison was provided by the carefully determined bulk threshold values reported by Fradin. The threshold field values for halides of sodium, rubidium and potassium were found to be in excellent agreement with the $N/n^2-1)$ relation. The potassium halide curve was displaced from the sodium

564-378 O - 74 - 2

and rubidium halide data, but was parallel to it. NaF was the only reported material widely variant from the proposed relation. In all cases, extrapolation of the empirical expression to the index value for air gave good agreement with reported air breakdown values.

C. J. Duthler and M. Sparks of Xonics, Inc., discussed two aspects of the damage problem, of particular relevance to laser window materials. In the first part of their talk, they revisited the problem of surface pit formation due to the heating of subsurface, absorbing inclusions. The failure mechanism they proposed is based, not on vaporization of the inclusion, but on the adiabatic heating of the inclusion to create a locally concentrated stress within the material, and then the rupture of the stressed material along a conical surface by microcrack propagation from the point of maximum stress. The energy required in this failure mode corresponds to breaking the bonds of the material only along the conical surface, rather than throughout the excavated volume. The cone angle of the pit decreases from 78°, for a deep-lying inclusion, towards 0° as the depth of the inclusion becomes comparable to the inclusion diameter.

If the heated inclusion lies very close to the surface, failure can occur by microcrack propagation from the surface into the material, towards the inclusion, resulting in a pinhole-type damage rather than a conical pit. Subsequent heating will, of course, expand this pinhole. Although the model presented contains a number of simplifying assumptions, the general agreement with experimental results is satisfactory. The delay time associated with this mechanism is the acoustical transit time to the surface, of the order of 10 ns for a particle 10 μm below the surface. No such delay has been observed experimentally, probably since the surface fails first at its weakest points, which correspond to inclusions which are very close to the surface, with correspondingly shorter delay times.

The second part of the paper dealt with the role of molecular impurities in determining the residual absorption of infrared window materials in regions of nominally high transparency. In KCl and KBr, absorptions greater than $10^{-4}cm^{-1}$ are seen in spectral regions in which theoretical estimates of intrinsic absorptions are at least an order of magnitude lower. Atomic impurities can lead to alteration of the lattice absorption due to the formation of local lattice modes, but these are felt to be at too low a frequency to contribute at 10.6 μm.

Diatomic ionic impurities, in general, exhibit too high a frequency to account for the extrinsic absorption. The hydroxyl ion, for example, with a resonant frequency of 3640 cm^{-1}, would have to be present at a concentration of 100 ppm to account for the observed absorption. The authors felt that the most likely candidates are polyatomic and multivalent molecular ions, such as NO_2^-, HCO_3^-, SO_4^{2-} and CrO_4^{2-}.

3. Recommendations

As has been mentioned many times, the greatest improvement in damage thresholds of optical elements yet to be realized is probably in the area of exposed surfaces, particularly if those surfaces are coated. While considerable advances have been made in this area, resulting in improved components for both CW and pulsed lasers operating in the visible and the infrared, it has been very difficult to identify the influence of any one factor and assess its specific role in the damage process. This stems from two main causes. First, it is generally impossible to isolate and vary a single factor without changing other influencing parameters. Secondly, due to the presence of synergistic effects, the role played by a given factor, such as surface roughness, will vary depending on other conditions of the material. From a standpoint purely of engineering and material utility, there is a genuine requirement for large area, defect free, homogeneous coatings. It is obvious from this year's symposium that the major controlling factors in coating damage resistance arise in the fabrication process. These include substrate preparation, ambient pressure, deposition technique, substrate finish, substrate temperature, geometrical arrangement, purity of starting material, selection of candidate materials, and rate of deposition. It is these factors which lead to specific film characteristics such as crystal structure, residual stress, defect concentration, uniformity, impurity concentration, scattering level, adhesion, etc. These are the observable properties to which the damage process must be related. Thus, there is considerable need for improved film characterization procedures so that these characteristics can be correlated with specifics of the fabrication process. In this way we may learn the influence of particular process factors in the specific film properties, such as impurity and defect concentration, and be better able to isolate the individual damage influencing factor such as stress, structure, etc. This program will require more application of advanced diagnostic techniques, such as Auger spectroscopy, LEED and Scanning Electron Microscopy, as well as the development or application of other more novel characterization techniques.

An area of increasing importance is metal mirror fabrication. Various techniques of fabrication, involving both coated and bare surfaces, are under investigation. It is to be expected that metal mirrors will show rapid improvement in damage resistance, because the subject is quite new. The current rate of improvement is impressive. As in other areas of damage studies however, empirical improvement often proceeds more rapidly than theoretical understanding. There is clearly a need for improved techniques of surface characterization, and the development of rapid scan, nondestructive test procedures. The elegant techniques available to determine surface roughness may form the basis for such instrumentation. At present, the exact relation between surface roughness and surface absorption remains to be elucidated. Additionally, there is some theoretical uncertainty in the relation between surface features and observed surface scattering.

There exists a large variety of physical probes to examine various features of surface structure. In order to gain a better understanding of what constitutes a "good" surface for high power laser use, very detailed characterization of surface conditions must be carried out. At a metal surface, for example, the damage threshold is seen to be sensitive to surface features on a scale of a few nm. This sensitivity is thought to be due to the influence of surface roughness on electron motion within the surface. A surface layer rich in defects or impurities would be expected to have a similar effect on the damage propensity of the material. The specific way that fabrication affects the surface layer, the detailed characterization of the surface layer, on the scale of electron motion as well as on the optical scale, and the consequent influence of surface properties or damage all need to be examined more carefully. It might be profitable, for example, to prepare a set of surface samples of controlled variation, by polishing with various grit sizes, for different periods of time, and so producing varying deposits of microfracture. These samples could then be polished to produce a smooth surface with varying degrees of subsurface structure. After testing, the smooth polished layer could be removed by etching to exposure the subsurface making it amendable to microscopic and other types of investigation. Alternately ground surfaces could be overcoated and a similar investigation carried out. This question of subsurface structure influences is probably the most significant area remaining to be addressed.

In the case of multilayer films, mechanical and thermal contact between film layers and at the substrate are also properties of overriding importance. The present preference for sputtered films over evaporated films may be a consequence of the substrate cleaning inherent in the sputtering process, and the better adhesion of sputtered films. Evaporated film techniques may be amendable to improvement in this regard.

It was reported at this conference that alkali halides grown by reactive atmosphere processing exhibit much higher damage thresholds than commercially available material. This improvement is amen- attributed to higher purity of the material. It was also reported that in RAP-grown material, not only were higher damage levels obtained, but that the relative levels of KCℓ and NaCℓ were reversed. This strongly suggests that impurities and defects play an important role mediating the onset of avalanche breakdown. It might be expected that currently quoted "intrinsic" damage strengths are actually amenable to improvement. There is still a need for developing a better understanding of damage processes, especially avalanche breakdown, from a detailed, solid-state theoretic point of view. The use of average electron properties is questionable, particularly in low-mobility materials, where the mean free path may be of the order of atomic dimensions.

Materials development and improvement continues to progress. The area of IR window materials is currently getting the major emphasis. There is substantial room for improvement in this area, as, for example, in the reduction of void concentration in ZnSe, the reduction of impurity absorption in a variety of materials, and the aforementioned improvement in alkali halide manufacture.

We can look forward to continuing development of materials for the UV and vacuum uv. Here the state-of-the-art is relatively primitive. The special problems of the uv, arising from the high probability of impurity ionization, the effect of two- and three-photon absorption, and the possibility of color center formation, remain to be enumerated fully and analyzed. Clearly, all of the problems of multilayer dielectric films and metal surfaces will carry over into the uv spectrum, with added complications.

As the understanding of various damage-related phenomena improves, and the capability of identifying relevant material parameters emerges, it becomes possible to formulate figures of merit for optical materials. An example of this is the analysis of thermal distortion in this proceedings. There is need for the identification, measurement, and tabulation of these figures of merit, for optical materials for high power lasers. The availability of this kind of information is, in fact, the ultimate goal of this symposium.

There is a growing appreciation of the importance of damage processes in designing large laser systems. Total system considerations must be taken into account in such a design. The interplay of material properties (as described by the figures of merit mentioned above), structural specifications, systems operating characteristics (beam quality, pulse length), and environmental factors comprise what we call synergistic effects. A material may exhibit a certain damage threshold under single pulse exposure, but respond quite differently when incorporated into a multi-pulse or CW system. The effect of flash-lamp irradiation on damage resistance can be important in pulsed solid-state lasers. Failure of one element may lead to the progressive failure of other, more expensive elements. There is evidence that when surface damage occurs, material may be splattered onto other parts of the surface, or even redeposited on adjacent surfaces, leading to damage on subsequent exposure. We must continue to emphasize that the ultimate use of laser materials is in laser systems, not solely in damage tests, and that the real environment must be considered in evaluating the material.

It seems clear that MIL-SPEC scratch and dig tests are of limited utility in specification of highly polished surfaces. The development of new surface specification standards, based on light scattering or FECO interferometry, is highly recommended, and would be an appropriate undertaking of the ASTM.

Finally, looking ahead to next year's symposium, we must seek to open up the discussion to new topics. The symposium attracts people interested in the interaction of intense light with optical materials, the development of new materials, and the design of high power laser systems. We are just beginning to emphasize system considerations. We have not addressed ourselves to the problems of fiber optics at all, to date. Our discussions of electro-optic materials have been very limited. These are a few of the directions in which the symposium might grow. The co-chairmen solicit and will welcome suggestions for new topic areas to be considered in the damage symposium in coming years.

4. Acknowledgement

We would like to acknowledge the invaluable assistance of Dr. Harold S. Boyne, Mrs. Pauline W. Smith, Mrs. Marjorie L. Wilson and Mrs. Florence M. Indorf of the National Bureau of Standards in Boulder, Colorado for their interest, support, and untiring efforts in the operation of this Symposium and in the preparation and publication of the proceedings. Also, we would like to take special note of Mrs Normal Lear and Mrs. Kay Jentsch, who added pleasurably to the conference operation particularly during the discussion periods following the formal presentations. The continued success of the Damage Symposia would not have been possible without their support.

5. Bibliography

[1] "Damage in Laser Glass", A. J. Glass and A. H. Guenther, Editors, ASTM Special Technical Publication 469, ASTM, Philadelphia, PA (1969).

[2] "Damage in Laser Materials", A. J. Glass and A. H. Guenther, Editors, NBS Special Publication 341, U. S. Government Printing Office, Washington, D.C. (1970).

[3] "Fundamentals of Damage in Laser Glass", N. Bloembergen, National Materials Advisory Board Publication NMAB-271, National Academy of Sciences, Washington, D.C. (1970).

[4] "Damage in Laser Materials: 1971", A. J. Glass and A. H. Guenther, Editors, NBS Special Publication 356, U. S. Government Printing Office, Washington, D.C. (1971).

[5] "High Power Infrared Laser Windows", N. Bloembergen, National Materials Advisory Board Publication NMAB-292, National Academy of Sciences, Washington, D.C. (1972).

[6] Proceedings of the Conference on High Power Infrared Laser Window Materials, (October 1971). C. S. Sahagian and C. A. Pitha, Editors, Special Report No. 127, Air Force Cambridge Research Laboratories, (1971).

[7] "Laser Induced Damage in Optical Materials: 1972", A. J. Glass and A. H. Guenther, Editors, NBS Special Publication 372, U. S. Government Printing Office, Washington, D.C. (1972).

[8] "Laser Induced Damage of Optical Elements, A Status Report", A. J. Glass and A. H. Guenther, Applied Optics 12, pp. 637-649 (1973).

[9] "Laser Induced Damage in Optical Materials: 1973", A. J. Glass and A. H. Guenther, Editors, NBS Special Publication 387, U. S. Government Printing Office, Washington, D.C. (1973).

[10] "Laser Induced Damage to Optical Materials, 1973: a Conference Report", A. J. Glass and A. H. Guenther, Applied Optics, 13, pp. 74-88 (1974).

A. J. Glass

A. H. Guenther

0.1 Opening Remarks

Alexander J. Glass

Lawrence Livermore Laboratory
P. O. Box 808
Livermore, California 94550

Speaking for Art Guenther and myself, I'd like to welcome you all to the Sixth Annual Symposium on Damage in Laser Materials. The National Bureau of Standards has again provided us with these superb accommodations, and has carried the burden of the preparation of the proceedings for this symposium over the years, and I want to reiterate the thanks that Haynes Lee has expressed to the Bureau, to the ASTM, and to ONR for their support in helping us carry out the work of the Symposium.

The organization of the meeting this year is the same as it has been in previous years, in that we have tried to group papers roughly according to subjects. We have a session this morning on damage and its consequences in glass systems, then we have a session that is devoted to basic theoretical investigations, and another on damage to crystals, particularly in nonlinear optical materials. Tomorrow, most of the day will be spent on a variety of papers on coatings, windows, and mirrors.

I think it is clear to everybody there are two fairly well delineated applications areas represented in these papers. One of them is short pulse, high peak power, essentially single shot lasers, mostly Neodymium glass for laser fusion. The other is high average power CW lasers for military and industrial application, which are primarily infrared lasers. In both areas very large systems are on line, or coming on line, depending on where you work. The topics that are being discussed here are not of purely academic interest. In the design of large systems it turns out that it is damage considerations that ultimately limit performance and dictate the design, and in many cases, determine the cost of the system. The cost sometimes becomes infinite, which means the system is infeasible. It is also true that because of the fact that the damage and the damage phenomena are the limiting factors, that real advances in the damage area lead to real benefits in terms of cost reduction, as well as in terms of improved system performance. Because of the fact that these are real problems that we are dealing with and real systems, you will find, in general that the subject seems to move ahead fairly quickly, and leaves behind it a number of fundamental investigations left undone. I think that it is typical of materials science and of applied science in general, that you learn how to deal with a problem long before you understand it, from the basis of first principles. The climate of applied science that exists in most places today is such that a lot of fascinating physics problems are going to be left behind. It is one of the minor regrets, but a necessary characteristic of this field, that we have to skip along the surface rather lightly, with the hope that someday, if people have sufficient motivation and there is a sufficiently hospitable climate to do so, some of these fascinating problems in materials science and in the interaction of high power light waves with quantum systems can be reviewed and dug into more deeply.

We take a very broad view of damage in the symposium. Many of the things we talk about don't really have to do with the catastrophic failure of materials but only, like small scale self focusing, with a reduction in the performance of the system. Along this line, we have a working definition of damage as being "whatever turns you off".

If you look at the schedule, you will find that there is nothing in it particularly associated with ultraviolet materials or ultraviolet systems. That is, not to say that damage problems don't exist in those systems. Even though ultraviolet lasers, excimer lasers, etc. operate at moderate powers in comparison to the IR and near visible systems, they are already damage limited. You even find people doing the calorimetry on ultraviolet lasers in terms of the damage to the coated elements. We know something about the damage mechanisms in the ultraviolet. We know that if one goes to short wavelengths one begins to get into circumstances in which two-photon absorption can become important in many materials. At the moment, my impression is that in the ultraviolet systems, extrinsic features such as impurities and imperfections in coatings are still dominant. We can look forward, however, as ultraviolet laser technology advances, to see more investigations in that area. We also have not, in any of the Damage Symposiums, addressed ourselves to synergistic problems that arise due to the influence of the environment on the elements of the system. This environmental influence alters the damage characteristics. Certainly, for military or industrial systems, one has a hostile environment consisting of dirt, sea water, or high altitude. A mirror or a coated surface which might bear up very well in the laboratory, may have an entirely different characteristic when it gets out into the working environment. The same is true of the high power, short pulse, Neodymium glass lasers for laser fusion. Ask yourself, what do 14 MeV neutrons do to reflecting surfaces, and do they retain their integrity and their reflecting properties at low absorption. I think that everyone working in laser fusion would be delighted to have that as a serious problem, but it is one that we undoubtedly will have to confront in future meetings of this kind.

1.1 Laser Beam Divergence and Damage in Glass Amplifiers

Keith A. Brueckner, Brian Guscott, Siebe Jorna,
Kent Moncur, and Larry Siebert

KMS Fusion, Inc.
Ann Arbor, Michigan 48106

The power limit in glass amplifiers is determined by the onset of non-acceptable beam distortion of self-focusing leading to glass damage, which results from the power-dependent index in the glass. Self-phase modulation due to the variation of index with power also can at very high power result in pulse distortion and gain loss. These effects can be analyzed quantitatively by integration of Maxwell's equations together with the equation for gain variation of the lasing medium. Under conditions of rapid intensity change, diffraction effects can be ignored and the eikonal equation used to determine beam propagation.

To study these problems for small amplitude disturbances we have analyzed the equations using dispersion theory. For larger amplitudes we have developed several computer codes which allow exact simulation of the laser system and of selected components which are essential for control of the beam intensity.

The intensity of the laser beam must be carefully controlled to avoid both large scale and small scale effects. The large scale effects which increase beam divergence result from the initial beam radial intensity variation combined with nonuniform gain in the laser amplifiers. The small scale effects usually result from diffraction and interference and can be minimized by reducing interference effects as far as possible. This can best be done by the use of graduated or "soft" apertures placed at critical points in the beam. The beam intensity profile can also be controlled by the use of attenuators with graduated transmission.

These techniques offer highly flexible and effective control of the laser beam and allow operation well above 5 GW/cm^2.

Key words: Apodizers; glass lasers; self-focusing.

1. Introduction

The power limit in glass amplifiers is determined by the onset of nonacceptable beam distortion or self-focusing leading to glass damage, which results from the power-dependent index in the glass. Self-phase modulation due to the variation of index with power also can, at very high power, result in pulse distortion and gain loss. These effects can be analyzed quantitatively by integration of Maxwell's equation, together with the equation for gain variation of the lasing medium. The integration of the electromagnetic wave equation can be simplified for small angular divergence. The relaxation processes in the lasing medium can be limited to transitions from the upper to the lower lasing level, for pulse lengths of a few nanoseconds or less. Under conditions of rapid intensity change, diffraction effects can be ignored and the eikonal equation used to determine beam propagation.

To study these problems for small amplitude disturbances, we have analyzed the equations using dispersion theory. For larger amplitudes, we have developed several computer codes which allow exact simulation of the laser system and of selected components which are essential for control of the beam intensity.

2. Self-Phase Modulation

The optical path-length in the lasing medium is

$$L_{opt} = \int n \, dz$$
$$= L\, n_0 + n_2 \int E^2 \, dz \tag{2.1}$$

For the present, ignoring the effects of gain saturation, beam nonuniformity, and beam divergence, the power variation in an amplifier rod is

$$E^2(z) = E^2(0) \exp Gz \tag{2.2}$$

with G the gain per unit length and $E^2(0)$ the field at the entrance to the rod. The variation of opitcal path-length with time shifts the frequency of the beam, with

$$\frac{\delta\omega}{\omega} = \frac{1}{c} \frac{\partial L_{opt}}{\partial t}. \tag{2.3}$$

Equation (2.1) then gives a wavelength shift per amplifier head of

$$\delta\lambda(\mathring{A}) \cong -2.81 \times 10^{-4} \frac{\partial P(GW/cm^2)}{\partial t(nsec)} G(cm^{-1}). \tag{2.4}$$

A typical gain is 0.064 cm^{-1}, corresponding in ED-2 glass to energy storage of 0.04 joules/cm^3. For a pulse rise time of 50 picoseconds, 5 amplifier heads at high power, and a peak power of 10 gigawatts/cm^2, equation (2.4) gives a shift of about 10 $\mathring{A}$, which is considerably less than the lasing line width. Thus, self-modulation can be avoided by reasonable choices of design parameters.

3. Large Scale Beam Divergence

The optical path-length change causes phase front distortion if the laser power is nonuniform. For small angular variations, the change in angle of the beam in a single amplifier is given by

$$\delta\theta(r) = \frac{\partial}{\partial r} \int_0^L d\ell n$$
$$= n_2 \frac{\partial}{\partial r} \int_0^L d\ell E^2(r,z). \tag{3.1}$$

We assume that the gain may be a function of r but not of z. Equation (3.1) then gives

$$\delta\theta(r) = \frac{4\pi n_0 n_2}{c} \frac{\partial}{\partial r} \left[P(r,z=0) \frac{(\exp G(r)L - 1)}{} \right]. \tag{3.2}$$

The angular variation of the beam can be compensated by a collimating lens provided that $\theta(r)$ varies linearly with r. We assume that the beam is collimated so that the divergence of the beam center is removed. We assume that $\exp G(r)L \gg I$ and use a typical value of $G(0) = 0.032$ for the gain at the rod center. We also neglect the variation of G(r) in the denominator of equation (3.2). The residual divergence then may be written

$$\delta\theta(r) - \delta\theta_0(r) =$$
$$= 2.64 \times 10^{-5} P_{GW}(\theta, z=L) \left\{ \frac{\partial}{\partial r} \frac{P(r,z=0)}{P(0,z=0)} \right.$$
$$\exp[G(r) - G(0)]L - r \left[\frac{\partial^2}{\partial r^2} \frac{P(r,z=0)}{P(0,z=0)} \right.$$
$$\left. \left. \exp[G(r) - G(0)L] \right]_{r=0} \right\}. \tag{3.3}$$

Equation (3.3) shows that the variation of gain with radius must be accurately compensated by the variation of the input beam, if residual divergences less than 10^{-4} radians is to be achieved for beam power in the range of 5 to 10 gigawatts.

4. Small Scale Beam Divergence and Damage

A laser beam may also undergo small scale self-focusing with resulting angular divergence. This effect is excited by small scale nonuniformities which are produced by diffraction effects or by index nonuniformities in the lasing medium.

In the gometric-optic approximation, the variation of the power in the beam is given by

$$\frac{\partial^2 P}{\partial z^2} = -\nabla_\perp \frac{P}{n} \nabla_\perp n. \tag{4.1}$$

The power dependence of n gives (for $n_2 E^2 << n_0$)

$$\frac{\partial^2 P}{\partial z^2} = \frac{-2\pi n_2}{c} \nabla_\perp^2 P^2. \tag{4.2}$$

Linearizing equation (4.2) for small variation of power P_1 gives

$$\frac{\partial^2 P_1}{\partial z^2} = \frac{-4\pi n_2}{c} P_0 \nabla_\perp^2 P_1. \tag{4.3}$$

The presence of diffraction adds to equation (4.1) the diffraction correction, valid for small angles of diffraction,

$$\left(\frac{\partial \delta P}{\partial z^2}\right)\text{diff} = \frac{1}{4K_L^2} (\nabla_\perp^2)^2 P \tag{4.4}$$

with $K_L = n_0 k_0$ and $\lambda_0 = 2\pi/k_0$ the laser vacuum wave number. Combining this with equation (4.3) gives the dispersion relation

$$k_z^2 = \frac{-4\pi n_2 P_0 k_x^2}{c} + \frac{k_x^4}{4k_L^2} \tag{4.5}$$

The growth rate is

$$P_1(z) = P_1(0) \exp \text{Im}\, k_z z. \tag{4.6}$$

The maximum growth is at

$$(k_x^2)_{max} = \frac{8\pi k_0^2 n_2 n_0^2 P_0}{c} \tag{4.7}$$

giving

$$\text{Im}k_z = \frac{4\pi n_2 n_0 k_0 P_0}{c} \tag{4.8}$$

At one micron wavelength, equation (4.7) and equation (4.8) give

$$(k_x)_{max} = 101 \text{ cm}^{-1} P_0(\text{GW})^{\frac{1}{2}}$$

$$\text{Im}k_z = 0.053 P_0(\text{GW}) \text{ cm}^{-1} \tag{4.9}$$

At a power of 5 gigawatts/cm^2, the e-folding length is only 3.8 centimeters, allowing for large growth in a typical path-length of 30-50 centimeters.

The growth of the instability also causes small angle divergence of the beam. The variation of angle with distance is given approximately by the eikonal equation.

$$\frac{d\theta}{dz} = \nabla_{\perp} n$$

$$= \frac{4\pi n_2}{c} \nabla_{\perp} P_1. \tag{4.10}$$

Thus,

$$|\theta(z)| \cong \frac{4\pi n_2}{c} \left|\frac{k_x}{k_z}\right| P_1(0) \exp |k_z| z \tag{4.11}$$

giving at the maximum growth

$$|\theta(z)|_{max} = \left(\frac{8\pi n_2}{cP_0}\right)^{\frac{1}{2}} P_1(0) \exp 0.053 P_0 (\text{GW}) z. \tag{4.12}$$

The linearization of equation (4.2) is valid only if the lateral displacement of the rays does not exceed the initial lateral structure of the perturbation P_1. This occurs when $\delta\theta dz \simeq k_x^{-1}$, at which point the angular deviation is

$$\theta(\Delta x = k_x^{-1}) = \left|\frac{k_z}{k_x}\right|. \tag{4.13}$$

At the maximum growth point,

$$\theta(\Delta x = k_x^{-1}) = \frac{2\pi n_2 P_0}{c} \frac{1}{2}$$

$$= 0.52 P_0 (\text{GW})^{\frac{1}{2}} \text{ milliradian.} \tag{4.14}$$

The growth reaches this amplitude when $2 P_1/P_0 \exp 0.53 P_0$ (GW) z is equal to unity. For an initial perturbation P_1/P_0 of 1% and a power of 5 gigawatts/cm^2, this occurs in 15 centimeters. The resulting angular deflection of about one milliradian can be a serious source of transverse energy loss from the beam.

The small scale self-focusing, which leads to angular divergence and hence of beam energy loss, also can cause glass damage. The self-focusing length is of the order of k_z^{-1} given in equation (4.5), with P_0 the power fluctuation which causes the self-focusing. Thus, a fluctuation of one gigawatt/cm^2 at the wavelength of maximum growth self-focuses in about 20 centimeters. The large increase of power then can cause breakdown and damage. The growth is less rapid for other wavelengths so that, in practice, damage appears to occur only for power fluctuations of 5 to 10 gigawatts/cm^2. The damage may also be prevented by lateral outscattering of energy from the self-focusing part of the beam. When this lateral outscattering of energy begins to occur, the laser beam changes from a sharp edged circular beam to a beam with a diffuse halo of energy around the outside of the gain energy. When this halo first begins to appear, there is no visible damage in the glass; however, microscopic damage may have already occurred. If the power density is increased, the halo becomes larger and the damage becomes visible in the form of small self-focusing tracks.

5. Intensity Control

The intensity of the laser beam must be carefully controlled to avoid both large scale and small scale effects. The large scale effects which increase beam divergence result from the initial beam radial intensity variation combined with nonuniform gain in the laser amplifiers. The small scale effects usually result from diffraction and interference and can be minimized by reducing interference effects as far as possible. This can best be done by the use of graduated or "soft" apertures placed at critical points in the beam. The beam intensity profile can also be controlled by the use of attenuators with graduated transmission.

The KMS Laser Amplifier System uses glass rods from 16 mm to 80 mm in diameter, then seven disc amplifiers with 100 mm clear aperture are used. Each disc amplifier has three glass slabs at Brewster's angle. In the design and use of optical components, we have extensively used our computer codes which solve Maxwell's equations for the propagation of the beam through the system. The code accurately determines the diffraction effects that are produced by the critical points of the system such as soft apertures.

A soft aperture with too sharp an attenuating edge will itself produce diffraction rings, while too gradual an attenuating edge wastes a large area of the rod; therefore, in the design of the soft apertures there is a trade-off between the area of the rod used and the diffraction pattern generated by the aperture. We have designed, tested and used several types of graduated apertures.

6. Film Apertures

Film apertures are inexpensive and easy to make, but are suitable only for low power application. The substrate the emulsion is on should be of good optical quality, and to avoid any phase front distortion by the emulsion, the aperture may be contained in an index matched liquid gate.

7. Variable Transmission Metal Layers on Glass

Metal layer apertures are more difficult and expensive to make than film apertures and can be used only in regions of low power density. The gold coated apertures we tested successfully attenuated the beam, but damaged at a lower power density level than the film apertures.

8. Dielectric Layers on Glass

Dielectric layers have a high damage threshold and can withstand 5 - 10 GW/cm^2. These work well as slowly graded attenuators to shape the intensity profile of the beam, but we have not been able to obtain any edges that are graded sharply and accurately enough to use as a graduated aperture in front of a rod and still effectively use most of the area of the rod.

9. Plano-spherical Lenses

Plano-spherical glass and quartz lens combinations have been used with index matched absorbing liquids for attenuation. Both saturable dye and non-saturable inorganic absorbers have been successfully used. These have worked very well as graduated apertures at all intensity levels. The major problem has been index matching the absorbing liquid to the glass of the lenses. Once the index match is obtained, the temperature must be regulated very closely.

We have also designed, but not fabricated, apodizers based on field dependent rotation on pockels cells and also an optical rotation in quartz.

Using these techniques, we have been able to operate the KMS laser well above 5 GW/cm^2 with a minimal amount of glass damage and a reduction in beam distortion.

COMMENTS ON PAPER BY BRUECKNER

The speaker noted that the beam divergence from the system is observed to be of the order of a few tenths of a milliradian at low power density, increasing significantly with power. He commented that without the use of apodized apertures and careful system design, up to 50% of the power of the beam is lost in the halo arising from small scale self focusing. With the use of apodized apertures, 80 to 90% of the energy can be maintained in the central beam.

1.2 Nonlinear Propagation Studies*

E. S. Bliss

Lawrence Livermore Laboratory
Livermore, California 94550

The desire to avoid damaging the components of high-power solid-state laser-systems being built for laser fusion experiments has led to increased interest in all aspects of intense pulse propagation. This paper describes a variety of observations of nonlinear propagation phenomena and the instrumentation used for measuring them, presents comparisons with theoretical predictions, and outlines some approaches to minimization of the resulting problems in large systems. The intent of the paper is to present an up-to-date summary of the progress being made in characterizing and controlling nonlinear propagation effects.

Key words: Apodization; beam breakup; instability theory; nonlinear propagation; propagation codes; self-focusing.

1. Introduction

The major problems of intense pulse propagation in a laser system are component damage and energy loss caused by whole-beam self-focusing, nonlinear enhancement of diffraction patterns, and beam instability with respect to small-scale intensity or phase irregularities. The development of a laser system producing 150 picosecond pulses with temporal and spatial noise of less than a few percent at 20 GW/cm^2 in a 7 mm diameter beam [1][1] has made it possible to perform new experiments in these areas. This paper discusses experimental and theoretical results and the implications for system optimization.

2. Whole Beam Self-Focusing

The self-focusing of all or part of an intense beam in solid state laser materials has been extensively studied both experimentally and theoretically [2]. The experiments, with an occasional exception [3], have consisted of observing the damage resulting from self-focusing, but it is possible with pulses having a smooth enough intensity profile to observe and measure the self-focusing of fairly large beams nondestructively.

One way to do this is to pass a collimated beam through a sample rod and observe the reduction in beam size that occurs several meters away. For comparison, a small fraction of the same pulse can be sent to the film over the same path length but without going through the rod. A representative result of such an experiment is shown in Figure 1. The multiple exposure-level photographs clearly show both an increased on-axis intensity and a reduction in diameter for the part of the beam which went through the sample. As expected [4], some distortion of the beam shape also occurs.

The beam photographs of Figure 1 are a time-integrated record of a dynamic process in which the focusing properties of the sample rod vary continuously during the pulse as the intensity varies from zero to its peak value and back to zero again. When the film is replaced by a 10-picosecond-resolution streaking-camera, the whole process can be time resolved as illustrated in Figure 2.

---

*This work was performed under the auspices of the United States Atomic Energy Commission.

[1]Figures in brackets indicate the literature references at the end of this paper.

In a large solid-state laser-system, dynamic whole-beam self-focusing occurs in every component. The details of the resulting distortion depend on the initial beam profile and virtually every other system parameter. These facts make meaningful system optimization strongly dependent on the ability to accurately compute the effects of parameter changes, so that only the most promising configurations need actually be tried. Using this kind of experimentally-verified computer-modeling combined with a knowledge of state-of-the-art capabilities in the production of such beam correcting elements as phase plates and apodizers, one can optimize a large system for a particular well-defined application.

Since self-focusing is a consequence of an intensity-dependent refractive index, the most fundamental observation one can make is an interferometric measurement of the refractive index change as a function of intensity. Figure 3 is a photograph of the time-resolved Mach-Zehnder interferometer used to obtain such measurements on samples of laser glass, Yag, and Faraday rotator glasses. The interferometer is adjusted to give a pattern of vertical fringes centered on the horizontal slit of the streaking camera, and index changes occurring in one arm of the interferometer but not in the other cause the fringes to move horizontally across the slit. The splitter reflectivities in the interferometer are chosen so that 99% of the pulse energy goes through the sample arm and only 1% through the reference arm. This guarantees that index changes in the reference arm are negligible even though it also contains a rod of the sample material for convenience in alignment. From the streaking-camera photographs one can plot the fringe shift, and therefore the index change in the sample, as a function of both time and position. Figure 4 is an example of the results.

The data obtained in any of these self-focusing experiments can be used to determine the nonlinear refractive index coefficient of the sample material. In fact, this was the main motivation for doing them, and we now know the value of n_2 for the materials being used in our large glass laser systems [5]. Similar measurements on a second group of materials have also been completed [6].

3. Diffraction Pattern Enhancement

Any laser system has limiting apertures which will generate diffraction patterns on the beam if light is allowed to hit them. Continuing to propagate such a beam through glass at high intensity leads to the familiar result [7]: the rings self-focus and damage the glass. To control the formation of diffraction patterns, the limiting aperture or apertures must exhibit a smooth transition from high to low transmission. A variable-thickness dye-cell such as shown in Figure 5 is a particularly simple version of such a graded aperture or apodizer, and we have used this type in one of our systems since late 1972 [8]. Other kinds of apodizers are now in use or under development as discussed elsewhere [9-14].

Of course, "smoothness" is not the only constraint on the transmission function of an apodized aperture. If the apodized beam has anything but a Gaussian radial-intensity-profile, there will always be a tendency for rings to form after a sufficient propagation distance; so a careful compromise has to be made between the desire to uniformly fill the system aperture for maximum energy extraction and the need to avoid damage caused by diffraction ring enhancement.

The importance of choosing the proper apodizing function for optimum propagation is illustrated in Figure 6. These results of calculations with a propagation code containing both diffraction and an intensity dependent refractive index [15] show that a slight increase in the steepness of the profile can cause a dramatic change in the generation and subsequent growth of diffraction features as an intense beam propagates through a disk amplifier chain [16]. Laboratory experience with various apodizing functions confirms this prediction.

4. Small-Scale Beam Instabilities

Everyone who has worked with large solid-state lasers is familiar with the highly structured beams and finely tracked rods or disks that can result from intense pulse propagation. Figure 7 shows how dramatically the beam profile can change in passing through a single glass rod. The growth of such structure from an input beam containing various degrees of modulation has been described by several forms of linearized instability theory and observed experimentally by a number of workers [17-26].

In an experiment aimed at obtaining a more detailed comparison between experiment and theory, we have propagated pulses with measured temporal profiles and well-characterized spatial-modulation through a glass rod at known intensities. The spatial structure is generated by passing the beam

through a shear plate composed of the inner surfaces of two closely-spaced quartz wedges. When the plates are at a small angle to each other, the interference between the main beam and the first forward reflected beam produces a sinusoidal intensity modulation in one dimension.

The simplest form of instability theory [17,21] predicts that small-scale noise grows exponentially with a gain coefficient having a maximum as a function of spatial frequency as shown in Figure 8. For wave numbers near the peak of this curve we do experimentally observe pronounced growth of the modulation as seen in Figure 9, but departures from this theory exceed the experimental error. A form of linearized instability theory which specifically treats the growth of shear plate type modulation does agree with the experiments, however, and a complete discussion of the results appears elsewhere [27,28]. The conclusion is that the growth of small-scale structure in a single rod is well understood.

Determining what happens when disks are substituted for the rod is more complicated both theoretically and experimentally. A qualitative difference between the two cases is observed when a 20 GW/cm^2 beam which has passed through 10 disks with a glass propagation distance of 24 cm is compared with the same beam after passing through a 24 cm long rod. From the representative beam photos in Figure 10 it is apparent that the dominant structure out of the rod is of a higher spatial frequency than that out of the disks.

The reason for this difference is shown schematically in Figure 11. For the beam as a whole, each disk acts as a very weak self-focusing lens and the effect of a series of disks is to reduce the beam size. For some smaller-scale beam irregularity of intensity height ΔI, the focusing effect of each disk is just cancelled by the tendency for the irregularity to diffract. Finally for very small-scale structure with the same ΔI, diffraction overcomes the self-focusing and the irregularities diffract away. To obtain quantitative information which can more readily be compared to computer calculations, a new experiment is being conducted. A single one-dimensional bump is superimposed on an otherwise smooth beam and propagated through a rod or an equivalent number of disks. The growth rate for the bump can then be measured as a function of its width for both rods and disks.

The glass damage caused by extreme beam breakup is an important concern in the design of large laser systems, but it is not automatically the over-riding one, since under some circumstances a frequent glass replacement program may be justified. The more fundamental concern is how the beam behaves after developing so much small-scale structure.

In an early experiment the ratio of the energy reaching a distant calorimeter to that reaching a nearby calorimeter after propagating through a rod was plotted against the input energy density. The result, shown in Figure 12, suggests that at high intensities some light is scattered into angles outside the aperture of the distant calorimeter. We are presently investigating the far field energy distribution of beams which have suffered various degrees of breakup to determine its effect on one's ability to focus the beam as a whole, because in the final analysis, optimizing a large system for laser fusion experiments will require maximizing the energy which can be focused through a target-size hole.

5. References

[1] Speck, D. R. and Bliss, E. S., Lawrence Livermore Laboratory Laser-Fusion Program Semiannual Report - January-June 1973, UCRL-50021-73-1, pp. 20-22. Available from the National Technical Information Center.

[2] See, for example, the proceedings of this symposium for the previous five years.

[3] Newman, B. E. and DeShazer, L. G., Proc. 3rd ASTM Symp. Damage in Laser Materials, NBS Spec. Publ. 356, 124 (1971).

[4] Dawes, E. L. and Marburger, J. H., Phys. Rev. 179, 862 (1969).

[5] Bliss, E. S., Speck, D. R. and Simmons,W.W., to be submitted for publication (1974).

[6] Moran, M. J., She, C. Y. and Carman, R. L., to be submitted for publication (1974).

[7] Fleck, J. A. and Layne, C., Appl. Phys. Lett. 22, 467 (1973).

[8] Speck, D. R. and Bliss, E. S., Lawrence Livermore Laboratory Laser-Fusion Program Semiannual Report - July-December 1972, UCRL-50021-72-2, pp. 18-19.

[9] Johnson, B. C., Lawrence Livermore Laboratory Laser-Fusion Program Semiannual Report - January-June 1973, UCRL-50021-73-1, pp. 29-31.

[10] Simmons, W. W., Leppelmeier, G. W. and Johnson, B. C., Appl. Optics, to be published (1974).

[11] Johnson, B. C. and Bliss, E. S., Lawrence Livermore Laboratory Laser-Fusion Program Semiannual Report - July-December 1973, UCRL-50021-73-2 (in press).

[12] Brueckner, K. A., Guscott, B., Jorna, S., Moncur, K. and Siebert, L., elsewhere in these proceedings.

[13] Campillo, A. J. Carpenter, B., Newman, B. E. and Shapiro, S. L., Optics Communications, to be published (1974).

[14] Costich, V. R. and Johnson, B. C., Laser Focus, to be published (1974).

[15] Fleck, J. A., J. of Computational Physics, to be published (1974).

[16] Morris, J. R., unpublished (1974).

[17] Bespalov, V. I. and Talanov, V. I., JETP Letters 3, 307 (1966).

[18] Chiao, R. Y., Kelley, P. L. and Garmire, E., Phys. Rev. Letters 17, 1158 (1966).

[19] Carman, R. L., Chiao, R. Y. and Kelley, P.L., Phys. Rev. Letters 17, 1281 (1966).

[20] Akhmanov, S. A., Khokhlov, R. V. and Sukhorukov, A. P., in Laser Handbook, ed. F. T. Arecchi and E. O. Schulz-DuBoi (North Holland, 1972), p. 1168.

[21] Glass, A. J., Proc. 5th Symp. Laser Induced Damage in Optical Materials, NBS Spec. Pub. 387, 36 (1973).

[22] Suydam, B. R., Proc. 5th Symp. Laser Induced Damage in Optical Materials, NBS Spec. Pub. 387, 42 (1973).

[23] Marburger, J., Jokippi, R., Glass, A. and Trenholme, J., Proc. 5th Symp. Laser Induced Damage in Optical Materials, NBS Spec. Pub. 387, 49 (1973).

[24] Campillo, A. J., Shapiro, S. L. and Suydam, B. R., Appl. Phys. Letters 23, 628 (1973).

[25] Jokippi, J. R. and Marburger, J., Appl. Phys. Letters 23, 696 (1973).

[26] Campillo, A. J., Shapiro, S. L. and Suydam, B. R., Appl. Phys. Letters 24, 178 (1974).

[27] Bliss, E. S., Speck, D. R., Holzrichter, J.F., Erkkila, J. H. and Glass, A. J., submitted for publication (1974).

[28] Erkkila, J., Bliss, E. S. and Glass, A. J., unpublished (1974).

6. Figures

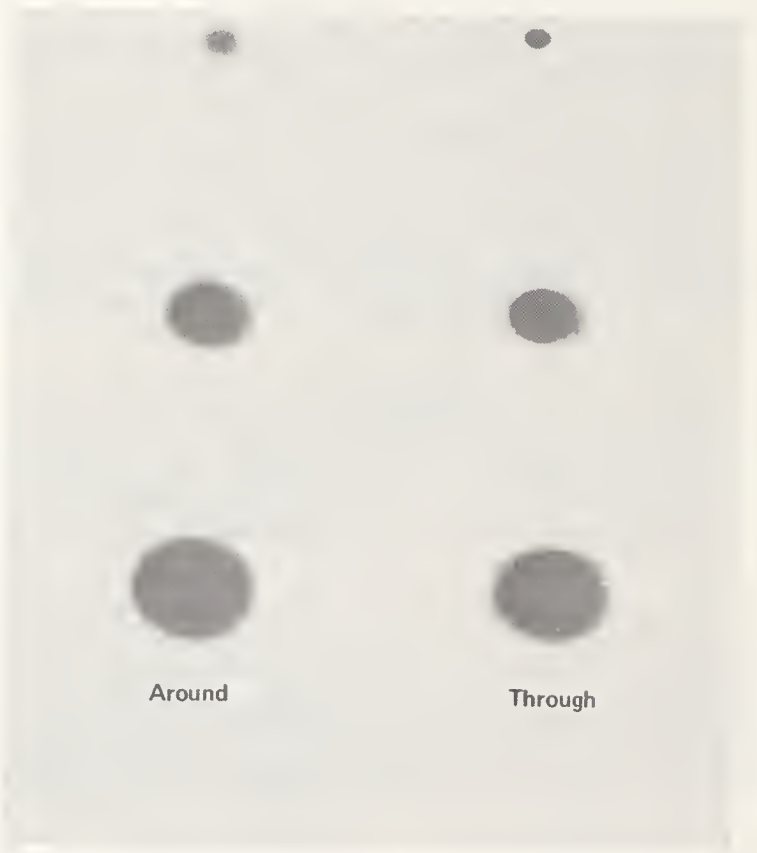

Figure 1. Photograph showing self-focusing of an approximately 7 mm diameter, 150 picosecond pulse with a peak intensity of 2.5 GW/cm^2 by a 50 cm long glass rod at a distance of 7 meters.

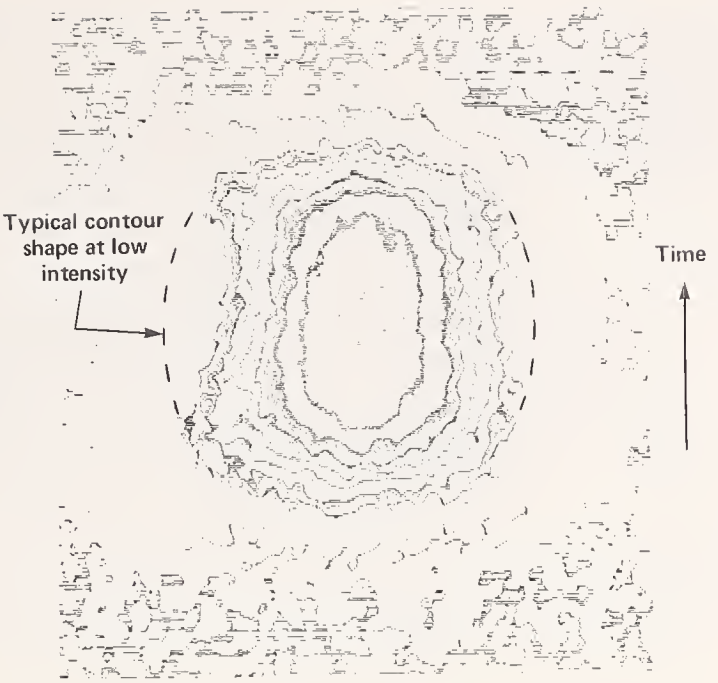

Figure 2. Isodensity contours of a streaking camera photograph showing the temporal dependence of the diameter of a self-focused beam.

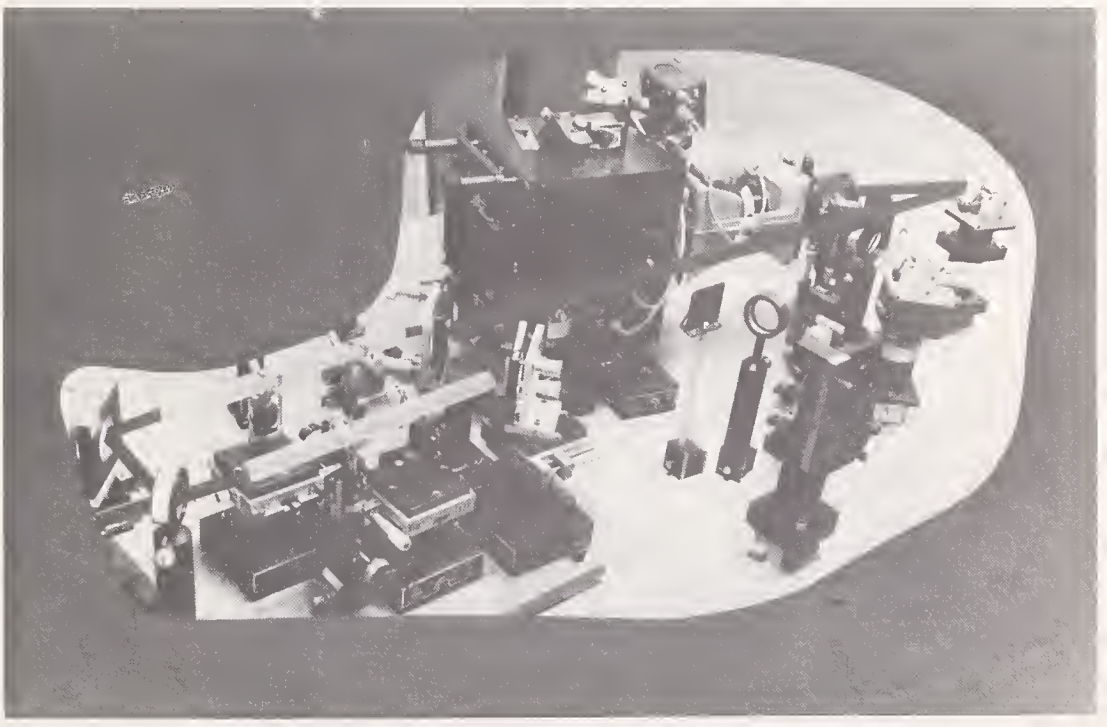

Figure 3. Time-resolved Mach-Zehnder interferometer for observing the intensity dependent refractive index change caused by intense laser pulses in transparent materials. The components positioned off of the main beam lines are on secondary beams used for streak camera triggering and for monitoring the temporal variation of the input pulse.

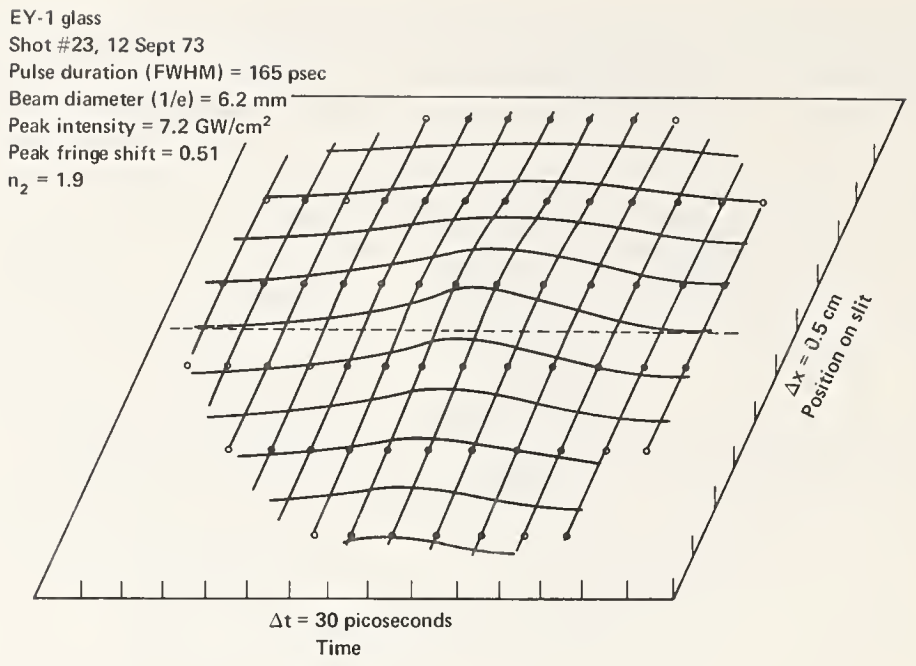

Figure 4. A representative plot of fringe shift (vertical axis) versus time and position on the slit from data obtained on the time-resolved Mach-Zehnder interferometer.

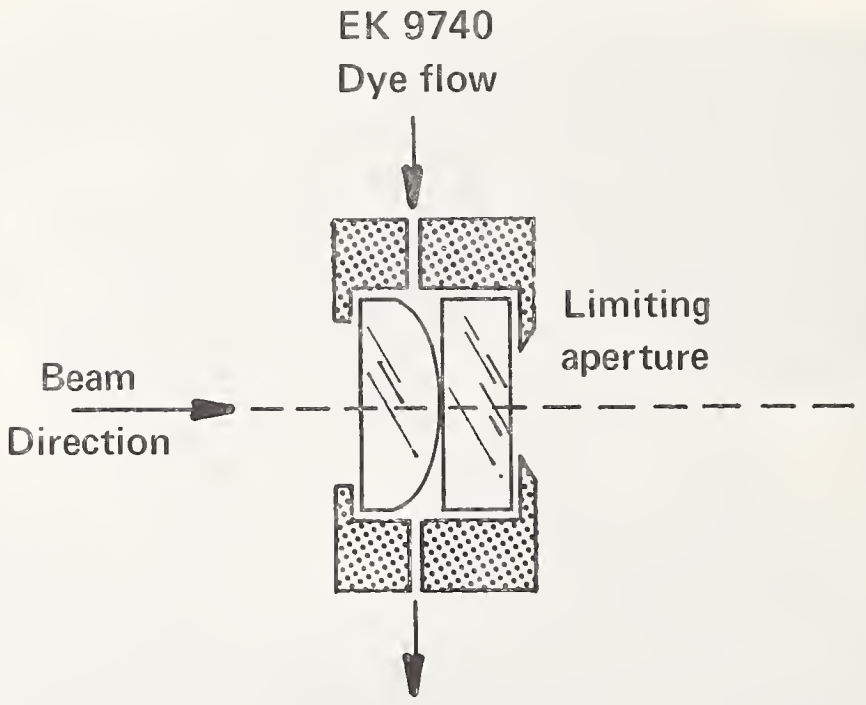

Figure 5. Variable thickness dye apodizer. Some versions use two curved windows and have slight curvatures on the outer surfaces as well to correct for index mismatch between the dye and window material.

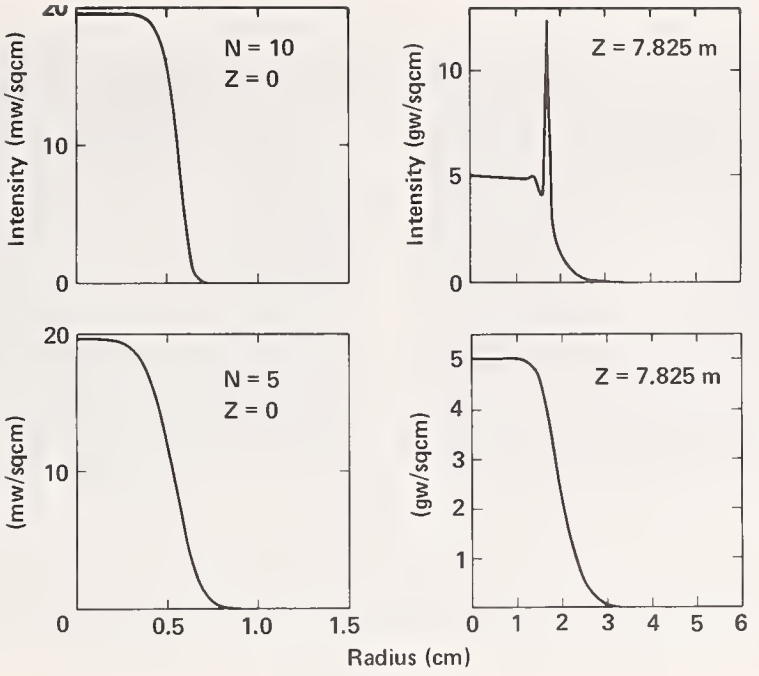

Figure 6. Propagation calculations for two intensity profiles of the form $I_o exp(-r/a)^N$. The left-hand curves are the input profiles for N = 5 and 10. The right-hand curves are the developing beam-shapes after propagating 7.8 meters at design intensities into the LLL developmental glass amplifier chain.

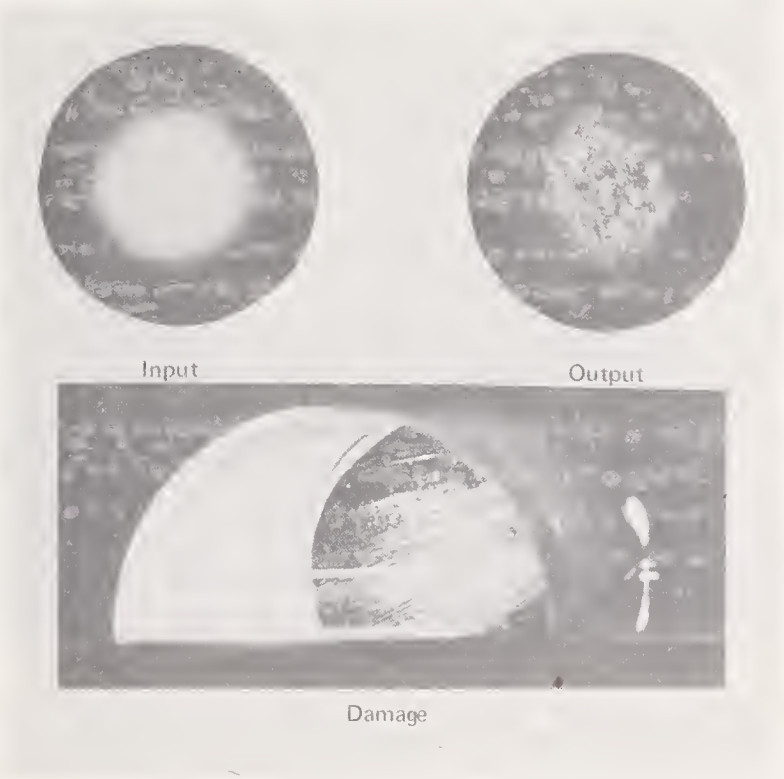

Figure 7. Small scale beam breakup at 20 GW/cm^2 in an unpumped 24 cm long glass rod. The photograph at the bottom shows the type of filamentary damage which results.

564-378 O - 74 - 3

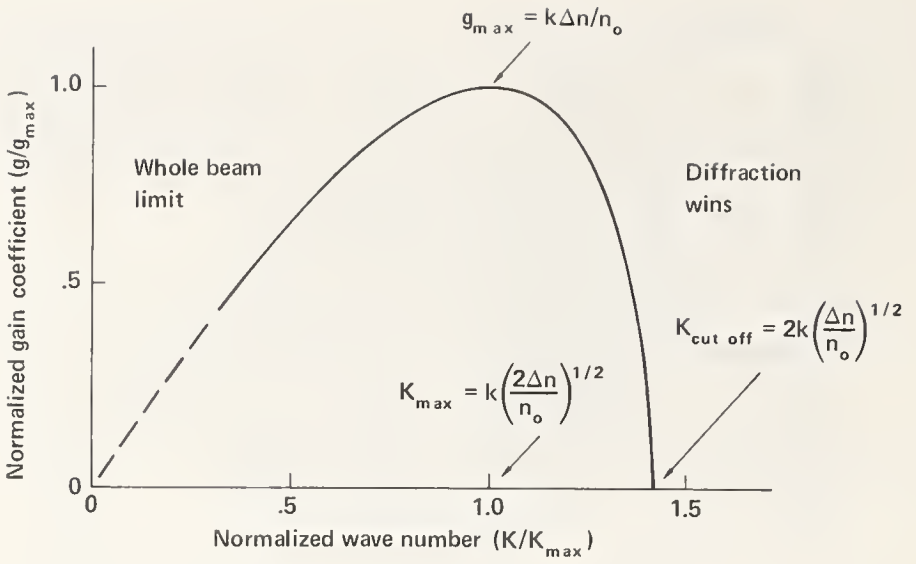

Figure 8. The variation of the exponential gain coefficient for the growth of small-scale intensity modulations as a function of modulation wave number as predicted by the simplest form of linearized instability theory.

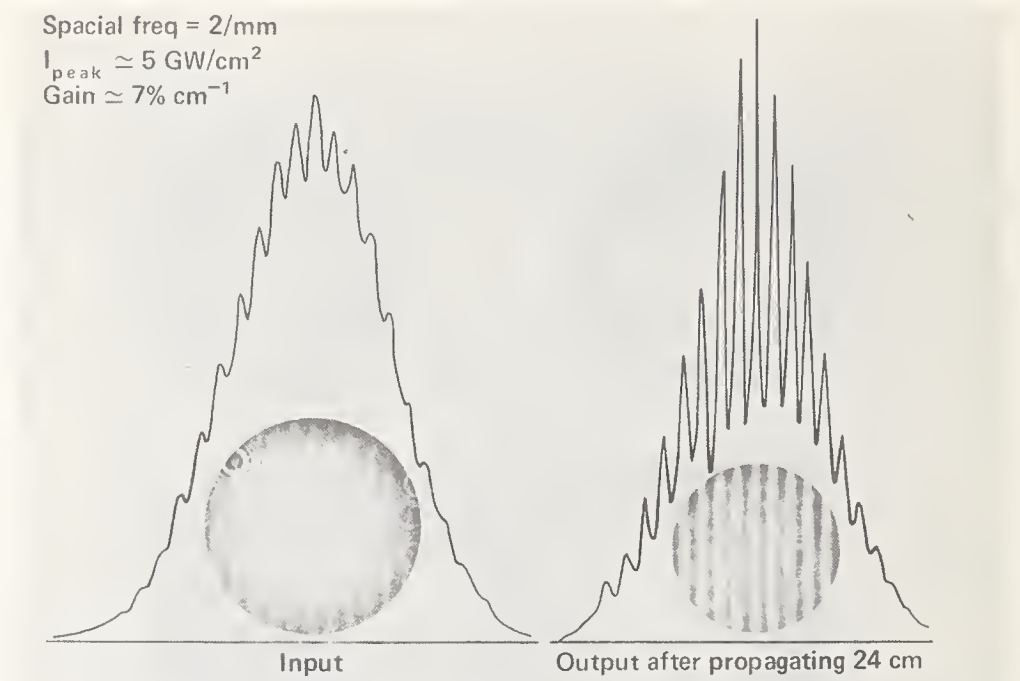

Figure 9. Beam photographs and densitometer scans showing the growth of shear-plate interference fringes spaced 2 mm apart (K = 119 cm^{-1}) on a pulse with a peak intensity of 5 GW/cm^2.

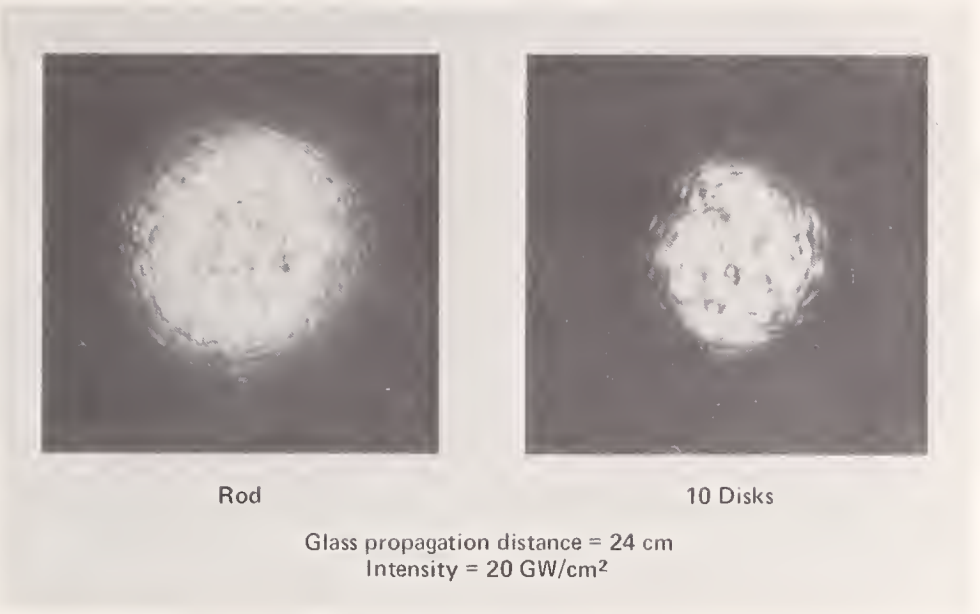

Figure 10. Comparison of the beam breakup caused by propagation through a rod with that caused by propagation through a series of disks.

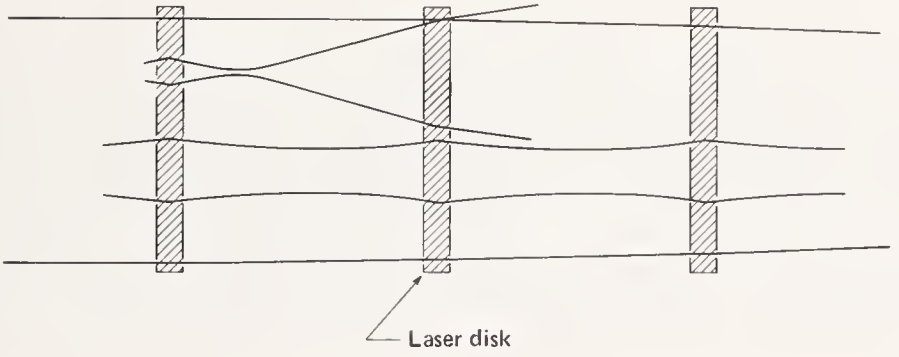

Figure 11. Schematic drawing of the behavior of various bumps when propagating through a series of disks.

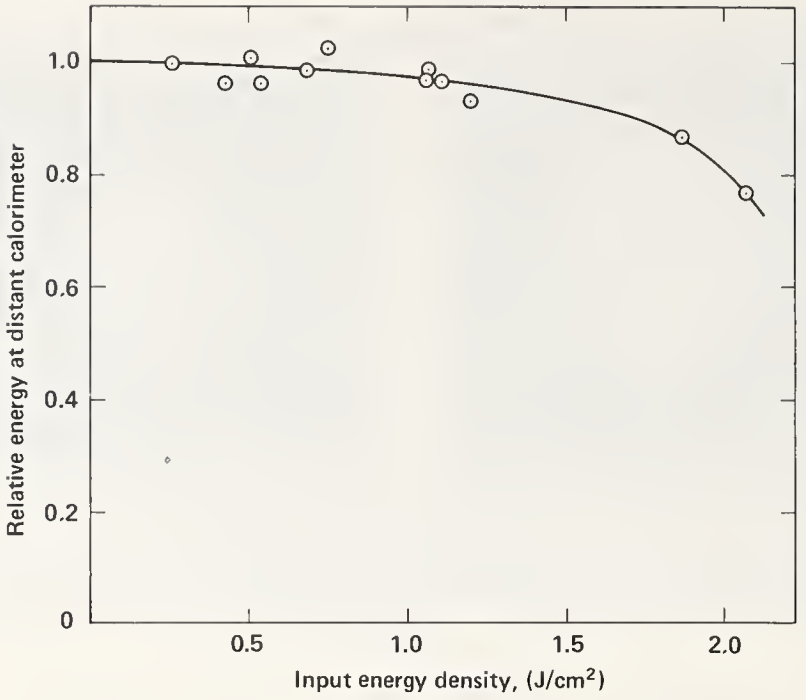

Figure 12. Energy collection at a distant calorimeter as a function of input energy density. For this plot "relative energy" is defined as that fraction of the energy exiting the rod which is still within the fixed 1.6 cm aperture of the calorimeter after propagating 6 meters.

COMMENTS ON PAPER BY BLISS

A number of points regarding the experimental setup used in the work described in this paper were clarified. The question was asked regarding the use of saturable dyes in the dye apolizers. The speaker commented that generally saturable dyes were used, but under the circumstances in which they responded in a linear fashion. With regard to the analysis of the experiment on the growth of the small self focusing, the importance of treating the initial conditions of the problem realistically, that is say, of reproducing in the analysis the relative phase of the intensity and phase modulation introduced at the entrance face of the glass sample by the shearing plate interferometer was emphasized. It was pointed out that the introduction of the appropriate initial conditions led to extremely good agreement between calculation and theory and that the analytic model was further substantiated by detailed numerical computation.

1.3 Suppression of Parasitic Oscillation In Laser Rod Amplifiers

J. M. McMahon, R. P. Burns and T. H. DeRieux

Naval Research Laboratory
Washington, D. C.

The most common glass laser rod amplifier geometry is one in which the laser rod is centered in a glass water jacket and pumped by Xenon flashlamps surrounding the water jacket. By suppressing parasitic modes in the amplifier much higher gains can be realized than previously achieved with a consequent increase in the short pulse damage threshold. 30-50% improvements have been attained in the NRL system and factor of two improvements are possible.

Key words: Disc lasers; laser amplifiers; laser design; parasitic suppression.

1. Introduction

The generation of intense subnanosecond laser pulses is required for laser fusion and related applications. Total energies in the kilojoule range and subnanosecond pulse require laser systems capable of operating routinely at intensities above 10^{10} W/cm^2. For neodymium glass laser systems nonlinear effects severely impact the ability to generate such peak powers with high system reliability and efficiency. The breakup of the laser beam into filamentary regions with consequent damage to laser components has been studied extensively in recent years as this represents the major limitation for high peak power laser design. Marberger has pointed out that the dominant effect is not beam collapse (self focusing of the entire beam) but the self focusing of intensity fluctuations on the beam which can have a much lower threshold than whole beam self-focusing. [1][1] Suydam has extended this analysis to laser amplifiers and finds that the gain coefficient for the growth of intensity fluctuations at the most unstable ripple frequency will be ~.73 of that given by Marburger's analysis for passive propagation since the intensity varies in the amplifier. [2] More importantly, he found that the safe operating level will vary directly as the gain coefficient α (for amplifiers where saturation is not present). Experiments at NRL & LLL are in reasonable agreement with these results.

Apodization techniques have resulted in improved laser performances by minimizing the spatial frequency "noise" (ripple) on the pulse but these cannot totally eliminate the problem since index inhomogeneities will always be present to some degree and will constitute a spatial noise source.[3,4,5] It is more appropriate to attempt to suppress beam breakup by increasing the gain coefficient per unit length since this will directly tradeoff with safe intensity.

Disc amplifiers offer distinct advantages at large aperture diameters over rod amplifiers, as there is no surface area to volume ratio constraint on the optical pumping. [6] Parasitic oscillation problems have been extensively investigated and adequate solutions appear in hand for practical systems. [7,8,9] On the other hand, the many surfaces in a disc amplifier present a maintenance problem and we have observed some indications of flashlamp induced damage to disc surfaces.

Rod amplifiers offer a number of significant advantages where they can be used. There is no surface problem, the pumping efficiency is much higher and it is a much cheaper geometry to construct. There have been reports in the literature of transient losses under very hard pumping, [10,11] as well as results showing a very fast roll off in the gain coefficient as the pump energy is increased. [12] Because of the possibly large benefit in high gain large aperture rods over moderate aperture disc amplifiers we decided to investigate the reasons for the reported behavior of rod amplifiers.

The CGE rod amplifiers provide a convenient test vehicle for this investigation as all the flashlamp pumping modules are identical and successive amplifiers have twice the beam area while the radius-neodymium doping product is held constant. This allows intercomparison of optical pumping efficiencies as well as giving different radial and axial gain aspect ratios (α D vs αL).

A further experiment was to retrofit the 64 mm laser head with a 44 mm aperture disc laser structure (shown in figure 1). This allowed a direct measure of the variation of gain with pump energy in a case where parasitics were stabilized and also allowed a direct intercomparison of the relative coupling efficiency to disc and rod structures. It was found that there was no fast roll off in the gain coefficient but rather that it increased as expected from earlier results of the ZAP

1. Figures in brackets indicate the literature references at the end of this paper.

optical pumping code. [9,13] It was further found that the pump geometry coupled three times more efficiently to the 64 mm rod than to the disc structure.

The disc laser results allowed us to predict the relative gain coefficient vs. pump energy for the 45, 32 and 23 mm amplifier rods. All three amplifiers were found to depart from the predicted values above $\alpha D = 0.19$. This factor strongly argued against a flashlamp induced loss coefficient as the cause of the rollover. The gain dependence argued that it was a parasitic oscillation dependence and the fact that αD and not αL was the relevant parameter argued that it was a radial parasitic rather than a longitudinal parasitic mode.

The pumping geometry for the three CGE amplifiers offers several possible parasitic paths. One radial mode (henceforth designated mode #1) has a ray path where the ray bounces around the rod at the critical angle. For the indices of refraction of ED-2 and water this ray can only run in the outer periphery of the amplifier ($R_m > (\sqrt{3}/2)R$; however scattering of some of the energy off the roughened sidewall into the center of the rod would deplete the gain. A second radial mode consists of light reflecting at the critical angle from the interface between the water jacket and air (Mode #2). There are two analogous longitudinal modes (Modes #3 and 4).

2. Suppression of Lowest Order Parasitic Mode

The approach attempted to suppressing the lowest order parasitic was to dope the water with Samarium salts to increase the index of refraction. The high 1.06μm absorption of the solutions employed would suppress modes involving long parasitic ray paths in the water jacket (Modes No. 2 and 4).

We can calculate a threshold condition for Mode No. 1 by noting that the mode will bounce off the sidewall m times per transit at the critical angle with some loss to scattering each bounce, hence

$$S\alpha_\tau = m \ell n R \tag{1}$$

Where S is the path around the rod ($\sim \pi D$) and α_τ is the gain value where the mode exceeds threshold (the gain at the periphery is 1.2 the central gain in these amplifiers). We can also calculate the number of bounces as a function of index mismatch as

$$m = \left[1 + \frac{180}{90\text{-}\arcsin(1-\epsilon)}\right] \tag{2}$$

where $\epsilon = \Delta n/no$.

For water in the jacket eqs. 1 and 2 give R = 91% which implies R_s = 9%. The Samarium solutions were then used to raise the index to n = 1.46 in several steps. The pumping efficiency was not affected by the Samarium solution. Figure 2 shows the variation in threshold vs. index mismatch. The fit to the calculation is quite good and implies that it is indeed mode #1 which first exceeds threshold. Figure 3 shows the improvement in the 45 mm amplifier. Further it can be inferred that with a solution with an index of 1.50 the CGE amplifiers would be stabilized ($\alpha D \leq .37$).

3. Results with High Index Solutions

The index of the Samarium solutions could not be increased above n=1.46 before the Samarium began to precipitate out at 20°C. Solutions of Zinc Chloride and Zinc Bromide were investigated.[14] Figure 4 shows the index of refraction vs. concentration for both the zinc and samarium solutions. $ZnCl_2$ solutions could be stably obtained with an index of 1.53 as determined by a minimum deviation prism technique.[14,15] While the $ZnBr_2$ solutions had higher indices of refraction, they were highly absorbing in the laser pump bands. The zinc chloride solutions were measured on a CARY 14 and found to be quite transparent in the neodymium pump bands. Experiments in the laser heads with zinc chloride solutions showed that optical pumping produced an undesirable chemical change. $Zn(OH)_2$, which is a white insoluble compound, was formed in a few shots. This reaction was prevented by adding 3-5% HCl to the solution.

Initially a $ZnCl_2$ solution with an index of 1.50 was tried in the 32 mm amplifier. It was found to perform almost as poorly as the same amplifier with water alone in the jacket. Some samarium chloride was added to the solution. There was a dramatic improvement. Figure 5 shows the results with the 32 mm amplifier with the various solutions.

Factor of two improvements in the gain (23% increase in α) were found with the best solutions compared to water cladding. However, it was clear that a parasitic involving paths in the water

jacket was also happening. The increase in gain when samarium was added to the water jacket corresponded to stabilization of the radial water jacket mode.

The only remaining possible parasitic mode corresponds to a longitudinal oscillation involving the rod faces, sidewalls and water jacket. To test for this mode, one end of the 23 mm rod was anti-reflection coated ($R \simeq .01$). As shown in figure 6, the gain curve followed the predicted curve almost all the way to peak energy. The roll off was due to the single AR coating being insufficient to avoid oscillation at the highest gains. With better AR coating(s) this mode would have been completely suppressed. The fact that the curve exceeds the predicted values is due to improved coupling between rod and lamps and is also an area where large increases in the gain coefficient may be possible. With the solution with an index of 1.52 and anti-reflection coatings the gain coefficients of the 23 and 32 mm CGE amplifiers can be increased by 47% and 55% respectively. The gain of the 45 mm amplifier is pump energy limited but it can be increased by 40%.

4. Pumping Efficiency of CGE Rod Amplifiers

It was found that while the achieved gain coefficient α varied as R^{-1} the pumping efficiency improved a great deal for the larger amplifiers. This fact was found to have a geometrical interpretation in the coupling of pump light to the water jacket. In this geometry the water jacket should be 1.33 times the rod diameter to image the rod as the full jacket diameter. This is in fact not quite the case with the CGE amplifiers as is shown in table 1. The optimum diameter is listed as D*. D_L is the center line diameter of the helical flashlamps.

Table 1.

Amplifier	Rod Dia.	Jacket Dia.	D*	Lamp Dia. (D_L)
V23A2	23 mm	36 mm	30.6 mm	53 mm
V32A4	32 mm	46.5 mm	42.6 mm	62 mm
V45A4	45 mm	58 mm	60 mm	75 mm

A comparison of the relative transfer efficiencies of the amplifiers shows that it scales as $(D^*/D_L)^2$ (figure 7). With the higher index solutions D* increases and a geometrical improvement in pumping efficiency of 23% for the 23 mm head and 19% for the 32 mm head would be expected if there were no additional absorption by the dopants in the water. With the samarium solutions, the efficiency stayed the same as samarium was added, indicating that the blue absorption of the samarium was sufficient to offset the geometrical improvement. The amount of samarium chloride in the high index zinc solutions was decreased to 5gm/100 ml (which was still sufficient to stabilize mode #2) and both the 23 and 32 mm amplifiers showed ~ 12% increases in pumping efficiency. This indicates that there was an 8-10% loss due to the solution which was more than counter-balanced by improvements in the geometrical coupling. Table 2 lists the initial and final results for the on axis gain coefficient for the three CGE amplifiers.

Table 2.

Amplifier	$(\alpha\ell)_o$	$(\alpha\ell)_F$
V23A2	2.9	4.25
V32A4	3.3	5.1
V45A4	2.25	3.10

With helical pumping in the CGE heads and parasitic suppression values of $\alpha D \sim 3.6$-3.8 can be attained. This does not represent the ultimate which can be achieved. With a zinc solution with an index of 1.53; an $\alpha D = 6$ can be attained without parasitic oscillation problems.

With close coupled linear flashlamp arrays values of αD in this range can be attained. Use of a pump geometry similar to the linearly pumped NRL disc amplifier would allow pumping to an $.65 < \alpha D < 0.7$. The results achieved at Rochester on a 9 cm amplifier are consistent with a pump limited $\alpha D \leq .7$ if it is noted that the water jacket parasitic is evident in their data beginning at $\alpha D \sim .19$ (figure 8). With state of the art pumping geometries energy storage efficiencies of $\simeq 2\%$ (at $\alpha D = .6$) appear realistic.

5. Summary

1. The dominant gain limitation in glass rod amplifiers is parasitic oscillation. By use of available index matching solutions the lowest threshold mode can be stabilized for $\alpha D \leq 0.6$.

2. The next lowest threshold mode involves reflection from the rod ends and can be suppressed in any one of a number of ways.

3. With helically pumped CGE amplifiers it has proven possible to increase the gain coefficient by 30-50% using solutions which are stable in the laser head.

4. With optimized linear pumping geometries it should be possible to achieve $\alpha D = 0.6$. From small scale self focusing theory and experiments this should result in a safe output power density from 64 mm rod amplifiers 3 times higher than with the standard CGE amplifier.

5. If disc amplifiers and rod amplifiers are equally susceptible to small scale self focusing the tradeoff point in terms of equivalent gains (9-10%/cm) will occur at 6-7 cm aperture diameters but the ~3 fold efficiency factor in favor of rods may make the economic tradeoff point occur at 10-11 cm aperture.

6. For a system with exponential gain throughout, measurements indicate a safe level of $I < 3 \times 10^{11} \alpha$ for stable beams with less than $\lambda/2$ wavefront distortion and no beam breakup. For an amplifier with $\alpha D = .6$, this implies that the safe level is $1.8 \times 10^{11} D^{-1}$ W/cm^2. For nanosecond pulses and $D < 10$ cm, surface damage will be the problem and not small scale self-focusing.

7. No pump induced loss was found in this study. If any such loss was present it could not have been greater than 1%/cm. The authors of the earlier reports which appeared to show this (present company included) were probably misled by using the rod fluorescence as an energy storage diagnostic when the "soft" parasitic was present.

6. Acknowledgements

The authors would like to acknowledge helpful discussions with Dr. J. R. Airey, Dr. J. L. Emmett and Dr. G. Dubé which materially assisted the successful completion of this effort.

7. References

[1] J. Marburger, NBS Spec. Publication 356, 51, (1971).

[2] B. R. Suydam, Los Alamos Sci. Lab Report LA-UR-73-671 (1973).

[3] J. Marburger, R. Jokipii, A. Glass, J. Trenholme, Laser Fusion Program Semi-annual Report Jan.-June 1973, UCRL-50021-73-1, 145 (1973).

[4] J. F. Holtzrichter, et al., "Laser Target Interaction Exps. at NRL", APS Plasma Physics Division Meeting, Monterey, California (Nov. 1972).

[5] R. Speck, E. Bliss, IEEE Conf. on Laser Engineering & Applications, Wash., D. C., May 1973.

[6] J. L. Emmett, et al., "High Peak Power Lasers", IEEE Int'l. Quantum Electronics Conf., Montreal, May 1972.

[7] S. W. Mead, R. E. Kidder, J. E. Swain, F. Rainer & J. Petruzzi, Appl.Optics 11, 345 (1972).

[8] J. B. Trenholme, NRL Memorandum Report 2480 (July 1972).

[9] J. M. McMahon, J. L. Emmett, J. F. Holtzrichter and J. B. Trenholme, IEEE J:Quant. Elect. QE-9, 992 (1973).

[10] J. M. McMahon, ASTM Spec. Technical Publication 469, 117 (1969).

[11] C. R. Jones, P. V. Avizones, P. Sivgals, NBS Special Publication 341, 28 (1970).

[12] J. Soures, S. Kumpan and J. Hoose, Laboratory for Laser Energetics, U. of Rochester, Report No. 20, 24 (1973).

[13] J. M. McMahon, O. C. Barr, and R. P. Burns, IEEE Proc. Int'l. Electron Devices Meeting (1973).

[14] G. Dubé and N. L. Boling, Applied Optics, 13, 4, 699 (1974).

[15] J. Strong, Concepts of Classical Optics, W. H. Freeman & Co., San Fran., (1958), p.214

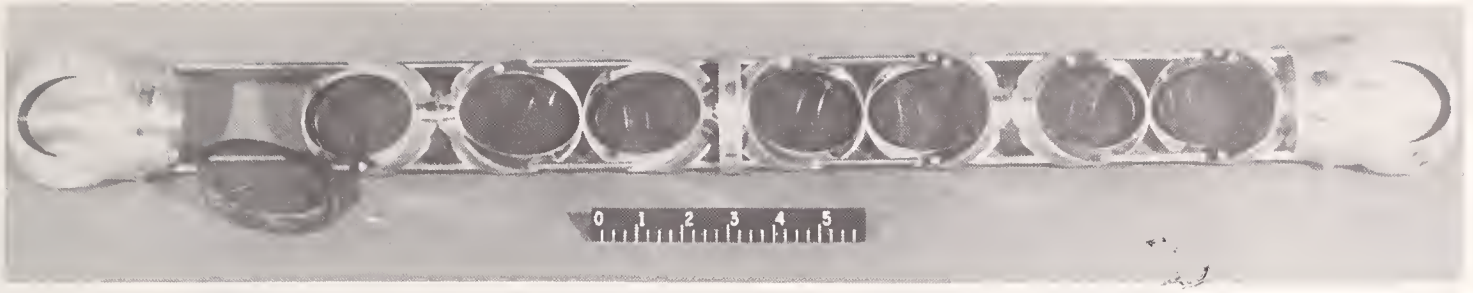

Figure 1. 44 mm aperture disc laser structure which was retrofitted in CGE V64AB amplifier head in place of a 64 mm laser rod.

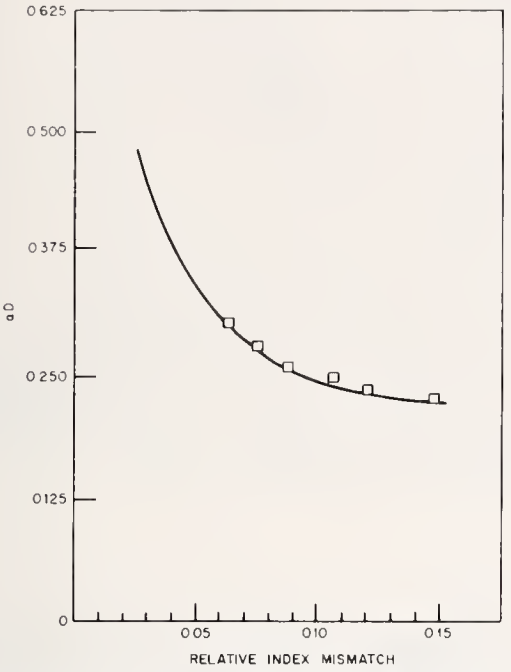

Figure 2. Threshold for radial mode #1. The data points are experimental, the curve is calculated from equations 1 and 2.

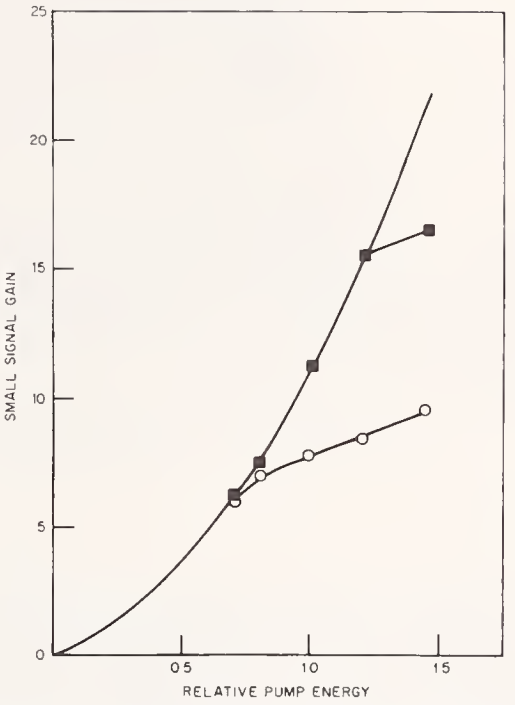

Figure 3. Gain vs. pump energy for V45A4 amplifier with water (0) and with a samarium chloride solution with an index of 1.46.

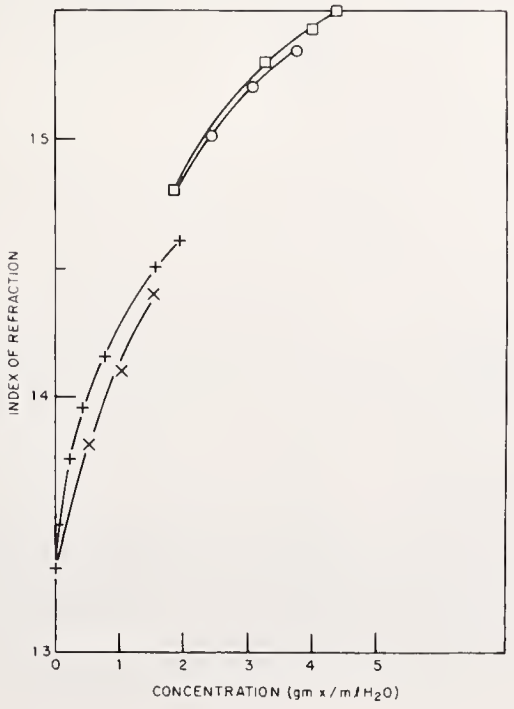

Figure 4. Index of refraction vs. concentration for solutions used. X-samarium nitrate; +-samarium chloride; o-zinc chloride; □-zinc bromate.

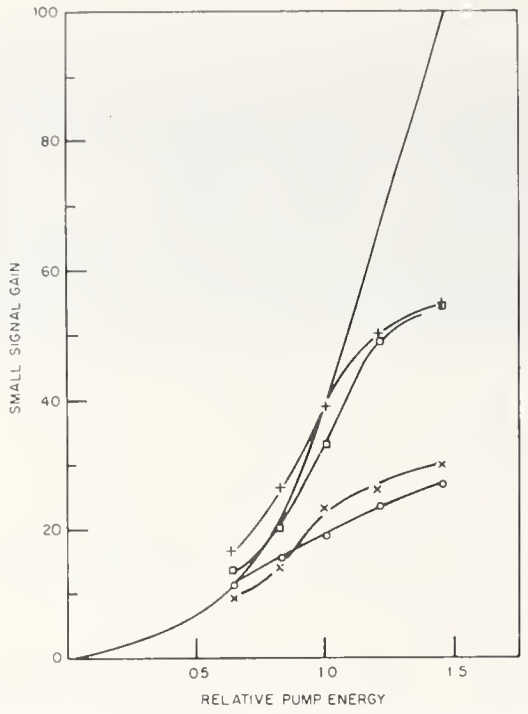

Figure 5. Gain vs. pump energy for V32A4 amplifier with various solutions. 0-H_2O; □-samarium chloride (n=1.44); X-zinc chloride (n=1.50); +-zinc chloride and samarium chloride (n=1.50).

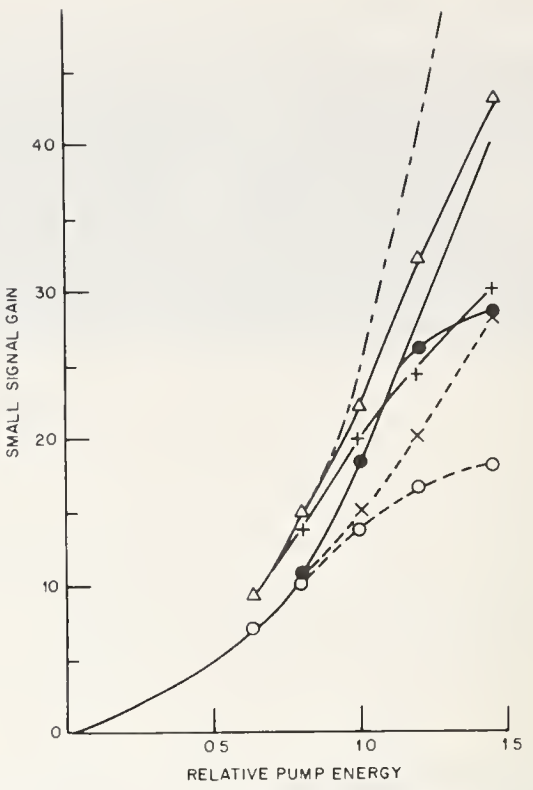

Figure 6. Gain vs pump energy for V32A2 amplifiers with various solutions. 0-H_2O; ●-samarium chloride (n=1.46); x-zinc chloride (n=1.52); + - zinc chloride + sm chloride (n=1.52); Δ- same as + but with laser rod end anti-reflection coated.

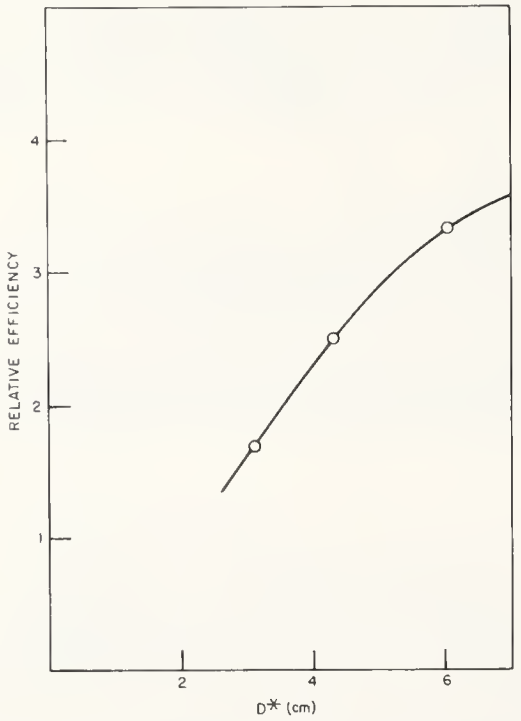

Figure 7. Relative pumping efficiency of 23, 32 and 45 mm laser heads. Curve is $(D^*/D_L)^2$ vs. D normalized to the 23 mm data.

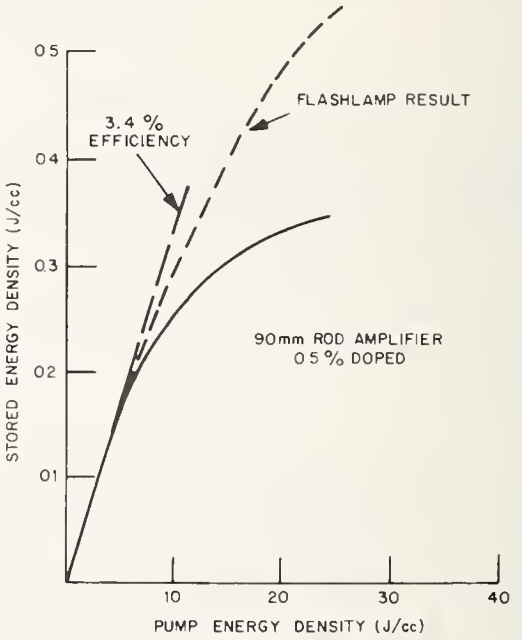

Figure 8. U. of Rochester result for a linearly pumped 90 mm rod amplifier. - Rochester data; --- expected result for flashlamp transfer.

COMMENTS ON PAPER BY McMAHON

The question was raised about the stability of zinc bromide in solution under aging. The speaker pointed out that the solution only needs to be stable in an inert atmosphere, but that long term stability was clearly a problem for any solution that was used. He commented that the lamp-induced or pump-induced surface damage may be a consequence of the pump-induced stress at the surface due to the strong absorption by cerium in the laser glass, especially in highly pumped discs. Even this type of damage was strongly dependent upon the condition of the surface. The tendency to damage was reduced by careful cleaning and by storing the glass discs in an inert atmosphere when not in use.

4.4 Optical Requirements for Laser Mirrors

H. E. Bennett and P. C. Archibald

Michelson Laboratory, Naval Weapons Center
China Lake, California 93555

The surface and coating requirements for mirrors used in laser systems are very severe. They may be summarized as follows: (1) excellent figure under thermal load, (2) high catastrophic damage threshold and an absence of localized sites where damage is likely to occur, and (3) low scattering levels. Backscattering is particularly important since it can easily damage the laser itself. The figure requirements for components increase rapidly when multicomponent "real world" optical trains are used. For example, to satisfy Maréchal's criterion for a 10 component system used at a wavelength of 3.8 μm, each component must have an initial figure of approximately 1/8th wave in the visible region and thermal distortion over the surface of less than 1000 Å. Very high reflectance coatings with excellent uniformity are thus required. Light scattering at short wavelengths provides a powerful, nondestructive tool for measuring microroughness (which reduces the infrared reflectance of metal coatings), and for identifying potential sites where damage is likely to occur. The damage threshold of a metal mirror is not necessarily determined by its absorption, and our understanding of the laser mirror problem is still incomplete.

Key words: Infrared absorption; laser damage; laser mirror; laser optical train; laser window; microroughness; optical figure; scattered light.

1. Introduction

Dr. Glass has defined "laser damage" as "whatever turns you off." One thing which can "turn you off" is the mirror train in a laser system. The surface and coating requirements for such mirrors are very severe, particularly in multielement systems. They may be summarized as (1) excellent figure even under thermal load, (2) high catastrophic damage threshold and an absence of localized sites where damage may occur, and (3) low scattered light levels (particularly low backscattering). The latter two requirements are necessary to avoid catastrophic damage to the laser system itself. The first requirement is of a different sort. Failure to meet this requirement will not result in damage to the laser system but the output beam will not be focussable, "turning you off." In this paper the requirements for laser mirrors used in an optical train will be discussed, and methods for evaluating and improving such mirrors will be given.

2. Figure Requirements

If the output beam from a laser is to be focussed, wave front distortion becomes extremely important. The primary sources of wave front distortion are (1) nonuniformities in the active medium, (2) distortion caused by figure errors in mirrors or windows in the optical train, (3) refractive index variations in the window, and (4) atmospheric nonuniformities. Both initial and thermally induced phenomena contribute to each of these effects. If the resulting wave front distortion is sufficiently large, it may be necessary to resort to techniques such as apodization or wave front correction using active optical elements. However the additional inefficiency, complexity and cost involved in such solutions makes it desirable to minimize wave front distortion rather than to correct for it. The crucial parameter in most laser applications is the on-axis focussed intensity. This on-axis intensity initially falls off very rapidly as wave front distortion increases, making the optical excellence required for maximum intensity more stringent than that required for high resolution optics. This situation is in sharp contrast to the relaxed criteria which apply when only a high flux level is required over an area large compared to the diffraction limit of the focussed beam. The reason for the stringent requirements on focussed optics is that, as wave front distortion increases, the shape of a focussed beam near maximum intensity changes very slowly. However the on-axis intensity decreases quite rapidly, the extra energy going into the diffraction wings. Therefore, although the generally accepted criterion for optical quality requires that the peak-to-peak wave front distortion not exceed

one quarter of the wavelength (the Rayleigh $\lambda/4$ criterion [1][1]) the resolving power of an optical system for two closely spaced, high contrast objects will remain near the Rayleigh theoretical resolution limit [2] up to wave front distortions as high as $\lambda/2$. For low contrast, extended objects the optical performance of a $\lambda/2$ system is degraded because of the halo surrounding each image point. Near theoretical resolving power is, however, only a necessary, not a sufficient condition for good focus, and higher quality optical systems are required to produce diffraction limited high intensity focussed spots than to produce diffraction limited optical resolution.

What are the tolerances on multiple elements used in a focussable laser optical train? Even in the intermediate infrared they are very severe, as can be seen from the following argument. Maréchal has shown [1] that to obtain 80% of the on-axis focussed intensity available from a true Gaussian beam the rms wave front distortion must not exceed $\lambda/14$. The peak-to-peak wave front error is then approximately the Rayleigh quarter-wave criterion. For small wave front distortions the ratio of the focussed on-axis intensity I to the undistorted wave front intensity I_o (the Strehl intensity) is given by [3]

$$\frac{I}{I_o} \cong 1 - \left(\frac{2\pi}{\lambda}\right)^2 \sigma^2 \tag{1}$$

where σ is the rms deviation of the wave front compared to that of an undistorted wave, expressed in units of wavelength λ. The Strehl relation is a good approximation [4] for intensity ratios above 60% or rms wave front errors of less than $\lambda/10$. In using it we also assume a uniform intensity along the wave front. In practice the intensity will either fall off as a Gaussian or vary in a more complicated manner along the wave front, requiring a more detailed analysis than that presented here. In our preliminary calculations, however, let us assume that there are N components in the system, all of which are allowed equal contributions to the resulting total wave front error σ. The contribution arising from the figuring error in a given component is assumed to be independent both of figuring errors in other components and of thermally induced errors. From eq. (1), then,

$$\sigma^2 = \sigma_T^2 + N\,\sigma_f^2 \tag{2}$$

where σ_T is the total thermally induced error in the wave front and σ_f is the figure-induced error in the wave front caused by an individual component. If the thermally induced wave front distortion σ_t in each component is also uncorrelated to that of other components, we obtain

$$\sigma_T^2 = N\,\sigma_t^2 \quad . \tag{3}$$

However, the thermally induced distortion in the different components is probably not uncorrelated to that of other components. For example, if the laser beam heats the center of one component more than its edge, the beam will probably do the same to the other components. If the thermally induced distortions of the various components are completely correlated, the resulting total thermal distortion will simply be the sum of the individual contributions, or

$$\sigma_T' = N\,\sigma_t \quad . \tag{4}$$

In optical shop practice the figure distortion is measured as a peak-to-peak value rather than an rms value. Approximate peak-to-peak values, represented by ρ's, can be obtained by multiplying the σ's by $2\sqrt{2}$. Then, from eqs. (1) to (4) we obtain for the case when both the initial figure errors of the individual components and the thermally induced errors are uncorrelated and the Maréchal condition is fulfilled:

$$\rho_t^2 + \rho_f^2 = \frac{0.4}{N}\left(\frac{\lambda}{\pi}\right)^2 \quad , \tag{5}$$

and when the thermally induced errors in individual components are correlated:

$$N\rho_t^2 + \rho_f^2 = \frac{0.4}{N}\left(\frac{\lambda}{\pi}\right)^2 \quad . \tag{6}$$

Equations (5) and (6) give the maximum peak-to-peak wave front distortion per component which may occur without seriously degrading the focus of the optical train. Even if the Maréchal criterion is relaxed, the allowable distortion increases by only a small amount. For example, if we double the intensity loss at focus and require only 60% of the theoretical intensity to be achieved instead of the 80% given by the Maréchal criterion, the allowable distortion only increases by a factor of 1.4.

The wave front distortion produced by a mirror is twice the physical distortion of the mirror surface. The normal optical shop tolerance on a prevision optical surface is $\lambda_v/4$ where λ_v is the visible test wavelength used, typically 5461 Å. The most stringent tolerance most optical shops will

1. Figures in brackets indicate the literature references at the end of this paper.

accept is $\lambda_v/8$. A plot of the mirror figure requirements for a 10 component laser system as calculated from eqs. (5) and (6) is shown in figure 1. The dashed lines indicate optical shop tolerances. The better the initial figure, the more thermal distortion is allowed, which translates into more relaxed tolerances on the absorption of mirror coatings or on mirror cooling requirements. In general, a $\lambda_v/4$ figure is quite adequate for CO_2 laser mirrors and even a $\lambda_v/2$ figure might be acceptable. If the figure is worse than 0.338 μm, or about 5/8 λ_v, however, the Maréchal condition cannot be met even if no thermal distortion is present. Also, if the thermal distortions in the different components are correlated, the maximum allowable thermal distortion is only 0.107 μm, or less than 1/3rd of that for the uncorrelated case. In practice the allowable distortion should be between these two values if the mirror is extremely well figured and will decrease as the figure becomes poorer.

Contrast the case for the CO_2 laser operating at 10.6 μm with that for the DF laser operating at 3.8 μm. Even a $\lambda_v/4$ surface is not good enough for a 10 component optical train used with a DF laser; at least a $\lambda_v/8$ surface is required. Also, the thermal distortion allowed is at best at the lower limit of that allowed for CO_2, and in most cases will be several times less than that. In the correlated case, assuming a $\lambda_v/8$ initial figuring error, it is only 316 Å, which is a very small number indeed and will require both very highly reflecting coatings and very efficient cooling if it is to be achieved.

The figuring requirements for windows may also be calculated from eq. (5). If we assume the figure errors on the two sides of the window are correlated (worst case but entirely possible if both sides are polished on the same lap), then the optical path difference per component will be

$$\rho_f = 2(n - 1)\ \tau \tag{7}$$

where τ is the error in the physical surface and n is the index of refraction of the window (assumed to be in vacuum or air). For KCl, where at 10.6 μm n = 1.45, tolerances on the surface figure are seen to be less than half as tight as on mirror surfaces, as shown in figure 2 for a 10 component system. A half-wave figure would be adequate for CO_2 lasers and even a full wave figure error would not necessarily be disastrous, although the thermal absorption required for such a component would have to be lower than for one with a better figure. As shown in figure 3 the situation for KCl is in marked contrast to that for ZnSe (n = 2.405 at 10.6 μm) where the figure and thermal distortion tolerances are over 3 times more severe than for KCl and are thus worse than for mirror surfaces.

3. Minimizing Thermal Distortion in Mirrors

The static figure of a laser mirror, although often very difficult to achieve, is obtained by more or less conventional optical shop techniques such as those used for producing astronomical mirrors and other high quality optics. However, an additional requirement on some laser mirrors is that they exhibit minimum figure distortion under thermal loading. Much of the heat absorbed by the mirror surfaces can be removed by cooling the mirror, but the greatest gains are made by using mirror coatings which do not absorb the energy to begin with. Both metal and metal-dielectric coatings are used, and in both cases the purity of the initial starting materials and the conditions under which the coatings are deposited are crucial to the resultant absorption the coatings will have. The substrate on which the coating is deposited must also be exceptionally smooth. Surface microirregularities as small as 30 Å rms can significantly affect the infrared absorption of silver and other metals. Optically polished metal surfaces typically have microroughnesses of the order of 70 Å rms, but by careful polishing, this value can be reduced to less than 30 Å rms. [5] By overcoating the metal with a sputtered film of the same material and then polishing that, surfaces having microroughnesses under 15 Å rms can be achieved. [5,6] In general, as the surface becomes smoother the absorption becomes lower. However, as shown by figure 4, the decrease in absorption is not determined solely by the rms height of the surface irregularities, and probably depends on the surface autocovariance function as well. The solid line represents the increase in absorption observed for surfaces roughened by depositing calcium fluoride on them and then overcoated with silver deposited in ultrahigh vacuum. Finely spaced irregularities are produced in this way, and the increase in absorption (over a factor of three for surfaces as smooth as 35 Å rms) is higher than for any of the polished metal surfaces tested. On the other hand, the increase in absorption of the 35 Å rms sputtered copper on copper sample was less than 30% and was nearly identical with that of the smoother copper samples. Work is now underway [7] to measure the autocovariance function of such surfaces with the hope that by appropriate modification of polishing technique and type of substrate the roughness requirement on laser mirror surfaces can be significantly relaxed.

4. Damage Threshold

In addition to the optical figure requirement, a laser mirror must have a high catastrophic damage threshold. As with dielectric materials, the damage process in metals is not entirely clear. Damage may occur at sites where localized defects such as scratches or inclusions exist, and techniques for detecting such defects are thus important. Scratches may be detected by scattered light meaurements, as described below. Auger spectroscopy, when combined with a sputter attachment for obtaining

depth profiles, is a powerful tool for inclusion detection. [8] Figure 5 shows an Auger scan of a copper surface polished with aluminum oxide powder in a water slurry. Even in this unfavorable case the sensitivity of the Auger system to polishing particles imbedded in the copper surface is about 10^{-7} gm/cm^2 of Al_2O_3 or 0.1% surface coverage.

The damage threshold of metal or metal-coated mirrors is not directly proportional to their absorption. It often is significantly higher for uncoated polished bulk metal mirrors than for the same mirrors coated with an evaporated metal film, even though the absorption is lower in the latter case. It also varies with substrate material. Beryllium copper has one of the highest damage thresholds. It is significantly better than pure OFHC copper (bulk copper) [9], as shown in figure 6. However, when the bulk OFHC copper was coated with a dispersion-hardened, sputtered copper film and then polished, the damage threshold increased almost four times [9], and was over 2 1/2 times higher than for bulk BeCu. When a silver film was evaporated onto the bulk OFHC copper (lower bar graphs) no change in damage threshold was observed, even though the absorption decreased by over a factor of two. When silver was evaporated onto the sputtered surface, the damage threshold was nearly twice as high as for the bulk sample. It was only about half that of the sputtered substrate, however, even though by coating the substrate the absorption was reduced by over a factor of two. When a sputtered silver coating was deposited on a sputtered substrate, the damage threshold went up almost, but not quite, to the uncoated sputtered substrate level. [9] The absorption of the sputtered silver film was nearly twice that of the evaporated film. This example demonstrates that the damage threshold of metal mirrors is determined not only by the energy the surface absorbs but also by other quantities such as thermal transfer, surface structure and film adherence. To minimize thermal distortion of the mirror low absorption coatings are essential, so conventionally sputtered silver coatings [10] are inadequate in spite of their high damage threshold. One possible solution is to improve the sputtering conditions with the objective of lowering the absorption of the sputtered silver coating to values comparable to those of evaporated silver films.

5. Scattered Light

If backscattered light from the mirrors in the optical train of a laser is allowed to pass back through the active laser medium, catastrophic damage to the laser can result. Various attenuation schemes to avoid this situation can be employed, but one of the best is to minimize scatter from the mirrors themselves. Scattered light is also a useful nondestructive tool for detecting inclusions, scratches and other localized defects in the mirror surface. If such defects are larger than the wavelength of light employed, the scattered light will have little wavelength dependence. Total integrated scatter (TIS) from microirregularities, on the other hand, usually follows a $1/\lambda^2$ law [11], as shown in figure 7. By scanning the mirror surface at several wavelengths in the visible region it is then possible, from TIS measurements, to separate and determine both the surface microroughness of the mirror and the presence of scratches or other localized defects which may lower the damage threshold of the mirror. Differential scattering measurements at the operating wavelength of the laser are also required, as are reflectance measurements.

An instrument for performing scattering and reflectance measurements on mirrors up to 40-cm diameter has been described previously. [12] It employs 18 laser lines extending from the ultraviolet through 10.6 μm in the infrared and is enclosed in a class 100 clean room. Results of scattering measurements on a gold coated, 25-cm diameter beryllium copper mirror with a polished sputtered surface are shown in figure 8. The average values of the scatter at different radii are given at the top of the circles indicating the scan positions, and the points indicate the deviation from these average values. This mirror is an exceptionally good one polished by the Perkin-Elmer Corporation and sent to us to evaluate by the Air Force Weapons Laboratory. The rms roughness at the center of the mirror is only 22 Å, as determined by scattered light measurements. [13] There are virtually no significant scratches on this mirror and the roughness has excellent radial symmetry about the mirror center, as can be seen from the uniform scatter points about the circles indicating average values. The mirror is thus completely polished out but does show a pronounced radial dependence of roughness. For the largest circle, which is 25 mm from the outer edge of the mirror, the average roughness is 29 Å rms, causing a 60% increase in scatter as compared to the mirror center. The reason for this increase in roughness is not known, but may be associated with the way in which a large optical surface polishes.

The increase in scattering level with distance from the mirror center is seen more easily in the radial scan shown at the left in figure 8. There was a small scratch near the edge of the mirror which also shows up graphically in the radial scan. The still smaller scratch seen halfway out was almost imperceptible visually, although it is easily located on the trace.

6. Conclusion

The requirements on the elements in the optical train of a laser are very severe, particularly if the train has several elements in it. If the beam is to be focussed for high energy density and techniques such as apodization are not used, the figure requirements are more stringent than are those for high resolution optics, and may demand state-of-the-art polishing procedures even for lasers used in

the intermediate infrared. Thermally induced distortion is also important, and coatings which absorb a minimum of the flux incident on the mirror are thus essential. Microroughness contributes significantly to the absorption of metal coatings but can be controlled by polishing sputtered coatings deposited on the substrate rather than by polishing the substrate itself. Another possibility now under investigation is the control of the surface autocovariance function by appropriate polishing techniques. Short wavelength scattered light is a powerful, nondestructive tool for checking mirror surfaces for microroughness as well as potential damage sites.

In addition to figure requirements, the laser mirror must have a high catastrophic damage threshold, and backscatter must be minimized. The damage threshold of metal mirrors is determined by more than simply the absorption of the surface. Examples have been reported in which the damage threshold for silver-coated copper doubled even though the absorption also doubled. The damage threshold per absorbed photon thus increased by nearly a factor of four without a change in mirror material. Such results are encouraging but indicate that our understanding of the laser mirror problem is still incomplete.

7. References

[1] Born, M. and Wolf, E., *Principles of Optics* (Pergamon Press, New York, 1959), p. 467; Conrady, A. E., *Applied Optics and Optical Design* (Dover Publications, Inc., New York, 1957), p. 136.

[2] Conrady, A. E., *Applied Optics and Optical Design, Part Two* (Dover Publications, Inc., New York, 1960), pp. 626-7.

[3] Born, M. and Wolf, E., *op. cit.*, p. 463.

[4] Winsor, H. V., *Proceedings of the Third Conference on High Power Infrared Laser Window Materials*, November, 1973 [AFCRL-TR-74-0085 (III)], p. 1069.

[5] Slomba, A., Perkin-Elmer Corp. (private communication); Soileau, M. J., Bethke, J. and Ashley, E. J., *High Energy Laser Mirrors and Windows* (Semi-Annual Report No. 4, ARPA Order 2175, Naval Weapons Center, March 1974), pp. 51-58.

[6] Stewart, R. W., *Investigate Material Systems for Mirrors Used in High Power CO and CO_2 Lasers* (BNWL-1780, ARPA Order 2175, December 1972).

[7] Bennett, J. M., elsewhere in these proceedings (1974).

[8] Porteus, J. O., *High Energy Laser Mirrors and Windows* (Semi-Annual Report No. 3, ARPA Order 2175, Naval Weapons Center, September 1973), pp. 88-90.

[9] Soileau, M. J. and Wang, V., Appl. Opt. 13, 1286 (1974).

[10] Stewart, R. W., *Investigate Material Systems for Mirrors Used in High Power CO and CO_2 Lasers* (BNWL-1781, ARPA Order 2175, August 1973).

[11] Bennett, H. E., Stanford, J. L. and Bennett, J. M., "Scattering from Mirror Surfaces Used in Space Optics" in *Space Optics*, B. J. Thompson and R. R. Shannon, eds. (National Academy of Sciences, Washington, D. C., 1974), pp. 717-738.

[12] Bennett, H. E., Archibald, P. C. and Stanford, J. L., *High Energy Laser Mirrors and Windows* (Semi-Annual Report No. 3, ARPA Order 2175, Naval Weapons Center, September 1973), pp. 5-24.

[13] Bennett, H. E. and Porteus, J. O., J. Opt. Soc. Am. 51, 123 (1961).

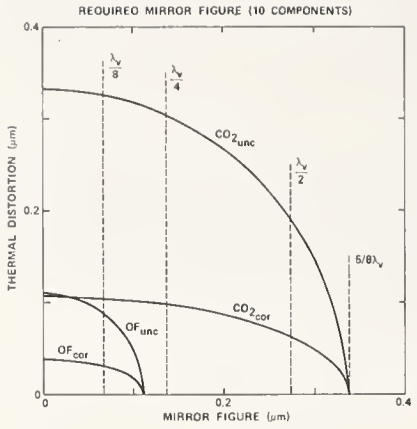

Figure 1. Figure requirements for mirrors used in the 10 component optical train of a laser operating at 10.6 μm (CO_2) or 3.8 μm (DF). Equal contributions to the wave front distortion by each component are assumed. The subscripts cor and unc refer to correlated and uncorrelated thermal distortions. Dashed lines refer to conventional figure tolerances used in optical shops, i.e., an eighth wave surface, quarter-wave surface, etc., at a wavelength λ_v = 5461 Å.

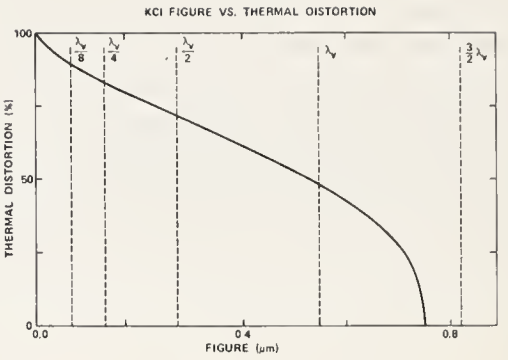

Figure 2. Figure requirements for KCl windows used in the 10 component optical train of a CO_2 laser. Equal contributions to the wave front distortion by each component are assumed. The ordinate gives the fraction of the total wave front distortion introduced by the window which can be thermally induced. Dashed lines refer to conventional figure tolerances used in optical shops.

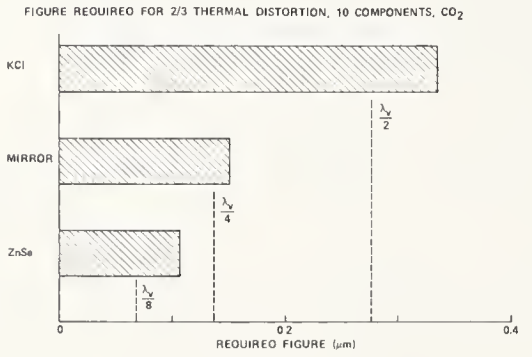

Figure 3. Figure requirements for a mirror, a KCl window, and a ZnSe window used in a 10 component CO_2 laser optical train with equal contributions to wave front distortion allowed for each component. Two-thirds of the allowable wave front distortion is assumed to result from thermal effects. The dashed lines refer to conventional optical shop figure tolerances.

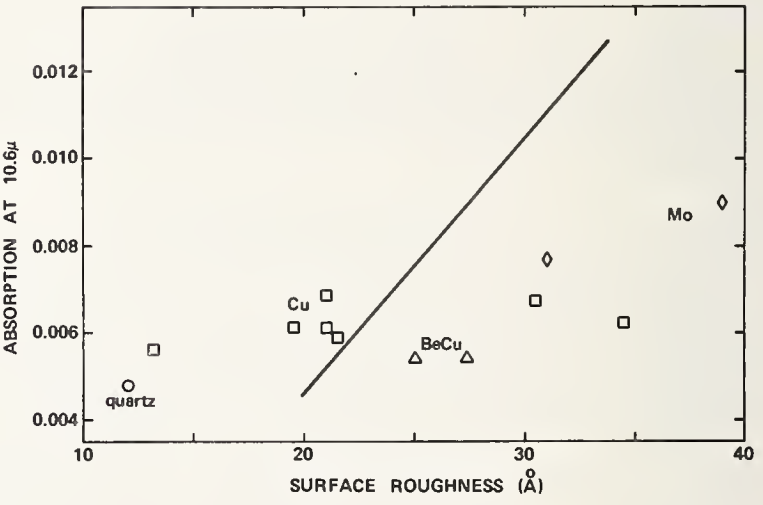

Figure 4. Absorption at 10.6 μm of silver films evaporated in ultrahigh vacuum (10^{-9} Torr) onto surfaces having various roughnesses, as determined by scattered light and FECO interferometric measurements on the silvered surfaces. The solid line shows the absorption for rough surfaces formed by depositing CaF_2 onto quartz substrates. The OFHC copper surface had a sputtered copper overlayer and is represented by the squares. There was no sputtered layer on the BeCu (triangles), the Mo (diamonds) and the quartz (circles). All surfaces were polished by bowl feed.

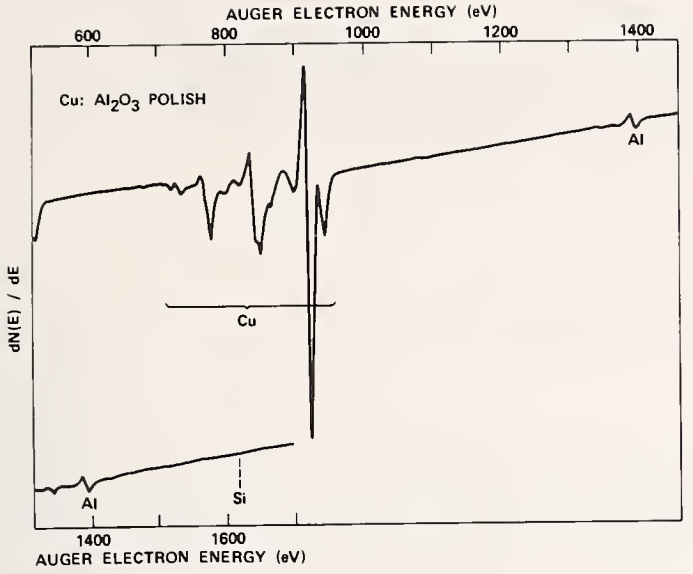

Figure 5. High-energy portion of the Auger spectrum from a copper surface polished with Al_2O_3. The Al peak from residual Al_2O_3 particles embedded in the surface is easily detected. Estimated sensitivity of this technique is 10^6 particles/cm^2 or a surface coverage of 0.1%. From reference 8.

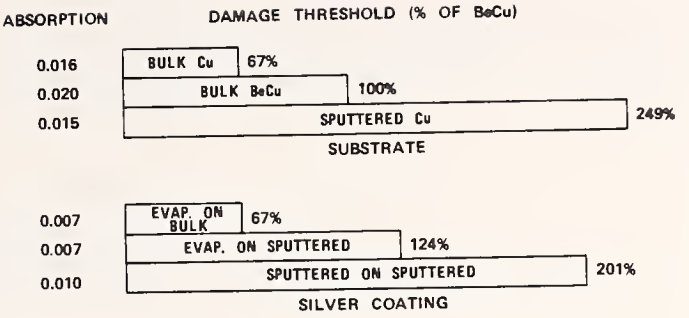

Figure 6. Damage threshold for copper mirrors at 10.6 μm. Absorption values for the different surfaces are shown on the left and percent improvement in damage threshold as compared to uncoated BeCu on the right. Data taken from reference 9.

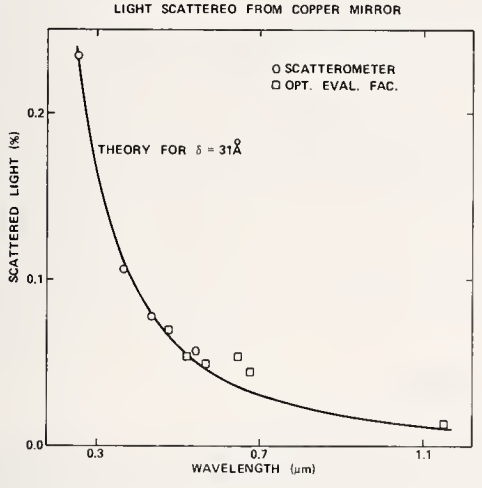

Figure 7. Scattered light from a copper mirror having a sputtered copper coating which was then polished. The circles represent measurements made with the NWC scatterometer, and the squares are measurements made on the Optical Evaluation Facility. The solid line is the hemispherical scattering function predicted from scalar scattering theory for a 31 Å rms roughness surface.

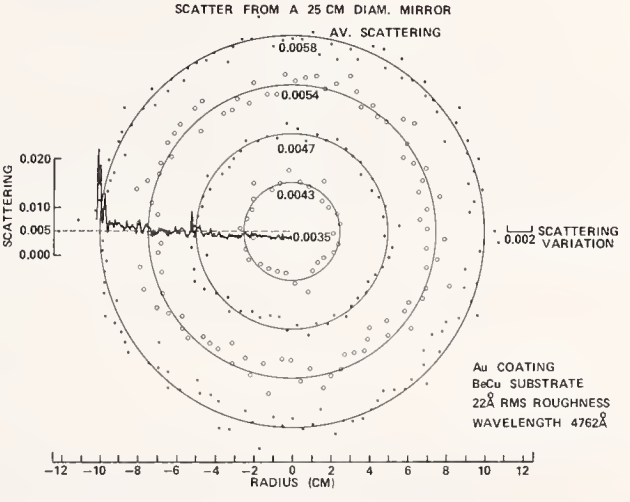

Figure 8. Scattered light as a function of position on a 25 cm diam. gold-coated beryllium copper mirror. The circular scans were made at radial increments of 2.5 cm. The average scattering value for each scan is shown at the top of the corresponding circle and the points show the variation about this average. The radial scan confirms that the scattering level, although radially symmetric, increases with radius by about 60% (corresponding to a change in roughness from 22 Å at the center to 29 Å near the edge of the mirror). The dashed line gives the average radial scatter excluding the scattering from the scratch near the edge of the mirror.

564-378 O - 74 - 4

COMMENTS ON PAPER BY BENNETT

It was pointed out that whereas a sample must be overcoated to use with FECO measurements, light scattering measurements require no alteration of the surface, and therefore are more suitable for survey examination. FECO measurements are thus sensitive to the care exercised in preparing the sample for measurement, as well as the surface condition of the sample prior to the test.

1.5 Diffraction Theory of Absorbing Windows*

M. Flannery and J. Marburger

University of Southern California
Los Angeles, California 90007

The diffraction-optical theory of coherent polarized beams incident on realistic absorbing windows is developed here with emphasis on tracing the origin of qualitative features of the diffraction field. The influence of incident polarization, stress induced birefringence, and other parameters, on the transmitted beam is described, and both analytical and numerical solutions for the transmitted diffraction field are presented. Our development of the theory allows the influence of the window material to be characterized by two parameters in the transient regime rather than the three previously believed to be necessary. Implications for IR window design are summarized.

Key words: Birefringence; laser windows; thermal distortion.

In assessing materials for use in laser systems, one must know how each material parameter influences critical properties of the laser output beam. Unfortunately, the relation between material properties and the transmitted optical field of an absorbing window can be quite obscure. Bendow and Gianino[1][1] have performed extensive numerical analyses of the diffraction field of a truncated Gaussian beam focussed through a weakly absorbing window which heats, expands, and produces an inhomogeneous stress induced birefringence. Because of the large number of parameters involved, the numerical results are difficult to summarize, and it is difficult to attribute specific features of the diffraction field to specific mechanisms in the window. In this paper, we describe a general diffraction theory of absorbing windows which is simple enough to allow analytical estimation of many important features of the transmitted field. These estimates show clearly how such features are related to the material parameters of the window. The basic formalism of the theory is general enough to allow the analysis of realistic window systems.

Our starting point is the slowly varying envelope equation for the amplitude $\vec{E}$ of the total optical field $\vec{E}_{opt}$ of frequency ω:

$$\vec{E}_{opt} = \mathrm{Re}\, \vec{E} e^{ikz} e^{-i\omega t} .$$

Here $k = n\omega/c$, and n is the mean refractive index of the medium through which the electromagnetic field is propagating. The envelope equation in an inhomogeneous medium is ($\nabla_T^2 = \partial^2/\partial x^2 + \partial^2/\partial y^2$)

$$2ik\frac{\partial \vec{E}}{\partial z} + \nabla_T^2 \vec{E} = \frac{-4\pi\omega^2}{c^2} \overleftrightarrow{\chi} \cdot \vec{E} \qquad (1)$$

where $\overleftrightarrow{\chi}$ is the inhomogeneous part of the linear susceptibility tensor defined through $\vec{P} = [(n^2-1)/4\pi]\vec{E} + \overleftrightarrow{\chi} \cdot \vec{E}$. We are using unrationalized cgs (Gaussian) units.

In free space (or in air, ignoring inhomogeneities), eq. (1) becomes

$$2ik\frac{\partial \vec{E}}{\partial z} + \nabla_T^2 \vec{E} = 0 \qquad (2)$$

which has the solution

$$\vec{E}(\vec{r},z) = \frac{-ik}{2\pi z}\int\int d^2r'\, e^{i\frac{k}{2z}(\vec{r}-\vec{r}')^2} E_{out}(\vec{r}',0) . \qquad (3)$$

---

*Research supported by the Defense Advanced Research Projects Agency, Department of Defense, monitored by Air Force Cambridge Research Laboratories under Contract No. F19628-72-C-0275.

[1]Figures in brackets indicate the literature references at the end of this paper.

The exit plane of the window is assumed to be at z = 0, and $\vec{E}_{out}$ is the field at that plane. If a thin lens of focal length R is placed at z = 0, then (3) should be replaced by

$$\vec{E}(\vec{r},z) = \frac{-ik}{2\pi z}\iint d^2r' \; e^{\frac{ik}{2z}(\vec{r}-\vec{r}')^2} \; e^{-i\frac{kr'^2}{2R}} \; \vec{E}_{out}(\vec{r}',0) \quad . \tag{4}$$

Eqs. (3) and (4) will be used to find the field beyond the window.

The field $\vec{E}_{out}$ at the exit plane of the window system can be obtained in simple form if the window is so thin that diffraction effects (arising from the $\nabla_T^2 E$ term in (1)) can be ignored inside the window. Then (1) becomes

$$2ik\frac{\partial \vec{E}}{\partial z} = \frac{4\pi\omega^2}{c^2}\vec{\vec{\chi}}\cdot\vec{E} \quad . \tag{5}$$

This can be integrated easily if $\vec{\vec{\chi}}(\vec{r},z)$ is locally diagonal in a coordinate system whose axes do not depend upon z. In this case

$$\vec{E}_{out}(\vec{r},0) = \left\{\exp\left[\frac{i2\pi\omega^2}{kc^2}\int_{-W}^{0}\vec{\vec{\chi}}(\vec{r},z)dz\right]\right\}\cdot\vec{E}_{in}(\vec{r},-W) \; , \tag{6}$$

where z = -W is the entrance plane of the window system. Figure 1 shows the geometry of a typical system.

The bracketed quantity in (6) is a two dimensional matrix which we call the aberration matrix $\vec{\vec{A}}$:

$$\vec{E}_{out}(\vec{r},0) = \vec{\vec{A}}(\vec{r})\cdot\vec{E}_{in}(\vec{r},-W) \tag{7}$$

This matrix depends upon the details of the incident field as well as upon material parameters. For a "perfect" window $\vec{\vec{\chi}} = 0$, $\vec{\vec{A}} = \vec{\vec{I}}$ and $\vec{E}_{out} = \vec{E}_{in}$ (except for a constant phase factor). But even in this case, eq. (4) for the transmitted field is difficult to evaluate except for special cases.

If the incident field has cylindrical symmetry, $\vec{E}_{in} = \hat{e}_{in}E(r)$, where $\hat{e}_{in}$ is a constant polarization unit vector, and if the window response is also cylindrically symmetric, then $\vec{\vec{A}}$ will be diagonal in polar coordinates in the window plane:

$$\vec{\vec{A}} = e^{i\Phi_r}\hat{r}\hat{r} + e^{i\Phi_\theta}\hat{\theta}\hat{\theta} \tag{8}$$

$$= \exp i\phi\begin{bmatrix}\cos\Delta + \sin\Delta\cos\theta & \sin\Delta\sin 2\theta \\ \sin\Delta\sin 2\theta & \cos\Delta - \sin\Delta\cos\theta\end{bmatrix}$$

The second form of writing is appropriate for a Cartesian coordinate system, where $\hat{r} = \hat{x}\cos\theta + y\sin\theta$, and

$$\phi \equiv \tfrac{1}{2}(\Phi_r + \Phi_\theta), \qquad \Delta \equiv \tfrac{1}{2}(\Phi_r - \Phi_\theta).$$

The principal phases Φ_r, Φ_θ, are simply the eigenvalues of the exponent in eq. (6). Eq. (8) is important because all θ dependence is explicit. This means that the angular part of the integration in the diffraction integral (4) can be performed. The result for the transmitted diffraction field may be written

$$\vec{E}(r,z) = \vec{E}_o(r,z) - \vec{\vec{R}}(\theta)\cdot\vec{E}_2(r,z) \tag{9}$$

where

$$\vec{\vec{R}}(\theta) = \begin{pmatrix}\cos 2\theta & \sin 2\theta \\ \sin 2\theta & -\cos 2\theta\end{pmatrix} \tag{10}$$

and

$$\vec{E}_o(r,z) = \frac{-ik}{z} e^{\frac{ikr^2}{2z}} \int_o^d r'dr' \times \left[e^{-\frac{1}{2}iur'^2} e^{i\phi} \cos\Delta \; J_o \vec{E}_{in} \right] , \tag{11}$$

$$\vec{E}_2(r,z) = \frac{-ik}{z} e^{i\frac{kr^2}{2z}} \int_o^d r'dr' \times \left[e^{-\frac{1}{2}iur'^2} e^{i\phi} \sin\Delta \; J_2 \vec{E}_{in} \right] . \tag{12}$$

Here $u \equiv k(R^{-1} - z^{-1})$, and the argument of the Bessel functions J_o and J_2 is krr'/z.

We can learn much about the transmitted field by meditating upon those equations. $\vec{E}_o$ and $\vec{E}_2$ both have the polarization of the incident field, and therefore by (9) all depolarization effects are proportional to $\vec{E}_2$. Eq. (9) also implies that departures from cylindrical symmetry in the transmitted field are also proportional to $\vec{E}_2$. The field $\vec{E}_2$ itself vanishes on axis (r = 0) because J_2 vanishes there, so the axial field has the same polarization as the incident field, and equals $\vec{E}_o(0,z)$. When there is no birefringence, $\Delta = 0$, and $\vec{E}_2$ vanishes. The intensity is easily obtained using $\vec{R}^2 = 1$:

$$|\vec{E}|^2 = |\vec{E}_o|^2 + |\vec{E}_2|^2 - 2 \operatorname{Re} \vec{E}_o \cdot \vec{R}(\theta) \cdot \vec{E}_2^* . \tag{13}$$

If the incident polarization is elliptical with ellipticity $\varepsilon = \tan\chi$ and with principal axes along the Cartesian coordinates, then the total intensity is

$$|\vec{E}|^2 = |E_o|^2 + |E_2|^2 - 2(\operatorname{Re} E_o E_2^*) \cos 2\chi \cos 2\theta . \tag{14}$$

For circularly polarized, or unpolarized light, this implies

$$|\vec{E}|^2 = |E_o|^2 + |E_2|^2 \qquad \text{(unpolarized, circularly polarized)}$$

while for linear polarization

$$|\vec{E}|^2 = |E_o|^2 + |E_2|^2 - 2(\operatorname{Re} E_o E_2^*) \cos 2\theta \qquad \text{(linearly polarized)} .$$

These formulas give the explicit azimuthal dependence of the transmitted intensity for any cylindrically symmetric incident beam with uniform polarization.

To appreciate the influence of ϕ and Δ upon the diffraction field, we must specify the incident mode structure and the window response more precisely. It is convenient to adopt as a fiducial case a Gaussian equiphase beam with weak truncation at the window aperture:

$$\vec{E}_{IN}(r,0) = \hat{e}_i E_{in} \exp -r^2/w^2 . \tag{15}$$

The truncation will be specified by the ratio $\alpha = d/w$, where d is the window radius. If d and the incident power in the whole Gaussian are fixed, then the focal intensity of the transmitted beam is a maximum for $\alpha = 1.122$. For this value of α, 92% of the incident power is transmitted, and the structure (e.g. Airy rings) introduced in the diffraction field by truncation is weak.

The simplest realistic model for window response is one in which the window is made of an isotropic material which heats in the beam and develops internal strains as the cooler periphery restricts the expansion of the warmer interior. These strains generate index changes proportional to the appropriate elasto-optic tensor elements p_{ij}. The total phase disturbances Φ_r, Φ_θ also contain contributions from the direct temperature coefficient of refractive index $\partial n/\partial T$, and from the slight change in path length as the heated portion of the window expands and bulges outward under the restraining periphery. The window is assumed to be freely supported at the edges with a medium with the same thermal and elastic properties as the window. For simplicity in what follows, we shall consider only short heating times during which the local temperature is not affected by thermal diffusion. Any of these simplifying conditions may be relaxed with consequent increases in the complexity of the theory, although analytical treatments are still feasible in most cases. The reader familiar with the work of Bendow and Gianino [1] will appreciate that even this restricted window model leads to very complex diffraction fields.

Bendow and Gianino[1] have shown that the principal phases can be written (for the window model just described) in the form

$$\Phi_n = C_1^n f(r) + C_2^n g(r) + C_3 , \qquad n = r,\theta \tag{16}$$

where f(r) is proportional to the local temperature increase and g(r) to the mean integrated temperature increase from the origin to the radial distance r. For example, during the initial heating regime before thermal diffusion sets in, a Gaussian incident beam leads to

$$f(r) = \exp(-2r^2/w^2) \tag{17}$$

$$g(r) = \frac{1 - \exp(-2r^2/w^2)}{r^2/w^2} \tag{18}$$

The coefficients in (16) are

$$C_1^r = H\left\{\frac{\partial n}{\partial T} + \bar{\alpha}(1+\nu)(n-1) + \tfrac{1}{2}\bar{\alpha}n^3\left[(1-\nu)p_{12} - \nu p_{11}\right]\right\}$$

$$C_1^\theta = H\left\{\frac{\partial n}{\partial T} + \bar{\alpha}(1+\nu)(n-1) + \tfrac{1}{2}\bar{\alpha}n^3\left[p_{11} - 2\nu p_{12}\right]\right\}$$

$$C_2^r = -C_2^\theta = H\bar{\alpha}n^3(1+\nu)(p_{11} - p_{12})/8 \tag{20}$$

$$H = (\beta kW/C')\int^t I_o(t')dt'$$

$$I_o = \frac{nc}{8\pi}|\vec{E}_{in}(0,0)|^2 .$$

Here $\partial n/\partial T$ is the rate of change of index with temperature at zero stress, $\bar{\alpha}$ is the coefficient of thermal expansion, ν Poisson's ratio, and p_{ij} the elasto-optic tensor elements. β is the absorption coefficient, C' the heat capacity per cm^3, and W the thickness of the unstrained window. With this notation, the aberration functions are

$$\phi = \tfrac{1}{2}(C_1^r + C_1^\theta)\, f(r)$$

$$\Delta = C_2^r[g(r) - 2f(r)] .$$

Introducing the new parameters

$$\tau \equiv \tfrac{1}{2}(C_1^r + C_1^\theta), \qquad \sigma \equiv 4C_2^r/(C_1^r + C_1^\theta) , \tag{21}$$

we find

$$\phi = \tau f(r) \tag{22}$$

$$\Delta = \sigma\tau[\tfrac{1}{2}g(r) - f(r)] . \tag{23}$$

These are plotted in figure 2 for an incident Gaussian in the pre-diffusion regime. The importance of these formulae is that the introduction of birefringence ($p_{11} \neq p_{12}$) requires only the additional lumped parameter σ for its description in this model. Previous formulations of the theory required two additional parameters equivalent to C_2^r/C_1^r and C_1^θ/C_1^r.

The significance of τ can be seen from the role of the mean phase shift ϕ in eq. (11). If ϕ is expanded in powers of r^2, we find

$$\phi(r) \approx \phi_o + \phi_2 r^2 + \phi_4 r^4 + \ldots .$$

The term in ϕ_o is of no interest here, but that in ϕ_2 is equivalent to a lens of focal length

$$R_{eff} = -\frac{k}{2\phi_2} . \tag{24}$$

For a Gaussian beam,

$$f(r) \approx 1 - 2r^2/w^2 + 2r^4/w^4 , \tag{25}$$

or one finds

$$R_{eff} = +\frac{kw^2}{4\tau} = \frac{kd^2}{4\alpha^2\tau} . \tag{26}$$

Thus τ is the ratio of the Gaussian diffraction length $kw^2/4$ to the instantaneous effective focal length of the center of the window. Higher orders in the expansion of ϕ are also proportional to τ. Thus the lowest order spherical aberration term is

$$\phi_4 = 2\tau/w^4 . \tag{27}$$

Using a modification of a criterion due to Rayleigh [3], we expect serious degradation of the focal intensity when $\phi_4 w^4 \approx \pi/2$, or $\tau \approx \pi/4$. If either the defocusing effect (26) or the aberration effect (27) were present, one would expect a substantial reduction of focal intensity when $\tau \approx 1$, but from (25) one can see that the effects can nearly cancel. In fact the focal intensity drops by half only after the rather long "time"

$$\tau_{1/2} \approx 3 .$$

This can be inferred either from numerical solutions or from the exact analytical expression for the focal intensity (when birefringence is absent) reported elsewhere [2]. Table 1 gives values of $\tau/w\int_o^t I\, dt$ for a variety of materials. This number, which should be small for negligible thermal lensing effects, is directly proportional to the absorption coefficient β.

When birefringence is present, $\sigma \neq 0$, the field $\vec{E}_o$ of eq. (11) is altered by the $\cos\Delta$ factor in the integrand of the diffraction integral. Because there is no birefringence at r = 0 in an isotropic window with axially symmetric strains, $\Delta(r)$ vanishes at r = 0. Thus $\cos\Delta$ is unity at the origin and decreases at finite r values, effectively replacing the smooth incident Gaussian field by one with radial minima on circles for which $\Delta(r) = (m + \frac{1}{2})\pi$, $m = 0, \pm1, \pm2 \ldots$. Figure 3 shows the effect of this factor on the focal intensity for various values of σ. One expects the frequency of the pronounced oscillations to be roughly proportional to σ, and this is indeed the case. The $\cos\Delta$ factor reduced focal intensity by decreasing the effective incident power (which is matched by an increase of power in the off-axis E_2 component) and by sharpening the effective mode structure thereby decreasing the diffraction length. The effect of birefringence on the time required for thermal lensing to cause the focal intensity to drop to half its original value is shown in figure 4. Of materials interesting for 10.6 μm operation, only KCl has a large effect, but birefringence could be a severe problem in the fluorides.

The off-axis structure in the focal plane is shown in figures 5 through 7 for $\sigma = 2$. Notice that the ring structure is contributed entirely by E_2 as anticipated in eqs. (12) and (13). The position of the ring in E_2 can be estimated by the following argument based upon eq. (12): The magnitude of E_2 at radius r is most strongly influenced by the value of $F \equiv r' \sin\Delta\, E_{in}$ at that value of r' for which $J_2(krr'/z)$ has its first maximum. Since this occurs at $J_2(3.1) \approx .486$, and since F(r') has a maximum at some value r'_m, we expect a maximum in $|E_2|$ near $r \approx 3.1\, z/kr'_m$. For the examples shown, this estimate agrees well with the ring radius in the numerical solutions. (The value of r'_m is easily determined from a plot of F(r').)

The aberration matrix formalism provides a convenient starting point for the analysis of more complicated window systems. Further applications of this formalism are described in the series of progress reports cited as reference [4].

Table 1. Dimensionless Times and Birefringence Parameters (Based on values tabulated in Ref. 1)

Material	σ	$\tau/w\int^{t} I_o(t')dt'$
KBr	-.598	-0.149
KCl	-1.344	-2.51
NaCl	-0.202	-6.30
KI	-0.296	-7.91
CsI	0?	-63.6
CsBr	0?	-80.7
CdTe	.0317	-181.4
KRS-5	0?	588.
ZnSe	.0746	1424.
GaAs	-.00886	2990.
InSb	0?	9790.
Ge	.0139	8570.
TI Glass #1173	0?	2890.
TI Glass #20	0?	3780.
Irtran-4 (ZnSe)	.0829	4310.
Irtran-6 (CdTe)	.0423	19500.

w = window thickness (cm)
I_o = incident axial intensity (Watt/cm^2)
t_o = time since turn-on (sec.)
σ and τ are dimensionless

References

[1] Bendow and Gianino, Applied Physics, 2, 1, 71 (1973), "Thermal Lensing of Laser Beams in Optically Transmitting Materials."

[2] Flannery and Marburger, Proceedings of Conference on High Power IR Window Materials (1971), "I.R. Window Criteria: 'Exact' Analyses of the Thermal Distortion Problem."

[3] R. V. Luneburg, Mathematical Theory of Optics, University of California Press, Berkeley, 1966.

[4] USCEE Report 469, I. R. Window Studies, F. A. Krüger and J. H. Marburger.

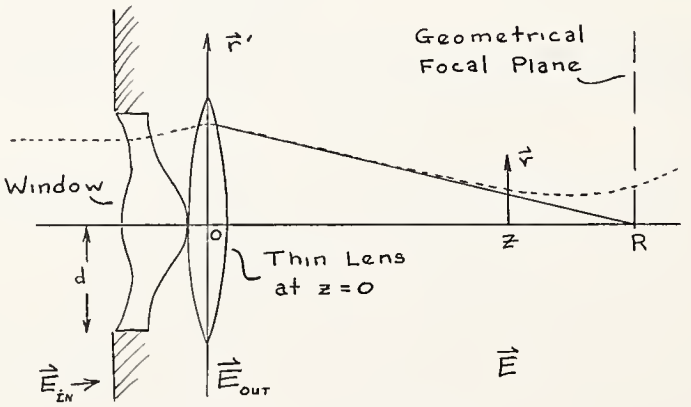

Figure 1. Window geometry.

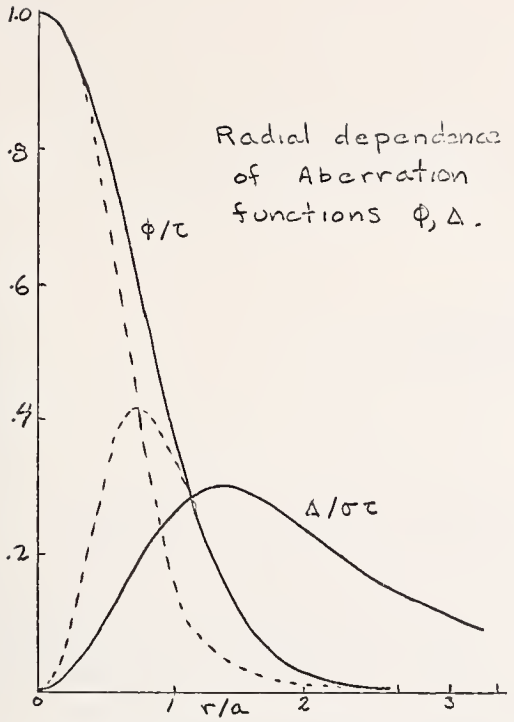

Figure 2. Radial dependence of aberration functions ϕ and Δ.

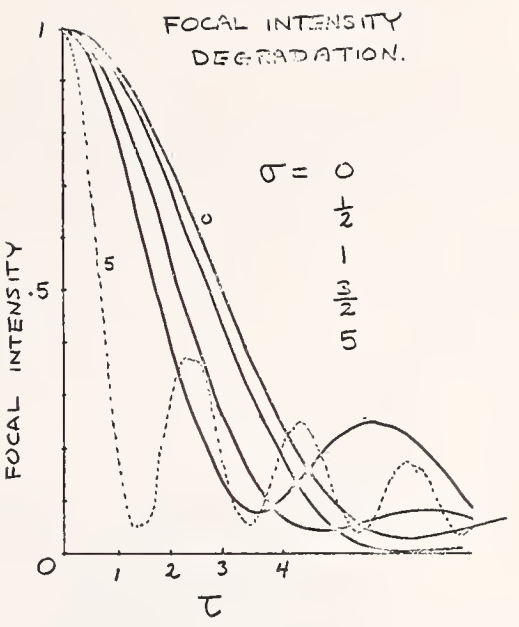

Figure 3. Focal intensity degradation with time for σ = 0, 0.5, 1, 1.5, 5.

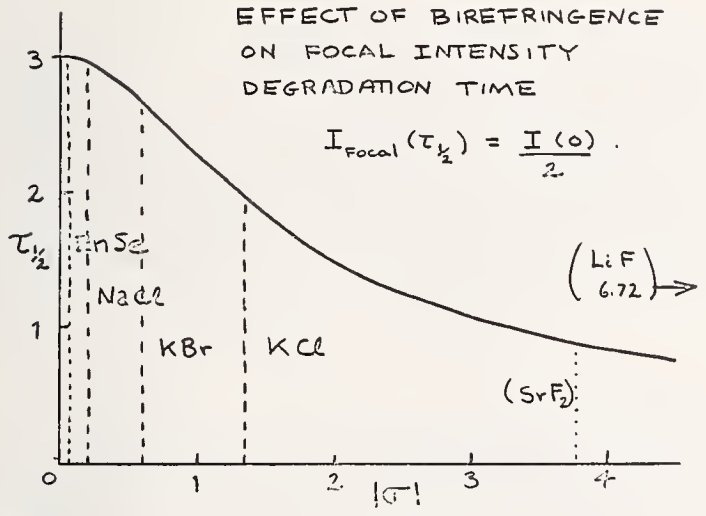

Figure 4. Effect of birefringence on focal intensity degradation time, $I_{focal}(\tau_{1/2}) = I_{focal}(0)/2$.

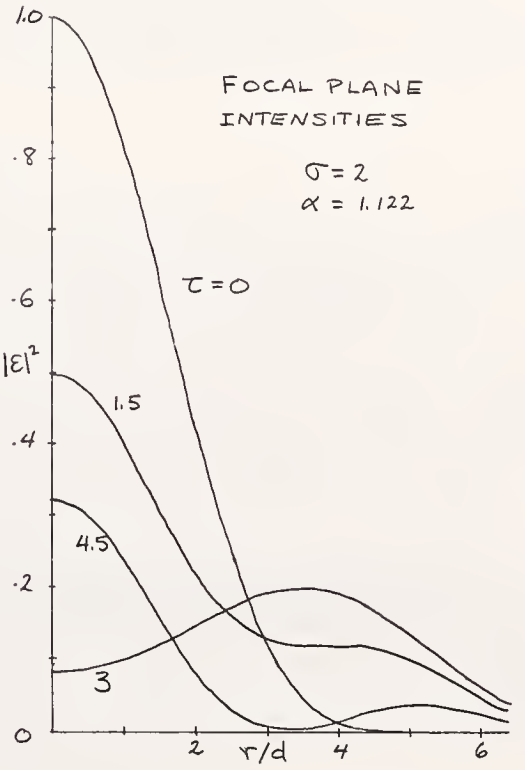

Figure 5. Focal plane intensities for σ = 2, α = 1.122, θ = 0 and $|\vec{E}|^2 = |E_o|^2 + |E_2|^2 - 2\,\mathrm{Re}\,(E_o E_2^*)$.

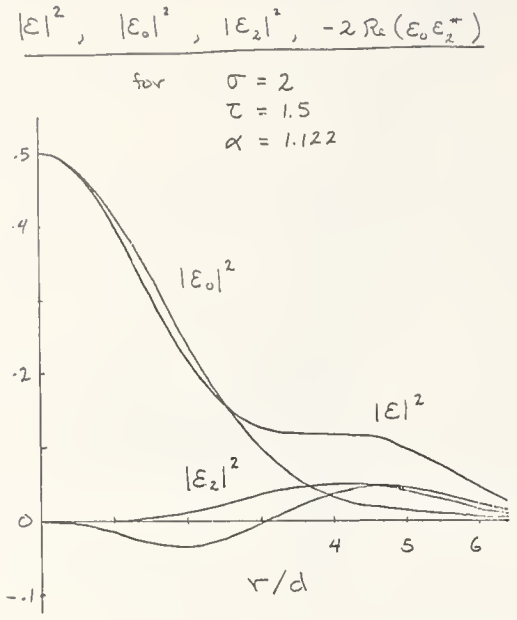

Figure 6. $|\vec{E}|^2$ for $\tau = 1.5$ from figure 5 plotted with its components $|E_o|^2$, $|E_2|^2$ and -2 Re $(E_o E_2^*)$.

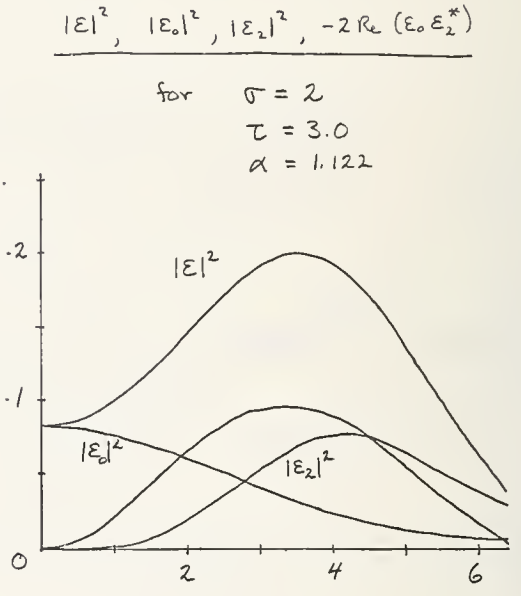

Figure 7. $|\vec{E}|^2$ for $\tau = 3.0$ from figure 5 plotted with its components $|E_o|^2$, $|E_2|^2$ and -2 Re $(E_o E_2^*)$.

COMMENTS ON PAPER BY FLANNERY

In response to a question on the intended empahsis of this work, the speaker commented that the aim of the work described was to call out effects of birefringence explicitly since the effects of uniform thermal lensing had already been well treated in the earlier literature. He also commented that the model presented predicted an asymmetric shift, or beam steering effect, which had subsequently been observed. This shift is sensitive to the geometry of the mount of the window in materials with large piezo elastic coefficients. In such materials, for example with a 3 point mount with the window tightly secured, a very large beam steering effect can be observed.

2.1 Damage Resistance of Dielectric Reflectors for Picosecond Pulses*

Brian E. Newnam

University of California
Los Alamos Scientific Laboratory
Los Alamos, NM 87544

A state-of-the-art survey has been conducted to determine the range of damage thresholds of electron-gun-produced dielectric reflectors irradiated by 30-ps laser pulses at 1.06 μm. Seven commercial coating companies, experienced in producing refractory-oxide coatings, supplied total reflectors of a specified TiO_2/SiO_2 design deposited on low-scatter glass substrates provided by LASL. Optional reflectors of ZrO_2/SiO_2 were also evaluated. Single-shot thresholds were determined by laser-induced scatter and photoelectric detection of spark radiation. Thresholds of TiO_2/SiO_2 reflectors ranged from 1 to 4 J/cm^2; those for ZrO_2/SiO_2 reflectors ranged from 0.5 to 2 J/cm^2. Reflectors which exhibited a large amount of diffuse, weak-signal scatter generally had low thresholds.

Key words: Damage thresholds; dielectric reflector; laser-induced scatter; picosecond pulses; spark thresholds; thin films; weak-signal scatter.

1. Introduction

The damage resistance of commercially-produced dielectric coatings is an important constraint in the design of short-pulse, high-power glass laser systems being built for laser fusion experiments. Heretofore, very few damage threshold values for subnanosecond pulses at 1.06 μm have been reported. In the present work, conducted with single 30-ps pulses, we have determined the range of damage thresholds of commercially-produced multilayer reflectors deposited by electron-gun evaporation. To evaluate the effect of only the coating preparation and deposition techniques used by each manufacturer, the coating design and materials were specified and low-scatter glass substrates were supplied. In addition, each company was invited to submit reflectors of alternate materials and/or designs which might be more damage resistant than the specified coatings. Results of these damage tests are presented in Section 7. Tests to determine the possible correlation of weak-signal scattering and damage thresholds are discussed in section 8.

2. Reflector Design and Materials

Seven commercial coating companies, experienced in producing refractory-oxide coatings, supplied two samples each of 20-layer TiO_2/SiO_2 reflectors according to the design specified in table 1. Reflectors of this design had the highest damage resistance in a previous study conducted with 13-ns ruby laser pulses. [1,2][1] Reflectors composed of ZrO_2 and SiO_2 were also submitted by four vendors. All reflectors were deposited on BK-7 glass substrates two inches in diameter and 0.5 inch thickness. Since it has been established that coating defects limit the practical damage threshold, it was desired that the surface finish of the substrates not initiate pits and grooves in the coatings. After examining the surfaces of BK-7 glass substrates submitted by several commercial polishers, the "super-polished" surfaces produced by Itek Corporation were selected for their minimal defects and surface roughness. The optical quality of the BK-7 glass was grade P which is specially selected from grade A melts. In selecting the best of the surfaces submitted by the several companies, it appeared that the number of surface defects might be related to the material grade. After polishing, further contact with the surfaces was prevented by shipping them to the coaters in special aluminum fixtures. Prior to coating deposition, it was suggested that the surfaces be wiped with methanol and lens tissue followed by a jet of nitrogen gas.

---

*This work was performed under the auspices of the U.S. Atomic Energy Commission.

[1]Figures in brackets indicate the literature references at the end of this paper.

Table 1. Damage resistance of dielectric reflectors (state-of-the-art survey)

A. Reflector parameters	
Coaters:	7 commercial vendors
Substrates:	BK-7 glass (grade P) Low-scatter surface polish obtained with bowl-feed method by Itek Corp.
Specified coating materials & designs:	20 layers TiO_2/SiO_2 with $G(HL)^9HL^2A$ layer configuration for normal incidence[a]
Optical coatings:	vendor's considered best[b]
B. Laser parameters:	
1. Wavelength:	1.064 μm
2. Pulsewidth:	30 ps
3. Beam spot-size radius at sample surface:	0.74 mm

[a]Configuration notation: G is the glass substrate, H and L are respectively high and low-index films of λ/4 thickness, and A is air.

[b]Four vendors submitted optional reflectors of ZrO_2/SiO_2.

3. Laser Apparatus

The diagnostic laser consisted of a mode-locked, Nd:YAG oscillator from which a single pulse was switched out by a Pockels cell/spark gap arrangement and augmented by two YAG amplifiers. The net output was approximately 50 mJ in a 30-ps pulse with a TEM_{00} spatial distribution. The energy was measured with accuracy of ± 5% with a calorimeter of LASL design [3], and a two-photon fluorescence camera measured pulsewidth. A fast Si photodiode and Tektronix 519 oscilloscope monitored the mode-locked pulse train.

For the present tests, the output was focused with a 2-m lens to a spot-size radius of 0.74 mm at the sample plane. The sample plane was located in front of the lens focal plane to avoid possible uncertainties in the axial intensity which can result from focusing truncated Gaussian laser beams.[2] A theoretical treatment of this topic has been performed by Farrukh. [4]

The beam profile was first measured at the lens plane by directing a small portion of the beam onto a Reticon RL 256EC linear scanner array (resolution of 0.05 mm) centered on the beam with a X-Y translation device. The signal was recorded on a Tektronic 556 oscilloscope and the resultant photograph allowed an instantaneous measure of the beam spot-size. The relative intensification of the focused beam at the sample surface was determined by measuring the energies required to barely damage unexposed, freshly developed, Polaroid 410 film at both lens and sample planes. (The damage threshold for 30-ps pulses of 1.06 radiation was measured to be 20 mJ/cm^2.) With such large spot-sizes it is also possible to measure the focused beam profile at the sample surface directly with the Reticon array, but a substantial error can result from inaccurate detector placement in a rapidly converging beam.

The damage test facility was housed in three adjacent rooms. One room contained the laser apparatus, the second was darkened and contained the damage experiment including energy and spark detectors, and the third contained the monitoring electronics. In this way, laser flashlamp emission and room lights did not interfere with visual and photoelectronic monitoring of damage, thereby enabling accurate detection of damage thresholds.

4. Detection of Damage

Damage was detected by two methods simultaneously (see figure 1). Optical breakdown accompanied by a high-temperature spark was detected with a photomultiplier (RCA 6655A) with a purple-transmitting filter (peaked at 4150 Å, 150 Å bandwidth) to discriminate against flashlamp energy. The photoelectric signal caused by the spark emission was measured with a Tektronix 556 oscilloscope. The sensitivity of the spark detection system was such as to detect a spark 10 μm in diameter with black-body temperature equal to the melting point of TiO_2 (2093°K).

Evidence of laser-induced disruption of the surface of a coating was manifested by increased scattering of He-Ne laser light. The beam from a low-power (2 mW) He-Ne laser, traveling collinearly with the pulsed laser beam, illuminated the test area. By comparing the level of scattering before, during (with N.D.9.0 safety goggles) and after pulse irradiation, changes in the coating structure could be detected. We found that visual detection of changes in the scatter level was much more sensitive than photoelectric detection of the same (i.e., with photomultiplier and lock-in amplifier). A third in situ technique of visual observation with a traveling microscope (30 X) was useful only for examining damage sites considerably above threshold.

5. Test Procedure

Each reflector was dusted with a jet of Freon gas to remove any possible dust particles. No other cleaning was considered necessary or desirable. In determining the damage thresholds, a given area of a sample was irradiated by one shot only. Sites of irradiation were spaced several millimetres apart. The energy of the laser beam was controlled by Schott neutral density filters to lie as close to the threshold as possible. Thus, easily visible damage rarely occurred. This care was necessary to prevent damage products from one area from influencing the thresholds of adjacent areas. An adequate sampling of the damage resistance was obtained with 30 to 40 shots.

6. Weak-Signal Scatter

Weak-signal scatter measurements were performed prior to the damage tests. A cw Nd:YAG laser beam (1 W) was directed at normal incidence onto the center of each reflector. A Si photodiode (EG&G YAG-44), subtending a solid angle of 3.3×10^{-3} sr, detected scattered radiation at 30° from the surface normal. It was considered important to use the same wavelength for these scattering tests as in the damage tests so as to have the same standing-wave electric field patterns in both cases. As shown in Figure 2, for defect-free films the laser light at the design wavelength, 1.06 μm, drops to a negligible value after eight layers. Imperfections in the layers (surface roughness and defects) alter the wave patterns and penetration depth somewhat, and the resultant scattering is dependent on the ratio of wavelength-to-imperfection dimension. This assertion is substantiated by McKenney and Mott [5] who found a strong wavelength dependence for the diffuse reflectance of dielectric films.

7. Test Results

The damage thresholds for TiO_2/SiO_2 and ZrO_2/SiO_2 reflectors are given in tables 2 and 3 in terms of peak energy density. Values ranged from 1 to 4 J/cm^2 for the former and 0.5 to 2 J/cm^2 for the latter. Thresholds were determined independently by spark detection and laser-induced scatter (LIS). Generally, thresholds determined by spark were lower than or equal to those by LIS monitoring. This occurred especially for reflectors with high levels of initial scattering. Occasionally, however, LIS changes were noted without any measurable spark, probably when an absorbing inclusion was irradiated. Therefore, net thresholds determined with both techniques are also tabulated and are considered the most useful.

The thresholds are given as a range of values instead of a single number. The larger value was the highest energy density which caused no damage; the lower value was the lowest energy density which caused threshold damage. Occasionally, a laser shot with energy density considerably higher than the determined threshold produced no damage. Likewise, an energy density significantly lower than the range indicated sometimes caused damage; such values are given in parentheses. Since the laser spot-size was large (0.74 mm), no statistical nature of damage should be inferred. [6] The range of threshold values is believed to be a measure of the variable damage resistance of the coatings from one area to another.

Although only two samples of TiO_2/SiO_2 reflectors were tested from each manufacturer, a relatively large range of damage thresholds was measured. Since coating design and materials were specified and equivalent low-scatter glass substrates were used for each coating, only variation in vacuum-deposition technique and possibly starting material purity remain to explain the differences.

Table 2. Damage thresholds of commercial TiO_2/SiO_2 multilayer reflectors[a]

Reflector Designation[b]	Peak Energy Density by spark	by LIS	net by spark & LIS combined
	J/cm²	J/cm²	J/cm²
A-1	2.9-4.0 (2.4)[c]	2.9-4.0 (2.4)	2.9-4.0 (2.4)
A-2	2.6-4.1 (2.1)	2.6-4.2	2.6-4.1 (2.2)
B-1	2.9-4.2 (4.7)	3.0-4.2	2.9-3.7 (4.2)
B-2	3.0-4.3 (2.5)	2.8-4.1 (2.5)	2.8-4.0 (2.5)
C-1	2.8-4.0 (1.9)	3.1-3.7	2.8-3.7 (1.9)
C-2	2.3-3.9 (1.9)	2.3-4.0	2.3-3.6 (1.9)
D-1	2.8-3.4 (2.4)	2.8-3.9 (4.3)	2.8-3.4 (2.4)
D-2	1.2-1.8 (2.3)	1.2-2.5 (3.7)	1.2-1.8 (2.3)
E-1	1.6-2.3	2.0-2.3 (1.7)	1.6-2.3
E-2	1.4-2.2	1.8-2.2	1.4-2.2
F-1	0.84-1.7	1.1-1.7	0.84-1.7
F-2	1.2-3.9	2.0-3.5 (1.5)	1.2-2.2 (3.2)
G-1	0.81-1.3	0.96-1.3	0.81-1.3
G-2	0.78-1.0	0.78-1.0	0.78-1.0

[a]Design: $G(HL)^9HL^2A$.

[b]Identification of coating manufacturers with reflector designation may be obtained from the author.

[c]Values in parentheses were for single shots considered outside the general range.

Table 3. Damage thresholds of commercial ZrO_2/SiO_2 multilayer reflectors

Reflector Designation[a]	Peak Energy Density by spark	by LIS	net by spark & LIS combined
	J/cm^2	J/cm^2	J/cm^2
A-3	0.71-1.0 (1.5)[b]	0.83-1.2 (1.5)	0.71-1.0 (1.5)
A-4	1.5-1.8	1.4-1.8	1.4-1.8
D-3	0.80-1.2 (1.6)	0.80-1.6	0.80-1.2 (1.6)
D-4	0.87-1.9	1.4-2.3	0.87-1.6 (1.9)
E-3	0.57-1.6	0.94-1.6	0.57-1.6
E-4	0.48-1.6 (3.3)	0.88-1.9	0.48-1.5
G-4	1.1-2.1	1.6-2.1	1.1-2.1

[a]Identification of coating manufacturer with reflector designation may be obtained from the author.

[b]Values in parentheses were considered outside of the general range.

8. Weak-Signal Scattering

The scatter measurements for the TiO_2/SiO_2 reflectors are plotted in terms of bidirectional reflectance versus damage threshold in Figure 3. Bidirectional reflectance is defined as the fraction of incident power P_0 of unit wavelength, incident from direction (θ_1, ϕ_1), which is reflected in direction (θ_2, ϕ_2) per unit solid angle Ω_2,

$$\rho_B(\theta_1, \phi_1; \theta_2, \phi_2, \lambda) = \frac{\pi}{\cos \theta_2 \Omega_2} \cdot \frac{P_2}{P_0} . \quad (1)$$

The factor of $\pi/\cos \theta_2$ is required so that the directional reflectance ρ_D (the quantity measured by integrating spheres) may be directly calculated by integrating ρ_B over the hemisphere according to the standard definition,

$$\rho_D(\theta_1, \phi_1, \lambda) = \frac{1}{\pi} \int_{\Omega} \rho_B \cos \theta_2 d\Omega_2 . \quad (2)$$

A general correlation of decreasing damage threshold with increasing bidirectional scatter is seen in Figure 3. The correlation is most apparent for reflectors with largely differing scattering levels and is weak for reflectors with scattering of the same magnitude. This same type of correlation was previously reported by Newnam and DeShazer [2] for scattering and damage by 13-ns ruby laser pulses. Results of that study for TiO_2/SiO_2 reflectors are presented in Table 4. For the eight ZrO_2/SiO_2 reflectors measured, the bidirectional reflectances were all in the range from 10×10^{-2} to $20 \times 10^{-2} sr^{-1}$.

That the damage thresholds were generally lower for coatings with high scatter is a reasonable result. The effective absorption coefficient of a coating can be enhanced via internal reflections of the scattered energy. [7] If the contribution of scattering to the net deposition of energy is great enough, the resultant damage threshold would be lower than the threshold for no scattering. It is also possible that the scattering process itself does not increase the absorption of energy significantly. Instead, the level of scatter may indicate the relative presence of other film defects which do control the threshold by another mechanism. As an example, grooves and pits can cause localized enhancement of the electric field. [8]

Table 4. Comparison of weak-signal scatter and spark threshold for TiO_2/SiO_2 multilayer reflectors designed for 6943 Å[a]

Reflector designation	Normalized scatter intensity at 6943 Å	Peak energy density threshold (by spark)[b]
		J/cm²
0104	1.0	107-127
0102	2.3	98-110
0101	3.5	83-103
0103	3.7	121-126
S101	6.5	44- 56

[a]Excerted from table 5 of reference 2.

[b]Damage thresholds were obtained with 13-ns pulses from a TEM_{00} mode ruby laser and spot-size radius of 0.06 mm at the sample surface.

9. Discussion

It is interesting that the best ZrO_2/SiO_2 reflectors had less than one-half the damage threshold (1-2 J/cm²) as that of the best TiO_2/SiO_2 reflectors (3-4 J/cm²). By considering only linear absorption in defect-free films, ZrO_2/SiO_2 reflectors should have been the more damage-resistant. This can be shown from the following analysis which includes standing-wave electric fields and thermal and optical properties of defect-free films. It is necessary to consider only the fields in and the properties of the high-index components, TiO_2 and ZrO_2, since these have much smaller damage thresholds than the low-index component, SiO_2.[2] In addition, the first high-index layer would be most likely to damage first, since the peak standing-wave electric field drops rapidly in subsequent layers (see Figure 2).

The absorbed energy required to melt a TiO_2 film is 6845 J/cm²; that to melt a ZrO_2 film is 9400 J/cm², which is ~35% larger. [1] But the normalized electric field, $|E/E_0^+|^2$ at the first H-L interface is also about 35% greater for a ZrO_2/SiO_2 reflector than for a TiO_2/SiO_2 reflector. [1] So, reflectors with TiO_2 and ZrO_2 high-index layers would be expected to have equal damage thresholds by thermal and electric-field property considerations alone. However, optical properties must also be included. The UV absorption resonances of ZrO_2 and TiO_2 are at 2480 Å [9] and 3200 Å [10], respectively. Considering also that the real part of the refractive index of ZrO_2 films is less than that of TiO_2 (~2.0 compared to ~2.3 at 1 μm), the linear absorption coefficient α of a ZrO_2 film would be less than for TiO_2. Thus, by linear absorption alone in defect-free films, ZrO_2/SiO_2 reflectors should be the more damage-resistant. This is opposite to the present experimental results.

If linear absorption was the only operable damage mechanism, unrealistically high values of the absorption coefficient would be required for both TiO_2 and ZrO_2 films. The corresponding coefficients for the thresholds measured would range from 1000 to 5000 cm^{-1}. We are, therefore, forced to consider nonlinear absorption processes, such as multiphoton absorption, and film defects. Two photon absorption of pure TiO_2 films was probably not the damaging mechanism since damage at the 4 J/cm² level would require a coefficient of ~140 cm^{-1} which is much larger than the ~1 cm^{-1} value measured by Waff and Park.[11] Defects and absorbing impurities, however, could result in both enhanced multiphoton absorption [12] and localized linear absorption greater than the average over the surface. The observed correlation between weak-signal scattering and damage threshold supports this latter premise. Previous investigations of dielectric films designed for 6943 Å have uncovered the role of film defects by measuring thresholds as a function of laser spot-size [13] and pulse duration.[14] It is probable that similar tests on the present state-of-the-art reflectors will further implicate film defects as the main limitation on damage resistance.

10. Summary

Several interesting results from this study may be listed:

1. The present electron-gun coating-deposition technology has resulted in higher damage thresholds for TiO_2/SiO_2 reflectors (1 to 4 J/cm²) than for ZrO_2/SiO_2 reflectors (0.5 to

2 J/cm^2) for 30-ps laser pulses at 1.06 μm.

2. The wide range of thresholds among the seven coaters surveyed appears to be due to the various coating techniques used.

3. Reflectors with a relatively large amount of scatter have low thresholds. Bidirectional scatter measurements can be a useful, nondestructive method to segregate low threshold reflectors.

11. Acknowledgments

The author is grateful to the following individuals and their coating companies who prepared reflector coatings for this study:

1. C. Broomer of Broomer Research Laboratories
2. V. Costich of Coherent Radiation
3. M. Grindel of Continental Optics
4. Y. Hahn of CVI Laser, Inc.
5. D. Sigler of Laser Energy, Inc.
6. M. Ogne of Optical Coating Laboratory, Inc.
7. G. DeBell of Spectra-Physics Corp.

The cooperation of E. Podbielski of Itek Corp. regarding the glass substrates is also acknowledged.

At Los Alamos Scientific Laboratory, the author was assisted by G. Hoffman in optical microscopy and K. Winn in preparing the diagnostic laser. Special thanks go to J. Hudson for assistance in data acquisition and reduction, and to Jo Ann Painter for skillful editing and typing of the manuscript.

12. References

[1] Newnam, B. E., "Laser-Induced Damage Phenomena in Dielectric Films, Solids and Inorganic Liquids," dissertation, Univ. of Southern California (1973). Available from University Microfilms, Ann Arbor, Michigan.

[2] Newnam, B. E., and DeShazer, L. G., in Laser Induced Damage in Optical Materials: 1972, edited by A. J. Glass and A. H. Guenther, (NBS Special Publication No. 372, October, 1972), pp. 123-134.

[3] Watt, B. E., Appl. Opt. 12, 2372 (1973).

[4] Farrukh, U. O., "Diffraction and Focusing of Truncated Gaussian Beams," dissertation, Univ. of Southern California (1974). Available from University Microfilms, Ann Arbor, Michigan.

[5] McKenney, D. B., and Mott, L. P., J. Opt. Soc. Am. 61, 665 (1971).

[6] Bass, M., and Barrett, H. H., in Laser Induced Damage in Optical Materials: 1972, op. cit., pp. 58-69.

[7] Winsor, H. V., in Conference on High-Power Infrared Laser Window Materials, edited by C. S. Sahagian and C. A. Pitha, (Air Force Cambridge Research Laboratories Report AFCRL-71-0592, 1971), pp. 351-368.

[8] Bloembergen, N., Appl. Opt. 12, 661 (1973).

[9] Travina, T. S., and Mukhin, Yu. A., Sov. Phys. J. 9, 40 (1966).

[10] Meehan, J., and Salomon, R. E., J. Phys. Chem. 70, 3642 (1966).

[11] Waff, H. S., and Park, K., Phys. Lett. 32A, 109 (1970).

[12] Braunlich, P., in Damage in Laser Materials, edited by A. J. Glass and A. H. Guenther (NBS Special Publication No. 341, December, 1970), pp. 102-104.

[13] DeShazer, L. G., Newnam, B. E., and Leung, K. M., in Laser Induced Damage in Optical Materials: 1973, edited by A. J. Glass and A. H. Guenther, (NBS Special Publication No. 387, December, 1973), pp. 114-123.

[14] Milam, D., Bradbury, R. A., and Bass, M., in Laser Induced Damage in Optical Materials: 1973, op. cit., pp. 124-132.

564-378 O - 74 - 5

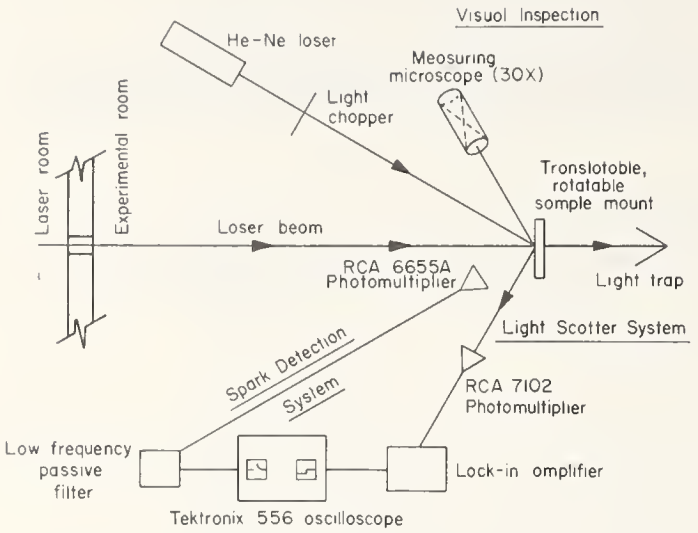

Figure 1. Methods for detecting laser-induced damage to optical components: 1) photoelectric spark detection, 2) laser-induced scatter (LIS) of a He-Ne beam (electronic and visual), and 3) visual inspection with a low-power microscope.

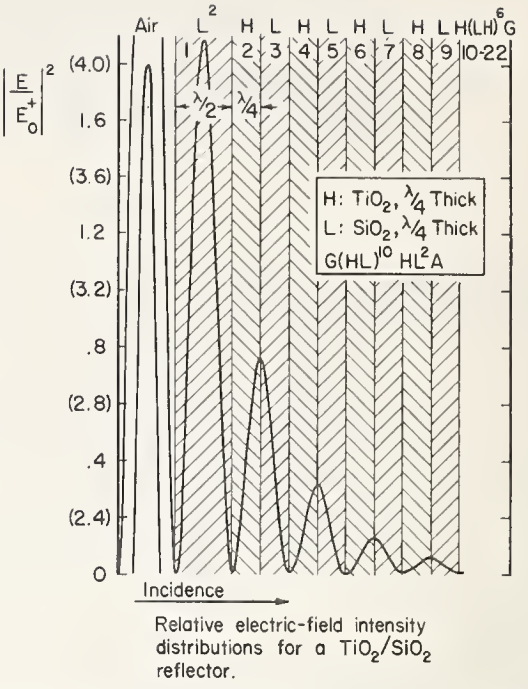

Figure 2. Relative electric-field intensity distributions for a TiO_2/SiO_2 multilayer reflector.

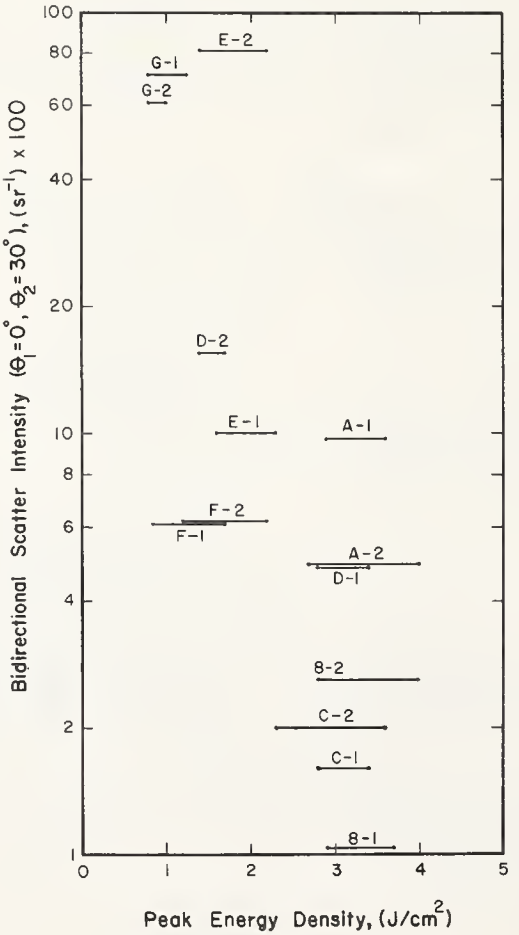

Figure 3. Initial weak-signal scatter at 1.06 μm versus damage threshold for TiO_2/SiO_2 multilayer reflectors.

COMMENTS ON PAPER BY NEWNAM

The speaker commented that the roughness of the substrate would be expected to have an effect on coatings of a few degrees, but for multilayer coatings, the effect of substitute roughness would not be observable. M. J. Soileau of the Michelson Laboratory indicated that films tested at that laboratory clearly showed roughness corresponding to the substitute roughness, even with many layers.

D. Milam of AFCRL commented that over large aperatures, it is the weakest area which determines the damage threshold. The speaker commented that regions of higher scattering damaged more readily than low-scattering regions of the same film. He also indicated that those manufacturers who produced the films with the highest damage levels also produced films with fewer weak spots (highly scattering regions). Thus, whether the low or high value of damage threshold was taken as representative of a given film, the rank ordering of samples was essentially the same. In all cases run, substrate damage thresholds were much higher than film damage values. All the film designs tested had a SiO_2 layer at the surface. Even though this gives a higher internal field value, it was chosen to give a compressive stress in the outside layer, for structural strength.

2.2 Damage Studies at 1.06μm With 100-200 ps Pulses*

G. W. Leppelmeier and M. Finkelstein

Lawrence Livermore Laboratory
Livermore, California 94550

Studies have been conducted of the damage threshold at 1.06 μm of multi-layer dielectric films used as polarizing beamsplitters, mirrors, and anti-reflection coatings, $K(H_x \ldots D_{2-x})PO_4$, several high Verdet constant glasses, and micro-machined silver. The laser pulse used had less than 4% spatial and temporal ripple. Pulse energy of up to 1 joule permitted using a collimated beam. Damage thresholds in the range 1-5 J/cm^2 were obtained.

Key words: Laser damage; mirror damage; thin films.

1. Introduction

Lasers for laser-driven fusion are characterized by subnanosecond pulse lengths, apertures of hundreds of millimeters, and energy densities approaching bulk material limits. Thus the optical components in such laser systems are subjected to very high stresses, in addition to the stringent requirements placed by large apertures and high optical beam quality. At present, the damage threshold of optical coatings, along with nonlinear beam distortion, poses a major limitation in the performance of laser-fusion lasers, particularly for Nd:glass lasers. For this reason we are interested in the macroscopic damage resistance of films and surfaces, and report here investigation of the damage threshold at 1.064 μm, for pulses of 100-200 picoseconds, of multi-layer dielectric coatings, as used for polarizing beam splitters, mirrors, and anti-reflection (AR) coatings, as well as several magneto-optic and electro-optic materials.

The laser system is indicated in the schematic of figure 1, and is designated the "Intermediate Laser System" (ILS). It consists of a Nd:YAG oscillator, single-pulse selection unit, two Nd:YAG pre-amplifiers (LLL-designed and built) and two CGE glass amplifiers, one with 16 mm diameter and one with 32 mm diameter. The spatial properties of the beam are determined by a spatial filter between the two Nd:YAG pre-amplifiers (in early experiments this was simply a pinhole, without lenses) and a soft aperture, or apodizer, near the input of the first glass amplifier. Temporal smoothness of the pulse is insured by etalons in the oscillator cavity which provide a time/bandwidth-limited pulse. Figures 2 and 3 show the spatial and temporal beam profiles, respectively. The absence of reproduction of the large features in successive traces permits the inference that the large features are due to film noise or the like, and that the actual ripple is less than 4%, both in space and time. In early experiments the streaking camera traces indicated that the full width at half maximum intensity was 200 ps ± 25 ps. Most of the data were obtained more recently with a characteristic FWHM time of 125 ps ± 25 ps. The maximum energy available from the ILS before beam breakup due to nonlinear effects is about 1 joule, which provides peak energy densities of up to 8-10 J/cm^2 in a collimated beam rather than a focused beam. Thus the damage measurements are obtained for "macroscopic" regions, i.e., 0.5-2 mm, rather than for small focal regions.

The experiment itself is described in figure 4, which shows the beam emerging from a 3:1 telescope and passing through an uncoated, wedged beam splitter. One of these diagnostic beams then goes to a 2.5 mm aperture in front of a high resolution LLL calorimeter [1][1]. The other diagnostic beam is used to produce a multiple reflection image, either on Polaroid film or Kodak 1-Z high resolution film. The main beam then passes to the test sample. The 2.5 mm aperture, the film plane, and the test sample are all the same distance away from the beamsplitter. For low eneregy densities (1-2 J/cm^2) the beam profile was approximately flat across the central 2.5 mm. As the energy rises (2-4 J/cm^2) some whole beam self-focusing occurs, making the peak energy

*This work was performed under the auspices of the U. S. Atomic Energy Commission.

1. Figures in brackets indicate the literature references at the end of this paper.

density somewhat higher than the average over the central 2.5 mm, which is what the calorimeter measures. At energy densities higher than 3-4 J/cm^2 the edges of the beam experience a severe self-focusing, causing the peak energy density to occur at the edge of the beam, rather than the center. When the beam is not extremely smooth, small-scale self-focusing causes the beam to break up into hot spots with peak energy densities much higher (2-4 X) than the average.

The results will be presented for average energy density over a 2.5 mm aperture. In cases where the peak energy density was notably higher than average a note will be made as to the necessary correction. The ratio of peak energy density to average energy density (E_p/E_{av}) is obtained by tracing the beam profile on the high resolution film with a microdensitometer. Since the ratio of exposures of adjacent spots on the multiple-image film is equal to the reflection of the partially transmitting mirror, each film is auto-calibrating. Plotting the exposure versus r^2 then allows us to use a polarimeter to obtain the ratio of peak exposure to average exposure, which is equal to E_p/E_{av}.

2. Experimental Results

Tables 1-4 contain summarized results of the damage tests.

Polarizing beam splitters: table 1 contains the results of damage testing of polarizers. All the polarizers were tested at an angle of incidence of 56.5 ± .2 (Brewster's angle for the substrate, which is BK-7 for all samples). The polarizers are designed as stop-band filters, with the transition to transmission occurring for the P-polarization at a shorter wave length than for the S-polarization, due to the oblique angle of incidence. Generally, the samples had twenty to thirty layers. Fluorescence analysis indicated that the high-index layers contained zirconium or titanium, sometimes with potassium or cerium added. We assume the low index material was SiO_2, which would be indistinquishable from the substrate. It was also evident from the angle and wavelength dependence of the transmission of the two polarizations that decidedly different coating designs are used. We found no correlation of damage threshold with coating materials or polarizer performance.

Table 1. Measured damage thresholds for multilayer dielectric coated polarizers

Substrate Material: BK-7

Unless otherwise noted, pulse times are 125 ± ps (FWHM) and energy densities are average over 2.5 mm circular aperture.

Manufacturer	Resisted Damage at (J/cm^2)	Damaged at ($J\ cm^2$)	Remarks
A	3.2 2.8-3.2 (3 shots)	3.8 3.1-3.8 (4 shots)	peak energy density, 200 ps x 1.3 = peak energy density
B	--	1.5-2.0	peak energy density, 200 ps
C	1.8-2.5 (3 shots)	2.5-3.0 (4 shots)	x 1.6 = peak energy density
D	3.6, 5.3 2.1, 2.1	4.3, 6.7 2.2, 2.2, 4.2	peak energy density, 200 ps x 1.5 = peak energy density
E	3.3-4.8 (10 shots)	5.2-5.9 (4 shots)	x 2.0 = peak energy density
F	3.3-5.8 (15 shots) on two spots)	6.7	beam badly broken up
G	2.9-3.7 (5 shots)	3.1, 3.5, 4.4	x 1.3 - peak energy density

Several manufacturers supplied anti-reflected coatings on EY-1 samples furnished by LLL. The damage tests of these samples are summarized in table 2. The best results are comparable to the best attained for polarizers, but not by the same manufacturers.

Table 2. Measured damage thresholds for anti-reflection coating on EY-1

Pulse times are all 125 ± 25 ps
Energy densities are average over 2.5 mm circular aperture

Manufacturer	Resisted Damage at (J cm^2)	Damaged at (J cm^2)	Remarks
A	2.6-3.6 (6 shots)	3.6, 4.8, 5.3	x 1.5 = peak energy density
D	4.0-5.4 (7 shots)	--	x 1.3 = peak energy density
F	2.0-2.9 (6 shots)	2.8-4.0	x 1.3 = peak energy density
G	3.0-4.7 (9 shots)	5.0-6.2	x 1.2 = peak energy density

Table 3 contains damage testing results for mirrors: micro-machined silver and a BK-7 prism as well as multi-layer dielectrics. The silver mirror was made at Y-12, in a single cut on 0.762 mm of electrolytically deposited silver on OFHC copper. While the thresholds for the dielectric coats are nearly as high as for the glass prism, they are definitely lower than for the polarizers and AR coats. As would be expected due to superposition of electric fields, the BK-7 prism damaged at the internal reflectance face.

Table 3. Measured damage thresholds for mirrors

Pulse times are 125 ± 25 ps

Manufacturer	Resisted Damage at (J/cm^2)	Damage at (J/cm^2)	Remarks
B	1.6	1.4, 2.0	$\theta_i = 0°$
H	2.0-2.5 (4 shots)	2.3, 2.7, 2.7	x 1.5 = peak energy density, $\theta_i = 45°$
μ-machined Ag	0. 6-1.0 (15 shots)	1.0, 1.0	
	Earlier tests at 200 ± 25 ps. Values are peak energy density.		
BK-7	3.0-4.2	4.7, 4.9	90° turning prism
D	2.6-3.1	3.3-3.9	$\theta_i = 45°$
B	2.5-3.3 (9 shots)	3.5-4.5	$\theta_i = 45°$

Lastly, table 4 gives damage thresholds for three Faraday rotator glasses and KDP and KD*P with deuterations of 86% and 97%. FR-4 is a cerium-doped glass made by Hoya Optical Company. FRN-5 is a terbium-doped glass from the same company, while EY-1 is a terbium-doped glass made by Owens-Illinois. As can been seen, all three glasses are very tough. The KDP samples were not subjected to energy densities any higher than 3.0 J/cm^2. The KDP samples were aligned close enough to k-vector matching to provide some doubling to 5320 Å, but not for maximum second harmonic generation, as this would have caused a reflection directly back into the glass amplifiers.

Table 4. Measured damage thresholds for several magneto-optic and electro-optic materials

Energy densities are peak values

Material	Resisted Damage at (J/cm^2)	Damaged at (J/cm^2)	Remarks
FR-4	4.0	7 (beam broken up)	200 ± 25 ps
FRN-5	7.4	--	125 ± 25 ps
EY-1	4.2		200 ± 25 ps
KDP	2.5-3.0 (7 shots)	--	125 ± 25 ps
KD*P (86%, 97%)	2.5-3.0 (6-8 shots)	--	125 ± 25 ps

3. Summary

The aim of these tests was to evaluate various components for the LLL Nd:glass laser systems, with the goal of obtaining reliable optical components at energy densities around 2 J/cm^2, for pulses in the range of 100-200 ps. In large part, this goal has been obtained, with the mirors remaining an item for improvement. Our experience underlines the necessity of very clean beams for nanosecond and subnanosecond work: the slightest modulation in the beam will self-focus and cause a local energy density far in excess of the average. It seems quite clear that damage resistance in dielectric coatings is process-dependent. Achievement over large apertures of the high damage resistance reported here remains a difficult and demanding challenge to the coater, as does further increase in the damage thresholds.

4. References

[1] S. R. Gunn, "Volume-Absorbing Calorimeters for High-Power Laser Pulses", Rev. Sci. Instr., July 1974, to be published.

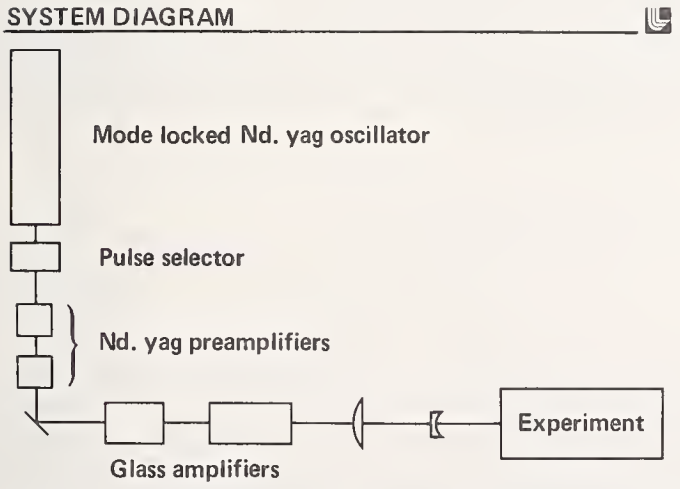

Figure 1. Diagram of the Intermediate Laser System. Generally a spatial filter is inserted between the ND:YAG pre-amplifiers and a soft aperture is placed near the input of the first glass amplifier. The two ND:glass rod amplifiers are made by CGE-Marcoussis and are 16 mm and 32 mm in diameter, respectively.

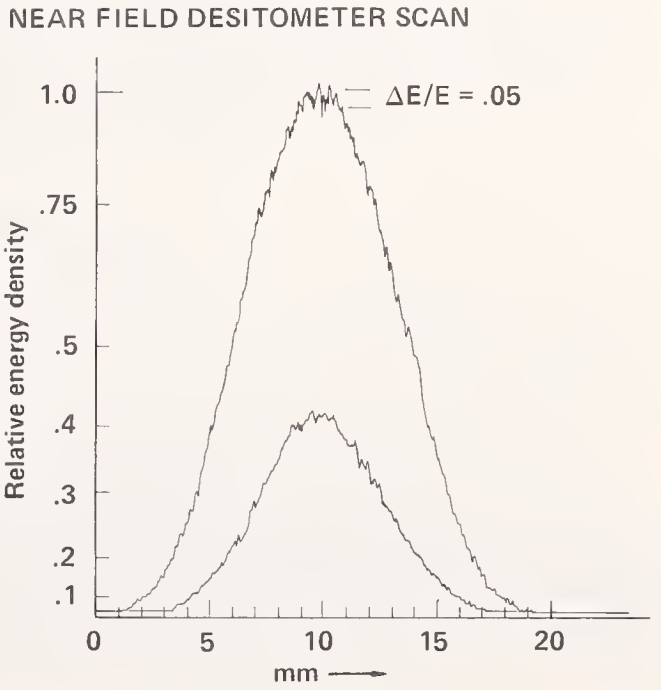

Figure 2. Typical microdensitometer traces of the time-integrated transverae beam profile.

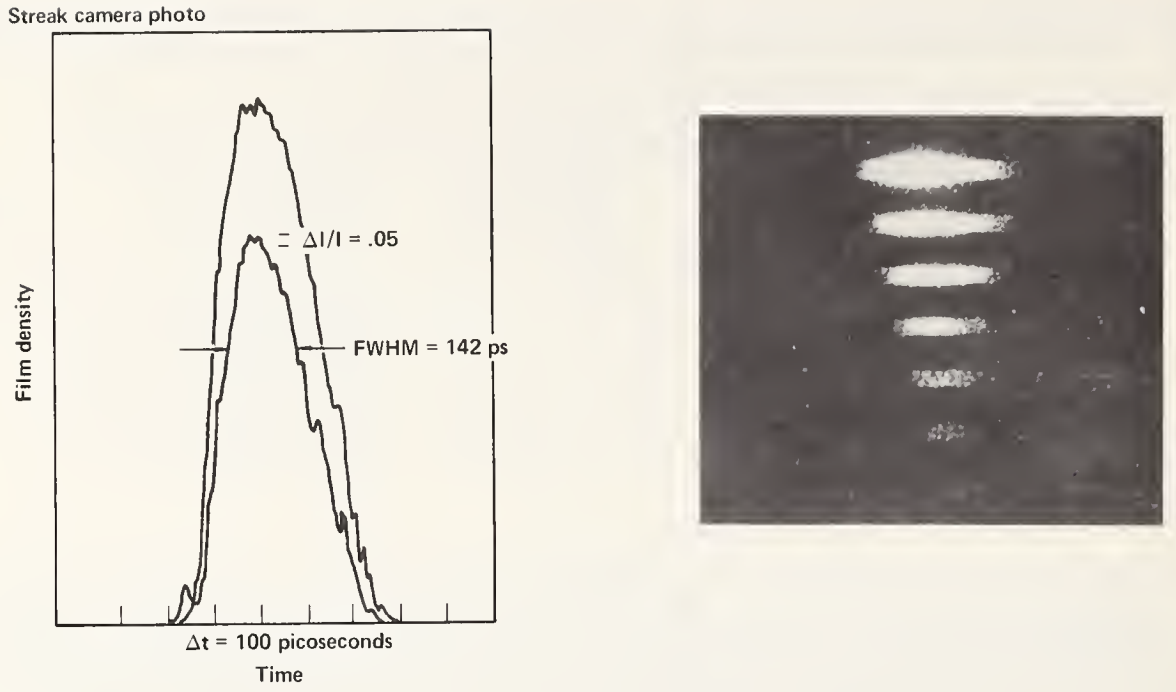

Figure 3. Typical microdensitometer traces of streaking camera records showing temporal character of the beam.

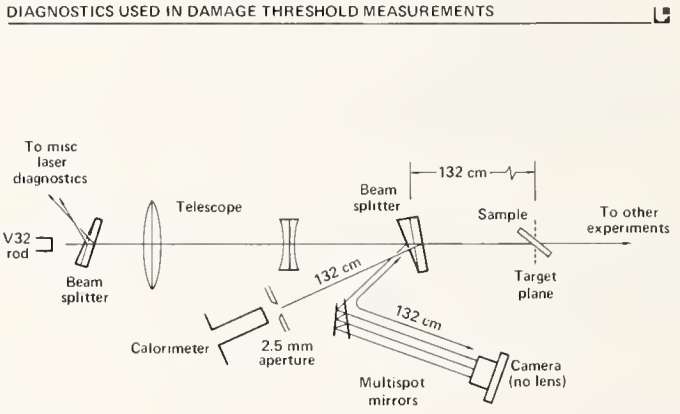

Figure 4. Diagram of the experimental set-up and diagnostics. See text for discussion.

COMMENTS ON PAPER BY LEPPELMEIER

It was asked if the presence of obscuring inclusions in multilayer dielectric structures was sufficient to disrupt the standing wave pattern, and therefore influence the damage threshold. Due to scattering in the material, this was thought to be unlikely. In inclusion-dominated damage in multilayer coatings, D. Milam of AFCRL reported damage at inclusion sites, not at the interfaces of the coating layers.

2.3 Damage Thresholds in ZnSe, A/R Coated NaCl and Micromachined Mirrors by 10.6 μm Multijoule, Nanosecond Pulses*

Eugene E. Stark, Jr. and Walter H. Reichelt

Los Alamos Scientific Laboratory
University of California
Los Alamos, NM 87544

Multijoule, nanosecond pulses at 10.6 μm were used to determine the damage thresholds of uncoated and antireflection (A/R) coated ZnSe, A/R coated NaCl and micromachined mirrors. The ZnSe results indicate that the A/R coatings have a higher damage threshold than the bulk material. Antireflection coatings on NaCl were found to have a damage threshold slightly lower than uncoated NaCl. Damage thresholds for micromachined copper and gold are greater than 4 joules/cm^2.

Key words: A/R coatings; damage thresholds; machined mirrors; ZnSe.

1. Introduction

The damage thresholds of various optical components are important parameters in the design of large, short pulse CO_2 systems. The threshold may be defined as the incident energy flux level which results in observable damage to the surface or bulk material of the component. Damage thresholds have been established for the two prime window material candidates, NaCl and KCl. [1][1] Recent emphasis by the Air Force in developing large ZnSe windows for CO_2 laser use has prompted an investigation of both uncoated and A/R coated ZnSe. The results of this investigation are discussed in this paper.

A/R coatings are necessary in order to reduce beam losses due to Fresnel reflections in the case of high index of refraction materials. This, of course, is an alternative to the use of Brewster angle windows. While these losses are of considerable importance in the case of ZnSe because of the high index of refraction, they also become important in the case of the alkali halides when a number of these components are involved in a system. In addition, due to the hygroscopic nature of the alkali halides, it may be prudent to use the A/R coating as a protective coating. Results from a preliminary investigation of A/R coated NaCl are also given in this report.

Gas laser systems require large numbers of metal mirrors for beam handling and focusing. Conventional fabrication techniques for these components are both costly and time consuming. Recent developments in the direct micromachining of optical surfaces [2] implies that this process will reduce mirror fabrication time and costs. Mirrors fabricated by means of micromachining have been used extensively in the Los Alamos Scientific Laboratory CO_2 laser system. Lower bound damage thresholds have been established for both copper and gold micromachined surfaces and are reported.

2. Experimental Configuration

The experimental configuration, pulse shapes, etc., have been described in the Damage Symposium Proceedings of 1973. [3] Consequently, they will be reviewed here briefly for completeness.

The Los Alamos Scientific Laboratory pulsed CO_2 laser was used to provide a well characterized joule level, nanosecond pulse. Joule level pulse generation is accomplished by amplifying a TEM_{00}, polarized, millijoule pulse in three electron beam pumped amplifiers as shown in figure 1. The TEM_{00} energetic pulse is focused into a clean-gas-filled tube by an R = 4m totally reflecting mirror. The sample is located in flowing clean gas to minimize dust effects. Reflecting surfaces are at a slight angle from normal in order to prevent reflections from traversing back into the still-active amplifier system. Average peak energies are determined by means of an aperture and calorimeter.

Damage observations are made visually and with the aid of a telescope. Damage sites are examined with the aid of optical and scanning electron microscopy.

---

*Work supported by the U. S. Atomic Energy Commission.

1. Figures in brackets indicate the literature at the end of this paper.

3. Results and Discussion

3.1 Dielectric Window Materials

a. Uncoated ZnSe

These samples were prepared by the CVD process at the Raytheon Research Laboratory. Optical microscopy reveals a high-density of voids and inclusions scattered throughout the volume. The fabrication process is such that these defects occur predominantly in layers. Sectioned and polished layers reveal these bulk defects as well as a highly stressed material as seen in figure 2(a). Some grain boundary separation is noted at or near the surface in some samples. Electric field enhancement [4] at these defects results in a lower damage threshold and may cause catastrophic damage.

ZnSe damages in the bulk material at an average incident energy of 1.5 joules/cm^2. There is a variation in the defect density from sample to sample that would account for variations in the damage threshold. The damage appears as a progressive clouding of the material with repeated pulses. The clouds consist of a large number of miniscule dots approximately 3 μm in diameter. These are presumably microcracks radiating from defect centers. The clouds have a defect density of the order of 10^5/cm^3. Surface damage was not observed when the surface was of optical quality. When surface damage did occur, it had the appearance of "pull-out", wherein whole grains were lifted from the surface as seen in figure 2(b).

A rather spectacular single shot, damage event is illustrated in figure 2(c). The incident laser beam (1 joule/cm^2) direction is indicated by the arrow. A magnified picture of the entrance surface is shown in figure 2(d). It is speculated that a surface defect such as grain boundary separation at the surface was responsible for the event. The high electric field resulting from field enhancement at the defect caused an "explosion" at the surface. Conical fracture occurred in a manner quite similar to that observed when a steel ball is shot onto a glass surface. [5] Figure 2(e) shows spallation at the entrance surface. Figure 2(f) is the center spike extending along the beam axis into the bulk of the material.

Both the observed bulk damage and damage originating at the surface indicate the importance of material integrity and purity. The electric fields associated with these short pulses require that the material be defect free. This is particularly true in the case of high index of refraction materials.

3.2 Antireflection Coated ZnSe

The relatively high index of refraction of ZnSe causes a high Fresnel reflection at each surface, In order to reduce these beam losses, it is necessary to A/R coat the surfaces. Several ZnSe samples were coated by the Hughes Research Laboratory and the Optical Coating Laboratory, Inc.

a. Optical Coating Laboratory (OCLI) A/R Coated ZnSe

Microscopic observation of these surfaces before irradiation reveal surface defects that might be in the coating. The defect appearance is a slightly different color cast than the rest of the surface. The defects were round or oval shaped. The bulk material was relatively defect free.

The irradiated sample surface was refinished by OCLI before coating. Under irradiation the dielectric surface damaged at 2.5 joule/cm^2. Characteristic damage is shown in figure 3(a). The shape and size of the damage spot is similar to the defect spots observed in the coating before irradiation. These results are indicative of a rather tenacious coating with good damage resistance.

b. Hughes Research Laboratories (HRL) A/R Coated ZnSe

As in the case of the OCLI coatings, surface coating defects were noted before irradiation. These defects were irregular in shape and were rather ragged. Damage was noted in these samples at an average incident energy of 1.7 joules/cm^2. A typical damage site is shown in figure 3(b). The shape of the site is similar to the surface defects noted in the unirradiated sample. Note the difference in the substrate finish between the samples shown in figures 3(a) and 3(b). This latter sample had more bulk defects than in the former sample. This fact may explain some of the difference in damage thresholds although the substrate surface finish was better in the OCLI sample. Once again this implies that resistant coatings are possible for ZnSe.

3.3 Antireflection Coated NaCl

These samples were prepared by C. Phipps of Lawrence Livermore Laboratory. They were conventional $\lambda/4$ NaF coatings on standard finish NaCl flats. The coating had a cloudy cast which apparently did not affect its efficiency at 10.6 μm. These samples damaged at $\sim$ 2.0 j/cm^2. A typical damage site is shown in figure 3(c). No special care was taken in surface preparation before coating. Improved surface finishing could result in significantly higher damage thresholds.

3.4 Conclusions

The optical quality of CVD ZnSe is presently not sufficient for short pulse CO_2 laser applications at high energy fluxes. It is recognized, however, that this situation is constantly improving. Damage thresholds of the order of 3 joules/cm^2 may be expected for both ZnSe and NaCl. The experimental results again point out the necessity for defect-free bulk material and surfaces. At pulse lengths shorter than a nanosecond, the electric fields associated with the same energy flux are greater, consequently material purity and surface quality will become increasingly important.

4. Micromachined Metal Mirrors

4.1 Micromachined Mirrors

Micromachined metal mirrors were prepared by the Y-12 facility at Oak Ridge, Tennessee. Copper substrates were machined from OFHC copper. The substrates were then electroplated with 0.013 cm of either gold or copper. The plated surfaces were then micromachined to optical quality. Some of the machining and plating parameters are:

Surface Material	Plating Bath	Purity Levels	Tool Material	Tool Radius	RPM of Part	Cutting Feed
Copper	Sel Rex	99.95	SC Diamond	1/8 in.	1000	200 μinch/rev
Gold	Temprex HO	99.99	SC Diamond	1/8 in.	1000	200 μinch/rev

Samples were irradiated as received from Y-12. No attempt was made to reclean the surfaces. They were dusted with clean N_2 although some dust particles were observed on the surfaces in the clean gas irradiation tube.

4.2 Copper Mirrors

The copper surfaces were irradiated to 4j/cm^2 with no permanent surface damage. Figure 4(a) shows an irradiation site with surface debris from a dust particle which exploded in the laser beam. The debris washed off in an alcohol bath leaving the surface appearing as it did prior to irradiation. The primary electron energy was varied in SEM studies of the surface and subsurface and no subsurface damage was noticed.

4.3 Gold Mirrors

Effects of dust debris were noted in the case of gold surfaces just as in the case of the copper sample. In one case damage to the surface was observed at an average incident energy of 2 joules/cm^2. This damage site is shown in the optical micrograph in figure 4(b). There is surface debris and some shallow cratering. A series of scanning electron micrographs taken with increasing primary electron energies is shown in figure 5. These photographs reveal subsurface damage structure as indicated by the darkening radial zone. A cross section of this damage site is shown in figure 4(c). It is evident that there is shallow cratering and subsurface layering - evidence for surface spalling and bulk separation. The speckled appearance of the gold is an artifact due to imbedded polishing compound. The exact cause of this damage characteristic is not known although there is a temptation to speculate that it originated with a dust particle explosion at the surface.

4.4 Conclusions

A reasonable lower bound to micromachined gold and copper surfaces is of the order of 4 joule/cm^2. The experiment reveals the necessity to keep the surface dust free when used in the high energy flux applications.

5. Summary

Table 1 lists the experimental damage thresholds for materials reported in this page. In addition, thresholds for NaCl and KCl are included for completeness.

Table 1. Damage Thresholds or 10.6 μm for Nanosecond Pulses (joules/cm^2)

Material	Coating	S.C.[a] S.F.[b]	S.C., HPLF[c]	Poly,[d] S.F.	Poly, HPLF	Machined
NaCl	uncoated	3.0	4.5		3.0	
KCl	"				1.5	
ZnSe	"			∿ 1.5		
ZnSe	A/R, OCLI				2.5	
ZnSe	A/R, HRL			1.7		
NaCl	A/R, NaF	2.0				
Copper	uncoated					> 4
Gold	"					> 4

(a) S.C. refers to single crystal materials
(b) S.F. refers to a surface finish of the order of 40-20 dig, scratch
(c) HPLF to a finish of the order of 10-5 dig, scratch
(d) Poly refers to polycrystalline material

6. References

[1] W. H. Reichelt and E. E. Stark, Jr., unpublished.

[2] J. B. Arnold, P. J. Steger and T. Saito, Oak Ridge, Y-12 Plant, Publication Y-DA-5786.

[3] W. H. Reichelt and E. E. Stark, Jr., Laser Induced Damage in Optical Materials, 1973, NBS Publication 387 (Dec. 1973), p. 175.

[4] N. Bloembergen, IEEE Journal of Quantum Electronics, QE-10, #3, p. 375 (1974).

[5] I. A. Fersman and L. D. Khazov, Soviet Physics-Technical Physics, 15, #5, p. 834 (1970).

7. Figures

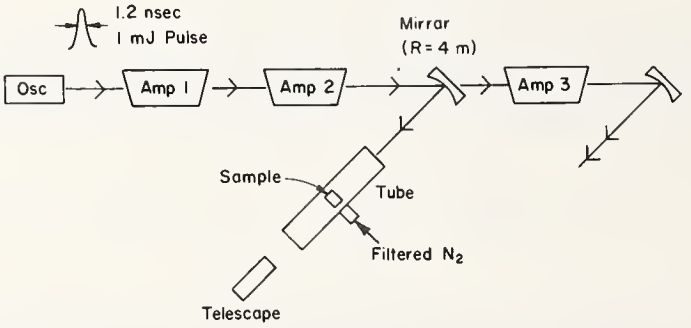

Figure 1. Experimental configurations for damage studies.

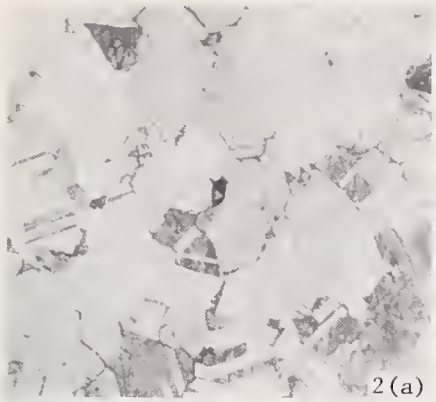

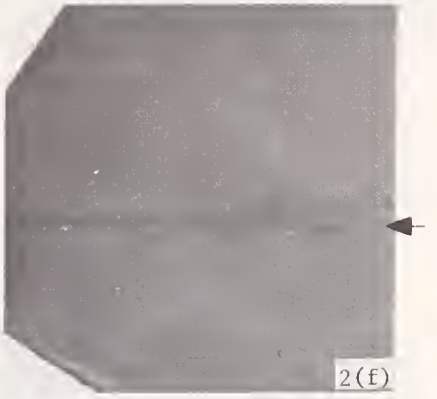

Figure 2. ZnSe samples, uncoated. (a) etched section, 250X; (b) exit damage, 300X; (c) conical fracture; (d) entrance damage, 40X; (e) entrance damage, 100X; (f) center damage spike, 100X.

Figure 3. A/R coated samples. (a) ZnSe 1000X; (b) ZnSe 1000X; (c) NcCl 25X.

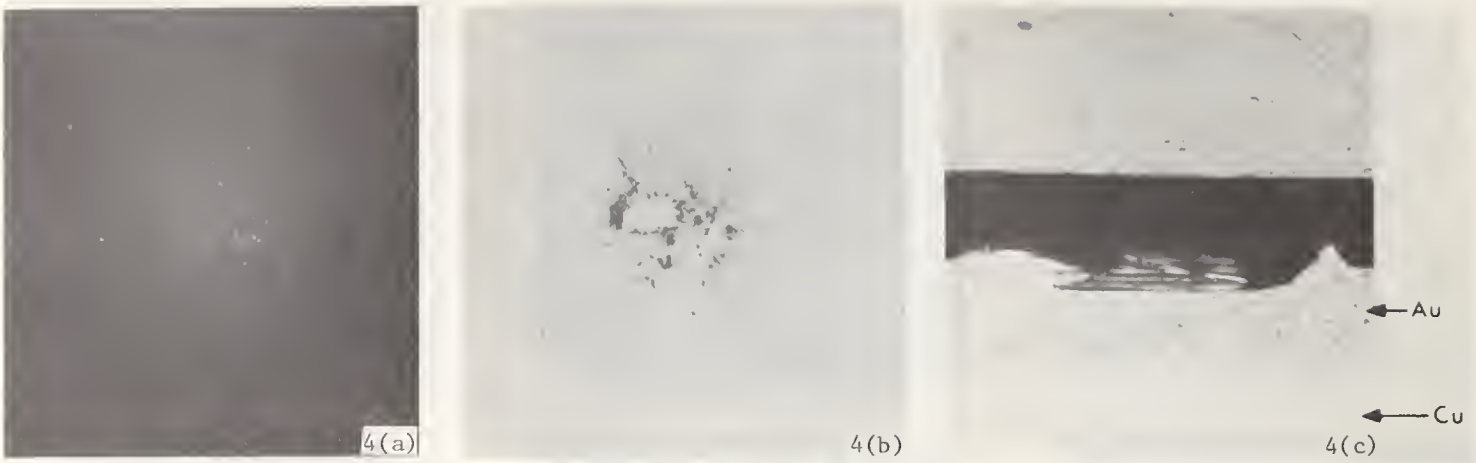

Figure 4. Micromachine surfaces. (a) copper 300X; (b) gold 300X; (c) gold 250X.

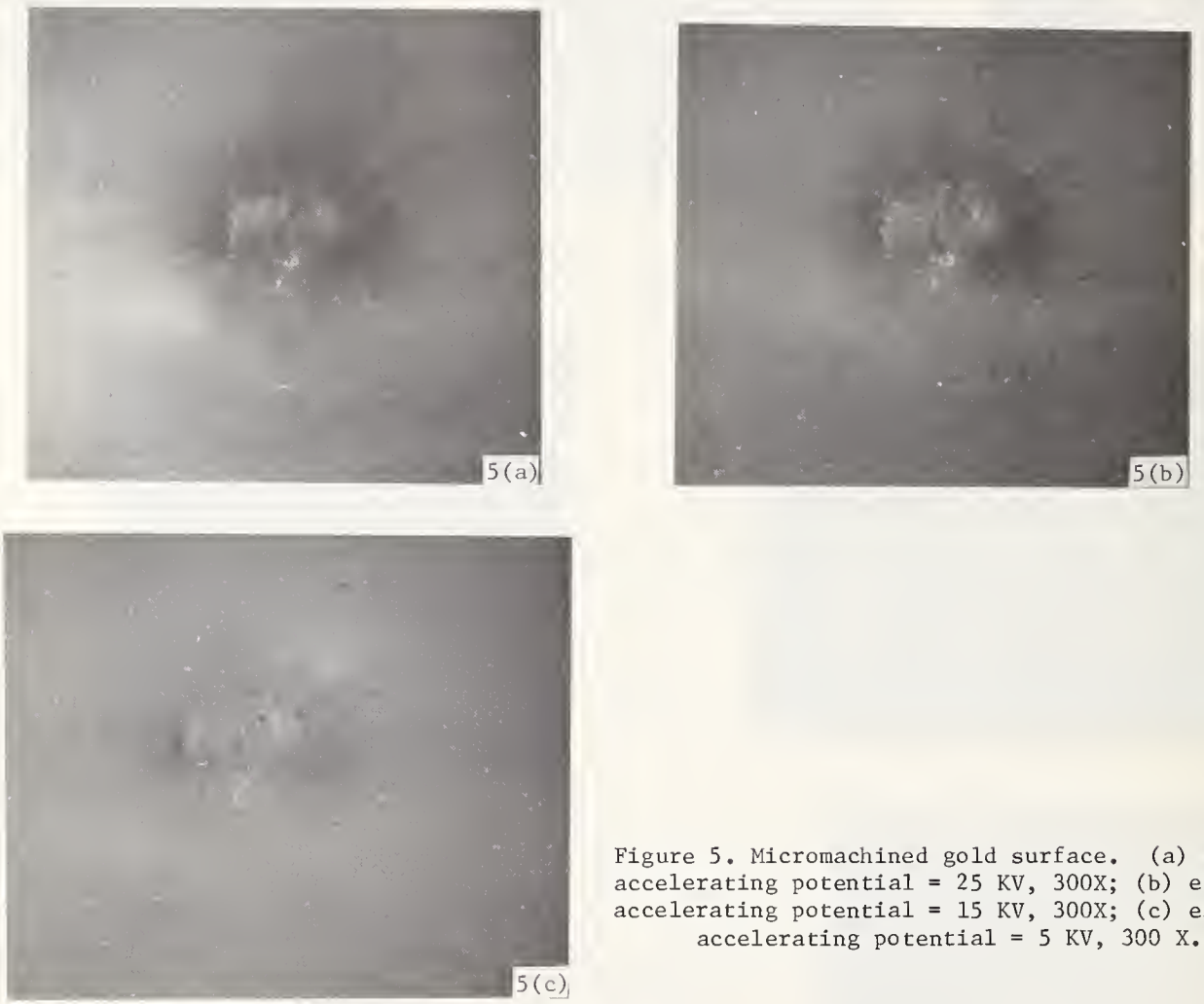

Figure 5. Micromachined gold surface. (a) electron accelerating potential = 25 KV, 300X; (b) electron accelerating potential = 15 KV, 300X; (c) electron accelerating potential = 5 KV, 300 X.

COMMENTS ON PAPER BY STARK

A. Braunstein of the Hughes Research Laboratory commented on the difficulty of obtaining a good finish, scratch-free, on ZnSe, if the banded structure intersects the surface. In pieces free from banding near the surface, this difficulty was not encountered.

2.4 Pulsed CO_2 Laser Damage in Windows, Reflectors, and Coatings*

V. Wang, J.E. Rudisill, C.R. Giuliano, M. Braunstein, and A. Braunstein

Hughes Research Laboratories
3011 Malibu Canyon Road
Malibu, California 90265

Recent 10.6 μm damage measurements using a TEM_{00} laser of 0.6 μsec pulse length are reported for a variety of windows, reflectors, and coatings. Reduction of the density of inclusions in ZnSe was found to have a large effect upon scatter but a smaller effect upon damage resistance. Absorptions and damage thresholds of thin films of ZnSe, As_2S_3 and ThF_4 were measured upon relatively defect-free KCl substrates, and then tested in antireflection and multilayer reflector configurations. Also reported is a five-fold increase in damage resistance of simple polished copper reflectors by surface etching.

Key words: As_2S_3; laser coatings; laser reflectors; laser windows; pulsed CO_2 laser damage; ThF_4; ZnSe.

1. Introdution

Since 1971 we have been involved in the development of damage resistant, low absorption, optical components at 10.6 μm.[1,2][1] Since our prior experiments have indicated that wide bandgap materials are as damage resistant as simple polished metal reflectors and that semiconductor materials are considerably less damage resistant, this paper reports upon recent development of three wide bandgap materials: ZnSe, As_2S_3, and ThF_4. These results are compared with recent progress in metal reflectors.

2. Experimental Conditions

An ultraviolet CO_2 TEA laser discharge 50 cm in length, operating at 550 Torr with 1:1:8 mixture of CO_2:N_2:He was used in this experiment. A two-meter, approximately hemiconfocal cavity operating in the TEM_{00} mode with an uncoated germanium resonant output reflector delivers an essentially untruncated gaussian beam to a folded optical train (illustrated in figure 1). A beam attenuator consisting of two wire grid polarizers on ZnSe substrates allows better than two orders of magnitude attenuation without rotation of the output polarization.[3] Wedged NaCl beamsplitters allow monitoring of the energy in each pulse by a polyvinylchloride (PVF) pyroelectric detector. Absolute calibration of the pyroelectric monitor is provided by a Hadron Model 100 cone thermopile with a 1 cm aperture located in the near field of the laser.

The output pulse of the laser consists of a 200 nsec gain-switched pulse followed by a nitrogen fed tail of ∿3 μsec. Figure 2(a) displays the output detected by a germanium photon drag detector, and figure 2(b) is an expanded trace showing a typical example of the partially self-mode locked beating in the output. Power density is measured at the peak of the gain switched spike by using a detector that averages the rapid pulsations from mode beating, as shown in figure 2(c). An equivalent pulse length is defined by measuring the area of figure 2(c) and constructing an equivalent rectangular pulse of equal area and height equal to the height in figure 2(c).

*Work partially supported by Air Force Weapons Laboratory, Kirtland Air Force Base and by Defense Advanced Research Projects Agency under the technical cognizance of Air Force Cambridge Research Laboratories.

[1]Figures in brackets indicate the literature references at the end of this paper.

For thermal damage mechanisms, the effect of nanosecond pulses is negligible with respect to the total pulse energy, so total pulse energy and pulse length closely characterize the pulse. For electrical breakdown mechanisms in inclusion-free dielectrics, simple considerations predict a pulse length dependence for the electric breakdown field due to the finite time required to form sufficient electrons through avalanche. Our extrapolation of calculations by Yablonovitch and Bloembergen [4] suggests that a pulse 2 nsec long would be expected to have a breakdown threshold 4 to 8 times higher in power density than a 0.2 μsec pulse. From figure 2(c), the peak intensity of this pulse is approximately 5 times the average intensity, so it is the average power in the gain switched pulse that is reported in both this paper and the paper by S.D. Allen, et al., [7] on surface and bulk damage in KCl.

Spot size for a given lens is measured by varying the energy focused on a heat-sensitive plastic film (3 M, Type 557) in a series of burn spots, and plotting the log of energy versus spot size squared (figure 3). A pulse of gaussian profile yields a straight line whose slope is a measure of the spot size. Measurements of spot size using the 12.5 cm germanium lens used for the majority of the tests indicate an essentially diffraction-limited spot size to beyond the $1/e^2$ intensity points. Measurements of spot size at the focus of the 6.2 cm lens give a diameter of between 0.059 mm and 0.073 mm (figure 3). The uncertainty in measurement for this lens is due in part to the difficulty of measuring the low energies used in this calibration. Energy densities quoted for this lens are calculated for the on-axis peak intensity of a 0.073 mm spot. If a diffraction-limited waist is assumed, energy and power densities would be 50% higher for this lens at the beam waist.

Both windows and reflectors are tested in a sample chamber evacuated below 1 Torr to eliminate spurious effects caused by dust and air breakdown induced near the surface of a sample. Damage threshold in this paper is defined as the first visible, permanent change in the appearance of the sample viewed at high magnification in an optical microscope, unless otherwise stated. During the tests the sample is observed at ∿10x.

3. Test Results

Zinc selenide has been of major interest as a high power window material. Previous results [2,5,6] have indicated that inclusions that visibly lie in bands within the material limit the damage threshold, as shown in figure 4. In an effort to explore the effects of improved materials process control, regions of low scatter were selected for damage testing. The ZnSe surfaces were etch polished with potassium ferricyanide on both the samples in tables 1 and 2 to remove a damaged surface layer. Scattering measurements at 10.6 μm show a tenfold reduction in scatter for the selected clear areas. However, the damage threshold, reported in table 1, shows only a small improvement in damage resistance.

Table 1. Measured Thresholds of Damage in ZnSe Windows

Material	Absorption cm^{-1}	Relative Scatter, 10.6 μm	Damage Threshold		Comments
			Energy Density, J/cm^2	Power Density,[a] MW/cm^2	
Banded region, R-26	0.0030	1	30 to 40	50 to 70	Inclusion damage
Unbanded region, R-26	0.0021	0.1	55	90	Inclusion damage or localized surface absorption sites

[a]Based on τ = 0.6 μsec.

Wide bandgap high and low index materials are useful for antireflection coating on windows and multilayer dielectric reflectors. Zinc selenide (n = 2.41) and As_2S_3 (n = 2.38) are promising materials for high index films and ThF_4 (n = 1.35) is the only nonhydroscopic material available of low index and low absorption at 10 μm. In order to evaluate the performance of individual films, λ/4 wave layers have been deposited on relatively defect-free surfaces of low absorption etch-polished RAP grown KCl. [7] These substrates allow accurate calorimetric absorption measurements to be made and also provide a damage-resistant substrate.

Table 2. Measured Damage Thresholds in Thin Films and AR Coatings

Coating and Substrate	Absorption	Measured Damage Threshold		Comments
		Energy Density J/cm^2	Power Density[a] MW/cm^2	
$\lambda/4$ ThF_4 on KCl	10 cm^{-1}	80 J/cm^2	130	
$\lambda/4$ As_2S_3 on KCl	<1 cm^{-1}	120 J/cm^2	200	
$\lambda/4$ ZnSe on KCl	<0.6 cm^{-1}	140 J/cm^2	230	Poor adhesion of film
ZnSe/ThF_4 AR on KCl	0.2% per surface	60	100	
ThF_4/ZnSe AR on ZnSe	N.A.	25 to 40 J/cm^2	40 to 70	Limited by substrate
ThF_4/ZnS AR on ZnSe	N.A.	30 to 40 J/cm^2	50 to 70	Limited by substrate

[a]Based on τ = 0.6 μsec.

To compare the values given in table 2 for ZnSe films with the bulk values in table 1, we can calculate the electric field distribution in the film as shown in figure 5. Assuming a plane wave entering from the left, figure 5 plots the normalized electric field versus depth into the $\lambda/4$ film in micrometers. The average electric field in the layer is within a few percent of the field in a bulk ZnSe window. While bulk ZnSe has an absorption coefficient of 0.002 to 0.003 cm^{-1} (assuming the absorption is uniformly distributed), the film has a coefficient of approximately 0.1 cm^{-1}. In this case the absorbed energy density in the film would be 30 to 50 times larger than that in the bulk samples, and its damage threshold would be expected to be correspondingly lower. Thus, the higher damage threshold observed in the film may be a result of the relative lack of absorbing inclusions. In the case of ThF_4, as a result of the relatively high absorption coefficient, linear absorption alone can account for a temperature rise to near the melting point. The performance of ThF_4, ZnSe, and ZnS coatings in an antireflection design on ZnSe substrates is shown in the bottom half of table 2. As expected, the incident flux is limited by damage due to substrate inclusions near the surface.

The performance of some of these films in reflector designs is summarized in table 3. Apparently because of localized absorbing centers, visible plasmas form near the surface at a low energy density, but gradual power increase removes these artifacts without damage to the overall integrity of the films. Since visible scattering remains relatively high in these preliminary samples, it might be expected that considerable improvement is possible. The last sample in table 3, a $(ThF_4/ZnSe)^2$ reflector on an electroless nickel substrate, exhibits a reproducible improvement by a factor of more than 4 over the several sites tested on its surface, without any intentional changes in the film deposition techniques. However, the scatter of this sample was lower than the previous ones. Figure 6 is an exact computer calculation of the electric field distribution within this dielectric reflector, including the effects of absorption. As can be seen, the peak electric field within the reflector occurs at the outermost interface between the high and low index films, and is approximately 20% higher than the $\lambda/4$ film on KCl. The field approaches zero on the outer surface of the stack and is also small at the metal substrate boundary. The substrate absorbs about 0.07% of the incident flux, or 32% of the total absorption of the reflector.

Whereas simple uncoated metal reflectors have proved to be among the most damage-resistant optical components examined, recent results have indicated an improvement of 3 to 4 in damage resistance by superpolishing of dispersion-hardened copper mirrors. [8] However, this improvement was not observed in superpolished molybdenum. In an effort to isolate the mechanism responsible for the improvement, samples of OFHC copper were polished and etched by metallographic techniques designed to remove all surface contaminents from abrasives, and to leave an unworked surface highlighting the grain structure. This surface is not an acceptable mirror in the visible due to high scatter, but exhibits a marked increase in damage resistance, similar to that seen in superpolished materials. Table 4 summarizes this development, and compares the results with a conventionally polished sample. Etch-polishing techniques to yield a smoother surface of low scatter are presently under consideration. It is necessary to qualify the applicability of these numbers to large-scale beams. Because of the small beam sizes incident upon some of the samples (120 μm), three-dimensional heat diffusion can be expected to cool the surface at a greater rate than one-dimensional heat diffusion, as experienced in large-scale beams. Large-scale beams would thus be expected to exhibit a lower damage threshold.

564-378 O - 74 - 6

Table 3. Measured Thresholds of Damage in ThF_4/ZnSe Multilayer Reflectors

Substrate	Coating	Absorption, %	Measured Damage Threshold		Comments
			Energy Density, J/cm^2	Power Density[a] MW/cm^2	
Mo	$(ThF_4/ZnSe)^2$	0.22	50	80	Conditions with gradual power increase
Mo	$(ThF_4/ZnSe)^3$	0.32	30	80	Conditions obvious scattering sites
Al/E-Ni	$Ag/(ThF_4/ZnSe)^2$	0.2	270	450	Scattering sites visible

[a]Based on τ = 0.6 μsec.

Table 4. Measured Thresholds of Damage in Metal Reflectors

Coating and Substrate	Damage Threshold		Comments
	Energy Density J/cm^2	Power Density[a] MW/cm^2	
Cu, conventional polish	90 150	150 250	25.4 cm focusing lens used 12.7 cm focusing lens used
Mo, sputtered Mo coating	4 to 8	7 to 13	25.4 cm focusing lens used
OFHC Cu, polish and etch	750	1200	No imbedded abrasive unworked surface High visible scatter 12.7 cm focusing lens used

[a]Based on τ = 0.6 μsec.

4. Summary

By careful measurement of spot sizes and temporal profile, we have attempted to precisely define the on-axis energy and power. Results of tests upon thin films currently indicate that wide bandgap materials are capable of damage thresholds comparable to metal reflectors, and that simple linear absorption can be the limiting factor rather than inclusion damage.

It has been further concluded that inclusions or surface contamination play an important role in limiting the damage resistance of copper mirrors. Improvements in surface preparation have improved damage resistance by better than a factor of four.

5. Acknowledgments

We wish to thank Roger Turk for his invaluable expertise in microscopy and in the metallographic preparation of the copper reflectors, Bernardo Garcia and John Bowers for the preparation of dielectric films, and Tomas Horne for aid in the construction of the experiments.

6. References

[1] Wang, V., Braunstein, A. I., Braunstein, M., and Wada, J. Y., "Investigation of Pulsed CO_2 Laser Damage of Metal and Dielectric-Coated Mirrors," NBS Special Publication 372, Laser Induced Damage in Optical Materials (1972).

[2] Wang, V., Braunstein, A. I., Braunstein, M., Rudisill, J. E. and Wada, J. Y., "Pulsed CO_2 Laser Damage Studies of Metal and Dielectric Coated Mirrors," NBS Special Publication 387, Laser Induced Damage in Optical Materials (1973); and Braunstein, A. I., Wang, V., Braunstein, M., Rudisill, J. E. and Wada, J.Y., "Pulsed CO_2 Laser Damage Studies of Windows and Window Coatings," NBS Special Publication 387, Laser Induced Damage in Optical Materials (1973).

[3] Garvin, H. L., Kiefer, J. E. and Somekh, S., "Wire-Grid Polarizers for 10.6 μm Radiation," 1973 IEEE/OSA Conference on Laser Engineering and Applications.

[4] Yablonovitch, E. and Bloembergen, N., "Avalanche Ionization and the Limiting Diameter of Filaments Induced by Light Pulses in Transparent Media," Phys. Rev. Lett. 29, 14, 2 October 1972.

[5] Fradin, D. W. and Bua, D. P., "Laser-Induced Damage in ZnSe," Appl. Phys. Lett. 24, 11, 1 June 1974.

[6] Braunstein, M., "Laser Window Surface Finishing and Coating Technology," Third Conference on High Power Infrared Laser Window Materials, November 12-14, 1973.

[7] Allen, S. D., Braunstein, M., Giuliano, C. and Wang, V., "Pulsed CO_2 Laser Damage Studies of RAP Grown KCl, this Proceedings.

[8] Soileau, M. J. and Wang, V., "Improved Damage Thresholds for Metal Mirrors," Appl. Opt. 13, 6 June 1974.

7. Figures

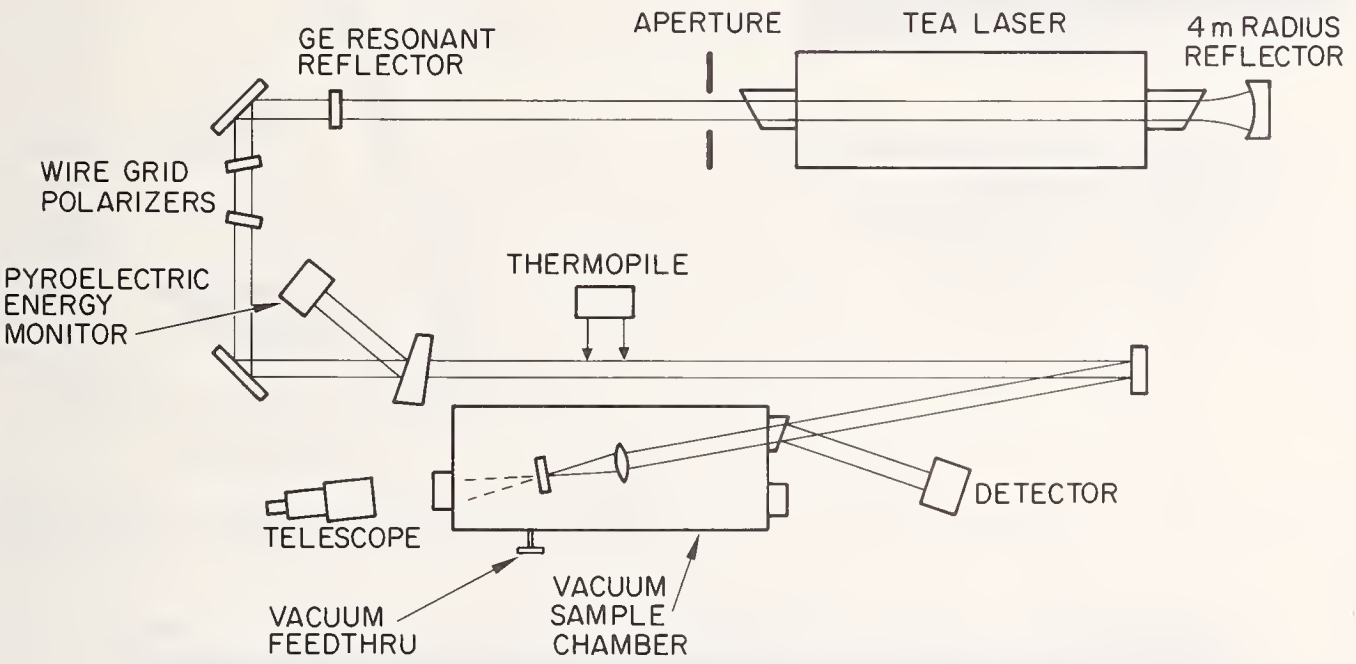

Figure 1. Schematic of laser, optical train, and sample chamber.

EXPERIMENTAL LASER PARAMETERS

ENERGY - 200 MJ TEM_{oo}, DIFFRACTION LIMITED

PULSE LENGTH (EQUIVALENT PULSE LENGTH) - 0.6 μSEC

BEAM DIAMETER AT OUTPUT (1/E ELECTRIC FIELD) - 0.5 CM

SPOT SIZES (1/E INTENSITY IN DIAMETER)

25.4 CM f.l. - 0.240 MM
12.7 CM f.l. - 0.120 MM
6.3 CM f.l. - 0.059 - 0.073 MM (EXP. UNCERTAINTY)

ATTENUATOR - WIRE GRID POLARIZERS

SAMPLE CHAMBER - EVACUATED TO <1 TORR

DIAGNOSTICS - VISUAL AT ~10X MAGNIFICATION

DETECTORS - HADRON MODEL 100 THERMOPILE, GE PHOTON DRAG DETECTOR, PYROELECTRIC DETECTORS

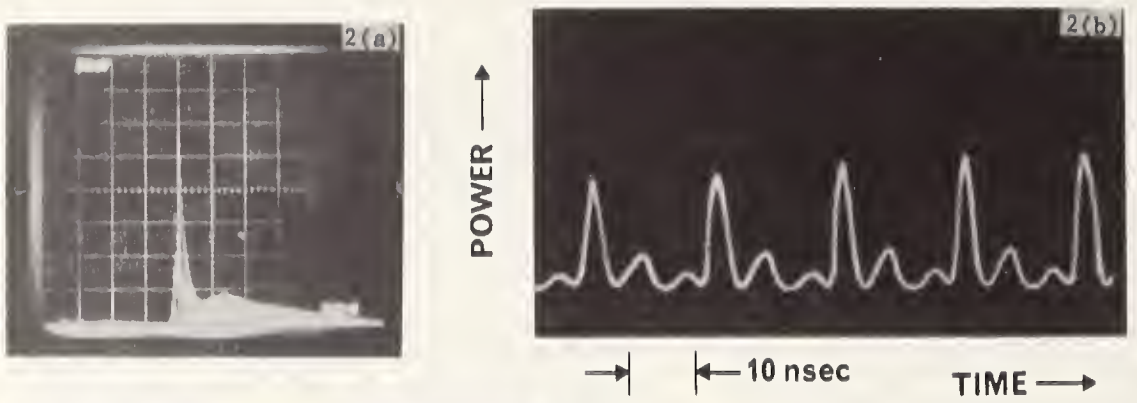

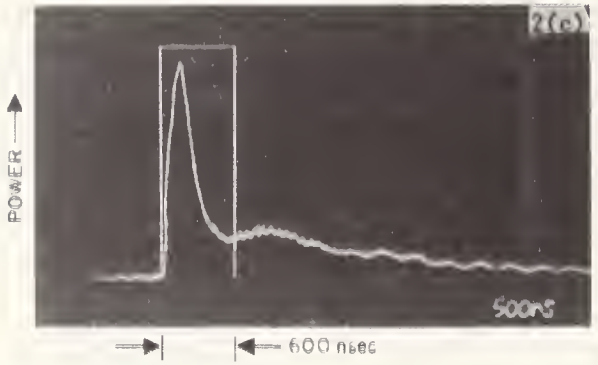

Figure 2. Pulse temporal profile

(a) Germanium photon drag detector plus 500 MHz oscilloscope.
(b) Expanded to 10 nsec/division.
(c) Definition of equivalent pulse (pyroelectric detector).

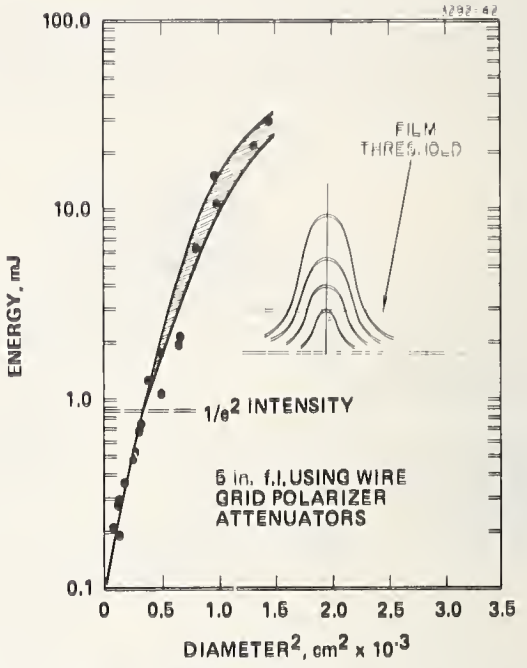

Figure 3. Beam spatial profile and spot size.

NOTE: BANDING (TOP DARK REGION). THIS COINCIDES WITH FACE WHICH POLISHED POORLY. BOTTOM EDGE COINCIDES WITH FACE GIVING EXCELLENT POLISH.

Figure 4. Zinc selenide cross section.

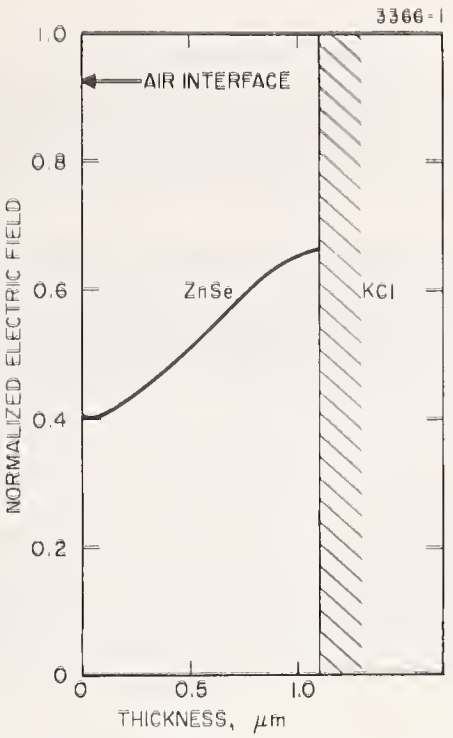

Figure 5. Computed electric field in λ/4 ZnSe on KCl.

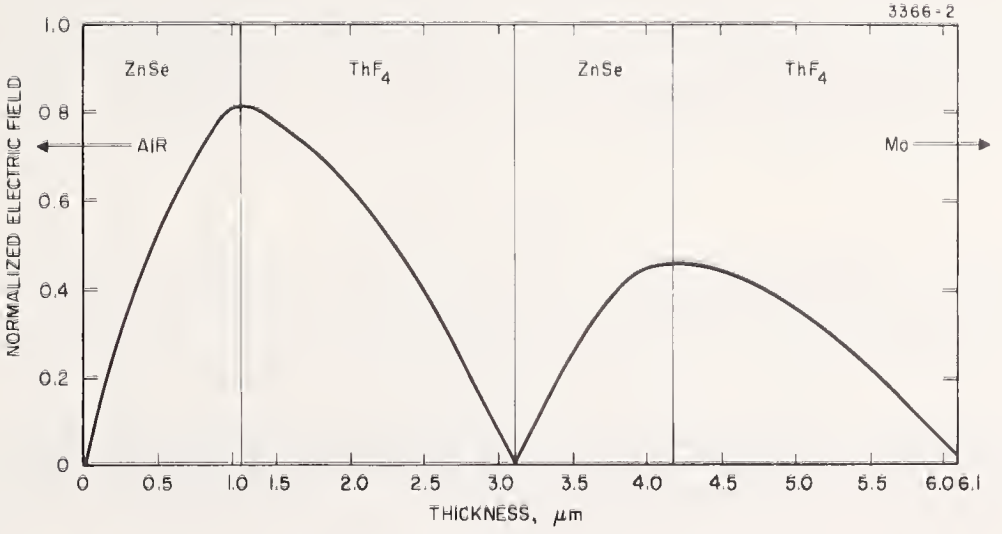

Figure 6. Electric field distribution on a Mo/$(ThF_4/ZnSe)^2$ reflector.

COMMENTS ON PAPER BY WANG

Although the etched surface reported in this paper exhibited substantial scattering, and was not an optically finished surface, the authors feel that the etching technique is applicable to optically figured surfaces as well. This type of etched surface shows a damage level close to the intrinsic melting limit of a bare copper surface. The material used in this test was otherwise off-the-shelf, oxygen-free material.

2.5 Pulsed CO_2 Laser Damage Studies of RAP Grown KCl*

Susan D. Allen, Morris Braunstein, Concetto Giuliano, and Victor Wang

Hughes Research Laboratories
3011 Malibu Canyon Road
Malibu, California 90265

ABSTRACT

Laser damage thresholds in high purity RAP (Reactive Atmosphere Processing) KCl were measured as a function of surface and bulk processing techniques. Single crystal and press forged material was prepared in a "conventionally" polished and HCl etch-polished manner and the bulk and surface damage thresholds measured and correlated with absorption (cw CO_2 laser calorimeter), Auger, LEED and SEM data. The damage measurements were made with a TEM_{00} CO_2 TEA laser with a 0.6 μsec pulse length.

Key words: Etch-polishing; KCl; laser damage; laser windows; 10.6 μm; RAP.

1. Introduction

The present results represent a continuation of work on Hughes Research Laboratories (HRL) Reactive Atmosphere Processing (RAP) KCl reported by A. Braunstein et al. [1][1] at the 1973 Laser Damage Symposium. Conventional methods of polishing KCl (Linde A and methanol on a flannel lap) are known to produce scratched and smeared surfaces, which contribute considerably to the 10.6 μm absorption [2] and scattering. A method of surface finishing which removes the damaged layer has been developed with a resultant improvement in the 10.6 μm calorimetric absorption, scattering, and laser damage measurements. Other techniques used to characterize the HRL-grown and finished RAP KCl include Auger spectroscopy, LEED, and SEM. Bulk laser damage threshold measurements on HRL RAP KCl raise interesting theoretical questions as the predicted trend for the damage threshold of KCl relative to that of NaCl is reversed.

2. Sample Preparation

The procedure for producing HRL RAP KCl has been described elsewhere. [3] The crystals produced exhibit some low-angle grain boundaries, but can be considered single crystal for most purposes. Press forged samples were fabricated from boules with minimum visible internal scatter and were essentially veil free. Press forging was done at 250°C to a reduction of 50% in height at a rate of 0.05 in. per minute per in. of remaining length. Grain size in the resulting windows was 5 to 10 μm average diameter.

Windows polished by conventional polishing techniques are extremely environment sensitive. Surfaces fogged over a period of several minutes on damp days. It was therefore difficult to establish standards of measurement for KCl windows as the data changed with time. Figure 1 illustrates the microscopic difference between fogged and unfogged surfaces. It was also believed that the surface quality was setting a limit to the absorption and scattering measurements, effectively masking any improvement in bulk crystal quality that had been achieved.

J.W. Davisson [4] of Naval Research Labs had reported that concentrated HCl was a good etch for single crystal KCl. We have developed a modification of Davisson's procedure which consistently produces high quality surfaces. Conventionally polished KCl windows are agitated in concentrated HCl for 1 to 2 minutes (depending on the quality of the polished surface and the depth of the scratches), rinsed quickly in isopropyl alcohol, and then immersed in the vapor of a Freon TF degreaser to remove the alcohol and any remaining HCl.

*Work partially supported by Defense Advanced Research Projects Agency under the technical cognizance of Air Force Cambridge Research Laboratories.

[1]Figures in brackets indicate the literature references at the end of this paper.

3. Sample Characterization

Optical micrographs of a conventionally polished and etch-polished KCl window are shown in Figure 2. In contrast to the scratches and digs observed in the conventionally polished window, the etch-polished surface shows no discernible features at this magnification. This smoothness is confirmed by SEM photographs at 18,000X (Figure 3).

Absorption coefficients measured calorimetrically at 10.6 μm for HRL RAP KCl, along with similar data for Optovac KCl for comparison, are given in Table 1. The values quoted for the absorption coefficient are total absorption of the sample, including surface contributions. The range of values for the etch-polished HRL RAP KCl is much narrower than that shown by conventionally polished KCl and consistently lower.* This behavior is an indication of not only improved surface quality, but also improved stability of the surfaces. It is also now possible for us to distinguish bulk quality differences, which were not noticeable in conventionally polished windows. As an environmental test, a window cut from an early boule measured α = 0.00032 cm^{-1} after etching. When measured after three weeks in a desk drawer, protected only from dust during a period of high humidity, α = 0.0004l cm^{-1}, and window was not visibly fogged.

Table 1. 10.6 μm Absorption of KCl

HRL RAP KCl	Absorption, cm^{-1}*
Single Crystal	
Conventionally Polished	0.0008 to 0.0020 cm^{-1}
Etch Polished	0.00013 to 0.00020 cm^{-1}
Press Forged	
Conventionally Polished	0.00045 to 0.002l cm^{-1}
Etch Polished	0.00022 to 0.00024 cm^{-1}
Optovac KCl	
Conventionally Polished	0.00l to 0.002 cm^{-1}
Etch Polished	0.0004 to 0.0014 cm^{-1}

*Total absorption of sample — includes bulk and surface.

*Preliminary experiments by us and others [5] indicate that the measured absorption coefficients in the 1 to 2 x 10^{-4} range might actually be instrument limited and represent upper limits to the actual absorption.

Auger analysis and LEED patterns [6] were recorded for four samples representative of different types of surface finishing: a cleaved Czochralski (Optovac) window, a similar cleaved window subjected to a 1 minute HCl etch as previously described, a polished HRL RAP window of unknown crystallographic orientation, and a polished blank from the same boule also etched for 1 minute; the results are given in Table 2. The initial Auger scans show the normal contaminants as all of the surfaces were prepared in air. Most of these trace contaminants are removed by 6 minutes of Ar^+ sputter cleaning. The residual oxygen can be ascribed to system contamination. The initial LEED patterns indicate some surface disorder in the cleaved Optovac sample and the etch-polished HRL RAP sample (B15-7), while the conventionally polished HRL RAP window (B15-8) displays essentially complete absence of surface order. The etched, cleaved Optovac window exhibited a great degree of surface order as shown by the appearance of first, second, and third order diffraction in the LEED pattern. A six minute Ar^+ sputter clean improved all of the LEED patterns with the exception of the conventionally polished sample (B15-8). An additional hour of Ar^+ sputter cleaning (removal of ~ 5 μm total) was necessary to obtain a diffuse LEED pattern for HRL B15-8. The data on the two samples of cleaved Optovac material (etched and unetched) indicate that a relatively thin layer ($\lesssim 0.4$ μm) of surface disorder is generated in the cleaving process, which is removed in the etch procedure. The residual diffusivity of the etch-polished HRL RAP window LEED pattern, can be at least partially attributed to the fact that the crystals were not cut along a symmetry axis. The resulting asymmetry of the LEED pattern makes it difficult to characterize. It is also quite possible that a longer etch time would have been necessary to remove all of the surface disorder caused by conventional polishing.

Table 2. Leed and Auger Data on Various KCl Samples

Sample	Initial		After 6.0 min Ar^+ Sputter-Clean (800 eV, 10 μA/cm^2)		After 1 Hour Ar^+ Sputter-Clean (800 eV, 10 μA/cm^2)	
	Leed Pattern	Auger Scan	Leed Pattern	Auger Scan	Leed Pattern	Auger Scan
1. Cleaved Optovac KCl	Diffuse	S, O, C	Sharp	O, C $O_f/O_i = 0.15$ $O_f < 1\%$		
2. Cleaved Optovac KCl Etched 1 min	Sharp (1st,2nd,3rd order)	O,C (Trace)	Sharp (Best)	O, I $O_f/O_i = 0.25$		
3. RAP B15-8 Polished	No	S, O, C (Trace)	No	O (Trace)	Weak, Diffuse	O (Trace)
4. RAP B15-7 Etched 1 min	Weak, Diffuse	S, O, C (Trace)	Sharper but still weak, diffuse	O (Trace)		

Relative total (surface and bulk) scattering at 10.6 μm was measured using a stabilized (0.1%) 200 mW cw CO_2 laser; these measurements are given in Table 3. The laser beam, focused to a 50 μm spot, was scanned across the sample and the scattering amplitude in the central portion of the scan was averaged and normalized to a similar measurement on conventionally polished HRL RAP KCl. As is indicated in the table, the lowest scattering is from etch polished, single crystal HRL RAP KCl. For the press forged material, etch polished windows show more scatter in the visible than conventionally polished blanks, but less at 10.6 μm as shown in Table 3. It is known that grain boundaries are preferentially etched in concentrated HCl and the enhanced grain boundaries contribute to the visible scatter, but do not affect the 10.6 μm scatter appreciably.

Table 3. Relative Scattering 10.6 μm

Single Crystal		
Mech Polished	KCl	1.0
Etched Polished	KCl	0.45
Press Forged		
Mech Polished	KCl	2.3
Etched Polished	KCl	0.72

4. Laser Damage Thresholds

The laser damage test facility, used to obtain the current results, is described in detail in another part of these proceedings. [7] Briefly, the laser is an ultraviolet preionized TEA laser operated in the TEM_{00} mode, with 200 mJ maximum output energy. The equivalent rectangular pulse length is 0.6 μsec, but the actual pulse consists of many 2 nsec longitudinal mode spikes. Damage thresholds are reported in terms of the average power in the equivalent rectangular pulse. The actual peak power is approximately 5X the average power. Both a 5 in. focal length and 2.5 in. focal length lens were used in measuring the damage thresholds with measured beam waist spot sizes of 120 and 70 μm, respectively. The measured spot size of 70 μm for the short focal length lens is probably an upper limit. The actual spot size lies in a range from 60 μm (the calculated diffraction limited spot size) and the measured 70 μm. (cf Ref. 7.)

All tests were conducted in an evacuated sample chamber equipped with an x-y translation stage. Sites to be tested were selected with a 6X microscope to be free of cosmetic defects observable at that magnification; the onset of damage was monitored with the same microscope. In the samples for which high damage thresholds were measured, damage was so catastrophic that sophisticated observational techniques were unnecessary. For those sites where the apparent threshold at 6X magnification could not be reached, microscopic evaluation at 220X revealed no additional damage morphology. The range of damage thresholds reported represent the lowest power at which damage occurred to the highest power at which damage could not be effected.

The surface damage thresholds for polished KCl, reported in Table 4, are given mainly for historical perspective. All of the values reported are for the laser focused on the exit surface using the 5 in. focal length lens. The thresholds vary over quite a range, and do not correlate well with the absorption data. Since the absorption data were, of necessity, taken before the damage measurements, changes in the surface quality that occurred between the two measurements cannot be tracked easily.

Table 4. Surface Laser Damage Threshold Polished KCl

Sample	Absorption (cm^{-1})	Damage Threshold Energy Density (J/cm^2)	Damage Threshold Power Density (GW/cm^2)
Single Crystal			
RAP B24-6	0.00078	70-85	0.12-0.14
RAP B11-11	0.00070	> 110	> 0.18
RAP B53-4	0.0022	350	0.58
Optovac	0.024	18	0.03
Harshaw "Polytran"	0.0016	15	0.025

The character of the exit surface damage morphology for polished KCl is illustrated in Figure 4. The central portion of the damage site has been melted and is surrounded by a ring with a relatively smooth topography as compared to the undamaged portion of the surface. Radiating from this "cleaned" area are shallow cleavage planes. This type of shallow damage is observed only on poor surfaces and at relatively low damage thresholds in KCl.

In contrast to polished KCl the etched HRL RAP KCl absorption data do seem to correlate with the laser damage performance. The highest exit surface damage thresholds for etched HRL RAP KCl (Table 5) are measured on those samples with the lowest absorption and vice versa. Those samples marked by an asterisk were measured with the 2.5 in. focal length lens and the others with the 5 in. focal length lens. The wide range of values reported for sample RAP B53-1 is an exception to the convention for reporting thresholds. This particular sample at any one site either damaged, at a relatively low energy density (600 J/cm^2), or did no damage to the limit of the laser power output. The best (and most recent) etched HRL RAP KCl samples have a measured damage threshold for exit surface damage at least an order of magnitude greater than the threshold for conventionally polished KCl.

Table 5. Surface Laser Damage Threshold Etch KCl

Sample	Absorption (cm^{-1})	Damage Threshold Energy Density (J/cm^2)	Damage Threshold Power Density (GW/cm^2)
Single Crystal			
RAP B53-2	0.00026	380-520	0.63-0.87
RAP B53-4	0.00043	330-450	0.55-0.75
RAP B53-1	0.00020	600-2500+	1.0-4.2+
*RAP B63-2	0.00015	1500-2700	2.4-4.5
Harshaw Cleaved	———	60-135	0.10-0.22
Press Forged			
*RAP B37-17	0.00023	1500-1800	2.4-3.0
*RAP B37-16	0.00024	1650	2.7

Exit surface damage thresholds for press forged HRL RAP KCl are lower than those for single crystalline material, although not enough samples have been tested to date to establish this trend as definitive. The presence of "V grooves" in the form of preferentially etched grain boundaries in the polycrystalline KCl would, according to the theory of Bloembergen, [9] lead to lower damage thresholds due to enhanced dielectric breakdown.

Exit surface damage morphology for etched HRL RAP KCl differs markedly from that for polished surfaces (Figure 5). The damage sites are several millimeters in diameter and are composed of radiating cleavage planes. This type of behavior — minor damage at low thresholds for "dirty" surfaces, catastrophic damage at high thresholds for "clean" surfaces — had been noted by Giuliano [8] in measurements on ion-polished sapphire at 0.69 μm. The cleavage planes of exit surface damage sites in etched polycrystalline HRL RAP KCl (Figure 6) are distorted, compared to those in etched single crystal material, and seem to indicate the presence of grain boundaries. Inclusion damage, both bulk and surface, is readily distinguishable by damage morphology. A typical inclusion damage site (Optovac KCl, bulk damage) is illustrated in Figure 7. The damage region extended for a length of 400 μm along the beam path with many inclusion damage sites observable.

The bulk laser damage thresholds for HRL RAP KCl are given in Table 6, with measurements on one sample of Optovac KCl given for comparison. Because of the instability of the laser at low output powers, the bulk damage threshold of this particular sample of Optovac material could only be crudely bracketed. On the other extreme, the maximum available output power of the laser was not sufficient to damage one sample of single crystal and one sample of polycrystalline HRL RAP KCl. (In all fairness, it must be mentioned that other workers [10] have noticed a great variability in Optovac samples, and that we tested windows from only one sample.) For these measurements, the arguments for using the calculated diffraction limited spot size are particularly strong as the samples are thick enough (≈1 cm) that a

small error in measuring the focal distance and/or placement of the sample would still place the beam waist in the bulk of the material. Using the diffraction limited spot size would increase the damage thresholds by a factor of 1.4. Bulk damage in material with a high damage threshold has a very similar morphology to that exhibited by high damage threshold surface sites. Again the damage sites are massive and consist of radiating cleavage planes.

Table 6. Laser Damage Threshold Bulk KCl

Sample	Absorption (cm^{-1})	Damage Threshold Energy Density (J/cm^2)	Damage Threshold Power Density (GW/cm^2)
Single Crystal			
*RAP B53-1	0.00020	2500-3100	4.2-5.2
*RAP B63-2	0.00015	> 4600	> 7.8
*Optovac		> 180	> 0.3
		< 520	< 0.9
Press Forged			
*B37-15 (End)	Veiled	3700	6.3
*B37-15 (Center)	0.00064†	> 4600	> 7.8

†Conventionally polished sample, all others etch polished.

5. Dielectric Breakdown

The most generally accepted theory of laser induced breakdown in low absorption solids is that damage occurs via electron avalanche breakdown, and thus is a function of the peak electric field in the laser pulse. A recent paper by N. Bloembergen [11] reviews the subject of dielectric breakdown in solids, and summarizes the experimental evidence to date. [12,13,14] The data of E. Yablonovitch [12] at 10.6 μm and Von Hippel [14] (dc measurements) are given in Table 7, along with the HRL data. The electric field strength and power densities were calculated and measured slightly differently in the Yablonovitch and HRL data. Yablonovitch used peak power measurements (≃ 2X average) [12] and the diffraction limited spot size in calculating the breakdown electric fields. The HRL measurements are calculated using the average power and a measured spot size. For comparison, the HRL breakdown thresholds calculated using the diffraction limited spot size are given in parentheses in Table 7. In order to eliminate the differences in experimental conditions between the Yablonovitch and HRL data, the KCl data was normalized to Harshaw NaCl. According to Yablonovitch, [15] commercial NaCl yields damage thresholds consistent from sample to sample and thus we used it as a standard. The theoretical prediction from periodic table trends was that NaCl should have a damage threshold at 10.6 μm greater than that exhibited by KCl. In data given by Yablonovitch, this trend holds true for samples of comparable purity for both compounds. The HRL RAP KCl, on the other hand, has a considerably higher damage threshold than Harshaw NaCl, effectively reversing the trend for KCl/NaCl. This data is seen to lend support to the hypothesis of Hellwarth [16] that electron avalanche breakdown is impurity mediated, i.e., the observation of dielectric breakdown does not necessarily indicate that the ultimate limit for damage has been reached for a given material. It is expected that damage thresholds on HRL RAP NaCl (presumed to be comparable to HRL RAP KCl in purity) would be higher than those measured on Harshaw NaCl, and would, perhaps restore the expected relationship: breakdown (NaCl) > breakdown (KCl).

6. Conclusions

We have developed a technique for generating high quality, relatively undamaged surfaces on HRL RAP KCl. The improvement in surface quality enables us to better evaluate bulk quality, and various characterizing measurements have been developed to judge surface and bulk quality. The results of these measurements seem to correlate qualitatively with the measured damage thresholds. The damage threshold of the surface has improved by at least an order of magnitude and approaches the bulk damage threshold in some samples.

The measurements of bulk damage threshold support the theory that sample purity affects the "intrinsic" electron avalanche breakdown damage threshold.

Table 7. Comparison of Laser Damage KCl and NaCl

	Yablonovitch (1972)		HRL (1974)*		Von Hippel (1937)	
	KCl	NaCl	KCl	NaCl	KCl	NaCl
Power (GW/cm^2)	3.7	7.5	>7.8(10.6)	4.8(6.5)		
	KCl/NaCL = 0.49		KCl/NaCl = 1.6			
Electric Field (MV/cm)	1.39	1.95	>2.0(2.4)	1.6(1.9)	1.0	1.5

*Parenthetical values were calculated using the diffraction limited spot size (60 μm) instead of the measured 70 μm.

7. Acknowledgments

The authors gratefully acknowledge the help and assistance of Roger Turk, Bernie Garcia, Paul Coker, and Don Williams. The many technical discussions with Art Braunstein were invaluable. The efforts of the HRL optical polishing shop, George Heussner and Matt Himber, are also appreciated.

8. References

[1] Braunstein, A. I., Wang, V., Braunstein, M., Rudisill, J. E., and Wada, J. NBS Special Publication Laser Induced Damage in Optical Materials, A. J. Glass and A. H. Guenther, Ed., 1973, p. 151.

[2] Braunstein, M. "Laser Window Surface Finishing and Coating Technology," ARPA Contract F19628-73-C-0234.

[3] Pastor, R. C., and Braunstein, M., "Advanced Mode Control and High Power Optics Technology," Tech. Report, AFWL-TR-72-152, Vol. II.

[4] Davisson, J. W., Conference on High Power IR Laser Windows, Vol. 2, November 1972, p. 525-534.

[5] Haas, M., Naval Research Labs, private communication.

[6] Physical Electronics Industries, Inc., Edina, Minn., Model #10-234G.

[7] Wang, V., et al., these proceedings.

[8] Giuliano, C., Appl. Phys. Lett., 21, 39 (1972).

[9] Bloembergen, N., Appl. Opt., 12, 661-664, 1973.

[10] Bernal, G., E., Honeywell, private communication.

[11] Bloembergen, N., IEEE J. of Quantum Electron., QE-10, 375-386, 1974.

[12] Yablonovitch, E., Appl. Phys. Lett., 19, 495-497, 1971.

[13] Fradin, D. W. and Bass, M., Appl. Phys. Lett., 22, 206-208, 1973.

[14] Von Hippel, A., J. Appl. Phys., 8, 815-832, 1937, Phys. Rev. 54, 1096-1102, 1938.

[15] Yablonovitch, E., private communication.

[16] Hellwarth, R. W., NBS Special Publication, Damage in Laser Materials, A. J. Glass and A. H. Guenther, Ed., 1970, p. 67.

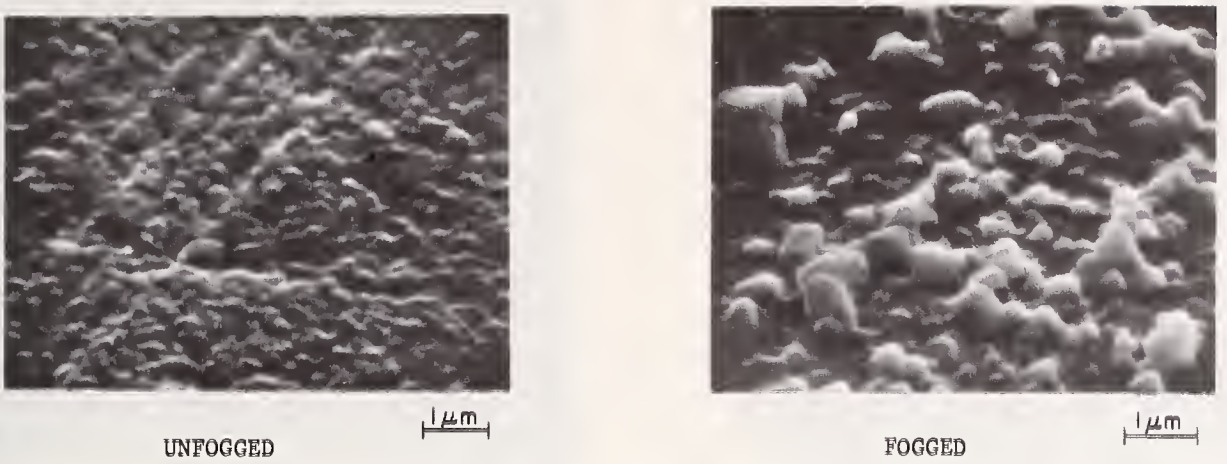

Figure 1. Scanning electron micrographs of KCl surfaces.

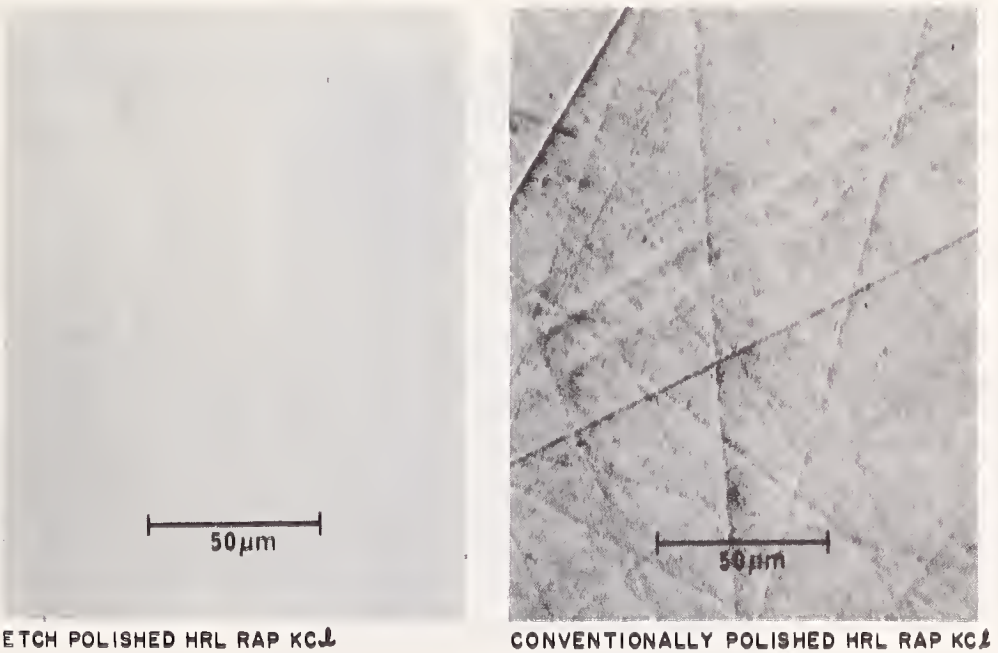

Figure 2. Optical finishing techniques.

Figure 3. HCl-etch polished KCl (SEM) 18,000X magnification.

Figure 4. Surface laser damage, conventionally polished single crystal HRL RAP KCl (B53-4).

32a

Figure 5. Surface laser damage, etch-polished single crystal HRL RAP KCl (B63-2).

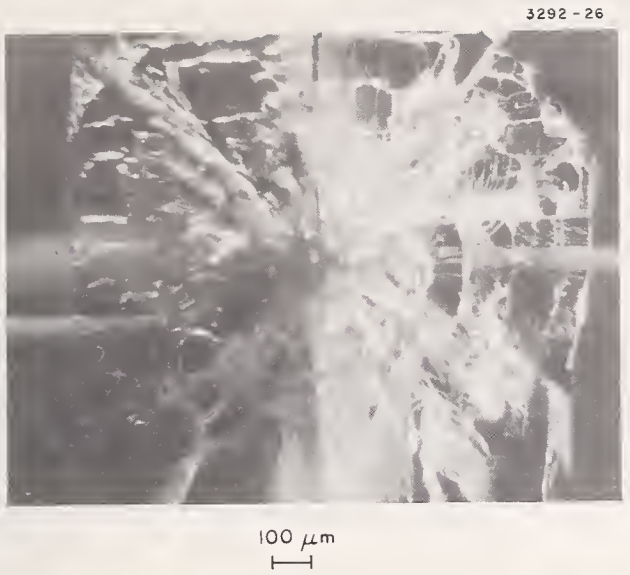

Figure 6. Surface laser damage, etch-polished press forged HRL RAP KCl (B37-16).

Figure 7. Bulk laser damage, single crystal Optovac KCl.

COMMENTS ON PAPER BY ALLEN

The improvement in "intrinsic" damage levels over the alkali halide results reported previously was attributed to the fact that RAP-grown material contains significantly less impurities and defects than previously available material. The presence of impurities is thought to initiate the avalanche ionization process. M. Bass of USC pointed out that, in case of the avalanche process, the damage threshold is sensitive to local field values, so the temporal history of the laser pulse is much more important than in the case of thermal damage. Although the absolute values of damage threshold are somewhat uncertain, the ratio of the value for KCl to that for NaCl should be less sensitive to details of the pulse shape, assuming the pulse to be fairly reproducible.

2.6 A Comparison of 10.6μm Pulsed Laser Damage in Sputtered vs Electron Beam Deposited Ge-Coated KCl*

A. Golubovic, W. Ewing, J. Bruce, J. Comer and D. Milam

Air Force Cambridge Research Laboratories
Solid State Sciences Laboratory
L. G. Hanscom Field
Bedford, Mass. 01730

Germanium films deposited on KCl substrates by electron beam and sputter techniques have been irradiated at 10.6μm. A comparative damage study of germanium films prepared by these techniques under pulsed irradiation is reported. A novel multiple beam pulsed laser damage apparatus was used for this study. Well characterized RAP Bridgeman and Czochralski grown KCl substrates with (100) and (111) orientation were used.

Key words: Characterization of laser damage; e-beam deposition of germanium; germanium coating; laser damage mechanism; laser induced damage; multiple beam damage apparatus; potassium chloride; sputtering of germanium.

1. Introduction

The alkali halides represent a class of materials which are presently under investigation as possible window materials for use in high energy laser (HEL) systems at 10.6μm. In particular, potassium chloride has been shown to have both very low absorption ($\beta<2X10^{-4}cm^{-1}$) and relatively high damage threshold. However, the halides in general are subject to hygroscopic deterioration and are mechanically poor. Thus, for practical application these materials must be environmentally protected against moisture and abrasion by suitable anti-reflective coatings.

Potassium chloride has an index of refraction of n=1.454 at 10.6μm. Since the index requirement for a single layer anti-reflective coating ($n_1=\sqrt{1.454}$) cannot be met practically, multi-layer films are required for zero reflectance at this wavelength. Germanium has an index of refraction of n=4.00 at 10.6μm and has been treated as a candidate for a first layer film for multi-layer anti-reflective coatings. [1][1] Further, this material is ideal for laser damage studies since it is mono-elemental, well characterized and may be deposited by almost all commonly used deposition techniques.

It is the objective of this investigation to compare the 10.6μm pulse laser damage thresholds of germanium films deposited on well characterized potassium chloride substrates by electron beam deposition and R. F. sputter techniques. Both of these techniques have their own characteristics which are reflected not only in the nucleation and growth processes during deposition, but in the final properties of the films as well. In this investigation we characterize not only the damage mechanisms of the germanium films but the substrate, film-substrate interfaces and films as well.

As part of this investigation a novel pulse laser damage experiment is described for the first time. This novel technique, involving the use of a multiple beam splitting wedge, greatly speeds laser damage studies of materials, and allows an accurate

*This research was supported jointly by the Air Force and the Advanced Research Projects Agency of the Department of Defense.

1. Figures in brackets indicate the literature references at the end of this paper.

determination of damage thresholds with few measurements. While the system is used for pulse damage measurements at AFCRL, the extension of this technique to C. W. damage studies is obvious.

2. Experimental

2.1 Substrate Preparation

Single crystal substrates of potassium chloride were cut from oriented boules of both Czochralski and reactive atmosphere process (RAP) Bridgeman material grown at AFCRL. For this study (100) and (111) orientations were used. Rough grinding was performed by hand on glass plates using 600 and 1000 mesh silicon carbide followed by 1μ Al_2O_3, all using kerosene as a vehicle. Fine polishing was performed by hand on a Politex "supreme" porometric lap (Geoscience Instrument Corp.) using Linde B (0.05μ Al_2O_3) with ethylene glycol as a vehicle. After mechanical polishing, the substrates were heated to 60°C for a period of 2-3 hours prior to chemical polishing. After cooling to room temperature, the substrates were chemically polished for 10-15 minutes in a 2:1 mixture of glacial acetic acid and concentrated hydrochloric acid, followed by a thorough rinsing in absolute ethanol and Freon 11. The resulting substrates were clear and unstained by residual contamination. Deposition was performed as soon as possible after this step, usually within one hour.

2.2 R. F. Sputtering of Germanium Films

To insure identical deposition conditions, a group of four samples, one of each orientation and growth method, was sputtered simultaneously. Prior to deposition, the KCl substrates were sputter etched for 15 seconds by argon bombardment at a power level of 100 watts. Optimal deposition conditions were established by variation of R. F. power levels (and hence both deposition rate and substrate temperature) while maintaining all other deposition parameters constant. With an R. F. power level of 50 watts the deposition rate was ~1Å/second and the substrate temperature was measured to be 75°C. At 100 watts, the deposition rate increased to ~3Å/second and the substrate temperature increased to 110-120°C. For all runs the argon pressure was maintained at 20 X 10^{-3} torr and the source to substrate distance was 40 mm. All sputter depositions were performed with a Randex model 2400 - 8L turbo-pumped system.

2.3 Electron Beam Deposition

All electron beam depositions were performed in a VEECO VE-400 vacuum system equipped with a Sloan BXV-6, six kilowatt 180° deflection electron beam gun. The pressure of this system was 5 X 10^{-8} torr prior to deposition, rising to ~2 X 10-5 torr during the depositions. For all samples prepared by this technique, the source to substrate distance was 18 inches (45.7cm) and the substrate temperature was 75°C. Substrate heating was accomplished with quartz iodide lamps directed at the surface of the substrates to be coated.

Using this arrangement, the depositions were rate limited due to source arcing. It was found that 20Å/second was optimum and this rate was used for all the depositions reported. Deposition control was maintained by an Inficon XMS-3 quartz crystal deposition controller.

2.3.1 Film Thickness

A film thickness of 1μ was chosen for these experiments. This thickness represents an arbitrary value chosen less than λ/4 to eliminate interference effects, yet thick enough to be representative for damage measurements. Film thickness was controlled by timing the deposition during sputtering at a known rate and by a quartz crystal thickness monitor during the electron beam evaporation. After each run the actual thickness was determined by stylus (Dektak) and Tolansky microscope techniques.

2.4 Film Characterization

Several techniques were used to characterize both the KCl substrate surfaces and the Ge films before and after deposition. The surface quality during the polishing and etching procedures was monitored by Nomarski interference contrast microscopy. Auger spectroscopy was used to analyze the chemistry of the film-substrate interface.

564-378 O - 74 - 7

The texture and the crystallinity of the Ge films were examined by transmission electron microscopy and electron diffraction techniques; the method of specimen preparation is described below in detail.

Films as deposited in this study were too thick for transmission electron microscopy. Both undamaged and damaged films were floated off the KCl substrates, thinned by floating on 1 part "superoxol" to 1 part water for 30-90 seconds, and washed by floating in deionized water before mounting on 1/8" specimen grids. The final thickness of the films was estimated to be 1000-2000Å. When damaged films were examined the surfaces were first coated with a thin film of collodion before separation to prevent breakage. The collodion was removed with amyl acetate before examination.

2.5 Pulsed CO_2 Laser Damage Experiment

The apparatus for performing pulsed CO_2 damage experiments is shown in figure 1. Provision is made for recording the energy incident at the sample, the spatial profile of the laser beam in the sample plane, and the waveform of the laser pulse as viewed by a 500 MHz detection system. These three measurements are discussed individually below. The characteristics of the TEA CO_2 laser are described in table 1.

Table 1. Characteristics of TEA CO_2 Laser Pulses

Pulse Energy	≈50 Millijoules, Reproducible to 5%
Peak Power	>200 Kilowatts
Repetition Rate	1PPS
Spatial Mode	TEM_{oo}, Gaussian to $I/I_o \leq 0.01$
Mode Diameter	6mm
Longitudinal Modes	Many
Pulse Profile	Unreproducible mode beating, 100% modulation. Duration of initial maximum of the pulse envelope is 75 nsec.

2.5.1 Beam Profile Measurements for CO_2 Lasers

The most difficult experimental aspect of CO_2 damage measurements is that of properly measuring the spatial profile of the laser beam at the sample plane. This is usually done by recording burns on some absorbing material during a series of firings in which the laser is successively attenuated. As a result, the laser profile cannot be monitored for a single firing which is used to actually cause the damage.

Multiple-beam devices [2] are commonly used for beam analysis in the visible. These devices can be adapted for use in the infrared. If an air-spaced wedge consisting of a 50%/100% reflector pair is placed downstream from the lens used to focus the beam onto the sample, multiple foci are generated. Furthermore, there is a well defined relative power level incident at successive foci. Ideally, beams are attenuated by 2:1 when generated in a 50%/100% reflective wedge. Here, the experimentally measured ratio was 2.1:1. The separation of the multiple foci in the sample plane can be adjusted by setting the angle of the wedge, and the path length accumulation in the wedge is minimized by operating with the smallest possible separation of the dielectric films comprising the wedge.

Beam profile measurements can be obtained from the set of n burns recorded on heavy carbon paper placed either in the weaker beams in the sample plane, or in the alternate sample plane shown in figure 1. These weaker of the burns presumably result from the melting of the gel containing the carbon. When illuminated at about 45° incidence, and viewed at normal incidence in an optical microscope, these burns are highly visible and readily photographed. An example is shown in figure 2. Using radii measured from such burns, and the relative attenuation factor of the wedge, the beam profile can be plotted for a single firing. The beam profile at the waist of the 50cm lens is shown in figure 3. The solid curve in that figure is a Gaussian profile fit to the data. The Gaussian parameter a^2, defined by the form,

$$E_d(r) = E_p e^{-r^2/a^2}$$

can be determined to within about 15%.

Additional confidence in the profile measurement can be obtained by producing multiple burns at a range of input powers. For example, if the entire laser output is incident on an ideal 50%/100% wedge, foci with energy densities proportional to the series 1, 1/2, 1/4, 1/8, etc are obtained. Attenuating the laser power to 75% of its total value produces the sequence 3/4, 3/8, 3/16 etc during a second firing. This can be extended to densely fill the range of possible focal power levels, thereby furnishing many points to document the beam profile.

In practice, if our TEA CO_2 laser is left running at 1pps, shot-to-shot variations in the focal size cannot be measured. The focal profile is measured at the first of each data set, and verified at the end of the set, but not recorded for each firing.

Damage experiments are performed by irradiating the sample with multiple foci of known profile. Typically eight laser pulses are used, with various attenuations, so that 8n sites are irradiated. A damage sample can be processed in about 10 minutes with most of the time being used to position the sample and return it to its container.

There are some practical limitations in the use of the multiple beam wedge. Since it must be placed downstream from the focussing lens, damage in the wedge will occur if lenses of too short focal length are used. This problem is increased due to the multiple beam interference in the wedge which results in the formation of intense fringe patterns on the wedge surfaces. There is also a slight astigmatism in the focal profile due to the existence of the wedge, but this is not a serious problem with relatively long focal length lenses.

2.5.2 Energy Calibration

By adjusting the wedge angle to collapse the fan of n beams into a single beam, the total energy passing through the focal plane can be compared with the portion of the pulse detected at the calorimeter in the side arm. This calibrated calorimeter response is recorded for each pulse, and the calculated total energy is assumed to be distributed among the n foci according to the wedge splitting factor, 2.1:1.

2.5.3 Pulse Waveform Measurements

The waveforms recorded by photon drag detector and Tektronix 7904 oscilloscope show irreproducible mode beating. These waveforms are not recorded in studies of absorbing materials.

3.0 Results and Discussion

3.1 Character of Undamaged Films

Nomarski photomicrographs of the various surface preparation stages are shown in figure 4. The effect of the chemical polishing was to remove most of the initial scratches due to mechanical polishing, although some gross scratches, pits and occasional grain boundaries may be seen. Bernal [3] et al, have reported non-preferential etching of 0.05μm/minute using the etching conditions used here. The existence of etched grain boundaries (found only in the Bridgeman crystals which were slightly polycrystalline) suggests shorter polishing times should be used for polycrystalline materials.

Preliminary substrate preparation using un-annealed crystals was unacceptable as substrate quality was inferior. J. W. Davison [4] has reported similar experience in his investigations of KCl polishing techniques. All of the Bridgeman KCl used in this investigation was annealed at 600°C prior to any cutting or polishing.

Film adhesion was measured qualitatively using the standard "scotch tape" test. Films produced by both sputtering and e-beam deposition were found to be weakly adherent to the chemically polished KCl, although stronger adhesion was observed for the sputtered films.

Auger analysis of the film-substrate interfaces of films produced by both methods show that for sputtered films the diffusion of Ge⇌KCl is more complete. The process seems to be describable by the following sequence: During the sputtering of Ge, the substrate is bombarded by secondary electrons which are produced as part of the sputter process. The bombardment of the KCl by these secondary electrons causes

chlorine depletion at the surface of the KCl, a phenomena observed in Auger and LEED measurements on alkali halides [5]. As the Ge is deposited, the heat generated locally at the substrate surface enhances the diffusion of the potassium rich KCl surface layer into the growing Ge film. The Auger profile of a sputtered Ge film on KCl is shown in figure 5. In contrast, the local heating of the KCl substrate during the conventional deposition process is not sufficient to enhance this diffusion process. However, it was noted that during initial stages of the e-beam deposition stray electrons from the source would cause color center production in the substrate. The Auger profile of an e-beam deposited Ge film on KCl shows the "leading" of the potassium at the Ge-KCl interface (figure 6).

Appreciable differences in texture were noted between sputtered and evaporated films as seen by transmission electron microscopy. A typical region of the evaporated film is seen in figure 7a. The film is essentially structureless at this magnification except for the many holes which result from the topography of the KCl structure. Thinner regions of the film around protrusions or depressions have been completely dissolved causing loss of parts of the film. Diffuse rings in the diffraction pattern (figure 7b) appear at the same positions reported by Donovan, Terence, Heineman and Klause for amorphous germanium [6].

The sputtered films show a spherulite growth seen in figure 8. The spherulites are composed of radiating fibers which are less than 100Å in width. Diffraction maxima from these films (seen in figure 9) were broader than those from the evaporated material.

3.2 Laser Damage Results

The multiple beam damage experiment produces an array of damage sites on the specimen, figure 10a. This photograph was taken with transmitted light, the array being formed by holes in the Ge film. Analysis of such arrays yield threshold values.

The laser damage thresholds for the different films are summarized in table 2.

Table 2. 10.6μm Laser Damage Threshold (J/CM^2) of Evaporated vs Sputtered Ge-Coated KCl

Specimen	Evaporated Film	Sputtered Film
KCl (RAP) (100)	0.53	1.06
KCl (RAP) (111)	0.73	0.98
KCl (CZOCH) (100)	0.82	0.96
KCl (CZOCH) (111)	0.56	1.18

For Laser Beam Parameters used, 1 Joule/cm^2 = 10^7 watts/cm^2.

The energy densities quoted represent the lowest energy densities which produce observable damage and represent an average of multiple irradiations performed at different positions on the sample surface. The threshold values quoted indicate a higher damage threshold for the sputtered films relative to the e-beam deposited films. However in this investigation no correlation of damage threshold to either the substrate crystallographic orientation or method of growth could be made.

The damage sites were examined by Nomarski microscopy; a typical damage site is shown in figure 10b. Here the Ge is completely gone from the KCl surface and several cleavage cracks were formed in the substrate during damage.

The Ge films were also studied after laser damage by transmission electron microscopy. Damaged regions were identified by holes in the film. Regions immediately surrounding the holes were crystalline in both the sputtered and evaporated films, in contrast to the amorphous nature of the film observed prior to damage. One of the regions in an evaporated film is shown in figure 11.

4. Conclusions

Several conclusions can be drawn from the observations made during this investigation. First, there exists an adhesion problem of the germanium coatings on the chemically polished KCl which is independent of the deposition technique described above. The sputtered films tended to show qualitatively better adhesion (see above), however, none of the films produced in this experiment were able to pass the

"scotch tape" adhesion test in a satisfactory manner.

The object of this investigation is to compare the damage thresholds of germanium films produced by sputtering and e-beam deposition. The observed damage thresholds for all the films tested were within a factor of two, indicating that sputtered germanium films can compete or as in this investigation excell in performance against e-beam evaporated films produced in medium high vacuum. However, the damage threshold measured are low in all cases suggesting that for high power laser application germanium is a poor first coating.

The damage mechanism observed is consistent with a thermal runaway damage model. The burn holes in the germanium film suggest a vaporization of a large part of the film with large amounts of heat being generated at the crater periphery. This is seen in the crystalline nature of the periphery of the crater edges. Further, the damage at the substrate surface suggests local heating at the beam site.

The damage profile of both sputtered and e-beam deposited films was essentially the same. That is, there appeared to be no significant differences in the mechanism for damage between films. Auger analysis of both kinds of films could show no measurable difference in the contamination, particularly for oxygen which is known to have an absorption band centered at about 13μm. Further, no correlation could be made between threshold level and the orientation or growth method of the substrates used in this investigation.

Finally, the multiple beam laser damage experiment described above has been shown to be effective in the laser damage studies at 10.6μm.

5. Acknowledgement

The authors thank H. Posen for his helpful suggestions in the course of this study. Potassium chloride was generously furnished for this investigation by J. O'Connor of AFCRL, to whom we are greatly indebted. Technical assistance was also provided by I. Berman and J. Fitzgerald of this laboratory.

6. References

[1] Loomis, J. S., "Evaluation of Coated Laser Windows". Proceedings of High Power Infrared Laser Window Materials Conference, Hyannis,MA., 30 Oct-1 Nov, 1972.

[2] I. M. Weiner, Appl. Opt. 5, 1437 (1966).

[3] Bernal, et al., "Preparation and Characterization of Polycrystalline Halides for use in High Power Laser Windows", ARPA Contract No. DAHC-73-C-0227, Final Report, Dec., 1973.

[4] Davisson, J. W., "Chemical Polishing of NaCl and KCl Laser Windows". Proceedings of High Power Infrared Laser Window Materials Conference, Hyannis,MA., 30 Oct-1 Nov, 1972.

[5] Palmberg, P. W., Todd, C. B. and Rhodin, T. N., J. Appl. Phys., 39, 4650 (1968).

[6] Donovan, T., et al., "Thin Film Coatings for Alkali Halide Windows", Proceedings of High Power Infrared Laser Window Materials Conference, Hyannis, MA., 12-14 Nov, 1973.

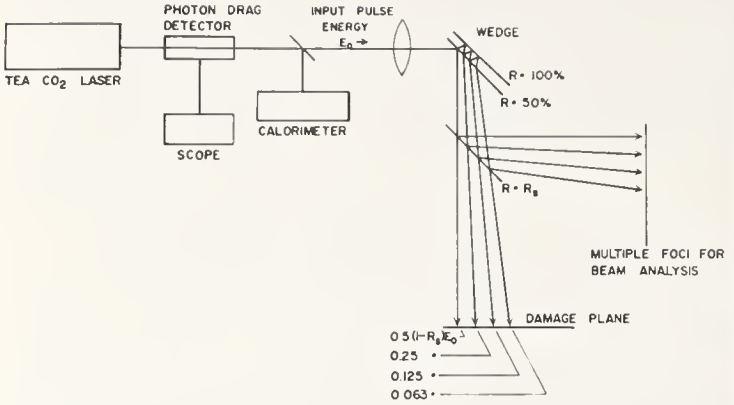

Figure 1. Diagram of apparatus for pulsed CO_2 multiple beam damage experiments.

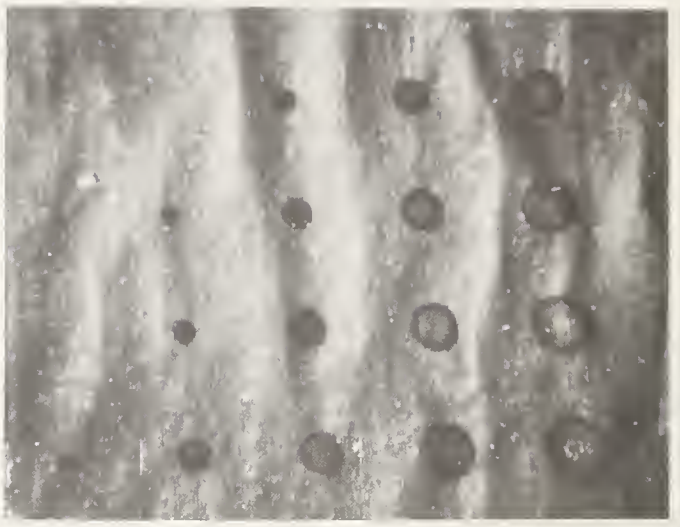

Figure 2. Burn pattern in carbon paper used in determining beam profile.

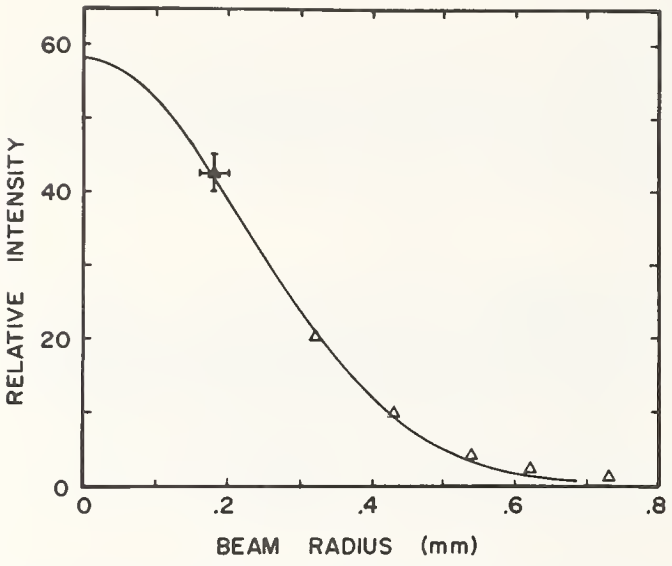

Figure 3. Profile of a focused CO_2 laser beam determined from data obtained during a single pulse.

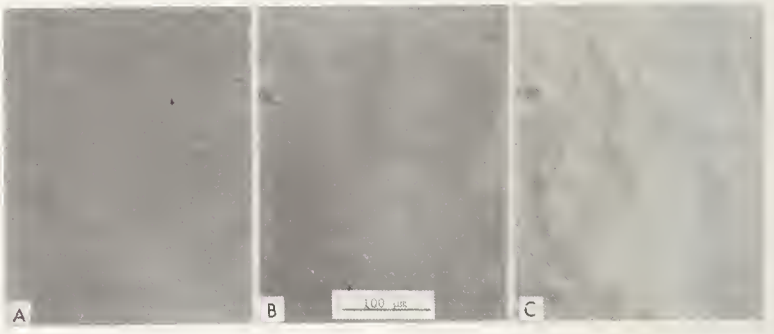

Figure 4. Nomarski micrographs of surface of KCl (100), Czochralski grown; (A) after mechanical polish with 0.05 μm Al_2O_3, (B) after 2:1 acetic/HCl chemical polish, (C) after 1 μm thick Ge sputter deposit.

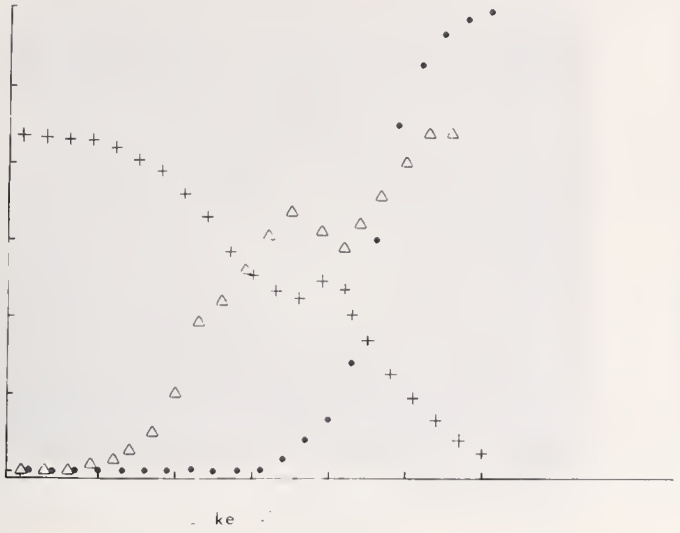

Figure 5. Auger profile of a sputtered Ge film on KCl.

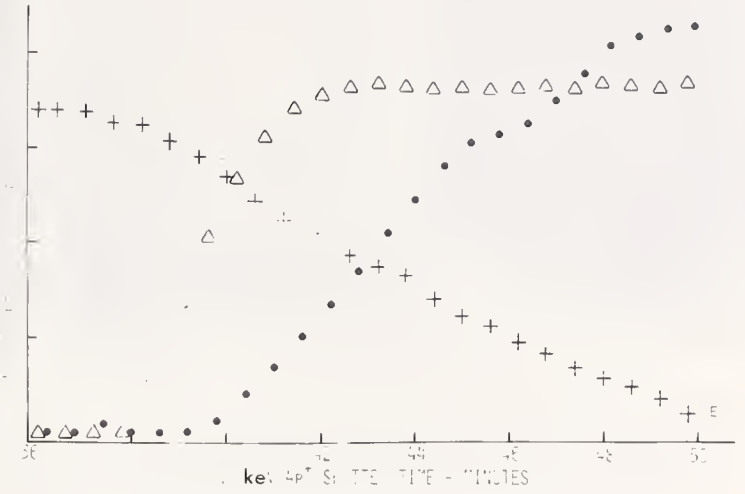

Figure 6. Auger profile of e-beam deposited film on KCl.

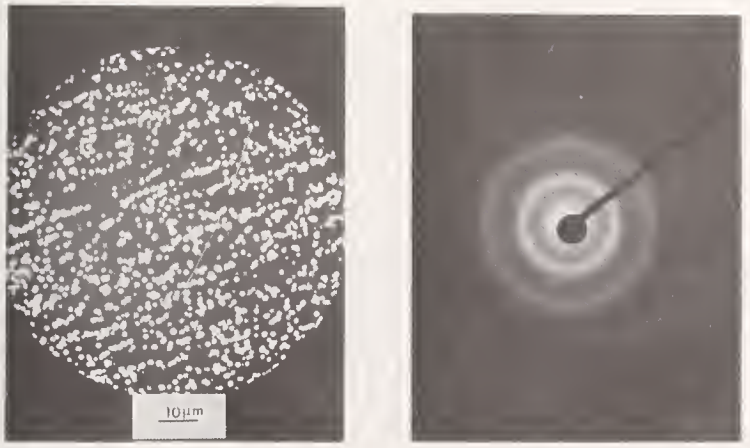

Figure 7. Structure in thinned evaporated Ge film.

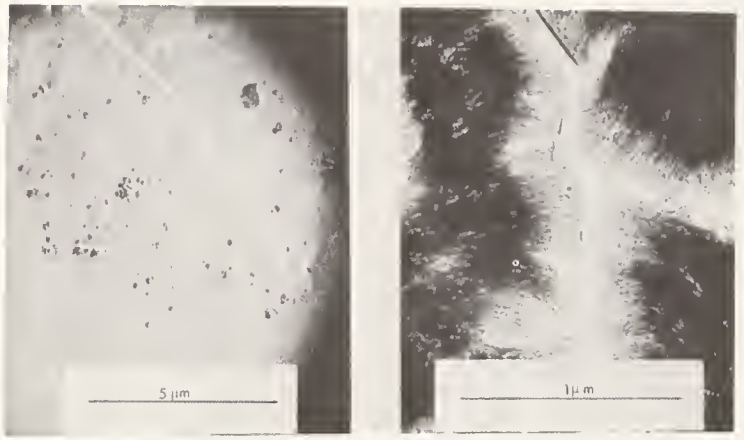

Figure 8. Transmission electron micrographs of a sputtered Ge film showing spherulitic growth.

Figure 9. Electron diffraction pattern from sputtered Ge film.

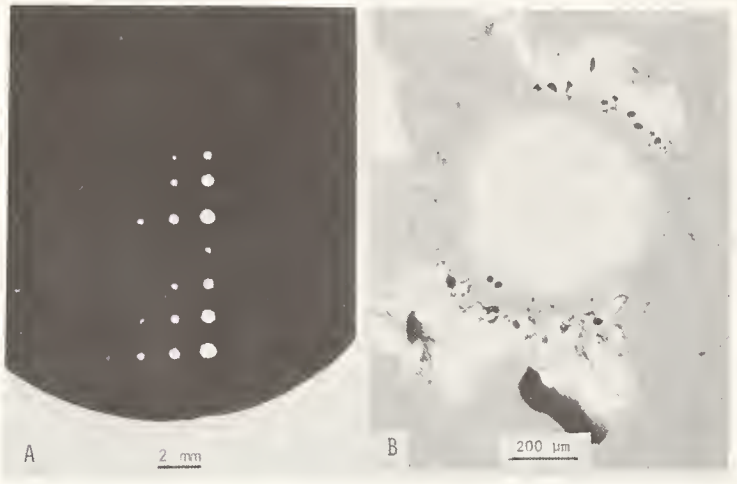

Figure 10. 10.6 μm pulsed laser damage of Ge-coated KCl; (A) Macrophotograph showing an array of damage sites, (B) Nomarski micrographs of a damage site.

Figure 11. Structure of a sputtered Ge film surrounding the 10.6 μm laser damaged region.

COMMENTS ON PAPER BY GOLUBOVIC

It was pointed out that the fact that measurements can be made at several power levels on a given shot, using the multiple reflectium technique, offers distinct advantages for damage studies. Care must be exercised however, to avoid synergistic effects due to spattering from one damage site to an adjacent site. The exact mechanism of the interaction between adjacent damage sites is still unclear, however.

2.7 10.6μm Pulsed Laser Damage in ZnSe

H. Posen, J. Bruce and D. Milam

Air Force Cambridge Research Laboratories
L. G. Hanscom Field
Bedford, Massachusetts 01730

The effect of 10.6μm pulsed laser radiation on large grain ZnSe is examined with respect to the local crystallography of the material. In particular, the presence of twin boundaries, a common defect in II-VI materials, is shown to have very little effect on the damage threshold. Damage effects were monitored by Nomarski interference contrast microscopy, electron microscopy and x-ray topography.

Key words: CO_2 pulsed laser damage; damage threshold; laser windows; twin structure; zinc selenide.

1. Introduction

The object of this study was to examine the thesis that the presence of specialized intergranular boundaries, albeit clean of defect material, may adversely affect the 10.6μm laser damage threshold in candidate window materials in high power CO_2 laser optics systems.

For cubic materials of the alkali halide family, which have the rock salt crystal structure, polycrystallinity prepared by in situ crystallization techniques such as the PIR method [1][1] reflect little deterioration in 10.6μm transmissivity and appear to exhibit no degradation in 10.6μm damage threshold, directly attributable to the presence of grain boundaries. These observations have been examined solely under CW conditions [2] and carefully graded pulsed measurements of damage thresholds as done in this study according to the method of D. Milam of AFCRL have not been made.

Another class of cubic materials, such as CdTe and ZnSe, because of their low absorption at 10.6μm and their comparatively larger yield strengths vis-a-vis those of alkali halides have been also considered as candidate window materials for 10.6μm laser systems. These II-VI materials are low band gap semiconductors, available only as polycrystalline aggregates. They exhibit a variety of large grain boundary misorientations, but characteristically, regardless of the crystal growth method exhibit highly rectilinear intergranular bands which are called twins.

Early experiments on CdTe under CW 10.6μm irradiation exhibited dramatic material failure [3]. There was evidence in these failures that the boundaries acted as local failure initiation sites, although again the width of the CW incident CO_2 laser beam did not permit an unambiguous assignment of failure initiation to the twins or their boundaries.

Some pulsed damage experiments on ZnSe by Fradin and Bua [4] emphasize the relation of 10.6μm damage threshold to the possible presence of particular defects rather than to the local morphology of the crystal. In other experiments on 10.6μm pulsed damage in ZnSe [5,6] using extremely short pulse lengths, again no attempt was made to correlate damage threshold with local crystallography.

For these II-VI materials we will demonstrate in the next section that the presence of twins necessarily implies boundaries of several atomic layers thick of non-cubic material. The presence of such non-cubic layers provide local variations in the refractive index. Grain boundaries in these materials on the other hand represent boundaries between single crystallites of different orientation, whose crystal structure remains the same. By their very nature they are large angle boundaries and represent convenient sites for "stranger" or garbage atoms, which may act as strong local absorptive sites. Early 10.6μm CW studies at AFCRL [3] clearly demonstrated the susceptibility of materials with dirty grain boundaries to low damage thresholds.

1. Figures in brackets indicate the literature references at the end of this paper.

The thrust of these experiments is confined to evaluating the effect of the presence of twins and their concurrent local variation in refractive index on the damage thresholds. Thus the boundaries of the twins are wurtzite polymorphs of ZnSe and are approximately 6.5Å thick.

In view of the coherence of these twins, the specific energy of the twin interface, because of the good atomic fit, is particularly low with respect to the specific energy of an interface between normal grain boundaries, and defect atoms would prefer grain boundaries as sites rather than twin boundaries. Thus the major possible structural contribution to damage threshold variation is the local variation in refractive index, arising from the different crystalline structure at the twin interface.

Figure 1, illustrates the ZnSe lattice stacked along the [111] polar axis. The symbols "a"and "c" are repeat distances along [110] and [111] directions. Figure 1(a) shows the normal zinc selenide structure with the usual close packed ABCABC type stacking along [111] while figure 1(b) shows the results of a growth error, in which the structure shown by full lines is a unit cell with hexagonal packing of another form of ZnSe. Because of the polarity of the structure, the whole lattice is turned 180° about the [111] normal after the twinning.

2. Crystal Twinning in ZnSe

One may regard twinning as a phenomenon that permits individual parts of a crystal to take up a new orientation, usually in response to a growth error, a thermal transformation or some mechanical impetus. The new crystal is of the same crystal species as the original crystal, and each is oriented with respect to the other, according some well defined laws. Only in the immediate vicinity of the boundary can there be a change of crystal structure. Such boundaries may be coherent or incoherent. Coherent boundaries are plane and parallel to the twin plane and do not give rise to macroscopic lattice stresses. Twins in ZnSe are classified as growth twins and have coherent boundaries.

Crystalline twinning was early recognized by mineralogists as a common phenomena occurring in many minerals. Friedel [7] was the first to systemize twinning according to specific laws. These twinning laws have been refined and expanded and put on a mathematical basis for all crystal systems by Jaswon [8],and Jaswon and Dove [9].

A predominantly phenomenological exposition of crystalline twinning is extensively reviewed by Cahn [10]. M. V. Klassen-Neklyudova [11] reviews in detail the development of mechanical twins. ZnSe belongs to the cubic zinc blende crystal structure class and may be regarded as two interpenetrating face centered cubic lattices, one of zinc and one of selenium shifted with respect to one another 1/4 unit along the main diagonal of the unit cell. The basic structural unit is a tetrahedron of Zn(Se) atoms, at the center of which is a Se(Zn) atom, covalently bonded to each of the Zn(Se) atoms. Thus the structure may be considered as the two-element analog of the diamond cubic structure, but because not all vertices of the tetrahedra have the same orientation, the structure has no center of symmetry, resulting in the familiar polarity of ZnSe crystals along the [111] direction.

Aminoff and Broomé [12] looked at the geometry of twin structures for zinc blende (ZnS), galena (PbS), diamond, gold and copper, and concluded that if two crystals form a twin, then the two lattices are directly in contact or the lattices are separated by a transition region. For monoelemental structures, the transition region corresponds precisely to the initial structure, whilst for structures like ZnSe, the transition region has a structure corresponding to one of the polymorphic forms of the initial structure. Aminoff and Broomé showed that there are fourteen possible modes of incorrect deposition when ZnS grows on a (111) face, but the only growth twins known are ones in which the transition region has the wurtzite structure, the hexagonal polymorph of zinc blende.

3. Experimental Procedure

Selected particular crystals within the ZnSe matrix were to be examined in detail with respect to their twin structure, exposed to 10.6μm pulsed laser radiation, and observed as to when and how damage occurs. However, the grain size of polycrystalline CVD ZnSe is too small to perform such a study, because of the desirability of indexing the damage area with other observations. Specimens of large grain multi-twinned ZnSe manufactured by Eagle Picher Industries, Inc. were selected. Figure 2 shows a macrophotograph of one of these specimens, a disk 17mm in diameter and 4mm thick. Its

structure is composed primarily of one large heavily twinned crystal and another smaller crystal. These specimens were grown in a carbon crucible by the Stockbarger technique and may contain traces of carbon impurity, as will be discussed later.

Specimens of both CVD and twinned ZnSe were polished using Linde A, and etched in $K_3Fe(CN)_6$ solution according to the method of Braunstein [13]. This etch not only removes the mechanically damaged surface layer but also reveals the grain structure and twin structure. The surface grain structure of both types of ZnSe was examined using Nomarski interference microscopy. Micrographs of typical grain structures found are shown in figure 3. The linear banding is typical of twin structure where the light and dark areas represents crystals of different crystallographic orientations, with a definite orientation relationship between the two.

The twinning relationship was established by determining the crystallographic orientation of each part of the twin and plotting this on a stereographic projection together with data on the direction of the composition plane. Figure 4 shows the resulting stereogram with some of the (100),(110) and (111) poles plotted. Solid and open symbols refer to the two parts of the twin; some poles are common to both twins. From this stereogram, both the twinning plane and the composition plane are found to be the (111) plane (dashed line).

The finer details of the ZnSe twin structure are shown by transmission electron micrographs of a two-stage replica of a ZnSe large grain twinned crystal. The crystal surface had been polished and etched as described previously. Figure 5(a) shows an electron micrograph of a 10μm twin band. The difference in texture is due to a difference in the etching characteristics of the twin surfaces with different crystallographic orientations. An area of multiple twinning is shown in figure 5(b). Here there are at least seven twin bands present in this particular 6μm region. Some twin bands are as small as 0.02μm. Twin bands smaller than this would not be seen by this replica technique on a surface of this quality.

The surface chemistry of the large grain twinned ZnSe was examined with Auger spectroscopy. The object here was two-fold: to identify the composition of numerous black particles seen throughout the bulk of the specimen as well as on the surface;and to look for any impurities in the grain boundaries or twin boundaries. Figure 6 shows spectra taken on a particle before and after sputter cleaning of the surface. The particle was identified as carbon. No impurities could be found in the boundary regions after sputter cleaning of the surface.

However consideration of the surface resolution of the Auger beam, and the low defect chemistry of these materials as established by IR spectroscopy and mass spectroscopy [14] mitigates against determining accurately the local chemistry of the twin boundaries.

To insure that the CVD and twinned ZnSe are of comparable optical quality, bulk absorption coefficients were measured at 10.6μm on both materials by the calorimetric method. The results are presented in Table 1.

Table 1. 10.6μm Optical Absorption of ZnSe

	$\beta(cm^{-1})$
ZnSe (CVD)	$0.0030 \pm .0004$
ZnSe (twin)	$0.0070 \pm .0002$

The large grain twinned material has an optical absorption about double that of the CVD material. This higher value is not surprising since the twinned material contains visible carbon inclusions which can act as absorptive and scattering centers.

3.1 Laser Damage Measurements

The experimental arrangement used to perform pulsed CO_2 damage experiments at preselected sites in ZnSe is shown in figure 7. A lens with focal length of 10cm was used. The profile of the focussed beam in a plane approximately 1cm downstream from the waist was determined by recording burns on carbon paper while successively attenuating the beam. The beam profile is shown in figure 8, where the solid curve is a Gaussian profile fit to the data.

The calorimeter in the side arm was calibrated by comparison with the total

energy arriving in the sample plane. Calorimeter readings were taken for each firing.

The specimen was placed in the above characterized plane and damage was induced at an arbitrary place on the sample. The HeNe laser beam was then focussed through the sample onto the damage site. Sites could then be preselected for damage experiments by using the HeNe beam as a site indicator.

Damage experiments were performed by successively removing CaF_2 attenuators from the beam until visible evidence of damage was observed on a given site. Faint yellow light, which may be either white light filtered by the transmission properties of ZnSe or blackbody radiation from heated sites, was seen on some sites, while the usual bright white sparks were seen on other sites. Several seconds were allowed between shots to limit heat accumulation in the sample.

4. Results

Pulsed laser damage was induced on several sites within the individual parts of the twin crystal as well as on twin boundaries, and in one case on a grain boundary. Figure 9 is a sketch of a specimen surface with the twin and grain boundaries indicated. Superimposed on this is the location of several numbered damage sites and the energy value in J/cm^2 at which damage was observed. Here all of the damage threshold values fall within the range of 4-11 J/cm^2, whether the irradiated site was within a twin or on a twin boundary. No particular trend in threshold energy with relation to damage site location was observed.

In eighteen out of twenty-three runs, damage occured at 10-11 J/cm^2, indicating that this value is the damage threshold energy for this material, and suggesting that at the five sites where lower threshold values were observed, there may have been a flaw in the material, such as a carbon particle, to cause premature damage. Actually two of these five sites show no visible damage, even when examined at 80X.

The damage sites were examined using optical microscopy at 80X. They appeared to be located primarily within the bulk of the material, although a few were observed on both front and back surfaces.

Figure 10 shows three typical damage sites, located below the surface. They appear to have two types of structure associated with them depending on which twin they are located in. That is, the crystallographic orientation of the twin has a definite effect on the damage morphology. Figure 10(a) is a micrograph of damage site number 34, with the twin surface orientation ~10° off (110). Damage occurs in the (110) plane, with numerous damage striations along (011) planes. Figure 10(b) shows damage site number 32, with the surface of this twin 13° off (100) plane. Here there are no (011) striations within the circular damage area. However, outside this area is another disturbed region where stepwise cleaving has occured. Figure 10(c) illustrates a damage site located at a twin boundary where both types of damage morphology were observed.

X-ray reflection topographs were taken of the large grain twinned ZnSe crystal. Here diffraction contrast can be obtained using either set of twins. X-ray reflections were selected using the computer program TOPOG [15]. Figure 11 shows x-ray topographs of [400] and [440] reflections for one set of twins. The crystal is strained thus eliminating some of the expected pattern. Figure 12 shows the same reflections after laser irradiation. Here only two surface damage sites (A & B) are seen, since this technique samples only about a 15μm surface layer. Most of the damage sites are located below the specimen surface.

5. Conclusions

Although no direct correlation between damage threshold at 10.6μm and site location was found, there is some indication that the morphology of the damage is related to the orientation of the twin relative to the surface. When failure did occur, it occurred by partition along the (110) cleavage planes.

The twinning theory indicates that in cubic ZnSe, the twin boundary has a hexagonal structure, probably a few layers thick. However, when the twin boundary was irradiated, the size of the laser beam used was so large relative to the boundary that it did not see local variation in index of refraction between these two structures at the interface. Thus, our original thesis has not yet been disproved, That the twinning is present and coherent actually serves to strengthen the material.

since it forms a barrier to dislocation propagation. However, the question requires more detailed experimental work.

6. Acknowledgements

The authors wish to thank H. Lipson for the optical absorption data, W. Ewing for the Auger spectra, J. Comer for the electron micrographs and C. Bergeron for specimen preparation.

7. References

[1] High Power Infrared Laser Window Materials (LQ-10 Program), Quarterly Progress Report No. 6, Air Force Cambridge Research Laboratories, AFCRL-72-0559.

[2] Posen, H. et al, Proceedings of Conference on High Power Infrared Laser Window Materials, AFCRL-TR-73-0372, (1972) Vol. II p. 383.

[3] High Power Infrared Laser Winsow Materials (LQ-,0 Program), Quarterly Progress Report No 2, Air Force Cambridge Research Laboratories, AFCRL-71-0405.

[4] Fradin, D.W. and Bua, D.P., Appl Phys Lett 24, 555 (1974).

[5] Wang, V., et al, elsewhere in these proceedings (1974).

[6] Stark, E.F. and Reichelt, W.H., elsewhere in these proceedings (1974).

[7] Fridel "Lecons de crystallographie", Paris: Berger-Levrault (1926).

[8] Jaswon, M.A., Acta Cryst 9, 621 (1956).

[9] Jaswon, M.A. and Dove, D.B, Acta Cryst 10, 14 (1957).

[10] Cahn, R.W., "Twinned Crystals" "Advanced in Physis" Vol. 3, (1954) p. 363.

[11] Klassen-Neklyudova, M.V., "Mechanical Twinning of Crystals", translated from Russian by J.E.S. Bradley, consultants Bureau, NY (1964).

[12] Aminoff, G. and Broome, B., Z. fur Krist. 80, 355, (1931).

[13] Braunstein, M., Proceedings of third Conference of High Power Infrared Laser Window Materials, Vol. III, Surfaces and Coatings, p. 863, (1973).

[14] Hunt, M., AFCRL, private communication.

[15] Posen, H. - TOPOG, a Computer Program to compute Penetration Depth and Setting Angles for Reflection X-Ray Topography, to be published.

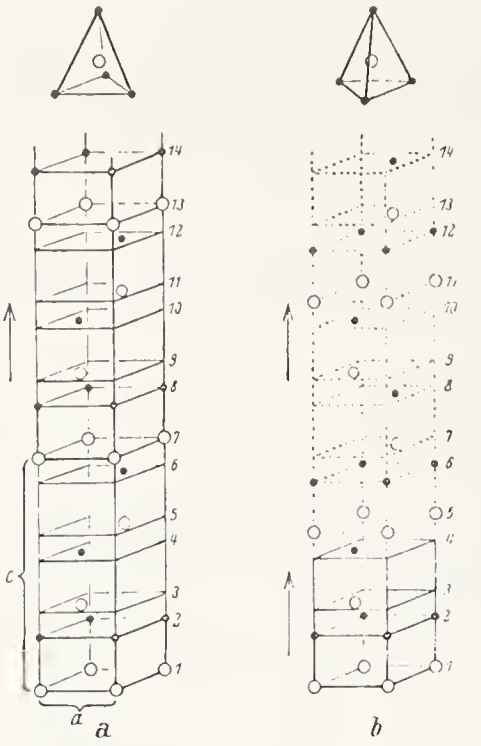

Figure 1. Atomic structure of twin development of ZnSe (from Aminoff and Broomé [12]).

Figure 2. Macrophotograph of a large-grain multi-twinned ZnSe crystal.

Figure 3. Nomarski micrographs illustrating the grain structure and twin structure in twinned and polycrystalline CVD ZnSe.

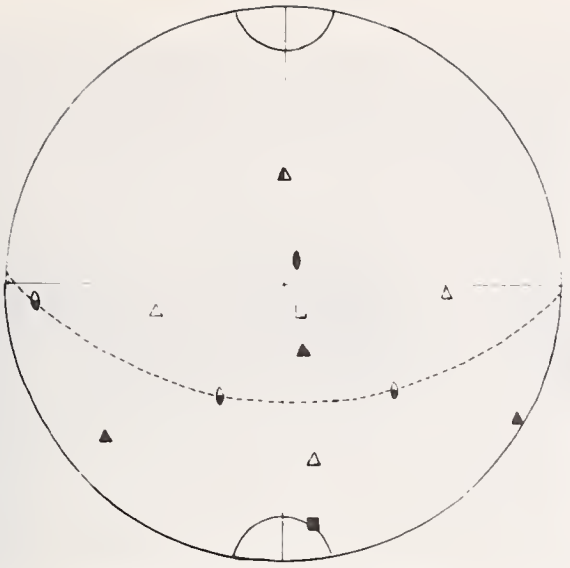

Figure 4. Stereogram illustrating twinning relationship in ZnSe.

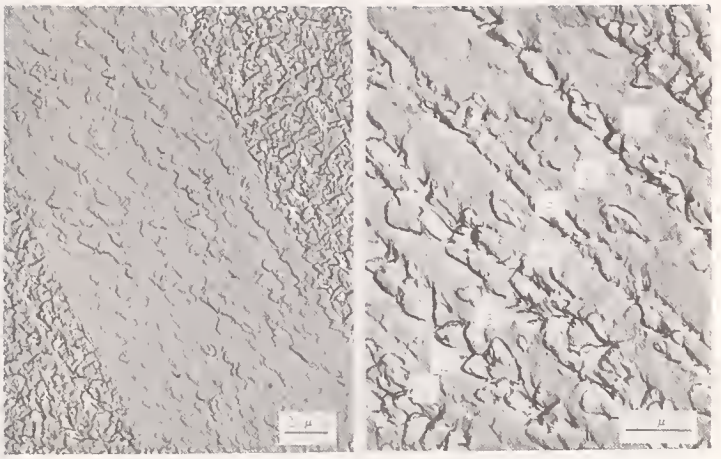

Figure 5. Electron micrographs of a replica of ZnSe surface, illustrating twin structure.

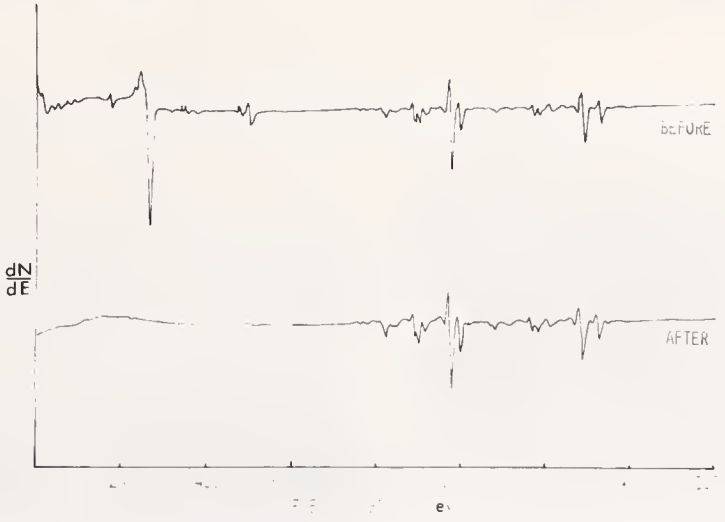

Figure 6. Auger spectra of a foreign particle in ZnSe before and after sputter cleaning of the surface.

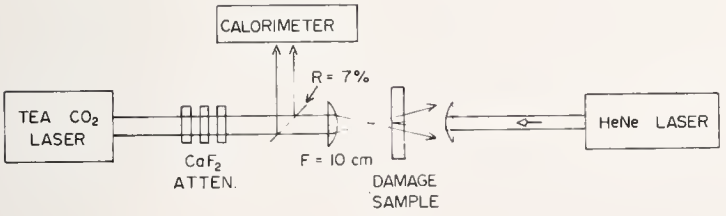

Figure 7. Experimental set-up for pulsed CO_2 laser damage experiments on preselected sites in ZnSe.

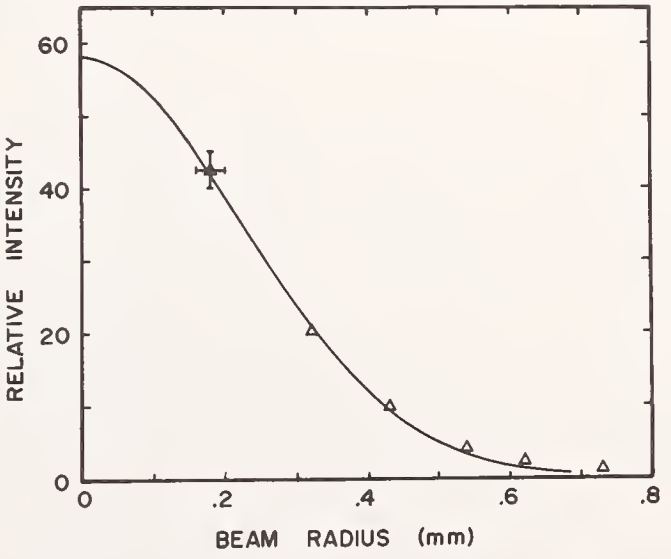

Figure 8. Profile of a focused CO_2 laser beam.

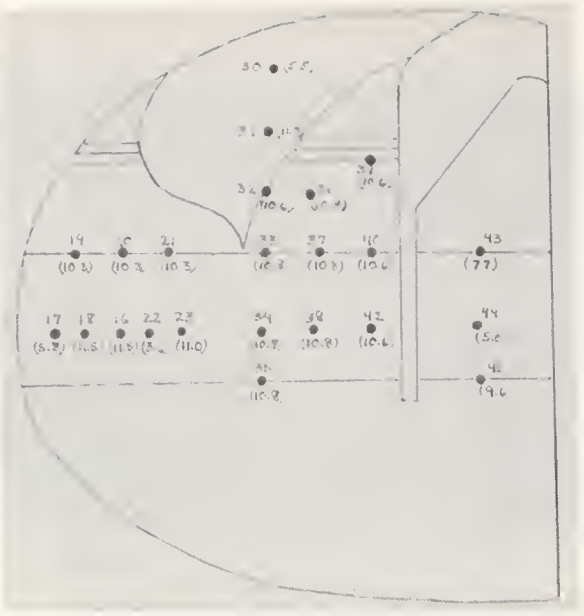

Figure 9. Energy values of observed pulsed CO_2 laser damage in J/cm^2 for ZnSe twinned crystal.

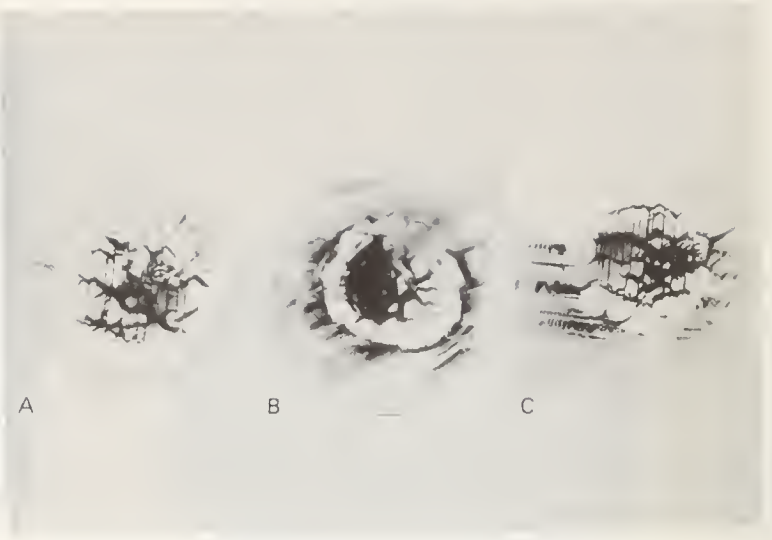

Figure 10. Micrographs of CO_2 laser damage sites in ZnSe twinned crystal.

Figure 11. [400] and [440] x-ray reflection topographs of ZnSe twinned crystal.

Figure 12. [400] and [440] x-ray reflection topographs of a damaged ZnSe twinned crystal.

NO COMMENTS ON PAPER BY POSEN

2.8 Evaluation of Single Crystal $LaCl_3$ AS CO_2 Laser Window Material

F. Varsanyi and L. G. DeShazer

Center for Laser Studies
University of Southern California
Los Angeles, California 90007

We report calorimetric measurements of the $LaCl_3$ absorption coefficient at 10.6 μm. Single crystal $LaCl_3$ of substantial size (one inch diameter, two or more inches long) were grown repeatedly in our laboratories in the past years, mostly for spectroscopic purposes. $LaCl_3$ is transparent in the visible extending up to 25 μm and, if pure, is only slightly hygroscopic. Its phonon spectrum has been well investigated and terminates around 260 cm^{-1}. A rather elaborate program of mechanical and optical property evaluation was initiated. In the preliminary experiments reported here, we studied a $LaCl_3$ single crystal (2 x 11 x 12 mm) with a CO_2 laser. We feel $LaCl_3$ compares favorably with KCl as a laser window material, but without some of its problems.

Key words: Absorption coefficient; $LaCl_3$; infrared materials; thin film material.

COMMENTS ON PAPER BY VARSANYI

H. Posen of AFCRL commented that in order for a material to be attractive as a 10.6 μm window material, it should be optically isotropic. However, the use of $LaCl_3$ as a coating material, in thin film form, is still attractive.

564-378 O - 74 - 8

2.9 LASER WINDOW DAMAGE FROM CW 10.6-μm RADIATION

J.S. Loomis and C.A. Huguley

Air Force Weapons Laboratory
Kirtland AFB, New Mexico 87117

Damage studies have been conducted using a CW, one-kilowatt CO_2 laser. Some analytic calculation of local temperature rise as a function of laser power, spot size, and irradiation time will be discussed. Results of optical distortion and stress-field observations on uncoated and coated samples of KCl, NaCl, and ZnSe are reported.

Key words: CO_2 laser radiation; CW laser damage; infrared windows; KCl; NaCl; optical distortion; ZnSe.

1. Introduction

Our initial investigation into CW laser-induced damage [1][1] was directed toward determining the various failure modes which may be encountered. For semiconductor materials such as ZnSe and CdTe, damage was accompanied by very high temperatures at the center of the damage spot which frequently resulted in holes being melted through the window. Alkali halide windows such as KCl and NaCl were most often damaged through fracture localized near the irradiated areas. Melting or burning of any coating usually accompanied the fracture; the latter almost always occured after the laser beam was turned off.

More recently our efforts have been directed toward exploring the temperature dependence on total power, spot size, and exposure time for windows transmitting CW infrared laser radiation. The desired theory was developed by solving the heat conductive equation, first by making some simplifying assumptions and then more exactly by numerical methods. We then attempted to demonstrate various aspects of the thermal problem with measurements of optical distortion and stress-fields during irradiation by various combinations of power, spot size and irradiation time.

2. Calculation of Local Temperature Rise

Consider first the case of a homogeneous window which is being irradiated by a uniform beam. One can make the usual assumptions that the absorption is low so that energy is absorbed evenly throughout the volume of window material, that the thermal properties remain constant during irradiation, and that the irradiation time is less than the typical time constant for external heat transfer. Under these conditions the temperature of the window will increase linearly with time and there will be no temperature gradients across the window. The window will have no thermally induced optical distortion or stress patterns, and damage will occur only when the temperature of the window reaches the melting point.

Contrast this situation to that of a window which is being irradiated at a small spot at the middle of the window. The temperature at the center of the spot can be obtained from a simple heat-balance equation:

$$\pi R^2 \, d \, C \, \frac{dT}{dt} = -Q + \beta \, d \, P \qquad (1)$$

1. Figures in brackets indicate the literature references at the end of this paper.

where $\pi R^2 d$ is the volume of material being irradiated (R is the spot radius and d is the thickness of the window), C is the specific heat of the window, β d P is the absorbed power (β is the absorption coefficient and P is the total incident power), and Q is the heat flow to the surrounding material. This heat loss term can be approximated as:

$$Q \simeq K \frac{A}{x} T \tag{2}$$

where K is the thermal conductivity, $A = 2\pi Rd$ is the heat transfer area and $x \simeq R$ is the average heat transfer distance. Equations (1) and (2) can be combined to give:

$$\pi R^2 C \frac{dT}{dt} = - 2 \pi K T + \beta P \tag{3}$$

which has the solution

$$T = T_o (1 - e^{-t/\tau}) \tag{4}$$

where

$$T_o = \frac{\beta P}{2 \pi K}$$

and

$$\tau = \frac{R^2 C}{2 K}$$

This simplified analysis suggests that, in the limit of small beam spot sizes, the temperature at the center of the spot will equilibrate to a temperature which is independent of spot size with a time constant τ which is proportional to the area of the spot. For the case of potassium chloride irradiated by a 1000 watt beam over a spot of 0.5 cm radius, there is a temperature rise of about 1.5°C and a time constant of about 2 seconds.

The actual experimental situation lies between the two extremes. To arrive at an actual temperature dependence, a numerical solution to the heat conduction equation was made [2] The solution assumed cylinderical geometry with azimuthal symmetry. Heat transfer was assumed to be governed by differential boundary conditions with a heat transfer coefficient of 0.002 watt/cm^2 - °C, which is appropriate for conduction into still air. The beam profile was assumed to be gaussian. An implicit finite-difference technique was used to calculate temperature as a function of time and position.

Figure 1 shows the calculated temperature rise for a potassium chloride window irradiated for 5 seconds by a gaussian beam with a $1/e^2$ spot diameter of 6 mm. The window itself is 3.8 cm in diameter by 1.0 cm thick. Note that the temperature gradient is established within 3-4 seconds. Afterward the temperature at each point in the window rises uniformly.

3. Apparatus

The experimental arrangement used is similar to that reported earlier [1]. That apparatus used a spherical mirror to focus the beam from the CO_2 laser (GTE/Sylvania model 971) onto the sample. Several such mirrors were tried in that system, but in each case the beam profile aberrated to an elliptical shape. The present experimental apparatus, shown in figure 2, uses a salt lens (25 cm focal length to focus the beam. Graphite apertures 1.3 cm in diameter are used to stop reflections from the uncoated surfaces of the lens. These components were mounted on a translation stage, allowing different spot sizes on the fixed sample. Measurements of spot size and transmission of this lens are given in an accompanying paper [3] . Window samples were positioned after the focus of the lens so that the intensity was largest at the front surface of the sample.

Before the laser beam reaches the test apparatus shown in figure 2, it passes through a diagnostic area containing beam switches, a 1-percent mirror chopper, and instruments to mea-

sure the power, wavelength, intensity profile and polarization of the laser beam. Exposure times are measured to 1 millisecond resolution and can be set to about 10 millisecond precision.

The interferometer used to measure optical distortion is an Optical Engineering "bench-top" interferometer using a HeNe laser beam. Fringe patterns were recorded either by a motion picture camera (20 frames/sec., F 5.6) or a 35-mm still camera (1/60 sec., F. 4). A television camera was used to record visual observations on video tape. Provision was made for viewing the sample between a polarizer/analyzer combination to observe stress patterns.

4. Optical Distortion

The fringe patterns in figure 3 demonstrate optical distortion in ZnSe, KCl, and NaCl. The photographs in the lower row were taken after the fringe patterns had stabilized, from 10-20 seconds after the start of irradiation. The aperture of the interferometer was 2.5 cm x 2.0 cm and the beam diameter was 4 mm and approximately centered in the interferometer aperture. Laser power incident on the samples was about 500 watts.

The optical pathlength difference (OPD) at any point over the interferometer aperture is proportional to the change in window temperature integrated along the path of the interferometer beam. Since the interferometer and the incident laser beam are approximately normal to the surface of the window, the observed OPD is proportional to the average radial temperature. The proportionality between pathlength and temperature can be written as:

$$\phi = \frac{d \chi T}{\lambda}$$

where ϕ is the optical pathlength difference (OPD) in fractions of a wavelength, λ , and χ is given approximately by [4].

$$\chi = \frac{dn}{dT} + (n - 1)(1 + \nu)\alpha$$

where n is the index of refraction, α is the linear coefficient of thermal expansion, and ν is Poisson's ratio.

The peak OPD measured from figure 3 was 3.3 fringes for ZnSe, 0.8 fringe for KCl, and 0.3 fringe for NaCl. An attempt was made to collect data for several different spot sizes and materials, calculate peak OPD's and normalize the results by a suitable combination of material properties and experimental variables. The result is shown in figure 4. Heat conduction calculations produced the solid line which shows that a change in spot area of a factor of 100 only produces a change of a factor of 2 in peak temperature. The experimental points were adjusted by making an arbitrary choice for χ. Neither the value of χ nor the shape of the curves which resulted were in agreement with theory. However, the uncertainties in power measurement, spot size, and OPD were large. Further experimental work will be required to improve the quantitative results.

The fringe patterns in figure 5 show optical distortion during irradiation at increasing laser powers until damage occurred. The peak OPD at each power level was directly proportional to the incident power. As can be seen in figure 5 damage is present in the last fringe pattern. Prior to that time, however, no permanent distortion of the fringe pattern was observed.

Interferometric measurements are sensitive to changes in the physical thickness of the window which may be caused by inelastic flow of material to relieve the compressive stress near the irradiated area. Such areas of flow are visible otherwise only by illumination from reflected light. Since the large scale spacing of fringes preclude observation of small damage areas, the interferometric technique is not a sensitive method of detecting microscopic damage spots. Permanent distortion of the fringe pattern without other physical damage present was observed only in one sample of KCl, coated with As_2S_3.

described measurements at powers up to 1000 watts and power densities as high as 70 KW/cm^2. No more than microscopic damage was observed on any of the uncoated specimens. The damage shown in figure 10 is typical of the damage spots produced on uncoated ZnSe. Sparkles were seen on the surface at power densities as low as 5 KW/cm^2, but were not seen at higher power densities. Even after small damage spots were visible to the naked eye, continued irradiation of that spot did not produce catastrophic damage. The left side of figure 10 does suggest, however, that multiple damage spots may have been produced by that continued irradiation. Although some of the damage spots seemed to be associated with black inclusions in the ZnSe, there was no evidence that all irradiated inclusions produced damage or that all damage was associated with inclusions. The smoky rings about the damage spots suggest vaporization of dust or contaminents at the surface.

Damage to uncoated NaCl and KCl was found on one of the two NaCl samples tested and on all of the four KCl samples tested. Damage appeared to be restricted to the surface in all cases and no fracture was observed on any uncoated sample. Sparkle was observed in the majority of the samples at low power levels. Continued irradiation of damage locations did not seem to enhance the amount of damage present.

Tests conducted on coated samples generally produced damage to both the coating and substrate and usually destroyed the sample. A description of the coated samples tested recently and the power levels which produced failure are given in table 1.

TABLE 1

EXPERIMENTAL PARAMTERS FOR COATED WINDOWS TESTED

Sample	Description	Absorption (Percent)	Power (watt)	Time (sec)	Power Density (KW/cm^2)
ZnSe 20	Raytran substrate with ZnS/ThF_4 AR coating	1.0	450	3.5	55
ZnSe 22 (no damage)	Raytran substrate with ZnS/ThF_4 AR coating	1.0	550	30.	65
KCl 30	Single crystal substrate As_2S_3 half-wave coating		500	4.0	60
KCl 38	Single crystal substrate As_2S_3 half-wave coating	1.7	360	3.5	45
KCl 39	Single crystal substrate As_2S_3/ThF_4 AR coating	2.2	1,000	3.0	1
KCl 40	Single crystal substrate As_2S_3/ThF_4 AR coating	1.6	150	--	20

5. Stress Effects

One of the early calculations for window performance was the dependence on stress in the window as a function of beam parameters and window properties. [4-5] The radial dependence of the radial and azimuthal stress in a typical window sample irradiated by a Gaussian beam is given in Figure 6. The conditions are the same as for Figure 1. The stress at the interior of the crystal is compressive, with the azimuthal and radial stress becoming equal at the center of the window and the radial stress becoming zero at the edge. The edge of the crystal is subjected to azimuthal tensile stress. Fracture was originally believed to be caused by the edge tensile stress exceeding the modulus of rupture of the window, which would result in cracks originating at the edge and propagating into the center of the crystal. It was further advocated that one way to minimize failure might be to subject the window to a hoop stress which would counteract the thermally induced tensile stress at the edge of the window.

Our results do not agree with this model of fracture. In most of the samples which fractured, fracture occurred after the laser beam was turned off and was localized to the vicinity of the irradiated area. To explain this, we first calculated the value of stress at the center of the sample and compared it to the azimuthal stress at the edge of the sample. The results from thin-plate equations [5] are that:

$$\sigma_{center} = \alpha E \left[T - \frac{1}{2} T_{center} \right]$$

$$\sigma_{edge} = \alpha E \left[2T - T_{edge} \right]$$

where σ is the stress, E is Young's modulus and T is the average temperature of the window. For a window irradiated over a small area at the center, the temperature at the center will be larger than either average temperature or the edge temperature. Thus the compressive stress at the center will be larger than the tensile stress at the edge. Although these compressive stresses are not likely to result in fracture, when the stress exceeds the elastic limit of the material, slip or flow may result. When the thermally-induced stress is relieved, by turning off the laser, tensile stress will be created at the boundary between the elastic-strained material and inelastic-strained material. These tensile stresses may in turn be large enough to cause fracture near this boundary. This explanation, coupled with the assumption of surface absorption, also accounts for the observation of fracture localized at the surface of the crystal.

The stress fields produced by a focussed laser beam can be observed by viewing the sample between crossed polarizers. Commercial polarizer material is available which combines a quarter-wave retardation plate with a half-wave plate. Two such pieces of material may be arranged so that the stress fields produce dark fringes on bright background instead of the bright fringes on a dark background produced by the usual half-wave plates. Figure 7 shows a sample of BaF_2 irradiated by a 35 watt CO_2 laser beam focused to a 1 mm spot size. A spectacular stress pattern is observed during irradiation. This pattern then disappears after the laser is turned off. Figure 8 shows a sample of As_2S_3/BaF_2 coated KCl before and during irradiation with a focussed beam. This time a residual stress pattern remained after irradiation, as seen in Figure 9. Also, shown in Figure 9 is the small damage spot of melted coating. In this case irradiation had been cut-off before either substantial burning or fracture resulted. As with the interferometer technique, viewing the sample does not detect small damage spots. The damage spot on the right hand side of Figure 9 is not seen in the macro photograph on the left hand side.

Samples of uncoated ZnSe, NaCl, and KCl were also irradiated at about 500 watts of power ($70 KW/cm^2$). No stress patterns appeared for either ZnSe or NaCl. A faint discoloration, which did not photograph well, appeared for KCl.

6. Damage Morphology

Several samples each of uncoated ZnSe, NaCl and KCl were tested during the previously

Two ZnSe samples AR coated at 10.6 μm with ZnS/ThF_4 were examined for optical distortion during irradiation. The first sample was subjected to a power of 450 watts into a 1 mm spot size. In less than 3 seconds the window reached its melting temperature and the burn pit shown in Figure 11 was created. Although it is not obvious from the picture, a hole was drilled through the window. The damage was accompanied by stress (revealed by crossed-polarizers) but no fracture of the window developed. A sister sample was then tested more cautiously. Successively higher exposures were made until the sample was subjected to 550 550 watts for 30 seconds, with no damage observed. One explanation for the difference between the two samples is that the damage may have been caused by a small blemish in either the coating or the sample. Another explanation is the the conditioning of the second sample may have improved its survivability.

Our previous work suggested that As_2S_3 was an excellent candidate for a damage-resistant coating on KCl or NaCl. Since that time we have tested three additional samples of As_2S_3-coated KCl, two of which damaged. One sample, viewed during irradiation through a polarizer/analyzer combination, is shown in Figure 8 and 9. The damage spot covers approximately 10% of the irradiated area and seems to be caused by melting or vaporiztation of the coating. Residual stress was observed due to laser exposures of 500 watts for 20-40 seconds ($60KW/cm^2$) at different places on the sample. However, the substrate did not fracture at any of these exposures. Another sample, from a different source, was tested for optical distortion (Figure 5) and failed (after a series of conditioning exposures) at 360 watts in less than 3 seconds (45 KW/cm^2). As can be seen in Figure 12, the damage spot consisted of a central region where the coating had burned away surrounded by a ring of ash. In this case the substrate did fracture (after the laser was turned off).

Two samples of KCl with an AR coating of As_2S_3/BaF_2 were also tested. The first sample failed at 1000 watts in 30 seconds (0.8 KW/cm^2). No damage to the coating was observed, but the substrate fractured at the point of irradiation after the laser was turned off. During irradiation of the second sample, the coating burned and the substrate fractured (see Figure 13) in about 1 second at 150 watts (20 KW/cm^2). The damage spot in this instance was smaller than the irradiated area.

7. Conclusion

During this series of measurements we have subjected samples of ZnSe, KCl, and NaCl both coated and uncoated) to CW radiation up to 1000 watts at power densities up to 70 KW/cm^2 and for times of 1-30 seconds. It was shown that temperature gradients within the sample stabilized within several seconds after the start of irradiation, but that the temperature at each point continues to rise linearly with time thereafter. Measurement of optical distortion can therefore be made under reasonably steady-state conditions. However, the analysis of interferometer patterns still requires a knowledge of the laser spot size and the thermal properties of the window. Viewing windows through a polarizer/analyzer combination is a useful technique for studying the time dependence of the stress distribution within the window in those materials which are sufficiently birefringent.

Much of the damage which has been observed, especially on uncoated materials, is seen at or near the surface. Conditioning of the surface at lower power appears to be of some benefit in increasing the survivability of the window. However, it is not clear what kinds of surface defects cause the window to damage catastrophically and which merely disturb the cosmetic quality of the window without unduly affecting its performance.

8. References

[1] Loomis, J.S. and Saito, T.T. Third Conference on High Power Infrared Laser Window Materials November 12-14, 1973, Volume III, Air Force Cambridge Research Labs, AFCRL-TR-74-0085 (111). 1974.

[2] Smith, G.D., Numerical Solution of Partial Differential Equations, Oxford University Press, 1965.

[3] Saito, T.T., Charlton, G.B., and Loomis, J.S., elsewhere in these proceedings, 1974.

[4] Sparks, M., J. Appl. Phys. 42, 5029 (1971)

[5] Horrigan, F.A., et.al., High Power Gas Laser Research, Raytheon Research Division, AD 676 226, September 1968.

9. Figures

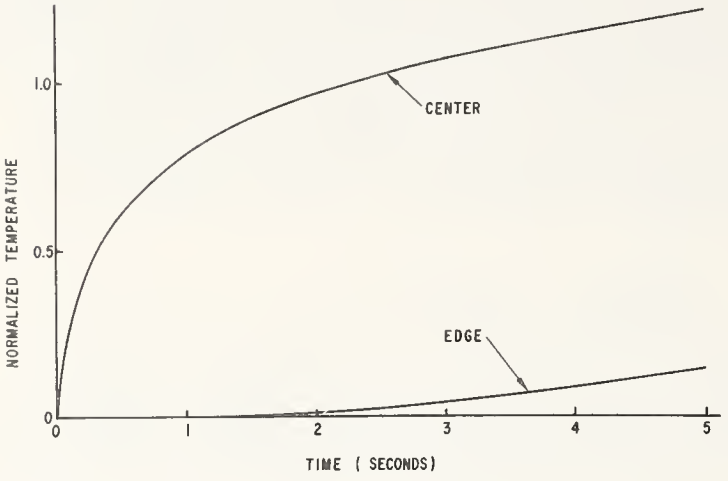

Figure 1. Average radial temperature at the center and edge of a potassium chloride window as a function of time. The actual temperature achieved is proportional to the absorbed power.

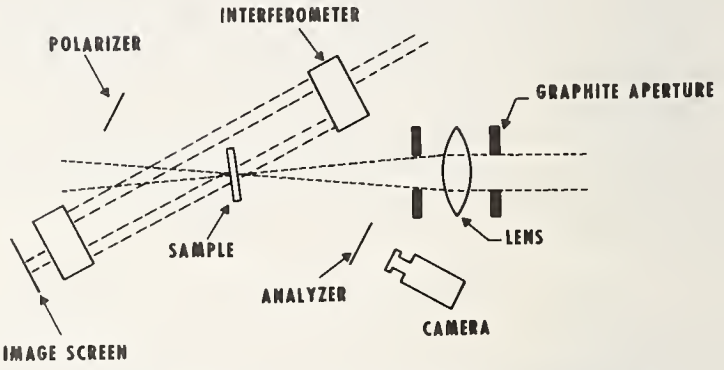

Figure 2. Schematic of experimental apparatus.

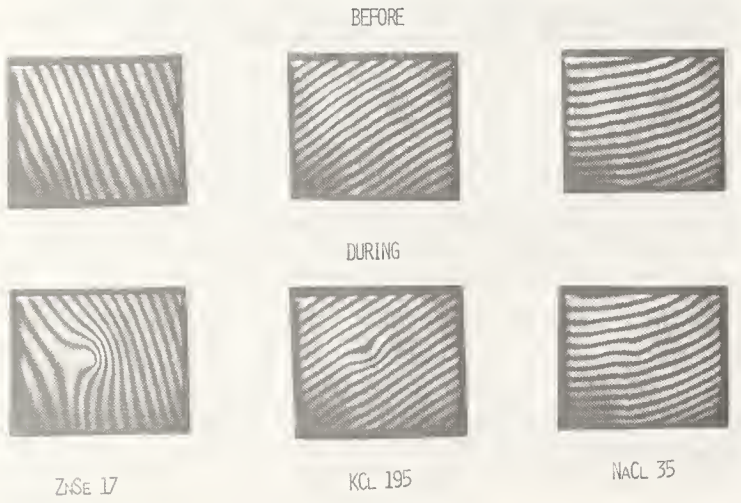

Figure 3. Interferometer patterns of three materials before and during irradiation by 500 watts CO_2 laser radiation. The top row is before irradiation and the second row is after the distortion had stabilized.

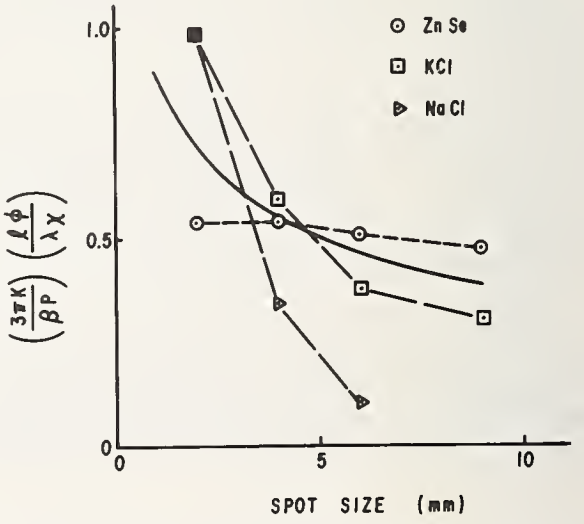

Figure 4. Correlation between peak distortion and spot size (in normalized form).

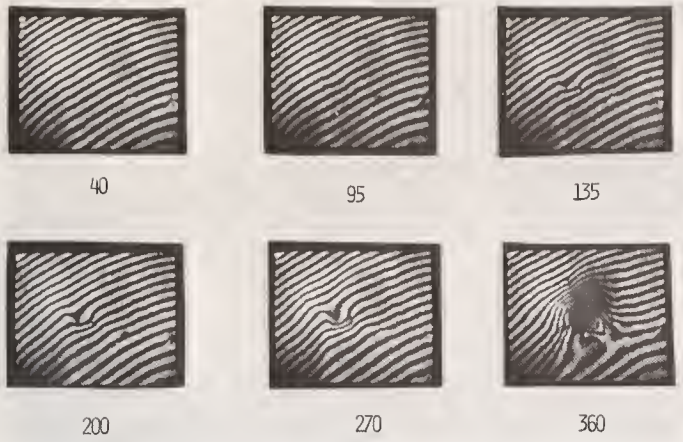

Figure 5. Interferometer patterns during irradiation of KCl 38 by the indicated laser power (watts) into a 1 mm spot size.

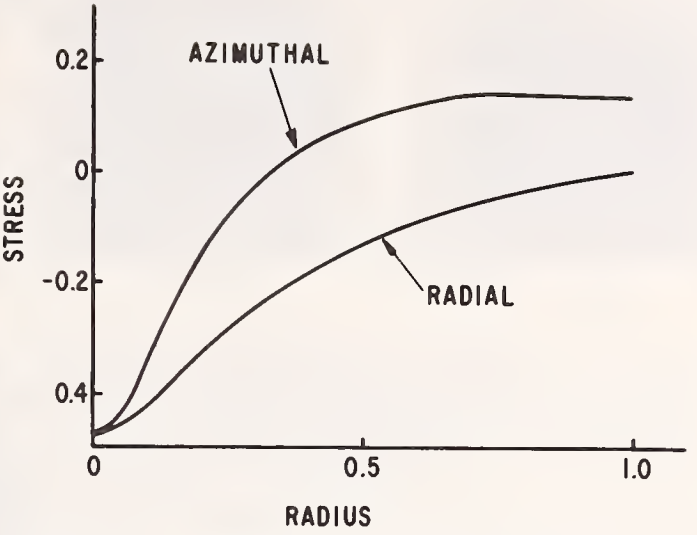

Figure 6. Azimuthal and radial stress as a function of radius (normalized units), for a potassium chloride window irradiated by a gaussian beam.

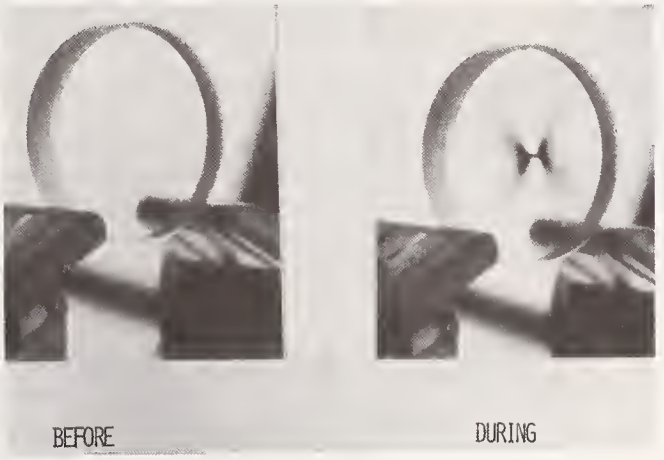

Figure 7. Barium fluoride viewed through a polarizer/analyzer before and during irradiation by 35 watts into a 1 mm spot size. The sample is 3.8 cm in diameter.

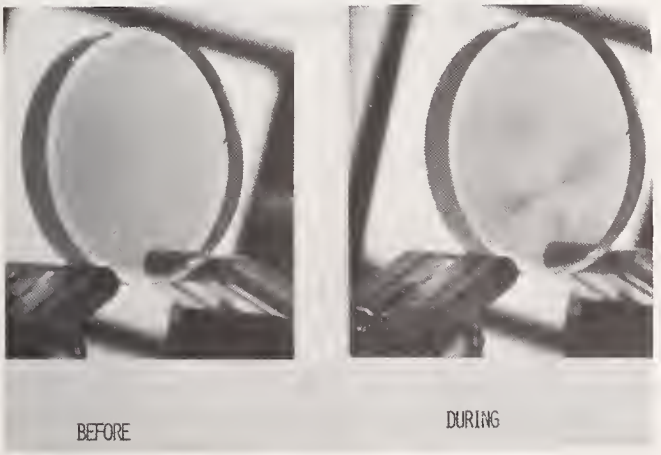

Figure 8. Coated KCl viewed through polarizer/analyzer before and during irradiation by 500 watts into a 1 mm spot size.

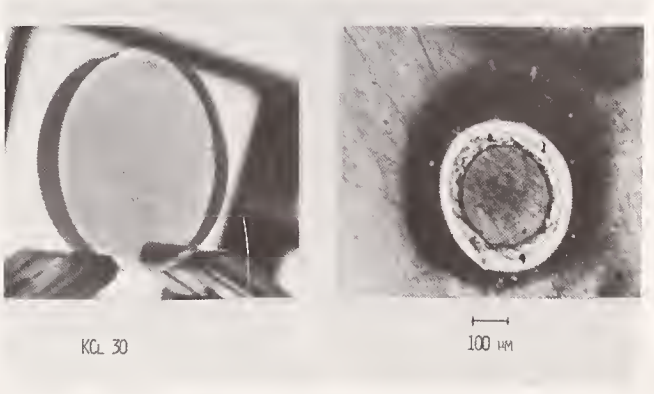

Figure 9. Same coated KCl after irradiation, photograph at right is magnified view of the damage spot.

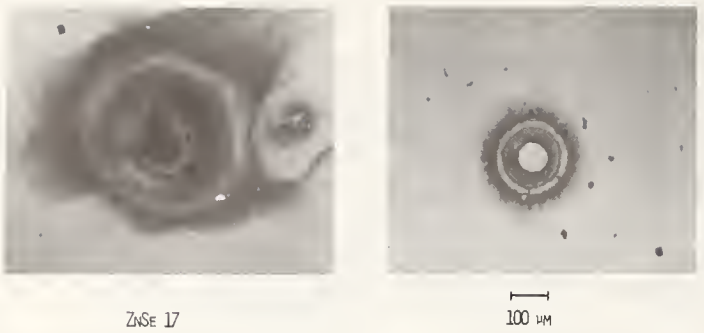

Figure 10. Magnified view of damage spots on surface of uncoated ZnSe sample, which has been repetitively irradiated.

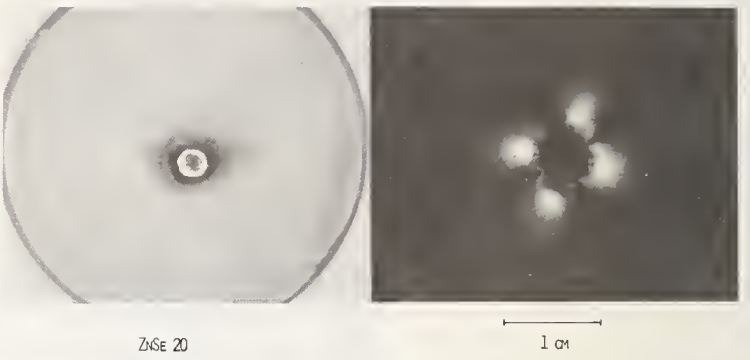

Figure 11. Damage crater in coated ZnSe sample, shown at the same magnification under normal illumination (left) and through crossed-polarizers (right).

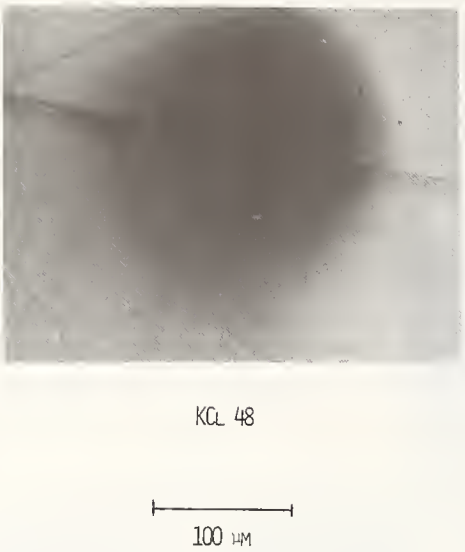

Figure 12. Micro-damage area on coated KCl sample.

Figure 13. Macro-damage on coated KCl sample.

NO COMMENTS ON PAPER BY LOOMIS

2.10 10.6 Micrometer CW Laser Damage Studies Of Metal Substrate Mirrors

T. T. Saito, G. B. Charlton, and J. S. Loomis

Laser Development Division
Air Force Weapons Laboratory
AFWL-LRE
Kirtland AFB, NM 87117

The CW damage properties of metal substrate mirrors were studied by focusing a 1 KW CW CO_2 laser onto the mirrors. Mirrors studies included polished and diamond machined bare metals, noble metal evaporated coatings, electroplated and then machined metals, and dielectric coated. Experimentally determined damage thresholds and damage statistics are discussed. Extensive efforts to characterize beam area of focused kilowatt beam is included. Evidence of a self-cleaning of mirrors by slowly raising laser power is described. Dust on mirrors reduces the damage threshold below 100 W/cm^2.

Key words: CW laser damage; diamond turned optics; dielectric enhanced metal mirrors; laser beam characterization; metal mirrors.

1. Introduction

We will describe our initial experiments studying the damage resistance of metal substrate mirrors illuminated by a focused 1 KW CO_2 laser. The experimental apparatus will be described. Theory of the propagation and focusing of a spherical-gaussian laser beam will be reviewed. Three techniques for measuring laser beam radius will be discussed including comparative results. An error analysis of the damage threshold will be given. Two very interesting results from our experiment are the evidence of self-cleaning by the laser and drastic effects of dust on reducing damage thresholds. Most samples were characterized by measuring the reflectivity/absorption, total integrated scatter, and examination by Nomarski microscope.

2. Experimental Apparatus

2.1 General

A single-mode Sylvania Model 971 CO_2 laser with maximum output power of about 1 KW was used for the damage experiment. A coincident He-Ne laser was used for alignment. A 25 cm focal length NaCl lens 330 cm from the laser was used to focus the beam onto the samples which were located 22.5 cm from the plano-convex lens. The convex side of the lens faced the laser in order to minimize aberrations. Two graphite blocks with 1.2 cm apertures were symmetrically spaced in front of and behind the lens in order to block the Fresnel reflections from the lens. The graphite blocks were 1.2 cm thick and spaced by 8.3 cm. A Coherent Radiation Model 213 power meter with a 5% (manufacturer's specification) accuracy was used to measure the incident power for each shot. The transmission of the lens aperture system was measured periodically and every time the laser was turned on or the laser was realigned. Eight measurements of the transmission at one given time yielded a result and standard deviation of 0.68 ± 0.02. The transmission measured throughout the series of experiments yielded an average and standard deviation of 0.68 ± 0.06. Contributions of the uncertainty of the transmission and power meter yield power readings uncertainty of 6% of the power measured.

2.2 Focusing of a Spherical Gaussian Beam

Let us now consider the propagation of a spherical-gaussian laser beam [1, 2][1] whose spatial dependence on the radial coordinate, r, of the intensity, I, is expressed in terms of the peak intensity, I_o, and the $1/e^2$ beam radius, w given in equation 1:

$$(1) \quad I = I_o e^{-2r^2/w^2}$$

The dependence of w on the propagation distance, z measured from the position of minimum waist radius, w_o, is given by:

1. Figures in brackets indicate the literature references at the end of this paper.

$$(2) \quad w = w_o \sqrt{1 + \left(\frac{\lambda Z}{\pi w_o^2} \right)^2}$$

For a lens of focal length f located a distance d from the waist minimum, the square of the beam radius can be expressed in terms of the distance from the lens, L, and the wavelength of light, λ, by

$$(3) \quad w^2 = \frac{\left(\frac{\lambda}{\pi}\right)\left(\frac{f - L}{f}\right)^2 \left(\frac{\pi w_o^2}{\lambda}\right)^2 + \left[d + L\,(1 - d/f)\right]^2}{\frac{\pi w_o^2}{\lambda f}\left[d + L\,(1 - d/f)\right] + (1 - L/f)\,(1 - d/f)\,(\pi w_o^2/\lambda)}$$

In general the smallest spot of a focused/laser beam does not occur at L = f. However in the case of our experiment equation 3 predicts the smallest spot occurs at 0.1 cm beyond the focal length. We measured the focal length of the lens using a method suggested by Spawr. [3] A razor blade was located on a translation stage so that it could be moved in the direction of propagation (along L) and also perpendicular to the direction of propagation. The L position of the blade was changed while observing the transmitted beam on an x-y detector array made by Laser Precision. The minimum spot size was defined as that L position where translating the razor blade into the beam attenuated both the x and y axis of the beam uniformly for the 971 laser operating at several hundred watts but chopped to transmit 1% of the power. Substracting the 0.1 cm theoretical difference of the distance to the minimum spot size yielded a focal length of 24.9 cm. This was in good agreement to the calculated focal length of 24.4 cm based on the measured radius of curvature and 10.6 μm index of refraction of 1.49 from the window materials compendium. [4].

2.3 Measurement of Beam Radius

Three methods were used to measure CO_2 laser beam sizes. One involved scanning an edge of a metal block (or sheet) through the beam and thereby progressively blocking the beam and reducing the power incident on a power meter head behind the scanning edge. The second method used a narrow slit which was scanned across the beam in the same fashion. The third technique scanned a wire across the beam, while monitoring the change in the wire's resistance caused by heating by the laser. Plotting resistance as a function of scan position of the wire yields a direct profile of the laser beam. This method was used to insure that the power profile of the model 941 Sylvania (3 watt) laser was gaussian. The 941 laser was used to validate the three methods of beam radius measurement. In the scanning edge measurement technique the edge was moved in discrete steps into the beam. The position along the scan direction (x) and power transmitted past the edge (P) were recorded. The incident power (or power transmitted with the block removed) (P_o) was also recorded. In order to take into consideration beam profiles which are not symmetric, such as those caused by aberration from a focusing mirror, we shall work with a bi-variate gaussian whose intensity distribution is

$$(4) \quad I = I_o \exp\left[-2\left(\frac{x^2}{w_x^2} + \frac{y^2}{w_y^2}\right)\right]$$

The ratio of P/Po is given by

$$(5) \quad P/P_o = 1 - \frac{1}{\sqrt{2\pi}} \int_{-\infty}^{Z_E} e^{-Z^2/2}\, dZ$$

where $Z_E = \frac{2x}{w_o}$.

P/Po is determined at each value of x and consequently the left side equation 5 is known. The table of the normal distribution function provides values for the integral on the right side of equation 5 and thus values of Z_E are determined. Then since

$$(6) \quad w_x = 2\,\frac{(x - x_o)}{Z_E}$$

(where x_o is the position of the intensity maximum).

$$(7) \quad x = \frac{wx}{2} \quad Z_E + x_o$$

A plot of x versus Z_E will yield a straight line whose slope is $w_x/2$. The procedure for acquiring data with the scanning slit is basically the same as for the scanning edge except that the incident power is not measured. For a narrow slit of width Δx the power through the slit Ps is given by

$$(8) \quad P_s = K \, e^{-2 \frac{(x-xo)^2}{w_x^2}} \Delta x$$

where K is a constant which depends on the integral in the y direction. The natural log of P_s is of the form

$$(9) \quad \ln P_s = a_2 x^2 + a_1 x + a_o$$

where $a_2 = \frac{-2}{w_x 2}$

Considerations of how narrow the slit width must be are given in the appendix. A plot of lnPs versus x yields a second order polynomial where the coefficient of the quadratic term is related to w_x. Figure 1 presents the results of scanning edge and scanning slit measurements on the Sylvania 941P CO_2 laser. The horizontal axis is the distance from the beam waist assumed to be at the inner surface of the output window. The waist size derived from the measured points is 0.164 cm. The waist size is produced from the measured points using a parabolic regression assuming the functional form of equation 2. The solid curve is the theoretical curve for a waist size of 0.16 cm. As can be seen from the figure there is a considerable discrepancy between the measured and theoretical profiles. Also, the waist size derived from the measured profile is smaller than the 0.19 cm predicted by laser cavity theory for this laser. The radius of curvature of the back mirror and cavity length were measured by us and found to be in agreement with the specifications. Consultations with the manufacturer did not resolve the discrepancy. In order to check the edge and slit technique we then utilized the scanning wire which was in good agreement with the edge and slit. A possible explanation for the smaller beam is that the inner diameter of the laser tube or some obstruction is aperturing the beam within the cavity. This would explain the smaller radius and possibly explain why the beam diverges more than predicted by equation 2 at distances greater than 100 cm.

Some comparisons between the techniques are appropriate. A detailed explanation of the techniques, and comparisons to burning plexiglass [5,6] will be given in a later publication. None of the techniques require an accurate power sensing device, only one that is linear over a decade of power. The scanning edge technique is the most flexible and yielded better statistical fits than the slit technique. The wire technique shows promise for very small beams. Tests of the upper level of power density for the wire and slit technique have not been completed.

A significant advantage of the scanning edge technique is that in-situ spot measurements can be made at the power density of this test. We found that a 1 cm thick milled aluminum block would serve well as an edge to be scanned across the beam of intensities greater than 200 KW/cm^2 for a 1 KW input. A razor blade burned in the focus. The beam size for this experiment was measured using the scanning edge technique at the same location (±0.2 cm) as the damage tests. Taking into consideration the statistical uncertainty (0.005) in determining w from the slope of x plotted versus Z_E and theoretical contributions of the uncertainty (±.005) of the distance L from the lens yields a spot radius w, of 0.042± .007 cm. The uncertainty in w due to uncertainty in L could have been reduced by performing the experiment at the minimum w of the focused beam.

2.3 Damage Threshold Uncertainties

Contributions of uncertainty in power (6%) and in area 24% yield an uncertainty of 25% of the power thresholds. Integrating equation 1 yields a relationship between the total power P_T, and peak intensity I_o

$$(10) \quad I_o = \frac{2 P_T}{\pi w^2} .$$

Damage threshold values are peak intensities given in KW/cm^2.

3. Procedure of Experiment

3.1 Illumination

Before each sample was mounted it was dusted using canned freon taking care to prevent the deposition of liquid freon on the mirror surface. The spot to be illuminated was identified by the coincident He-Ne laser. The first illumination was for 1 second at 25 KW/cm^2 in order to "clean" the sample. Then 1 second illuminations were made at various levels. As soon as the illumination was completed investigation with a 5X eye-loupe was made while slowly cutting off the He-Ne. This method is especially powerful for determining in-situ damage when the damage site scatters light. We were able to detect all damage spots in this way except for the case of copper and KCl. More than one illumination was made on the same mirror. If no damage was observed the last shot was at maximum power for 10 seconds. For the case of uncoated mirrors we observed no damage in-situ so we went from the cleaning shot to maximum power 10 second illuminations. On coated mirrors we tried to increase the intensity in 50 KW/cm^2 increments to obtain an estimate of damage threshold.

3.2 Definition of Damage

After the experiment was completed samples were examined with a Nomarski differential phase-contrast interference microscope. Typical magnification was 100x. Damage is defined as sites which are observable by microscope. Laser damage sites exhibit a characteristic chromaticity when viewed with a Nomarski. One problem with this method is the possibility of overlooking a damage site because they are so small. We found that some mirrors would have a spark of light during illumination but no damage was detected. [5, 6, 7]

4. Results

4.1 - Characterizations of Samples

Various characterizations of the mirrors were made. The reflectivity and/or absorption at 10.6μm were measured in the multiple-bounce reflectometer [8] or the absorption calorimeter [9]. Surface roughness for selected samples was measured using a Fringes of Equal Chromatic Order (FECO) interferometer and a Talystep profile-meter for mirror M-106. [10] Total-Integrated-Scatter (TIS) at He-Ne wavelength was also measured. The FECO and TIS instrument were built by Perkin-Elmer. [11]

4.2 Bare Metal Mirrors

Table 1 presents the results of our damage study. Identification of the mirror and substrate are given in the first column. In general the mirrors marked with an M are molybdenum substrate mirrors. The reflectivity or absorption are given in the second column, with the absorption given as 1-A and so indicated by an asterisk. The % TIS values are given in the third column. In the case where no damage was observed the damage threshold (expressed in KW/cm^2) are indicated as being greater than the maximum intensity of illumination. It is noteworthy that damage was not observed in molybdenum but was observed in copper. Pulsed (0.8 microsecond) laser studies have indicated that molybdenum has about a three times lower threshold than copper. [12, 13]

It is important to note that our experiments were done in the atmosphere, and it is possible that oxidation of the copper upon heating increases the absorption and thus results in laser damage. Stark and Reichelt, who performed their experiment in a nitrogen atmosphere, reported copper to have a higher damage threshold than gold. [7]

In this experiment, damage on the copper was not observable in-situ. Figure 2 presents a Nomarski photograph of a damage site. This damage is different than what is observed under pulse conditions. SEM studies indicated that near pulse threshold copper fails along grain boundaries. [13]

Table 1. Results of CW 10.6μm Damage Study

Mirror	R	%TIS	I_t (KW/cm^2)	Comments
BARE				
M114-Moly	0.98	3	>200	7805 Molybdenum
M115-Moly	0.981	0.2	>170	7805 Molybdenum
T-1-Cu	0.992	0.1	<210	OFHC; 37Å RMS Rough
T-3-Cu	0.991	0.4	<210	OFHC; 187Å RMS Rough; Cloth Polished
DIAMOND TURNED				
L^3-Cu	0.989	1	<220	64Å RMS Rough; Oxidized
Y-12-2(6")Cu	0.988*	0.2	<210	Electroplated Cu
L^3-Brass	0.984*	2	<200	137Å RMS Rough;Oxidized
L^3-Au	0.988*	0.6	>220	74Å RMS Rough; Brass Substrate
C4 Au on Cu	0.991	0.07	>220	46Å RMS Rough
C1 Ag on Cu	0.993	0.05	>210	
NOBLE METAL EVAPORATED				
C44-BeCu-Cu	0.9898*	1	>210	UHV+O.C. 21Å RMS Rough
			>210	Area with Fingerprint
T-32 TZM-Mo	0.9933*	0.05	>190	UHV Ag 23Å RMS
GBC-44 BeCu	0.993	0.9	>200	Badly Scratched
T-20FHC Cu	0.985	0.3	>210	Au; 50Å RMS Rough
T-4 OFHC Cu	0.984	0.3	220	Au; 200Å RMS Rough; Cloth Polish
SINGLE QUARTER WAVE DIELECTRIC				
M128 Cr/Ag/ThF_4	0.87*	0.9	140	Rs=0.991
M104 ThF_4	0.907*	6	>170	Rs=0.977
M164 KCl	0.9615*	20	200	Rs=0.982
M163 ZnS	0.837*		48	Gallard Schlessinger ZnS; Rs=0.982
M119 ZnS	0.963*		>210	Irtran 2; Rs=0.983
M161 AsS_3	0.902*	10	90	
DIELECTRIC STACKS				
M128	0.977*	1	>230	Rs=0.991; Cr/Ag (ThF_4/ZnSe)
M106	0.995	7	180	Rs=0.925; 123Å Tally; Cr/Ag(ThF_4/ZnSe)
OCLI	0.999*	0.5		See Text
5-22-73	0.998*	0.2	200	See Section 4.6 Ag (ThF_4/CdTe)^3 on Kanigen

*1-Absorption

4.3 Diamond Turned Optics

Diamond turning of optics can be defined as the use of a diamond tool on a precision lathe under very precisely controlled machine and environmental conditions to fabricate a finished optical component. [14] Damage values for machined copper are comparable to those of conventionally polished copper. Future studies may be able to differentiate between the two. Pulsed laser damage studies have shown diamond turned optics to be inferior to super-polished copper but this difference may be due to the machined copper being an early product of the diamond turning research program. [12] The gold and silver for these mirrors were first electroplated on the sample before the final cut was made. A damage site from machined electroplated copper (on a copper blank) is shown in figure 3.

4.4 Noble Metals - Evaporated

Only one sample in this series failed, the gold on copper. The mirror was made similar to T-3 and it is not surprising that damage occurred since the gold decreased the reflectivity of the bare copper. It is interesting that mirror T-2 did not fail. This indicates that the threshold is near 220 KW/cm^2 for gold coated copper. It is interesting that mirror C-44 did not fail even though there was a finger print in the tested area. GBC-44 was a badly scratched mirror and also survived the damage test.

4.5 Single Quarter-Wave Dielectric

The reflectivity of the uncoated substrate, R_s, is also given for this series in the comments column. The failure of M-128 is attributed to high absorption in the ThF_4. Both M104 and M128 exhibited high absorption. The TIS values for M-104 and M-128 indicates that M-128 has a superior surface finish. One may obtain better damage threshold for KCl in combination with other dielectrics to protect it from moisture. The test was made several days after the coating was made. Although efforts were made to minimize water absorption the coatings absorption degraded several percent from their optimum. The difference in the damage threshold of the ZnS is probably due to the differences in the absorption of the coating, which in turn may be related to the starting material. All substrates for this series were molybdenum. Figure 4 presents a Nomarski photograph of the damage site of ThF_4 and also the coating peeling off near the damage site. Figures 6 and 7 demonstrate the structure of KCl damage. Lack of a burned appearance may be a result of failure near threshold.

4.6 Dielectric Stacks

The performance of M-128 is very encouraging because it is the same mirror that failed with just a ThF_4 single layer. M-128 was masked and one-half of the mirror had an additional quarter wave stack of ZnSe which decreased the total absorption by 0.17 and probably explains why the coating survived. Decreasing the absorption of the ThF_4 may yield durable coatings using this combination. A possible explanation for the failure of M-106 is the exceptionally rough (123 Å RMS) surface. The value given for the reflectivity of the substrate is without the $Cr/Ag/ThF_4$ coatings. Earlier measurements yielded a reflectivity of 0.991 reflectivity for a Cr/Au coating on the same substrate. OCLI has developed a high reflectivity coating which is reproducibly greater than 0.998 in reflectivity. Unfortunately this sample was damaged in an earlier test because of dust on the surface. The damage site was large enough that we suspect contaminant from the damage may degrade the performance in this test. However, we found places which did not damage when illuminated with 200 KW/cm^2. Further test of this coating is planned.

4.7 Evidence of Self Cleaning by the Laser

We mentioned earlier that sparks from the surface were observed without any laser damage. We also noted that if the power was raised in 50 KW/cm^2 increments after the cleaning shot that 5-22-73 would survive 200 KW/cm^2. However, the coating failed when illuminated with 190 KW/cm^2 on the first shot in a new spot. Since it is difficult to differentiate between differences in damage threshold due to non-uniformities and method of illumination, further study of this phenomenon is warranted. Indications of self-cleaning by the laser was observed on other coated mirrors.

4.8 Effects of Dust

A $Cr/Ag/ThF_4$ coating on a molybdenum mirror was tested earlier to survive at 1 KW/cm^2 illumination for 20 seconds. The surface was then covered with dust by shaking a dust rag over it. Half of the mirror was cleaned and then was illuminated so that the dust line bisected the beam. Damage was observed on the dust half of the mirror at less than 100 W/cm^2. This was a drastic demonstration of the effect of dust in reducing the damage resistance of mirrors.

5. Conclusions and Summary

We have described a method to perform in-situ measurement of CW CO_2 laser beams with intensities greater than 200 KW/cm^2. This test has shown that copper exhibits a lower damage threshold than molybdenum in the CW case which is opposite the findings for the pulsed case. Silver and gold evaporated on metal substrates to yield a reflectivity greater than 0.99 should survive 200 KW/cm^2 illumination of small spots. Diamond turned optics compete well with conventionally polished optics. Not surprisingly coating absorption is the major factor influencing coating survivability. Dielectric stacks in this test survived illuminations greater than 175 KW/cm^2. Care must be taken in extrapolating the damage threshold values of these experiments to cases of the same intensity by larger beam illumination. We hope to perform theoretical analysis on the effect of beam size on damage threshold.

6. Acknowledgments

We gratefully acknowledge the advice, assistance and measurements of C. Huguley regarding spot size, contributions of L. B. Simmons and R. L. Lester, and the contribution of samples from J. Buckmelter, J. Staal, D. L. Witt, and J. Bryan.

7. Appendix
Effects of Slit Width on Accuracy of Scanning Slit Beam Measurement

In order to reduce scanning slit data, equation 8 was obtained by approximating the integral of the intensity to describe the power transmitted by a slit vertical in the x-y plane

$$(11)\qquad \int_{x-\Delta x/2}^{x+\Delta x/2} e^{\frac{-2(x-x_o)^2}{w^2}}\, dx \sim \Delta x \; e^{\frac{-2(x-x_o)^2}{w^2}}$$

where Δx is the width of the slit. We can estimate how narrow a slit is necessary in order to have a fraction error of ε by breaking the interval of the integral in half and consider an arbitrary x dependence of intensity, f (x)

$$(12)\qquad \int_{x-\Delta x/2}^{x} f(X)\, dX + \int_{x}^{+\Delta x/2} f(X)\, dX \sim f\left(x-\frac{\Delta x}{4}\right)+f\left(x+\frac{\Delta x}{4}\right) \quad \frac{\Delta x}{2}$$

The requirement that the fractional error be ε is expressed in terms of the difference of equation 12 and the generalized form of equation 11.

$$(13)\qquad \Delta x f(x) - \left[f\left(x-\frac{\Delta x}{4}\right) + f\left(x+\frac{\Delta x}{4}\right)\right] \quad \frac{\Delta x}{2} = \varepsilon f(x)\, \Delta x$$

Equation 13 can be simplified to read

$$(14)\qquad 1 - \frac{1}{2} \quad \frac{f\left(x-\frac{\Delta x}{4}\right) + f\left(x+\frac{\Delta x}{4}\right)}{f(x)} = \varepsilon$$

For a gaussian distribution, the maximum rate of change of the slope occurs at $x = x_o$. Therefore, the most stringent requirement on Δx is established by evaluating equation 14 at $x = x_o$. Setting $x_o = 0$ and using a series for the exponentials yields the relationship between the slit width and error.

$$(15)\qquad \frac{\Delta x^2}{8w^2} = \varepsilon$$

For the 3 watt model 971 laser, $w \geq 0.16$ cm and our 200μm slit width, the approximation of equation 11 creates an error less than 0.2%.

564-378 O - 74 - 9

8. References

[1] A. E. Siegman, An Introduction to Laser and Masers, McGraw-Hill, San Francisco, Calif., 1971.

[2] H. Kogelnik, Bell Tel Syst Tech J 44:455 (1965).

[3] W. J. Spawr, Private Communication, 1974.

[4] C. S. Sahagian, and C. A. Pitha, Compendium on High Power Infrared Laser Window Materials (LQ-10 Program), AFCRL-72-0170, Air Force Cambridge Research Laboratories, Bedford Mass., March 1972.

[5] V. Wang, A. Braunstein, M. Braunstein, J. E. Rudisill, and J. Y. Wada, Laser Induced Damage in Optical Materials: 1973, U. S. Department of Commerce 1973.

[6] J. S. Loomis and T. T. Saito, Third Conference on High Power Infrared Laser Window Materials November 12-14, 1973 Volume III: Surfaces, Coatings, Air Force Cambridge Research Labs, AFCRL-TR-74-0085 (III) 1974.

[7] E. E. Stark Jr. and W. H. Reichelt, Laser Induced Damage in Optical Materials: 1974, to be published.

[8] Wetzel, M. G., Saito, T. T., and Patterson, S. R., App Opt. 12:1558 (1973).

[9] Saito, T. T., L. B. Simmons, and A. B. Callender, "10.6μm Absorption Calorimeter for Metal-Substrate Mirrors," J. Opt. Soc. Am. 64:536 (1974) Presented to 1974 Optical Society Meeting.

[10] Saito, T. T., "10.6μm Absorption on Molybdenum Mirrors," to be presented to the AIAA/ASME Heat Transfer Conference, July 74.

[11] J. R. Kurdock, "Low Absorptance Metallic Coatings for Metallic Substrates," A. F. Weapons Lab Technical Report AFWL-TR-74-28, March 1974.

[12] M. J. Soileau, and V. Wang, to be published, App. Opt. 1974.

[13] T. T. Saito, W. J. Spawr, V. Wang, to be published, 1974.

[14] T. T. Saito, Microinch Machining of Optical Components for Infrared Optics AFWL-TR-73-290, A. F. Weapons Laboratory, Kirtland AFB, NM Feb 1974.

9. Figures

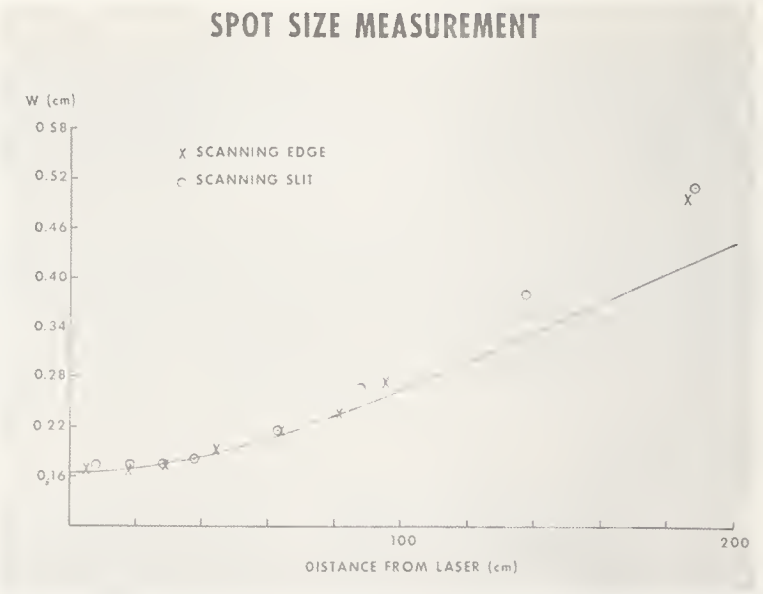

Figure 1. Measurement of spot size using the scanning edge and scanning slit technique versus distance from the laser. The solid line is the theoretical propagation of a spherical-gaussian laser beam with a minimum w of 0.164.

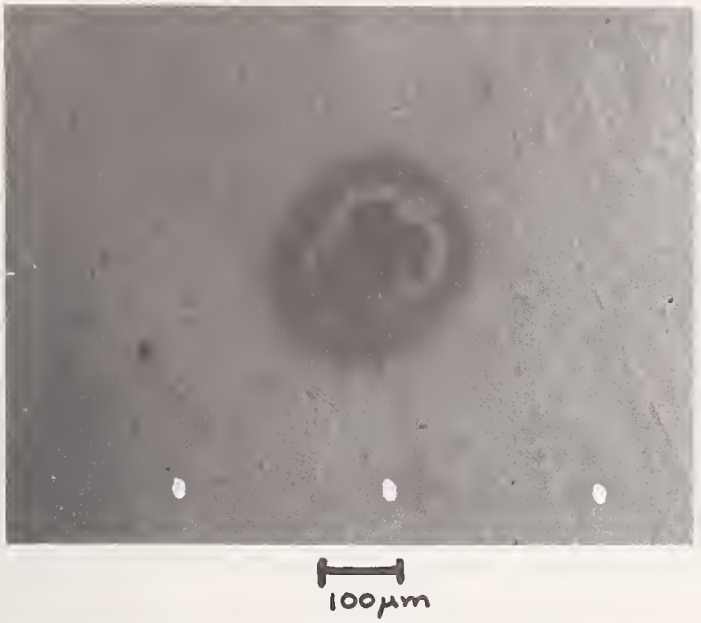

Figure 2. OFHC cloth polished copper with 187 Å roughness damaged at 210 KW/cm^2. Nomarski photograph at 100χ.

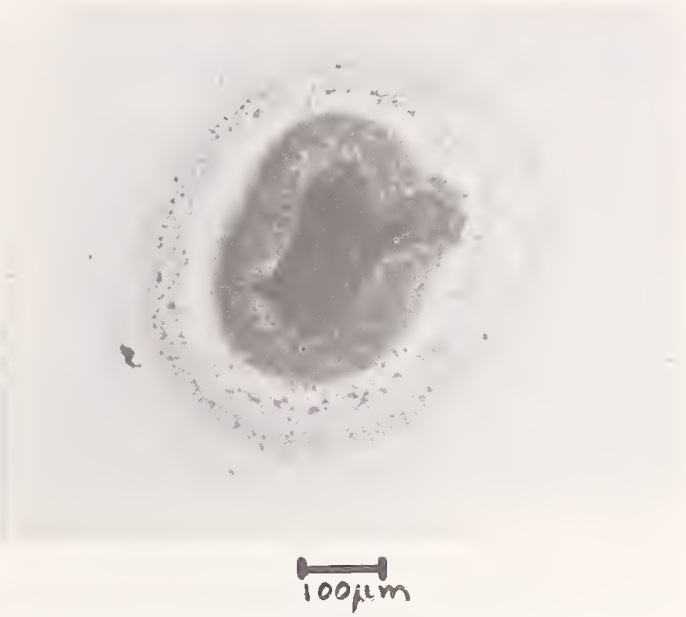

Figure 3. Electroplated copper then machined: Damage site of illumination at 210 KW/cm^2. Nomarski photograph at 100χ.

Figure 4. Molybdenum substrate mirror coated with Cr/Ag/ and λ/4 at 10.6 micrometer of ThF_4. Notice the coating peeling off near damage site created by laser. Nomarski photograph at 100χ.

Figure 5. Molybdenum substrate mirror with λ/4 at 10.6 micrometer of As_2S_3 illuminated at 90 KW/cm^2. Nomarski photograph at 100χ.

Figure 6. Molybdenum substrate mirror with λ/4 at 10.6 micrometer of KCl damaged at 200 KW/cm^2. Nomarski photograph at 100χ.

Figure 7. Molybdenum substrate mirror with λ/4 at 10.6 micrometer of KCl damaged at 200 KW/cm^2. Nomarski photograph at 475χ.

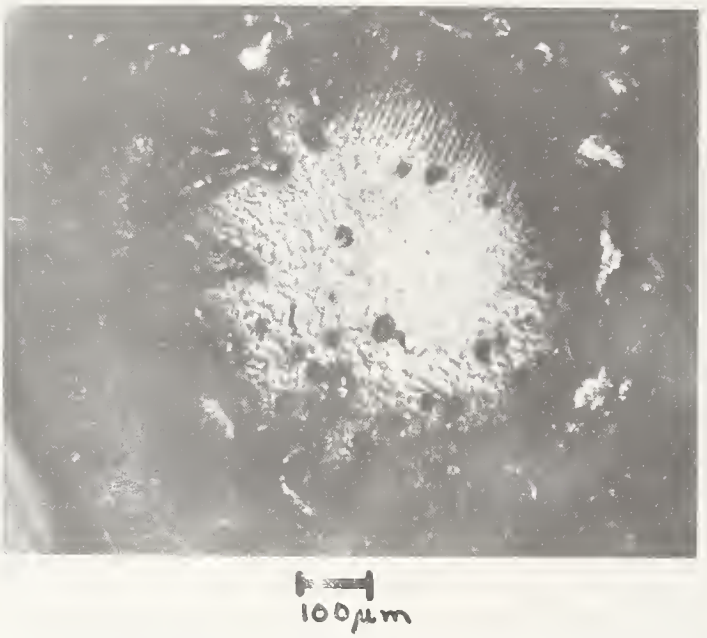

Figure 8. Ag and 3 pairs of ThF_4/CdTe on a kanigen substrate, center of damage area where the coating was not destroyed, probably because of non-uniformity of damage resistance observed. Nomarski photograph at 100χ.

COMMENTS ON PAPER BY SAITO

W. Spawr of Spawr Optical commented on the difficulty of identifying damage in post-mortem examination of surfaces which were initially of poor quality, i.e., in excess of 100 Angstroms rms roughness. On surfaces of high quality with roughness of the order of 30 Angstroms rms, however, small scratches, digs and damage-induced local variations stand out much more clearly. Thus, damage levels quoted for rough surfaces may actually be higher than the true threshold.

2.11 High Absorption Damage in Infrared Filters

W. S. Otaguro

McDonnell Douglas Astronautics Company
Huntington Beach, California 92647

The damage morphology, degradation of filter transmission, and thresholds for damage of infrared filters subjected to a hostile environment where the radiation incident on the filters includes high power densities in a wavelength region of high absorption have been examined. Infrared filters cooled to 10 Kelvin exhibited damage thresholds at 5 megawatts per square centimeter when illuminated with a Q-switched ruby laser. A thermodynamic model based on intrinsic absorption of the material composing the multilayer coatings is compared to the measured damage thresholds.

Key words: High absorption damage; infrared filters; laser-induced damage.

1. Introduction

Optical filters are used to pass radiation in a prescribed wavelength band and reject radiation outside of this passband. The optical absorption properties of materials are used to achieve the desired out of band rejection. Normally, the radiant energy being absorbed by these filters is relatively low, and the performance of the filters is not seriously degraded by heating due to absorption. However, in the application of various radiation sensor systems, the amount of radiant power density outside of the passband of the infrared filters may be as high as 5 megawatts per square centimeter. Under these "hostile" conditions, the high absorption of radiation by optical filters outside of their passband may result in serious degradation in the transmission properties of these filters.

The damage threshold for an infrared filter composed of multilayers of germanium and zinc sulfide was determined by irradiation with a Q-switched ruby laser. A thermodynamic model based on intrinsic absorption of the material composing the multilayer dielectric coating is compared to the measured damaged thresholds.

2. Infrared Filters

The commercial infrared filters obtained for these tests are composed of multilayers of low (zinc sulfide) and high (germanium) index materials. The index of refraction of zinc sulfide is 2.84 and the index of refraction of germanium is 4.0. The surface layer is zinc sulfide. X-ray fluorescence analysis indicates traces of aluminum, tungsten, iron and chromium in the multilayer coatings. Also, an ambiguous peak which could be due to traces of phosphorus, platinum, gold and/or zirconium was detected. The surface of the infrared filters has small mounds 1 to 7 microns in diameter. The multilayers ranged in thickness from 0.65 to 2.4 microns. The substrate material is germanium. The passband of the filters is from 8 to 14 micrometers.

3. Experimental Apparatus

The experimental arrangement is shown in figure 1. The Q-switched ruby laser produced a TEM_{oo} mode with a 20 nanosecond pulse width. The pulse was monitored by a biplanar photodiode. The spatial uniformity of the laser pulse was recorded on polaroid film. A helium-neon alignment laser was used to define the beam path of the ruby laser. The infrared filters, cooled to 10 Kelvin in a helium dewar, were irradiated with the unfocused ruby output. The laser beam entered the dewar through a potassium chloride window.

The transmission of the infrared filter was measured with a modified Perkin Elmer Model 621 Spectrophotometer. The modification involved the addition of a chopper between the spectrophotometer source and the infrared filter. This modification prevented the detector from seeing the emitted energy of the infrared filter as a signal and allowed the measurement of the infrared transmission spectra of the filters at cryogenic temperatures.

4. Test Procedure

The damage threshold for the infrared filters was defined as the irradiation level of the ruby laser where the transmission in the passband of the filter changed by 4%. The 4% transmission change was selected because the spectrophotometer had a ± 1% measurement precision.

The transmission of the filter was measured in the dewar at ambient conditions and then at 10 Kelvin. After being irradiated by the ruby laser, the transmission of the filter was measured. The process was repeated until damage occurred.

5. Results

The infrared filters exhibited damage thresholds due to the Q-switched ruby laser at power densities of 5 megawatts per square centimeter. The irregular removal of several layers of the coating material accompanied the reduction of the filter transmission.

A portion of the filter not radiated by the laser is shown in figure 2. The mounds range from 1 to 7 microns in diameter. Debris from the damaged areas in the form of white flakes was deposited in the undamaged area.

In figure 3 the filter transmission after an incident pulse of power density 7.2 megawatts per square centimeter is shown. Although the filter transmission was reduced, the overall bandpass structure is unchanged. The damage morphology of this filter is shown in figure 4. The damage seems fairly uniform with a rather clean demarcation between the regions of material removal and those of no damage. The color of the damaged area is gray-white in contrast to the black metallic luster of the undamaged areas. Even in regions where a high density of pits was produced, small, undamaged portions of the filter surface remained.

A highly magnified view of the damage morphology is shown in figure 5. The damage is evidenced by the removal of the top zinc sulfide and germanium layers and the heating of the layers below them. The breaks are sharp indicating the clean, perhaps explosive, removal of the surface layers. The morphology of the areas within the pitted regions exhibits a structure similar to the material formation produced by intense heating to boiling, followed by rapid cooling. The dark spots are areas where the local heating was intense. Zinc sulfide has recrystallized near the edge of the pits. Flakes of zinc sulfide are also present. The depth of the damage in figure 5 is 1 to 2 microns. An edge view of the damage area indicates that the surface damage and layer delamination does not extend more than 4 layers into the filter coating. Transparent fragments of the filter material, probably the zinc sulfide top layer were found deposited on the front window through which the laser beam entered the dewar.

The infrared transmission of the filter decreased anywhere from 10% to 40% depending on the severity of the damage.

6. Analysis

According to the Beer Law the intensity of light transmitted through a material, I, is given by:

$$I = I_o e^{-\alpha d} \qquad (1)$$

where

I_o = incident intensity

α = absorption coefficient, cm^{-1}

d = path length, cm

For germanium at $\lambda = 6943\text{Å}$ and 77 Kelvin, the absorption coefficient is equal to 5×10^4 cm^{-1}.

Therefore:

$$\frac{I}{I_o} = e^{-\alpha\lambda/4n} = 0.036$$

Approximately, ninety-six percent of the laser energy incident on the germanium layer will be absorbed by this layer. For an extinction coefficient of 0.069, and an index of 4, the amount of radiation transmitted into the first germanium layer through one layer of zinc sulfide is 82%. The total energy absorbed by the first germanium layer is approximately 0.79 I_o (π r^2) where I_o represents the incident energy density and r is the radius of the laser beam. The surface layer of zinc sulfide is assumed to affect only the amount of radiant energy incident on the first germanium layer.

A classical thermodynamic formalism is used to calculate the damage thresholds. [1][1] The laser photons are absorbed by interaction with electrons where the electrons in the valence band are excited to the conduction band. The excited electrons in the conduction band impart energy to the lattice by collisions with phonons which result in the heating of the material. During the pulse duration, 2×10^{-8} seconds, the excited electrons will collide among themselves and deliver this energy to the lattice phonons. The energy deposited by the laser pulse in the multilayer coatings may be considered as being turned instantaneously into heat in the area where the laser pulse is incident. Under these conditions, the usual equations for heat flow are applicable. [1, 2]

$$\nabla^2 T\,(x, y, z, t) - (1/k)\,\frac{\partial T\,(x, y, z, t)}{\partial t} = \frac{-P\,(x, y, z, t)}{K} \qquad (2)$$

where T = temperature
t = time
k = thermal diffusivity
P = heat production per unit volume per unit time
K = thermal conductivity

The solution to this differential equation is complicated by the temperature and hence, the time dependence of the thermal diffusivity, k, and the thermal conductivity, K. However, in order to obtain a solution to eq. (2), k and K will be assumed to be constant. The effect of their variation on the solution will then be evaluated. The solution to eq. (2) for $\alpha = 5 \times 10^{-4}$ cm^{-1} and for a laser pulse flat in time and uniform in the x-y plane is given by: [1, 2]

$$T\,(z, t) = [2\,F_o\,(kt)^{1/2}/K] \quad \text{ierfc}\,[z/2\,(kt)^{1/2}] \qquad (3)$$

For z = 0:

$$T\,(0, t) = (2\,F_o/K)\,(kt/\pi)^{1/2} \qquad (4)$$

The results of eq. (4) are shown in Table 1.

Table 1. Surface temperature of a germanium layer with $F_o = 5 \times 10^6$ watts/cm^2 and $t = 20 \times 10^{-9}$ seconds. The values of k and K are for T_o.

T_o (°K)	T (°K)
20	975
100	585
200	710
800	1275
1000	1295

The irradiated germanium layer will reach the temperatures given in a time, $\tau = d^2/4k$ where d is equal to the thickness of the germanium layer. Accounting for the variation in k, the largest τ is of the same magnitude as the pulse duration.

1. Figures in brackets indicate the literature references at the end of this paper.

7. Discussion

The damage structure indicates intense heating of the multilayer coatings. The analysis shows that a 5 megawatt per square centimeter pulse can heat the germanium layer uniformly within the pulse duration to a temperature range where germanium will melt (1209 Kelvin) and the zinc sulfide layers will sublime (1401 Kelvin).

The heating of the first germanium layer and the subsequent sublimation of the zinc sulfide layers above and below the first germanium layer accounts for the observed damage morphology. The blow off of the first germanium layer due to pressure produced by the sublimation of the zinc sulfide layer below it created the surface pitting. The irregular structure within the pits is due to the sublimation of the zinc sulfide coating during the presence of the laser pulse followed by the rapid cooling due to the 10 Kelvin environment after the laser pulse had terminated. It is unlikely that the 5 megawatts per square centimeter laser pulse would be able to vaporize the germanium. Since the damage was confined to the top four layers of the coating, the overall filter transmission shape was not altered except for the reduction of the filter transmission due to scattering and reflection losses resulting from the surface damage.

Although the damage as seen in figure 4 appears to be uniform, figure 5 reveals that the damage structure is made up of many micro-pits. The exact absorption mechanism in materials of such high absorption is quite complex. However, it is the creation of a suitable electron density which will stimulate absorption. [3, 4] The presence of material inhomogeneities in the form of defects, particulate inclusions and impurities will aid the electron growth once the initial electrons are excited from the valence to the conduction band by the laser photons. The presence of metals detected in the coatings and the hot spots in figure 5 indicate that the pitted nature of the damage is probably due to the enhancement of the electron density around these regions of inhomogenieties.

8. Acknowledgement

The many helpful suggestions of Dr. Isaac Richman during the course of this investigation are gratefully acknowledged.

9. References

[1] Ready, J. F., "Effects of High Power Laser Radiation," Academic Press, New York, 1971.

[2] Carslaw, H. S. and Jaeger, J. C., "Conduction of Heat in Solids," 2nd ed., Chap 2 Oxford Univ. Press, London and New York, 1959.

[3] Hellworth, R. W., Proc. 2nd ASTM Symp. Damage in Laser Mat'ls., NBC Spec. Pub. 341, 67 (1970).

[4] Bliss, E. S., Proc. 2nd ASTM Symp. Damage in Laser Mat'ls., NBC Spec. Pub. 341, 105 (1970); also Optoelectronics 3 99 (1971).

10. Figures

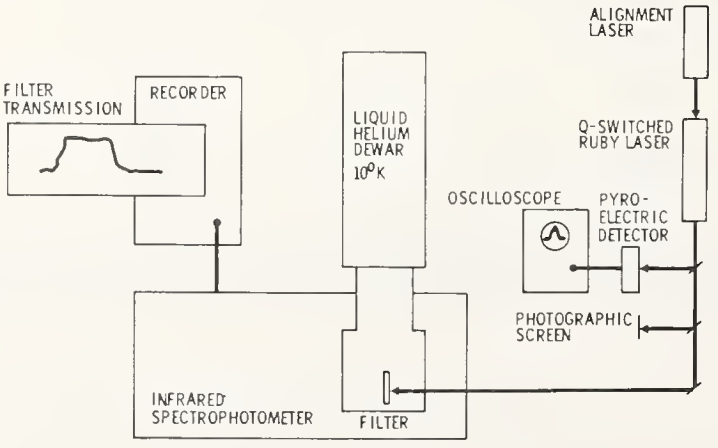

Figure 1. Experimental arrangement.

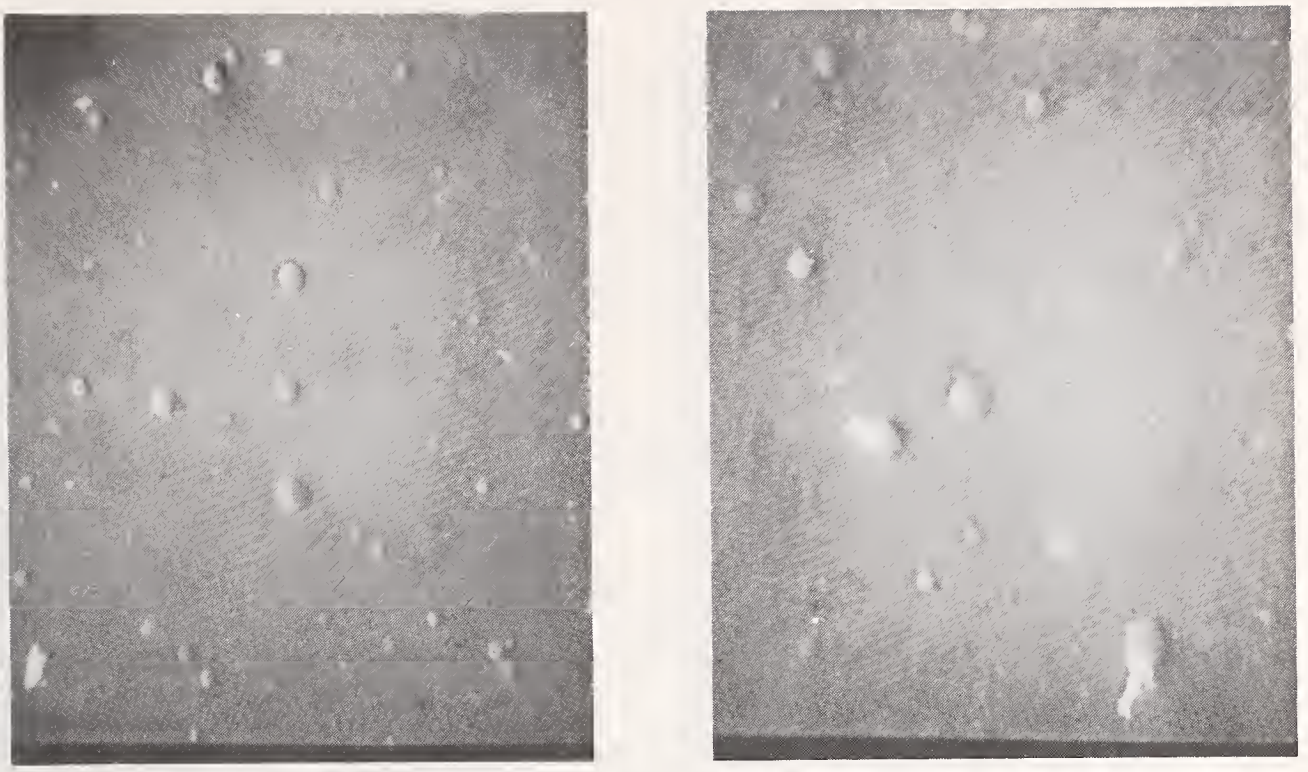

Figure 2. Portion of infrared filter not irradiated by ruby laser. The figure on the left is 164 microns wide. The figure on the right is 82 microns wide. The mounds range in diameter from 1 to 7 microns. The white flakes are debris from damage areas.

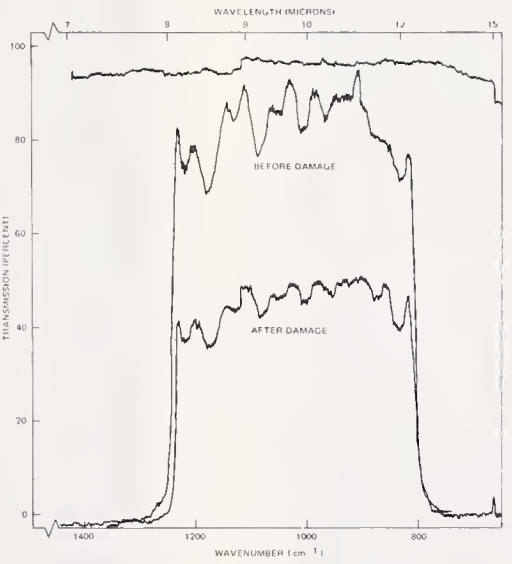

Figure 3. Transmission of infrared filter before and after damage due to 7.2 megawatts per square centimeter output from a ruby laser.

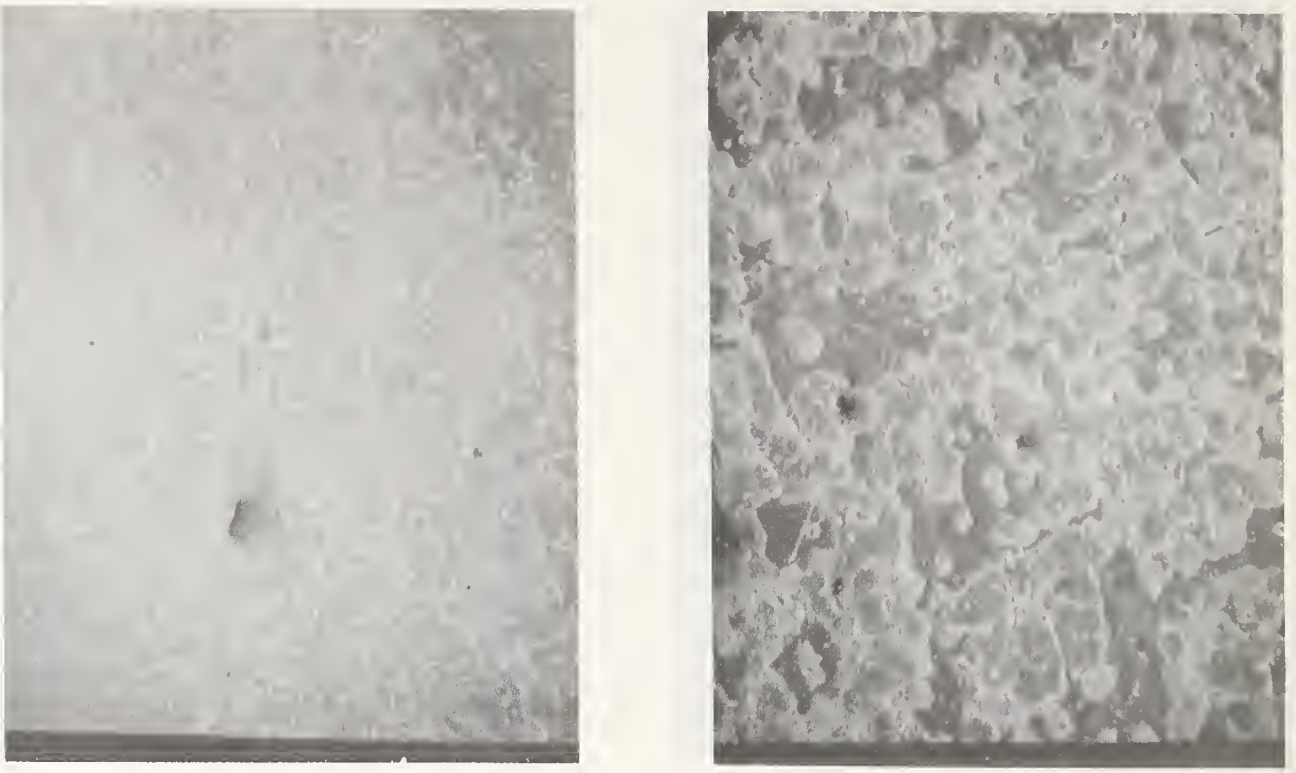

Figure 4. Surface morphology of infrared filter irradiated with 7.2 megawatts per square centimeter ruby laser output. The figure on left is 4.3 mm wide. The figure on right is 820 microns wide.

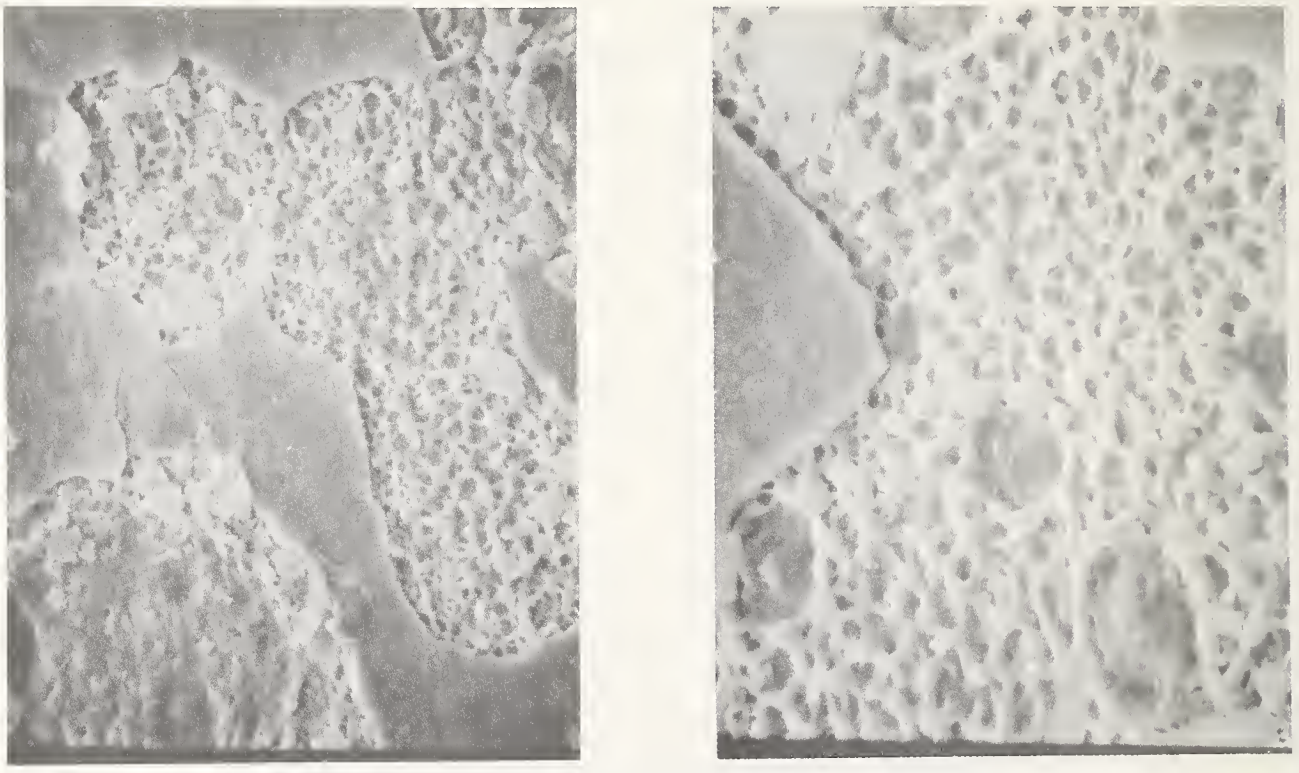

Figure 5. Higher magnification of damage areas irradiated by 7.2 megawatts per square centimeter ruby laser output. The figure on left is 82 microns wide. The figure on the right is 41 microns wide.

NO COMMENTS ON PAPER BY OTAGURO.

3.1 Q-Switched Laser Induced Surface Damage at 1.06 Microns*

N. L. Boling, J. A. Ringlien and G. Dubé

Owens-Illinois, Inc.
1700 North Westwood Avenue
Toledo, Ohio 43666

Our studies of the effect of ''superpolishing'' on the surface damage threshold indicate that such polishing does not increase the practical threshold on ED-2 laser glass. Impurities introduced in the polishing process often outweigh any advantages that might be gained in longer polishing to reduce geometrical defects.

On commercially available, ''conventionally'' polished laser glass, the surface threshold is about 150 J/cm^2 (5 GW/cm^2). This is at least an order of magnitude below the intrinsic bulk threshold. Some problems encountered in using small beams to measure the surface-to-bulk ratio are discussed.

The effect of treating ED-2 laser glass with boiling nitric acid is also briefly described. This treatment can permanently raise the threshold by as much as a factor of three, while leaving the surface in good optical condition. The efficacy of the treatment is highly dependent on the polishing history of the sample.

Key words: Electron avalanche; laser; laser induced damage.

1. Introduction

In this paper we explore the following three questions concerning 1.06 μm Q-switched damage to laser glasses:

1) What is the ratio of the practical damage threshold on ''conventionally'' polished surfaces to the bulk breakdown threshold?

2) Does ''superpolishing'' of laser glass lead to higher damage thresholds?

3) If the answer to 2 is no, what approach should be taken to achieve higher surface thresholds?

We use the terms ''conventionally polished'' and ''superpolished'' very loosely. By ''superpolishing,'' we generally refer to a ''bowl-feed'' process that, if done carefully, leads to a surface with fewer and smaller scratches and a low rms roughness value. However, the effect of the polishing process on the surface depends on many factors. Among these are the type and size of the grinding materials used, the composition of the polishing compound, the type of lap, the pressure used on the sample, the polishing time, the amount of water used on the lap, etc. Seemingly insignificant changes in any one of these can lead to large changes in the modified surface layer created by polishing (see [1][1], for example). Because of this complexity, we stress that the terms ''super'' and ''conventional'' are not sufficient to describe polishing. We use them only because they have been used to describe the results of other damage studies.

---

* This work was supported by the Advanced Research Projects Agency under Contract DAHC 15-72-C-0170.

1. Figures in brackets indicate the literature references at the end of this paper.

2. Surface Threshold vs. Bulk Threshold on Conventional Surfaces

To address the question of bulk vs. surface threshold and to provide reference material for question 2 above, we refer to the work of Olness and Swain [2,3]. They investigated the effect of hydrofluoric acid etching on the entrance surface threshold of three commercial laser glasses. A 5 ns, TEM_{00} pulse from a glass laser was used in the studies. The glasses as they were received from the manufacturer exhibited thresholds of 35 J/cm^2 (7 GW/cm^2). We have made measurements at 4 ns at Owens-Illinois that agree well with these values. Upon etching in HF acid and glycerin for approximately two hours, the threshold increased by a factor of two to three, a significant increase. But when they refinished the samples using barnesite and a pitch lap, the result was even more dramatic. The threshold increased more than an order of magnitude, going as high as 380 J/cm^2 (76 GW/cm^2).

Since these measurements refer to the entrance surface and since the electric vector on the entrance has the same magnitude as in the bulk, these values can be used to indicate a minimum value of the bulk threshold. That is, since Olness and Swain saw no internal damage [4], we can conclude that the bulk threshold was at least an order of magnitude higher than the conventional surface threshold.

We have found further evidence for this in other work. Feldman has measured a minimum intrinsic bulk threshold of 50-60 GW/cm^2 at 25 ns for laser glasses [5]. At Owens-Illinois, we have regularly been obtaining entrance thresholds of 4 to 6 GW/cm^2 (30 ns), again at least an order of magnitude below the minimum bulk threshold.

On the other hand, recent measurements have been made of the ratio of bulk to surface breakdown levels using the same test setup for both measurements [6]. In these measurements, a small beam ($\approx$ 20 μm) was focused first inside the sample and then on the surface. The probability of breakdown [7] in these two positions was measured. For conventionally polished BSC glass, a bulk-to-surface ratio of only 1.7 was obtained. Thus, there is a rather wide discrepancy among reported bulk-to-surface ratios. To resolve this discrepancy is important, since one would like to know the maximum improvement that can be expected in surface thresholds.

One reason for the discrepancy could be that in the work of [6] shots on which it was judged inclusions were struck were not counted, nor were the levels at which these inclusions damaged reported. That is, only shots on which it was judged that intrinsic damage had occurred were counted. This could lead to the high reported values for surface breakdown (34 GW/cm^2 or $\approx$ 400 J/cm^2 at 12 ns).

Another reason for the discrepancy could lie in the subtleties involved in using very small beams for damage studies. as was done in . [7] If we accept as a premise the idea that, for small enough beams, there is no sharp damage threshold, but rather only a probability for damage at given energy density, it is profitable to analyze an experiment that compares the probability of bulk breakdown to surface breakdown. In such an experiment damage is due to at least one free electron gaining enough energy to begin an avalanche.

Consider figure 1. The laser beam is focused through a microscope lens of focal length f to a spot of diameter d on a sample surface that has no inclusions and is perfectly uniform. Let's suppose in this ideal experiment that the beam profile is square and not Gaussian as in most real experiments. That is, it is possible to associate unambiguously an energy density to any shot that causes damage. In this way we can ascertain the electric field "seen" by the electron that starts an avalanche. One proceeds to hit the sample with a large number of shots at a constant energy level, counts the number of these that cause damage, and then determines the probability $P_S(E)$ of damage at that energy level. Now suppose d is doubled while maintaining the energy density constant, and the experiment is repeated in a second series of shots. It is obvious that if the beam is small enough to see statistics, the probability for damage will be greater in the second series. The reason for this, of course, is that the probability of damage depends on the initial number of free electrons available to initiate damage in the irradiated volume.

The point of this argument is that, for a beam small enough to see statistics on a uniform surface, the parameter of practical interest is not the probability of damage at a given energy level, which is system-dependent, but rather the probability of damage per unit area of surface irradiated. In fact, even this is over simplifying things. The breakdown occurs not at an idealistic two-dimensional surface, but in a surface layer of probably a few hundred angstroms depth. (We consider this depth to be roughly that of the modified surface layer left by the polishing process. It is in this layer that one expects higher free electron densities due to stresses, impurities, etc.) Thus, one should really consider the probability of damage per unit surface volume.

Let us imagine next that the beam is now focused inside the sample to measure the probability of bulk breakdown $P_B(E)$, as in figure 2. Again, it is obvious that the number of free electrons in the focal volume V_B is system-dependent, and therefore that $P_B(E)$ is system-dependent.

If we consider the ratio $P_B(E)/P_S(E)$, it might appear that the system-dependence cancels. That this is not the case can be seen by considering that the ratio V_B/V_S (in figures 1 and 2) changes as the focal length of the lens changes. That is, V_B is roughly proportional to f^3, while $V_S \propto f^2$.

Thus, the ideas of electron avalanche and damage probability lead us to conclude that the ratio of bulk-to-surface breakdown levels cannot be measured with very small beams. However, one might make the seemingly obvious argument that if the sample surface is placed in the middle of the beam waist, as in figure 3, and the bulk is seen to damage before the surface, then surely the surface breakdown level is at least that of the bulk. After all, the beam has to pass through the surface to get to the bulk! Again, this argument is wrong if one accepts the idea of damage probability. This can be seen by considering again that V_B/V_S (figure 3) changes with f. If f is doubled. for example, the number of free electrons in the surface volume is quadrupled, while the number of free electrons in the half of the focal volume in the bulk goes up by about a factor of nine, and therefore $P_B(E)/P_S(E)$ is not constant.

We have gone on at some length with this analysis of small beam results in an attempt to resolve the discrepancy in reported ratios of bulk-to-surface breakdown. On the basis of this analysis and reported large beam results, we conclude that on conventionally polished laser glass. which exhibits entrance thresholds of 4-6 GW/cm^2 at 30 ns, the surface threshold is at least an order of magnitude below the bulk threshold.

3. The Effect of Scratches on the Practical Damage Threshold

The observation that the electric field of a laser beam incident on a surface is enhanced at scratches and digs has led Bloembergen [8] to conclude that scratches and digs lead to a lower damage threshold. This lowering of the threshold by defects would take place whether damage was due to either avalanche or inclusions. However, because small enough inclusions do not damage, and because free electrons can diffuse out of the high electric field regions around small enough scratches before an avalanche can build up, it was theorized [8] that scratches smaller than about 100 Å should not lower the threshold. Recent experimental work on the comparison of intrinsic bulk breakdown to intrinsic breakdown of superpolished surfaces has seemed to support this theory [6]. In fact, the work of [6] implies that glass surfaces do not have to be polished very carefully to raise the intrinsic surface threshold to that of the bulk. (Again, inclusion damage was excluded in the data.) BSC glass with scratches as large as 2000 Å was found to have an intrinsic surface threshold of about that of the bulk. (We note that the analysis of Section 2 causes us to question the surface-to-bulk ratio obtained in small beam experiments. However, such experiments, if the geometry is maintained, should reflect changes in the surface-to-bulk ratio from sample to sample.)

The work of Olness and Swain [2,3] on HF etched laser glass is pertinent in evaluating the roles of surface imperfections in damage. After deep etching of the commercial laser glasses they tested, which could have been expected to exhibit occasional scratches of a few thousand angstroms, the surfaces were left in extremely rough condition. Defects as large as 3 to 4 microns can be seen in the optical micrographs. [3]. In this case, then, the change has been from a fairly smooth surface to a very rough one, and yet the damage threshold has increased by an order of magnitude. This suggests two points. First, increasing the surface geometrical defects does not necessarily decrease the damage threshold. Second, surface impurities play the major role in determining the damage threshold.

We have measured the damage threshold of several samples that have been bowl-feed polished. Figures 4 and 5 juxtapose two surfaces on ED-2 laser glass. Both have been polished in the same manner, except that the one in figure 4 was polished longer in an attempt to further remove scratches. This surface did in fact present a slightly better appearance when viewed in its entirety. Yet the damage threshold in this longer polished surface was only 45 J/cm^2 (1.5 GW/cm^2), while the threshold of the other surface was 90 J/cm^2. These two surfaces, however, were polished with jewelers rouge, which is known to cause low damage thresholds at 1.06 μm. Initial damage is always due to inclusions on rouge-polished surfaces. But two points again can be made from these data. First, a longer polishing to get rid of scratches can lead to a much lower threshold. Second, the polishing history, aside from geometrical defects, is of prime importance in damage.

Figures 6 and 7 show two fused quartz surfaces polished in the same manner by conventional techniques. The surface in figure 7 has been subjected to an acid treatment, leaving pits of about 1000 Å. The thresholds for figures 6 and 7 were respectively 310 and 360 J/cm^2, about the same within the accuracy of the measurements.

Still another set of comparison surfaces is shown in figures 8 and 9. In figure 8 is an ED-2 surface conventionally polished with barnesite. Defects as large as 1000 Å can be seen. In figure 9 is a very good bowl-feed polished ED-2 surface. No scratches larger than 100 Å can be seen. The damage thresholds of the two surfaces were the same, 150 J/cm^2 (5 GW/cm^2).

In those cases we have described and in others we cannot discuss here, we have been unable to find an example of an increase in threshold by decreasing the geometrical surface defects. In fact, the opposite has sometimes been the case. What can we infer from this? There can be no doubt that the field is enhanced at these defects, although as pointed out by Bloembergen [8], the degree of enhancement can only be estimated. Given that all other conditions are equal, it seems that a badly scratched surface must damage before a smooth one. This might be the case. The key would seem to be in getting all other things equal. In the examples we have discussed, the surfaces compared were always different in ways besides the size of scratches by virtue of having been etched or not, or polished for different times. etc.

There are, however, also theoretically plausible reasons why some defects are not important. Perhaps electron diffusion out of the highly localized high field region around the scratches is faster than has been estimated. One can also make the argument that a single 1000 Å spherical pit, for example, would probably not be the first region to damage, simply because the probability of finding a free electron in the approximately 10^{-15} cm^3 high field region around it is very small. An extension of this argument is that the density of defects on a surface should be considered if avalanche is to be considered the breakdown mechanism.

Whatever the case, there are two points that are clear from these experiments:

1) Surface impurities are in practice often more important than scratches and digs in lowering the threshold.

2) ''Superpolishing'' is not a panacea for raising the surface threshold, and sometimes, because of the greater introduction of impurities, it can even be detrimental.

4. Raising the Surface Damage Threshold by Acid Treatment

Since we have concluded that polishing deposited impurities are of prime importance in the damaging process, it seems reasonable to investigate ways to remove these impurities. We have been studying various acid treatments of ED-2 laser glass to this end. Acid treatments to raise the damage threshold are, of course, nothing new. Several workers have tried various acids. Swain [3] used HF to achieve large, permanent increases in the threshold, but this acid attacks the silicate structure of the glass leaving the surface in an optically unacceptable condition. Others, including ourselves, have tried various other acids at room temperature with no effect or only a temporary effect on the threshold.

Recently, we have been using boiling 0.4 N nitric acid on glass surfaces. The damage threshold of ED-2 laser glass can be changed greatly by this treatment, going from 150 J/cm^2 (5 GW/cm^2) to as high as 470 J/cm^2. We have subjected samples to this acid treatment, damage tested them almost two months later, and found the same high threshold. Furthermore, the nitric acid does not attack the silicate structure of the glass, so the surface is left in good optical condition.

The key to the success of this process lies in the high temperature of the acid. We have evidence that diffusion plays an important role, and diffusion coefficients in glass can change as much as three or four orders of magnitude as the temperature goes from 25°C to 100°C. This perhaps explains the negative results obtained by us and others when room-temperature acid treatments were used.

The effectiveness of the boiling nitric acid treatment is highly dependent on the polishing history of the sample. We have worked with several sets of ED-2 samples that have been polished either by different compounds or in different polishing shops. The increase in threshold after the acid bath has ranged from 0 to the factor of three discussed above. But the effect is repeatable within a given set of samples that have all been polished in the same manner. Again, we are seeing the importance of details of the polishing process.

Since we suspect that diffusion plays a dominant role in the acid treatment, an increase in the bath temperature might render the effectiveness of the treatment less sensitive to polishing details. Therefore, rather than monitor very closely the polishing process in an attempt to find out what is responsible for the differences in threshold, our next step will probably be to work at higher temperatures.

5. Conclusions

The surface damage threshold on commercially obtained laser glass is about 150 J/cm^2 at 30 ns. This is at least an order of magnitude below the bulk threshold. Results obtained by using very small beams to measure this bulk-to-surface ratio are questionable.

So-called superpolishing of laser glass is not a panacea for raising the threshold. and can even be detrimental. Impurities introduced by the polishing process are the major cause of damage at 30 ns, whether it be from inclusions or electron avalanche. Hot acid treatment of laser glass can be very effective in increasing the damage threshold by removing these impurities and/or modifying the surface layer. By paying close attention to polishing and surface treatment, we have seen the entrance threshold vary between 45 J/cm^2 (on rouge-polished ED-2) and almost 500 J/cm^2 (on acid-treated ED-2).

6. Acknowledgement

We wish to express our appreciation to W. Barnes of Itek Corp. for supplying the bowl-feed Cerox polished ED-2 sample.

7. References

[1] Bennett, J. M. and King, R. J., Applied Optics 9, 236 (1970).

[2] Olness, D., J. Applied Physics 39, 6 (1968).

[3] Swain, J., ASTM Damage Symposium, 1969, Boulder, Colo., ASTM STP 469, Ed. A. Glass and A. Guenther.

[4] Personal communication with J. Swain, Lawrence Livermore Laboratories, Livermore, Calif.

[5] Personal communication with A. Feldman, NBS, Gaithersburg, Md.

[6] Fradin, D. W. and Bass, M., Appl. Phys. Letters 22, 157 (1973).

[7] Bass, M. and Barrett, H. H., IEEE J. Quantum Electron. QE-8, 338 (1972).

[8] Bloembergen, N., Applied Optics 12, 661 (1973).

8. Figures

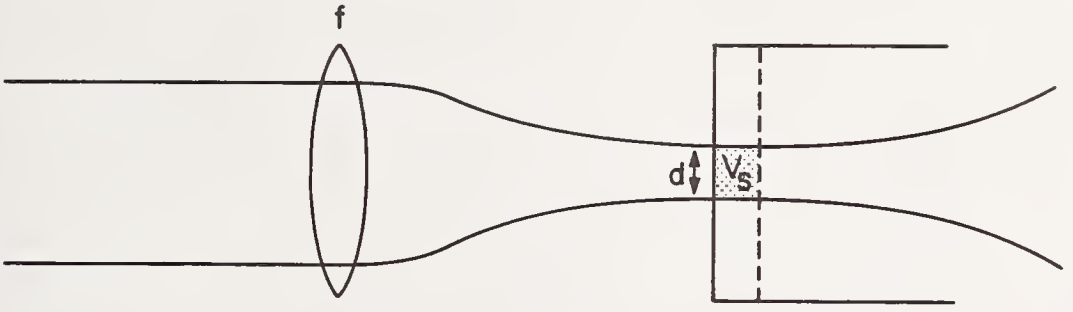

Figure 1. Small beam irradiating a surface volume V_S to measure surface breakdown probability.

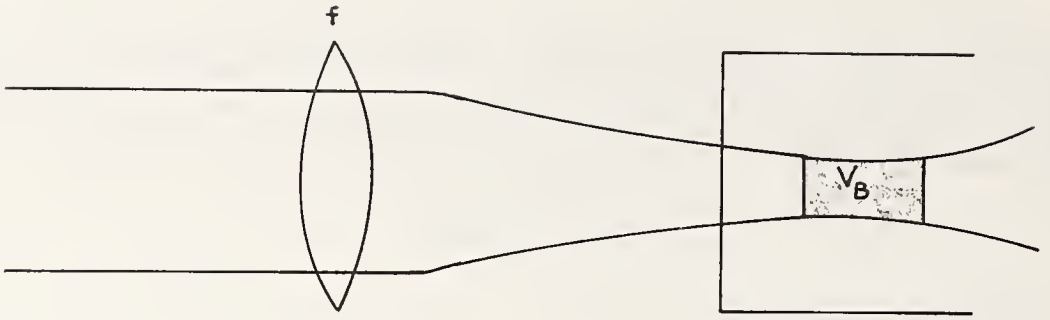

Figure 2. Small beam irradiating a bulk volume V_B to measure bulk breakdown probabilities.

Figure 3. Sample placed in center of beam waist to determine the surface threshold relative to the bulk threshold.

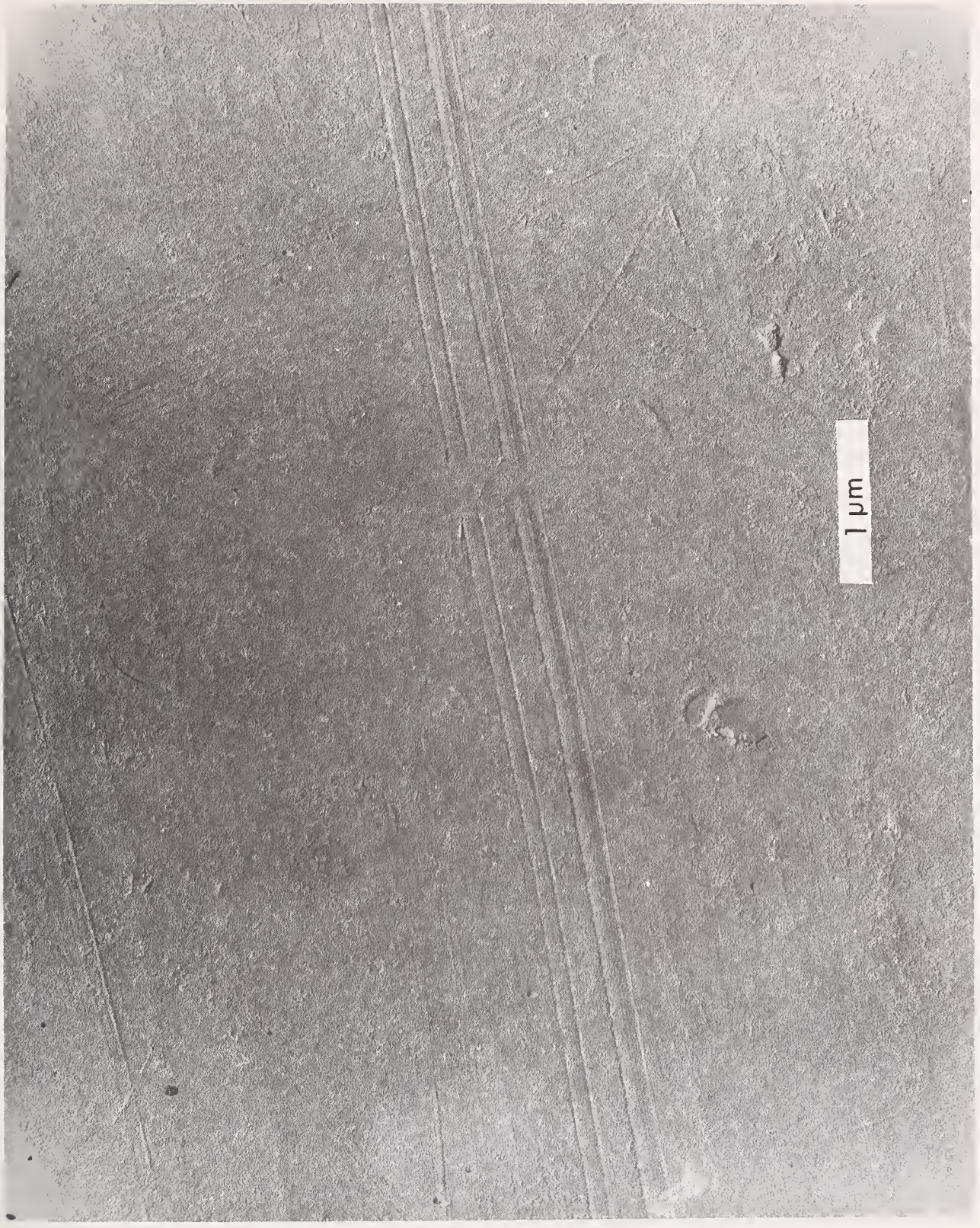

Figure 4. ED-2 laser glass - bowl-feed polished with rouge.

564-378 O - 74 - 10

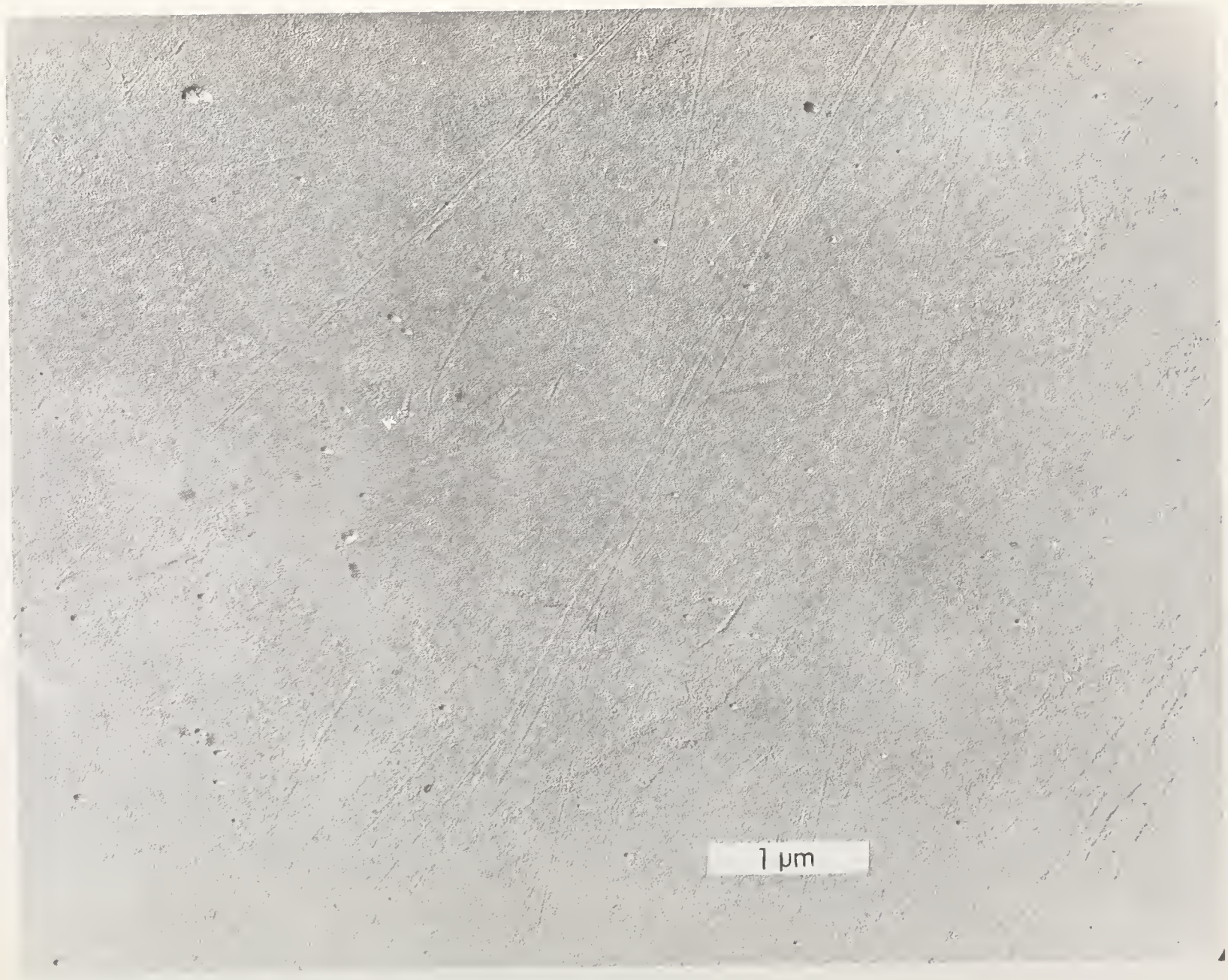

Figure 5. Ed-2 laser glass - bowl-feed polished with rouge.

Figure 6. Conventionally polished fused quartz.

Figure 7. Conventionally polished fused quartz after acid etch.

Figure 8. Ed-2 laser glass conventionally polished with Cerox.

Figure 9. Ed-2 laser glass bowl-feed polished with Cerox.

COMMENTS ON PAPER BY BOLING

The speaker was asked how well the surface roughness was characterized and how well the presence of surface impurities was measured in these experiments. He commented that qualitative measures of surface roughness such as measurements of the root mean square deviation of the surface were not used, but that a characterization of rougher or smoother was obtained solely on the basis of visual inspection of electron micrographs. With regard to surface impurities some microprobe analysis, particularly auger analysis was used, but not to a very large degree. Nevertheless, he emphasized the main point that what is crucial in determining the damage resistance of a surface is not simply the surface roughness, no matter how it is characterized, but the history of surface preparation. There was considerable discussion of the difference between polishing methods which bring about a removal of a surface layer and those methods which smooth a surface by means of plastic flow and the creation of a subsurface layer of defects and impurities. It is to be expected that in the former case, higher damage will be observed. Mike Bass of the University of Southern California, offered some clarifying comments with regard to his work which had been referred to in Boling's talk. Bass commented that they took great pains to insure that their studies were carried out on small areas in order to avoid the ambiguity of large area irradiation. They found, he said, that a significant difference was observed in the morphology of surface damage between surfaces polished by conventional methods, which exhibited lower thresholds, and those polished by so-called super polishing techniques, which exhibited higher thresholds. He emphasized that in their work the term roughness or smoothness of the surface referred to small scale effects observed on small illuminated areas. He indicated that it was crucial in obtaining consistent results to the experiments that the beam size at the damage surface be kept constant, that the focusing geometry be maintained. To this end, short focal length lenses were employed.

3.2 Damage in Nonlinear Optical Materials at 1.06 μm: Surface Treatment of $LiNbO_3$ in Ar-O_2 Plasmas and High Pressure O_2 Environment*

John C. Potosky and Concetto R. Giuliano

Hughes Research Laboratories
3011 Malibu Canyon Road
Malibu, California 90265

and

Christopher F. Klein
Hughes Aircraft Company
Culver City, California 90230

Surface damage in $LiNbO_3$ has been studied at 1.06 μm as a function of different surface treatments. While the use of ion beam polishing on $LiNbO_3$ has resulted in general degradation of surface finish and decrease in damage resistance, a different type of plasma treatment shows a distinct improvement. This method of surface treatment is one in which the sample is bombarded in a low energy rf-excited plasma of argon and oxygen. Under this type of plasma treatment, the damage resistance is substantially improved ($\sim$ 50%) over that of the conventionally polished surface of the same sample. To avoid complications of possible cumulative effects in the damage experiments, each point on the surface is laser irradiated only once at any given power. The results are presented in terms of the fraction of surface which resists damage for a given incident energy.

That this improvement in threshold involves a surface-oxygen effect is supported by another series of preliminary measurements in which damage tests were performed on $LiNbO_3$ at 10 to 15 atm O_2 pressure. Under these conditions, the surface was usually seen to completely resist damage at levels of irradiation at least twice that at which damage occurred at ambient conditions or in a high pressure nitrogen environment.

Key words: $LiNbO_3$; 1.06 μm; oxygen deficiency; surface damage; surface treatment.

1. Introduction

The relatively low laser-induced surface damage threshold of lithium niobate, $LiNbO_3$, poses stringent limitations on its use as a Q-switch or second harmonic generator. However, its large electro-optic tensor elements and its nonhygroscopic nature render it one of the most useful Q-switch crystals. Thus, a method for increasing its surface damage threshold would certainly be valuable.

It has been reported [1,2][1] that the surface of $LiNbO_3$ is apparently deficient in oxygen although there are various speculations as to its exact role in the damage mechanism. This deficiency is hypothesized to result in greater absorption and thus a lower damage threshold at the surface than in the bulk material. Experimental verification of this hypothesis is presented herein.

It has been found that surface damage in $LiNbO_3$ can be significantly reduced by supplying an excess of oxygen utilizing either of two methods. One method consisted of exposing the $LiNbO_3$ to a low energy rf excited plasma of argon and oxygen. This appeared to supply an excess of oxygen at the near surface, resulting in a residual increase in the surface damage threshold. The other method consisted of surrounding the sample with pressurized oxygen, also resulting in a significantly increased surface damage threshold. However, when the sample was removed from the chamber, no residual effects were observed.

---

*This work was supported in part by the Defense Advanced Research Projects Agency through Air Force Cambridge Research Laboratories.

[1] Figures in brackets indicate the literature references at the end of this paper.

2. Surface Damage Threshold Measurement Procedure

The technique employed for the determination of the damage thresholds in these experiments was developed to provide a quantitative threshold value and to detect small changes caused by the surface conditioning experiments. It was realized that there are several damage mechanisms in simultaneous operation, some of which are probabilistic in nature. Also, damage in $LiNbO_3$ has been reported to be complicated by multiple shot cumulative effects. [1] For this reason, single pulse damage thresholds were sought. In addition, previous experience had shown that sample crystals of $LiNbO_3$ available had significantly high densities of inclusions which obscured measurements of the intrinsic surface damage threshold.

It was assumed that each point on the surface was characterized by a damage threshold value lying between a power density below which no point on the surface would ever be damaged, and one above which every point on the surface would always be damaged. Thus a surface would have a range of damage thresholds which could be measured by firing the laser one time at a particular site, looking for the occurrence of damage, and moving to another site while keeping the laser output constant. A series of such measurements taken over the range of damage thresholds yields the probability that the single shot damage threshold lies below a given power density.

In order to determine the surface damage threshold for a sample, a single shot Nd^{3+}:YAG laser operating in the TEM_{00} mode at 1.06 μm was focused through a 3.3 cm lens at the entrance surface of the $LiNbO_3$ sample as shown in figure 1. The laser had a pulsewidth of 17.5 nsec (FWHM) and a focused spot size of 64.5 μm (1/e diameter for intensity). The output was varied by rotating crossed polarizers. The damage site* was observed with a microscope focused at the $LiNbO_3$ entrance surface utilizing an annular mirror oriented at 45° to the laser axis. The laser output was monitored with a beam splitter and an ITT biplanar photodiode whose output was electrically integrated and displayed on an oscilloscope.

3. Ion Bombardment Treatment

The threshold for laser induced surface damage in optical materials is determined in part by the physical condition of the surface. [3] Previous work by Giuliano [4] has shown that bombardment of sapphire crystal surfaces with energetic Ar^+ ion beams resulted in a substantial increase in the surface damage threshold over that of conventionally polished surfaces. Subsequently, attempts were made to similarly condition $LiNbO_3$ surfaces.

A series of experiments was performed to determine whether the surface of $LiNbO_3$ could be made more resistant to laser damage. One mechanically polished surface was subjected to various conditioning plans in which time, energy, and current density of an incident Ar^+ ion beam were varied. The damage threshold of this surface was then measured and compared with that of another surface of the same crystal which had not been ion bombarded. The results showed that the ion bombarded surfaces were usually slightly more resistant to damage, although the increase in threshold was insignificant.

Considering the surface deficiency of oxygen in $LiNbO_3$, an attempt was made to condition the surface by oxygen ion bombardment and increase the surface oxygen concentration. A surface was sputtered in an MRC rf plasma sputter system. The plasma pressure was 4 mTorr argon with 1 mTorr oxygen. The surface was sputtered for 30 min at 300 V bombardment energy. When the damage threshold of this surface was compared with that of an untreated surface on the crystal, it was found that a significant ($\sim$ 50%) increase resulted. The procedure was repeated on several crystals with similar results as summarized in figure 2. The time between sputtering and damage testing varied from 30 min to several weeks, indicating a retention of oxygen by the surface. From the data shown in figure 2 it can be seen that the treated and untreated surfaces have the same low power damage behavior, but differ significantly for high incident fluxes. Thus for the treated surface, the power density above which damage is observed on every shot is about 50% higher than for the untreated surface. This is interpreted to mean that the damage resistance is improved in the more resistant areas of the surface, (i.e., inclusion-free regions) while the treatment has no effect in improving the less resistant areas of the surface (included regions).

It was found that the power level below which no damage was ever observed was essentially a constant. However, the level above which damage was observed on every shot varied significantly from sample to sample and from conditioned to unconditioned surface on a particular sample.

*Damage is defined here as being characterized by the appearance of a small crater or pit generally accompanied by a plasma spark.

4. Pressurized Oxygen Treatment

For the damage tests performed in a pressurized oxygen environment, a windowed chamber was built to house the sample. The surface damage threshold measurement technique is identical with that outlined above, except for the addition of the chamber (see figure 1). With the chamber open to the atmosphere, damage threshold measurements were made. The chamber was then pressurized with oxygen to 250 psig and the same procedure repeated. In the $\sim$ 100 sites on $\sim$ 5 different crystals from one vendor, some of which were uncoated and some ThF_4 coated, surface damage was rarely detected with the crystals in 250 psig oxygen. Only internal damage was usually seen at a level of approximately twice that for surface damage. However, crystals grown and polished by others did show more surface damage in the oxygen environment substantiating the need for high quality polishing techniques. [3] In addition, some surfaces coated with materials other than ThF_4 showed significant surface damage. This suggests that ThF_4 may be porous enough to allow oxygen to diffuse through it in order to be in contact with the $LiNbO_3$ surface.

One important difference was noted between surface damage observed in an oxygen environment and that observed without. Without oxygen, surface damage rapidly avalanched to the catastrophic level. In pressurized oxygen, a surface damage site may begin to form, but it either becomes no worse with additional shots or worsens only slightly. It was never seen to rapidly avalanche into catastrophic damage, as such a site would always do without oxygen.

In order to verify that the oxygen was responsible for the changed surface damage characteristics of $LiNbO_3$ rather than some other effect due to the presence of pressurized gas, nitrogen was substituted for the oxygen. The pressurized nitrogen had no discernable effect upon the surface damage characteristics. As an additional test, another material, yttrium vanadate, YVO_4, was substituted for the $LiNbO_3$ in the pressurized oxygen with no perceptible change in the surface damage characteristics.

To determine the minimum pressure and exposure time required to produce an observable effect upon the damage threshold, these two parameters were individually varied. Minimum pressure appeared to be $\sim$ 50 psig. Below this level, no observable improvement was detected. Above $\sim$ 100 psig, no additional improvement was seen, but the remaining tests, however, were conducted at 250 psig in order to be assured of maximum benefit. The time during which the sample was exposed to pressurized oxygen prior to being irradiated was varied from a few minutes to $\sim$ 24 hours with no perceptible difference. When the sample was removed from the oxygen, no residual damage resistance was observed.

5. Conclusions

The surface damage characteristics of $LiNbO_3$ are significantly altered by the presence of oxygen. An increased surface damage threshold resulted as well as a marked tendency away from the usual rapid buildup of a damage site with each additional shot.

Two methods for introducing excess oxygen at the $LiNbO_3$ surface were used. One method — bombarding the surface with an argon-oxygen plasma — had the residual effect of increasing the damage threshold after removal from the plasma. The other — immersing the sample in pressurized oxygen — had no residual effect. While in the oxygen, however, the surface damage threshold was increased and the tendency for a damage site to avalanche into catastrophic damage with additional shots was significantly reduced.

Certainly, additional work must be performed in order to more quantitatively describe the effects of oxygen on the surface damage threshold of $LiNbO_3$. However, these results clearly indicate that it is significantly improved by the addition of surface oxygen.

6. Acknowledgments

The authors wish to express their appreciation to Dr. Eric Woodbury for discussions which led to the investigation of pressurized oxygen treatment of $LiNbO_3$ and to Dr. H. Garvin for guidance and assistance in the sputtering processes.

7. References

[1] G. M. Zverev, et al., "Laser-Radiation-Induced Damage to the Surface of Lithium Niobate and Tantalate Single Crystals," Soviet J.Q.E. 2[2] (1972) pp. 167-169.

[2] J. O. Porteus, E. A. Teppo, and J. H. Dancy, "Characterization of Polished $LiNbO_3$ Surfaces Using Auger Spectroscopy and Transmission Electron Microscopy," High Energy Laser Window Conference, Air Force Cambridge Research Laboratory, Hyannis, Massachusetts, 12-14 November 1973.

[3] N. Bloembergen, "Role of Cracks, Pores, and Absorbing Inclusions on Laser Induced Damage Threshold at Surfaces of Transparent Dielectrics," Applied Optics 12 [4] (1973) pp. 661-664.

[4] C. R. Giuliano,"Laser-Induced Damage in Transparent Dielectrics: Ion Beam Polishing as a Means of Increasing Surface Damage Thresholds," Appl. Phys. Lett. 21 [1] pp. 39-41.

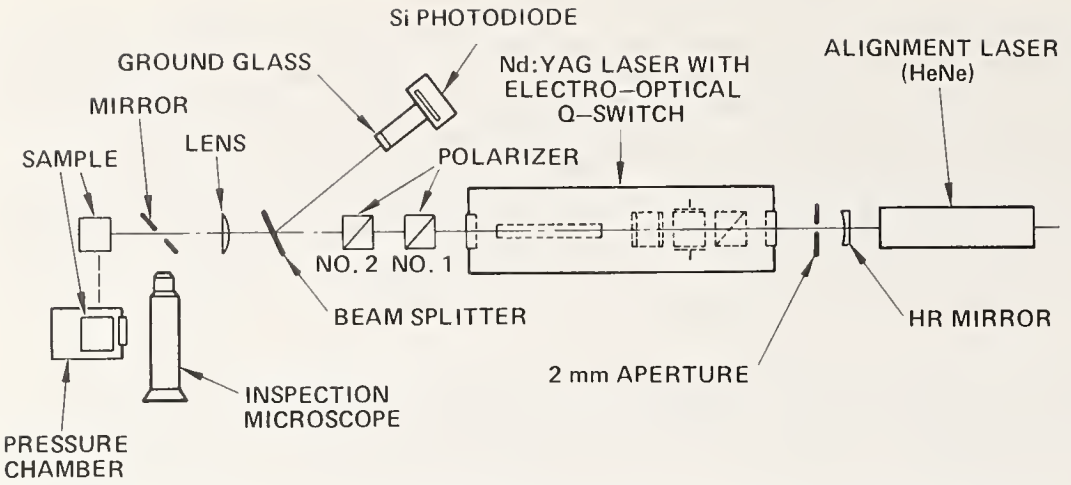

Figure 1. Equipment arrangement for determining laser surface damage thresholds.

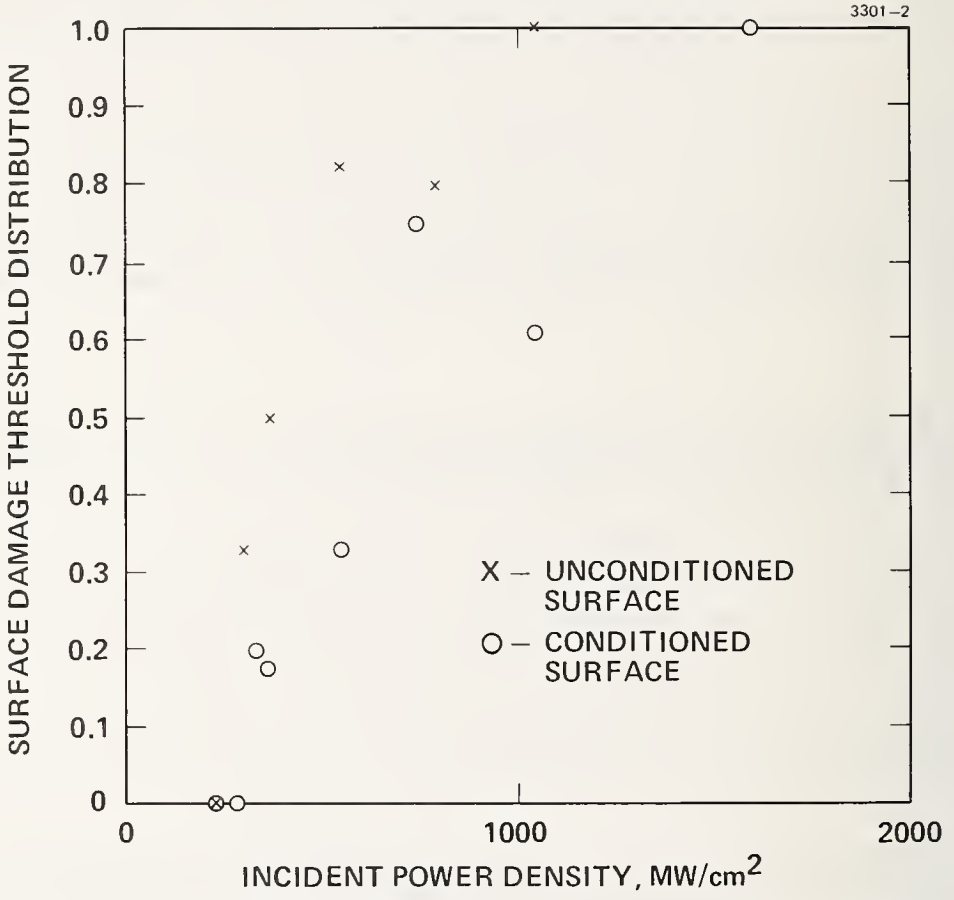

Figure 2. Laser surface damage threshold distributions for unconditioned and oxygen ion conditioned surfaces of $LiNbO_3$.

NO COMMENTS ON PAPER BY POTOSKY.

3.3 Surface Characteristics Related to Laser Damage of Lithium Niobate and Potassium Chloride Surfaces*

J. O. Porteus, E. A. Teppo, and J. H. Dancy

Michelson Laboratory, Naval Weapons Center
China Lake, California 93555

Laser damage of transparent materials is promoted by irregularities in topography and surface composition. Changes in these characteristics following laser irradiation can provide insight on damage mechanisms. Transmission electron micrographs of replicated $LiNbO_3$ surfaces which have been chemically etched show submicroscopic pitting similar to that previously observed following laser irradiation. Experiments designed to explore a possible role of surface-acoustic waves in the laser-induced pitting are in progress. Auger analysis of coated $LiNbO_3$ surfaces following visible laser damage have helped to identify redistributed surface material. Profiling of the coating shows evidence of C contamination layers near the substrate surface. Preliminary Auger spectra of KCl surfaces show promise for similar studies on this material.

Key words: Auger electron spectroscopy; ion beam profiling; laser-induced damage; lithium niobate; potassium chloride; surface acoustic waves; surface characterization; transmission electron microscopy.

1. Introduction

The results reported here represent recent progress in a continuing program on the surface-physical characteristics of laser optical materials. [1,2][1] An understanding leading to better control of laser damage mechanisms is sought via (1) detecting undesirable initial characteristics, such as surface irregularities or contamination, which are the result of improper preparation and handling, and (2) analysis of characteristics induced or altered by laser irradiation. Submicroscopic topography is monitored by transmission electron microscopy (TEM). Surface composition and material distribution are determined by Auger electron spectroscopy (AES), including ion beam profiling. Previous work in this program has concentrated mainly on uncoated $LiNbO_3$ surfaces, where a laser-induced submicroscopic pitting effect was observed. [1,2] The present paper deals with further efforts to understand this effect and Auger analyses of visibly damaged, coated $LiNbO_3$ surfaces. Preliminary work on uncoated KCl surfaces was performed to demonstrate the applicability of AES methods to this material.

2. Experimental Apparatus and Technique

The TEM measurements were performed with a JEOLCO Model 120U electron microscope, using a two-stage replication procedure. [2,3] The resolution of the resulting micrographs is limited by the grain of the replica to approximately 50 Å. The AES measurements were performed using conventional cylindrical mirror analyzer systems (Physical Electronics Industries, Model 5000; Varian Associates, Model 981-2607). [2,4] One of these (PEI) is equipped with a multiplexor and sputter-ion gun for ion beam profiling. [5] To minimize surface charging the electron probe beam was inclined 60° relative to the sample normal and typically operated at a primary energy of 2 KeV. Lateral resolution, as determined by the probe beam cross section, is 300 μm or better. Analyses were normally performed in an unbaked ion-pumped system operating in the low 10^{-8} Torr range. Profiling was done at 5×10^{-5} Torr Ar using a 2 KeV ion beam.

3. Samples

Uncoated $LiNbO_3$ samples were kindly supplied by Isomet Corporation. These are of the form conventionally used for laser Q-switch modulation. Dimensions are 8 x 8 x 24 mm with the long dimension parallel to the z-axis. The ends have been optically polished using a variety of polishing compounds

---

*This work was supported by the Defense Advanced Research Projects Agency and by Navy Independent Research Funding.

1. Figures in brackets indicate the literature references at the end of this paper.

including Al_2O_3, diamond dust, SiC in glycerol and Syton. Two coated $LiNbO_3$ samples showing visible laser damage were provided through the courtesy of C. F. Klein of Hughes Aircraft Corporation. The coating on one of these is proprietary; available information suggests ThF_4 or $ThOF_2$ with a protective overlayer of Al-containing material, possibly Al_2O_3. The coating on the other sample, which was analyzed by profiling, is nominally $ThOF_2$. Both coated samples have the usual gold electrodes used to apply a modulating field parallel to the x-axis. The KCl samples consist of a freshly cleaved single crystal and a polished Harshaw Econoflat.

4. Uncoated $LiNbO_3$

4.1 Submicroscopic Pitting

It has been demonstrated that exposure of uncoated polished $LiNbO_3$ to laser power densities as low as 12 MW/cm^2 can lead to submicroscopic surface pitting. [1,2] The pits are ~ 100-500 Å in diameter with depths in excess of twice the diameter; they are not confined to the directly irradiated area, but may extend over the entire polished surface. The pit density and power density required for formation appear to be strongly influenced by topographical irregularities and quality of surface finish. The significance of this effect for catastrophic damage is that the pits may act as direct absorption sites for energy from the laser beam. [2]

4.2 Energy Transport Mechanism

An explanation of the nonlocalized pitting effect requires a mechanism for transporting energy along the surface. One possibility is the scattering of light by dust or inhomogeneities in the surface. [6] Another mechanism is suggested by the excellent propagation characteristics of $LiNbO_3$ for surface acoustic waves [7], combined with the possibility of exciting these waves by laser irradiation. [8]

Two experiments designed to test for these mechanisms are now in progress. One of these involves deliberate generation of surface acoustic waves on a $LiNbO_3$ surface and subsequent inspection for pits. The sample in this case is a YZ-cut acoustic-wave delay line having Al interdigital transducers at either end for sending and receiving acoustic signals. [9] An unexpected problem was immediately encountered with the procedure used to mount the transducers. An etchant (Electrotec #CAE-600) customarily used to remove the excess Al was found to produce a submicroscopic pitting which is more dense, but otherwise essentially indistinguishable from that observed following laser irradiation. This may be seen by comparing figure 1 with figures 8-10 of reference 2. Etching between the transducers can be avoided by a modification of present procedures, as will be done in future experiments. Nevertheless, pit formation by an alternative means emphasizes the importance of carefully monitoring sample preparation procedures.

The second experiment is illustrated in figure 2. One end of the uncoated $LiNbO_3$ sample is slotted with a wire saw as indicated, dividing the surface into four areas designated by letters. The sample is irradiated through area B using a collimating mask. The surface is then examined by TEM for submicroscopic pitting in each of the four areas. Pitting confined to area B alone would support the acoustic wave mechanism, since the slots effectively block the progress of acoustic waves along the surface. Pitting in other areas, on the other hand, would support an alternative mechanism, such as that involving scattered light. Initial studies show slight evidence of pitting in area D, as well as B. However, in view of the weakness of the effect and the experience with the acoustic delay line it is possible that the pitting may have been present before irradiation and was overlooked in the control examination. The experiment must therefore be repeated to establish confidence in the result.

5. Coated $LiNbO_3$

5.1 Sample With Proprietary Coating

The previously described sample with a proprietary coating was analyzed with AES in an effort to identify visible changes in the surface outside the damage site. An optical micrograph of the damaged portion of the surface taken after analysis is shown in figure 3. A crater and surrounding peripheral damage area appear as a roundish black spot to the lower left of center. Irregular, lighter-than-average spots spaced at regular intervals across the field are the result of coating discoloration by the Auger probe beam. This imaging of the beam permits accurate determination of the analyzed area. A large, slightly darkened area, made more evident by contrasting surface scratches, covers most of the lower half of the field. Another large area approximately 2 mm wide, part of which is visible on the extreme right-hand side of the field is relatively clear (undarkened). However, the darkening again occurs further to the right, out of the field of view.

Auger spectra were obtained at the damage site and at 1 mm intervals along a line passing through that position. Normalized peak-to-peak intensities are plotted in figures 4-6. The positional relationship to visible surface features is indicated at the top of these figures. The elements represented

in figure 4 show a maximum Auger intensity in the clear sample area, while those represented in figure 5 generally show a minimum here. Figure 6 shows the results for the C and N peaks which do not fall obviously into either category. Strangely, no Th peak was observed, evidently because of the protective Al-containing overlayer and the shallow sampling depth. The F atom either diffuses to the surface because of its relatively small atomic size or is a normal constituent of the overlayer. Unfortunately, we did not have the opportunity to profile the sample in order to clarify this point.

On the basis of these results the clear area of figure 3 represents undisturbed coating, while the large darkened areas represent overlying material consisting mainly of compounds containing Nb, S, and Cl. The origin of the last two elements is not certain. The association with Nb suggests a relationship of S and Cl to the damage event, i.e., as coating impurities ejected from the crater. However, without either profiling studies or repeating the damage in a controlled environment, the possibility of preferentially adsorbed atmospheric contaminants cannot be excluded. Judging from the maxima in Nb and O, and the minima in Al and F signals near the crater, a substantial area of $LiNbO_3$ is exposed here. The failure of the maxima to coincide exactly with the crater position is attributed to surface roughness within the crater area. The roughness suppresses both secondary electron emission and Auger emission. The suppressed secondary emission promotes surface charging which may also influence the observed Auger intensity distribution via deflection and defocusing effects. Except for a minimum in the crater area due to roughness, the intensity of the C signal is essentially constant over the surface, as might be expected from superficial contamination occurring after the damage event. The N signal, on the other hand, shows a single pronounced maximum near the crater, attributed to the formation of nitrogen compounds in a spark which accompanied the damage.

5.2 Sample With $ThOF_2$ Coating

The damage on the second coated sample is shown in figure 7. The damage pattern here is much more complex, and shows a definite periodicity of 40 μm in the direction of the modulating field. The origin of the periodicity has not been definitely determined. The facts point to spatial modulation of the light intensity by interference, possibly a result of misaligned optical surfaces. Intense monochromatic surface acoustic waves are also excited by optical interference [8] and may have an effect on the plasma distribution via their associated electric fields. The excitation of surface acoustic waves of the proper frequency (~ 100 MHz) by the Q-switch modulating field is ruled out by its slow rise time (~ 300 nsec).

The depthwise composition of the damaged surface was investigated by profiling at selected points along the surface. It was found that certain areas within the damage pattern, such as the partially clear circular area near the bottom center of figure 7, are intact except for an overlayer of ejected substrate material. Cratered areas near the center of the pattern show spectra characteristic of bare $LiNbO_3$, whereas those near the edge of the pattern are covered with a thin layer of coating material. This indicates more rapid removal of material from the original coating than from the bottoms of the craters. Either the craters are more shielded, possibly by plasma, or the original coating is inherently more absorbing, possibly due to impurities.

An attempt was made to detect light-absorbing impurities which may have led to coating damage by profiling an undamaged area on the opposite end of the sample. The results are shown in figure 8. The initial turn-on of the electron probe beam in the presence of Ar results in rapid removal of superficial C and an increase in signal from the coating constituents Th, O and F. When the ion profiling beam is turned on the spectrum shifts due to a change in surface charge, which necessitates retuning the multiplexor. Resumption of the scan with both beams on provides a measurement of the relative concentration vs depth for each element monitored in the remaining portion of the coating. The profiling rate is estimated at approximately 35 Å/min.

A significant feature of the results for laser damage is the marked rise of the C peak at the coating-substrate interface, indicating C contamination of the $LiNbO_3$ surface. Another significant feature is contamination of the coating, as indicated by oscillations in the profiles. The prominent maxima in the C profile, which coincide with minima in the Th profile, are produced by inhomogeneities where C replaces Th to a large degree. These C-rich layers also appear to be abnormally rich in F at the expense of the O content. The marked predominance of C as a contaminant, both in the coating and at the coating boundaries, strongly suggests its involvement in absorption of energy from the laser beam.

6. KCl Samples

The feasibility of similar Auger studies on KCl laser window samples was investigated by preliminary AES scans on this material. Figure 9 shows the spectra from the Harshaw Econoflat. In addition to the peaks due to K and Cl, peaks from O and Na were observed. Spectra obtained from a freshly cleaved control sample were similar, except for the absence of the Na peak. Prolonged exposure to the Auger probe beam was observed to reduce the intensity of the Cl peak relative to that of K, indicating some surface decomposition. [10] A related problem is the tendency toward surface charging, which is promoted by the reduced secondary emission coefficient of the K-rich surface. However, decomposition proceeds at a sufficiently slow rate that it is not considered to be a serious problem.

7. Summary and Conclusions

Submicroscopic pitting, which has been observed on uncoated $LiNbO_3$ surfaces following laser irradiation insufficient to cause visible damage, can also be produced by chemical etching. Experiments designed to explore the role of surface acoustic waves in the laser-induced pitting have not yet yielded conclusive results. Auger analysis of a coated $LiNbO_3$ sample with visible laser damage shows large areas covered with Nb, Cl and S, which appear to be related to the damage event. Auger studies on a second coated sample show a thin layer of coating material within craters lying near the edge of the damaged area, indicating preferential destruction of the original coating. Profiling shows evidence of C-containing layers both within the coating and at the substrate interface, suggesting that C plays a major role in surface absorption and damage. Preliminary Auger spectra of KCl surfaces show promise for laser damage studies on this material.

8. References

[1] Porteus, J. O., Defense Advanced Research Projects Agency, ARPA Order 2175, Semi-Annual Report No. 3, Apr. 1973-Sept. 1973, pp. 87-104; Porteus, J. O., Teppo, E. A., and Dancy, J. H., Defense Advanced Research Projects Agency, ARPA Order 2175, Semi-Annual Report No. 4, Sept. 1973-Mar. 1974, pp. 84-94.

[2] Porteus, J. O., Teppo, E. A., and Dancy, J. H., Proceedings of the Third Conference on High Power Infrared Laser Window Materials, Hyannis, Mass., 12-14 Nov. 1973, pp. 947-964.

[3] Murr, L. E., *Electron Optical Applications in Materials Science* (McGraw-Hill, New York, 1970), Section 5.3.3.

[4] Bauer, E., Vacuum 22, 539 (1972).

[5] Morabito, J. M., Thin Solid Films 19, 21 (1973).

[6] Emmony, D. C., Howson, R. P., and Willis, L. J., Appl. Phys. Letters 23, 598 (1973).

[7] Slobodnik, A. J., Appl. Phys. Letters 14, 94 (1969).

[8] Cachier, G., Appl. Phys. Letters 17, 419 (1970).

[9] White, D. J. and King, R. L., Defense Advanced Research Projects Agency, ARPA Order 2175, Semi-Annual Report No. 3, Apr. 1973-Sept. 1973, pp. 114-122.

[10] Palmberg, P. W. and Rhodin, T. N., J. Phys. Chem. Solids 29, 1917 (1968).

9. Figures

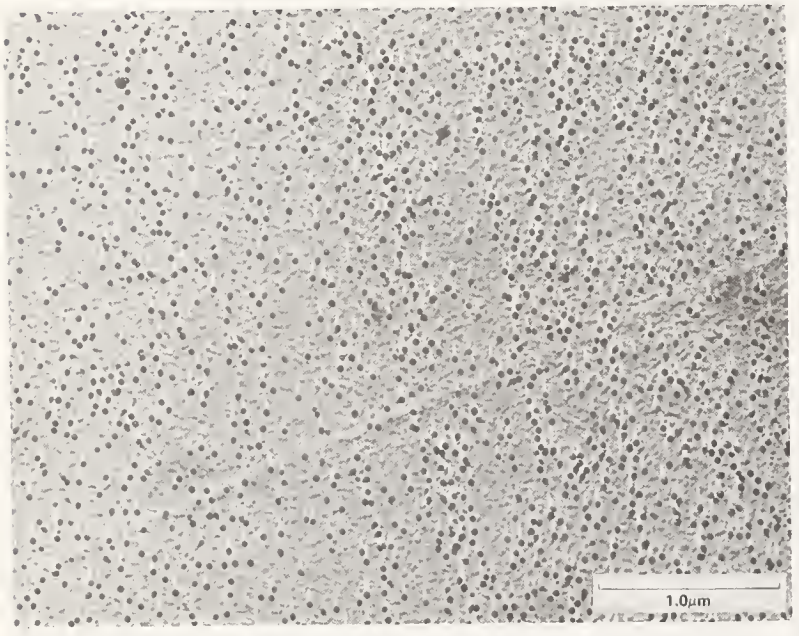

Figure 1. Transmission electron micrograph of pitted $LiNbO_3$ acoustic delay line after application of Al etch. Compare with micrographs of laser-induced pitting in references 1 and 2.

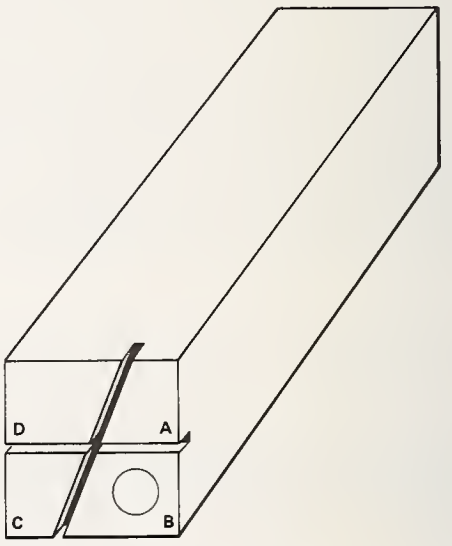

Figure 2. Slotted $LiNbO_3$ sample used in testing for surface acoustic wave pitting mechanism. Laser irradiation is at normal incidence through a mask which exposes a 2-mm diameter circle in area B.

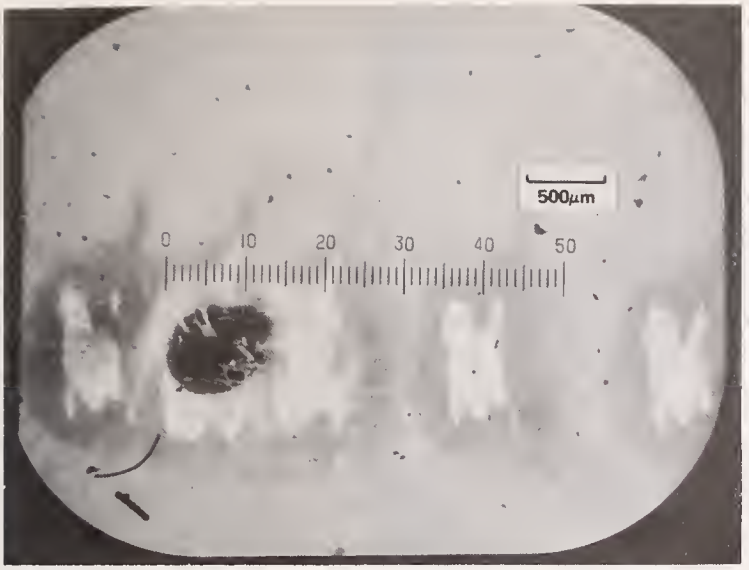

Figure 3. Optical micrograph of laser-damaged portion of a coated $LiNbO_3$ surface after Auger analysis. The black spot is the damage crater, while excessively light spots are images of the Auger probe beam.

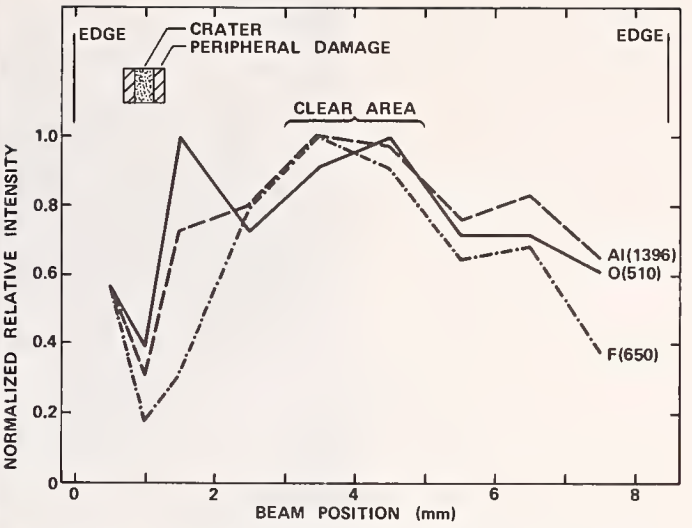

Figure 4. Auger intensity distribution across a damaged, coated $LiNbO_3$ surface for those elements included in the coating material. Auger peaks used are identified by element and by energy in eV at the right.

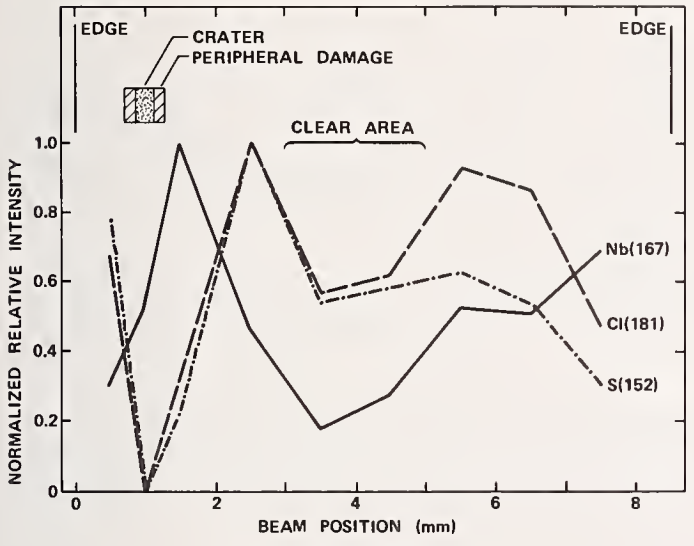

Figure 5. Figure corresponding to figure 4 for elements probably ejected from the damage crater.

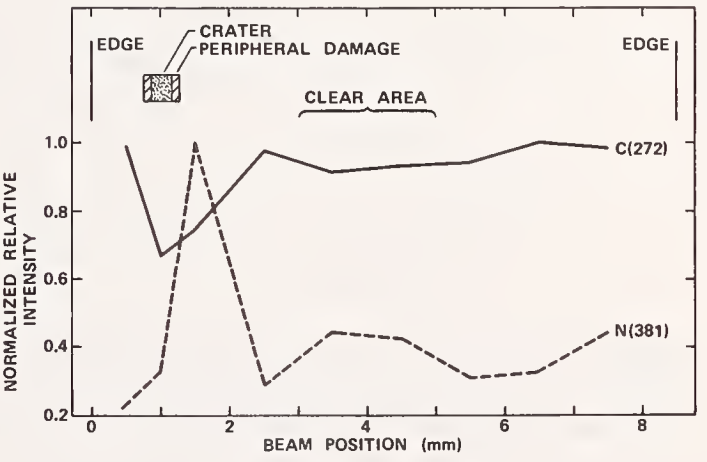

Figure 6. Figure corresponding to figure 4 for contaminants originating mainly from the sample environment.

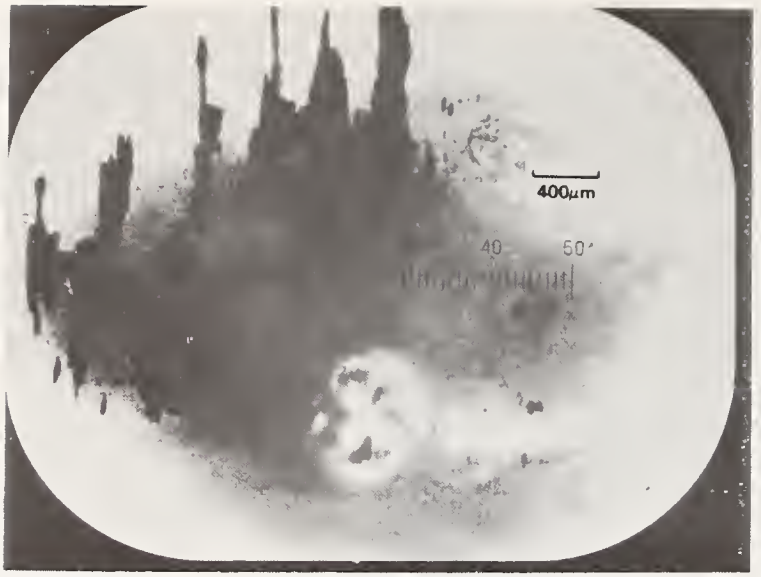

Figure 7. Laser-damaged $ThOF_2$-coated $LiNbO_3$ surface. Note the periodic damage pattern consisting of vertically elongated damaged areas which are evenly spaced in the horizontal direction.

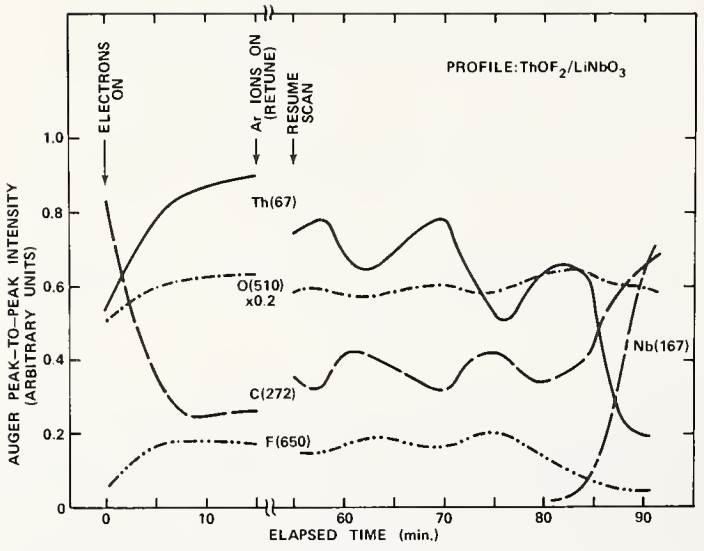

Figure 8. Ion beam profile of $ThOF_2$-coated $LiNbO_3$ surface using Auger analysis. Curves on the left show removal of a superficial C layer by the Auger probe beam before ion profiling has begun.

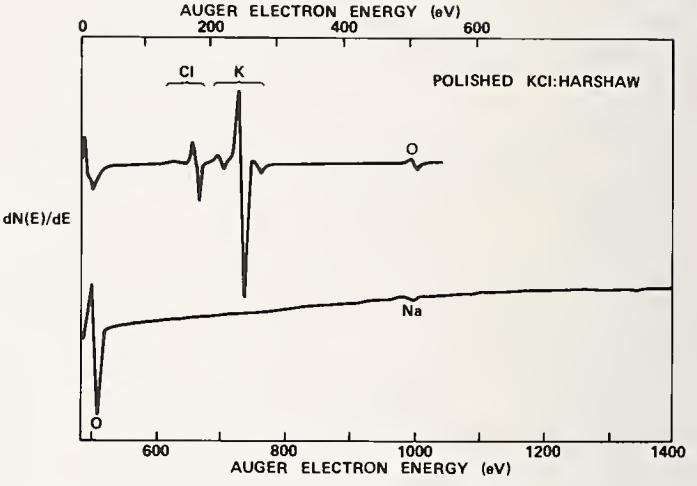

Figure 9. Auger spectrum from polished KCl window material.

COMMENTS ON PAPER BY PORTEUS

The speaker commented on the sensitivity of Auger analysis to surface defects and impurities and quoted results from an experiment done with an aluminum impurity on a copper surface generated by polishing the copper with aluminum oxide. Using the Auger analysis, an impurity level of about 100 nanograms per square centimeter could be detected. He commented further that the Auger probe only penetrates the surface to a depth of about 10 Å and therefore it is appropriate to characterize its sensitivity in terms of the fraction of the surface layer covered by the impurity. In these terms, in the aforementioned experiment, a sensitivity of about 0.1% surface coverage by the aluminum impurity on copper could be detected. Fritz Zernicke of Perkin-Elmer raised the point that the pitting of the surface may not be due entirely to the etch used to remove the aluminum coating from the surface, but to the original aluminum coating process. He said in experiments that he had carried out, no such pitting was observed, when surfaces were coated with manganese. The speaker indicated that he had not investigated this point.

4.1 Characterization of Infrared Laser Window Materials at the National Bureau of Standards*

A. Feldman, I. Malitson, D. Horowitz, R. M. Waxler, and M. Dodge

National Bureau of Standards, Washington, D. C. 20234

A program has been established for measuring refractive index, n, stress-optical constants, q_{ij}, change of index with temperature, dn/dT, thermal expansion coefficient, α, and elastic compliances, s_{ij}, of infrared laser window materials. These parameters are necessary for determining the optical distortion that occurs in windows due to heating by the absorption of high power laser radiation. n and dn/dT are measured over a spectral range 0.2 to 50 μm by the method of minimum deviation on precision spectrometers. Twyman-Green and Fizeau interferometers, which operate at 0.6328 μm, 1.15 μm, and 10.6 μm, are used for measuring q_{ij}, α, dn/dT and s_{ij}. Materials currently under study are polycrystalline ZnSe, As_2S_3 glass, chalcogenide glass (Ge 33%, As 12%, Se 55%), and KCl. Results are given for n and dn/dT in KCl, and q_{ij} and s_{12} in ZnSe, As_2S_3 glass, and chalcogenide glass.

Key words: As_2S_3; chalcogenide glass; coefficient of thermal expansion; elastic constants; infrared laser window materials; KCl; photoelasticity; polycrystalline ZnSe; refractive index; stress-optical constants; thermal coefficient of refractive index.

1. Introduction

Laser systems of high average power are currently under development. As the output power increases, the optical components in these systems undergo optical and mechanical distortion due to absorptive heating. If the distortion is sufficiently severe, the optical elements become unusable. The parameters necessary for determining this optical distortion [1,2][1] are absorption coefficient, refractive index, change of index with temperature, thermal expansion coefficient, stress-optical coefficients, elastic compliances, specific heat, thermal conductivity, and density.

The temperature change that occurs in a laser window due to absorptive heating will produce three effects: (1) an expansion, (2) a direct change of refractive index, and (3) a system of internal stresses due to thermal gradients, which changes the refractive index through the stress-optical effect.

Although some information is available [3,4] on thermal expansion and change of index with temperature of laser window materials, there is very little data on the stress-optical effect [5]. In the past stress-optical coefficients have been measured in the visible region of the spectrum using interference methods [6,7]. We have now constructed Twyman-Green and Fizeau interferometers for making these measurements at 1.15 μm and 10.6 μm as well as at 0.6328 μm. This is the first time that interferometers have been used for measuring stress-optical coefficients in the infrared. These interferometers are also useful for measuring thermal expansion, change of index with temperature, and elastic compliance coefficients.

In this paper we present the methods used for measuring refractive index, n, change of index with temperature, dn/dT, thermal expansion coefficient, α, stress-optical coefficients, q_{ij}, and elastic compliances, s_{ij}. We also report on results obtained on As_2S_3 glass, a chalcogenide glass (Ge 33%, As 12%, Se 55%), polycrystalline ZnSe, and single crystal KCl.

---

*This research was supported in part by the Advanced Research Projects Agency of the Department of Defense.

[1]Figures in brackets indicate the literature references at the end of this paper.

564-378 O - 74 - 11

We discuss measurements of n and dn/dT by using precision refractometry methods in section 2. The quantity dn/dT is obtained near room temperature by measuring n at 20°C and at 30°C. Results are reported for KCl.

In section 3 we discuss the measurement of thermal expansion and dn/dT up to a temperature of 800°C. These measurements involve the use of Fizeau fringes.

In section 4 we discuss the measurement of stress-optical coefficients and elastic compliances. In isotropic materials there are two independent elastic constants and two independent stress-optical coefficients. The use of Twyman-Green and Fizeau interferometers in conjunction with samples under uniaxial and hydrostatic compression supplies us with sufficient data for obtaining all the constants.

In section 5 we present the results of measuring q_{ij} and s_{12} on the chalcogenide glass, As_2S_3 glass, and polycrystalline ZnSe.

2. Refractive Index and Change of Index with Temperature

In the search for potential window and auxiliary optical component materials for high-power lasers, KCl appears to be one of the most promising candidates. It has useful transparency from $\sim$ 0.2 to 20 μm (with 90% transmittance between 0.45 and 14 μm). This covers window utilization in both the ultraviolet and infrared.

2.1 Index Data

A KCl prism cut from a commercially grown crystal was used in this study. The prism faces are 10 x 10 mm and the refracting angle near 60°. The refractive index was measured by means of the classical minimum deviation method with two precision spectrometers. The spectrometer schematic shown in figure 1a is designed for visible region refractometry and is capable of accuracy of several parts in 10^6. The spectrometer schematic shown in figure 1b employs mirror optics and is used in the non-visible spectral regions. It is capable of accuracy of several parts in 10^5. Both instruments and procedures for high-precision refractive index measurements have been described in previous publications [8,9].

Refractive index measurements were made at controlled room temperatures near 20°C at 60 wavelengths from 0.22 μm in the ultraviolet to 14.3 μm in the infrared. The wavelengths were selected from the spectra of emission sources of Hg, Cd, He, Cs and Zn, and from calibrated absorption bands of H_2O, polystyrene, and methylcyclohexane. A series of calibrated narrow-band filters was also used in the infrared in the 3.5 to 10.6 μm region.

The experimentally determined index values at 20°C for KCl are represented by the solid curve in figure 2. The refractive index decreases from a value of 1.6360 at 0.224 μm to 1.4374 at 14.3 μm, an over-all change of 2×10^{-1}. At 10.6 μm the value of the refractive index is 1.4542 at 20°C.

The refractive index measurement program is being supplemented with a compilation of critically evaluated refractive indices of key laser materials. A literature search has turned up fourteen published papers dealing with refractive index of KCl. The data cover the wavelength range from $\sim$ 0.16 to 220 μm and were obtained by a variety of experimental techniques. It is interesting to note that in the spectral regions of interest to laser designers, the most accurate measurements were made in 1901 [10], 1908 [11], and 1927 [5]. The crystals measured were natural salt, and the minimum deviation method was employed with the sample in prism form. The excellent agreement between the NBS and the early data is shown in figure 2. The NBS values are lower in index by an average value of 2×10^{-4}.

2.2 Thermal Coefficient of Index

Refractive index measurements in KCl were repeated at 22 selected wavelengths at a controlled room temperature near 30°C. The refractive index values at 20°C and 30°C were used to calculate the thermal coefficient of index, dn/dT. The dependence on wavelength is shown in figure 3. The value of dn/dT varies from -2.1×10^{-5} K^{-1} at 0.27 μm to -2.5×10^{-5} K^{-1} at 14.3 μm; dn/dT remains relatively constant at about -3.0×10^{-5} K^{-1} in the infrared between 3 μm and 6.0 μm. The fact that dn/dT is negative indicates that the variation in index with temperature is essentially due to the change in density of the crystal. At the extremes, where dn/dT is less negative, the influence of temperature suggests a shift of the ultraviolet and infrared absorption edges to longer wavelengths.

The dn/dT values of Gyulai [12] and Paschen [13] are shown in figure 3 for comparison. Gyulai's values for a mean temperature of 33°C cover the wavelength range 0.20 to 0.61 μm. Paschen's data, for which the mean temperature is unknown, covers the wavelength range 0.59 to 17.7 μm. It can be seen that the absolute values of the earlier work are generally higher than those of NBS. It has been observed in halide crystals that the absolute value of dn/dT increases with increasing temperature.

3. Thermal Expansion and Change in Refractive Index with Temperature

The thermal expansion and change of refractive index with temperature dn/dT may be measured up to a temperature of 800°C by an interferometric method that uses Fizeau type fringes [14]. In the visible part of the spectrum these measurements can be made simultaneously.

The interferometer assembly as used in the visible is shown in figure 4. The set of fringes on the left is obtained between the top and bottom surfaces of the lower fused silica plate, T, and is calibrated in terms of temperature so that the fringes serve as an optical thermometer. The center set of fringes is obtained between the top and bottom surfaces of the index sample, R, and is used to calculate the change in refractive index. Beneath this sample is a frosted area on the lower plate so that no fringes are formed at the interface. The third set of fringes is formed by the slight wedge introduced between the upper plate, E, and the lower plate, T, when these fringes are separated by the expansion sample, S, which is cut from the same material as the index sample, R. These fringes are used to obtain the thermal expansion. The assembly is heated by a vertical tube furnace and the shifts in the three sets of fringes are recorded simultaneously on a single strip of 35 mm film as a function of temperature.

The interference pattern generated by the sample of thickness, t, and refractive index, n, is expressed by the equation,

$$N\lambda = 2nt, \tag{1}$$

which relates the optical path, nt, and the fringe number, N, when monochromatic light of wavelength, λ, passes twice through the sample at normal incidence. By differentiating with respect to temperature, T, and rearranging, it is found that

$$\frac{dn}{dT} = \frac{\lambda}{2t}\frac{\Delta N}{\Delta T} - \frac{ndt}{dT} \quad . \tag{2}$$

We calculate the change of refractive index as a function of temperature from the number of fringes that pass a point of reference and from the change of thickness obtained from the thermal expansion sample [15].

Using a modification of the above method, we intend to extend the measurement of dn/dT to the infrared.

4. Measurement of Stress-Optical Coefficients and Elastic Constants

The importance of measuring all the stress-optical coefficients in the infrared is not always well understood. Several laboratories have been measuring stress-induced birefringence at 10.6 μm. However, these data are not sufficient for determining the optical wavefront distortion due to thermal stresses, because they measure only the relative stress-optical coefficients [$(q_{11} - q_{12})$ and q_{44} for cubic materials]. We know of only one paper which presents measurements of q_{11} and q_{12} separately at 10.6 μm [5], and these measurements, which were done on Ge, did not give the sign of the coefficients. Both q_{11} and q_{12}, in combination with the elastic constants, are necessary for calculating the optical distortion due to stresses from thermal gradients in optical materials [1,2]. Index changes due to these stresses can be even greater than changes in index due to a rise in temperature. For example, in a material tailored to have dn/dT = 0, the changes of index will be due solely to the stress-optical effect.

4.1 Apparatus

Conventional Twyman-Green interferometers are used [16]. The Twyman-Green interferometer at 0.6328 and 1.15 μm uses helium-neon lasers as sources. The fringes are observed with a silicon matrix vidicon camera.

The Twyman-Green interferometer at 10.6 μm uses a CO_2 laser source, a germanium beam expander, and a germanium beam splitter. The fringes are viewed either on a liquid crystal detector or on a commercial thermal image plate.

For uniaxial loading, the specimen, in the form of a rectangular parallelepiped is compressed in a rectangular frame screw clamp equipped with a calibrated load cell and a digital readout voltmeter. A photograph of the stressing apparatus with the voltmeter is shown in figure 5.

4.2 Experimental Procedure

The sample is placed within one arm of the Twyman-Green interferometer. The fringe shift per unit of applied stress is measured for stress parallel to the polarization of the radiation, $\Delta N_1/\Delta P$, and for stress perpendicular to the polarization of the radiation, $\Delta N_2/\Delta P$.

The sample, itself, functions as a Fizeau interferometer if the faces are properly polished; interference fringes are obtained from reflections from the sample surfaces. The fringe shifts obtained for stresses parallel and perpendicular to the polarization of the radiation are, respectively, $\Delta N_1'/\Delta P$ and $\Delta N_2'/\Delta P$.

For an isotropic material we obtain

$$s_{12} = \frac{\lambda}{2t}\left(\frac{\Delta N_1}{\Delta P} - \frac{\Delta N_1'}{\Delta P}\right) = \frac{\lambda}{2t}\left(\frac{\Delta N_2}{\Delta P} - \frac{\Delta N_2'}{\Delta P}\right) \tag{3}$$

$$q_{11} = \frac{\lambda}{n^3 t}\frac{\Delta N_1}{\Delta P} + \left(\frac{2}{n^3}\right)(n-1)\, s_{12} \tag{4}$$

$$q_{12} = \frac{\lambda}{n^3 t}\frac{\Delta N_2}{\Delta P} + \left(\frac{2}{n^3}\right)(n-1)\, s_{12} \tag{5}$$

Additional experimental data can be obtained by measuring the stress-induced birefringence. The experimental arrangement is shown in figure 6. The stress is applied 45° with respect to the plane of polarization. The analyzer is oriented parallel to the incident polarization. The uniaxial load applied to the sample is increased until extinction is obtained. The loaded specimen then acts effectively as a half-waveplate, and considering the double passage of the light through the specimen, the load is that which creates a single pass quarter wave retardation in the sample. The relative stress-optic coefficient is

$$q_{11} - q_{12} = \lambda/(2n^3 P t). \tag{6}$$

The value of $q_{11} - q_{12}$ from the measurement of birefringence is more precise than the value of $q_{11} - q_{12}$ obtained from eqs (4) and (5). Thus, we calculate q_{11} and q_{12} from the sum $q_{11} + q_{12}$, obtained by adding eqs (4) and (5), and the difference $q_{11} - q_{12}$ from eq (6). This assures us that the birefringence calculated from the numerical values of q_{11} and q_{12} equals the measured value.

Equation (3) gives the value for s_{12}. In order to obtain s_{11}, we use a method similar to the method for measuring dn/dT. The sample which acts as a Fizeau interferometer is compressed in a pressure vessel. Figure 7 shows the pressure vessel. Hydrostatic pressure is generated by compressing a fluid. From the shift in fringes per unit pressure, $\Delta N/\Delta P$, we obtain for an isotropic material

$$s_{11} + 2s_{12} = \frac{\lambda}{2nt}\frac{\Delta N}{\Delta P} - \frac{n^2}{2}(q_{11} + 2q_{12}) \tag{7}$$

Using s_{12} obtained from eq (3) together with eq (7), we can solve for s_{11}.

The procedures described in this section are for measuring stress-optical constants and elastic constants of isotropic materials. These constants can be measured with the same procedures on crystalline materials. Because stresses must be applied along several crystallographic axes, more samples are required for measurements on crystalline materials than for measurements on isotropic materials.

4.3 Results

Measurements of absolute and relative stress-optical coefficients have been made on chalcogenide glass, As_2S_3 glass, and polycrystalline ZnSe. The results are given in Table 1. The data for As_2S_3 are presented for three wavelengths, 0.6328 μm, 1.15 μm, and 10.6 μm. Data for the same wavelengths are presented for polycrystalline ZnSe although absolute values are lacking at 10.6 μm. We have assumed the ZnSe to be an isotropic material. Data for the chalcogenide glass are presented at the infrared wavelengths.

Table 1. Stress-optical constants, q_{11} and q_{12}, and elastic compliance, s_{12}, in units of 10^{-12} m^2/N.

	n[a]	q_{11}[b]	q_{12}[b]	$q_{12}-q_{11}$[b]	s_{12}[b]
As_2S_3					- 18.6, - 18.8[c]
0.6328 μm	2.606	7.63	6.36	- 1.27	
1.15 μm	2.452	7.64	6.54	- 1.10	
10.6 μm	2.354	8.23	6.95	- 1.28	
Chalcogenide Glass (Ge 33%, As 12%, Se 55%)					- 12.0, - 12.2[d], - 11.5[e]
1.15 μm	2.5704	5.32	4.89	- 0.43	
10.6 μm	2.4919	5.42	4.94	- 0.48	
Polycrystalline ZnSe					- 4.0
0.6328 μm	2.578	- 1.34	0.29	1.62	
1.15 μm	2.465	- 1.37	0.62	1.98	
10.6 μm	2.408			1.96	

[a] These values were not measured in this work, but are given because they were used to calculate the q_{ij}. The values for ZnSe are from single crystal data.

[b] Estimated accuracy of numbers from this work is ±2%.

[c] F. W. Glaze, D. H. Blackburn, J. S. Osmalov, D. Hubbard, and Mason H. Black, J. Res. Natl. Bur. Std. 59, 83-92 (1957).

[d] Ray Hilton, private communication -- value for Texas Instruments.

[e] Ray Hilton, private communication -- value for Bell Laboratories.

The birefringence of the above infrared glasses is of opposite sign to most optical glasses [17]. The q_{11} is greater than the q_{11} of most optical glasses by a factor of ten, and q_{12} is greater than the q_{12} of most optical glasses by a factor of three [18].

From the theory of photoelasticity and from the data, we expect that the refractive index of the ZnSe will decrease under hydrostatic pressure. This behavior has been observed previously in single crystal ZnS [19]. Since dn/dT for ZnS is positive [20], it would be of interest to observe whether the same is true for ZnSe. In addition, for ZnSe there is a large dispersion in q_{12}.

Also included in Table 1 are the values we have obtained for s_{12}. Agreement with the values of other workers is very good.

5. Summary

We have outlined the program of optical materials characterization at the National Bureau of Standards. The properties that we are measuring are refractive index, change of index with temperature, thermal expansion, stress-optical coefficients, and elastic constants. At the present time, primary interest is in laser window materials at 10.6 μm. Data have been presented on chalcogenide glass, As_2S_3, polycrystalline ZnSe, and crystalline KCl. Measurements on these materials and on other infrared

laser window materials are in progress. In addition, we are developing more sensitive techniques for measuring the stress-optical coefficients in materials that exhibit a small stress-optical effect.

A similar need exists for optical materials characterization in the ultraviolet. Techniques similar to those we have used in the infrared can be employed in the ultraviolet should the need arise.

6. Acknowledgments

We would like to acknowledge the receipt of samples from Carl Pitha of AFCRL, Bennett Sherman of the Servo Corporation, Ray Hilton of Texas Instruments, Phillip Klein of NRL, and Colonel William Goldberg of AFML. We would like to thank W. J. McKean for his technical assistance.

7. References

[1] B. Bendow, P. D. Gianino, A. Hordvik, and L. H. Skolnik, Optics Commun. 7, 219 (1973).

[2] B. Bendow and P. D. Gianino, Appl. Phys. 2, 1 (1973).

[3] C. S. Sahagian and C. A. Pitha, AFCRL-72-0170, 9 March 1972, Special Reports No. 135.

[4] C. A. Pitha, AFCRL-TR-73-0372(1), 19 June 1973, Special Reports No. 162, Vols. I and II.

[5] R. L. Abrams and D. A. Pinnow, J. Appl. Phys. 41, 2765 (1970).

[6] F. Twyman and J. W. Perry, Proc. Phys. Soc. London 34, 151 (1922).

[7] K. Vedam and S. Ramaseshan, in Progress in Crystal Physics, Vol. I, edited by R. S. Krishnan (Interscience Publishers, New York, London, 1958), pp. 102-138.

[8] C. Weir, S. Spinner, I. H. Malitson, and W. J. Rodney, J. Res. Natl. Bur. Std. 58, 189 (April 1957), RP2751.

[9] L. W. Tilton, J. Res. Natl. Bur. Std. 2, 909 (1929), RP64.

[10] F. F. Martens, Ann. d. Phys. 6, 603 (1901).

[11] A. Smakula, Office of Technical Services, U. S. Department of Commerce (October 1952), p. 81.

[12] Z. Gyulai, Z. Phys. 46, 80 (1927).

[13] Reference 11, page 66.

[14] J. B. Saunders, J. Res. Natl. Std. 35, 157 (1945), RP1668.

[15] R. S. Krishnan, in Progress in Crystal Physics, Vol. I (Interscience Publishers, New York and London, 1958).

[16] N. Born and E. Wolf, Principles of Optics, (Pergamon Press, 1970), p. 303.

[17] R. M. Waxler and A. Napolitano, J. Res. Natl. Bur. Std. 69A, 325 (1965).

[18] K. Vedam, Proc. Indian Acad. Sci. [A] 31, 450 (1950).

[19] R. M. Waxler, IEEE J. Quant. Electron. QE-7, 166 (1971).

[20] Reference 15, page 146.

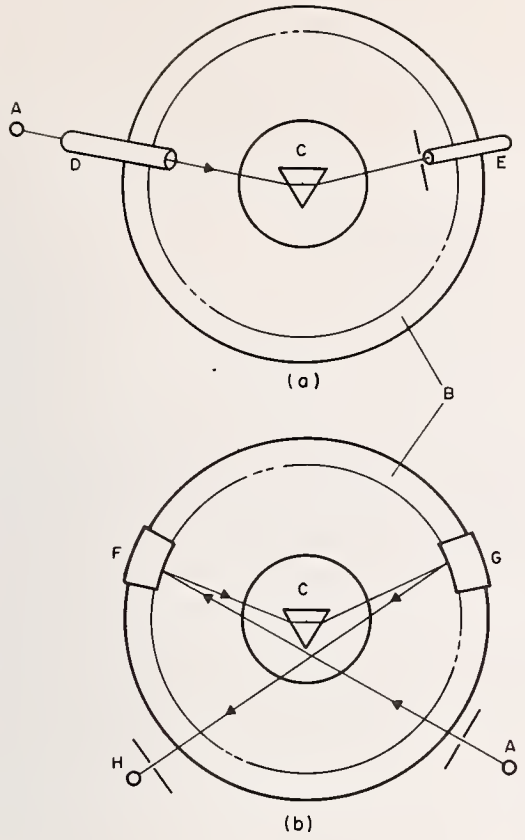

Figure 1. (a) Schematic of spectrometer used for visible-region refractometry. A. source; B. divided circle; C. prism table; D. collimator; E. telescope. (b) Schematic of spectrometer used for non-visible-region refractometry. A. source; B. divided circle; C. prism table; F. collimating mirror (fixed); G. movable mirror; H. detector.

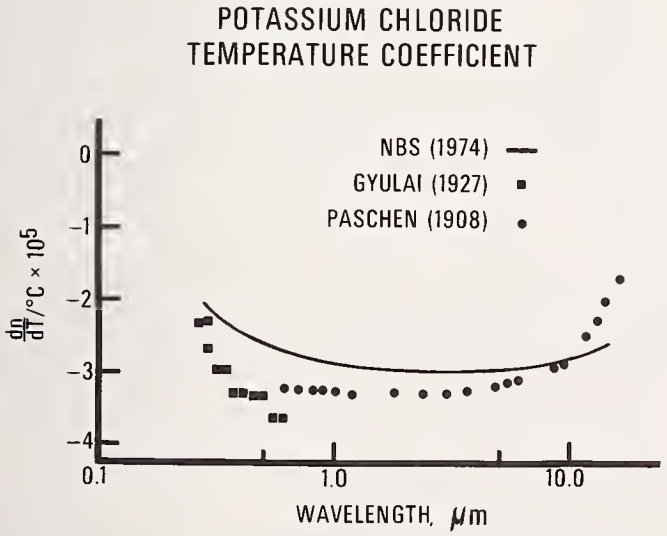

Figure 3. Temperature coefficient of refractive index of KCl.

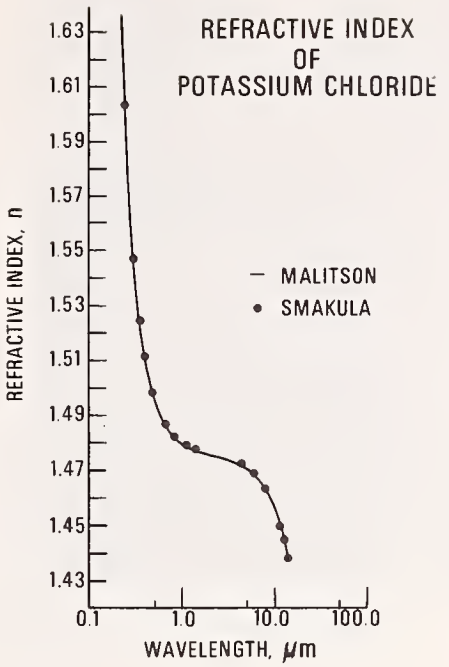

Figure 2. Refractive index of KCl at 20°C.

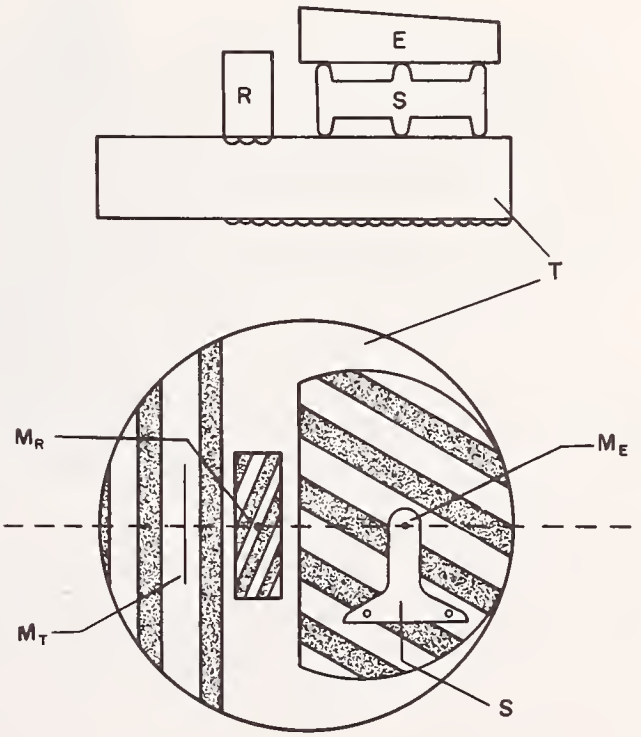

Figure 4. Interferometer assembly for the measurement of thermal expansion and thermal change in refractive index. E. an interferometer plate; S. thermal expansion specimen; R. refractive index specimen; T. interference thermometer; M_E, M_R, and M_T, reference lines for the interference fringes of thermal expansion, refractive index change and temperature change.

Figure 5. Stressing apparatus with specimen, load cell, and digital voltmeter readout.

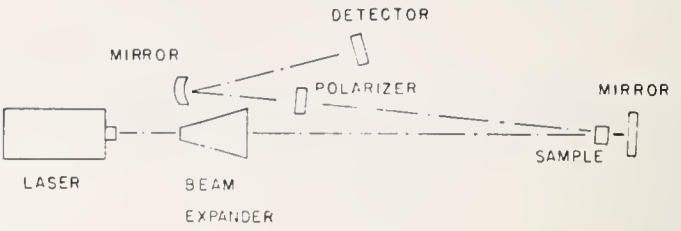

Figure 6. Experimental arrangement for measuring stress-induced birefringence.

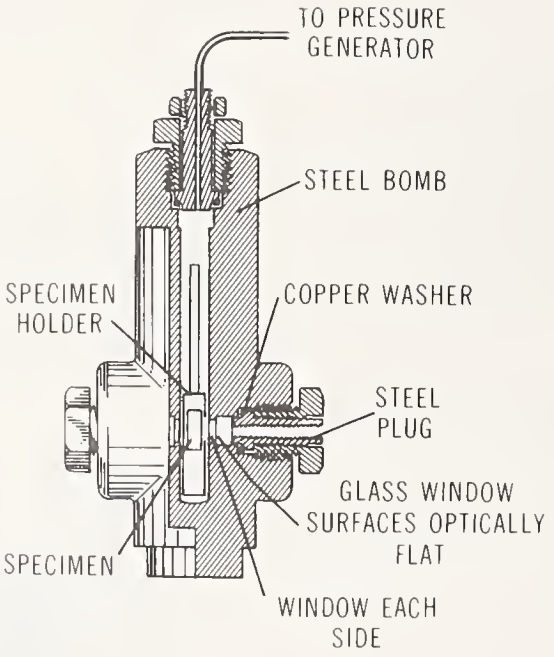

Figure 7. Pressure vessel.

NO COMMENTS ON PAPER BY FELDMAN.

4.2 Testing the Surface Quality of Laser Materials

M. J. Soileau and H. E. Bennett
Michelson Laboratory, Naval Weapons Center
China Lake, California 93555

Research presented at the 1973 Laser Damage Symposium clearly showed that surface microcracks and pits influence laser damage thresholds for optical materials. In addition, backscatter from laser amplifiers can result in damage to oscillator optics in high power oscillator-amplifier systems. The scratch and dig specifications presently used to specify optical surface quality are inadequate since (1) they address only the problem of surface irregularities larger than 2 μm (Bloembergen has shown theoretically that pits or scratches as small as 100 Å can significantly reduce damage thresholds), and (2) compliance is determined in a subjective manner. The relationship between surface quality and light scattering from transparent optical components is discussed, and an instrument for measuring bulk scattering and surface quality described. Quantitative measurements on a set of standard scratches and digs are presented, as well as measurements of surface imperfections and bulk scattering in optical materials used in infrared laser systems.

Key words: Laser damage; light scattering; optical surface quality; scratch detection.

1. Introduction

Surface quality is extremely important in determining the resistance of an optical element to laser damage. Some of the surface properties which influence laser damage thresholds are: (1) surface defects such as pits and microcracks, as proposed by Bloembergen [1][1], (2) subsurface defects caused by polishing damage, suggested by Giuliano [2], and (3) surface microroughness which may lead to resonant absorption, as proposed by Decker. [3] The surface quality specification presently being used (MIL-O-13830A, the so-called scratch and dig specification) is inadequate since (1) it treats only the problem of surface irregularities larger than 2 μm (Bloembergen has shown theoretically that pits or scratches as small as 100 Å can significantly reduce damage thresholds) and (2) compliance is determined in a subjective manner. Other techniques commonly used to determine surface quality are visual inspection, inspection under a microscope, and specifying the type of polish that should be used to produce the surface, i.e., "super polish" as opposed to standard polish. The various microscopic techniques (Nomarski, dark field, SEM, etc.) serve a very useful purpose in qualitative assessment of surface quality, but give little quantitative information. The term "super polish" is used to describe surfaces prepared by bowl feed, recirculating slurry, or other similar techniques which differ from classical fresh feed polishing procedures. The use of nonstandard polishing techniques does not ensure superior surface quality; thus, specifying the type of polish does not specify surface quality.

In addition to the surface-related problems, bulk imperfections such as voids and inclusions can cause lower damage thresholds. Scattered light from surface and bulk imperfections can also result in damage to components in high gain oscillator-amplifier systems. In this paper an instrument for measuring bulk scattering and surface quality is described, and preliminary results on laser window materials are reported. Quantitative measurements on a set of standards using light scattering techniques can form the basis for surface and bulk quality specifications for laser windows.

2. Instrument Design

The basic concept used in the design of the Optical Functional Tester (OFT) [4] was to make an instrument which could characterize optical components objectively in terms of scattered light from the optical element and also in terms of present standards. The instrument was to be capable of measuring both reflecting and transparent optics in the visible and the infrared. An additional design constraint was that the instrument be capable of measuring scattering from the surface and the bulk of the component to be evaluated.

1. Figures in brackets indicate the literature references at the end of this paper.

The OFT is shown in figures 1 and 2 in its present configuration. A schematic diagram of the instrument is shown in figure 3. A light beam from a HeNe laser, operating at either 0.6328 μm, 1.15 μm, or 3.39 μm, is filtered, chopped at 13 Hz, and transmitted through the sample. (The sample is mounted on a fixture that allows it to be accurately aligned and rotated so that all of it can be scanned. It is positioned using a fiber optic microprobe.) The transmitted light passes through the Coblentz sphere (collecting mirror, M_c) and is measured by pyroelectric detector D_2. The scattered light strikes the Coblentz sphere M_c and is imaged on pyroelectric detector D_1. The signals from both detectors are fed into lock-in amplifiers, and the outputs are ratioed by a digital voltmeter. This ratio of the scattered light to the transmitted light (or reflected light if a mirror is being evaluated) is displayed on a chart recorder.

The system can be used to evaluate reflecting optics by placing the laser in the position indicated as Laser Mirror Mode. In this case the detector D_2 would be moved slightly off-axis to allow clear passage of the illuminating beam, and would be used to collect the specularly reflected beam. The scattered light would be collected by the Coblentz sphere in the same manner as before.

An additional element, not shown in the diagram, is an infrared filter placed between the laser and the sample that is used whenever the system is operating in the infrared. The purpose of the filter is to eliminate stray, incoherent visible light from the laser which is always present when the laser is tuned for an infrared line. Apertures, also not shown, are inserted between the chopper and the sample to constrain the light beam and eliminate light diffracted from the edges of the chopper blades.

The OFT uses only reflecting optics and broad band pyroelectric detectors. Thus, it can operate over an extended wavelength range from the ultraviolet through the visible and into the infrared merely by changing the laser source. Laser sources now commercially available extend from about 0.25 μm to 10.6 μm.

In its present configuration, the instrument measures total scattering from both the surfaces and from the bulk of the component being tested. Because of the small f number of the collecting sphere, the depth of focus at the detector is small. Contributions from the bulk of the sample and from either of the two surfaces could thus be separated by restricting the detector aperture and by fine focusing.

3. Evaluation of Surface and Bulk Scattering

The OFT measures scattered light from both surfaces of the sample as well as volume scattering from the bulk of the material. Since the Coblentz sphere has an f number of about 0.5, the depth of focus at the detector is quite small. The detector itself has a fairly large sensitive area (5x5 mm), but by aperturing it to the size of the incident laser beam, a small depth of field at the sample position is achieved. In this way, the contribution from a particular surface or volume element in the sample is maximized. Consider a sample of thickness t positioned so that the front surface of the sample (z = 0) is in focus on the detector aperture. Letting S_ℓ be the total amount of scattered light passing through the aperture, we have

$$S_\ell = aS_o + b(t)S_t + \int_o^t \gamma(z)S_b dz \qquad (1)$$

where S_o is the light scattered in the forward direction by the front surface, S_t forward scattering from the back surface, and S_b forward scattering per unit volume in the bulk of the material. The quantities a, b and $\gamma(z)$ are geometrical acceptance coefficients determined by the aperture and the angular dependence of the scattering. If the front of the sample is positioned at the focus, $a \cong 1$. The back surface will then be out of focus so that the coefficient $b(t) \ll 1$. It will vary depending on sample thickness, refractive index, and the angular dependence of the scattering from the back surface as well as on the aperture used. Bulk scattering occurs between z = 0 and z = t so that γ will have limits $a > \gamma(t) > b$ provided the angular dependence of surface and bulk scattering are not too different.

Approximate values of the acceptance coefficients can be determined experimentally for a "typical" component by measuring a sample one of whose faces scatters heavily. If we assume that without the aperture the detector records essentially all of the forward scattering from the sample, then if the high scatter surface is in the back position, the ratio of signals recorded with and without the aperture gives b. The value of a can be determined by positioning the high scatter surface at the focus, and the value of γ can be determined approximately by translating the high scatter surface between the back position and the focus position.

If the fractional scattering per unit volume is the same throughout the specimen, we can remove S_b from under the integral in eq. (1) and obtain

$$S_b = \frac{S_\ell - aS_o - bS_t}{\int_o^t \gamma(z)dz} \quad . \tag{2}$$

In the general case all quantities on the right side of eq. (2) are now known except S_o and S_t. The backscatter from the sample surfaces can be determined by coating the surfaces with an opaque metal film and measuring the total integrated scatter in reflection using the Optical Evaluation Facility. [5] If we assume that the forward and backscattering from a surface are approximately equal (there is experimental evidence to support this assumption as discussed below), we can obtain the bulk scattering from eq. (2). Thus we have, on a "first cut" basis, separated the surface and volume scattering coefficients and have obtained approximate values for each.

4. Scattering Levels in KCl and ZnSe

The OFT was used to measure surface and bulk scattering parameters of several candidate infrared laser window materials, including hot rolled KCl [6], hot forged Eu^{++} doped KCl [7], laser grade "polytran" KCl [8], and ZnSe grown by chemical vapor deposition. [9] A crucial assumption in the separation of bulk and surface scattering is that the total integrated scatter in the forward and back directions from such surfaces be approximately equal. To check this assumption, the forward scattering of two of the KCl samples and two polished quartz samples was measured at 6328 Å. No bulk scattering could be observed visually from these samples, eliminating the third term of eq. (1) and making it possible to measure forward scattering from the surfaces unambiguously. The samples were then coated with silver and the backscattering measured using the Optical Evaluation Facility. [5] Care was taken that exactly the same area of the samples was measured with each instrument. The results are given in table 1 in terms of derived surface roughness. There is good agreement between the backscattering and forward scattering results, indicating that for these quite rough samples and also for the relatively smooth samples the assumption that forward and backscattering are approximately equal is valid. (The roughnesses of the KCl blanks reported in table 1 are typical of many polished KCl surfaces. However, smoother KCl surfaces can be obtained. Using bowl feed with a triacetin slurry we have produced optically flat surfaces with roughnesses under 40 Å rms on both hot rolled KCl and polytran.

The Eu^{++} doped KCl and the ZnSe specimens exhibited significantly more bulk scattering than did the other KCl samples. A preliminary analysis of bulk scattering in these materials was performed at 0.6328 and 1.15 μm using eq. (2); the results are given in table 2. Based on these two wavelengths, the bulk scattering from the KCl sample seems to decrease with wavelength approximately as $1/\lambda^2$, whereas the ZnSe goes approximately as $1/\lambda$. One should be extremely cautious about extrapolating these results to longer wavelengths, but if the trend continues, at 10.6 μm the forward scattering from the bulk would be 2 to 4 x 10^{-4} cm^{-1} for both materials. The total amount of light scattered per cm of path would be twice these values and would be comparable to that absorbed per cm at 10.6 μm. Such scattering levels would result in increased window absorption for geometries where significant total internal reflection occurs, as well as increasing the possibility of damage to the oscillator-amplifier part of the laser. The scattering centers may also act to reduce the threshold for laser damage of the materials.

Table 1. Roughness of polished KCl and quartz surfaces

Specimen	Roughness (Å rms)	
	TIS (backscatter)	OFT (forward scatter)
Hot rolled KCl	164	151
Polytran (KCl)	115	124
Quartz No. 1	13.1	12.4
Quartz No. 2	17.8	20.9

Table 2. Bulk scattering measurements (forward scattering)

Specimen	0.6328 μm	1.15 μm
KCl (Eu^{++})	0.028 cm^{-1}	0.010 cm^{-1}
ZnSe No. 556	0.026 cm^{-1}	0.016 cm^{-1}
ZnSe No. 554	0.069 cm^{-1}	0.036 cm^{-1}

5. Scratch Detection

The laser damage threshold of laser windows is significantly lowered if scratches are present on the window surface. [1] Scratches also contribute to scattered light, although in a well polished surface most of the scattered light results from closely spaced microirregularities only a few tens of angstroms in height, not from the few scratches on the surface. If a scratch is present on a surface which is scanned by a light beam, when the light strikes the scratch the scattered light level goes up. Thus, by relating the scattered light to the scratch size, we may hope to develop a rapid, simple, reliable and inexpensive method for checking laser components for scratches.

The currently accepted technique for determining the surface quality of optical elements is described in MIL-O-13830A, the scratch and dig standard specification. This test is difficult, only semiquantitative, and must be performed visually by a skilled and painstaking inspector if it is to be meaningful. A comparison is made between the scratches that can be seen on the surface to be tested and those on a MIL Surface Quality Standard for Optical Elements. The finer scratches on this standard are extremely difficult to see. However they can be revealed by using Nomarski (Differential Interference Contrast) Microscopy as shown in figure 4. Dig standards are also shown. [10] Both are scribed on 1.5 inch diameter glass substrates that are mounted in a glass case through which measurements are made.

An attempt was made to measure the scattering of the standard scratches through the glass case. However, this was unsuccessful because of the high level of scattering from the encapsulating surfaces. The standards were then removed from the glass case and evaluated with the OFT. The results of these measurements are summarized in figures 5 and 6. The scattering levels of each of the standard scratches are plotted in figure 5 along with 600X Nomarski micrographs of each scratch. Note that the scattering level of the #10 scratch is higher than that of the #20 scratch. In addition, the average scattering from the substrate on which the #10 scratch is scribed is higher than the peak scattering for the #20 scratch. This discrepancy on the standard designed to evaluate surface quality as related to scattering illustrates the importance of surface microirregularities as well as scratches and digs in determining the quality of an optical surface.

Figure 6 illustrates the sensitivity of the OFT. The trace on the left is identical to that shown in figure 5. In the trace to the right the system gain was increased by a factor of 100 to bring out the #20 scratch. As can be seen in the micrograph of this scratch in figure 5, the substrate for the #20 scratch is markedly smoother than than for the #10 scratch and the scratch is narrower and better defined.

The ability of the OFT to identify and make quantitative measurements on scratches and digs on actual components is demonstrated from measurements of the surface quality of an infrared transmitting dome. In figures 7-9, actual scattered light scans of the clear dome at 0.6328 μm are presented. The three traces in figure 7 correspond to complete circular scans at various positions off the dome optical axis (5°, 10.0° and 20.4° from the dome center). A large scratch is indicated in the 5° off-axis scan. The scattering level from this scratch corresponds to that of a #60 scratch.

Figure 8 illustrates the ability of the OFT to identify and track a surface scratch. The dome was displaced 0.5° (approximately 1/3 mm) between each successive scan. The two large "bumps" in the curves in figure 8 correspond to the same scratch. The dome was 50% overscanned to demonstrate the repeatability of the data. Thus, each scan corresponds to approximately one and one-half times around the dome at a given position off the dome axis. From this type of measurement one can determine the number of scratches, their location on the surface, the length of the scratches and the average scattering level of the dome caused by microirregularities.

In figure 9 two complete scans displaced by 1/3 mm from the dome center are shown. The scratch indicated in this scan corresponds to a #40 standard scratch. Note that the scratch is in both scans, whereas the dig is present in only one. The double peak between the #40 scratch and the dig in the trace to the left in figure 9 is indicative of a scratch on the order of a #10 standard scratch or smaller.

6. Conclusion

Scratches or pits in optically polished surfaces, and voids, impurity clusters and other volume defects all act to reduce the damage threshold of laser windows. They also produce scattered light which can damage components in a laser optical train. The sensitivity of scattering to bulk and surface defects can, however, be used to advantage in testing for the presence of such defects. For maximum sensitivity the measurements should be made at as short a wavelength as is feasible, since the scattering cross section of most defects increases with decreasing wavelength.

An instrument, the Optical Functional Tester (OFT) has been built for evaluating surface and volume defects in optical components. By scanning a narrow beam across the sample, both the surface and the volume may be checked for defects in a fraction of the time required for visual inspection. In addition, the scattered light test is quantitative, not subjective, and can detect defects which are virtually impossible to see visually. Scratch and dig standards currently used to specify optical surfaces can be extended by defining scratch size in terms of light scattering at a given wavelength. The position and size of even minute scratches on the surface can then be readily determined. It should then be possible to relate scratch size to damage threshold quantitatively. In addition, since microroughness as well as scratches and digs affects surface scattering, a better measure of true surface quality can be achieved.

Finally, measurement of scattered light at the operating wavelength of the laser furnishes a functional test of the component performance in use. The system designer can then intelligently specify what scratch/dig value and what microroughness the surface should have for a given application. He can also test for volume defects by determining volume scattering levels. For example, scattering measurements made with the OFT show that some CVD grown ZnSe has high volume scatter as does some KCl doped with Eu^{++} for high strength. It will be interesting to see if these defects cause a significant reduction in damage threshold or result in large scattering levels at 10.6 μm.

7. Acknowledgment

The authors are grateful to Mr. G. J. Hutcheson of the Army MICOM for use of the OFT, which was built by NWC under contract to MICOM. In addition, we are grateful to Dr. E. Bernal G. of Honeywell and Mr. John Fenter of AFML for providing such interesting specimens for measurement.

8. References

[1] Bloembergen, N., Appl. Opt. 12, 661 (1973).

[2] Giuliano, C. R., in *Laser Induced Damage in Optical Materials: 1972*, A. J. Glass and A. H. Guenther, eds. (NBS Spec. Pub. No. 372), pp. 55-57.

[3] Decker, D. L., *High Energy Laser Mirrors and Windows* (Semi-Annual Report No. 4, ARPA Order 2175, Naval Weapons Center, March 1974), pp. 66-83.

[4] Bennett, H. E., Soileau, M. J., and Hutcheson, G. J., U.S. Army Missile Command Technical Report QR-TR-74-1, March 1974.

[5] Bennett, H. E., and Archibald, P. C., elsewhere in these proceedings (1974).

[6] Produced and sent to us by Dr. R. Bernal G. of Honeywell, Inc. for evaluation.

[7] Produced by Honeywell, Inc. and supplied to us for evaluation by John Fenter, Air Force Materials Laboratory.

[8] Produced by Harshaw, Inc.

[9] Produced by Raytheon, Inc. and supplied to us for evaluation by John Fenter, Air Force Materials Laboratory.

[10] The scratch standards, Serial No. F-66-1268 and dig standards, Serial No. F-66-1277 were kindly provided by Mr. Nate Scott of the Frankford Arsenal, U.S. Army, Philadelphia, Pennsylvania.

9. Figures

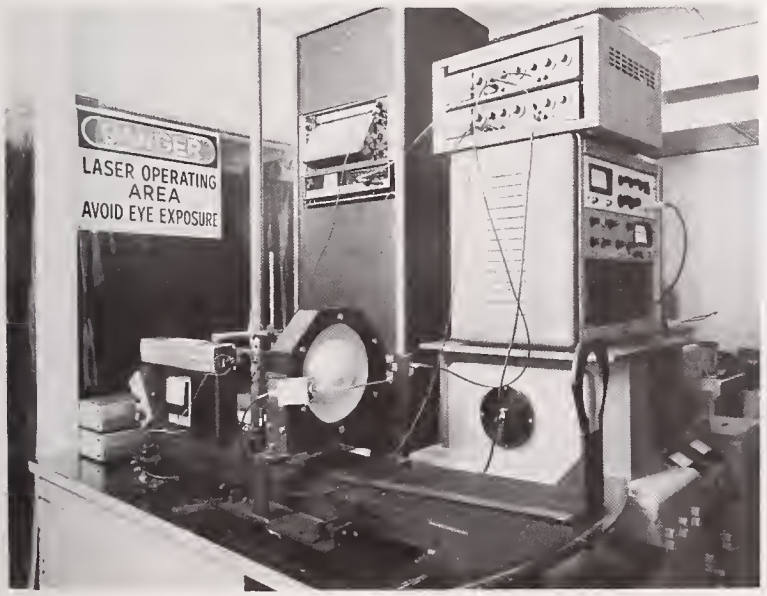

Figure 1. Photograph of the Optical Functional Tester showing overall view and associated electronics.

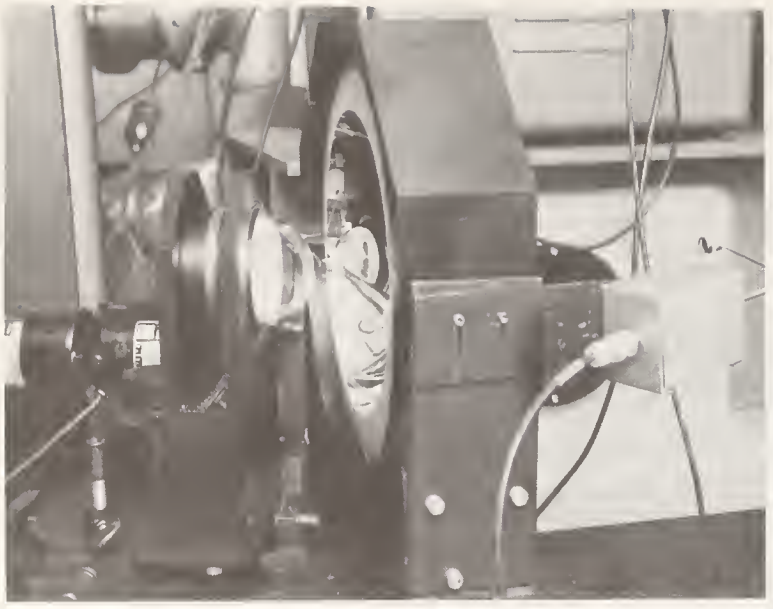

Figure 2. Close-up of OFT. The fiber optics sample positioner, Coblentz sphere, transmitted and scattered light detectors, and an infrared transmitting dome are shown.

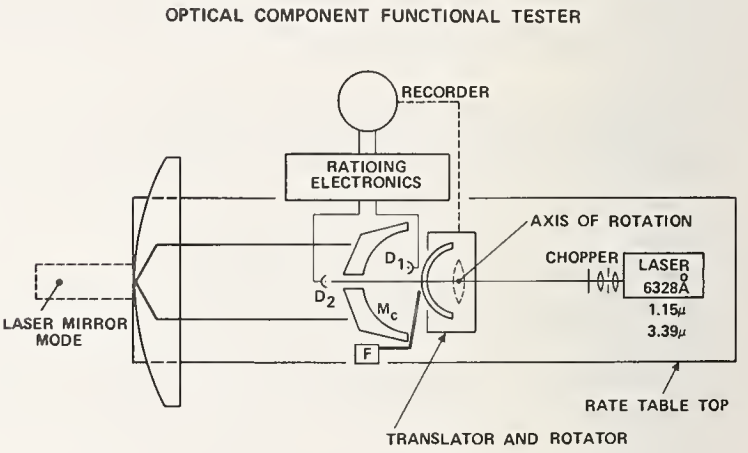

Figure 3. Schematic diagram of the OFT. Light from a laser source is used to illuminate the sample being tested. The transmitted light is measured by detector D_2, and the scattered light is collected by the Coblentz sphere, M_C, and imaged on detector D_1.

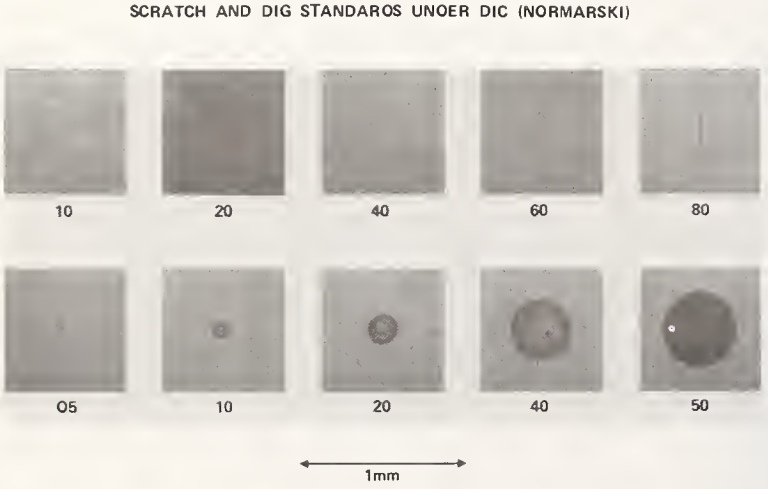

Figure 4. MIL Surface Quality Scratch and Dig Standards for Optical Elements. Photographs are 600X Nomarski micrographs taken through the sealed glass case in which the standards are stored.

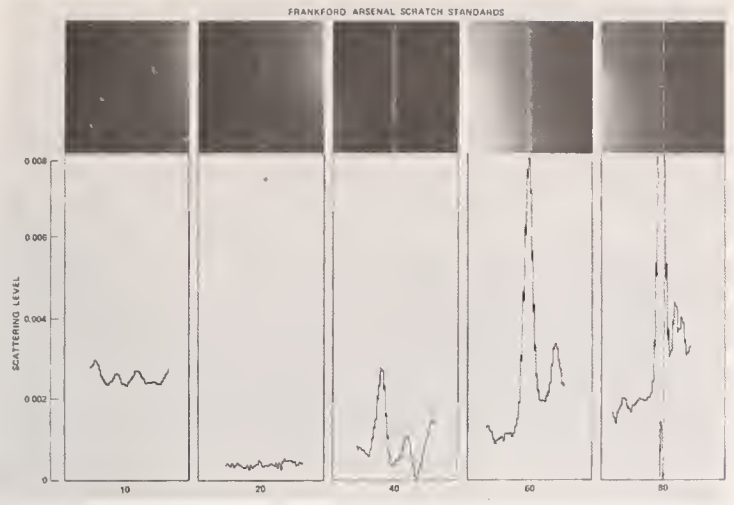

Figure 5. Nomarski micrographs and OFT traces of the scattering levels from standard scratches at 0.6328 μm.

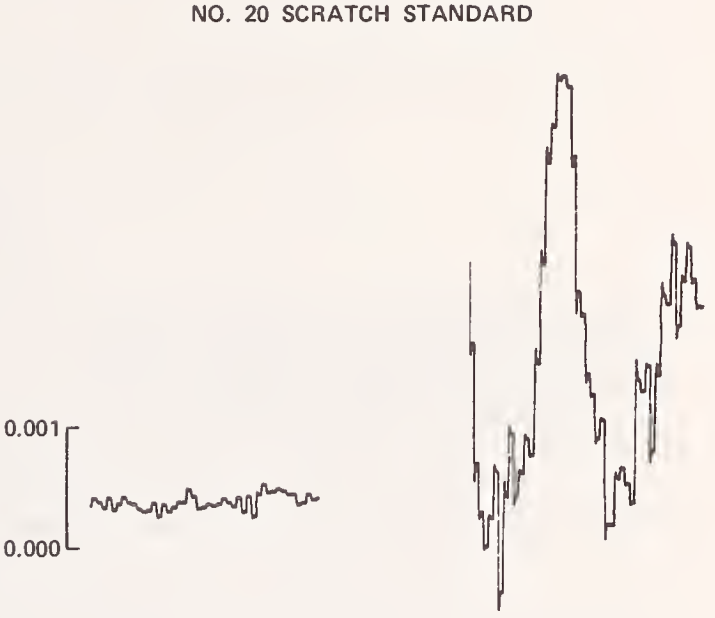

Figure 6. OFT trace of the scattering from the #20 standard scratch at 0.6328 μm. The scale on the left is the same as in figure 5. The trace on the right was generated using a factor of 100 increase in gain in the detector electronics. This figure illustrates the sensitivity of the OFT to extremely low levels of scattered light.

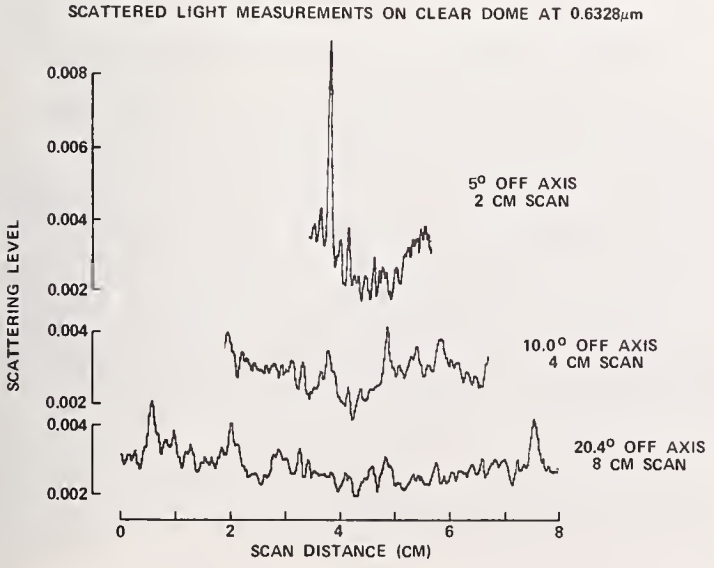

Figure 7. Representative scans of the scattering level of the infrared dome at various distances off-axis. The scale at the bottom of the figure corresponds to the circumference of the dome at the position of the scan.

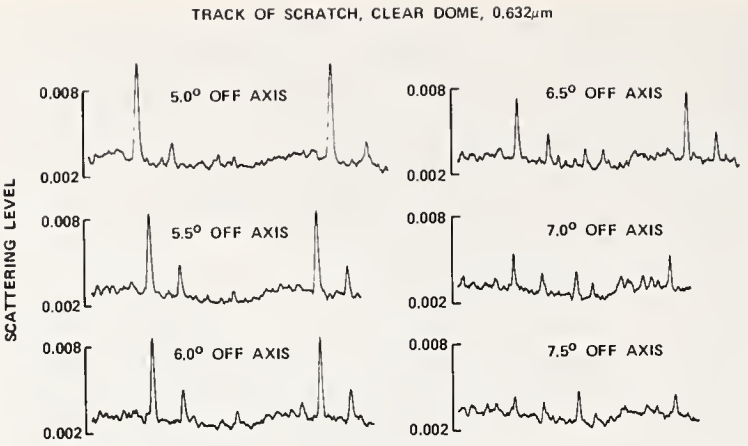

Figure 8. Scans made 5 to 7.5° off axis on the infrared transmitting dome at 0.6328 μm. The dome was overscanned by about 50% to demonstrate repeatability. Thus, the two large peaks in each scan represent the same scratch on the dome surface. This scratch corresponds to a #60 standard scratch.

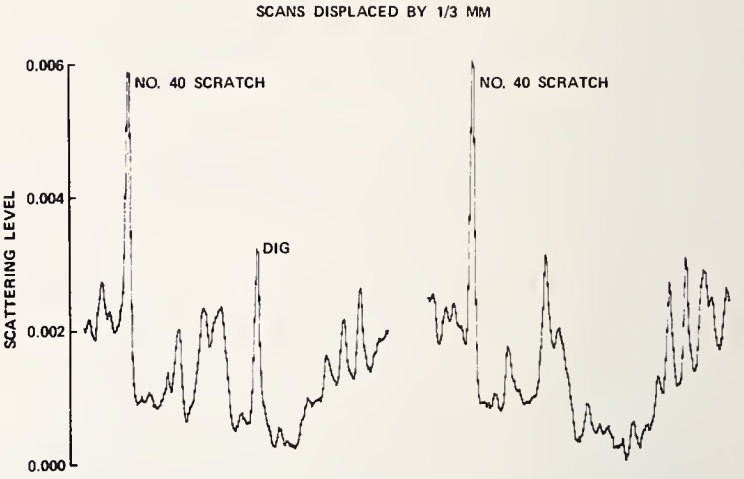

Figure 9. Illustration of the ability of the OFT to detect digs as well as scratches. The scans were generated by displacing the dome by 1/3 mm off axis.

COMMENTS ON PAPER BY SOILEAU

Norman Boling of Owens-Illinois commented that since it seemed rather easy to obtain surfaces with RMS roughness of 30 Å and that according to Bloembergen's theory, cracks and crevices of less than 100 Å dimension did not lead to significant field enhancement, that current polishing techniques would seem to be entirely adequate to raise surface damage thresholds to their intrinsic levels. It was pointed out, however, in discussion that with a 30 Å RMS variation of the surface there would be a significant number of 100 Å cracks and scratches in the surface. Harold Posen of the Air Force Cambridge Research Laboratory pointed that the measurement of the RMS roughness of the surface was not in itself entirely indicative of the damage resistence of the surface, but instead that the correlation distance across the surface was also a significant perameter. In response to a question as to the origin of the scattering that was observed, the speaker commented that it was probably from gross scratches on the surface rather than from the RMS micro roughness. This was further supported by results obtained using FECO interferometry. A further test of the scattering mechanism would be the polarization dependence of the scattering which, however, had not been measured at the time of the preparation of the paper.

4.3 Statistical Characterization of Mirror and Window Surfaces

Jean M. Bennett

Michelson Laboratory, Naval Weapons Center
China Lake, California 93555

In order to evaluate the contribution of surface structure to laser damage and to calculate the magnitude and angular distribution of scattered light from laser mirrors, windows, and other optical surfaces, the autocovariance function, rms roughness and height distribution functions are required. These and other statistical parameters for optical surfaces can now be determined with a FECO Scanning Interferometer, which consists of a FECO interferometer, slow scan television camera, signal averager, minicomputer, and teletype. Wavelengths are measured at 512 equally spaced points along the length of an interference fringe (which contours irregularities on the optical surface under investigation). The fringe length corresponds to a total length of 1 mm on the interferometer surface. The statistics for the surface are obtained from the wavelength data. The system has the advantages that it does not depend on visual estimates of fringe width to yield a value of the rms roughness, and additional statistical information such as the autocovariance function and height distribution function can be obtained which cannot be determined visually.

Key words: Autocovariance laser damage statistical characterization of surface; FECO interferometry; scattered light; surface roughness.

1. Introduction

The surface structure of optical elements, and in particular the surface microroughness, is of importance in laser applications for three main reasons. First, surface microroughness produces scattered light. Unwanted scattering not only decreases the intensity of the main beam, but more importantly it can produce spurious signals and, in the case of backscattering, it can cause damage to the laser components. Surface absorption can also be caused by surface microroughness. In mirrors, surface roughness can increase the absorption by as much as a factor of three; the situation for windows is not so clear, but some experiments indicate that here also the surface absorption is related to surface microroughness. Finally, surface structure plays a role in laser damage in windows. Theoretical studies indicate that microcracks of dimensions as small as 100 Å may induce dielectric breakdown in transparent solid materials [N. Bloembergen, Appl. Opt. 12, 661-664 (1973)].

It is not possible to deduce the surface structure unambiguously from measurements of scattered light, and at best measurements of this type give indirect evidence about the surface roughness and whether or not the surface has Gaussian statistics. We have developed a method for directly measuring the statistical parameters of plane optical surfaces. These parameters include the rms roughness, rms slope, autocovariance function, height distribution function, and slope distribution function. The lateral resolution limit of the measurements is about 2 microns, but the depth resolution is of the order of a few angstroms. In this paper we will describe the FECO Scanning Interferometer with which we obtain the data, and give examples of typical results we have obtained to date.

Figure 1 shows a photograph of the FECO Scanning Interferometer and a schematic view is shown in figure 2. White light from a xenon arc Z is collimated by lens L_1 and directed onto the sample at normal incidence by means of beam splitter B. The sample, which has been overcoated with an opaque layer of silver to increase its reflectance, is placed nearly in contact with a supersmooth optical flat (roughness less than 10 Å rms) that has been coated with an ~ 95% reflectance semitransparent silver film. Fringes of equal chromatic order (FECO fringes) are formed by interference of multiply-reflected beams between these two surfaces, and contour irregularities on each surface. Lens L_2 focuses an image of the interferometer on the slit S of a constant deviation prism spectrograph, and the FECO fringes can be observed visually in the image plane, photographed, or detected with a slow scan TV-type camera. By scanning one line at a time with the TV camera, information in digital form is obtained from the signal averager, which when analyzed by the minicomputer yields the wavelength of the portion of the fringe contained in the scan line. Thus, wavelengths at 512 equally spaced discrete points along the length of the fringe are obtained. These are then converted by another computer program into height differences above and below the mean surface level, and the statistics of the sample are then obtained. The spacing between the scan lines is set approximately equal to the resolution of the optical system, so that statistical information is obtained at approximately 2 micron

increments along the fringe. The fringe actually corresponds to a rectangular area on the sample 1 mm in length. The width of the rectangle is determined by the width of slit S, which is approximately 2 microns. Thus, the statistics of the surface roughness are effectively for little squares on the surface, 2 microns on a side.

We have studied various types of surfaces including very smooth polished optical glasses (Cervit, fused quartz), polished fluorides (magnesium fluoride, calcium fluoride), polished alkali halides (potassium chloride, sodium chloride), polished metals (molybdenum, copper, TZM, titanium, stainless steel), and machined copper. Results for representative samples will be given here. Figure 3 shows data for Cervit, a polycrystalline quartz with a very low expansion coefficient. This sample had a roughness of 8 Å rms, as determined from visual measurements of the fringe width and corroborated by scattered light measurements. The Polaroid photograph shows the general nature of the fringe, which in this case is quite straight and structureless. We think that the variations shown in the trace from the scanning camera in this case are mainly variations in the reproducibility of the system rather than structural details on the fringe. For the rougher surfaces, there is excellent correspondence between structure shown in the Polaroid photographs and in the scanning camera traces. The autocovariance function in the lower part of the figure shows that the primary correlation on extremely smooth surfaces is short range in nature, and that there is very little long range waviness on the surface.

The height and slope distribution functions for the same Cervit surface are shown in figure 4. In both cases the histograms are the measured distribution functions and the smooth curves are Gaussians that have the same areas under the curves as do the measured ones. Notice that both the height and slope distribution functions are very close to Gaussian. This was found to be generally true for the surfaces we have examined, with a couple of exceptions to be noted later. Surfaces such as very smooth polished calcium fluoride, magnesium fluoride and the smoothest polished copper have height distribution functions and autocovariance functions which look quite similar to those we have just shown for Cervit.

As an example of a polished alkali halide surface, figure 5 shows data for one of the smoothest polished KCl surfaces which we have seen, having a roughness of 29 Å rms. The jagged character of the fringe is not much different from that of a polished plate glass surface, and the autocovariance function has the same general form as some polished metals, as will be seen later. However, in figure 6 we see that there are a few parts of the surface that have very large values of slopes, very large points and deep scratches. These curves are averages of 8 different scans, so the statistics should be reasonably good. In addition to the microstructure of scratches which is measured by the FECO Scanning Interferometer, polished KCl surfaces have large macroscratches which are clearly visible to the naked eye. Light scattered from these surfaces is affected by the macrostructure as well as by the microstructure. For this reason, rms roughness values derived from measurements of scattered light are always larger than the FECO values. The rms roughness of this surface deduced from scattered light measurements was 51 Å.

Figure 7 shows a photograph of the FECO fringe, the TV scanning camera trace, and the autocovariance function for a very smooth polished molybdenum surface, having a visually measured roughness of 22 Å rms. This material clearly has long range roughness characteristics as shown by the almost regular oscillations of the autocovariance function around zero. Histograms for the height and slope distribution functions for the same polished molybdenum surface are shown in figure 8. It is clear that both height and slope distribution functions are quite good Gaussians, although there are some rather large deviations from the Gaussian height distribution curve.

Figure 9 shows a photograph of the FECO fringe and other information for a 32 Å rms polished titanium surface. The interference fringe is very jagged, indicating scratches and peaks on the surface. This structure causes a very rapid oscillation of the autocovariance function around zero and an initial extremely precipitous drop from a maximum value at a zero correlation distance. Figure 10 shows that the height distribution function of the titanium surface has a general Gaussian shape, but there are some rather large excursions from the smooth curve. Part of this structure may be caused by the small number of scans on different parts of the surface used in the analysis. The slope distribution function is a very well behaved Gaussian with a majority of the facets having small slopes.

As a final example, figure 11 shows a copper surface that was prepared by single point diamond machining. Under Nomarski illumination one can sometimes see a pattern of grooves of varying periodicity from such a surface. For the better machined surfaces the groove patterns become indistinct and sometimes disappear entirely. A grooved pattern also shows up on the FECO fringes, and the extremely sharp character of the fringes clearly indicates that the grooves have smooth sides. In this figure we see an excellent correspondence between the undulations of the FECO fringe in the photograph and the undulations of the TV tracing of the fringe center line. This machined copper surface had a measured roughness of 47 Å, but the light scattered was equivalent to that from a much smoother surface. Measurements on a rougher machined copper sample gave a FECO roughness value of 70 Å, and a scattered light roughness value of about 35 Å. The structure in the autocovariance

function is undoubtedly related to the grooved nature of the surface. In figure 12 we see an anomaly in the slope distribution function, the only one of its kind we have observed. The first three slopes are equally probable rather than the smallest slope being the most probable. Also, the height distribution function is very jagged, undoubtedly because of the semiperiodic nature of the grooves.

In figure 13 we compare roughness values obtained from visual measurements of the peak-to-peak roughness to values obtained from the statistical analysis using scanning camera data. There is a good linear relationship between the two techniques which is very encouraging considering the subjective nature of the visual measurements. The main reason why the scanning camera measurements are consistently smaller is that the scanning camera picks out the center line of the fringe and ignores its width. Since the fringe width is caused by unresolved surface roughness as well as by the finesse of the interferometer, there is good theoretical justification why the scanning camera roughness values are smaller. Because of the linear relation between the two sets of roughness values, even though the slope of the graph differs from 45°, the scanning camera values can be corrected to give the visual roughnesses. The minimum visually determined roughness is 8 Å, while the minimum roughness value yielded by the scanning camera is about 3 Å. The latter value is determined by the reproducibility of the system. Thus, any structure in the fringe that is larger than about 3 Å can be detected by the scanning camera.

We are in the process of calculating the magnitude and angular dependence of the scattered light from the surface statistics we have shown here. We will then compare the calculations with direct measurements of scattered light using the Optical Evaluation Facility described by H. E. Bennett. Merle Elson is making the theoretical calculations.

In conclusion, I have described a FECO Scanning Interferometer which is capable of yielding statistical information on the roughness characteristics of optical surfaces. The system has the advantages that it does not depend on visual estimates of the fringe width to yield a value of the rms roughness, and additional statistical information such as the autocovariance function and height distribution function can be obtained which cannot be determined visually.

2. Figures

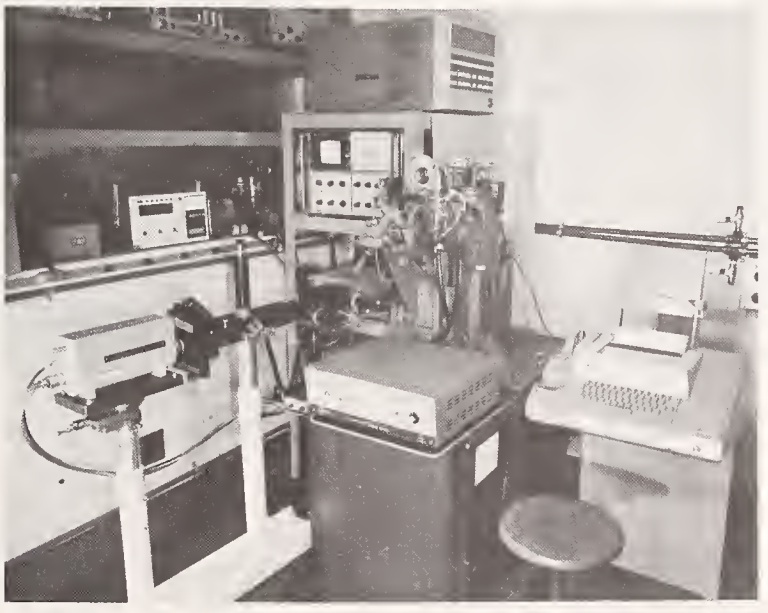

Figure 1. Photograph of the FECO Scanning Interferometer. The interferometer and light source are located near the upper center, the scanning camera is at left, signal averager and computer are at top center, and the teletype, used to communicate with the computer, is at right.

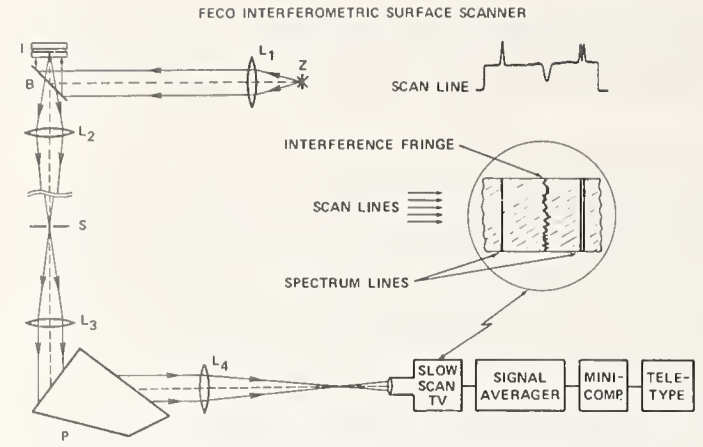

Figure 2. Schematic diagram of the FECO Scanning Interferometer. The spectrum, containing the interference fringe that contours irregularities on the optical surface, is scanned one line at a time by the slow scan TV camera, averaged by the signal averager, and processed by the mini-computer. Wavelengths at 512 equally spaced points along the fringe yield statistical information about the surface. The symbols are explained in the text.

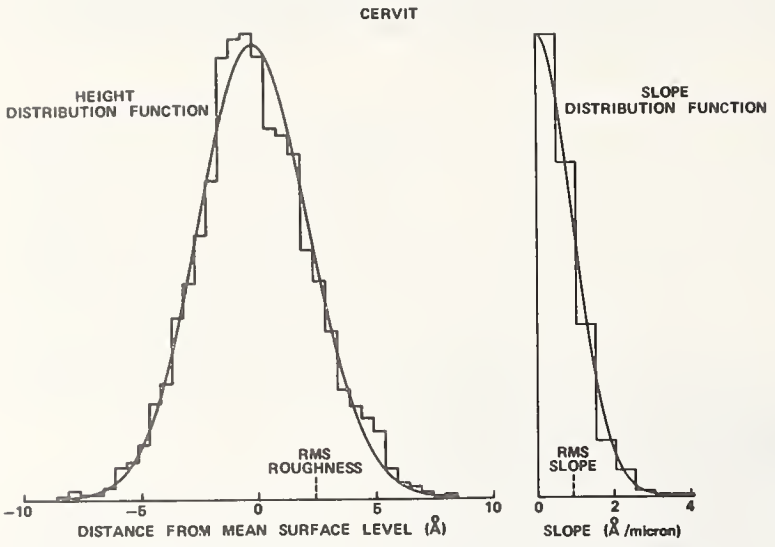

Figure 4. Height and slope distribution functions for the same Cervit surface. The smooth curves are Gaussians that have the same area under the curves as the measured histograms.

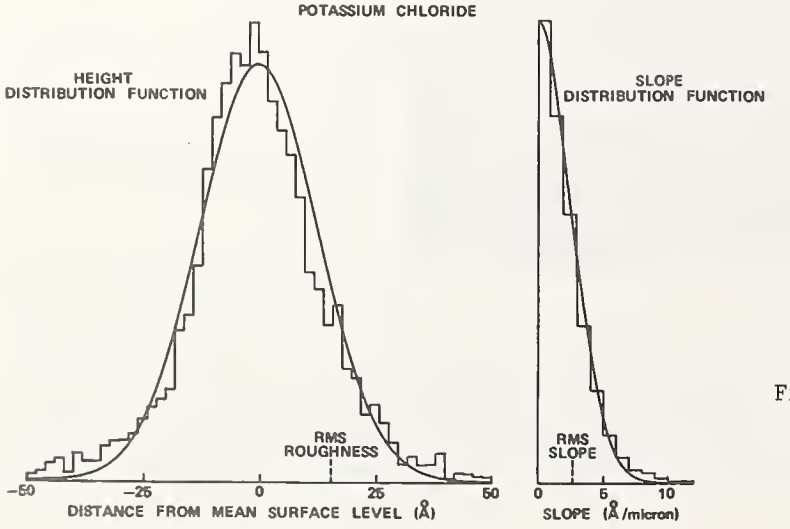

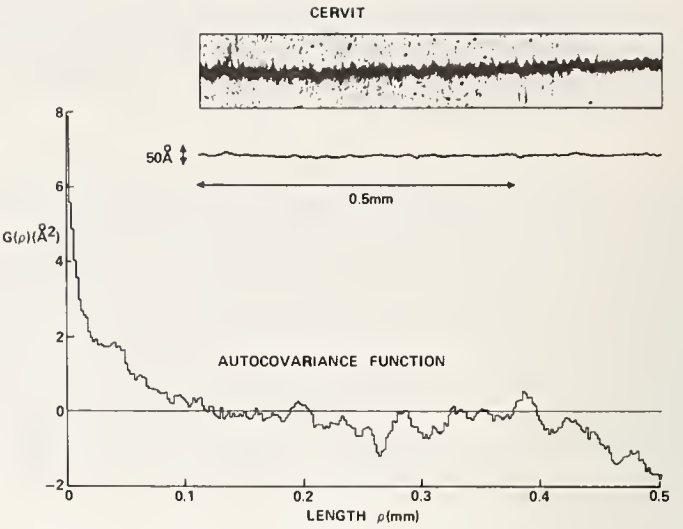

Figure 3. Photograph of the FECO fringe, TV scanning camera trace, and autocovariance function for an 8 Å rms roughness polished Cervit surface.

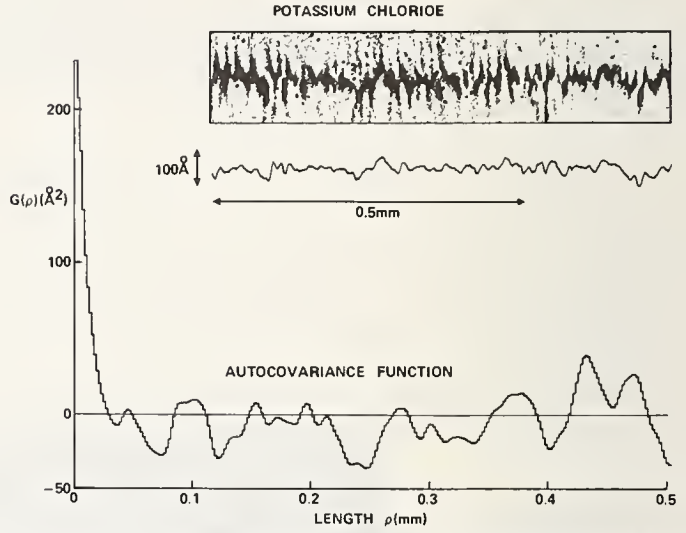

Figure 5. Photograph, TV scan, and autocovariance function for a 29 Å rms polished potassium chloride surface.

Figure 6. Height and slope distribution functions for the same potassium chloride surface.

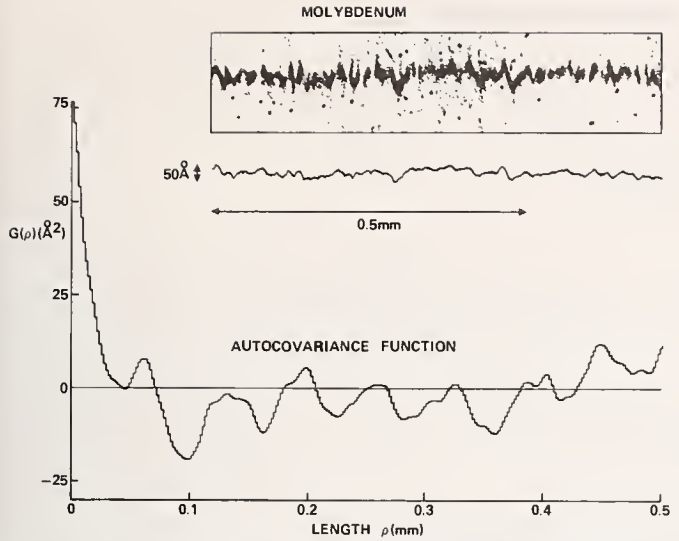

Figure 7. Photograph, TV scan and autocovariance function for a 22 Å rms polished molybdenum surfaces.

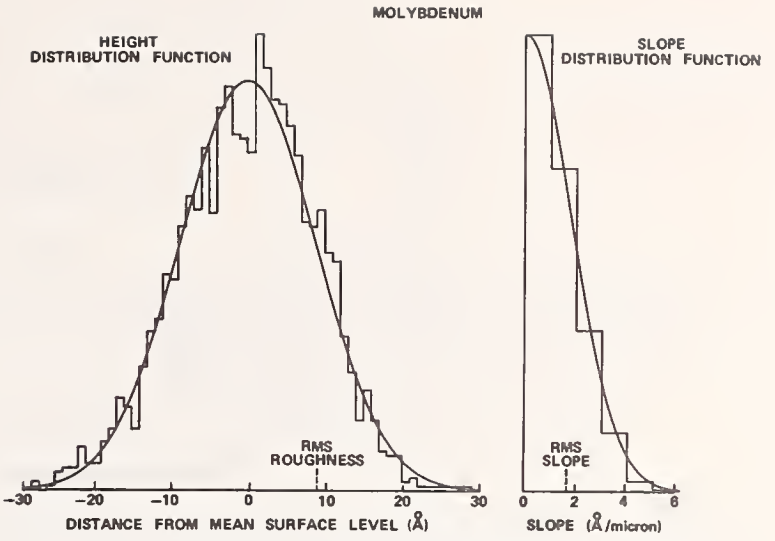

Figure 8. Height and slope distribution functions for the same molybdenum surface.

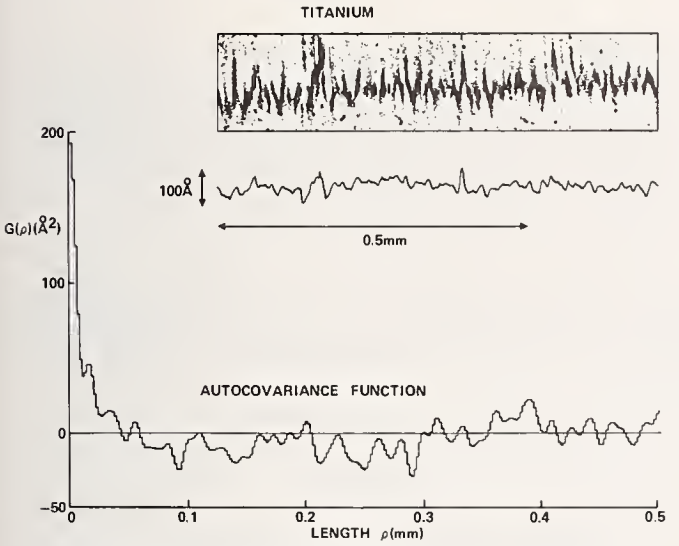

Figure 9. Photograph, TV scan and autocovariance function for a 32 Å rms polished titanium surface.

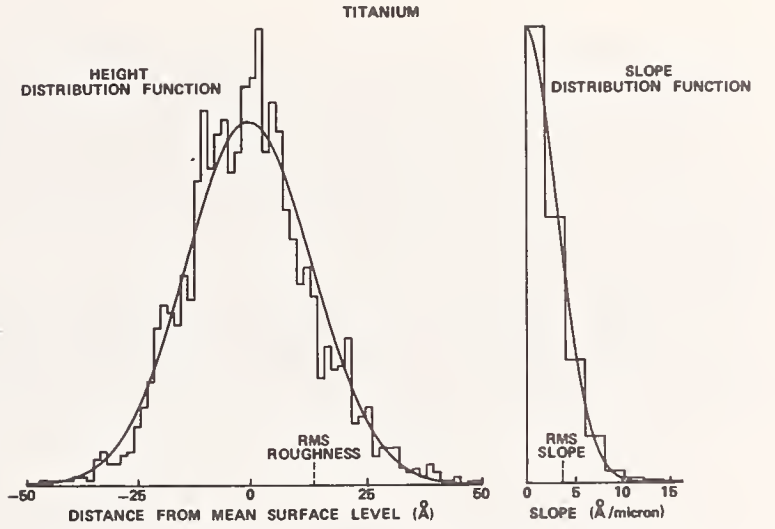

Figure 10. Height and slope distribution functions for the same titanium surface.

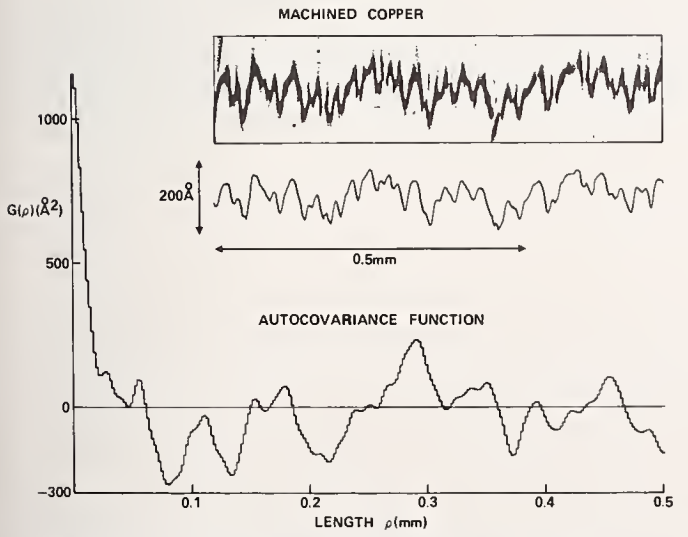

Figure 11. Photograph, TV scan and autocovariance function for a 47 Å rms machined copper surface.

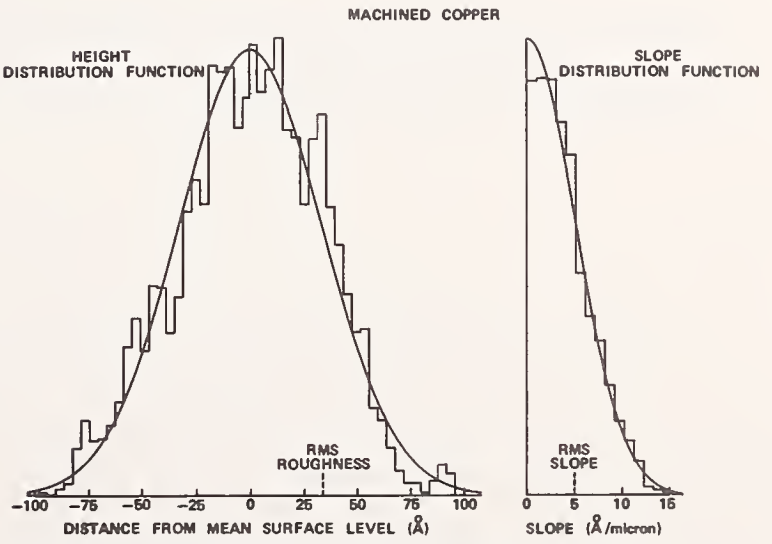

Figure 12. Height and slope distribution functions for the same machined copper surface.

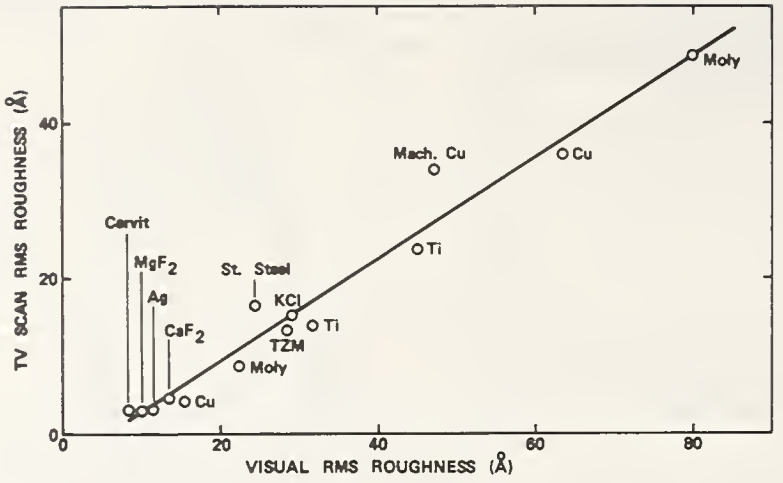

Figure 13. Relation between visual measurements of rms roughness and values obtained from scanning camera data.

COMMENTS ON PAPER BY BENNETT

The effect of surface absorption on fringe width was discussed, although this factor has not been included in the present analysis. At present, data obtained using the FECO method and scattering data are compared to obtain an objective evaluation of the FECO method. Some uncertainty remains in the interpretation of surface scattering data, particularly in the theoretical relation of scattering signatures to surface profiles.

In response to a question about surface quality of CaF_2 and MgF_2 surfaces, it was stated that samples polished by special techniques showed an rms surface variation of under 20 Angstroms, whereas conventionally polished samples of the same material typically showed an rms variation of 80 Angstroms. Also, densified rolled KCl showed an extremely good surface finish.

4.4 Roughness Measurement by Light Scattering*

John C. Stover

Dow Chemical U.S.A., Rocky Flats Division
Golden, Colorado 80401

Theoretical and experimental descriptions of how light scatters from sinusoidal gratings lead to the relationship between light scattered from an arbitrary surface and the spatial power spectral density function of that surface. With an appropriate measurement system, this relationship lends itself to studying the correlation between damage threshold and surface topography for surfaces in the 10 Å to 500 Å (rms) range. Experimental results are given for various types of sinusoidal gratings (variation in magnitude, frequency and material) and several arbitrary surfaces. Measurements of samples submitted by outside laboratories have been taken.

Key words: Light scattering; sinusoidal grating diffraction; spatial spectral density function; surface roughness.

1. Introduction

Beam damage of laser mirrors is related to the surface roughness and is probably a function of both the root mean square roughness (σ) and the autocorrelation length (T) of the surface (generally not found by conventional rougness measurement systems). This paper gives theoretical and experimental results describing the relationship between light scattered by mirrored surfaces (out of the specular beam) and the spatial spectral density curve of the surface. This curve can be used to compute both σ and T, but contains more information about the surface than just these numbers.

Any arbitrary surface profile can be thought of as being composed of a large number of sinusoidal surfaces of various magnitudes and frequencies, running in various directions which add to compose the actual surface. Relatively smooth sinusoidal surfaces (peak to valley less than 2 microinches or 500 angstroms) will reflect most of the light into the zero order (the specular direction) and diffract small fractions of the light (+1 and -1 orders) on either side of the zero order. The magnitude of this light is determined by the sinusoidal magnitude and frequency, while the position (angle of diffraction) is determined by the grating frequency and direction. Any arbitrary surface composed of many sinusoidal surfaces should then diffract in many directions where each direction and magnitude defines a sinusoidal component present on the surface. Measurement of the magnitude and direction of the scattered light then produces the magnitude and frequency of the sinusoidal components present once it is known exactly how sinusoidal gratings scatter their light. Measurement of these quantities amounts to measurement of the surface spatial power spectral density function. This curve defines the surface statistics but not the exact surface profile.

This paper gives first a theoretical explanation (scalar theory) of how light should scatter from a sinusoidal surface (or grating) and from a surface composed of many sinusoidal gratings. Then the production and measurement of sinusoidal gratings are described. Scattering measurements are given from each grating and compared to the theoretical model and the theoretical equation is accordingly adjusted. Finally, the adjusted theoretical description is applied through a computer to predict how light should scatter from a known non-sinusoidal surface with favorable results.

*This work was performed under the auspices of the United States Atomic Energy Commission.

2. Predictions of Scalar Diffraction Theory

Scalar diffraction theory can be used to develop a relationship between the first-order diffraction (magnitude and position) and a sinusoidal grating given by the surface:

$$z = \frac{d}{2} \sin(2\pi f x) \tag{1}$$

In eq (1), d is the peak-to-valley depth of a sinusoidal wave of frequency, f, imposed on the x,y plane. Figure 1 shows the orientation of the grating with respect to the incident and reflected light waves at angles ψ and θ, respectively.

Application of the Helmholtz Diffraction Integral* results in eq (2) and (3).

$$\sin \theta = \sin \psi + q\lambda f \tag{2}$$

Eq (2) gives the position of any order (q) in terms of ψ, f_0, and λ, the light wavelength. This relationship is known as the grating equation and is the expected result.

Eq (3) gives the ratio of the power diffracted in the first (P_1) and zero (P_0) order directions as:

$$\frac{P_1}{P_0} = \left[\frac{(\cos \psi + \cos \theta)\, J_1(h)}{2 \cos \psi \qquad J_0(h)} \right]^2 \tag{3}$$

In eq (3), $J_1(h)$ and $J_0(h)$ are the first- and zero-order Bessel Functions of the argument h given by:

$$h = \frac{\pi d}{\lambda} \ (\cos \theta + \cos \psi) \tag{4}$$

Eq (3) is plotted in figure 2 for various spatial wavelengths ($\Lambda = 1/f$) as a function of the peak-to-valley grating distance, d.

The Fourier transform of an arbitrary surface will consist of an infinite number of sinusoidal gratings running in an infinite number of directions at an infinite number of frequencies. However, the surface can be represented satisfactorily by a finite number of gratings running in discrete directions at discrete frequencies. Following the notation of the last section, such a composite surface is given by

$$z(x,y) = \sum_{m=1}^{M} \sum_{n=1}^{N} \frac{d_{mn}}{2} \sin\left[2\pi f_{mn} (x \cos\phi_m + y \sin\phi_m) \right] \tag{5}$$

where ϕ_m is the angle measured clockwise from the x-axis to a line perpendicular to the grating lines and $d_{mn}/2$ and f_{mn} are the magnitude and frequency of the nth grating in the mth direction.

If the surface is assumed to be isotropic, then measurements need be made only in one direction (i.e., for one value of m) in order to get all the information about the surface. The ratio P_{1n}/P_0 (any first order power in the incident plane over the specular reflection) becomes

$$P_{1n}/P_0 = \left[\frac{(\cos \theta_n + \cos\psi)\, J1(h_{1n})}{2 \cos \psi \qquad J_0(h_{1n})} \right]^2 \tag{6}$$

which is identical to eq (3). For $d_{1n}/2 \leq 1\mu$" then $h_{1n} \leq .25$ and $J_1(h_{1n}) \simeq \frac{h_{1n}}{2}$ and $J_0(h_{1n}) \simeq 1$. Thus

$$P_{1n}/P_0 \simeq \left[\frac{\pi\, d_{1n}}{4 \lambda \cos \psi} \right]^2 (\cos \theta_n + \cos \psi)^4 \tag{7}$$

This equation allows calculation of the magnitude of any spatial frequency present on the surface that diffracts into the plane of incidence.

*Scalar diffraction theory based on the Helmholtz Diffraction Theory is inadequate to accurately predict the behavior of the first order as the spatial wavelength Λ approaches the optical wavelength λ. For this reason the derivation of eq (3) is not given.

3. Production and Measurement of Sinusoidal Gratings

Sinusoidal gratings were produced by interfering two beams from a He-Ne laser on 10E75 Agfa-Geraert high resolution holographic film. The resulting fringes produce a sinusoidal density variation in the developed film and a proportional surface variation. Grating frequency is adjusted by changing the angle between the two beams and grating magnitude by changing the exposure time or fringe contrast. The resulting gratings were then coated with a layer of aluminum or copper.

Measurement of the sinusoidal gratings has been accomplished by several interferometric techniques. A Leitz microscope, both with and without a multiple beam attachment, was used for spatial wavelengths above 500 microinches. A Reichert metallurgical microscope with a polarization interferometer attachment (with a Michel-Levy color chart) was used for most of the gratings with spacing below 500 microinches. In addition, several gratings have been sent outside to labs for comparison measurements.*

4. Light Diffraction Measurements

The experimental system is shown in figure 3. It consists of a photomultiplier tube that measures the power through a small aperture set at any point on an eighteen-inch circular track. The DVM is a ratio meter adjusted to read P_{1n}/P_0. Light scattered at the source is eliminated by an aperture in front of the sample and by a spatial filter in the detector head. The light source is a He-Ne 5 mW laser polarized perpendicular to the plane of incidence.

For mirrored surfaces the observation path is divided up into sections. One measurement is taken inside each section and the total power scattered to that section is calculated. This number is then used to calculate the magnitude of the sinusoidal surface component that diffracts to the center of that section. When enough sections are used, the sinusoidal composite surface (composed of M elements per section) will have the same statistics as the actual surface.

The experimental results have been plotted in figure 2. As expected, they are in disagreement at short spatial wavelengths. For the purposes of calculating d_{1n} from P_{1n}/P_0, eq (7) can be modified to an approximate fit of the experimental data including small values of Λ.

$$P_1/P_0 = \left[\frac{\pi\, d_{1n}\,(.25 + .00075\,\Lambda)}{4\,\lambda\cos\psi}\right]^2 (\cos\theta_n + \cos\psi)^4 \tag{8}$$

A good theoretical explanation of closely spaced sinusoidal gratings is needed.

5. Roughness of Sinusoidal Composite Gratings

The rms deviation from the mean (σ) which normally is thought of as the surface roughness is defined as

$$\sigma = \frac{1}{\ell^2}\left[\int_0^{\ell}\int_0^{\ell} z^2(x,y)\,dxdy\right]^{1/2} \tag{9}$$

where the surface in question is square of edge ℓ. When eq (5) for $z(x,y)$ is substituted, σ becomes

$$\sigma = \left[\frac{M}{8}\sum_{n=1}^{N} d_{1n}^2\right]^{1/2} \tag{10}$$

where it has been assumed that the surface is isotropic (i.e., uniformly rough in all directions). The individual values of d_{1n} can be found experimentally by using eq (8) which allows computer calculation of σ.

---

* NBS in Washington, D.C., c/o Clayton Teague and China Lake Weapons Laboratory in California, c/o Hal Bennett.

The autocorrelation function $C(\tau)$ defined as

$$C(\tau) = \frac{\int_0^{\ell}\int_0^{\ell} z(x,y)\, z(x-\tau_x,\, y-\tau_y)\, dxdy}{\int_0^{\ell}\int_0^{\ell} z^2\,(x,y)\, dxdy} \tag{11}$$

can be found in a similar manner for isotropic surfaces to be

$$C(\tau) = \frac{\sum_{n=1}^{N} d_{1n}^2 \cos(2\pi\, f_{1n}\, \tau)}{\sum_{n=1}^{N} d_{1n}^2} \tag{12}$$

where τ_x and τ_y are the displacements in the x and y directions respectively and τ is the total displacement. The autocorrelation length T can be defined as the value of τ for which

$$C(\tau) = e^{-1} \tag{13}$$

σ and T have been popularly suggested as the two quantities needed to adequately define a surface. The method introduced in this paper, however, allows measurement of a more valuable quantity -- the spatial power spectral density function (SDF). This function contains more than just the information necessary to calculate σ and T. The data presented later gives all three quantities. The approximate SDF for an unknown surface is established from the SDF of the composite surface, $S_c(f)$. This is taken from the measured values d_{1n} as

$$S_c(f) = \sum_{n=1}^{N} \frac{d_{1n}^2}{8}\, \delta(f - f_{1n}) \tag{14}$$

where δ is an impulse function. The integrals over f of the SDF for both the composite surface and the real surface must be equal if both surfaces are to have the same statistics. Thus the values $(d_{1n}^2/8\Delta f)$ at fn must be points on the actual SDF [S(f)] where Δf is the frequency segment on which the nth measurement is centered.

$$S(f)\Big|_{f=f_{1n}} = \frac{d_{1n}^2}{8\,\Delta f_{1n}} \tag{15}$$

6. Spectral Density Function as a Measure of Roughness

Eq (15) allows calculation of the SDF of the real surface. Examples of what this curve can be expected to look like are given in figure 4. Note that the zero frequency component is considered to be zero (because the interest is in measuring deviations from a zero frequency surface) and that the curve approaches zero as f increases. This should be true as long as Λ is much greater than atomic distances on the surface. For various applications, roughness in certain spatial frequency regions may be more important. The SDF allows discrimination on this basis.

A complete SDF then defines all the roughness present on the surface, allowing comparison of various measurement systems (stylus, FECO, TIS, scattering vs angle, etc.).

A well-known problem with stylus instruments is that the stylus tip tends to "ride over" surface valleys that are much smaller than the stylus diameter. Thus the stylus instruments are not capable of measuring the high frequency roughness. Since the rms roughness is proportional to the area under the SDF, it is important to know the cut-off point of each instrument if rms results are expected to compare well.

FECO (fringes of equal chromatic order) interferometers with appropriate computer analysis (such as the system built by J. M. Bennett) [1][1] are capable of making measurements of the rms roughness, the autocorrelation function (and length) and the SDF out to about $f = 0.2 - 0.4\,\mu^{-1}$ (resolution is about 2μ or $f = 0.5\mu^{-1}$). Comparison of FECO results to the scattering angle measurements described in sections D and E is currently being carried out over this part of the SDF. Another instrument developed at China Lake [2] measures the total integrated scatter (TIS) out of the specular beam. The percentage of light scattered out of the specular beam is related to the rms roughness by a scalar scattering theory [2,3] that assumes a Gaussian distribution of the surface roughness. One would expect TIS devices to have a high frequency cutoff in the neighborhood of 0.6μ (roughly the spatial wavelength at which He-Ne laser light is diffracted along the surface for normal incidence). However, since the analysis is based on the scalar theory, it suffers in the same manner as eq (3) and (7). As can be seen in figure 2, the result is that a TIS measurement does not give enough weight to high angle scatter. The point at which this effect becomes severe is about 2.5μ (100μ") where the first order diffraction is almost one order of magnitude below scalar expectations. Thus one would expect the effective TIS cutoff to be in the $2.5\text{-}5\mu$ ($f = 0.2 - 0.4\mu^{-1}$) region, very close to the FECO cutoff. In fact, good agreement has been reached between FECO and TIS measurements [1][1].

Figure 5 shows the results of using the angle scattering technique on a polished copper sample. The lower curve is $d_{1n}/2$ as calculated by eq (8), which is proportional to the square root of the SDF. The upper curve is the calculated rms roughness as a function of the highest frequency component considered. The sample was measured at China Lake on a TIS device at about 18.2Å rms which compares favorably to 17Å at the $f = 0.3\mu^{-1}$ cutoff obtained by angle scattering.

Note that angle scattering for this angle of incidence (20°) and this wavelength (6328Å) has not yet reached the point where the SDF starts to approach zero. This is thought to be caused by two effects. First, eq (8) is probably inaccurate above $f = 0.8\mu^{-1}$ (interferometric data goes only to $f = 0.4\mu^{-1}$) and second, the system bandwidth may not be large enough yet. Electron microscope pictures [4] of super-finished metals show relatively large surface features with lateral dimensions in the 0.1μ to 1μ range so the roughness, as indicated, may simply have larger bandwidth than the measurements taken.

7. Summary

By examining the first order diffraction from sinusoidal gratings as a function of grating depth and wavelength, a relationship has been developed to measure the approximate spectral density function of optical surfaces. Use of this curve allows a basis of comparison for different measurement devices and should be useful as a means of examining different optical production techniques and laser damage dependence on surface geometry. The technique offers a method measurement that does not depend on surfaces having a Gaussian distribution and measures roughness out to higher spatial frequencies than many devices presently in use.

8. Acknowledgment

The author is grateful to G. Wayne Dutton for making the sinusoidal gratings, to L. William Utley for making the interferometric measurements on them, and to Dick Skulski (Dow Chemical) and Jean and Hal Bennett (China Lake Navel Weapons Center) for many helpful discussions.

[1] Figures in brackets indicate the literature references at the end of this paper.

9. References

[1] Bennett, J. M., "Statistical Characterization of Mirror and Window Surfaces," Proc. of ASTM-NBS-ONR Symposium on Damage in Laser Materials, Boulder, Colo. May 1974.

[2] Bennett, H.E., Bennett, J.M., and Stanford, J.L., "Surface Irregularities and Scattering," Proc. of The Infrared Information Symposium, Huntsville, Ala. Jan. 16, 1973.

[3] Porteus, J.O., "Relation between the Height Distribution of a Rough Surface and the Reflectance at Normal Incidence," J. Opt. Soc. Amer. 53, p. 1394. Dec. 1963.

[4] Discussion with H. E. Bennett at the China Lake Naval Weapons Center in California of pictures taken at that facility.

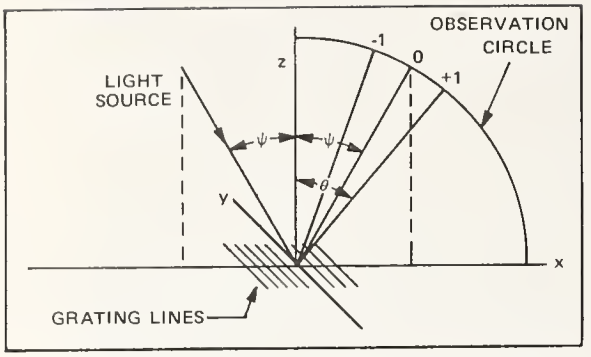

Figure 1. Position of sinusoidal grating, incident beam, specular reflection and first order diffraction spots.

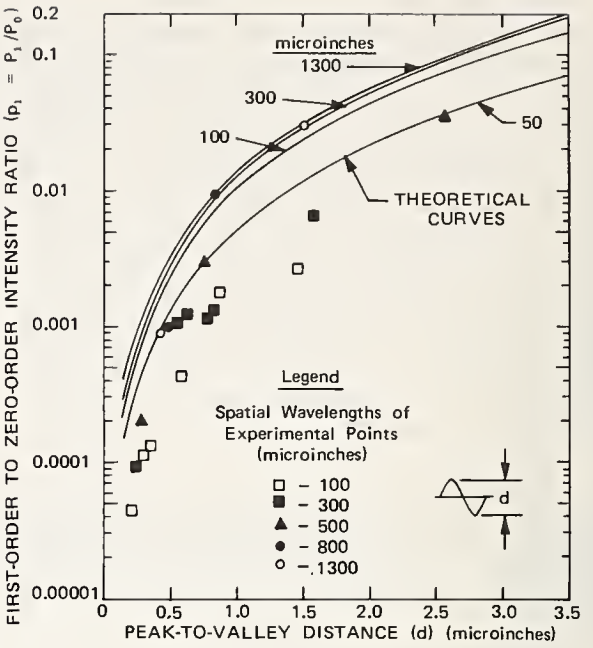

Figure 2. Theoretical and experimental results for sinusoidal gratings at several spatial wavelengths

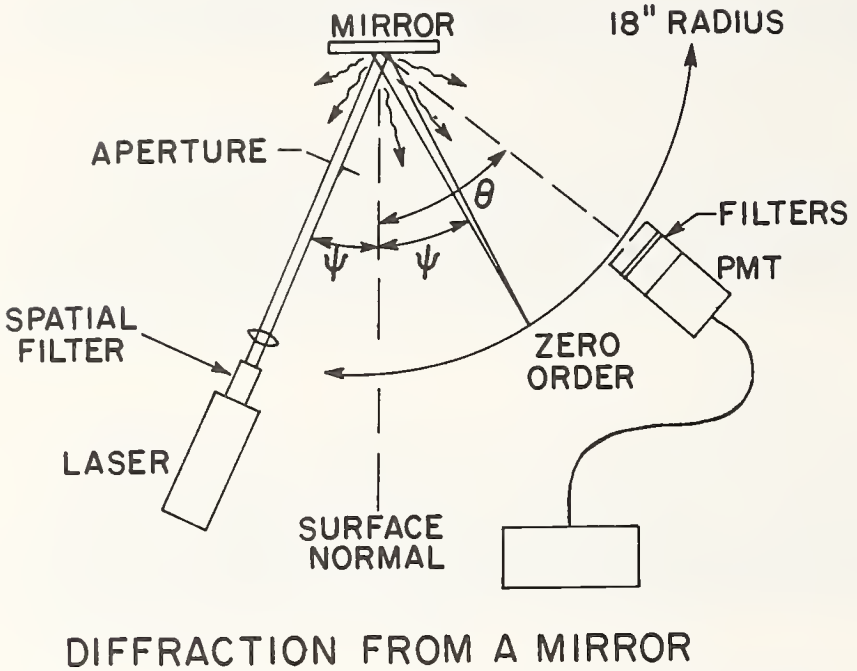

Figure 3. Experimental system to measure scattering as a function of angle from a mirrored surface.

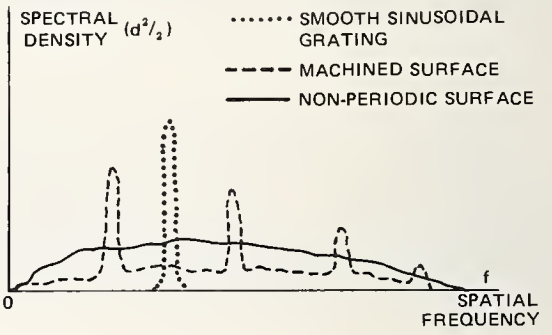

Figure 4. Spectral density functions of several types of surfaces.

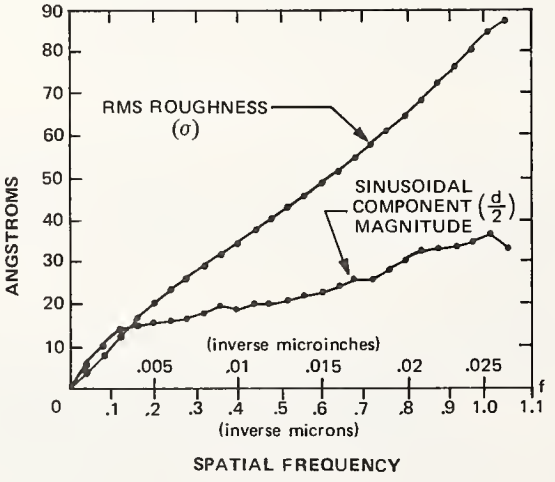

Figure 5. RMS roughness and sinusoidal component magnitude as a function of spatial frequency.

COMMENTS ON PAPER BY STOVER

The effects of polarization and coherence in the scattering source were discussed, as possibly influencing scattering results. No effects due to coherence have been observed in scattering measurements carried out at the Michelson Laboratory.

5.1 Laser-Damage-Mechanism Identification by the Measurement of Survival Times

D. Milam, R. A. Bradbury, and R. H. Picard

Air Force Cambridge Research Laboratories
Optical Physics Laboratory
Laser Physics Branch
L. G. Hanscom Field
Bedford, Massachusetts 01730

and

M. Bass

Center for Laser Studies
University of Southern California
Los Angeles, California 90007

The mechanism responsible for laser-induced damage can be determined from the statistical fluctuation in the times required to produce damage at many sites which were sequentially irradiated by equally-intense, square-waveform pulses. Damage mechanisms are readily separated into three general categories: (1) Homogeneous absorption, (2) damage due to material defects or inclusions, and (3) intrinsic damage due to electron-avalanche breakdown or other fast intrinsic mechanisms.

The statistical technique for identifying damage mechanisms will be contrasted with threshold measurement schemes which have been unfruitful in identifying mechanisms.

Key words: Absorbing inclusions; absorption; bulk dielectrics; dielectric films; dielectric surfaces; electric field enhancement; electron-avalanche breakdown; laser-damage statistics.

1. Introduction

It has previously been shown that laser damage in transparent materials at small focal spots is statistical in nature. Damage may or may not occur at a given incident power level. The nature of the damage statistics was used [1][1] to identify electron-avalanche breakdown as the intrinsic damage mechanism for nanosecond duration laser pulses. Another statistical manifestation of breakdown has been observed in damage studies of dielectric films. [2,3] For most films, the damage threshold is dependent on the size of the damage site, presumably because the film contains absorbing inclusions or mechanical defects. Such imperfections can be avoided on some firings if the irradiated area is sufficiently small.

Experimental observations of statistical behavior in small-spot damage experiments have been challenged on a number of significant points. The statistics could result from many effects other than avalanche breakdown, such as fluctuations in the laser output, improper positioning of the sample, a lack of material homogeneity or the presence of internal defects, or residual scratches, dirt, or polishing compound on the sample surface.

1. Figures in brackets indicate the literature references at the end of this paper.

A complication in the interpretation of damage statistics observed to date is due to the fact that single-mode laser pulses with non-constant temporal waveforms have been used. Though the waveform is highly reproducible from pulse to pulse, the fact that the intensity varies during each pulse makes it difficult to identify the cause of the damage event. For example, the optical field required to heat a small absorbing inclusion to a damaging temperature is so large [4], and the thermal time constant of these inclusions is sufficiently short, that the inclusion can cause damage at an intensity comparable to that which causes avalanche breakdown. One way to try to remove this ambiquity is to classify the damaging events into two sets [5]: (1) the set of events in which the transmitted laser pulse is cleanly and rapidly terminated by the damage and (2) events in which termination of the transmitted pulse is not abrupt, or perhaps incomplete, indicating that a large absorbing defects has been encountered. The statistics of the first set of damage events are consistent with avalanche breakdown. [6]

In order to evaluate the merits of the statistical observations and of the objections to these observations, an experiment using constant-intensity irradiation of small sites was designed at AFCRL. Our efforts, which began as a test of the hypothesis that avalanche breakdown was the intrinsic mechanism responsible for damage to transparent materials, have led to a generalized statistical technique for identifying the cause of laser damage. It is the purpose of this paper to describe that technique in its current state of development.

2. Description of the Technique

Consider an ensemble of identically irradiated sites, N_0 in number, which are being damaged at an instantaneous rate h(t). If N(t) is the number of sites undamaged at time t, then

$$\frac{dN(t)}{dt} = - h(t)\, N(t),$$

or

$$\ln \left(\frac{N(t)}{N_0}\right) = - \int_0^t h(t')\, dt'.$$

The function $N(t)/N_0$ is related to the damage statistics, since it is the probability of a site surviving for a time t without damaging. We define the plot of $\ln (N(t)/N_0)$ versus t to be the survival curve and note that it depends only on the integral of the rate function h(t) which presumably is determined only by the damage mechanisms in operation and the waveform of the irradiation.

The problem is in every way analogous to fluorescence decay, with irradiated but undamaged sites being the analogue of excited molecules and h(t) being the analogue of the fluorescence decay rate. The damage rate may depend on several mechanisms, just as fluorescent de-excitation may proceed via several different channels. Accordingly, we define h(t) as a sum

$$H(t) \equiv \sum_{j=1}^{n} h_j(t)$$

where one term $h_j(t)$ is included for each of the n damage mechanisms under consideration. If the computed functional forms $h_j(t)$ are sufficiently unique, and if one term dominates the sum in a given sample, the limiting damage mechanism can be ascertained simply by comparing the experimentally determined survival curves with those computed for the various possible damage mechanisms.

A particularly important advantage of the procedure outlined above is that damage mechanisms can be identified without determining the absolute level of irradiation. Mechanism identification is based solely on a comparison of functional forms. Absolute power density measurements, which have traditionally been the most difficult aspect of damage experiments can be avoided if one only wishes to determine the damage mechanism.

3. Qualitative Features of Survival Curves

3.1 Electron-Avalanche Breakdown

The rate of damage by electron-avalanche breakdown has been given in the form

$$h_{ea}(t) = A_0 e^{-K/E(t)},$$

where K is a material constant and E(t) is the applied optical electric field. If E(t) has the form

$$E(t) = \begin{cases} 0 & (t < 0) \\ E_0 & (0 \leq t \leq t_1) \\ 0 & (t > t_1) \end{cases},$$

the rate $h_{ea}(t)$ is also a constant,

$$h_{ea}(t) = A_0 e^{-K/E_0} \equiv \Gamma(E_0).$$

In this case, the survival curve found at a particular power level E_0 is a linear function of time, as shown in figure 1.

Following the observation by Crisp and Boling [6] that the local value of the optical electric field within the dielectric was the controlling factor in many damage experiments, Bloembergen [7] described the electric-field enhancement at mechanical defects of various shapes. The enhanced field will lead to enhanced probabilities for avalanche development. We can use the curves shown in figure 1 to illustrate the survival curves appropriate to defect-enhanced avalanche breakdown. Assume that we apply the field E_0 to N_0 sites, and that some sites contain mechanical defects. If, for simplicity, we consider only two types of defects, some sites will experience enhanced fields E_1 and E_2, such that

$$E_2 > E_1 > E_0.$$

Then, instead of observing only sites damaging at the intrinsic avalanche breakdown rate $\Gamma(E_0)$, we will also observe subsets of sites which damage at the higher rates $\Gamma(E_1)$ and $\Gamma(E_2)$. The observed survival curve will be a nonlinear function of time whose slope is initially large and then decreases, since the survival probability is the sum of three exponentials with different time constants. Similar survival curves will be observed if many types of mechanical defects are considered.

If the field E_0 is reduced until only the enhanced rate $\Gamma(E_2)$ is observable experimentally, the survival curve, even though resulting from enhanced avalanche breakdown, will be linear in time. It is only by generating survival curves at a number of optical power levels, beginning with the lowest that produces a measurable damage rate, that the intrinsic avalanche breakdown of a perfect dielectric can be distinguished from the breakdown at sites containing defects. For a perfect dielectric the survival curve is a linear function whose slope increases with increasing field amplitude. On the other hand, for a dielectric with mechanical defects, the survival curve is linear only at lowest field which produces damage, but become nonlinear as the field is increased.

3.2 Homogeneous Absorption

If the sample is a homogeneous absorber, all equivalently irradiated sites will survive until they simultaneously reach a damaging temperature T_d. The damage probability per unit time for absorption will approach a delta function centered about the time t_a at which the sites damage. The fractional number of survivors $N(t)/N_0$ will remain at unity until t_a, then fall rapidly to zero.

An increase in the applied field E_0 will decrease t_a. The manner in which t_a decreases with increasing E_0 will reveal whether the absorption is linear or nonlinear. Observation of the proper relationship between E_0 and t_a is possible only if the irradiated area is sufficiently large so that heat diffusion out of the irradiated area is negligible.

3.3 Absorbing Inclusions

If metallic or other highly absorbing inclusions are present at some sites, these sites will normally damage at incident power levels below that required to damage the host material. For spherical inclusions with diameters greater than $\sim \lambda/20$, where λ is the laser wavelength, simple heat-transfer arguments show that, under irradiation and with conduction cooling, the temperature of an inclusion of radius R initially increases as $1/R$ but reaches a final value proportional to R. This is illustrated in Figure 2. Small inclusions are heated more rapidly, but reach a lower final temperature.

Damage to a particular inclusion is deterministic. The statistical aspects of inclusion damage are due to the spatial distribution of the inclusions. If the irradiated spot area is sufficiently small so that some sites irradiated will be free of inclusions, the damage will be a statistical process.

Exact calculation of the inclusion damage rate $h_i(t)$ is difficult, but it is possible to obtain the qualitative features of the survival curves appropriate to inclusion damage from the heating curves shown in figure 2. At a given level of irradiation, all absorbers with radius less than some minimum value R_{min} will escape damage, their equilibrium temperatures being less than the temperature T_d required to produce damage. Slightly larger inclusions will be heated to T_d by time t_1, when the first damage events will occur. Damage events will cease at time t_2 when the largest inclusion present on any site has reached T_d, or when irradiation ceases. The fraction of survivors $N(t)/N_0$ is unity until t_1. Sites containing inclusions that can be heated to damaging temperatures will damage betwen times t_1 and t_2. Following time t_2 the survival curve will again have constant value because some sites are free of damageable inclusions.

An increase in the irradiation level E_0 will reduce both the time to first damage t_1 and the fraction of sites that remain undamaged. More damage events are expected under increased irradiation intensity for two reasons: (1) Some smaller and larger inclusions, which previously escaped damage, can be heated to a damaging temperature at the increased irradiation level, and (2) the effective area of the site will increase with increasing power due to the Gaussian spatial profile of the beam.

In practice, it must be realized that the thermal time constant of the submicron-sized absorbers in question may be less than the temporal resolution of the experiment. The delay until first damage at time t_1 may be the time required for the material to respond to the thermally generated stress[8] instead of the time required to heat an inclusion to T_d.

3.4 Typical Survival Curves

Typical survival curves for the damage mechanisms discussed above are shown in figure 3. Hopefully, in a given experimental situation, one of the damage mechanisms will predominate, so that mechanism identification will be possible by comparing the shape of the experimentally determined survival curves to the characteristic shapes shown in figure 3.

4. Experimental Apparatus for Measuring Survival Curves

The constraint of using step-function waveform irradiation, which was assumed for calculation of the damage rate h(t), is met by using a Pockels cell shutter to extract square-waveform pulses from the most intense portion of the smoothly varying pulses emitted by a single-mode ruby laser. The initial laser pulse, with the central switched-out portion missing, and the square pulse removed by the shutter are shown in figures 4a and 4b, respectively. The risetime of the pulse is 0.7 nsec, and its duration can be adjusted from 1.5 to about 50 nsec. Since the intensity of the primary laser pulse decreases as its duration increases, square pulses 40 - 50 nsec in duration are limited in power to approximately 50 kw. A 20 nsec pulse at a power level of approximately 200 kw is used for most experiments.

The damage experiment is shown in figure 5. A portion of the pulse energy is picked off before the pulse strikes the sample to serve as an intensity monitor. The remainder of the square pulse is focussed into the damage sample and then recollimated so that the entire beam is recorded. Both the transmitted pulse and the monitor pulse are recorded on the same oscilloscope trace by delaying one of them. A hypothetical trace is shown in figure 6. The pulse intensity is obtained by calibrating the height of the monitor pulse against the energy arriving in the sample plane. The occurrence of damage and the survival time for each site are indicated by a change in the transmission through the sample when damage occurs.

There are two difficult aspects to these experiments: (1) proper measurement of the spatial profile at the waist of the tightly focussed beams and (2) proper positioning of the damage samples when they are thin films or when it is desired to damage a sample surface.

Focal diameters (FWHM) ranging from 3 μm - 100 μm are used. Beam waists down to about 6 μm FWHM can be measured with reasonable accuracy from densitometer scans across multiple images[9] of the waist magnified 300 times. Smaller beam waists, obtained by using microscope objectives as focussing lenses, are more difficult to measure, since they are near the diffraction limit of our imaging system. As a result, absolute laser irradiation levels determined from focal diameters 10 μm (FWHM) or smaller could easily be in error by a factor of 2, even if reasonable care is taken when measuring the beam. We emphasize again that the damage mechanisms are identified by the shape of the survival curves and that a knowledge of the absolute damage power level is not required. However, the absolute power levels are of interest in order to establish intrinsic damage levels when possible, and an effort is made to measure these levels accurately.

When optical surfaces or thin films are studied, with small diameter spots, great care must be exercised to ensure that the surface is accurately parallel to the precision x-y translation stage used to carry the sample; otherwise the sample will be carried in and out of the beam waist as it is translated from site to site. The sample-to-stage parallelism can be achieved using light from the He-Ne laser alignment beam that is reflected from the surface of the damage sample. As illustrated in Figure 7, this reflected light, when transmitted back through the focussing lens and viewed at a distance large relative to the focal length, forms a magnified image of the intensity distribution in the focal plane of the lens. The distance between the sample and lens is adjusted until the beam waist is on the sample. The angular orientation of the sample is then adjusted until the magnified image of the beam waist remains invariant as the stage is translated indicating that the translation stage and the sample are parallel. The final adjustment is to correct the sample-to-lens distance for lens dispersion so that the waist of the ruby laser beam will be on the sample.

A simplified experiment is illustrated in figure 8. Here $N_0 = 8$ sites are irradiated at field strength E_0. An oscilloscope trace is recorded for each of the eight firings. The data is not sorted after the experiment in any way except to verify that the applied electric field remains at a value E_0, within acceptable limits, throughout each laser pulse. All data meeting this criterion are reduced, and a table of experimental results is compiled from which the survival curve is generated. The curve is then examined for correlation with computed curves.

564-378 O - 74 - 13

5. Experimental Results

We have experimentally determined survival curves for a sufficient number of samples to demonstrate the utility of the technique for determining damage mechanisms. We present below selected data gathered in damage studies of dielectric films, polished dielectric surfaces, and bulk dielectrics.

5.1 Damage due to Homogeneous Linear Absorption

Linear absorption in a TiO_2 - SiO_2 multilayer dielectric film is indicated by data shown in figure 9. At a given power level, all sites survive until a well defined time t_a at which damage occurs. An increase in irradiation level from 1.5 Gw/cm^2 to 3.9 Gw/cm^2 results in a proportional decrease in t_a revealing damage due to linear absorption.

An example of the oscilloscope data for an absorbing sample is shown in Figure 10. The deterministic behavior seen in the survival curves is reflected in the well-defined damage time for a given irradiation level.

5.2 Damage due to Absorbing Inclusions

Damage due to absorbing inclusions in a single-layer film of ZrO_2 is revealed by the survival curves shown in Figure 11. The delay to first damage, 3.0 nsec, and the leveling trend as damageable inclusions are exhausted, are both apparent. The data is plotted for $N_0 = 60$ sites (0) and for a smaller subset, $N_0 = 20$ (Δ), which were the first 20 sites irradiated. Notice that the basic characteristics of damage due to heating inclusions are already apparent from the survival curve generated by irradiating only a relatively small number of sites. For example, either curve reveals that damage occured at a greater rate between 4 and 6 nsec after irradiation commenced, and that about half of the sites survive undamaged.

We commonly observe absorbing inclusions in electron-gun-deposited dielectric films, in agreement with earlier morphological studies. [4,10]

5.3 Electron-Avalanche Breakdown

Survival curves indicative of avalanche breakdown in the bulk of samples of Suprasil 1 fused quartz are shown in Figure 12. Since the focal spot used for these measurements was about 3 μm in diameter FWHM, the total laser power incident on the sample is recorded instead of the power density at the focus. [11]

Survival curves at two power levels, 58 kw and 63 kw, are linear to within limits reasonably expected for the small number of samples in each case. However, data at a higher power level, 68 kw, is definitely nonlinear. That curve falls rapidly at first and then falls much more slowly. Beyond 8 nsec, the remaining sites damage rather abruptly with absorption-like behavior. The two linear curves and the initial nonlinearity of the third curve are strongly indicative that the limiting damage mechanism is field-enhanced avalanche breakdown. The abrupt drop for long survival times, characteristic of homogeneous absorption, is thought to be an independent effect and has been seen at very high power levels in several dielectric films, in the bulk of Owens-Illinois ED-4 glass, and in Dynasil fused quartz. A number of possible causes for the absorptive behavior at high power levels have been proposed. It could, for example, be due to actual low-level linear or two-photon absorption, or thermal self-focussing could reduce the spot size and enhance the avalanche rate.

The indication that the limiting damage mechanism in Suprasil 1 fused quartz is defect-enhanced avalanche breakdown, rather than intrinsic breakdown, is a new result and may appear somewhat surprising. However, the experiment has been repeated, producing essentially the same survival curves. Moreover, this behavior is consistent with known properties of fused quartz. Bubbles are generally present in each melt, and even the best quartz, which has been selected from high-purity melts to contain no bubbles larger than some pre-selected standard size, should still contain very small voids which enhance the field.

6. Conclusions

We have described the current status of development of a generalized scheme for determining the cause of laser-induced damage. The technique readily detects absorption with a sensitivity considerably better than a previously described double-pulse [10] method. Absorbing inclusions in electron-gun-deposited, metal-oxide films, which are known to be present as a result of earlier studies [4,10] are also readily detected. Electron-avalanche breakdown is seen in the bulk of high quality dielectrics, also in agreement with prior observations. [5]

There are numerous extensions of the technique yet to be made, and some features, such as the absorptive behavior of many samples at high field strengths, are poorly understood. However, even at the present stage of development, the technique described here is the only known way to identify damage mechanisms within a given single sample without resort to measurements in a series of materials or at a series of pulse durations.

7. Acknowledgment

The authors thank C. C. Gallagher, of AFCRL, for assistance with the design and assembly fast electronic circuitry, and Marilyn Sweeney, also of AFCRL, for assistance in preparation of the manuscript.

8. Figures

[1] Bass, M. and Barrett, H. H., IEEE J. Quant. Elect. QE-8, 338 (1972).

[2] DeShazer, L. G., Newnam, B. E. and Leung, K.M., Appl. Phys. Lett. 23, 607 (1973). Newnam, B. E. and DeShazer, L. G., in Proceedings of the 5th ASTM/NBS Symposium on Damage in Laser Materials, (U.S. GPO, Washington, 1973).

[3] Bliss, E. S., Milam, D. and Bradbury, R. A., Appl. Opt. 12, 602 (1973).

[4] Milam, D., Bradbury, R. A. and Bass, M., Appl. Phys. Lett. 23, 654 (1973). It has been demonstrated that intensities as large as 10^{11} watts/cm^2 are required to heat submicron diameter inclusions.

[5] Bass, M. and Fradin, D., IEEE J. Quant. Elect. QE-9, 890 (1973).

[6] Crisp, M. D., Boling, N. L. and Dube, G., Appl. Phys. Lett. 21, 364 (1972).

[7] Bloembergen, N., IEEE J. Quant. Elect. QE-10, 375 (1974).

[8] Duthler, C. J., Appl. Phys. Lett. 24, 5 (1974).

[9] Winer, I. M., Appl. Opt. 5, 1437 (1966).

[10] Milam, D., Bradbury, R. A. and Bass, M., in Proceedings of the 5th ASTM/NBS Symposium on Damage in Laser Materials, (U.S. GPO, Washington, D. C., 1973).

[11] Subject to statements in Section 4 concerning the difficulty in accurately measuring small beam waists, we note that a 1 kw Gaussian-mode beam focussed to 3 μm (FWHM) has an on-axis power density of about 10 Gw/cm^2. Many small sites in Suprasil 1 fused quartz withstand irradiation at 500 Gw/cm^2, give or take a factor of two, for 20 nsec.

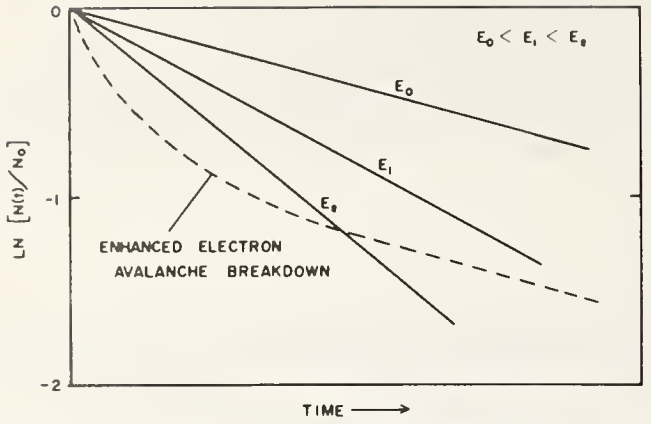

Figure 1. Survival curves characteristic of electron-avalanche breakdown. Intrinsic breakdown of the perfect dielectric at field strengths E_0, E_1, and E_2 produce three linear curves. If field E_0 is applied to N_0 sites, and field E_1 and E_2 are generated at some of these sites by field enhancement, all three curves will be observed simultaneously, resulting in a non-linear function.

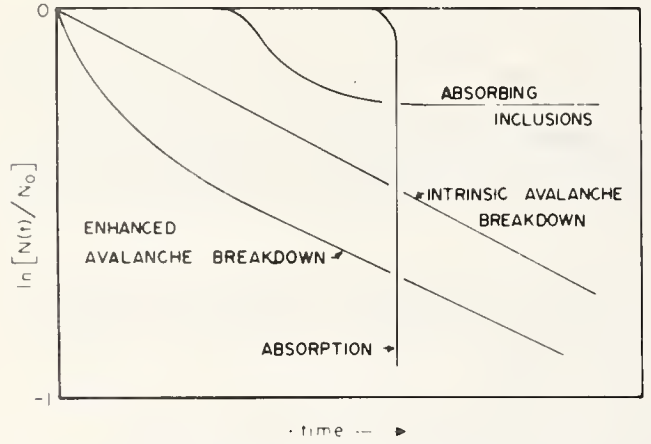

Figure 3. Survival curves characteristic of four damage mechanisms.

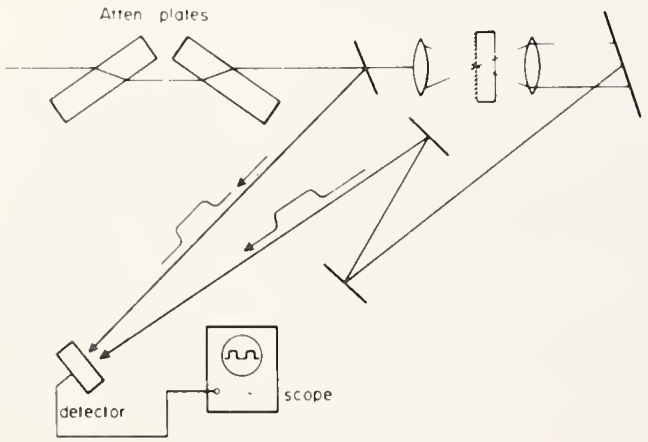

Figure 5. Damage experiment. Both the intensity monitor pulse and the pulse transmitted through the damage sample are displayed on the same oscilloscope trace.

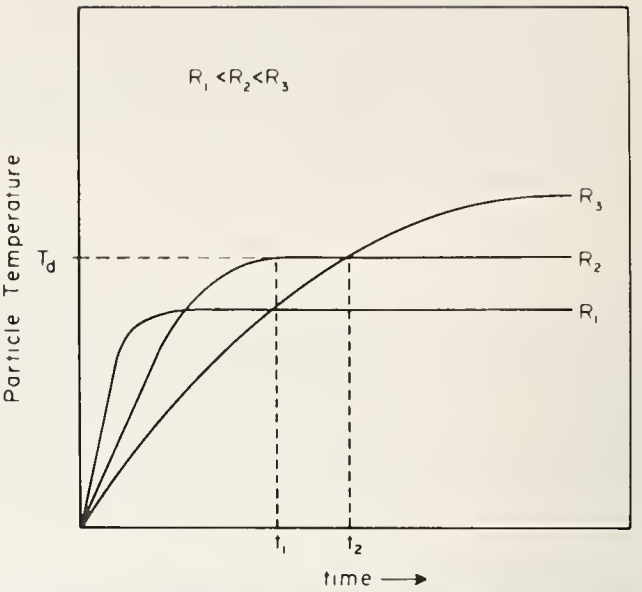

Figure 2. Temperature as a function of time for spherical absorbing inclusions heated by an optical field.

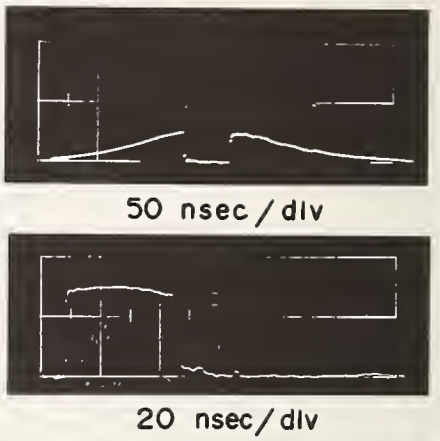

Figure 4. Upper: Pulse emitted by a single-mode ruby laser, with central portion shuttered out. Lower: Square-wave pulse selected by the shutter.

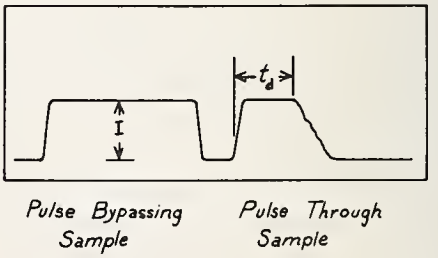

Figure 6. Idealized oscilloscope trace recording during damage measurements. Intensity is monitored by the first waveform while the time at which damage occurred is marked by termination of the pulse transmitted through the sample.

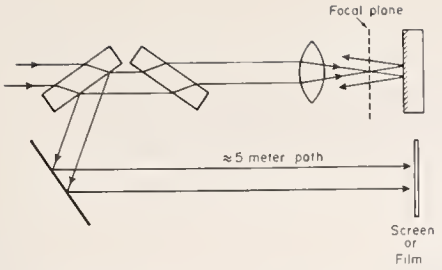

Figure 7. Technique for aligning the damage sample with the translation stage on which it is carried. Light reflected from the sample is used to form a highly magnified image of the intensity distribution in the focal plane of the lens. The sample orientation is adjusted until the image of the focal plane remains invariant as the sample is translated.

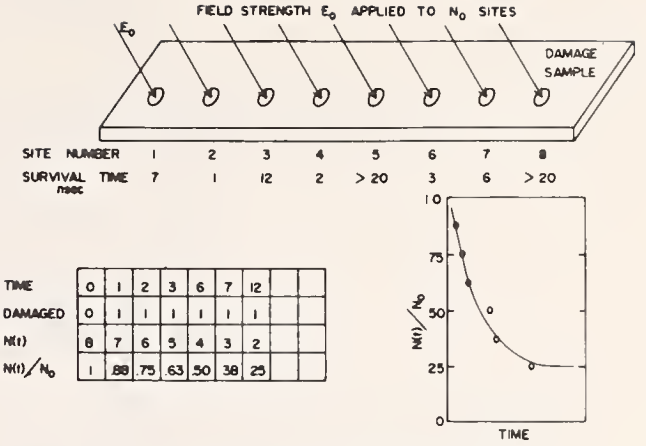

Figure 8. Conceptual damage experiment and resultant survival curve.

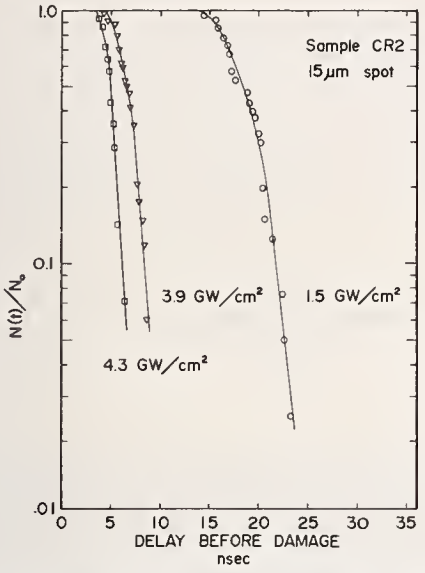

Figure 9. Survival curve indicating damage due to linear absorption. The survival time until damage is proportional to the intensity incident on the sample.

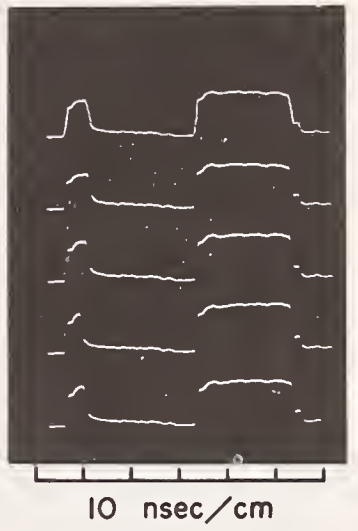

Figure 10. Typical damage data for an absorbing sample. The time until termination of the pulse transmitted through the sample (that pulse on the left of each trace) is proportional to the pulse intensity. The upper trace has been retouched on the rise and fall of the pulses.

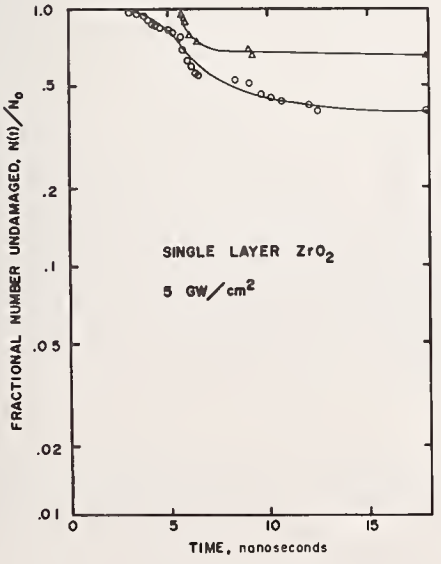

Figure 11. Survival curves indicating damage due to absorbing inclusions: A total of 60 sites were irradiated (data given by circles). The first 20 sites irradiated yield the data shown by triangles

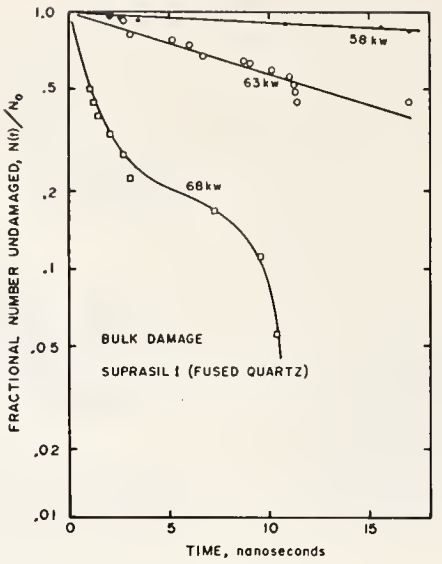

Figure 12. Survival curves indicating damage by electron-avalanche breakdown. The initial concave-upward curvature of the data at 68 kw indicates that limiting damage is due to avalanche breakdown at sites where the electric field is enhanced. The cause for final downward curvature on that curve is not understood.

COMMENTS ON PAPER BY MILAM

The speaker was asked if it was possible to identify the nature of the inclusion which led to a particular damage site. He responded that the damage morphology is determined by the portion of the illuminating pulse which intersects the damage site after damage is initiated and therefore it is insensitive to the actual initiation process. He also commented that it was not possible to find or identify submicron inclusions which are felt to be responsible for the damage, prior to damage, particularly since they are widely spread and there is no way of knowing which inclusion will damage beforehand. He further commented, in general, that despite the fact that inclusions are distributed in size, results obtained by this method are almost always unambiguous regarding identification of the mechanism of damage. Out of 50 runs only 2 or 3 cases were found in which a clear identification could not be made.

5.2 The Dynamics of Transmitted, Reflected, and Scattered Laser Pulses Above and Below Damage Threshold: The Search for Precatastrophic Damage*

Concetto R. Giuliano

Hughes Research Laboratories
3011 Malibu Canyon Road
Malibu, California 90265

This paper deals with a detailed study of the temporal shapes on a nanosecond time scale of laser pulses that are transmitted, back reflected, Brewster reflected, and backscattered at small angles for different powers below and above surface damage threshold. The sharp cutoff in transmitted light above damage threshold is accompanied by a corresponding cutoff in reflected light while the small angle backscattered light shows a sharp increase at the same time. The shapes of the transmitted and reflected pulses are essentially the same over a wide range of powers from below damage threshold to ∿ 10x above threshold. The small angle backscattered intensity is the most sensitive measure of the very onset of surface damage in that while the transmitted pulse shows essentially no change in shape for powers slightly above damage threshold, the backscattered component shows a marked increase in intensity. These results, along with the intensity dependence of Brewster reflected pulses, are discussed in terms of possible precatastrophic damage effects.

Key words: Back-scattering; 0.694 μm; precatastrophic damage; pulse dynamics; reflection; ruby laser; surface damage; temporal pulse monitoring; transmission.

1. Introduction

The problem of laser-induced damage over the past several years has been attacked by a variety of approaches, both experimental and theoretical. [1][1] There have been attempts to carefully quantify the measurements and characterize the phenomena involved. Morphology of damage has been studied in detail and a great deal of useful interpretation has arisen from these studies. [2-5] Damage mechanisms have been proposed both as a result of theoretical first principles and interpretation of experimental results. [2,6-9] Many ingenious experimental schemes have been devised to isolate the effects of different mechanisms and to probe details of the damage process. [10-13] New techniques have been developed for monitoring and characterizing both the sources used for damage studies and the materials being damaged, and a number of successful attempts have been made to increase the damage resistance of optical materials. [14-17]

The motivation for the work presented here has been first, to examine the dynamics of damaging pulses in more detail than has been done previously simply to obtain more information for characterizing details of the damage process and second, to explore the possibility of observing a subtle indication of the onset of damage at levels of irradiation that are lower than those for generating irreversible changes. To this end we have studied surface damage by characterizing the behavior of pulses transmitted through, reflected by, and scattered by samples over a range of incident fluxes from below to many times above damage threshold. Time-integrated and time-resolved data have been obtained for transmitted pulses and for both back-reflected and Brewster-reflected pulses. In addition to examining the light that is specularly reflected, we also measured the temporal and spatial properties of the light that is scattered out of the main reflected beam at moderate angles. The amplitude of backscattered light is very sensitive to the surface damage process and temporal irregularities in the backscattered light have been observed in the absence of any detectable catastrophic damage. However, this precatastrophic behavior was observed only a small percentage of the time (<5%) when the incident intensity was just below damage threshold; the remainder of the time a normal linear reflectivity was observed.

---

*This work was supported by the Defense Advanced Research Projects Agency through Air Force Cambridge Research Laboratories.

[1]Figures in brackets indicate the literature references at the end of this paper.

Hence, this monitoring technique, at least within the constraints with which it was explored in this work, does not appear to represent a practical means for detecting a damage precursor. There have been attempts by other investigators [18-23] to observe precatastrohpic or precursory damage indications, but none has led to a practical solution to the problem. There is no doubt that a nondestructive technique for determining the damage threshold of an optical component would be of great value to those working with high power lasers, and it is the strong conviction of this worker that damage investigations with this goal in mind should be pursued further.

2. Experimental Conditions

The data presented in this paper were obtained using a single longitudinal mode TEM_{00} Q-switched ruby laser that has been described in detail elsewhere. [24] The light was focused onto the surface of samples using a 19 cm lens; the focused spot radius is 55 μm (1/e for electric field). The material used for all the data presented in this paper was sapphire, but the behavior was essentially the same for other materials examined in a less detailed manner and, hence, is believed to be general. Also, whereas the quantitative results may differ slightly for different focusing conditions, the qualitative behavior is essentially the same.

3. Time-Integrated Transmission and Reflection of Laser Damage Pulses

In this section we report time-integrated percent transmission and reflection as a function of power for laser pulses. The main motivation for this work has been to determine whether the decrease in transmission of damaging pulses is accompanied by a corresponding increase in reflection as might be expected if the surface plasma density reaches a sufficiently high value.

The experimental setup for monitoring the pulses is shown in Figure 1. For the transmission experiments, the output from the detector located after the sample (detector No. 2) is integrated electrically and displayed on one trace of a dual beam oscilloscope (Tektronix 555) while the signal from the detector that monitors the incident energy (detector No. 1) is displayed on the other trace. Appropriate ratios are measured over a range of incident power from below damage threshold to many times above threshold. In a similar manner the percent reflected energy was measured in another set of experiments in which the reflected light that passes back through the focusing lens is monitored by detector No. 3 and displayed on the oscilloscope in place of the transmitted signal. The results of these measurements are shown in Figure 2 where the percent transmission data are presented for comparison with the reflectivity data. We see from these curves that both transmission and reflection show a monotonic decrease as the power increases above damage threshold.

4. Temporal Study of Transmitted and Reflected Damaging Pulses

A series of experiments was carried out to simultaneously study the temporal shape of transmitted and reflected pulses as a function of incident power. The purpose of these experiments was twofold: first, to determine whether the sharp drop in transmission at the time of damage formation is accompanied by a corresponding change in reflectivity, and second, to explore the possibility that some temporal irregularities might be detectable in the back-reflected pulse in the absence of catastrophic damage.

As we will see later, examination of the back-reflected light showed no indication of precatastrophic behavior, but there was evidence for such behavior when small-angle backscattering away from the directly back-reflected beam was studied.

For these experiments the outputs from detectors 2 and 3 in Figure 1 were individually displayed on separate Tektronix 519 oscilloscopes. The use of either line filters or Wratten No. 70 red filters assured that only laser light was detected. Both oscilloscopes were externally triggered by a pulse taken from an additional biplanar photodiode that is normally used to monitor the laser output. This external triggering scheme ensured that the two oscilloscopes are triggered at the same time (within less than 1 nsec). In this way variations in pulse shape for transmitted and incident light can be temporally related, even though they are separately recorded.

For each of the oscillographs recorded, a double exposure was taken. In the first trace, we recorded the signals when the laser was fired at the sample with the focusing lens removed from the optical path. For the second trace, the lens was appropriately positioned so that the light was focused on the surface of interest and the laser was fired again. The reproducibility of the ruby laser-amplifier combination is such that in each case (i.e., with lens and without lens) the total energy incident on the sample was the same (within $\sim$ 5%). Hence, in the absence of damage, each transmitted and reflected oscilloscope photograph shows a pair of traces of the same shape and amplitude. When damage occurred the temporal variations of the damaging pulse can be compared relative to the nondamaging pulse, both with respect to transmitted light and reflected light.

Experiments of this type were carried out in detail for both entrance and exit surface damage on sapphire, and the results of representative shots for different incident laser power are shown in Figures 3 and 4. Because of the difficulty in reproducing high-speed oscilloscope photographs, tracings of these photographs are shown.

The following features should be pointed out concerning the traces in the figures under discussion:

- The back-reflected pulse cuts off at the same time as the transmitted pulse.
- Most temporal irregularities in the transmitted pulse are duplicated in the reflected pulse.
- The back-reflected intensity for a damaging pulse is always less than or equal to that of the reference pulse. That is, the specular reflectivity of the interface during the occurrence of damage is always less than that of the undamaged interface.

Because of the lens diameter (2.54 cm) and distance from the sample surface (20.7 cm) the total amount of reflected light collected in the experiments described above would have spanned a maximum half angle of 3.5°.

5. Spatial Properties of Back-Reflected Light From Damaging Pulses

The experiments described in the preceding sections involved measurements of the reflected light collected over a half angle of 3.5°. It was of interest to obtain information concerning the spatial properties of the light being collected and to compare it with truly specularly reflected light. To this end an experiment was carried out, as illustrated in Figure 5, where the specularly reflected light was allowed to strike a photographic film (Polaroid Type 47). In addition to photographing the reflected beam as a function of incident total energy, the spot was photographed for different diameter apertures placed in the beam between the lens and the sample. In this way angular information could be obtained for some of the off-axis features.

Qualitative features of these beam profiles are shown in Figures 6 and 7. At low powers a smooth circular spot is seen that remains essentially unchanged when damage threshold is reached and even substantially above damage threshold ($\sim 2x$). At higher powers (above twice threshold) signs of off-axis features begin to appear and an increasing amount of light is detected in the form of irregular rings and bright spots.

The angular extent over which the pattern is detected was measured by varing the size of the aperture between the lens and the sample. It was found that an aperture diameter between 5.5 and 7 mm was the smallest that could be used to give the same pattern as obtained with no aperture in the system (Figure 7). (The effective limiting aperture caused by the lens would be 12 mm at that position.) Hence the off-axis features in the photographs extend over a half angle of from 1.5° to 2°.

It should be pointed out here that the measurements of "specularly" reflected light discussed earlier included the light that is shown in the photographs of Figures 6 and 7. Because of the setup used in those experiments, the angular acceptance of the detected light was on the order of 3.5° half angle. Hence, even though a detectable amount of light is scattered out of the specular beam, the total amount of light collected over the 3.5° half angle shows the general decrease with power above damage threshold.

6. Measurements of Backscattered Laser Light From the Surface During Damage

Since both the transmitted and reflected pulses show a sharp decrease in intensity following the creation of damage, one might be inclined to attribute the loss of light to absorption by the damaged region and/or surface plasma. However, there is also the possibility that an appreciable amount of the laser light is scattered out of the forward and back direction as well as absorbed.

A measurement of the total amount of scattered light would require the means for collecting and measuring the light scattered over all directions or a knowledge of the scattering distribution and subsequent sampling of the light over a particular solid angle. Measurements of this type were not carried out in our experiments but a few experiments were conducted that were directed toward determining the temporal behavior of scattered light. Again, the purposes were (1) to explore the possibility that an appreciable amount of light might be scattered out of the main beam, (2) to obtain a temporal correlation between the scattered light and transmitted or specularly reflected light, and (3) to explore the possibility that some indication of precatastrophic damage might be found in the temporal characteristics of the scattered light.

The experimental setup used for these experiments is shown in Figure 8. It is similar to the previous setup, except that a white card (7 cm sq.) with an aperture was placed approximately halfway between the focusing lens and the sample. Detector No. 3 was placed to monitor the diffuse laser light

scattered back from the sample surface onto the white card. The aperture diameter (6.5 mm) was substantially larger than the convergent beam diameter (1.7 mm) at the point where it passed through the hole in the card.

The experimental data were obtained in a similar way that the previously described data were taken; the laser was fired once with the lens removed and the second time with the lens placed appropriately in the beam, both pulses being recorded on the same oscilloscope photograph.

The results of a number of these experiments are illustrated in Figure 9. Here the data are displayed differently from before in that the scattered pulse has been inverted relative to the transmitted pulse so that the temporal relationship can be seen more easily.

The general qualitative features seen in these traces are

- The scattered light for damaging pulses is characterized by a sharply rising spike followed by a more slowly decaying tail.
- The peak of the scattered spike occurs at the same time that the transmitted pulse begins its sharp cutoff.
- The scattered intensity begins to rise from its background level before the transmitted pulse shows any appreciable irregularity.
- In cases where very slight damage occurs so that the transmitted pulse shows little or no change in shape, there is still an appreciable amount of scattered light detected. (Relative detector sensitivities are about 50:1.)

The sensitivity of the backscattered amplitude shown in the above experiments indicates that this type of monitoring is a more sensitive indication of surface damage than examination of either the transmitted or the specularly reflected light. Moreover, the fact that the backscattered light begins to rise in intensity relative to the background before the transmitted light shows signs of cutoff suggests that some evidence for precatastrophic damage may be indicated from this kind of measurement.

6.1 Precatastrophic Damage Experiments

Tentative evidence for precatastrohpic damage indications were seen in a few instances in the absence of damage where the scattered light showed a definite irregularity compared with the background pulse. In these cases the transmitted pulses were essentially identical with or without the focusing lens in place, whereas the backscattered pulse with the lens in place had a different shape than the pulse observed with the lens removed.

Examples of this behavior are shown in Figure 10. We see that the scattered pulse with the lens in place is different in shape from the one in which the lens is removed. In these examples the laser power incident on the surface was very close to the value where damage occurred but not sufficiently large to produce any detectable damage on that particular shot. All the pulses in the examples shown were followed by damage-producing pulses of slightly higher energy. Because of the detector sensitivity, it is difficult to obtain large signals at these levels of illumination.

The amplitude of the backscattered signal for the nondamaging reference pulse depends on the size of the aperture chosen and the alignment of the sample. Sometimes the unfocused beam was not reflected completely through the hole in the white card and the reference signal would be correspondingly larger than that obtained for normal incidence. Since the background pulse in these experiments is one in which the lens is removed from the system, the diameter of the beam in passing through the 6.5 mm aperture is different in the two cases. (The diameter of the focused beam at the $1/e^2$ intensity points is 1.7 mm and that for the unfocused beam is $\sim$ 4 mm.) Also the fact that the reference pulse is not focused means that it strikes a larger surface area (and hence may be scattered differently) raising some question as to the validity of comparing the pairs of pulses on the double exposure oscilloscope pictures.

In later experiments we changed the procedure for taking data so that the reference pulse could be employed more meaningfully. For these experiments the focusing lens was left in place for both shots obtained on the double exposure oscillogram. For the first shot recorded (the low power nondamaging reference trace) a Wratten neutral density filter ND 0.3 was placed in the laser beam just past the Glan-Kappa polarizers (Figure 8). The laser intensity in this part of the beam was never high enough at the levels we used to cause any bleaching or damaging of the filter and the $\sim$ 2x filter attenuation was reproducibly obtained. For the second shot of the double exposure oscillogram (the high power, potentially damaging shot) the ND 0.3 filter was removed from the main beam and placed in front of detector No. 3 (the one that monitors scattered light) and another filter with the same attenuation as separately

measured was placed in front of detector No. 2 (the one that monitors transmitted light). In this way signals seen by detectors 2 and 3 would be the same for both pulses as long as the sample behaved in a linear fashion. This linearity was confirmed in detail for a series of pairs of low power pulses, neither of which was intense enough to create damage. The result was a number of double exposure oscillograms in which both pulses were essentially superimposed.

Using the above technique, we carried out a detailed series of experiments for different laser powers very close to but usually below damage threshold. We confirmed the results obtained earlier using focused and unfocused beams and satisfied ourselves that the reference beam trances as depicted in Figures 9 and 10 are, in fact, valid comparison traces.

Most of the measurements performed using the above described method were directed toward exploring whether signs of precursory damage could be detected reliably and reproducibly by monitoring the backscattered temporal profile. Occasionally (less than 5% of the time), we would obtain traces similar to those illustrated in Figure 10 where the transmitted pulse showed no change from the reference pulse but where the backscattered pulse was distinctly different from its reference pulse and where there was neither a visible spark of any kind nor any detectable surface damage on subsequent microscopic examination. Possible explanations for this behavior are local heating causing a slight surface irregularity that could scatter or deflect the beam temporarily off axis or the formation of a microscopic plasma that could scatter light. Another possibility that cannot be ignored is the chance encounter of a scattering dust particle that happens to be illuminated somewhere between the screen and the sample surface.

The practical result of these backscattering measurements is that while definite precursory effects are observed in the absence of catastrophic damage, they are too subtle to be easily characterized and at this point do not indicate a practical reproducible means for nondestructive damage threshold determination.

7. Summary of Pulse Temporal and Spatial Experiments

The results of the above measurements can be summarized as follows:

1. The damaging pulse shows a sharp temporal cutoff both in transmission and reflection for light collected over a cone of 3.5° half angle.

2. Photographs of the back-reflected light show that a considerable amount of this light is scattered out of the main beam at small angles (less than 2°) in the form of bright spots and diffuse rings.

3. In addition to the small angle backscatter seen in the photographs, an easily detectable amount of light is scattered back at larger angles that is not seen photographically.

4. The light scattered back at larger angles (within a 23° half-angle cone) shows a sharp temporal spike at the time the transmitted light and specularly reflected light cuts off.

5. Some evidence of precatastrophic effects has been seen through observation of this large angle backscattered component.

6. Although it is almost certain that the damaged surface site and associated plasmas absorb a measurable amount of the incident pulse, it is not possible to obtain an accurate measure of the light absorbed during damage without integrating all the scattered light.

8. Brewster Angle Reflectivity as a Function of Incident Intensity

During the latter stages of our backscattering measurements in search of precursory damage phenomena we decided to explore for nonlinearities in the reflectivity at Brewster's angle. The rationale for this type of experiment was based on the fact that the nonzero value of the reflection coefficient for real dielectrics at Brewster's angle is attributed to slight residual absorption and that if some subtle surface disturbance were occurring prior to catastrophic damage, it might be detectable as a power dependence in this reflectivity. To explore this possibility we set up an experiment shown schematically in Figure 11 in which the incident energy, the Brewster reflected, and the transmitted light were all monitored. The signals from detectors 2 and 3 were displayed on Tektronix 519 and 7904 oscilloscopes so that we could look for temporal irregularities in the Brewster reflected light compared with the transmitted light. Reference pulses in the double exposure oscillograms were obtained in a similar manner to that described earlier. Figure 12 shows a series of double exposure oscilloscope traces comparing the transmitted and Brewster reflected pulses over a range of powers from the onset of damage to about 3.5 times damage threshold.

The results of these experiments are summarized below:

- Over a range of incident power from 1/10 damage threshold up to damage threshold the total energy reflected at Brewster's angle is a linear function of input energy corresponding to a reflectivity of $\sim 10^{-4}$.
- Over the range of incident powers below damage threshold the temporal shapes of the Brewster reflected pulse and the transmitted pulse are identical showing no evidence for precatastrophic effects.
- The Brewster reflected light shows a cutoff similar to that of back-reflected light (Figures 3 and 4) but occurring slightly later than the cutoff in transmission.
- While the transmitted and back-reflected pulses remain at a low level from the time of cutoff throughout the remainder of the pulse, the Brewster reflected pulses return to a "normal" level before the pulse ends (i.e., the Brewster and reference traces meet again before the end of the pulse while the transmitted pulse remains cut off).

The fact that the Brewster reflected light cuts off later than the transmitted light suggests that the point where the initial breakdown occurs is far enough below the surface that it does not affect the reflected beam initially. Also supporting the idea that the initial point of breakdown is below the surface is the fact that there is no increase in Brewster reflectivity as a function of power as would be expected if there were an increase in surface absorption; the amplitude of the Brewster reflected pulse is always equal to or less than the reference pulse. The back-reflected beam, however, would be expected to cut off at the same time as the transmitted beam because the back-reflected light is affected by subsurface effects as well. The situation is further complicated by plasma effects at the surface. Earlier work on surface plasmas [10,25] has shown that there are two types of plasmas formed during surface damage, an air plasma that extends along the light direction and a material plasma (explosion plasma) that extends in the direction of the surface normal. The latter plasma is caused by the deposition of energy in the material and subsequent explosion. For surfaces tilted away from normal incidence the two plasmas point in different directions, and the extent of their interactions with reflected light beams will depend on the surface tilt. In particular, the explosion plasma will not interact with the incident light as strongly for tilted surfaces as for surfaces at normal incidence.

9. Conclusion

The dynamics of damaging pulses have been studied for a number of different conditions of surface damage. Monitoring of backscattered light at moderate angles (2° to 25°) shows it to be an extremely sensitive means for detecting subtle aspects of damage initiation. Some signs of precursory damage behavior are noted in monitoring of backscattered light, but within the limits of the experiments performed, this does not appear to be a practical means for nondestructive testing of laser materials. Areas for further exploration along these lines are to monitor light scattered out of the main beam at angles other than the ones reported in this paper. Probing of the irradiated region with other types of optical probes are also recommended as possible means of investigating the more subtle aspects of surface damage.

The damage process is obviously very nonlinear, and once the critical conditions are met there is a rapid catastrophic runaway. But under suitable experimental conditions it should be possible to observe the initial stages in a reversible way. It is this author's recommendation that this type of approach be applied whenever possible by workers active in this field in order to uncover the most subtle fundamentals of the laser damage phenomenon.

10. References

[1] For detailed references on the bulk of work done in this area the reader is referred to the contents of National Bureau of Standards Special Publications No's. 341, 356, 372 and 387 (U.S. GPO, Washington, D. C., 1970-1973).

[2] Giuliano, C.R. and Marburger, J. H., Phys. Rev. Lett. 27, 905 (1971).

[3] Boling, N. L., Dubé, G., Crisp, M. D., National Bureau of Standards Special Publication No. 387 (U.S. GPO, Washington, D.C., 1973) p. 69.

[4] Wang, V., Braunstein, A., Braunstein, M., Rudisill, J. E. and Wada, J. Y., ibid., p. 157.

[5] Giuliano, C. R. and Tseng, D. Y., ibid., p. 239.

[6] Hellwarth, R. W., NBS Special Publication 341 (U.S. GPO Washington, D. C. 1970) p. 67.

[7] Hopper, R. W. and Uhlmann, D. R., J. Appl. Phys. 41, 10 (1970).

[8] Bass, M. and Barrett, H. H., IEEE-JQE 8, 338 (1972).

[9] Zverev, G. M., Mikhailova, T. N., Pashkov, V. A. and Solov'eva, N. M., Soviet Physics-JETP 26, 1053 (1968).

[10] Giuliano, C. R., IEEE-JQE 8, 749 (1972).

[11] Milam, D., Bradbury, R. A. and Bass, M., NBS Special Publication No. 387 (U.S. GPO, Washington, D. C. 1973) p. 124.

[12] Bliss, E. S., this publication.

[13] Milam, D., et al., this publication.

[14] Giuliano, C. R., Appl. Phys. Lett. 21, 39 (1972).

[15] Swain, J. E., IEEE-JQE 4, 362 (1968).

[16] Allen, S. D., Braunstein, M., Giuliano, C. R. and Wang, V., this publication.

[17] Potosky, J. C., Giuliano, C. R. and Klein, C. F., this publication.

[18] Belikova, T. P., Savchenko, A. N. and Sviridenkov, E. A., Soviet Physics-JETP 31, 1021 (1970).

[19] Belikova, T. P. and Sviridenkov, E. A., JETP lett. 3, 257 (1966).

[20] Bräunlich, P., Carrico, J., Rosenblum, B., and Schmid, A., NBS Special Publication No. 387 (U.S. GPO, Washington, D.C. 1973) p. 91.

[21] Parks, J. H. and Alyassini, N., NBS Special Publication No. 372 (U.S. GPO, Washington, D.C. 1972) p. 104.

[22] Edwards, D. F., Harker, Y. D., Masso, J. D. and She, C. Y., ASTM Special Technical Publication 469 (American Society for Testing and Materials, Philadelphia, Pa., 1969) p. 128.

[23] Edwards, D. F., She, C. Y., Masso, J. D., Harker, Y. D. and Schade, H. C., NBS Special Publication No. 341 (U.S. GPO, Washington, D.C. 1970) p. 102.

[24] Giuliano, C. R. and Hess, L. D., NBS Special Publication No. 341 (U.S. GPO, Washington, D.C. 1970) p. 76.

[25] Giuliano, C. R., NBS Special Publication No. 372 (U.S. GPO, Washington, D.C. 1972) p. 46.

11. Figures

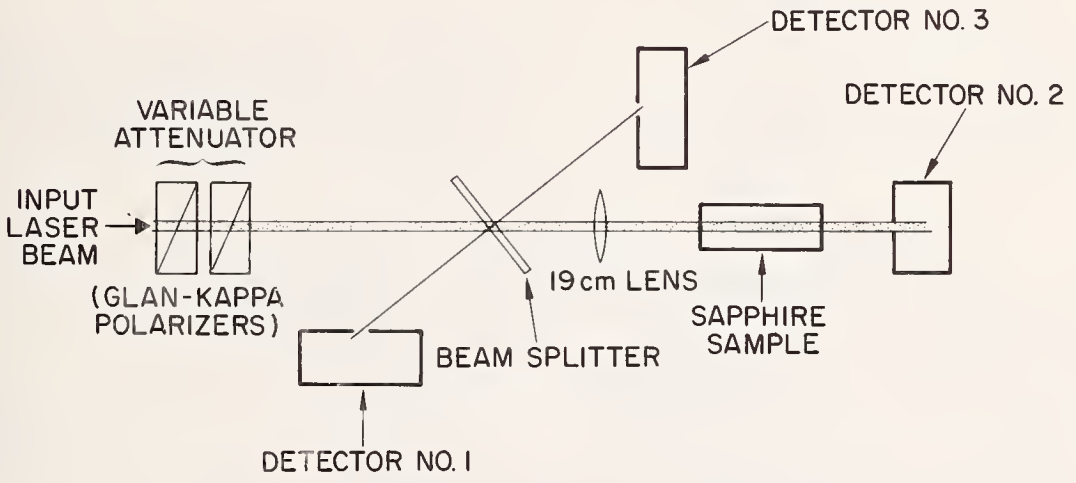

Figure 1. Experimental setup used in transmission and surface reflection measurements.

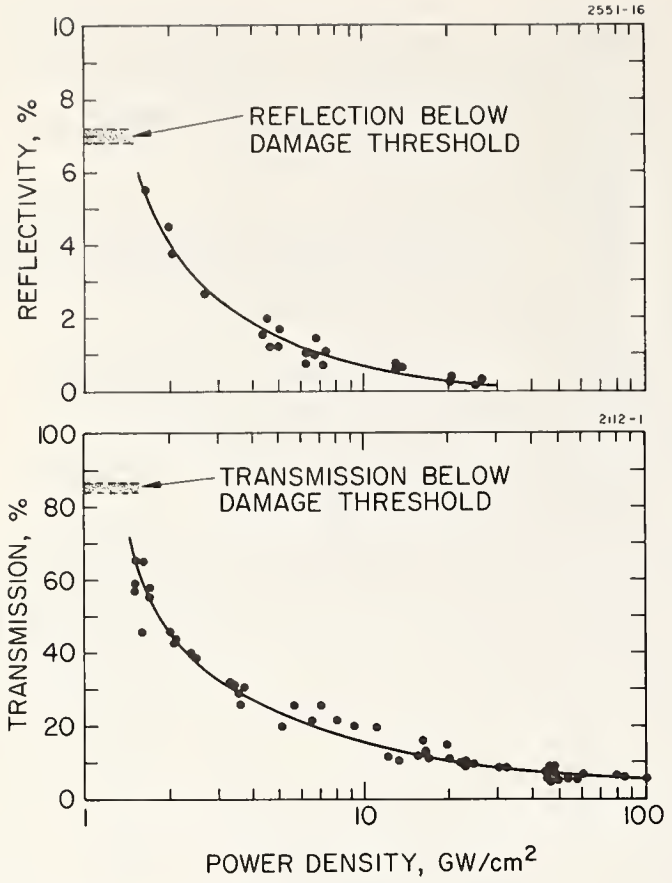

Figure 2. Integrated transmission and reflectivity of damaging laser pulses as a function of incident power on sapphire surfaces.

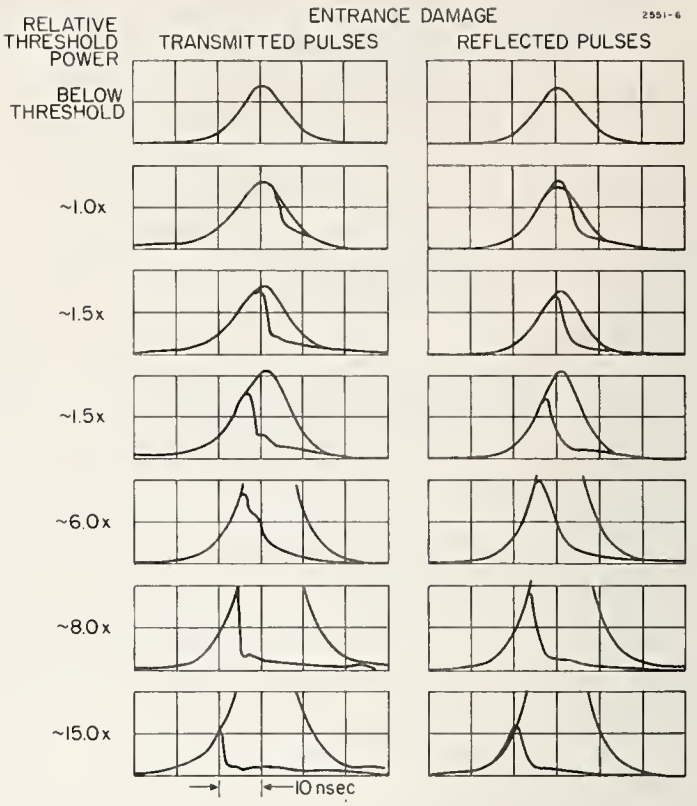

Figure 3. Temporal shapes of transmitted and reflected pulses for different powers relative to threshold for entrance damage.

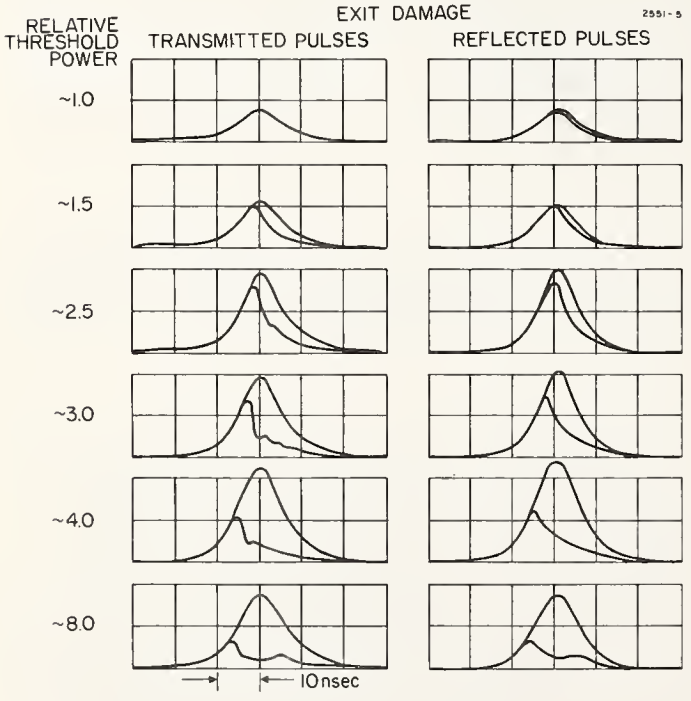

Figure 4. Temporal shapes of transmitted and reflected pulses for different powers relative to threshold for exit damage.

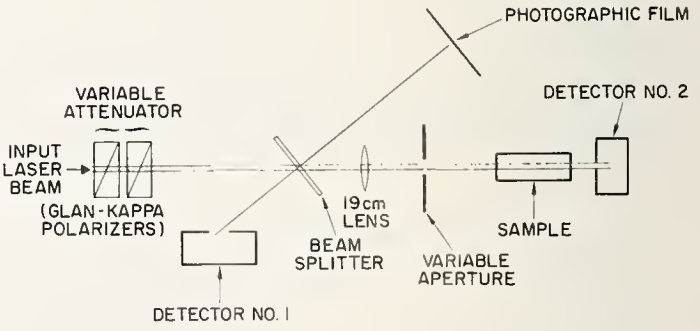

Figure 5. Experimental setup for photographing spatial features of specularly reflected light.

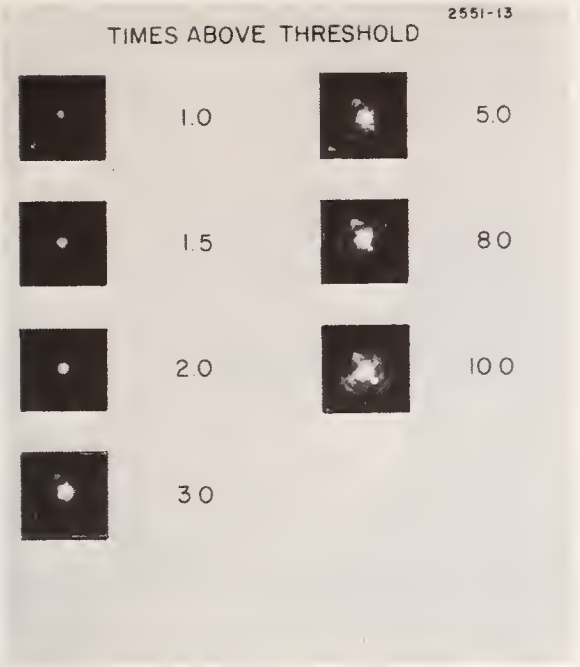

Figure 6. Photographs of back-reflected beam for increasing laser power above damage threshold (from 1 to 10x).

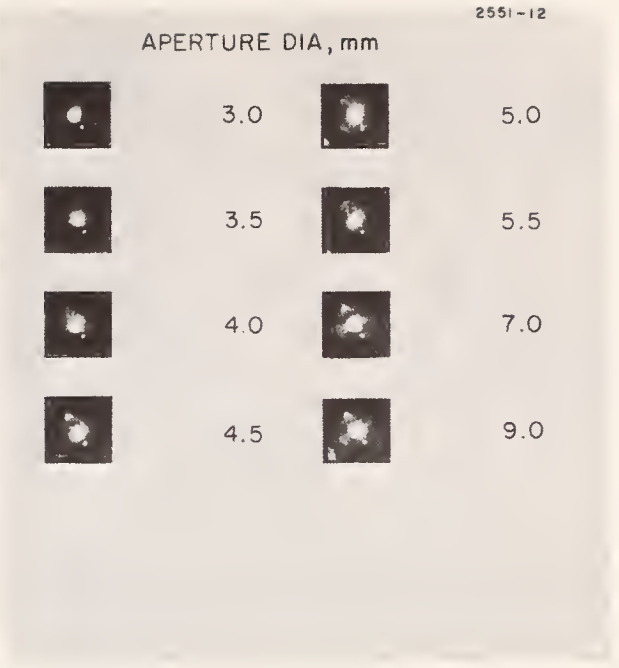

Figure 7. Photographs of back-reflected beam for different aperture sizes between lens and sample. Constant laser power for each shot ~10x threshold.

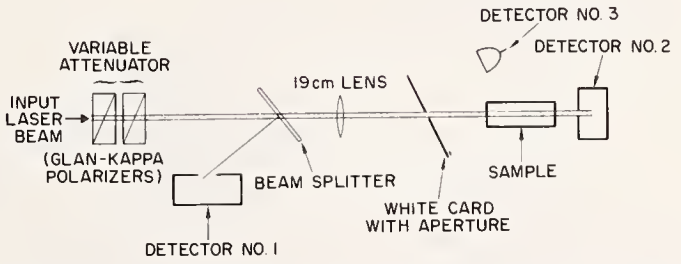

Figure 8. Experimental setup used in backscattering measurements.

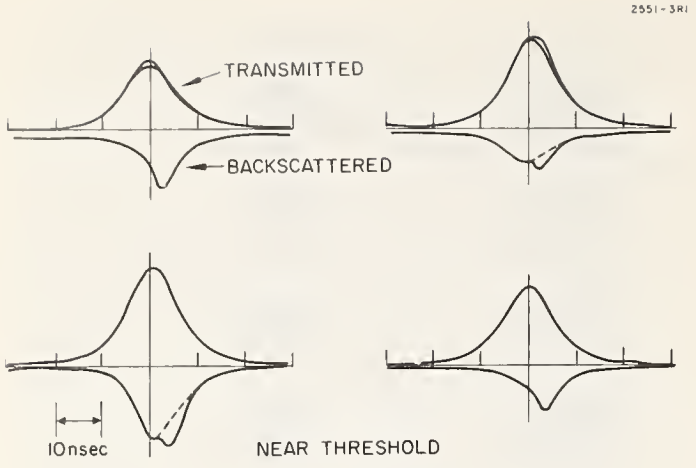

9(a)

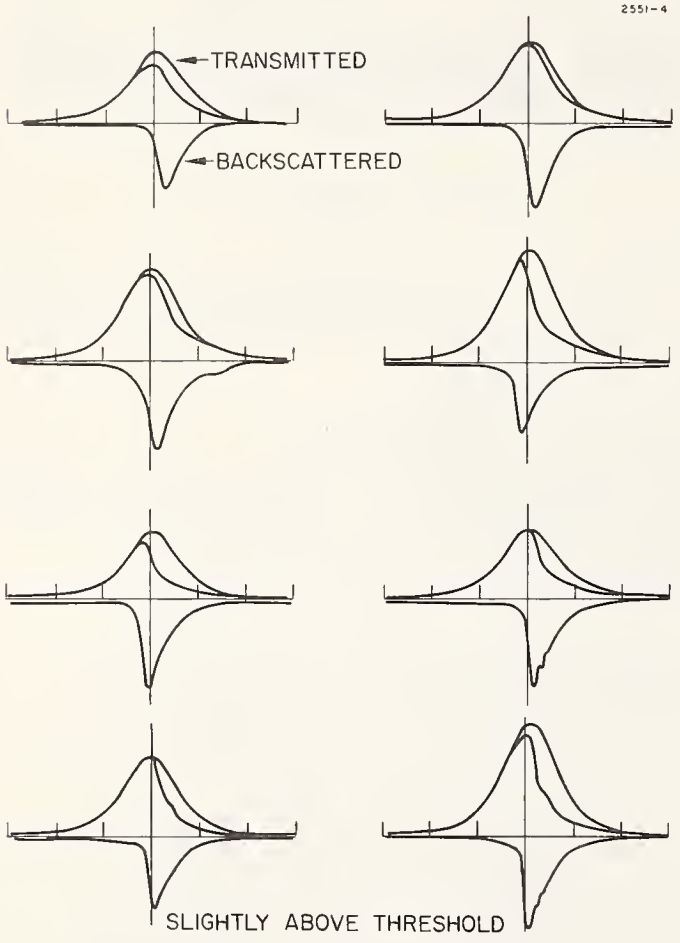

9(b)

Figure 9. Temporal profiles of laser pulses transmitted through and backscattered by sapphire samples at different powers relative to entrance surface damage threshold.

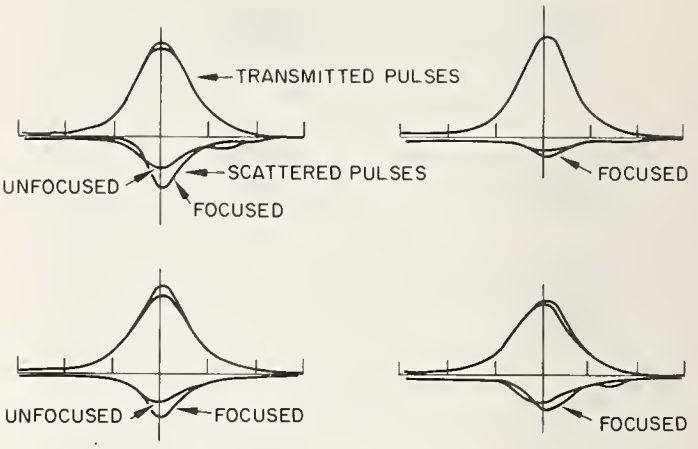

Figure 10. Backscattered pulses compared with transmitted pulses below damage threshold showing temporal irregularities in the backscattered pulse.

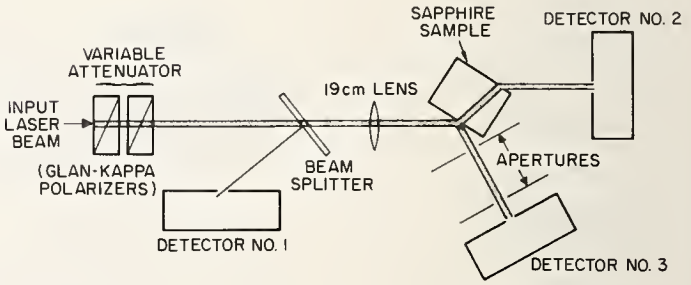

Figure 11. Experimental setup used in transmission and Brewster reflection measurements.

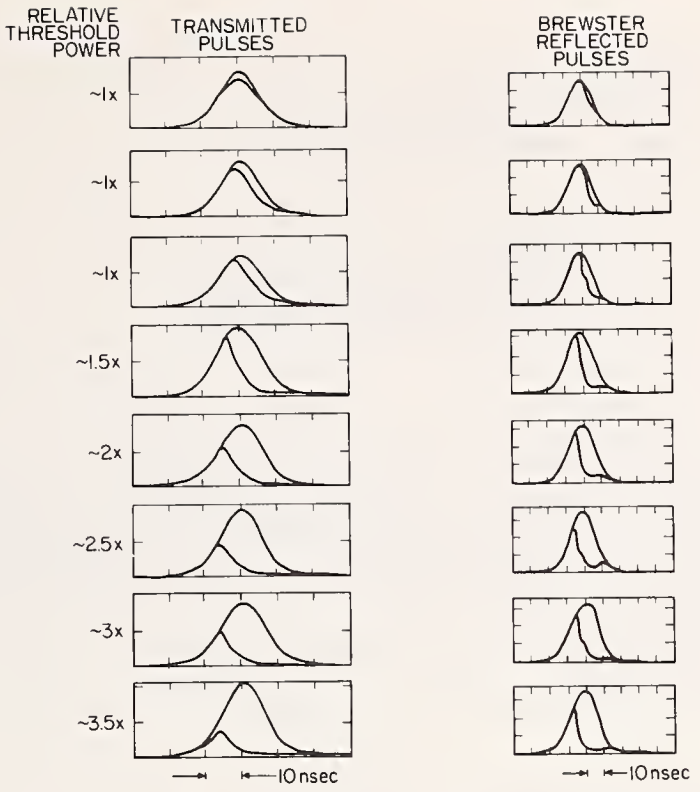

Figure 12. Temporal shapes of transmitted and Brewster reflected pulses for different powers relative to damage threshold.

COMMENTS ON PAPER BY GIULIANO

David Milam of the Air Force Cambridge Research Laboratory commented that he had observed damage precursors only on pulses in which damage occurred later in the pulse, that is to say, the observed change in the material properties only occurred on pulses sufficiently energetic to create damage. The speaker commented that in general it was true that suitable observables must be chosen in order to obtain precatastrophic damage information. He referred to the work of Parks and Alyassini on the increased scattering observed in thin films in the presence of high power laser pulses. In response to a question concerning the permanent nature of the scattering diagnostic, the speaker commented that increased scattering was only observed during high power pulses and that there was no permanent effect. It was pointed out that it is very hard to interpret diagnostic tests like scattering when the damaging pulse is very far above threshold, due to the fact that a large number of independent scattering sites are created and due to the presence of competing processes. Finally, it was mentioned that in this work, damage was always accompanied by the creation of a plasma. This was attributed to the absence of absorbing inclusions and to the fact that the Sapphire material involved was of good quality and therefore very near its intrinsic damage limit.

564-378 O - 74 - 14

5.3 Rutherford Backscattering Diagnostics of Laser-irradiated GaAs

R.R. Hart, C.R. Giuliano, and H.L. Dunlap

Hughes Research Laboratories
3011 Malibu Canyon Road
Malibu, California 90265

The Rutherford backscattering of 280 keV He^{++} has been used to study the amount and depth distribution of lattice disorder introduced in GaAs by intense laser irradiation. The lattice remains largely intact after irradiation at a laser power level of three times the damage threshold (optical) except within a 175 Å surface layer. In this surface layer the number of scattering centers increases to about 2.5 times the number of Ga and As atoms present in the surface oxide on undamaged GaAs.

Key words: Ion channeling; laser-damaged GaAs; Rutherford backscattering; scattering centers.

1. Introduction

The energy spectrum of Rutherford backscattered light ions, which are incident along a major channeling axis of a target crystal, can provide quantitative information of both the amount and depth distribution of lattice disorder. Such measurements have been especially useful for the study of ion-implantation-produced disorder in Si [1,2].[1] We have extended this technique to the study of laser-damaged GaAs. See Khan [3] for a general discussion of measurement techniques.

The experimental arrangement is illustrated in figure 1. In the present work, a 280 keV He^{++} ion beam was used for all measurements. The beam was mass analyzed and was restricted to a divergence of less than 0.02° and to a diameter of about 0.3 mm by a final 0.3 mm diameter aperture. The aperture could be moved parallel to the target surface to permit measurements across the diameter of the laser-damaged area. Backscattered He particles were detected at an angle of 160° with respect to the incident beam with a cooled Si detector. The GaAs sample was mounted on a goniometer to permit either <100> or random alignment of the crystal with the incident beam. A biased Faraday cup arrangement was utilized for target current measurements. The GaAs sample used for this work was an n-type wafer which was <100> oriented and polished. The present study was limited to the B face of the wafer.

A local area of the sample was irradiated with the unfocused output of a single transverse and longitudinal mode Q-switched ruby laser that has been described in detail elsewhere.[4] The pulse duration was 20 nsec and the beam spot size at the sample surface was 1.2 mm (1/e radius for intensity). Under these conditions the entrance surface damage threshold for the sample for which data is presented in this paper ranged from 12 to 15 MW/cm^2.[2] Here, damage is defined as a visual change at the surface as viewed in the damage setup at 30x magnification. At this low magnification the damage appeared as a change in the surface reflectivity and a fine speckled texture. Under higher magnification, scanning electron micrographs showed a general micro-molten appearance characterized by damage pits from 2 to 4 μm in diameter scattered over the entire laser damaged area. The damage morphology is similar to that shown by Smith.[5]

Backscattered energy spectra of 280 keV He^{++} incident in a random direction and along the <100> axis of both an undamaged area and near the center of the laser-damaged area are shown in figure 2. Consider first the random spectrum. The edge at a backscattered energy of 226 keV corresponds to the backscattering of He^{++} from Ga and As atoms at the sample surface. The yield at decreasing backscattered energies corresponds to backscattering from Ga and As atoms at progressively deeper depths below the surface. The depth scale indicated on Figure 2 (16 Å/keV) was estimated by extrapolation of stopping power data of He in Ge. [6]

---

[1] Figures in brackets indicate the literature references at the end of this paper.

[2] This is defined as the total power divided by πa^2 where a is the 1/e intensity radius giving the power density on axis.

The strong decrease in yield of the <100> spectrum from the undamaged crystal, as compared to the random yield, is caused by ion channeling effects in a crystalline lattice. [1] The peak at the sample surface is attributed to backscattering from Ga and As atoms in the surface oxide. The <100> spectrum obtained by He^{++} analysis near the center of the laser-damaged area is also shown in figure 2. In comparison to the <100> spectrum from the undamaged area, a substantial increase in the area of the surface peak, as well as an increased yield at deeper depths, are noted. The increase in area of the surface peak is caused by an increased number of scattering centers near the surface of the laser-damaged area. Note that the widths of the surface peaks correspond to the detector resolution, i.e., $\sim$ 175 Å for the GaAs surface. Thus, the actual widths are less than or equal to 175 Å. The scattering centers which contribute to the increased area of the surface peak may be either Ga and As atoms displaced from lattice sites by greater than $\sim$ 0.1 Å or Ga and As atoms present in an increased thickness oxide layer. The increase in <100> yield at deeper depths is primarily due to dechanneling of the He^{++} in traversing the damaged or altered surface region; however, some deep disorder or strain cannot be ruled out. Nevertheless, it seems significant that at depths greater than 175 Å a large fraction (greater than 80%) of the beam remains channeled, indicating that the GaAs lattice is largely intact.

The areas of the surface peaks, the cross-hatched areas of figure 2, were determined on the assumption of linear dechanneling corrections as indicated by the dashed lines. Based on the Rutherford scattering cross section the areas of the surface peaks were converted to the number of scattering centers per cm^2. These results are plotted in figure 3 as a function of distance across the laser-damaged region of the sample. The profile of energy density of the laser beam is also shown in figure 3, and the damage threshold (optical) is indicated. It can be seen in Figure 3 that the number of scattering centers per cm^2 begins to increase above the undamaged level near the energy density corresponding to the damage threshold. Moreover, the number of scattering centers per cm^2 increases nonlinearly with the energy density towards the center of the laser irradiated area to a maximum of about 2.5 times the number in the undamaged regions of the sample.

In conclusion, we have shown that the technique of He^{++} backscattering and channeling provides quantitative information regarding the number and depth of scattering centers introduced into a crystalline surface region by intense laser irradiation. For the case studied here, i.e., GaAs irradiated at a laser power level approximately three times the damage threshold (optical), the lattice is largely intact except within 175 Å of the surface. In this surface layer the number of scattering centers increases to about 2.5 times the number of Ga and As atoms present in the surface oxide on undamaged GaAs.

2. References

[1] Davies, J. A., Denhartog, J., Eriksson, L. and Mayer, J. W., Can. J. Phys. 45, 4053 (1967).

[2] Hart, R. R., Rad. Effects 6, 51 (1970).

[3] Khan, J. M., NBS Special Publication No. 372 (U.S. GPO, Washington, D.C. 1972) p. 75.

[4] Giuliano, C. R. and Hess, L. D., NBS Special Publication No. 341 (U.S. GPO, Washington, D.C. (1970).

[5] Smith, J. L., J. Appl. Phys. 43, 3399 (1972), also in NBS Special Publication No. 372, (U.S. GPO, Washington, D. C. (1972) p. 70.

[6] Chu, W. K. and Powers, D., Phys. Rev. 187, 478 (1969).

3. Figures

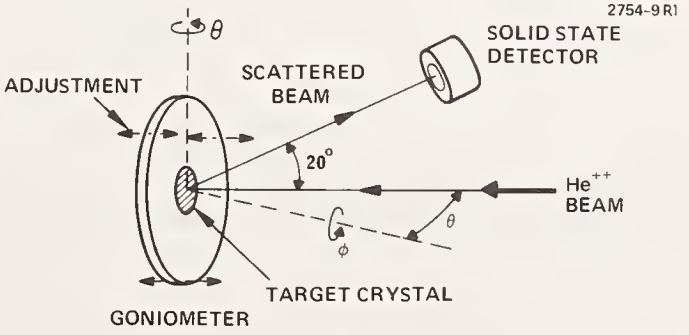

Figure 1. Schematic of backscattering setup.

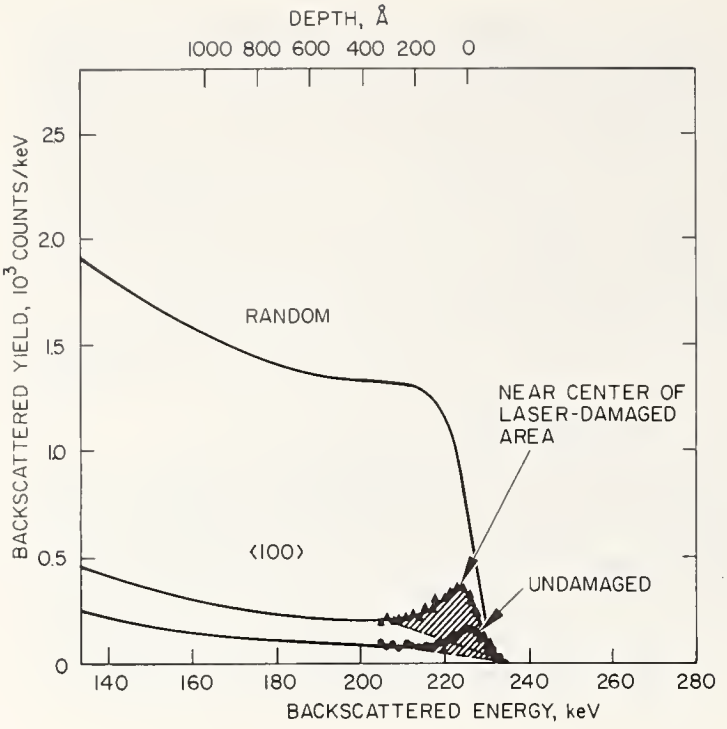

Figure 2. Backscattered energy spectra of 280 keV He^{++} incident in random and <100> directions on undamaged and near the center of the laser-damaged area of a GaAs sample. The cross-hatched areas are proportional to the number of scattering centers within 175 Å of the surface.

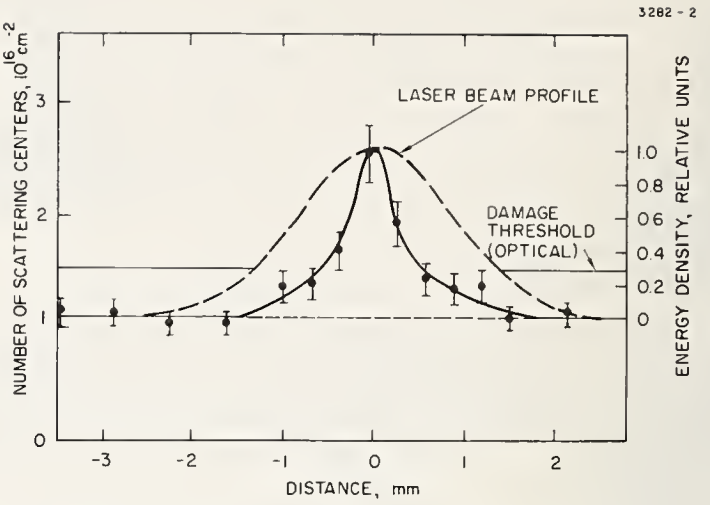

Figure 3. The number of scattering centers per cm^2 within 175 Å of the surface as a function of distance across a laser-damaged area of GaAs. The profile of the energy density of the laser beam together with the damage threshold (optical) are also indicated.

COMMENTS ON PAPER BY GIULIANO

Harold Posen of the Air Force Cambridge Research Laboratory indicated that he was not as optimistic as the speaker about using Rutherford back-scattering as evidence of crystalline disorder. He suggested it might be better to use, for example, transmission electron microscopy to ascertain that the material was indeed disordered. The speaker commented that in this work they were not able to identify the origin of the disorder, but only that the back-scattering had increased as a result of laser illumination. This increase in back-scattering might, for example, be due to a chemical process in which the gallium or arsenic atoms in the lattice were replaced by chemical compounds. In any case, any distruption of the lattice would be expected to lead to an increase in the back scattering. Jahn Khan, of Lawrence Livermore Laboratory, commented that he was surprised that in the presence of such pronounced damage morphology that only a small change in the channeling in the crystal was observed. In the presence of such massive changes in the material surface he indicated that he would expect a pronounced change in the back-scattering signal. The speaker indicated that this was indeed his expectation until the work was performed and that he too was surprised by the relatively low back-scattering signal that corresponded with significant surface damage. In the discussion, the question was raised of the possibility that the damage mechanism consisted of melting and recrystallization. The possibility was also raised that the damage process might involve the complete removal of strongly disordered material.
Jean Bennett of the Michelson Laboratory indicated surprise that significant visible damage was observed when the Rutherford back-scattering indicated that the extent of the damage was only of the order of 300 (Angstroms) into the surface. The speaker commented that no diagnostics other than back-scatter were employed in the analysis of these samples.

5.4 Surface Defects on Crystals of TiO_2 and YVO_4 Studied by Laser-Induced Damage Effects

K. M. Leung and L. G. DeShazer

Center for Laser Studies
University of Southern California
Los Angeles, California 90007

The nature of surface defects on single crystals of rutile (TiO_2) and yttrium orthovanadate (YVO_4) was investigated by laser-induced damage effects using a TEM_{00} Q-switched ruby laser. It was demonstrated that damage to these crystal surfaces can be distinguished as defect damage and intrinsic damage, where the damage thresholds decreased with increasing focal spot-size of the laser beam. The dependence on the directions of crystallographic axes and electric field was studied. The morphology of the surface damage sites was examined by the scanning electron microscope revealing that polishing imperfections were the cause of damage on TiO_2 surface and inclusions were the cause of damage in the case of YVO_4.

Key words: Damage morphology; polishing compounds; spot-size dependence; surface defects; rutile crystal damage; yttrium orthovanadate crystal damage.

1. Introduction

At the Fifth Annual Symposium on Laser Damage, we demonstrated that the distribution of coating defects can be related to the focal spot-size of the laser beam when measuring the damage threshold of a dielectric thin film. [1][1] However, since it is very difficult to identify what type of defect on thin films enhances laser damage, we transferred our defect investigations to surfaces of single crystals. We report here that surface defects on transparent dielectrics, either imperfections due to polishing or inclusions due to impurities, can be revealed by using the same approach as to the dielectric coatings.

The nature of surface defects on two uniaxial single crystals was investigated. By measuring the lowest damage threshold on the samples as a function of laser beam spot-size and by examining the morphology of the corresponding damage sites, we find that polishing imperfections were the cause of damage on rutile surface and inclusions were the cause of damage in the case of yttrium orthovanadate surface. The damage dependence on birefringence can be fully explained by Fresnel reflection losses, not requiring Bloembergen's model for explanation[2].

2. Experimental Procedure and Preparation of Samples

The experimental setup and procedure used in measuring the damage threshold of crystal surfaces is similar to that in the case of dielectric thin films. [1] The laser-induced scatter (LIS) technique is emphasized for damage diagnosis in our work. The spot-size is the $1/e^2$ radius of the intensity profile of the near Gaussian TEM_{00} ruby laser beam, and is measured by a pinhole scan detector. Focal spot-sizes ranging from 52μm to 215μm were used and areas of a test sample were irradiated by one shot only. The energy density in the laser beam was

[1]Figures in brackets indicate the literature references at the end of this paper.

varied by means of a liquid $CuCl_2$ filter while the output energy of the laser was kept constant. Defect and damage site morphology were studied using a scanning electron microscope as well as an optical microscope.

A single crystal of rutile (TiO_2) and a synthetic single crystal of yttrium orthovanadate (YVO_4) were used to study surface defects by laser-induced damage effect in this work. Both crystals are important optical materials since TiO_2 is a very common coating compound and YVO_4 has great potential to be a substitute for calcite and is an important solid-state laser host. They both have a large birefringence (see table 1). The samples used in this work were cut from single crystal boules and hand-polished to a block. The polishing compounds used were the usual types of roughing powder, with Linde A and C as the final finishing agents. A detailed spectrochemical analysis of the Al_2O_3 finishing compounds is displayed in table 2. The dominant trace elements are Si, Fe, and Pb. In general, the quality of the YVO_4 surfaces is better than that of the TiO_2 surfaces.

Table 1. Indices of refraction of three uniaxial crystals at 6943 Å

Material	n_E	n_O	Birefringence $n_E - n_O$
Calcite	1.486	1.658	(-) 0.172
Rutile [3]	2.88	2.58	(+) 0.30
YVO_4 [4]	2.20	1.98	(+) 0.22

Table 2. Semiquantitative analysis of the polishing compounds [5]

Element	Linde A	Linde C
Al	52. %	52. %
Si	0.062	0.023
Fe	0.005	0.0025
Mg	0.0011	0.0011
Ca	0.00071	0.0012
Cr	0.00041	0.00030
Cu	0.00031	0.00013
Ga	0.0036	0.0036
Pb	0.01	0.031

3. Laser-induced Damage Effects on Rutile and YVO_4 Surfaces

Damage threshold was measured as a function of the ruby laser beam spot-size. Figures 1 and 2 show the experimental data along with theoretical curves fitted using the same model as for the case of dielectric thin films [1, 6]. It is seen that the damage threshold depends strongly upon the focal spot-size of the laser beam. For TiO_2, the threshold of defect damage was measured to be about 10 J/cm^2 while it was 8 J/cm^2 for YVO_4. In both cases a factor of 3 on damage threshold was observed as the spot-size decreased from 190 μm to 52 μm. It is found that the LIS method is more sensitive than the spark detection method for the case of rutile surface, but not for the case of YVO_4.

Since both crystals have large birefringence, we have attempted to correlate the laser-induced damage effects to the orientation of the incident laser electric field to the crystallographic axes. For the rutile crystal, three different configurations were used in the experiment: axial, transverse P (optic axis parallel to the incident field) and transverse S (perpendicular to the field). Figure 3 displays these three configurations. For YVO_4, only the transverse S and P configurations were studied. It was thought that, by variation of spot-size, different defect damage thresholds could be observed since the enhancement factor depends on the refractive index of the material which is different for the S and P configurations. The experimental results are shown in figures 4 and 5. For each crystal surface, the S and P data were obtained and fitted with theoretical curves. However, when the Fresnel reflection [7] was taken into account to calculate the internal field intensity, the S and P data became identical. For example, table 3 compares the incident and internal field intensities for the intrinsic and defect damage thresholds of the two crystal surfaces. We conclude that Bloembergen's type of enhancement factor does not explain these results and the effect on the crystalline birefringence is only present for the incident field. The morphology of damage sites also reveals this aspect.

Table 3. Incident field intensity versus internal field intensity. All intensities are in units of Joule/cm^2.

Crystal	Configuration	Incident I_i	Internal I_i	Incident I_d	Internal I_d
TiO_2	S	36.3	29.3	12.0	9.2
	P	38.3	29.3	12.0	9.6
YVO_4	S	20.3	18.1	8.0	7.1
	P	22.0	18.9	8.0	6.9

4. Damage Morphology

The damage sites were examined by an optical microscope and a scanning electron microscope (SEM). Typical morphologies of the surface damage sites are illustrated in the following ten SEM pictures (figures 6 to 15). In general, small damage sites induced by a 50 to 80μm spot-size laser beam are similar for both crystals. Figure 6 shows an example of this small site for the TiO_2 surface. It appears like a 2μm crater. Large damage sites induced by a laser beam of at least 150μm spot-size show different morphology for the two crystals. They are different in several aspects. For the rutile crystal, a single shot damage site creates many irregularly distributed small craters within the irradiated area (see figures 7, 8 and 9). When a plasma was observed on a particular damage site, fracture on the site follows some crystallographic orientation which may reveal the crystal structure (see figure 10). For YVO_4 crystal, no fracture with any pattern was found on large damage sites and occasionally there were some irregularly distributed small craters within a site but not as numerous as those of the rutile crystal. However, there is one distinct feature of damage morphology which was not found on the rutile crystal. Figures 11, 12, and 13 show some of these damage sites. They appear like "popcorn" where the inclusion is popping out of the surface [8]. In brief, on rutile the crater morphology is dominant, while on YVO_4 surface, the "popcorn" morphology is overwhelming. This indicates that surface defects due to inclusions have enhanced the damage level.

When we compared damage sites corresponding to the S and P configuration tests, no morphology differences could be found. Also it was observed that damage was not always initiated by the structural discontinuity of a scratch, but by some entrapped absorbing compound, presumably a chemical from the polishing powders. Figure 14 shows a site struck by 150μm

beam with five small damage craters along a surface scratch. In addition, figure 15 shows a similar damage site on the YVO_4 surface except that the craters do not appear on an obvious scratch. Thus it seems that an enhancement of the laser electric field was not produced by the scratch but by absorbing chemicals entrapped in the surface. Recall that traces of iron oxide were present in the polishing powders.

5. Summary

Two dielectric crystals, rutile and yttrium orthovanadate, were tested for their damage resistance to the laser irradiation at 0.69μm. It was demonstrated that the measured damage threshold of these materials could be distinguished as intrinsic damage and defect damage. Surface defects are easily studied by this approach. The morphology of the surface damage sites reveals that entrapped polish particles were the cause of damage on TiO_2 surface and inclusions were the cause of damage in the case of YVO_4. The fact that the defect damage threshold is independent of the directions of crystallographic axes with respect to the optical field supports this conclusion.

6. Acknowledgements

The authors wish to thank Mr. Jack Worrall at the University of Southern California for his SEM work. This study was supported by Crystal Products Department, Union Carbide Corporation, San Diego, California. Both the rutile and yttrium orthovanadate crystals used in this study were grown by Union Carbide Corporation.

7. References

[1] L.G. DeShazer, B.E. Newnam and K.M. Leung, in Laser Induced Damage in Optical Materials: 1973, edited by A.J. Glass and A.H. Guenther (NBS Special Publication 387, December 1973), pp. 114-123.

[2] N. Bloembergen, App. Opt. 12, 661 (1973).

[3] W.L. Bond, J. Appl. Phys. 36, 1674 (1965).

[4] E.A. Maunders and L.G. DeShazer, J. Opt. Soc. Am. 61, 684 (1971).

[5] Spectrochemical analysis was performed for USC by Pacific Spectrochemical Laboratory Inc., Los Angeles, California 90064.

[6] L.G. DeShazer, B.E. Newnam and K.M. Leung, Appl. Phys. Lett. 23, 607 (1973).

[7] See for example, M. Born and E. Wolf, Principles of Optics, 4th ed. (Pergamon Press, New York, 1970).

[8] C.J. Duthler, Appl. Phys. Lett. 24, 5 (1974).

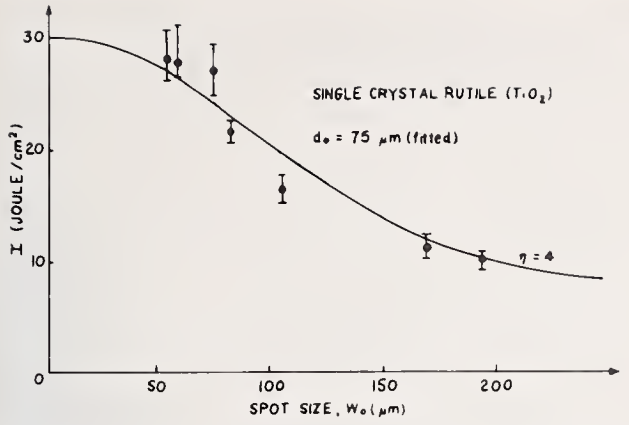

Figure 1. Spot-size dependence of surface damage on a single crystal of rutile (TiO_2) in the axial configuration test. The bars on the data points indicate the range of measured values and are not error bars. The intrinsic damage threshold I_i is the upper limit and the defect threshold I_d is the lower limit.

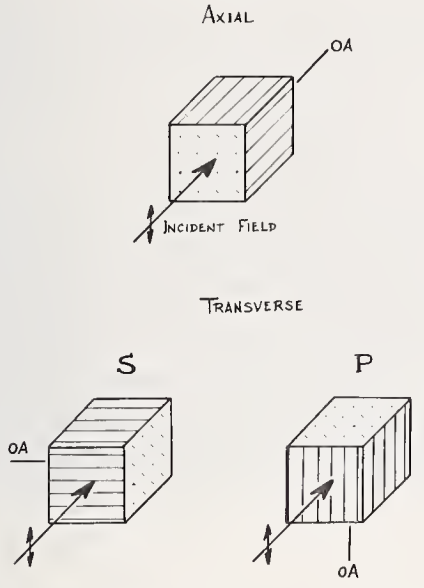

Figure 3. Schematics of crystal orientations with respect to incident laser electric field. Optic axis (OA) of the crystal is indicated by the parallel lines.

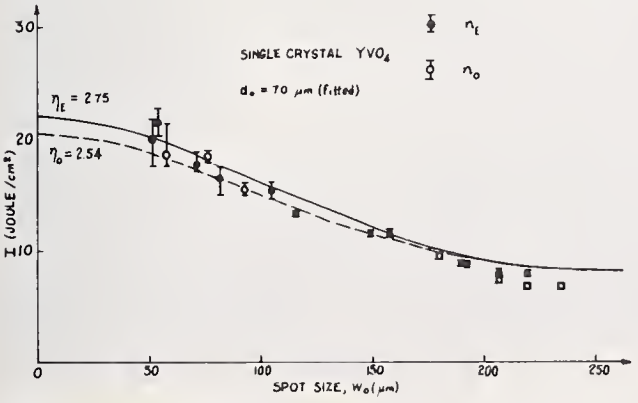

Figure 5. Spot-size dependence of surface damage to YVO_4 crystal for transverse S and P configuration tests.

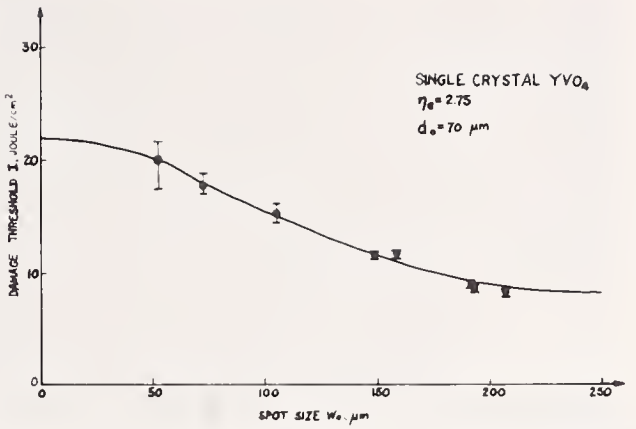

Figure 2. Spot-size dependence of surface damage on a single crystal of yttrium orthovana-date (YVO_4) in transverse P configuration.

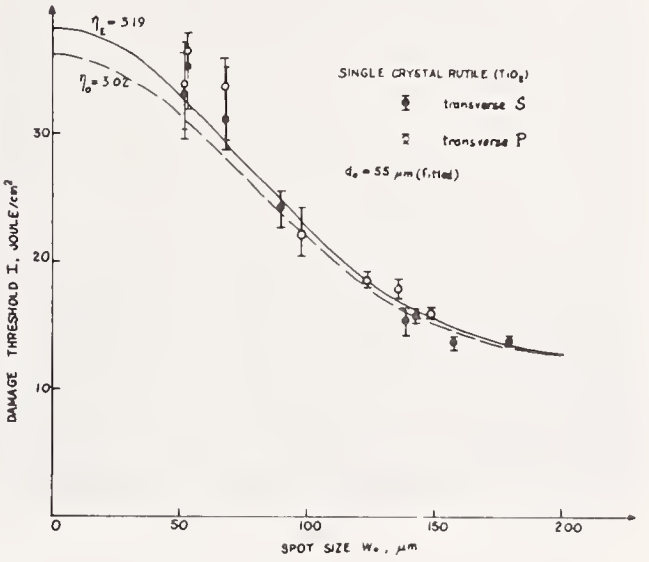

Figure 4. Spot-size dependence of surface damage to TiO_2 crystal for transverse S and P configuration tests.

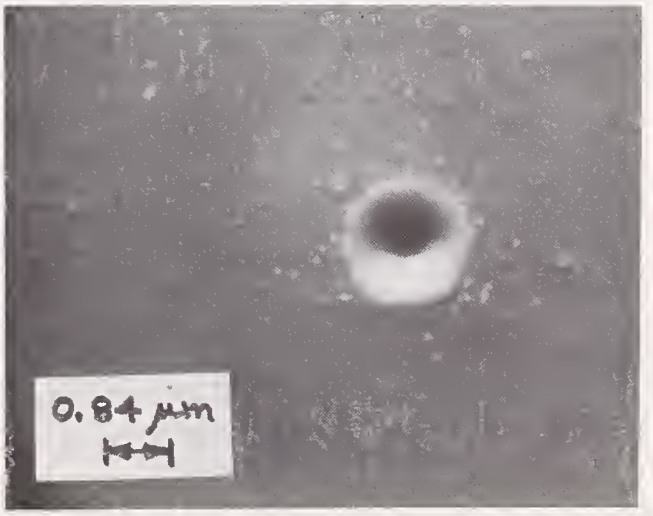

Figure 6. SEM photograph of a small damage site on TiO_2 surface; the spot-size is 52 μm. The crater is 2 μm in size.

Figure 7. SEM photograph of a large damage site on rutile surface; the spot-size is 160 μm. Note that this is a single shot damage site and the small craters are irregularly distributed.

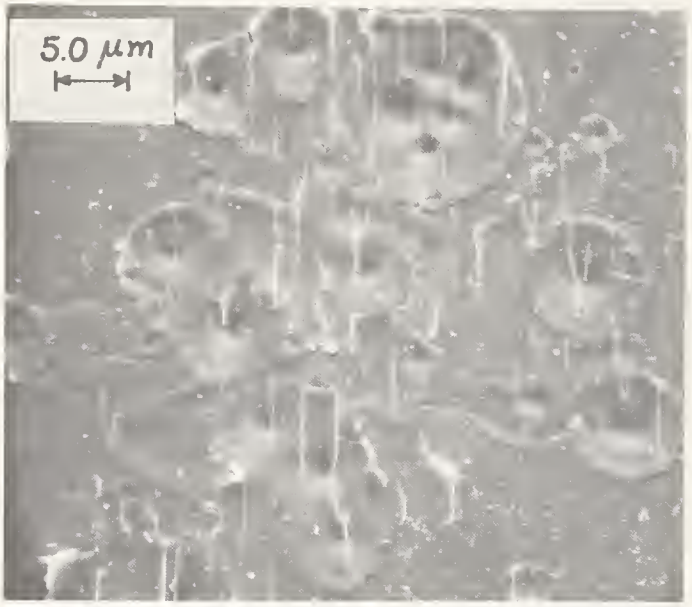

Figure 9. SEM photograph of larger damage site on rutile surface using transverse P configuration. The spot-size is 160 μm and no spark was observed.

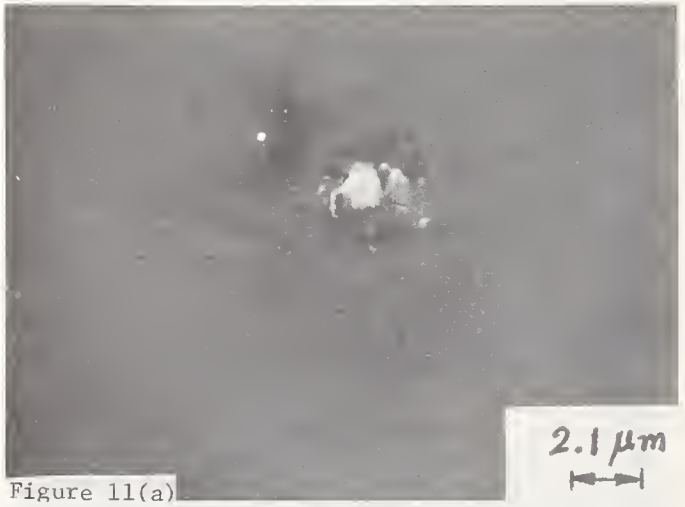

Figure 11(a)

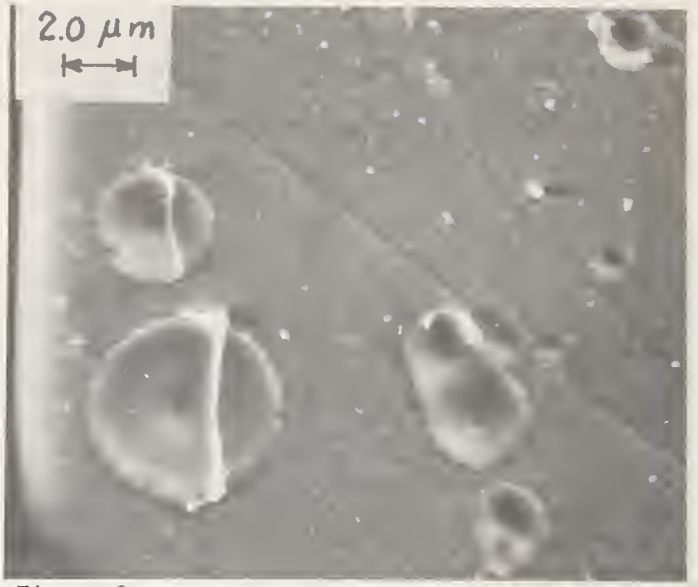

Figure 8. SEM photograph of a large damage site on rutile surface using transverse S configuration. The spot-size is 150 μm.

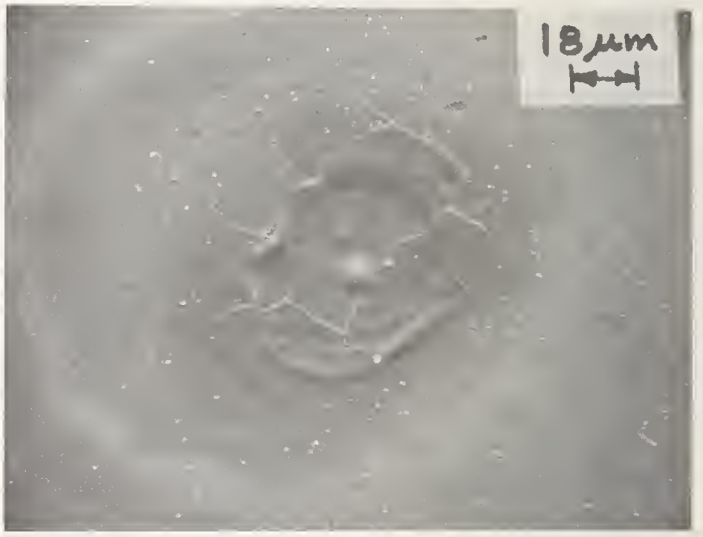

Figure 10. A very large damage site with a surrounding white ring on the rutile surface. A spark was observed in this case and the spot-size is about 190 μm.

Figure 11(b)

Figure 11. (a) SEM photograph of a large damage site on YVO_4 surface; a spark was observed and the spot-size is 160 μm. (b) Close-up view shows that the damage is due to a nonmetallic inclusion, 1.2 μm in diameter, which was about 0.2 μm below the plane surface. The morphology has crack nucleation similar to that in reference 8.

Figure 12(a)

Figure 12(b)

Figure 12. SEM photograph of another damage site on YVO_4 surface; a huge spark was observed and the spot-size is only 72 μm. The initial LIS level is high. (a) The top view of the site suggests that a cluster of inclusions was at the center of the site to initiate the damage. (b) Close-up view was taken with the electron beam at 84° with respect to the surface. No crater is observed on the site.

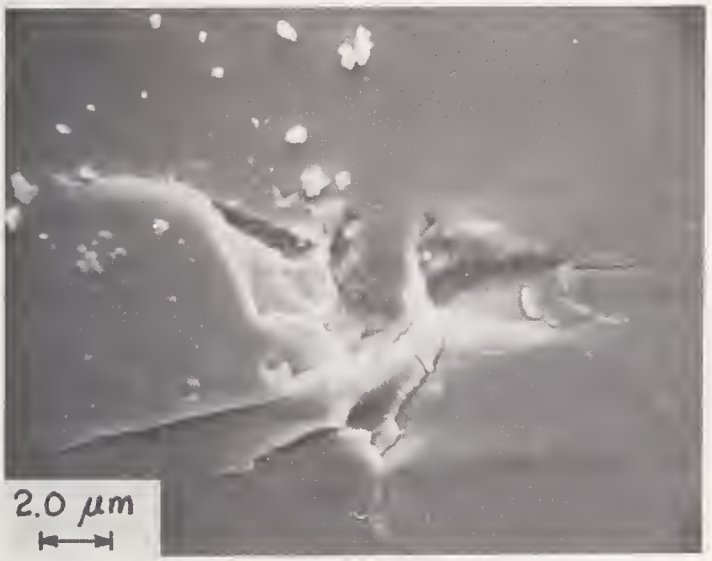

Figure 13. SEM photograph of another damage site on YVO_4 surface; a spark was observed and the spot-size is about 150 μm. It can be seen that material pops out of the site.

Figure 14. A large damage site on YVO_4 surface but no spark was observed. Note that this is a single shot using spot-size of 150 μm and the distinct small sites distributed along the surface scratch.

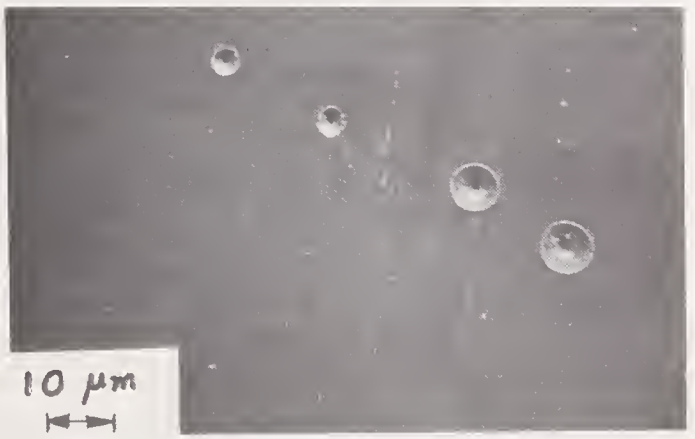

Figure 15. A similar damage site as shown in figure 14, except one cannot observe any scratch along the four collinear damage craters.

NO COMMENTS ON PAPER BY LEUNG.

6.1 Pulsed CO_2 Laser Window Damage Processes

R. A. Shatas, J. D. Stettler, L. M. Narducci,*
S. S. Mitra,† and H. C. Meyer

Quantum Physics, Physical Sciences Directorate
U. S. Army Missile Command
Redstone Arsenal, Alabama 35809

We examine the applicability of the extended avalanche breakdown process to describe the semiconductor window surface damage by pulsed high pressure CO_2 lasers. In the extension to optical frequencies of Shockley's avalanche theory construed originally for a dc electric field, a hard momentum-reversing collision of the free carrier is required to occur at the instant of optical field reversal. In contrast to alkali halides, the mobility is very high in semiconductors, and the probability of a momentum-reversing collision is too small to account for experimental observations of damage thresholds. Alternate models of damage processes are discussed. They are based on quantum mechanical photon assisted tunneling probability calculations between the bound and the quasi-free states and resonant collective excitations of carriers in the quasi-free state. Theoretical predictions for maximum pulsed CO_2 laser fluxes are made for some typical semiconducting window materials.

Key words: Damage threshold of GaAs; extended Shockley avalanche; pulsed laser damage; semiconductor infrared windows; solid state plasma; two-stream instability threshold.

1. Introduction

Recent reviews [1,2][1] of laser pulse damage to infrared transparent materials explain the damage mechanism in terms of the optical electric field-initiated avalanche ionization. The dominant features of this damage process are ascribed to the ionizing collisions of a few free carriers present initially which are accelerated above the band gap energies by the alternating field. After several generations of the free carrier creation, the Drude absorption (absorbance independent of light intensity) is taken to be of sufficient magnitude to make the material no longer transparent to the incident laser radiation. Although this process is expected to dominate the breakdown in materials such as alkali halides, in semiconducting window materials such as GaAs, CdTe, and others which exhibit high free carrier mobilities and low band gaps, collective solid state plasma excitations may play a dominant role in interactions leading to damage. In particular, the collective excitations may cause plasma instabilities to occur which lead to an intensity-dependent absorbance.

In section 2, we review the phenomenological theory of avalanche breakdown. In this context, we regard the avalanche as a single-electron initiated process analogous to the gas breakdown. We consider the two distinct limits of the electron-lattice collisional damping mediated by the free carrier interaction with phonons which determines the carrier behavior in the optical electric field. The strong damping condition is satisfied when ω_ℓ, the angular laser frequency, is less than the collisional frequency ν_e. However, for some semiconductor materials, the reverse is true; because of the relatively weak damping of a free carrier by collision with the lattice, the free electron-electron interaction allows for the collective electron excitation of the solid state plasma.

In section 3, we show that the Shockley dc avalanche breakdown can be extended to optical electric field frequencies if $\nu_e > \omega_\ell$. However, the extension of the Shockley avalanche breakdown cannot be justified for the case of $\nu_e < \omega_\ell$, primarily because of the lack of momentum-reversing collisions. We demonstrate these differences numerically for two IR window materials, namely NaCl and GaAs.

In section 4, we consider the resonant interaction of carriers with the laser light which occurs when the carrier plasma frequency approaches that of the laser. Above certain amplitudes of the optical

---

*Permanent address: Department of Physics, Worcester Polytechnic Institute, Worcester, MA.

†Permanent address: Department of Electrical Engineering, University of Rhode Island, Kingston, RI.

1. Figures in brackets indicate the literature references at the end of this paper.

electric field, the free carrier plasma is driven unstable and absorbs the laser light anomalously. Thresholds for the two-stream and the parametric instabilities are deduced; their numerical values agree within an order of magnitude with experiments.

2. Acceleration of Free Carriers in an Optical Electric Field

The energy distribution function of initially present free carriers is altered by the application of the optical electric field. Hyperthermal carriers at the high energy tail of the altered distribution undergo collisions when their kinetic energy exceeds the ionization potential and consequently create a new generation of free carriers. The exact description of the time dependence of the carrier distribution function requires solving some form of a transport equation. Treatment of this problem within the framework of the Fokker-Planck equation has been considered by several authors [3,4]. In the lowest order of approximation, however, the transport problem can be considered in terms of a single average carrier. The kinetics of this average carrier is described by Euler-Lagrange equations for a nonconservative free carrier-electric field system in which the carrier-lattice interaction is expressed by a phenomenological dissipation function containing the effective carrier-lattice collision frequency ν_e. Let $L = T - V$ be the Lagrange function of the system and let us express the Rayleigh dissipation function by

$$\mathcal{F} = \frac{1}{2} m\dot{q}^2 \nu_e \quad .$$

The Euler-Lagrange equations of motion for a nonconservative system formally are written as follows:

$$\frac{d}{dt}\frac{\partial L}{\partial \dot{q}} - \frac{\partial L}{\partial q} + \frac{\partial \mathcal{F}}{\partial \dot{q}} = 0 \quad . \tag{1}$$

In our case, they assume the familiar form

$$m\ddot{q} + e E_o \exp(-i\omega_\ell t) + \nu_e m\dot{q} = 0 \quad , \tag{2}$$

where m designates the free carrier mass and E_o is the electric field amplitude associated with the normally incident laser flux S_i. For crack and bubble free materials, E_o is given by the expression

$$E_o = \frac{\sqrt{32\pi S_i/c}}{1 + \sqrt{\epsilon}} \quad . \tag{3}$$

Cracks and bubbles encompassing domains smaller than the wavelength of the laser can lead to a local enhancement of E_o as shown by Bloembergen in his consideration of the electrostatic boundary problem for cracks and inclusions [5].

The steady-state solution of eq. 2 for the carrier velocity is given by

$$\dot{q} = -\frac{e}{m} E_o \exp(-i\omega_\ell t)\left(\frac{1}{-i\omega_\ell + \nu_e}\right) \quad . \tag{4}$$

The free carrier extracts energy from the laser electric field at a rate

$$\dot{W} = \frac{1}{2}\mathcal{R}e(\vec{\dot{q}} \cdot e\vec{E}^*) = \frac{\nu_e}{\nu^2 + \omega_\ell^2}\frac{e^2E^2}{m} \quad , \tag{5}$$

where E is the rms value of the electric field $E = E_o/\sqrt{2}$.

The case of a relatively weak carrier-lattice interaction $\omega_\ell > \nu_e$ is known as the "high frequency" limit [6] of the Fröhlich model [7]. In this case, eq. (5) becomes

$$\dot{W}_1 = \frac{\nu_e}{\omega_\ell^2}\frac{e^2E^2}{m} \quad . \tag{6}$$

Note that the lowest order of the expansion of the carrier distribution function also yields eq. 5 (see eq. 12 of ref. [3]). The opposite case $\omega_\ell < \nu_e$ yields the dc limit of the Fröhlich model used in his construction of the dc avalanche breakdown [7]. Here, the average rate of energy extracted from the electric field by a free carrier is given by

$$\dot{W}_2 = \frac{1}{\nu_e} \frac{e^2 E^2}{m} \quad . \tag{7}$$

A phenomenological dc breakdown model which incorporates the essential features of the electron avalanche initiated by the accelerated free carriers has been constructed by Shockley [8]. In the next section, we will consider the extension of his model to optical alternating fields for alkali halide and semiconductor-type window materials.

3. Shockley Breakdown in an Optical Electric Field

The argument for the avalanche breakdown is essentially built on the extension to an ac field [9] of Shockley's phenomenological theory originally conceived for a dc field. This extension is possible if a few "lucky electrons" experience momentum-reversing collisions which occur just at the time of the reversal of polarity of the alternating field. Thus, the acceleration of the electron continues throughout the several optical cycles needed to impart to the electron kinetic energy in excess of the ionization potential. This argument predicts that the rms value of the alternating field must be higher than that of the dc field to obtain an avalanche breakdown. A slight increase in the breakdown field in alkali halides indeed has been demonstrated by Fradin and Bass for the bulk damage [10]. A much larger increase is ascribed for the reactive-atmosphere processed KCl [11]. However, the threshold for surface damage of GaAs not only decreases with increasing frequency, but it also takes place at an order of magnitude smaller field than the dc breakdown [12]. Thus the qualitative behavior of the GaAs surface damage does not agree with that predicted by the avalanche theory (see table 2 of ref. [13]). A fully quantitative comparison between theory and experiment requires solving of transport equations of hyperthermal carriers in strong alternating fields as mentioned in the preceding section. Also, the properties of ionizing electrons (such as mobility, effective mass, etc.) are generally significantly different from those that determine the macroscopic mobility and relaxation times at low applied fields. Nevertheless, some quantitative comparisons between GaAs and NaCl can be made on the basis of macroscopic energy deposition considerations, ionization rates, and the applicability of the dc theory extended to the ac electric fields associated with the laser radiation.

It is convenient to recast eq. 5 in terms of the time between collisions $\tau = 1/\nu_e$ and the macroscopic mobility μ which are related by the expression $e\tau = m\mu$. This yields

$$\dot{W} = \frac{\mu e E^2}{(1 + \omega_\ell^2 \tau^2)} \quad , \tag{8}$$

which we evaluate for GaAs by taking the effective mass of a free carrier to be 0.1 of the electron mass [14]. In table 1 values of $\omega_\ell \tau$ for both GaAs and NaCl are listed for the laser frequencies of interest.

Table 1. Angular frequency-average carrier scattering time product for different laser frequencies. The average scattering time τ is calculated from room temperature mobility of 3000 $cm^2\ V^{-1}\ s^{-1}$ for our GaAs and of 10 $cm^2\ V^{-1}\ s^{-1}$ for NaCl

Laser		$\omega\tau$	
λ Wavelength (μm)	ω_ℓ (rad sec^{-1})	GaAs $\tau = 1.9 \cdot 10^{-13}$ sec	NaCl $\tau = 5.7 \cdot 10^{-15}$ sec
10.6	$1.78 \cdot 10^{14}$	$3.4 \cdot 10$	1.01
1.06	$1.78 \cdot 10^{15}$	$3.37 \cdot 10^2$	10.1
0.694	$2.71 \cdot 10^{15}$	$5.14 \cdot 10^2$	15.5

This shows that the term $\omega_\ell^2\tau^2$ in the denominator in eq. (8) will dominate. Thus for the same value of field an order of magnitude less total power will be pumped into the GaAs compared to NaCl. However, the τ used in table 1 is a macroscopic parameter whereas the breakdown is initiated by hot electrons for which $\omega_\ell\tau$ in NaCl may be nearly constant [15].

For avalanche formation the ionization rate per centimeter path length η is the controlling quantity. For $E = 10^6$ V cm^{-1}, experimental data indicate that $\eta = 3 \cdot 10^2$ cm^{-1} for NaCl [16] and $\eta = 2.2 \cdot 10^4$ cm^{-1} for GaAs [17]. Thus GaAs dc breakdown would be expected at lower fields relative NaCl as the case probably is. The surface damage we observe occurs at electric fields slightly less than 10^5 V cm^{-1}. For these fields

$$eE\lambda/E_R \sim 0.5 \tag{9}$$

where E_R is the energy of the optical phonon and $\lambda \approx 15$ Å is the effective mean free path obtained by fitting photocurrent near breakdown to the general theory of Baraff [18]. For values of this ratio less than one the acceleration theory of Shockley [8] holds so that

$$\eta/E \sim \exp(-E_i/eE\lambda) \tag{10}$$

where E_i is the effective ionization energy. The number of ionizations per free electron occuring within a laser pulse of length Δt is

$$N = \exp(\mu E\eta\Delta t) - 1 \quad . \tag{11}$$

For GaAs where $E_i \approx 1.8$ eV [18], eq. (10) leads to the estimate of $\eta \sim 10^{-43}$ cm^{-1} for $E \sim 10^5$ V cm^{-1}, and thus for $\Delta t \sim 10^{-7}$ sec, a negligible value is obtained in eq. (11).

Shockley's theory for the dc ionization rate has been extended to ac laser electric fields by considering the probability of a hard momentum reversing collision occurring during the time interval in which the field reverses its direction [9]. If ℓ is the mean free path between hard collisions and $\Delta t = 1/\omega_\ell$ is the time interval during which the laser field of frequency ω_ℓ changes direction, then the criterion of applicability is that

$$2v\,\Delta t/\ell > 1 \tag{12}$$

where v is the carrier velocity directed along the field and can be estimated from the low field mobility $v = \mu E$. In NaCl the mobility is both low and determined by hard collisions; thus, a reasonable estimate is that $\ell \approx v\tau$. The condition given by inequality (12) therefore reduces to that previously discussed, namely $\omega_\ell\tau \leq 1$. However, in the case of GaAs, the situation is less clear. The estimate $\ell \approx v\tau$ gives, for $E = 10^5$ V cm^{-1}, $\ell = 5.1 \cdot 10^{-5}$ cm which is obviously way too large. We therefore elect to follow Robson [19] and use the estimate $\ell = (\mu/e)(2\langle\varepsilon\rangle m)^{\frac{1}{2}}$ where $\langle\varepsilon\rangle$ is the average energy per electron. For $\langle\varepsilon\rangle$ given by the room temperature thermal energy, we find the mean free path to be $\ell \approx 6.3 \cdot 10^{-6}$ cm and therefore take it to be independent of the field. (The estimates for NaCl for $E = 10^6$ V cm^{-1} are $\mu E\tau = 5.6 \cdot 10^{-8}$ cm and $(\mu/e)(2\langle\varepsilon\rangle m)^{\frac{1}{2}} = 6.6 \cdot 10^{-8}$ cm.) The assumption of a constant mean free path was used by Baraff [18] in his theory of ionization rates in semiconductors which fits quite well the experimental data [17] on doped GaAs. These estimates may not hold for pure GaAs where polar optical phonon scattering dominates and leads to a mobility strongly varying with temperature [20]. In GaAs specimens doped to the level of most of our window materials, the mobility is not very temperature sensitive because ionized impurity scattering predominates [14]. As a comparison to the chosen value $\ell \approx 6.3 \cdot 10^{-6}$ cm, the effective mean free path for ionization for hot electrons has been found to be $\lambda_i \approx 1.5 \cdot 10^{-7}$ cm [17]. Next, the velocity in inequality (12) estimated by use of the mobility μ is so large that it takes at least 10 half-cycles of the CO_2 laser field to achieve it. Thus v in eq. (12) should be an average velocity over those half-cycles with the value $v \approx 0.29\,\mu E$. With these two modifications for GaAs and $E \sim 10^5$ V cm^{-1}, we have

$$2v\,\Delta t/\ell \sim 0.16 \tag{13}$$

which is below the criterion given in eq. (12). This is sufficient to rule out the applicability of Shockley's theory to our results on GaAs for two reasons: First, the sensitive exponential dependence of the theory on this parameter generates large changes in the predictions. Second, and more importantly, the high mobility used in eq. (12) should not hold for hot electrons in GaAs as the recent work by Robson indicates [19].

4. Calculation of Flux Thresholds for Carrier Plasma Instabilities in Semiconductors

Difficulties associated with the extension of the Shockley dc breakdown model to the multiplication of free carriers in semiconductors driven by the electric field component of the laser flux have led us to consider alternate processes to explain the damage threshold. Qualitatively speaking, if the carrier collisions with the lattice are not sufficiently hard to insure the reversal of carrier momentum at the instant of the reversal of the optical electric field, then perhaps the mutual free carrier interaction within the carrier plasma may provide an alternate mechanism of an anomalous absorption. Experimentally, the morphology of surface damage in GaAs [12] implies that the absorbance at the damage site by the end of laser pulse is larger than 10^4 cm^{-1}. Since the damage sites are not contiguous but consist of micron-sized depressions, this localization enables us to consider the creation of quasi-free states in which carriers interact collectively with the laser radiation in distances comparable to a few multiples of the Debye shielding length. For such semilocalized excitations, the effective pseudo-gap between the bound and the semifree state need not assume values ascribed to the crystalline gap. In ref. [13], we calculated the conditions for attaining a local carrier density needed in a nearly resonant carrier plasma interaction with the laser flux. A semiclassical treatment of bound to quasi-free transition probability of an electron in a model potential acted upon by a moderately strong monochromatic Maxwell field has been carried out elsewhere [21]. It also supports the contention that conditions for a near resonance can be attained in GaAs for experimentally observed surface damage fluxes if the effective pseudo-gap is of the order of 1/3 to 3/4 of the crystalline gap. The higher value corresponds to use of the effective carrier mass in GaAs instead of the electron mass. Because of the smallness of the excited site, linear absorption is not sufficient to account for the damage. Therefore, the catastrophic damage must involve a nonlinear, intensity dependent absorbance. Since we start with a neutral solid producing the carrier plasma, charge conservation requires the creation of an equal number of electrons and holes. The carrier plasma is analogous to a gaseous plasma of electrons and ions. We therefore should expect the same instabilities that develop in gaseous plasmas and lead to anomalous heating by lasers to arise in our semiconductor plasma. Since the two-stream instability [22,23] has one of the lowest thresholds for gaseous plasmas, we calculate its threshold first. In this instability, the laser radiation excites an electron wave and an ion acoustic wave in the plasma. In deriving the threshold condition [22,23], we begin with the electron and ion continuity equations:

$$\frac{\partial n_j}{\partial t} + \nabla \cdot (n_j \vec{v}_j) = 0 \quad ; \tag{14}$$

the electron and ion momentum conservation equations

$$m_j n_j \left(\frac{\partial \vec{v}_j}{\partial t} + \vec{v}_j \cdot \nabla \vec{v}_j \right) = -\nabla p_j + n_j e_j \left(\vec{E}_o \sin (\omega_\ell t) + \vec{E} \right) - m_j n_j \vec{v}_j \nu_j \tag{15}$$

and the Poisson's equation

$$e \nabla \cdot \vec{E} = 4\pi \sum_j e_j n_j \quad . \tag{16}$$

The subscript j refers to either electrons or ions, $E_o \sin \omega_\ell t$ is the laser electric field, the ν's are the relevant collision frequencies, and p_j denotes pressure. One then proceeds to linearize the coupled set of eqs. (14) to (16) in the dipole approximation and solve quasi-statically by transforming into the oscillatory frame of carriers with the smallest effective mass. Inspection of their dispersion relation shows that a positive imaginary part and hence an instability occurs if

$$\frac{e E_o}{m \omega_\ell} \gtrsim \sqrt{6}\, s_e \left(1 + \frac{T_i}{T_e} \right)^{\frac{1}{2}} \left(\frac{\nu_e}{\omega_B} \right)^{\frac{1}{2}} \quad , \tag{17}$$

where s_e is the electron thermal velocity given by $s_e^2 = \gamma_e (T_e/m_e)$ (γ_e is a numerical factor), and ω_B is the plasma Bohm frequency of the smallest-effective mass carriers. Inspection of eq. (17) shows that for small effective mass highly mobile carriers, the threshold for plasma instability can be quite low. Recasting of eq. (17) in terms of the macroscopic carrier mobility $\mu = e/(m\nu_e)$ and rewriting the threshold condition in terms of the laser flux S_t [W cm^{-2}], we obtain

$$S_t \gtrsim c\, T_e\, \omega_\ell\, m \nu_e = c\, e\, T_e \frac{\omega_\ell}{\mu} \tag{18}$$

for the case $T_e \sim T_i = 0.025$ eV and $\omega_\ell \sim \omega_B$.

The numerical constant c in eq. (18) is evaluated by comparison with ref. [24] and also takes into account eq. (3). With GaAs parameters listed with table 1, the threshold flux for the two-stream instability is calculated to be $S_t \sim 10^9$ W cm^{-2}. The onset of this instability leads to an enhancement of the high-frequency resistivity of the solid state plasma in GaAs and hence to the onset of anomalous absorption and heating.

Another solid state plasma instability of interest in laser induced damage in GaAs is the parametric instability formulated in terms of plasmons in solids by Gersten and Tzoar [25]. However, for this instability, the plasma is purely electronic, and we have to assume that the holes are immobile. The instability of interest here is the direct conversion of two identical photons into two plasmons. One considers that the onset of the instability occurs when the electron distribution function in phase space $f(\vec{x},\vec{p},t) = f_o + F$, in the presence of a laser electric field, undergoes a large spatial fluctuation F with respect to the zero-order distribution f_o.

One considers the solution of the Vlasov and Poisson equations given by eqs. (19) and (20) for both components of the distribution function:

$$\frac{\partial f}{\partial t} + \vec{v} \cdot \frac{\partial f}{\partial \vec{x}} + e \frac{\partial \varphi}{\partial \vec{x}} \cdot \frac{\partial f}{\partial \vec{p}} - e \vec{E}(t) \cdot \frac{\partial f}{\partial \vec{p}} = 0 \quad , \tag{19}$$

$$\epsilon \nabla^2 \varphi = 4\pi n_o e \left[-1 + \int f \, d\vec{p} \right] \quad . \tag{20}$$

Kane's nonparabolic Hamiltonian is

$$H = \left[(mc^{*2})^2 + (c^* p)^2 \right]^{\frac{1}{2}} \quad , \tag{21}$$

where $c^{*2} = \mathcal{E}_g/2m$ and $\mathcal{E}_g$ denotes the band gap. Using Hamilton's equations of motion $\partial H/\partial p = \dot{q}$ and $\partial H/\partial q = -\dot{p}$, we get the free carrier velocity $\dot{\vec{q}} = \vec{v}$ expressed by

$$\vec{v} = c^* \vec{p} \left[(mc^*)^2 + p^2 \right]^{-\frac{1}{2}} \quad . \tag{22}$$

One then transforms (19) and (20) into the oscillatory coordinates of the electrons and considers the threshold for plasma instability given by the onset of a net positive growth rate of plasma waves. In terms of solid state parameters, the parametric instability threshold is exceeded when the following inequality is satisfied

$$S_t \geq 8 \cdot 10^{-3} \, \mathcal{E}_g \, \omega_\ell / (e\mu) \quad .$$

We use again GaAs parameters quoted in table 1 to obtain $S_t \gtrsim 7 \cdot 10^7$ W cm^{-2} as the threshold flux for the onset of this instability. Experimental values [12] seen for 40 to 100 nsec CO_2 laser pulse damage of GaAs surfaces agree within an order of magnitude with our calculations. It should be noted that both the parametric and two-stream instability thresholds are proportional to the ratio ω_ℓ/μ.

5. Discussion

Using lowest order approximations, we have attempted in this contribution to demonstrate analytically that the physical damage processes may be quite different for low mobility, large band gap insulators such as the alkali halides and small band gap large mobility infrared transparent materials such as certain semiconductors. Although further work including higher-order contributions is still needed, the implications of our considerations encompass more than merely materials for windows. For example, in large MOPA CO_2 laser systems, Faraday rotators comprise about the most significant class of nonreciprocal devices. Currently, InSb is the only material with which successful isolators at 10.6 μm wavelength have been constructed [26]. Because of a high mobility and a small effective mass of carriers in InSb at 77°K, the pulse damage threshold could be primarily determined by the onset of solid state plasma instabilities discussed in the preceding section.

Despite the difference in the probable damage processes in these two classes of infrared window materials, the practical prescriptions for increasing the damage threshold are very similar. The threshold in avalanche damage for KCl and NaCl increases with the laser frequency; a similar increase is predicted for both plasma instabilities discussed in the preceding sections, albeit it is severely moderated by the lowering of the order of multiphoton transitions in the low band gap semiconductors. Furthermore, the increase in the energy gap between the bound and the free carriers and decrease in their mobility contribute to the increase in the threshold of damage initiated by the solid state

564-378 O - 74 - 15

plasma instabilities. At the surface, any condition which either increases the local electric field or provides an easy source of free electrons, also contributes to the lowering of damage threshold. In this sense, pulse damage experiments which determine the state of material before and after the illumination are not sufficient to differentiate between various processes of damage under consideration. However, in understanding the physics of damage, the distinction between various predicted processes will be quite useful.

6. References

[1] Bloembergen, N., IEEE J. Quantum Electron. QE-10, 375-386 (1974).

[2] Bloembergen, N., Paper 0-1, 8th Internat. Quantum Electron. Conference Digest, 74 CHO-858-1-QECON.

[3] Holway, Lowell H., Jr., Phys. Rev. Letters 28, 280-283 (1972).

[4] Epifanov, A. S., The Process of Development of Avalanche Ionization in Solid Transparent Dielectrics under High-Power Pulsed Laser Radiation, Lebedev Physical Institute preprint, Moscow, 1974

[5] Bloembergen, N., Appl. Opt. 12, 661-664 (1973).

[6] Zverev, G. M., Mikhailova, T. N., Pashkov, V. A., and Soloveva, N. M., Sov. Phys.-JETP 26, 1053 (1968).

[7] Fröhlich, H., Proc. Roy. Soc. (London) A160, 230 (1937).

[8] Shockley, W., Solid State Electron. 2, 35-67 (1961).

[9] Bass, M. and Barrett, H. H., IEEE J. Quantum Electron. QE-8, 338-342 (1972).

[10] Fradin, D. W. and Bass, M., Appl. Phys. Letters 22, 206-208 (1973).

[11] Allen, S. D. Braunstein, M., Giuliano, C., Wang, V., Pulsed CO_2 Laser Damage Studies of RAP Grown KCl, elsewhere in these proceedings.

[12] Smith, J. Lynn, NBS-SP-387 Report, p. 103 (Nov. 1973).

[13] Shatas, R. A., Narducci, L. M., Smith, J. Lynn, Meyer, H. C., and Mitra, S. S., NBS-SP-387 Report, p. 217 (Nov. 1973).

[14] Rowland, M. C., The Preparation and Properties of Gallium Arsenide in Gallium Arsenide Lasers, Gooch, C. H., ed. (Wiley-Interscience, New York, 1969), pp. 133-192.

[15] Yablonovich, E. and Bloembergen, N., Phys. Rev. Letters 29, 907-910 (1972).

[16] Fradin, D. W., Bloembergen, N., and Letellier, J. P., Appl. Phys. Letters 22, 635-637 (1973).

[17] Logan, R. A., Chynoweth, A. G., and Cohen, B. G., Phys. Rev. 128, 2518-2523 (1962).

[18] Baraff, G. A., Phys. Rev. 128, 2507-2517 (1962).

[19] Robson, R. E., Phys. Rev. Letters 31, 825-828 (1973).

[20] Wolfe, C. M., Stillman, G. E., and Lindley, W. T., J. Appl. Phys. 41, 3088-3091 (1970).

[21] Shatas, R. A. and Narducci, L. M., Interband Transitions in an Intense Infrared Radiation Field in Trans. 19th Conference U. S. Army Mathematicians, ARO-D Report 74-1.

[22] Kaw, P. K. and Dawson, J. M., Phys. Fluids 12, 2586 (1969).

[23] Nishikawa, K. J., Phys. Soc.-Japan 24, 1152 (1968).

[24] Meyer, H. C. and Shatas, R. A., Phys. Fluids 15, 1542 (1972).

[25] Gerstein, I. I. and Tzoar, N., Phys. Rev. Letters 27, 1650 (1971).

[26] Bicknell, W. E., Tomasetta, L. R., and Bates, D. H., Paper X.11, 8th Internat. Quantum Electron. Conference Digest, 74 CHO-858-1-QECON.

COMMENTS ON PAPER BY SHATAS

The theory proposed in this paper was characterized as a first cut at the problem. The use of the concepts of one-electron effective mass and differential mobility may be invalid as the electrons become energetic, due to non-paralolicity of the bands. In fact, the speaker commented on the role played in avalanche breakdown of a typical electron, not described by the Maxwellian distribution. He proposed that a rigorous treatment of the problem would involve a detailed numerical solution of the Boltzmann equations, which would be an expensive undertaking.

6.2 Frequency Dependence of the Nonlinear Optical Susceptibility of Five Glasses*

Robert Hellwarth, Joel Cherlow, and Tien-Tsai Yang

Electronics Sciences Laboratory, University of Southern California
Los Angeles, California 90007

The frequency dependence of the nonlinear susceptibility throughout the optical region of fused quartz, ED-4, LSO, SF-7, and LaSF-7 glasses is derived in a novel and useful form from Raman-scattering and intensity-induced polarization change measurements.

Key words: ac Kerr effect; glasses; nonlinear optical effects; nonlinear optical susceptibility; self-focusing; three-wave mixing.

1. Introduction

We have recently determined the frequency dependence of the nonlinear optical susceptibilities of five glasses, and used these to determine the relative contributions of "electronic" and "nuclear" mechanisms to their indices for self-focusing. We demonstrated how the nonlinear optical susceptibility is simply related to the frequency spectrum of polarized and depolarized Raman-scattering cross-sections and the coefficient for intensity-induced polarization changes (IIPC) in glasses. We used our own measurements of Raman cross-sections and Owyoung's measurements of IIPC to determine the nonlinear optical susceptibilities of fused quartz and the glasses ED-4, LSO, LaSF-7 and SF-7. The first account of this work is being published elsewhere, but we reproduce it in the Appendix (Sec. 6) of this paper. In this Appendix the necessary theoretical relations are derived and the experimental data are summarized, by which the nonlinear susceptibilities and mechanisms are determined. In the following section 2 we present some transformations of the original results which are of direct use in predicting a variety of nonlinear optical effects in the glasses.

2. Nonlinear Susceptibilities of Glasses

We have studied the "third order" nonlinear susceptibility tensor in glasses, i.e. the tensor which gives the term in the expression for the nonlinear polarization of a glass that is third-order in the propagating macroscopic optical electric fields. (By "optical" we mean fields whose frequencies are smaller than the bandgap and higher than lattice vibration frequencies.) The third-order term is the only nonlinear term that is important below damage thresholds. In the Appendix we show that whereas the "electronic" contribution to the nonlinear polarization can be expressed in terms of one real parameter σ, as in eq. (A1),[1] the "nuclear" contribution requires two real functions of time, a(t) and b(t) in eq. (A2), for its determination. Since a(t) and b(t) represent causal response functions of nuclear motions (a=b=0 for t<0), the real and imaginary parts of their Fourier integral transforms, A_ω and B_ω, are related by the usual Hilbert transform of eq. (A7).

In figure 1 of the Appendix are given our measured Raman-scattering cross-sections, to which the imaginary parts of A_ω and B_ω are related by the simple multiplicative function given in eq. (A6). Because the self-focusing indices considered in the Appendix involved only σ and the real parts of A_ω and B_ω at $\omega=0$, the Hilbert transforms at Δ of the imaginary parts of A_ω and B_ω were given in Table 1 only at $\Delta=0$. However prediction of other nonlinear effects requires a knowledge of Re A_ω and Re B_ω at arbitrary ω. For example, consider the three-wave mixing observed in glasses by Levenson (ref. [9] of the Appendix). In these experiments, Levenson superimposed two nearly colinear optical beams so that the macroscopic electric field at any point equalled

---

*This work was supported by the U.S. Atomic Energy Commission under U.C. Lawrence Livermore Laboratory subcontract 2713005.

[1]The numbered equations (1),(2),etc., in the Appendix will be referred to as eqs. (A1), (A2), etc.

5. Figures

The Fourier transforms A_ω and B_ω of the time-dependent nuclear response functions a(t) and b(t) for five glasses, in terms of which the nonlinear susceptibilities are expressed in the Appendix. The curves represent a) Re $(A_\omega + B_\omega)$, b) Im $(A_\omega + B_\omega)$, c) Re B_ω, and d) Im B_ω. The ordinates are 10^{15} timés the values in esu. The abscissae give the frequency ω in wavenumbers (cm^{-1}).

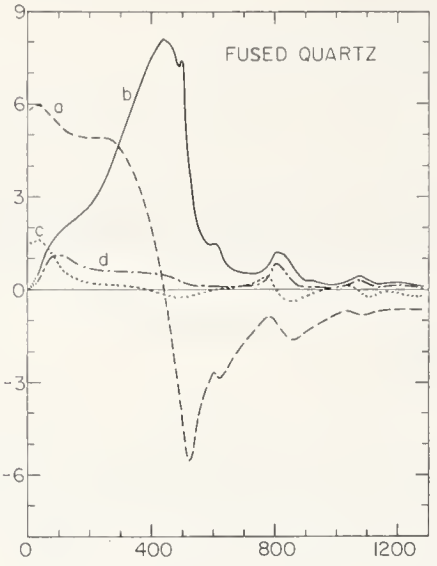

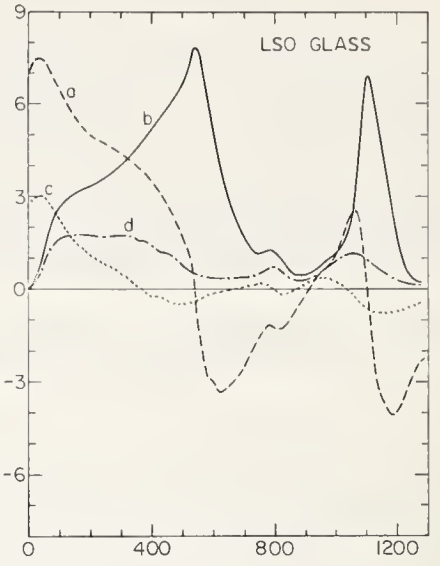

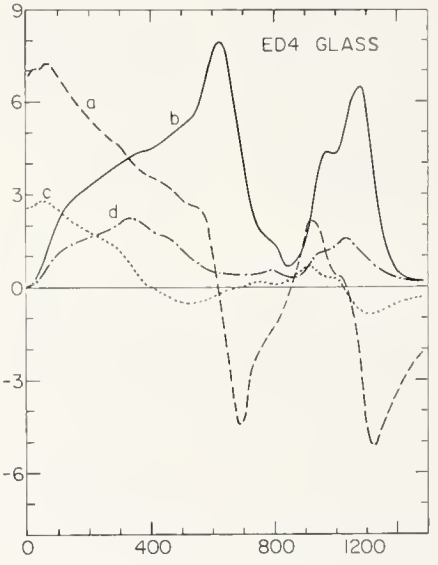

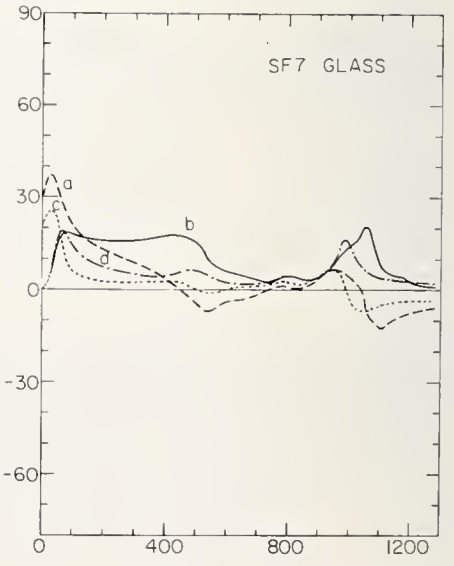

$$\underset{\sim}{E}(t)=\mathrm{Re}[\underset{\sim}{U}e^{-i\omega_u t}+\underset{\sim}{V}e^{-i\omega_v t}] \tag{2.1}$$

where U and V are complex amplitudes, depending on the strength and polarization of the two beams. Levenson then observed the light radiated at the "mixed" frequency $\omega=2\omega_u-\omega_v$ from a nonlinear polarization density which, from eqs. (A1) and (A2), has a complex amplitude

$$\frac{1}{4}\underset{\sim}{U}\underset{\sim}{U}\cdot\underset{\sim}{V}^*(\sigma+2A_\Delta+B_\Delta)+\frac{1}{8}\underset{\sim}{V}^*\underset{\sim}{U}\cdot\underset{\sim}{U}(\sigma+2B_\Delta) \tag{2.2}$$

where $\Delta\equiv\omega_u-\omega_v$. Here the involvement of the entire functions A_ω and B_ω is evident.

As a second example of the usefulness of the functions A_ω and B_ω, consider the "ac Kerr effect" in which colinear waves of the form of eq. (2.1) are again superposed in the medium, and a change in the optical susceptibility tensor $\delta\underset{\sim}{\chi}_v$ at frequency ω_v is observed because of the presence of the U-wave. To lowest order in U^2 this change is seen immediately from eqs. (A1) and (A2) to be expressible in the dyadic form

$$\begin{aligned}\delta\underset{\sim}{\chi}_v=&\frac{1}{4}\,\underset{\sim}{U}\underset{\sim}{U}^*(2A_\nu+B_o+\sigma)\\&+\frac{1}{4}\,\underset{\sim}{U}^*\underset{\sim}{U}(B_\nu+B_o+\sigma)\\&+\frac{1}{4}\,\underset{\sim}{1}(B_\nu+2A_o+\sigma)\underset{\sim}{U}^*\cdot\underset{\sim}{U}\end{aligned} \tag{2.3}$$

where $\nu\equiv\omega_v-\omega_u$. Again the entire functions A_ω and B_ω are needed for calculation of this effect, at least at frequency shifts ν small enough (typically $\lesssim$1000 cm^{-1}) so that A_ν and B_ν are not negligible.

Therefore, we have performed numerical computations of the Hilbert transform eq. (A7), for all transformed frequency variables below 1300 cm^{-1}, and obtained the numerical results for A_ω and B_ω, for the five aforementioned glasses, which are displayed in the figure at the end of this section.

3. Summary

We have re-expressed a previous experimental determination (reprinted in the Appendix) of the entire frequency dependence of the nonlinear optical susceptibility of fused quartz, ED-4, LSO, SF-7, and LaSF-7 glasses. This re-expression is summarized in curves of the real and imaginary parts of the Fourier transforms A_ω and B_ω of two scalar lattice response functions defined in the Appendix (where the electronic nonlinear susceptibility contributions are also tabulated).

4. Acknowledgments

The authors gratefully acknowledge the helpful conversations with A. Owyoung, A. Glass and M. Levenson.

6. Appendix A: reprint of article to be published in Physical Review in slightly expanded form.

Origin and Frequency Dependence of Nonlinear Optical Susceptibilities of Glasses*

Robert Hellwarth, Joel Cherlow and Tien-Tsai Yang
Department of Physics, University of Southern California
Los Angeles, California 90007

We have determined the frequency dependence of the nonlinear optical susceptibilities of fused quartz and four other glasses, and determined the relative contributions of "electronic" and "nuclear" mechanisms to their nonlinear optical indices. This is the first such determination in solids. Our method has been to analyze our own absolute measurement of ordinary differential Raman scattering cross-sections in conjunction with the coefficients for intensity induced polarization changes measured by Owyoung in the same glasses.

The nonlinear optical polarization density $\vec{P}^{(3)}(\vec{r}t)$, which is third order in the electric field in a material, manifests itself in a variety of commonly observed nonlinear optical effects such as beam self-focusing, self-phase modulation, frequency mixing, and intensity induced polarization changes (IIPC). Here we point out a relation between differential Raman scattering cross-sections and $\vec{P}^{(3)}$ which we use to determine both the frequency dependence and physical origins of the nonlinear polarization in five optical glasses. This is the first such determination in solids. We use our own Raman scattering measurements in conjunction with the IIPC data of Owyoung[1][1] to characterize $\vec{P}^{(3)}$ at "optical" frequencies; that is, at frequencies too low to excite electronic transitions and too high for nuclear motions to follow.

There are, in this case, two distinct physical contributions to $\vec{P}^{(3)}(\vec{r}t)$ (apart from electrostriction induced strains which we ignore). First, there is an "electronic" contribution from the nonlinear distortion of the electron orbits around the average positions of the nuclei. This polarization responds rapidly to field changes, within a few electronic cycles ($\sim 10^{-16}$ sec). In isotropic materials it contributes a term to $\vec{P}^{(3)}$ well approximated by the instantaneous form

$$\frac{1}{2}\sigma\vec{E}(\vec{r}t)E^2(\vec{r}t) \tag{1}$$

for frequencies well below the electronic band gap. The scalar coefficient σ is independent of temperature at fixed density.

A second, "nuclear," contribution arises from an optical field induced change in the motions of the nuclei; about these changed motions the electronic currents respond linearly to the optical fields. This contribution can be observed after the sudden impression of a field only following a time lapse of the order of the time ($\sim 10^{-12}$ sec) required for a nucleus to execute a vibrational or rotational cycle. In isotropic materials this contribution to $\vec{P}^{(3)}$ must be of the form (at some position $\vec{r}$)[2]

$$\vec{E}(t)\int_{\infty}^{\infty} ds\, a(t-s)E^2(s) + \int_{\infty}^{\infty} ds\vec{E}(s)b(t-s)\vec{E}(t)\cdot\vec{E}(s) \tag{2}$$

for frequencies well below the electronic band gap. The nuclear response kernels, a(t) and b(t), vanish for $t < 0$ by causality, and generally exhibit a marked temperature dependence at constant density. We determine the electronic coefficient σ and the Fourier transforms of a(t) and b(t) for several glasses using measurements of IIPC and Raman effect in the theoretical relations which we develop below.

That $\vec{P}^{(3)}$ should cause the elliptical state of polarization of a strong monochromatic beam to change was first predicted and observed by Maker, et al.[3] For a plane wave of frequency ω propagating in an isotropic medium, this "intensity induced polarization change" (IIPC) manifests itself by a rotation of the axes of the polarization ellipse through an angle $\theta(z)$ which increases with the distance z along the beam. An expression for θ in terms of σ, a(t), and b(t) is easily found by inserting such a plane wave E in (1) and (2), and then verifying that Maxwell's equations are satisfied (to order E^3) with this nonlinear polarization density, provided that [1,2]

---

*This work was supported by the U. S. Atomic Energy Commission under U.C. Lawrence Livermore Laboratory subcontract 2713005

[1]Figures in brackets indicate the literature references at the end of this paper.

$$\theta = \frac{\pi\omega z \langle E^2(t)\rangle (\sigma + 2B_o) \cos 2\phi}{8nc} \tag{3}$$

where c is the velocity of light, tan ϕ is the ratio of right to left circular polarization amplitudes, and B_o is the value of the Fourier transform B_Δ of b(t) evaluated at $\Delta = 0$ (esu used throughout). We define $B_\Delta \equiv \int dt\, b(t) \exp i\Delta t$, and A_Δ similarly. We next see how A_Δ and B_Δ can be determined from differential Raman scattering cross sections. Knowing B_Δ and A_Δ we can determine σ, and thereby the entire nonlinear polarization (1) and (2), through IIPC measurements which according to (3) give $\sigma + 2B_o$.

Consider first the well known nonlinear optical effect of ordinary (non-phased-matched) stimulated Raman scattering in which the presence of a strong plane polarized "pump" wave $\hat{x}F \cos(\nu t - k_o z)$ in a medium causes a second weak wave $\mathrm{Re}\, \hat{e}E \exp[i(\omega t - \vec{k}\cdot\vec{r})]$ to experience exponential gain. If $\vec{E}$ in (1) and (2) is the sum of these two optical fields, then Maxwell's equations are satisfied to order F^2E for real ν, k_o, and ω, if $\vec{k}$ is a complex vector $\hat{s}(k' + ig/2)$ where g, the "stimulated power gain per cm," is

$$g_{\parallel} = \frac{2\pi\omega F^2}{nc} \mathrm{Im}(A_\Delta + B_\Delta) \tag{4}$$

when $\hat{e} \parallel \hat{x}$, or

$$g_{\perp} = \frac{\pi\omega F^2}{nc} \mathrm{Im}B_\Delta \tag{5}$$

when $\hat{e} \perp \hat{x}$. $\Delta \equiv \nu - \omega$.

There exists a well known relation between these stimulated gain coefficients and the differential Raman scattering cross sections $d^2\sigma_i(\nu,\Delta)/d\Omega d\Delta$, defined as the fraction of incident photons of frequency ν inelastically scattered per unit distance into solid angle $d\Omega$ and angular frequency range $d\Delta$ about $\nu - \Delta$ when the incident and scattered polarizations are either parallel ($i = \parallel$) or perpendicular ($i = \perp$).[4] Substituting (4) and (5) into eq. (4) of ref. [4] gives the general relations which we seek:

$$\mathrm{Im}B_\Delta = \frac{\pi c^4}{\hbar\nu\omega^3} \frac{d^2\sigma_\perp}{d\Omega d\Delta} \left(1 - e^{-\hbar\Delta/kT}\right), \tag{6}$$

and a similar relation with A_Δ and $\frac{1}{2}\sigma_\parallel - \sigma_\perp$ substituted for B_Δ and $\sigma_\perp$ respectively. Because of the causal nature of a(t) and b(t), the real parts of their Fourier transforms can be calculated from their imaginary parts by the usual Kramers-Kronig integrals:

$$\mathrm{Re}\, B_\Delta = \frac{1}{\pi} \int_{-\infty}^{\infty} \frac{d\nu}{\nu - \Delta} \mathrm{Im}B_\nu, \tag{7}$$

and similarly for A_Δ.

We can see therefore from (6) and (7) how the entire transforms of a(t) and b(t) can be deduced from our measured Raman scattering cross-sections in figure 1 for the five glasses: 1) Homosil fused quartz (Amersil, Inc.), 2) LSO (American Optical Co.), 3) ED-4 (Owens Illinois, Inc.), 4) SF-7 (Schott) and 5) LaSF-7 (Schott). The curves in figure 1 were obtained from 90° Raman scattering measurements using the 514 nm line of an argon ion laser and a double monochromator whose spectral sensitivity was calibrated with a quartz-iodine standard lamp. The absolute cross-sections were obtained by comparison with the 992 cm^{-1} line of liquid benzene for which the absolute cross-section has been determined to within 5% by Kato and Takuma[5]. Index corrections of the type described by these authors were performed. Our measurements of the polarized Raman cross-sections of fused quartz yield Raman gains in (4) about 20% greater than those reported by Stolen and Ippen[6], but within their limits of error.

To obtain the values of B_o (required to determine the electronic coefficient from IIPC measurements) and A_o (required later to calculate the self focusing index n_2) we use (6) in (7) finding

$$B_o = \frac{2c^4}{\hbar\nu} \int_0^{\infty} \frac{d\Delta}{\omega^3\Delta} \frac{d^2\sigma_\perp(\nu,\Delta)}{d\Omega d\Delta} \left(1 - e^{-\hbar\Delta/kT}\right) \tag{8}$$

and similarly for A_o. Using the cross-sections of figure 1 in (8) gives the values for A_o and B_o listed in table 1. Also listed there are Owyoung's IIPC measurements of $\sigma + 2B_o$ (taken at 694 nm) from which we deduce the listed values of σ. This completes our characterization of the nonlinear optical polarization $\vec{P}^{(3)}$ for these glasses.

Table 1. Nonlinear polarization parameters defined in text as derived from our Raman data and intensity induced polarization change (IIPC) measurements. From these are derived the self-focusing index n_2 of eq. (3) and the fraction f_e that is electronic in origin. All quantities are in esu.

Material	n	$10^{16}B_o$ [a]	$10^{16}(A_o+B_o)$ [a]	$10^{15}(\sigma+2B_o)$ [b]	$10^{15}\sigma$	$10^{14}n_2$ (eq.4)	$10^{14}n_2$ (meas.)	f_e(%)
Fused Quartz	1.46	14±2	57±5	31±2	28±2	11±1	18±3 [c]	79±3
LSO Glass	1.52	28±4	70±6	46±3	40±3	15±1		81±3
ED-4 Glass	1.56	26±4	68±7	57±4	52±4	18±1.3	26±3 [c] 15±2 [d] 15±3 [e]	85±3
SF-7 Glass	1.65	210±20	315±30	202±20	160±20	58±7		79±3
LaSF-7 Glass	1.93	380±30	540±50	252±25	176±25	61±8		71±3

[a] This work [b] Ref. [1,12] [c] Ref. [9] [d] Ref. [8] [e] Ref. [7]

Our results may be compared with recent measurements of the self-focusing index n_2 for a monochromatic beam. Since the change in refractive index for linear polarization is defined as $n_2\langle E^2(t)\rangle$, we see from (1) and (2) that, in our terms,

$$n_2 = \pi\left(\frac{3}{2}\sigma + 2A_o + 2B_o\right)/n \qquad (9)$$

where n is the linear refractive index. Our predictions for n_2 in Table 1 (which depend mainly on Owyoung's data[1]) are seen to be consistent with the absolute interferometric, time resolved pulse measurements of Bliss et al.[7], and also with the interferometric comparisons with liquid CS_2 made by Moran et al.[8] Ours are, however, lower than the values obtained by Levenson [9] from 3-wave mixing experiments near 530 nm. This is most probably due to his less certain calibration. Estimates of dispersion from phenomenological theories of n_2 indicate that n_2 should not be more than 5% greater in the green. [9-12]

The phenomenological theories of n_2, developed to aid in the design of low-n_2 glasses, have assumed that n_2 is mainly electronic in origin. This is verified by our values in Table 1 for its electronic fraction f_e, which, according to (9), is $[1 + 4(B_o + A_o)/(3\sigma)]^{-1}$.

The authors gratefully acknowledge helpful conversations with A. Owyoung, A. J. Glass, E. Snitzer, N. Boling, E. Bliss, M. Moran and R. L. Carman, and thank S. P. S. Porto for the use of his facilities.

6.1 References for Appendix

[1] A. Owyoung, IEEE Journ. of Quantum Electronics 9, 1064 (1973); A. Owyoung, "Laser Induced Damage in Optical Materials: 1973," ed. A. J. Glass and A. H. Guenther (National Bureau of Standards Special Publ. 387, Dec. 1973); A. Owyoung, R. W. Hellwarth, and N. George, Phys. Rev. B5, 628 (1972).

[2] R. W. Hellwarth, A. Owyoung, and N. George, Phys. Rev. A4, 4 (1971).

[3] P. D. Maker, R. W. Terhune, and C. M. Savage, Phys. Rev. Letters 12, 507 (1964).

[4] R. W. Hellwarth, Phys. Rev. 130, 1850 (1963).

[5] Y. Kato and H. Takuma, J. Opt. Soc. Am. 61, 347 (1971); J. Chem. Phys. 54, 5398 (1971).

[6] R. H. Stolen and E. P. Ippen, Appl. Phys. Lett. 22, 275 (1973).

[7] E. R. Bliss, D. R. Speck, and W. W. Simons (to be published).

[8] M. Moran, C. She, and R. L. Carman (to be published).

[9] M. D. Levenson, IEEE Journ. of Quantum Electronics QE-10, 110 (1974).

[10] C. C. Wang, Phys. Rev. B2, 2045 (1970).

[11] J.F.Fournier and E. Snitzer, IEEE Journ. of Quantum Electronics QE-10, 473 (1974).

[12] N. L. Boling, A. J. Glass and W. Owyoung (to be published).

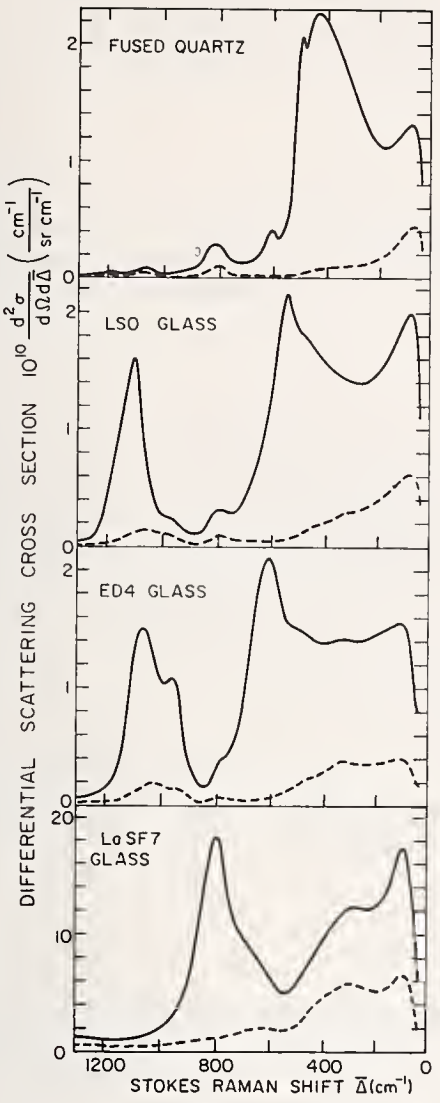

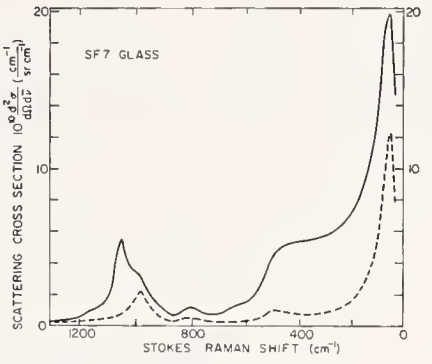

Figure 1. Differential Raman scattering cross-sections vs. (Stokes) frequency shift $\bar{\Delta}$ from 514 nm incident beam for five glasses ($\bar{\Delta} \equiv \Delta/(2\pi c)$ cm^{-1}). Solid lines are polarized ($\parallel$) and dashed lines are depolarized ($\perp$) cross-sections.

COMMENTS ON PAPER BY HELLWARTH

The presence of Neodymium in the glass samples did not directly affect the observed Raman spectrum. It did tend to introduce absorption at the exciting wavelength, and a consequent fluorescent background. When the absorption was strong, a resultant loss of signal was seen to occur.

6.3 The Refractive Index Dependence of Pulsed Laser Induced Damage

Jerry R. Bettis* and Arthur H. Guenther
Air Force Weapons Laboratory
Kirtland Air Force Base, New Mex 87117

and

Alexander J. Glass
Lawrence Livermore Laboratory
Livermore, California 94550

The dependence of the laser induced damage threshold on refractive index has been investigated. A simple theoretical expression, based upon several factors such as the local electric field and avalanche mechanisms, has been derived. Comparison is made with several series of previously published results to verify the proposed dependence. Strikingly good agreement is obtained between theory and experiment for materials with refractive indices ranging from 1.38 to 2.36. The available experimental data used for comparison were obtained (1) on the surface of uncoated dielectrics, (2) in the bulk of alkali halides, (3) with $\lambda/4$ dielectric coatings and (4) with vapor phase mixture thin films. Extrapolations of these results to conditions for air at STP give remarkable agreement with reported values of pulsed laser induced air breakdown.

Key words: Bulk; electro-absorption; electron avalanche, laser damage; local field corrections; refractive index; surfaces; thin films.

1. Introduction

An early observation of the damage of optical elements by intense pulsed laser radiation showed that the damage threshold is generally dependent upon the index of refraction of the dielectric. Notably, in the work of Turner [1][1] a hierarchy of damage sensitivity appeared to exist which indicated that high index materials were less damage resistant than low index materials. This paper attempts to elucidate that conclusion.

Since refractive index is a measure of the polarizability (distortion) of electronic distributions by the local optical electric field in the medium, it is pertinent to ask how laser induced damage is related to the optical field. Numerous observations over the past several years have indicated that the appropriate quantity in short-pulse, laser-induced damage is indeed the optical electric field. Dube first showed that this assumption readily explained the asymmetry in the entrance and exit damage thresholds by recourse to Fresnel considerations [2]. Bloembergen asserted that the difference in surface and bulk damage thresholds could be explained by the enhancement of the optical electric field at geometrical or mechanical imperfections and dielectric discontinuities such as absorbing inclusions [3]. It was further observed that the damage threshold at total internal

---

*Submitted in partial fulfillment for the degree of Doctor of Philosophy at the Air Force Institute of Technology, Wright-Patterson AFB, Ohio 45433.

1. Figures in brackets indicate the literature references at the end of this paper.

reflecting surfaces depended on the polarization of the light wave incident on the reflecting interface. By calculating the resulting electric fields for p and s polarizations, Fersman and Khazov [4] demonstrated that whereas the energy and power density at threshold depended on polarization, the electric field assumed a constant value. Finally, Fradin, Yablonovitch, and Bass [5] concluded that the damage mechanism in alkali halides is the field-dependent process of electron avalanche. By so doing they were able to explain both the frequency and pulse length dependence of laser-induced damage. At most operative pulse lengths and wavelengths of interest the breakdown field was nearly identical to DC breakdown values for the wide gap insulators studied.

2. Local Field Considerations

Granted, then, that the damage process is field dependent. How does this relate to the index dependence? The refractive index and the local electric field are related through the induced polarization and the Clausius-Mossotti relation. For a dielectric subjected to a local electric field, $\vec{E}_\ell$, the induced polarization per unit volume, $\vec{P}$, for a linear isotropic medium is

$$\vec{P} = N\alpha(\omega)\,\varepsilon_o\,\vec{E}_\ell \tag{1}$$

where N is the density of polarizable species (e.g., molecules), $\alpha(\omega)$ is the molecular polarizability, and ε_o is the permittivity of free space. By definition, the polarization is the sum of the displacements from equilibrium of each charge carrier times the charge. Taking $\langle\vec{x}\rangle$ as the total average displacement per molecule one obtains

$$N q_e \langle\vec{x}\rangle = N\alpha(\omega)\,\varepsilon_o\,\vec{E}_\ell \tag{2}$$

where q_e is the electronic charge. For dense dielectrics approximating cubic symmetry the Clausius-Mossotti relation between polarizability and refractive index yields

$$\vec{E}_\ell = \frac{n^2 + 2}{3\varepsilon_o(n^2 - 1)}\; q_e N \langle\vec{x}\rangle \tag{3}$$

By applying the Lorentz local field correction to obtain the macroscopic field, E, in the dielectric one obtains the desired relation

$$\vec{E} = \frac{q_e N \langle\vec{x}\rangle}{\varepsilon_o(n^2 - 1)} \tag{4}$$

The supposition is made that there exists a critical displacement, x_{cr}, not necessarily an average $\langle\vec{x}_{cr}\rangle$, depending undoubtedly on ionization potential, dispersion, band and energy level structure as well as other related quantities such as effective charges and masses, beyond which an electronic distribution cannot be displaced without liberating electrons. Since an electron avalanche is a process by which free electrons are accelerated to ionizing energies by the application of an electric field, the ease with which electrons can be freed would seem to have a decided effect on a material's damage threshold. Under these assumptions the magnitude of the threshold macroscopic electric field (E_{th}) should vary as

$$E_{th} \sim \frac{KN}{n^2 - 1} \tag{5}$$

Several other detailed approaches to this relation is given in a paper by Bettis, et al [6]. These include first principle consideration of polarizability and a rate dependent energy gain and loss calculation for electron avalanches produced by high intensity optical radiation interacting with dielectric media. Of course, to treat the problem explicitly, one should treat the total assembly of interacting species individually with careful consideration of their specific environment, density, locations, and intrinsic polarizability.

3. Test of Theory

To test the validity of this approach, one can compare the expression in eq. (5) to data obtained by various experimentalists. First consider the damage work of DeShazer, et al., [7] in which films of various thicknesses and material composition were applied to glass substrates. A tabulation of their results for $\lambda/4$ films is given in table 1. Included is the function $KN/(n^2-1)$ where the value of K has been chosen arbitrarily to facilitate comparison. In the final column is listed values of $KN/(n^2-1)$ relative to the thin film damage thresholds for the density and index of air. The values correspond closely to the reported values for air breakdown of 4.3×10^8 V/m [8] to 5.0×10^8 V/m [9].

Table 1. Tabulation of results for $\lambda/4$ films.

Material	E_{th} (10^7 V/m)	$\frac{KN}{n^2-1}$	E_{th} Air Breakdown
ZnS	5.71	5.53	5.0×10^8 V/m
TiO_2	6.59	6.67	4.69×10^8 V/m
ZrO_2	7.58	8.03	4.41×10^8 V/m
SiO_2	16.54	18.78	4.13×10^8 V/m
MgF_2	16.55	30.67	2.53×10^8 V/M

Comparison of the observed threshold electric field for damage vs. the function $\frac{KN}{n^2-1}$. The value of K was arbitrarily chosen to be 9.68×10^{-22} V-M^2. The values of air breakdown are the ratios of the function for the density and index of air vs. the material multiplied by the observed threshold field for the material.

In addition, films of TiO_2 of thicknesses $\lambda/4$, $\lambda/2$, and 3 $\lambda/4$ were damaged with the damage being indicated by laser induced scattering (LIS) rather than spark detection as in the values quoted in table 1. The appropriate threshold field values were 5.13×10^7, 3.78×10^7, and 3.69×10^7 V/m, respectively. These closely grouped values more nearly relate to an intrinsic property of TiO_2 than do the widely variant incident threshold power densities of 3.45, 0.6, and 1.8 GW/cm^2. The difference in threshold power density would vanish if the index of film and substrate were the same. Thus, we note for the case of SiO_2 (n = 1.456) applied to BSC-2 glass (n = 1.51) the values of threshold field vs incident power density for $\lambda/4$ and $\lambda/2$ films were 1.65×10^8, 1.58×10^8 V/m; and 10.5, 9.9 GW/cm^2, respectively.

A second set of experimental data, this by Boling, Dube', and Crisp [10] was reduced to figure 1. The data are the results of surface damage studies conducted on seven laser glasses, fused silica, and sapphire. Approximate values of molecular densities were obtained [11] and although detailed molecular densities have not been included in expression [5] one can still have confidence in the comparison since the approximate molecular densities, as supplied by the manufacturers, were sensibly constant.

Another set of available data is the vapor phase mixture results of Austin, et al [12]. In this study, vapor phase mixtures of various percentages of ThF_4 and ZnS were applied in $\lambda/2$ films to glass substrates. Perhaps the very nature of these complex mixture films negates exact comparison with the $N/(n^2-1)$ function, for although the threshold field does decrease with increasing index as evidenced in figure 2, the graph of E_{th} vs $N/(n^2-1)$ is reversed in slope. We cannot at present explain this apparently anomalous behavior. Thus, more careful treatment of binary mixture films is warranted as well as a detailed look at the surprisingly high optical strength of ThF_4.

Perhaps the most comprehensive data in which extrinsic influences have been all but eliminated is that gathered by Fradin and coworkers on wide-gap insulators [5]. This research is different in character in that threshold conditions for bulk damage were measured in 11 different alkali halides at 10.6 μm and 1.06 μm and compared to values obtained from D.C. breakdown studies. The results are quite striking when threshold electric field is plotted against $N/(n^2-1)$. From the previous discussion we would expect such graphs to be monotonically increasing straight lines and to within reasonable tolerances such is the case. Similar data at 1.06 μm is presented in figure 3. The potassium halides depart systematically from the sodium and rubidium halides. The value taken for the threshold value in NaI was extrapolated from the D.C. and 10.6 μm data, since the investigators report that the crystal was extremely hydroscopic and as a result exhibited an anomalously low threshold field at 1.06 μm. The breakdown field for KF at 1.06 μm was also extrapolated from the D.C. and 10.6 μm data since no value was given for 1.06 μm. The straight lines which result differ in slope by less than 10% with the only point deviating strongly being the single point for NaF. In passing, it is worthwhile mentioning that fluorides exhibit a tendency to deviate from expected behavior and therefore should be studied more closely. Extrapolating the threshold values to the conditions for air yields values of 4.2×10^8 V/m to 4.87×10^8 V/m for the potassium group and 6.4×10^8 V/m to 7.6×10^8 V/m for the Rb and Na group. These extrapolated values are in close agreement with experimental results for air breakdown at the appropriate frequency and pulse duration.

One can envision the interaction process as consisting of a catastrophic distortion of electron distributions. At the very high fields generated by focussed laser beams, second order effects may become important. Indeed, the second order correction to the refractive index leads to the well documented onset of self-focussing. Other effects which may become important at elevated fields are the process of electro-reflectivity and electro-absorption. It has been shown [13] that due to the quadratic Stark effect an increase in absorption may occur at elevated fields. Any such increase can lead to an enhanced deposition of energy within a lattice.

While the simple theory presented here gives more than fortuitous agreement with experiment, it is obvious that a more detailed examination is called for. Obviously for a proper treatment one should avoid taking average quantities but must instead deal with individual quantities. For example, the molecular polarizability of glasses is a gross average of the polarizabilities of each species and one would hope that a more detailed look at this facet of the problem would result in better understanding. Such things as impurities and structures need be considered as well as the total range of energy states in a solid lattice. Such considerations would naturally lead to investigation of low lying energy traps and the reduced effective mass of electrons lying near the top of Fermi bands.

4. References

[1] Turner, A. Francis, Damage in Laser Materials: 1971, NBS Spec. Pub. 356, 119-123 (1971).

[2] Boling, N. L. and G. Dubé, Laser Induced Damage in Optical Materials: 1972, NBS Spec. Pub. 372, 40-45 (1972).

[3] Bloembergen, N., Applied Optics 12, No. 4, 661-664 (April 1973).

[4] Fersman, I. A. and L. D. Khazov, Sov. J. of Quantum Electronics 2, No. 4, 319-323 (Jan-Feb. 73).

[5] Fradin, D. W., Eli Yablonovitch, and Michael Bass, Applied Optics 12, No. 4, 700-709 (April 73).

[6] Bettis, Jerry R., Arthur H. Guenther and Alexander J. Glass, Optoelectronics and Laser Technology, 1974 IEEE Region Six Conference Record, 43-55 (1974).

[7] DeShazer, L. G., B. E. Newnam and K. M. Leung, Laser Induced Damage in Optical Materials: 1973 NBS Spec. Pub. 387, 114-124 (1973).

[8] Nelson, P., P. Veyrie, M. Berry and Y. Durand, Phys. Letters 13, 222 (1964).

[9] Akmanov, S. A., A. S. Kovrigin, M.M. Strukov and R.V. Khokhlov, JETP Letters 1, 25 (1965).

[10] Boling, N.L., G. Dubé and M.D. Crisp, Laser Induced Damage in Optical Materials: 1973 NBS Spec. Pub. 387, 69-79 (1973).

[11] Boling, N. L., Private Communication.

[12] Austin, R. Russel, Raymond C. Michaud, Arthur H. Guenther, Joseph M. Putman and Richard Harniman, Laser Induced Damage in Optical Materials: 1972, NBS Spec. Pub. 372, 135-165 (1972).

[13] Boling, N.L., A.J. Glass and Adelbert Owyoung, Accepted for Publication in Journal of Quantum Electronics.

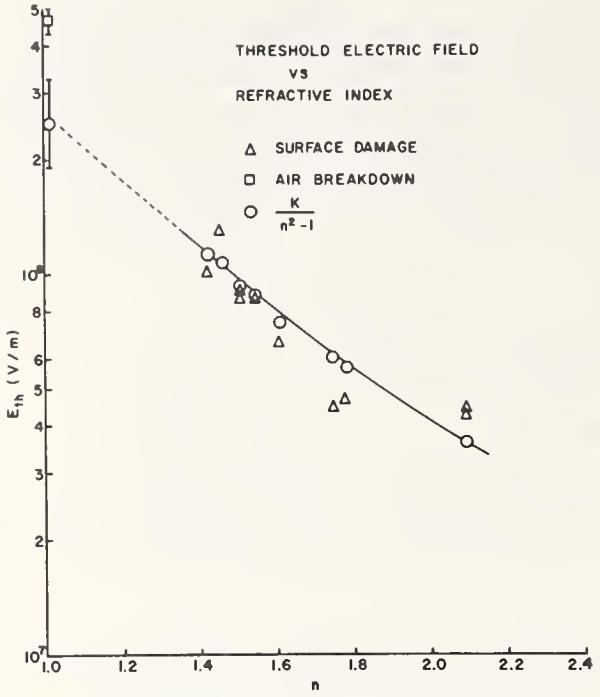

Figure 1. Threshold electric field for damage vs refractive index for glass, sapphire, and fused silica.

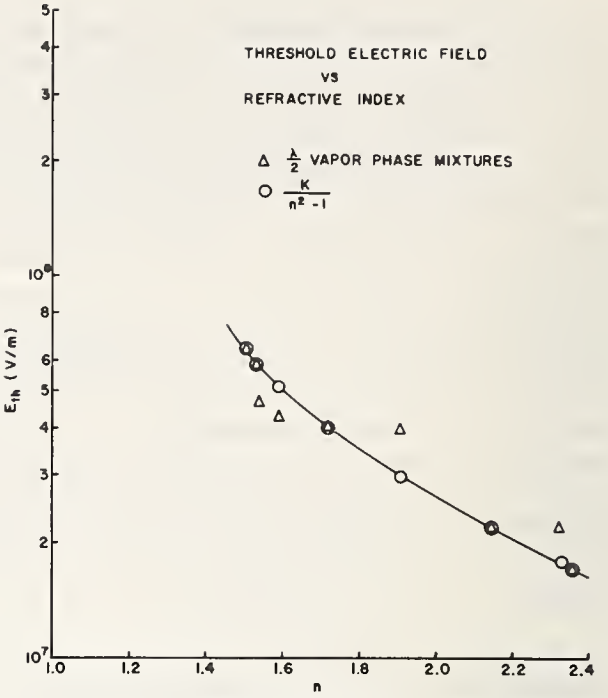

Figure 2. Threshold electric field for damage vs refractive index for vapor phase mixtures of ThF_4 and ZnS.

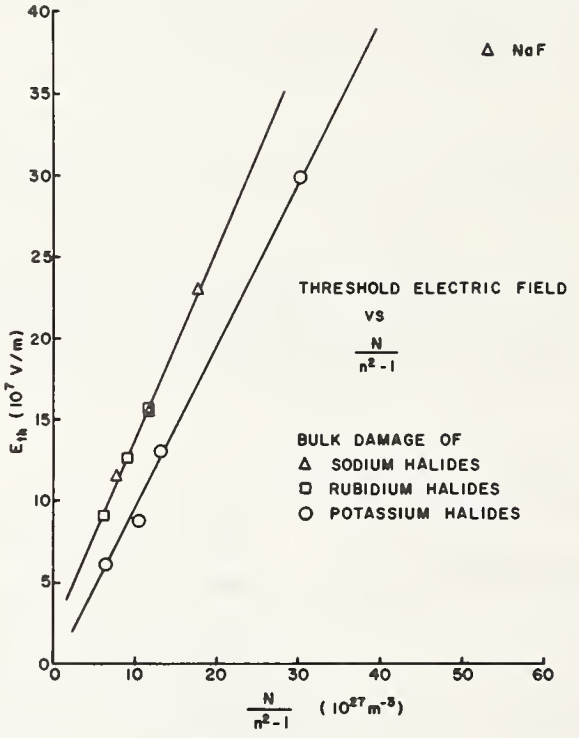

Figure 3. Threshold electric field for damage vs $\frac{N}{n^2-1}$ for 11 alkali halides.

COMMENTS ON PAPER BY BETTIS et al

The first question related to whether or not the breakdown mechanism proposed in this paper would be probabilistic. The speaker indicated that since this description only refers to the initiation of the breakdown, the avalanche process would still be probabilistic even though the initiation process is deterministic. The use of air breakdown values as a low index limit to the proposed scaling law was questioned, particularly since the numbers given for air breakdown values referred to dust laden air rather than pure air. The speaker indicated that these points were included for comparison purposes only. He was further questioned on the use of the data of Fradin and Bass on the breakdown strengths of alkali halides. He replied that in using those data where values were available at 1.06 micrometers, those values were used, but where 1.06 micrometer data were not available, data taken at other wavelengths were extrapolated to 1.06 micrometers according to the $1 + \omega^2\tau^2$ dependence.

6.4 Extrinsic Absorption in Laser Window Materials*

C. J. Duthler and M. Sparks

Xonics, Incorporated, Van Nuys, California 91406

Two types of extrinsic absorption are discussed. First, our calculations on absorbing inclusions, presented at the 1973 symposium, have been extended to explain the cone-shaped surface pits observed by Boling. For a spherical inclusion of radius a located a distance d below the surface, the cone half-angle is $\theta_m = \cos^{-1}(a/d)$. The second type of absorption is that due to polyatomic molecular-ion impurities in alkali halides. A literature survey indicates that concentrations of less than 0.1 ppm of NO_2^-, HCO_3^-, SO_4^{2-}, or CrO_4^{2-} will result in a bulk absorption coefficient $\beta(10.6\,\mu m) > 10^{-4}$ cm^{-1}.

Key words: Absorbing inclusions; alkali halides; impurity absorption; laser damage.

1. Introduction

We have previously reported our calculations of infrared absorption and materials damage in transparent materials containing inclusions. [1][1] We have extended our studies of extrinsic absorption in transparent laser materials to include two new effects. First, the mechanism is described for producing cone-shaped surface damage sites that are observed when certain materials are irradiated with a high-power, short-pulse-length laser at the threshold for damage. Second, certain molecular-anion impurities that substitute for the halide ion in alkali-halide crystals can contribute substantially to the extrinsic 10.6 μm absorption in these materials.

2. Conical Surface-Damage Pits

At the symposium last year, Boling, Dube', and Crisp [2] presented electron micrographs of several materials which suffered pre-plasma surface damage when irradiated with a 30 nsec, 1.06 μm laser pulse of energy from 7 to 25 J/cm^2. These damage sites are nearly perfectly conical having diameters of a few microns and depths of the order of one micron.

Due to the statistical distribution of the pits on the sample surface, it was proposed that the damage was initiated by an absorbing inclusion located just below the surface. Differing damage thresholds observed when various polishing compounds are used indicate that the inclusions may be polishing grits that somehow become embedded below the surface. Similar damage sites have been observed with thin films by Milam, Bradbury, and Bass. [3]

During the discussion following the talk by Boling, it was proposed that the conical pit was a crater resulting from the explosion of the inclusion as with conventional explosives. With conventional explosives the crater radius is related to the 1/3 power of the energy, and it was suggested that this may apply in the case of laser damage.

In a discussion with Dr. Robert Hellwarth after the meeting, we realized that the explosive mechanism is incorrect since it implies that the material in the conical section is completely broken up. A simple calculation reveals that there is only enough energy absorbed by the inclusion to disrupt the chemical bonds along the conical surface and that there is not enough energy available to further disrupt the cone.

---

*This research was supported by the Advanced Research Projects Agency of the Department of Defense and was monitored by the Defense Supply Service, Washington, D. C.

[1]Figures in brackets indicate the literature references at the end of this paper.

Consider a conical pit of 7 μm diameter and 2 μm depth resulting from absorption by a 1 μm radius inclusion. The absorption cross-section of a dielectric inclusion is given by

$$\sigma_{abs} = A \beta_I \pi a^3 , \quad (1)$$

where β_I is the absorption coefficient of the inclusion material, a is the inclusion radius, and A is a constant of order unity. [1] If we use $\beta_I = 10\,cm^{-1}$ and a laser fluence of $15\,J/cm^2$, the energy absorbed is 3×10^9 eV. Assuming that there is one chemical bond of energy 1 eV per $4 \times 10^{-16}\,cm^2$ of surface, the energy required to remove the conical section is 1×10^9 eV.

Therefore a mechanism is needed whereby the conical section is removed intact, or in a small number of fragments. One is led to consider shock waves which, however, can be quickly ruled out by mechanical equilibrium considerations. [4] In order for a compressive shock propagating outward from the inclusion to be able to produce fracture, the pulse length of the shock must be short compared to the time for sound to travel from the inclusion to the surface. In sapphire the velocity of sound is 1.1×10^6 cm/sec. This yields a round-trip time for sound of less than 10^{-9} sec which is less than even the 30 nsec rise time of the compressive pulse. For the sake of completeness, we mention that Fox and Barr [5] have observed laser-induced shock-wave damage in the back face of aluminum samples.

Hence the inclusion is viewed as acting as a source of quasistatic hydrostatic pressure within the cavity in the host material. The situation is sketched in figure 1. Neglecting heat flow out of the inclusion, the pressure P at the inclusion-host interface is found by equating the volume change of the heated and compressed inclusion to the volume change of compressed but unheated cavity in the host material, which yields

$$P = 3 \alpha_I B_{eff} T . \quad (2)$$

In eq. (2) T is the temperature of the inclusion, α_I is the linear thermal expansion coefficient of the inclusion, and B_{eff} is an effective bulk modulus given by $B_{eff}^{-1} = B_I^{-1} + B_H^{-1}$, where I and H denote inclusion and host.

If hydrostatic pressure P is applied within a spherical cavity in an infinite medium, the tensile stress along the spherical surface is given by $\sigma_t = P/2$. However, due to the proximity of the plane surface in the present case, the tensile stress is no longer uniform over the spherical cavity.

The exact solution for the 3-dimensional problem of stresses surrounding a spherical cavity near a plane boundary is very difficult, and approximate solutions converge very slowly. Fortunately, the exact solutions have been obtained for the qualitatively similar problem of a long cylindrical cavity aligned with its axis parallel to the plane surface. [6] These solutions can be used to gain insight into the present problem.

It is found that the tensile stress along the cylindrical cavity is anisotropic and is enhanced above the value that would be obtained in an infinite medium. The stress along the cylindrical surface σ_t is a maximum at the angle $\theta_m = \cos^{-1}(a/d)$ as is sketched in figure 1. Along the plane surface, maximum stress σ_x occurs at $x = 0$.

The dependence of the stresses $\sigma_t(\theta = \theta_m)$ and $\sigma_x(x = 0)$ on the depth of the inclusion is drawn in figure 2. For an inclusion near the plane surface ($d/a \to 1$), the stresses are very much enhanced over the infinite medium values. As d becomes large compared to a, the stresses approach the infinite medium values of $\sigma_t = P$ and $\sigma_x = 0$. The two curves cross at $d = \sqrt{3}\,a$.

Due to symmetry, the maximum stress along the surface of a spherical inclusion is expected to occur at the same angle θ_m as is shown in figure 1. However, the exact dependence of the stress on d/a will be slightly different from those shown in figure 2. First, the infinite-medium value for the stress on the spherical surface is

$\sigma_t = P/2$. Second, since the stress in the medium surrounding a sphere falls off more rapidly with distance than those surrounding a cylinder, the σ versus d curves are expected to be more strongly peaked near $d/a = 1$ than in figure 2.

The mechanism proposed for producing a conical pit is that a crack is nucleated at the point of maximum stress. For d greater than approximately $\sqrt{3}\,a$, this maximum stress occurs at the angle θ_m on the spherical cavity. The crack then propagates normal to the surface of the spherical cavity until it reaches the plane surface, directly forming a cone-shaped cavity. This is sketched in figure 3(a). The half-angle of the cone is θ_m, which is given as a function of d/a in figure 2.

Inclusions very close to the surface ($d/a < \sqrt{3}$) will produce maximum tensile stress at the point $x = 0$ on the plane surface. As is sketched in figure 3(b), a crack will first propagate from the point $x = 0$ to the cavity surface. Further expansion of the inclusion could result in additional failure near θ_m to produce a cone-shaped damage site.

The following considerations favor fracture first occurring at θ_m as in figure 3(a) rather than at $x = 0$ as in figure 3(b): Fracture in bulk materials is strongly dependent on surface cracks and imperfections which have the same size as the inclusion. Similar, but smaller, defects are expected to affect the fracture in the present case. If the inclusion is formed by melting surface material over an embedded polishing grit, more defects are expected on the surface of the inclusion than on the highly polished plane surface. In addition, there is much more surface area, hence more probability of finding a defect, along the circumference of the inclusion at the angle θ_m than at the point $x = 0$.

Calculated laser pulse energies It for failure are very imprecise due to large uncertainties in the failure strength σ_f for the material in the vicinity of the inclusion and in the bulk absorption coefficient β_I of the inclusion material. The failure strength σ_f for sapphire is estimated to be between 6×10^4 psi, observed in bulk samples, and the theoretical strength $\sigma_{theor} = 6 \times 10^6$ psi estimated from $\sigma_{theor} = \frac{1}{10}E$, where E is the Young's modulus. Assuming $\sigma_f = 2P$ at the point of failure and using $\sigma_f = 6 \times 10^5$ psi, we estimate that failure occurs at approximately $It = 400\ J/cm^2$ accurate to only about two orders of magnitude. Pulse energies for damage observed by Boling et al [2] are well within the range of reasonable theoretical values.

For the 30-nsec pulse durations used in many experiments, the assumption of no heat transfer to the host material is not valid. It is reasonable to expect that heating has little effect on the failure strength and that the principal effect will be to lower the pressure at the inclusion-host interface, hence increase the required energy for damage, due to thermal expansion of the cavity in which the inclusion is contained. [7]

Apart from the time for the crack to propagate to the surface, with very short pulses $t < \tau_s$, damage could be delayed until the time τ_s after the laser pulse. This will occur if the initially formed isotropic stresses are insufficient to cause damage but the quasiequilibrium anisotropic stresses, established after the time τ_s for sound to make a round trip to the plane surface, are enhanced sufficiently to cause damage. Delayed surface damage on dielectric mirrors has been observed by Bliss et al, [8] but it is uncertain whether this is the result of crack propagation or stress enhancement.

3. Molecular-Ion Impurities

In this section we consider increases in the overall absorption coefficient due to molecular-ion impurities. This applies mostly to 10.6 μm wavelength cw systems, in contrast to the previous section which was concerned with fracture due to localized heating in pulsed systems. The increased absorption heats the windows and can result in either undesirable thermal defocusing of the beam or fracture of the window. [9]

Among the most promising materials for use with CO_2 lasers are the alkali halides, in particular KCl and KBr. The absorption coefficient as a function of frequency in a typical material is sketched in figure 4. At low frequency, the mechanism for absorption is the creation of phonons, with the fundamental Reststrahl peak

564-378 O - 74 - 16

occurring in the far infrared. It has been well established experimentally [10] and theoretically [11] that the intrinsic absorption coefficient decreases exponentially with increasing frequency in the multiphonon region.

In the ultraviolet, the mechanism for absorption is the excitation of an electron across the band gap to create an electron-hole pair. In the Urbach-tail region, β decreases exponentially with decreasing frequency. In between the two exponential regions, the absorption is thought to be dominated by impurities and imperfections. The absorption coefficient β in this region is represented by a wavy line in figure 4.

At the CO_2 laser frequency of 943 cm^{-1} (10.6 μm wavelength), the absorption for KCl and KBr samples is extrinsic, having $\beta > 10^{-4}\,cm^{-1}$. This is to be compared to the extrapolated intrinsic values of $8 \times 10^{-5}\,cm^{-1}$ for KCl and $5 \times 10^{-7}\,cm^{-1}$ for KBr.

Last year we showed that infrared absorbing inclusions dispersed throughout the crystals can contribute to the overall absorption. [1] In what follows, evidence will be presented showing that another important type of impurity limiting 10.6 μm wavelength transmission in the alkali halides is molecular-ion impurities that substitute for the halide ions in these materials.

As an example, the case of NO_2^- substituting for the Cl^- ion in KCl is drawn to scale in figure 5. [12] This ion fits loosely into the lattice and suffers little distortion. Consequently the internal vibrations of NO_2^- and other substitutional anions are only slightly affected by the presence of the host crystal. Frequency shifts of the molecular modes and splittings of degenerate modes are small. Infrared inactive modes may be weakly absorbing in the crystal.

Because of the small interaction with the host crystal, spectroscopists have used the technique of alkali-halide matrix isolation for a number of years to concentrate and isolate ions for convenient study using conventional absorption spectroscopy. A literature survey has been made of those ions that have been studied in KCl and KBr crystals. Those that most severely limit 10.6 μm transmission are presented below.

To estimate the absorption at the laser frequency of ν = 943 cm^{-1} due to an impurity mode at ν_0, a Lorentzian line shape

$$\beta(\nu) = (\text{const})\,\frac{\Delta\nu}{(\nu-\nu_0)^2 + (\Delta\nu/2)^2} \tag{3}$$

is assumed. In eq (3), $\Delta\nu$ is the full width at half maximum, which is assumed to be frequency independent. When available, measured line strengths and line widths were used for extrapolation to 943 cm^{-1}. Typically for a crystal with 0.1% impurity concentration, the absorption coefficient $\beta(\nu_0)$ at the center of an allowed transition ranges from 10^2 to $10^3\,cm^{-1}$, with $\Delta\nu$ ranging from 4 to 50 cm^{-1} depending on the particular molecular species and host.

Impurities that substitute for lattice ions can be grouped into a few general types. First, atomic impurities can either yield an infrared active local mode of the lattice, or can activate normally infrared inactive phonons. However, because the frequencies of these modes are generally small compared to 943 cm^{-1}, little absorption occurs at the CO_2 laser frequency. The U center at 500 cm^{-1} has the highest frequency of this group and we estimate that more than 10 ppm H^- is needed to produce $\beta(\nu = 943\ cm^{-1}) = 10^{-4}\,cm^{-1}$. [13]

Diatomic ionic impurities that have been studied in KCl and KBr crystals, on the other hand, have absorption frequencies that are too large to result in significant absorption at 943 cm^{-1} in spite of their large line widths. The hydroxyl ion (OH^-) with ν = 3640 cm^{-1}, is a member of this group. There has been concern regarding the hydroxyl ion because of the difficulty in removing this ion from alkali-halide crystals. [14] However, using $\Delta\nu$ = 50 cm^{-1} in eq. (3), we estimate that greater than 100 ppm of OH^- at isolated lattice sites is needed to yield

$\beta(943\ cm^{-1}) = 10^{-4}\ cm^{-1}$. [15] At high impurity concentrations, the OH^- may combine with other impurities to absorb more strongly at 943 cm^{-1}.

Polyatomic impurities have several infrared active modes, some of which may occur near 943 cm^{-1} and produce considerable CO_2 laser absorption. This group can be further subdivided into small and large ions. Small polyatomic ions such as NO_2^- fit loosely into the lattice and have large, temperature dependent line widths due to rotational and translational degrees of freedom. Larger ions such as HCO_3^- fit tightly into the lattice and have several narrow, temperature insensitive lines.

In addition to the above groups, polyvalent ions such as SO_4^{2-} can substitute for the singly charged halide ion. In order to preserve the charge neutrality of the crystal, these ions must be accompanied by a compensating vacancy or by a divalent cation impurity such as Mg^{2+}. The infrared spectrum and 943 cm^{-1} absorption is dependent on the particular compensating species.

Our literature survey indicates that 0.03 ppm of either NO_2^-, HCO_3^-, SO_4^{2-}, or CrO_4^{2-} will result in $\beta(\nu = 943\ cm^{-1}) = 10^{-4}\ cm^{-1}$. Calculated spectra using an assumed Lorentzian line shape along with experimental frequencies and line widths are shown in figures 6-8 for NO_2^-, HCO_3^-, and SO_4^{2-}. [16]

In each of the cases shown in these figures, the laser frequency, 943 cm^{-1}, falls at the edge of a small number of peaks representing the infrared active internal modes of the impurity. It would seem from looking at these figures that it would be easy to measure the spectrum of a crystal containing an unknown impurity and hence determine the impurity. However, there are two difficulties. First, the absorption coefficient at the peaks is only $10^{-2}\ cm^{-1}$ so that it would be difficult to make high resolution measurements using conventional spectroscopy. Second, and more important, there will be more than one impurity present in a real crystal so that the actual spectrum will look more like that of figure 4 than figures 6-8.

In figure 9 we represent a real crystal by adding the absorption coefficient in the previous three figures. The individual lines near 1200 cm^{-1} have merged to form a relatively featureless, broad peak. The only distinctive lines remaining are the two HCO_3^- lines at 840 cm^{-1} and 971 cm^{-1}. If in addition we decrease the amount of HCO_3^- and add different compensating divalent cations such as CO^{2+} along with a small amount of CrO_4^{2-}, even the calculated spectrum would appear featureless from 1000 to 1500 cm^{-1}.

The above examples serve to illustrate the importance of molecular-ion impurities on 10.6 μm transmission in alkali halides. A more complete survey of the ions that have been studied in KCl and KBr crystals will be published elsewhere. [17]

4. References

[1] C. J. Duthler and M. Sparks, Laser Induced Damage in Optical Materials, NBS Spec. Pub. 387, 208 (1973); J. Appl. Phys. 44, 3038 (1973); Appl. Phys. Lett. 24, 5 (1974).

[2] N. L. Boling, G. Dube', and M. D. Crisp, Laser Induced Damage in Optical Materials, NBS Spec. Pub. 387, 69 (1973); Appl. Phys. Lett. 23, 658 (1973).

[3] D. Milam, R. A. Bradbury, and M. Bass, Laser Induced Damage in Optical Materials, NBS Spec. Pub. 387, 124 (1973).

[4] For a review of shock wave induced fracture see H. Kolsky and D. Rader in Fracture, Vol. 1, edited by H. Liebowitz (Academic, New York, 1968).

[5] J. A. Fox and D. N. Barr, Appl. Phys. Lett. 22, 594 (1973).

[6] G. B. Jeffery, Phil. Trans. Roy. Soc. Lond. 221, 265 (1921).

[7] R. W. Hopper and D. R. Uhlmann, J. Appl. Phys. 41, 4023 (1970).

[8] E. S. Bliss, D. Milam, and R. A. Bradbury, Appl. Opt. 12, 677 (1973).

[9] M. Sparks, J. Appl. Phys. 42, 5029 (1971); M. Sparks and H. C. Chow, J. Appl. Phys. 45, 1510 (1974).

[10] T. F. Deutsch, J. Phys. Chem. Solids (to be published).

[11] M. Sparks and L. J. Sham, Phys. Rev. B 8, 3037 (1973) and references therein.

[12] A. R. Evans and D. B. Fitchen, Phys. Rev. B 2, 1074 (1970).

[13] A. A. Maradudin in Solid State Physics, edited by F. Seitz and D. Turnbull (Academic, New York, 1966), Vol. 18, p. 274 and Vol. 19, p. 1.

[14] R. C. Pastor and M. Braunstein, Hughes Research Laboratories Technical Report No. AFWL-TR-72-152, Vol. II (1973).

[15] B. Wedding and M. V. Klein, Phys. Rev. 177, 1274 (1969); M. V. Klein, B. Wedding, and M. A. Levine, Phys. Rev. 180, 902 (1969); D. F. Smith, J. Overend, J. C. Decius, and D. J. Gordon, J. Chem. Phys. 58, 1636 (1973).

[16] The data used for NO_2^- in KCl are obtained from V. Narayanamurti, W. D. Seward, and R. O. Pohl, Phys. Rev. 148, 481 (1966); V. P. Dem'yanenko and Yu. P. Tsyashchenko, Sov. Phys. - Solid State 11, 3043 (1970); R. Kato and J. Rolfe, J. Chem. Phys. 47, 1901 (1967); R. Bonn, R. Metselaar, and J. van der Elsken, J. Chem. Phys. 46, 1988 (1967); A. R. Evans and D. B. Fitchen, Phys. Rev. B 2, 1074 (1970). The HCO_3^- data from D. L. Burnitt, K. O. Hartman, and I. C. Hisatsune, J. Chem. Phys. 42, 3553 (1965). The SO_4^{2-} data from J. C. Decius, E. H. Coker, and G. L. Brenna, Spectrochim. Acta 19, 1281 (1963); E. H. Coker, J. C. Decius, and A. B. Scott, J. Chem. Phys. 35, 745 (1961); D. N. Mirlin and I. I. Reshina, Sov. Phys. - Solid State 10, 895 (1968).

[17] C. J. Duthler, J. Appl. Phys. (to be published).

5. Figures

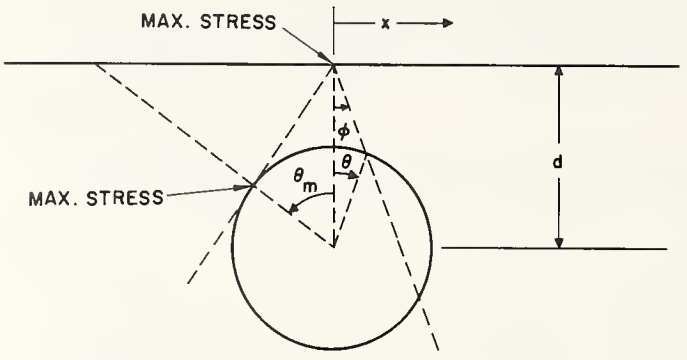

Figure 1. Sketch of an inclusion of radius a at a distance d below the host surface.

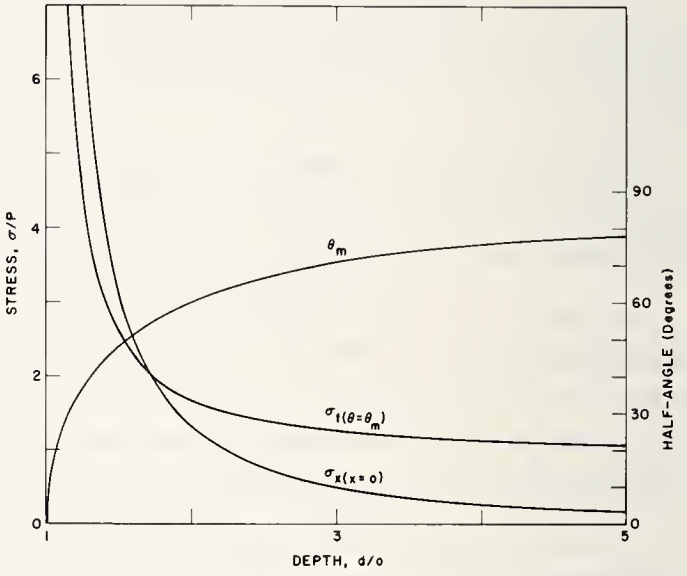

Figure 2. Tensile stresses and cone half angle as a function of inclusion depth.

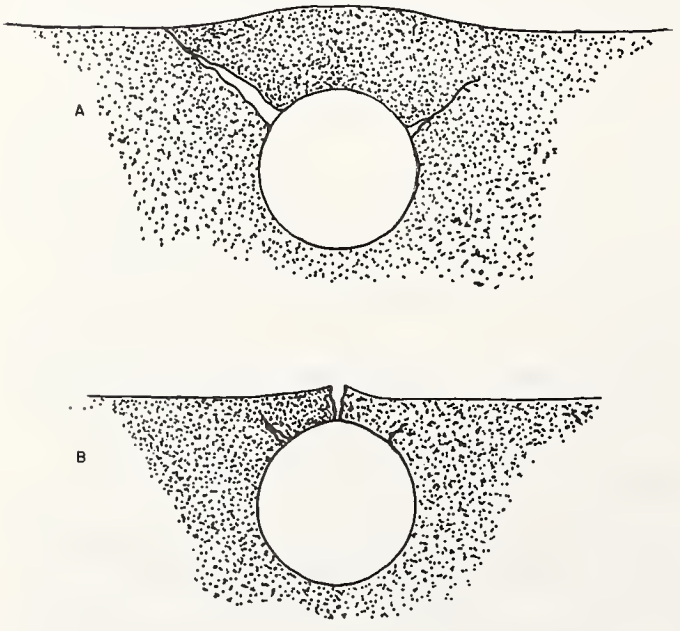

Figure 3. Cone-producing fracture for crack nucleation at inclusion surface (a) and at plane surface (b).

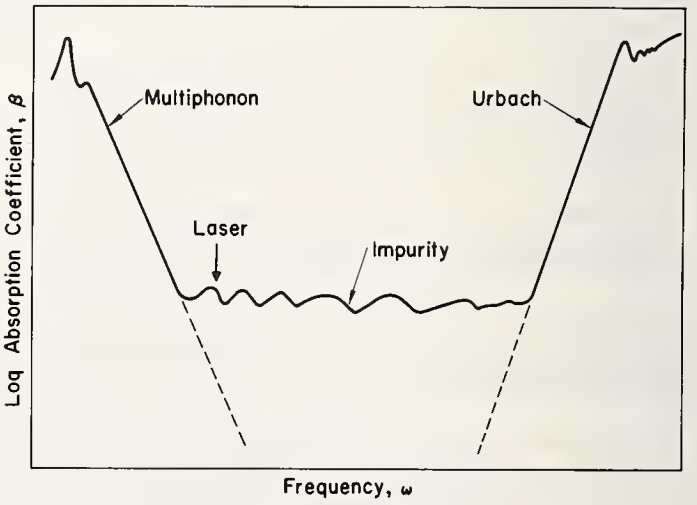

Figure 4. Semi-log plot of absorption in alkali halides as a function of frequency.

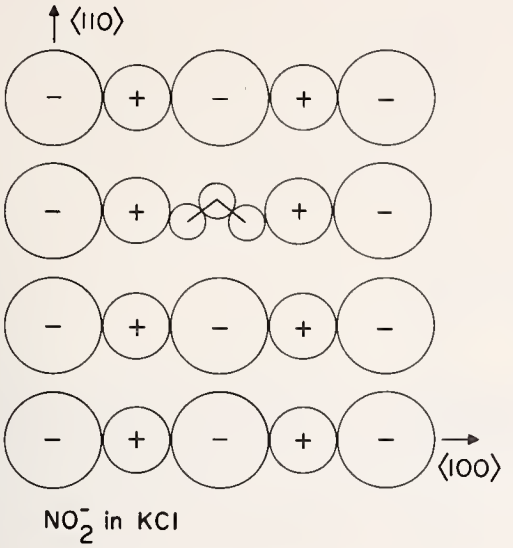

Figure 5. Orientation of NO_2^- impurity in KCl at low temperature.

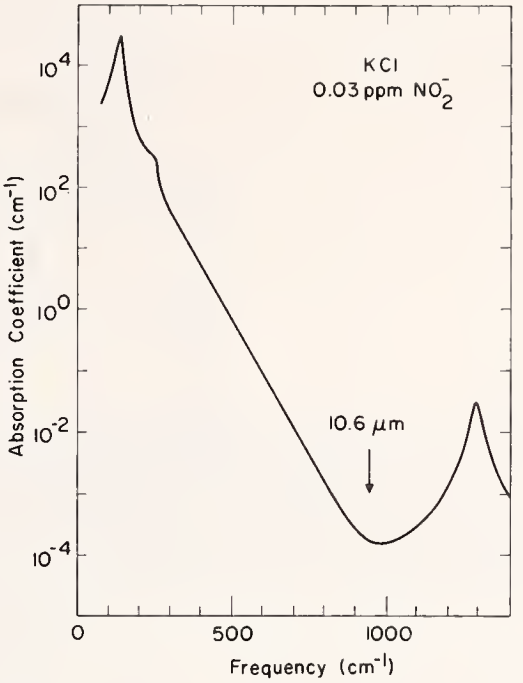

Figure 6. Calculated absorption coefficient of a KCl crystal containing 0.03 ppm NO_2^-.

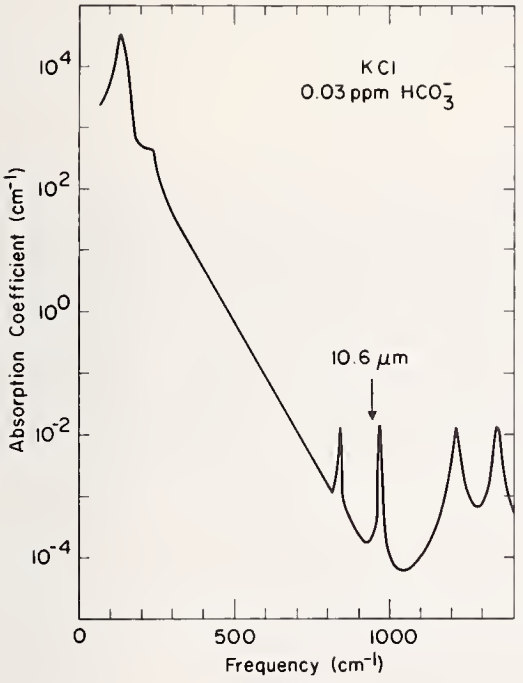

Figure 7. Calculated absorption coefficient of a KCl crystal containing 0.03 ppm HCO_3^-.

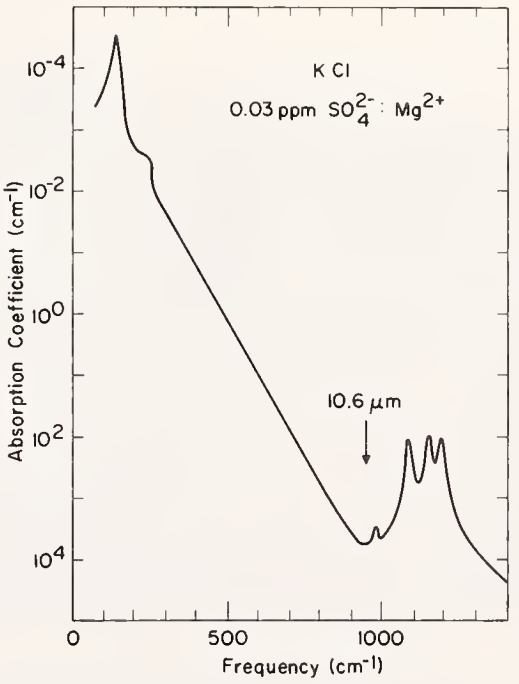

Figure 8. Calculated absorption coefficient of a KCl crystal containing 0.03 ppm SO_4^{2-}:Mg^{2+}.

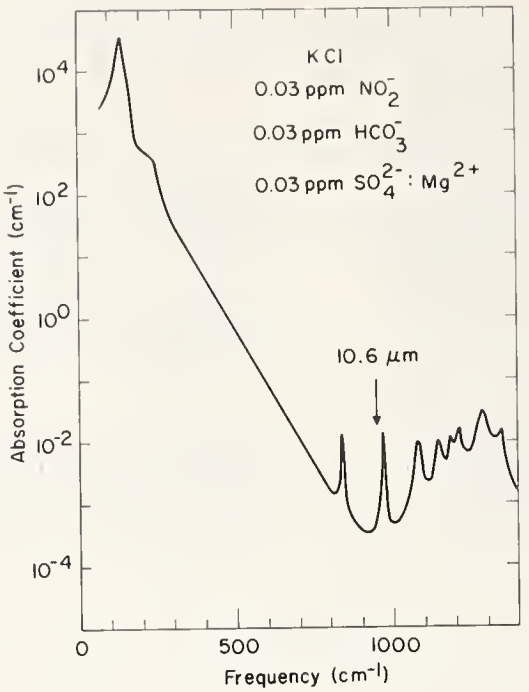

Figure 9. Calculated absorption coefficient of a KCl crystal containing a few impurities.

COMMENTS ON PAPER BY DUTHLER

Herbert Lipscomb, from Air Force Cambridge Research Laboratory, commented that his own recent work had shown that chlorate ions should be included as possible sources of absorption at 940 and 960 cm^{-1}. The speaker commented that the chlorate ion does not enter the lattice purely in a substitutional way, but represents instead, a local chemical change in the composition of the alkali halide. He had two comments to make on the work of Hopper and Uhlmann, reported at an earlier Damage Symposium. He commented that he felt that in their analysis of inclusions deep in the bulk of transparent materials, that Hopper and Uhlman did not use the correct absorption cross section. He further commented that when the inclusion lies near the surface the anisotropy in the stress must be considered, and the simple spherical geometry is no longer applicable. It was commented that crystalline material is not really accurately described by continuum elastic theory, but should be described in terms of the discrete lattice and that the positioning of an impurity with respect to the lattice could be of considerable importance in determining the effect of that impurity in the response of the material. The speaker commented that this was indeed the case, that he was in total agreement, but that to abandon continuum mechanics would introduce inordinate complexity in the calculation which was already only an order of magnitude estimate. David Milam, of Air Force Research Laboratory, noted in passing that in the case of extremely short pulses of picosecond duration, the first pulse, even though it may exceed the damage threshold of a reflecting surface, is still processed by that surface because it is reflected before the damage has time to occur.

APPENDIX I

MACHINING OF OPTICS WORKSHOP

AN INTRODUCTION TO THE MACHINING OF OPTICS

T. T. Saito
Air Force Weapons Lab
AFWL-LRE
Kirtland AFB, NM 87117

ABSTRACT

This paper will introduce machining of optics, presenting some of the history of machining progress, critical machining variables, material and geometrical capabilities and some new results on optical evaluation of machined surfaces. A most significant development is electroplating of materials which are otherwise not presently machineable. For example, molybdenum has been electroplated with silver or gold and then successfully diamond turned. Research and development ideas for future machining studies will be briefly discussed.

THE INFLUENCE OF TOOL FEED RATE ON THE MACHINABILITY OF CO_2 LASER OPTICS

J. B. Arnold
P. J. Steger
Oak Ridge Y-12 Plant
Oak Ridge, Tennessee
T. T. Saito
AFWL-LRE
Kirtland AFB, NM 87117

ABSTRACT

The influence of tool feed rate on reflectivity of diamond-machined surfaces was evaluated using materials (gold, silver, and copper) from which CO_2 laser optics are primarily produced. Fifteen specimens were machined by holding all machining parameters constant except tool feed rate, and allowing it to vary only by controlled amounts. Inspection results of the specimens indicated that tool feed rates significantly higher than 200 microinches per revolution produced detrimental effects on the machined surfaces. In some cases, at feed rates as high as 500 microinches per revolution, visible scoring was evident. Those surfaces produced with tool feed rates less than 200 microinches per revolution had little difference in reflectivity. Measurements indicated that their reflectivity existed in a range from 96.7 percent to 99.3 percent.

MIRROR MACHINING WITH CONVENTIONAL MACHINES

W. Ranbauske
Raytheon (Missile Systems Division)
Hartwell Road
Bedford MA 01730

ABSTRACT

A method is described for fabricating highly aspheric reflective optical elements using only conventional machines and fabrication processes. Employment of the method appears to be very practical for the fabrication of mirrors of apertures as large as 1.5 meters diameter for high energy lasers in the 3 to 10 micron wavelength region. Accuracies in curvature figuring for diffraction limited performance for a current system design and surface finish to better than one microinch have been achieved. The mirrors produced have as generatrices conical sections or straight lines, they are all metallic with a substrate of low thermal expansion, a hard upper surface, and a top layer of high reflectivity.

EFFECTS OF THE RESIDUAL SURFACE ROUGHNESS OF DIAMOND TURNED OPTICS

E. L. Church
J. Zavada
Frankford Arsenal
Philadelphia PA 19137

ABSTRACT

The residual roughness of diamond turned surfaces is expected to contain grating-like components. We explore the optical (infrared) properties of such components using Rice's perturbation theory for a statistically rough surface[1], by taking a roughness autocorrelation function of the form $z^2 \mathrm{Cos}(2\pi x/d)$; that is, a delta-function power spectrum corresponding to a surface wavelength d. The Rayleigh wavelengths $\lambda\pm=d(1\pm\mathrm{Sin}\theta)$ are critical parameters in describing such properties. For example, when $\lambda>\lambda+$, the surface has the reflectivity approaching that of a perfectly smooth surface, and when $\lambda<<\lambda-$, the reflectivity is that of the smooth surface reduced by the usual factor: $1 - (4\pi z\mathrm{Cos}\theta/\lambda)^2$. Here z is the rms vertical roughness, θ is the angle of incidence, and λ is the illuminating wavelength. When $\lambda\sim\lambda\pm$, additional interesting effects appear as functions of λ, θ, the groove direction, the polarization of the incident radiation, and the optical constants of the surface. The possibilities of observing these effects in reflectometry, ellipsometry, and scatterometry are considered as means for characterizing and evaluating surfaces of this type.

MEASUREMENT OF SURFACE FIGURE AND SURFACE FINISH AT THE Y-12 PLANT

R. E. Sladky
Union Carbide Y-12
Box Y
Oak Ridge, Tennessee 37830

ABSTRACT

The Y-12 Plant is expanding its optical inspection facilities to provide data for diamond knife machine tool development programs and for certification of the reflectors that have been produced. Measurements of reflectivity, diffraction pattern, and surface finish by FECO fringes will be made routinely in the near future. At present, surface finish is measured with double- and multiple-beam interferometers and Nomarski polarization. A comparison of results from various materials will be presented. The Foucault knife edge and Ronchi grating are used to evaluate surface figure.

APPLICATION OF ELECTROPLATING TO THE FABRICATION OF OPTICS

F. B. Waldrop
R. C. Waldrop
M. J. Bezik
W. E. Tewes
Oak Ridge Y-12 Plant
Oak Ridge, Tennessee

ABSTRACT

Copper, silver, and gold electroplates are sources of high-purity, flaw-free metal from which high-quality optical surfaces may be machined. The nature of the electrodeposit can be varied over wide limits, and this fact is demonstrated by using copper as an example. Superfinished metal surfaces can be replicated by electroforming as an alternate fabrication method.

ION POLISHING OF METAL SURFACES

R. A. Hoffman
W. J. Lange
W. J. Choyke
Westinghouse Electric Corporation
Research Laboratories
Pittsburgh, Pennsylvania 15235

ABSTRACT

An ion polishing apparatus that uses a focused beam of low energy Xe ions incident at a glancing angle is described. The sample to be polished is rotated and the beam scanned across the surface to produce uniform removal of material. Starting with single crystal copper which had been mechanically polished, and by using combinations of ion polishing and vacuum annealing the absorptivity, determined by calorimetry, was reduced from 0.92% to 0.76%. SEM pictures show that the surface features become smoother with ion polishing. A similar experiment was performed on a single crystal copper sample that had been electropolished, and the combination of ion polishing and annealing lowered the absorptivity from 0.97% to 0.89%.

ION MILLING FOR SURFACE FINISH IMPROVEMENT ON MACHINED METAL MIRRORS

J. Quella
Dow Chemical
Rocky Flats - Golden, Colorado 80401

ABSTRACT

An ion beam directed at a surface at a low angle of incidence removes a small amount of the surface material from the high points of the surface. Results of a preliminary study indicate that one microinch arithmetic average surface finishes can be improved 25 to 40 percent.

The process used by Commonwealth Scientific and the results of a preliminary study at Rocky Flats will be discussed on an informal basis.

EFFECTS OF POLISHING ON DIAMOND KNIFE MACHINED MIRRORS

R. L. Gordon
Battelle-Northwest Laboratories
Richland, WA

ABSTRACT

Work is in progress to determine effects of post machining treatment on diamond-knife machined copper mirrors prepared by Union Carbide Corporation, Nuclear Division, Y-12. Machined surfaces are in copper electrodeposited on oxygen-free copper substrates. Primary emphasis is placed on sample characterization both before and after different postmachining treatments. A relative scatterometer is used to estimate rms surface roughness and angular distribution of light scattered in the plane of incidence. The balance of the characterization includes interferometric observation of mirror figure, Nomarski microscopy for visualization of surface topography, and calorimetric absorption measurements at λ=10.6μm.

Results to date indicate that 1.52 in. diameter mirrors can be machined flat to within two fringes. At positions of minimum scattering, as-machined surfaces exhibit roughness near 27Å rms. Angular distribution of scattered light suggests that the as-machined surfaces approximate saw-tooth gratings with spacings near those predicted by machining parameters. Observation of diffraction maxima as a function of position on the sample indicate an increasing groove depth with increasing radius, with shallowest grooves lying near mirror center. These results are verified by SEM stereomicrographs. Scattering data further indicate a slight asymmetry in groove shape.

Absorption measurements on as-machined surfaces indicate the presence of non-negligible scattering at λ=10.6μm, and an optical absorption at that wavelength of about 0.9%. It has been demonstrated that a 9 minute polish in a slurry of colloidal carbon black reduces roughness from 27Å rms to less than 15Å rms. Some periodicity in the surface can still be detected after that duration of polishing. No increase in absorption due to final polishing of fine-grained deposits was observed.

Future work will determine effects of grinding with 1μ and 3μ diamond grits before final polishing on mirror scattering and absorption.

APPENDIX II

PARTICIPANTS

A

S. D. Allen	Hughes Research Labs., 3011 Malibu Canyon Rd., Malibu CA 90265
T. H. Allen	McDonnell Douglas Corp., P. O. Box 516, St. Louis MO 63166
L. J. Aplet	Hughes Aircraft Co., Centinela & Teale Sts., Culver City CA 90230
D. N. Aspinwall	Lockheed Research Labs., 3251 Hanover St., Palo Alto CA 94304
R. R. Austin	Perkin-Elmer Corp., Main Ave., Norwalk CT 06856

B

F. D. Baird	Lawrence Livermore Lab., P. O. Box 808, Livermore CA 94550
L. M. Ball	Optical Industries, Inc., 3006 Enterprise St., Costa Mesa CA 92626
W. P. Barnes, Jr.	Itek Corp., 10 Magire Rd., Lexington MA 02173
M. Bass	Center for Laser Studies, University of California, Los Angeles CA 90007
J. H. Bechtel	Gordon McKay Lab., Harvard University, Cambridge MA 02138
J. M. Bennett	Michelson Lab., Code 6018, Naval Weapons Centers,China Lake CA 93555
H. E. Bennett	Michelson Lab., Naval Weapons Center, China Lake, CA 93555
R. B. Bennett	Battelle-Columbus Labs., 505 King Ave., Columbus OH 43201
J. R. Bettis	Air Force Weapons Lab/DYX, Kirtland AFB NM 87117
E. Bliss	Laser Division, Lawrence Livermore Lab., P. O. Box 808, Livermore CA 94550
N. L. Boling	Owens-Illinois, 1700 N. Westwood, Toledo OH 43666
H. S. Boyne	Quantum Electronics Division, National Bureau of Standards, Boulder CO 80302
R. A. Bradbury	AF Cambridge Research Lab., Hanscom Field, Bedford MA 01730
A. Braunstein	Hughes Research Labs., 3011 Malibu Canyon Rd., Malibu CA 90265
M. Braunstein	Hughes Research Labs., 3011 Malibu Canyon Rd., Malibu CA 90265
N. J. Brown	Lawrence Livermore Lab., P. O. Box 808, Livermore CA 94550
J. A. Bruce	Air Force Cambridge Research Lab/LQO, Hanscom Field, Bedford MA 01730
W. F. Brunner	Lawrence Livermore Lab., P. O. Box 808, Livermore CA 94550
J. Bryan	Lawrence Livermore Lab/L-140, P. O. Box 808, Livermore CA 94550
D. L. Burdick	Code 6013, Naval Weapons Center, China Lake CA 93555

C

W. Caithness	Applied Optics Center, 10 B St., Burlington MA 01803
J. C. Camm	Avco-Everett Research Lab., 2385 Revere Beach Pkwy., Everett CA 02149
R. Carbone	L Division, Los Alamos Scientific Lab., Los Alamos NM 87544
G. E. Chamberlain	Quantum Electronics Division, National Bureau of Standards, Boulder CO 80302
P. W. Chan	Dept. of Elect. Engr., Colorado State University, Ft. Collins CO 80521
J. M. Cherlow	Physics Dept., University of Southern California, Los Angeles CA 90007
E. L. Church	L4100-150-2, U. S. Army - Frankford Arsenal, Philadelphia PA 19137
G. N. Cobham	Union Carbide Corp., P. O. Box Y, Y-12 Plant, Oak Ridge TN 37830
C. V. Collins	Air Force Cambridge Research Lab/LQO, Hanscom Field, Bedford MA 01730
J. J. Comer	Air Force Cambridge Research Lab., Hanscom Field, Bedford MA 01730
J. N. Cooper	Dept. of Physics, Naval Postgraduate School, Code 61CX, Monterey CA 93940
V. Costich	Coherent Radiation, 3210 Porter Drive, Palo Alto CA 94304

D

L. G. DeShazer	Center for Laser Studies, University of Southern California, Los Angeles CA 90007
J. A. Detrio	University of Dayton Research Institute, 300 College Park, Dayton OH 45469
T. M. Donovan	Code 6018, Naval Weapons Center, China Lake CA 93555
R. Doussain	Laboratoire National D'Essais, 1 Rue Gaston Noissier, 75 Paris 15°, France
C. J. Duthler	Xonics, Inc., 6837 Hayvenhurst Ave., Van Nuys CA 91406

E

J. M. Eastman	Optics Dept., Spectra Physics, 1250 W. Middlefield Rd., Mountain View CA 94042
S. J. Ekstrom	Lawrence Livermore Lab/L-214, P. O. Box 808, Livermore CA 94550
B. G. Enrique	Honeywell Research Center, 10701 Lyndale Ave. So., Bloomington MN 55420
W. S. Ewing	Air Force Cambridge Research Labs/LQO, Hanscom Field, Bedford MA 01730

F

A. Feldman	Materials A-259, National Bureau of Standards, Washington DC 20234
J. R. Fenter	Air Force Materials Lab/LPL, Wright-Patterson AFB OH 45433
C. W. Fountain	Code 5525, Naval Weapons Center, China Lake CA 93555
D. L. Frazen	Quantum Electronics Division, National Bureau of Standards, Boulder CO 80302

G

J. F. Giuliani	Code 5551, Naval Research Lab., 4555 Overlook Ave., Washington DC 20390
C. R. Giuliano	Hughes Research Labs., 3011 Malibu Canyon Rd., Malibu CA 90265
A. J. Glass	Lawrence Livermore Lab/L-215, P. O. Box 808, Livermore CA 94550
A. Glassman	Lawrence Livermore Lab/L-140, P. O. Box 808, Livermore CA 94550
A. Golubovic	Air Force Cambridge Research Lab., Hanscom Field, Bedford MA 01730
R. L. Gordon	Battelle-Northwest, P. O. Box 999, Richland WA 99352
A. H. Guenther	Air Force Weapons Lab., Kirtland AFB NM 87117

H

T. Harris	Raytheon Co./LADC, 4 Standish Circle, Andover MA 01810
G. A. Hayes	Code 5585, Naval Weapons Center, China Lake CA 93555
R. Hellwarth	Physics Dept., University of Southern California, Los Angeles CA 90007
R. A. Hoffman	R&D Center, Westinghouse Electric Corp., Beulah Rd., Pittsburgh PA 15235
S. J. Holmes	Laser Technology Labs., Northrop Corp., 3401 W. Broadway, Hawthorne CA 90250
R. A. House II	Air Force Weapons Lab/DYX, Kirtland AFB NM 87117
C. A. Huguley	Air Force Weapons Lab/LRE, Kirtland AFB NM 87117

I

J

E. G. Johnson	Quantum Electronics Division, National Bureau of Standards, Boulder CO 80302
G. T. Johnston	University of Dayton Research Institute, 300 College Park, Dayton OH 45469
F. W. Jones	Union Carbide Corp., P. O. Box Y, Oak Ridge TN 37830
T. Judd	Laser Optics, Inc., P. O. Box 3, Danbury, CT 06810

K

J. C. Kershenstein	Code 5503, Naval Research Lab., 4555 Overlook Ave., Washington DC 20375
J. M. Khan	Lawrence Livermore Lab., P. O. Box 808, Livermore CA 94550
C. Klein	Hughes Aircraft Co., Centinela & Teale Sts., Culver City CA 90230
A. Klugman	Dept. 630, Northrop Corp., 3401 W. Broadway, Hawthorne CA 90250
P. Kraatz	Research & Technical Center, Northrop Corp., 3401 W. Broadway, Hawthorne CA 90250
C. S. Krishnan	Materials Technology, TRW Systems, Space Park, Redondo Beach CA 90278
J. Kurdock	Perkin-Elmer Corp., 77 Danbury Rd., So. Wilton CT 06897
R. G. Kurtz	Dow Chemical Co., P. O. Box 888, Golden CO 80401

L

J. Lancelot	C.E.A. Limeil France, B. P. 27 Villeneuve, St. Georges 94, France
H. Lee	Owens-Illinois, 1035 N. Westwood Ave., Toledo OH 43666
G. W. Leppelmeier	Lawrence Livermore Lab., P. O. Box 808, Livermore CA 94550
K. M. Leung	Center for Laser Studies, University of Southern California, Los Angeles CA 90007
H. G. Lipson	Air Force Cambridge Research Lab/LQS, Hanscom Field, Bedford MA 01730
J. S. Loomis	Air Force Weapons Lab/LRE, Kirtland AFB NM 87117

M

D. MacGrath	Owens-Illinois, 1020 N. Westwood Ave., Toledo OH 43666
R. W. MacPherson	Electro-Optics Division, CRDV/DREW, P. O. Box 880, Courcelette, Quebec, Canada
T. J. Magee	Stanford Research Center, 333 Ravenswood, Menlo Park CA 94025
I. H. Malitson	A-251, National Bureau of Standards, Washington DC 20234
J. Marburger	University of Southern California, Los Angeles CA 90007
R. B. McGraw	MS 283, Research Dept., Perkin-Elmer Corp., Main Ave., Norwalk CT 06856
T. McJilton, Jr.	General Electric Co., Court Street Plant, Syracuse NY 13201
J. M. McMahon	Naval Research Lab., Washington DC 20390
D. Milam	Air Force Cambridge Research Lab., Hanscom Field, Bedford MA 01730
T. B. Milam	Pratt & Whitney Aircraft, West Palm Beach FL 33403
N. K. Moncur	KMS Fusion, Inc., P. O. Box 1567, Ann Arbor MI 48106
M. Monsler	Science Applications, Inc., 6 Preston Ct., Bedford MA 01730

N

B. E. Newnam	Los Alamos Scientific Lab/L-2, P. O. Box 1663, Los Alamos NM 87544

O

D. F. O'Brien	Air Force Materials Lab., Wright-Patterson AFB OH 45433
R. W. Ohlwiler	U. S. Air Force Systems Command Hdqs/DLSP, Andrews AFB MD 20334
W. Otaguro	MS 28, McDonnell Douglas, Huntington Beach CA 92708
A. Owyoung	Division 5214, Sandia Labs., P. O. Box 5800, Albuquerque NM 87111

P

R. J. Phelan, Jr.	Quantum Electronics Division, National Bureau of Standards, Boulder CO 80302
J. O. Porteus	Michelson Lab., Naval Weapons Center, China Lake CA 93555
H. Posen	Air Force Cambridge Research Lab/LQO, Hanscom Field, Bedford MA 01730
J. C. Potosky	Ion Physics Dept., Hughes Aircraft Co., 3011 Malibu Canyon Rd., Malibu CA 90265
R. F. Prater	Air Force Weapons Lab/LRE, Kirtland AFB NM 67117

Q

R

W. Rambauske	Missile Systems Division, Raytheon, Hartwell Rd., Bedford MA 01730
J. E. Rudisill	Hughes Research Labs., 3011 Malibu Canyon Rd., Malibu CA 90265
P. M. Rushworth	MP 276, Martin-Marietta Corp., P. O. Box 5837, Orlando FL 32808

S

T. T. Saito	Air Force Weapons Lab/LRE, Kirtland AFB NM 87117
R. J. Salmon	Dept. 52-21, Lockheed Missile & Space Co., 3251 Hanover St., Palo Alto CA 94304
S. R. Sheele	Hughes Aircraft Co., Centinela & Teale Sts., Culver City CA 90230
R. A. Shatas	Physical Sciences Lab., U. S. Army Missile Command, Redstone Arsenal AL 35809
C. Y. She	Physics Dept., Colorado State University, Ft. Collins CO 80521
J. L. Siemasz	U. S. Air Force Det 36, Hughes Aircraft Co., Centinela & Teale Sts., Culver City CA 90230
D. R. Sigler	Laser Energy, Inc., 320 N. Washington St., Rochester NY 14625
R. E. Sladky	Y-12 Plant, Union Carbide Corp., Oak Ridge TN 37830
D. M. Smith	RESD, General Electric Co., P. O. Box 8555, Philadelphia PA 19101
R. L. Smith	Quantum Electronics Division, National Bureau of Standards, Boulder CO 80302
T. H. Smith	Chemical Laser Technology, TRW Systems, 1 Space Park, Redondo Beach CA 90278
M. J. Soileau	Michelson Lab., Code 6018, Naval Weapons Center, China Lake CA 93555
W. J. Spawr	Spawr Optical Research, 130 N. Sherman Ave., Corona CA 91720
J. L. Stapp	Air Force Weapons Lab/LRE, Kirtland AFB NM 87117
E. Stark, Jr.	Los Alamos Scientific Lab., P. O. Box 1663, Los Alamos NM 87544
P. J. Steger	Nuclear Division, Union Carbide, Box Y, Oak Ridge TN 37830
C. M. Stickley	Materials Sciences Office, Dept. of Defense - ARPA, 1400 Wilson Blvd., Arlington VA 22209
D. L. Stierwalt	Code 2600, Naval Electronics Lab. Center, 271 Catalina Blvd., San Diego CA 92152
J. Stover	Dow Chemical Co., P. O. Box 888, Golden CO 80401
V. R. Stull	Tempo, General Electric Co., P. O. Box QQ, Santa Barbara CA 93102

T

U

V

K. Vedam	Pennsylvania State University, University Park PA 16802

W

F. B. Waldrop	Union Carbide, P. O. Box Y, Bldg. 9202, Oak Ridge TN 37830
V. Wang	Dept. 30-25, Hughes Research Corp., 3011 Malibu Canyon Rd., Malibu CA 90265
S. W. Warren	ITT Components Group Europe, Edinburgh Way, Harlow, Essex, England
R. Webb	Materials Research Center, Allied Chemical Corp., P. O. Box 1021-R, Morristown NJ 07960
E. D. West	Quantum Electronics Division, National Bureau of Standards, Boulder CO 80302
R. Wick	Air Force Weapons Lab/LRE, Kirtland AFB NM 87117
C. B. Willingham	Research Division, Raytheon Co., 28 Seyon St., Waltham MA 02154
R. Windebank	Laser Optics, Mill Plain Road, Danbury CT 06810
G. I. Wong	Bldg. R-1, TRW Systems Group, 1 Space Park, Redondo Beach CA 90278
S. M. Wong	Dow Chemical Co., P. O. Box 888, Golden CO 80401
R. A. Woodruff	Ball Brothers Research Corp., P. O. Box 1062, Boulder, CO 80302
D. L. Wright	Dept. of Electrical Engineering, Colorado State University, Ft. Collins CO 80521

X

Y

N. F. Yannoni	Air Force Cambridge Research Lab/LQS, Hanscom Field, Bedford MA 01730

Z

F. Zernike	Research Dept., Perkin-Elmer Corp., Norwalk CT 06856

U.S. DEPT. OF COMM. BIBLIOGRAPHIC DATA SHEET	1. PUBLICATION OR REPORT NO. Spec. Publ. 414	2. Gov't Accession No.	3. Recipient's Accession No.

4. TITLE AND SUBTITLE

Laser Induced Damage in Optical Materials: 1974

5. Publication Date: December 1974

6. Performing Organization Code

7. AUTHOR(S) Edited by Alexander J. Glass and Arthur H. Guenther

8. Performing Organ. Report No.

9. PERFORMING ORGANIZATION NAME AND ADDRESS

NATIONAL BUREAU OF STANDARDS
DEPARTMENT OF COMMERCE
WASHINGTON, D.C. 20234

10. Project/Task/Work Unit No. 2710900/2710569/2712585

11. Contract/Grant No.

12. Sponsoring Organization Name and Complete Address (Street, City, State, ZIP)

American Society for Testing & Materials, Phila., PA 19103
Dept. of the Navy, Office of Naval Research, Arlington, Va. 22217
Quantum Electronics Division, National Bureau of Standards, Boulder, CO 80302

13. Type of Report & Period Covered: Final

14. Sponsoring Agency Code

15. SUPPLEMENTARY NOTES

Library of Congress Catalog Card Number: 74-26935

16. ABSTRACT (A 200-word or less factual summary of most significant information. If document includes a significant bibliography or literature survey, mention it here.)

The Sixth ASTM-ONR-NBS Symposium on Laser Induced Damage in Optical Materials was held at the National Bureau of Standards in Boulder, Colorado on May 22-23, of this year. These Symposia are held as part of the activities in Subcommittee II on Lasers and Laser Materials, of the ASTM. Subcommittee II is charged with the responsibilities of formulating standards and test procedures for Laser materials, components, and devices. The Chairman of Subcommittee II is Haynes Lee, of Owens-Illinois, Inc. Co-chairmen for the Damage Symposia are Dr. Arthur Guenther, Chief Scientist of the Air Force Weapons Laboratory, and Dr. Alexander J. Glass, Head, Theoretical Studies, Y Division, Lawrence Livermore Laboratory.

Over 150 attendees at the Symposium heard 31 papers on topics relating to laser induced damage in crystalline and non-linear optical materials, at dielectric surfaces, and in thin film coatings as well as discussions of damage problems in the infrared region due both to cw and pulsed irradiation. In addition, several reports on the theoretical analysis of laser-materials interaction relative to the damage process were given, along with tabulations of fundamental materials properties of importance in evaluation of optical material response to high power laser radiation. Attention was given to high power laser system design considerations which relate to improved system performance and reliability when various damage mechanisms are operable in such systems.

(continued on reverse)

17. KEY WORDS (six to twelve entries; alphabetical order; capitalize only the first letter of the first key word unless a proper name; separated by semicolons)

IR windows and mirrors; laser damage; laser materials; self-focusing; thin films.

18. AVAILABILITY

[X] Unlimited

[ ] For Official Distribution. Do Not Release to NTIS

[X] Order From Sup. of Doc., U.S. Government Printing Office Washington, D.C. 20402, SD Cat. No. C13.10:414

[ ] Order From National Technical Information Service (NTIS) Springfield, Virginia 22151

19. SECURITY CLASS (THIS REPORT): UNCLASSIFIED

21. NO. OF PAGES: 256

20. SECURITY CLASS (THIS PAGE): UNCLASSIFIED

22. Price: $3.15

USCOMM-DC 29042-P74

Because of the growing importance and acceptance of machined components in high power laser systems, a workshop on the machining of optics was held, under the coordination of Captain T. T. Saito of the Air Force Weapons Laboratory. Nine papers on various facets of the topic were presented dealing with machining procedures, surface characterization of machined elements, coating of machined components, and the polishing and damage resistance of polished, coated, and bare metal reflectors. Abstracts on these papers are included in the Symposium Proceedings proper.

The proceedings of these Symposia represent the major sources of information in the field of laser induced damage in optical materials. The Symposia themselves, along with the periodic meetings of Subcommittee II, provide a unique forum for the exchange of information regarding laser materials specifications among the manufacturers and users of laser devices, components, and systems. The Symposia also serve as a mechanism of information gathering to enable the Subcommittee to write informed and realistic specifications.

NBS TECHNICAL PUBLICATIONS

PERIODICALS

JOURNAL OF RESEARCH reports National Bureau of Standards research and development in physics, mathematics, and chemistry. Comprehensive scientific papers give complete details of the work, including laboratory data, experimental procedures, and theoretical and mathematical analyses. Illustrated with photographs, drawings, and charts. Includes listings of other NBS papers as issued.

Published in two sections, available separately:

- **Physics and Chemistry (Section A)**

Papers of interest primarily to scientists working in these fields. This section covers a broad range of physical and chemical research, with major emphasis on standards of physical measurement, fundamental constants, and properties of matter. Issued six times a year. Annual subscription: Domestic, $17.00; Foreign, $21.25.

- **Mathematical Sciences (Section B)**

Studies and compilations designed mainly for the mathematician and theoretical physicist. Topics in mathematical statistics, theory of experiment design, numerical analysis, theoretical physics and chemistry, logical design and programming of computers and computer systems. Short numerical tables. Issued quarterly. Annual subscription: Domestic, $9.00; Foreign, $11.25.

DIMENSIONS/NBS (formerly Technical News Bulletin)—This monthly magazine is published to inform scientists, engineers, businessmen, industry, teachers, students, and consumers of the latest advances in science and technology, with primary emphasis on the work at NBS.

DIMENSIONS/NBS highlights and reviews such issues as energy research, fire protection, building technology, metric conversion, pollution abatement, health and safety, and consumer product performance. In addition, **DIMENSIONS/NBS** reports the results of Bureau programs in measurement standards and techniques, properties of matter and materials, engineering standards and services, instrumentation, and automatic data processing.

NONPERIODICALS

Monographs—Major contributions to the technical literature on various subjects related to the Bureau's scientific and technical activities.

Handbooks—Recommended codes of engineering and industrial practice (including safety codes) developed in cooperation with interested industries, professional organizations, and regulatory bodies.

Special Publications—Include proceedings of high-level national and international conferences sponsored by NBS, precision measurement and calibration volumes, NBS annual reports, and other special publications appropriate to this grouping such as wall charts and bibliographies.

Applied Mathematics Series—Mathematical tables, manuals, and studies of special interest to physicists, engineers, chemists, biologists, mathematicians, computer programmers, and others engaged in scientific and technical work.

National Standard Reference Data Series—Provides quantitative data on the physical and chemical properties of materials, compiled from the world's literature and critically evaluated. Developed under a world-wide program coordinated by NBS. Program under authority of National Standard Data Act (Public Law 90-396).

Building Science Series—Disseminates technical information developed at the Bureau on building materials, components, systems, and whole structures. The series presents research results, test methods, and performance criteria related to the structural and environmental functions and the durability and safety characteristics of building elements and systems.

Technical Notes—Studies or reports which are complete in themselves but restrictive in their treatment of a subject. Analogous to monographs but not so comprehensive in scope or definitive in treatment of the subject area. Often serve as a vehicle for final reports of work performed at NBS under the sponsorship of other government agencies.

Voluntary Product Standards—Developed under procedures published by the Department of Commerce in Part 10, Title 15, of the Code of Federal Regulations. The purpose of the standards is to establish nationally recognized requirements for products, and to provide all concerned interests with a basis for common understanding of the characteristics of the products. The National Bureau of Standards administers the Voluntary Product Standards program as a supplement to the activities of the private sector standardizing organizations.

Federal Information Processing Standards Publications (FIPS PUBS)—Publications in this series collectively constitute the Federal Information Processing Standards Register. The purpose of the Register is to serve as the official source of information in the Federal Government regarding standards issued by NBS pursuant to the Federal Property and Administrative Services Act of 1949 as amended, Public Law 89-306 (79 Stat. 1127), and as implemented by Executive Order 11717 (38 FR 12315, dated May 11, 1973) and Part 6 of Title 15 CFR (Code of Federal Regulations). FIPS PUBS will include approved Federal information processing standards information of general interest, and a complete index of relevant standards publications.

Consumer Information Series—Practical information, based on NBS research and experience, covering areas of interest to the consumer. Easily understandable language and illustrations provide useful background knowledge for shopping in today's technological marketplace.

NBS Interagency Reports—A special series of interim or final reports on work performed by NBS for outside sponsors (both government and non-government). In general, initial distribution is handled by the sponsor; public distribution is by the National Technical Information Service (Springfield, Va. 22151) in paper copy or microfiche form.

Order NBS publications (except Bibliographic Subscription Services) from: Superintendent of Documents, Government Printing Office, Washington, D.C. 20402.

BIBLIOGRAPHIC SUBSCRIPTION SERVICES

The following current-awareness and literature-survey bibliographies are issued periodically by the Bureau:

Cryogenic Data Center Current Awareness Service (Publications and Reports of Interest in Cryogenics). A literature survey issued weekly. Annual subscription: Domestic, $20.00; foreign, $25.00.

Liquefied Natural Gas. A literature survey issued quarterly. Annual subscription: $20.00.

Superconducting Devices and Materials. A literature survey issued quarterly. Annual subscription: $20.00. Send subscription orders and remittances for the preceding bibliographic services to the U.S. Department of Commerce, National Technical Information Service, Springfield, Va. 22151.

Electromagnetic Metrology Current Awareness Service (Abstracts of Selected Articles on Measurement Techniques and Standards of Electromagnetic Quantities from D-C to Millimeter-Wave Frequencies). Issued monthly. Annual subscription: $100.00 (Special rates for multi-subscriptions). Send subscription order and remittance to the Electromagnetic Metrology Information Center, Electromagnetics Division, National Bureau of Standards, Boulder, Colo. 80302.

U.S. DEPARTMENT OF COMMERCE
National Bureau of Standards
Washington, D.C. 20234

OFFICIAL BUSINESS

Penalty for Private Use, $300

POSTAGE AND FEES PAID
U.S. DEPARTMENT OF COMMERCE
COM-215

U.S.MAIL